Buckling of Thin-Walled Cylindrical & Conical Metal Tanks: Analysis, Test Evaluation & Design

Dissertation by

Medhanye B. TEKLEAB, M.Sc.

submitted to

Faculty of Civil Engineering Sciences

Graz University of Technology

Reviewed by

Werner GUGGENBERGER, Ao.Univ.-Prof. Dr.techn.

Institute for Steel & Shell Structures, Graz University of Technology

and

Ali LIMAM, Prof. Dr.

URGC-Structures, Department of Civil Engineering, INSA Lyon, France

Graz, December 2009

Acknowledgements

My heart-felt thanks will go to my supervisor Ao.Univ.-Prof. Dipl.-Ing. Dr.techn. Werner Guggenberger for his tireless, patience full, very close, smart and critical way of advising and the many important discussions we had during the course of my study. I really am in shortage of words to express my appreciation to him. I thank Prof. Ali Limam for reviewing my work who also is my external examiner. I would like to thank Univ.-Prof. Dipl.-Ing. Dr.techn. Richard Greiner, head of the Institute for Steel and Shell Structures at Graz University of Technology, for his valuable comments, encouragement and kind treatment. I am grateful to the institute and its nice hard working people for the resource-full and very good working environment I had during my stay. I specially thank Dipl.-Ing. Burkhard Krenn who has been a good friend to me and who helped me a lot in all administrative matters both in and off the university starting from the very first day I arrived in Graz.

My special thanks will also go to Gent University, Belgium, and specially to Prof. Guy Lagae and Dr. Wesley Vanlaere for providing me with a complete data and necessary explanations on the laboratory tests made at Gent University over 30 years ago.

This work wouldn't be true with out the financial support I was granted from the Austrian Academic Exchange Service through the North-South Dialogue scholarship for which I am grateful and would like to express my gratitude to all its staff members. I thank the Afro-Asian Institute in Graz and its staff members for the support I had with regard to housing matters. I thank Mekelle University, Ethiopia, the young yet vibrant university, of which I am an employee since nine years, for offering me a study leave even though there was shortage of lecturers with an increase in the number of incoming students.

Last but not least, I would like to acknowledge my father Biedebrhan Tekleab and my mother Me'aza Baraki for their unending true love, encouragement and moral assistance they showed me all the way in life.

Medhanye B. Tekleab

Abstract

This work re-searches the stability of cylindrical and conical thin-walled tank shells from the basic level in view of both analysis and previous test results. Detailed discussions on failure modes, numerical simulations and re-investigation of test results have been made. The axisymmetric elastic-plastic buckling phenomena, buckling modes and strengths of meridionally compressed and internally pressurized perfect and imperfect cylindrical and conical shells have been investigated in detail. The effects of imperfection wavelength, location along the meridian, orientation, and amplitude of sinusoidal & local imperfections have been thoroughly studied. The worst possible combined effect of an edge restraint and an imperfection in destabilizing such shells has also been discussed. All results are represented and interpreted in such a way that they can easily be understood and used for design purposes. Simplified expressions are obtained for the prediction of axisymmetric elastic-plastic buckling strength of general thin-walled cylindrical and conical shells under the mentioned loading situations. Design recommendations have been proposed. Comparisons with and critical review of few previous research works have as well been thoroughly carried out.

Detailed investigation of the numerous Gent laboratory test results (obtained about 30 years ago at the Laboratory of Model Testing at Gent University, Belgium) on liquid-filled conical shells, shortly called LFC, that have been made in response to a structural disaster in Belgium along with detailed discussions, explanations, and conclusions have been done. Previous LFC-related research works on nonlinear simulation of liquid-filled conical shells with and without geometric imperfections have as well been discussed and few cases have been re-examined for confirmation and further studying purposes. Relevant explanations and conclusions have been given to the outcomes of those works. Moreover, the Belgium (1972) and Canada (1990) steel water tower failure cases have been carefully examined to check and compare their elastic buckling strengths with the applied loads during failure; and to check for any possible roles played by plasticity effects during the collapse. Previous research works related to the collapse of the water towers have also been discussed. The notion of a “corresponding cylinder” of a liquid-filled conical shell has been introduced which behaves in exactly the same way as the LFC. Detailed and comprehensive investigation of this “corresponding cylinder” was then made with the simple outcome that the liquid-filled cone behaves like a “wet cylinder”, i.e. with respect to its axisymmetric deformation and buckling behavior.

Contents

Notation

Cylindrical shells:

R	radius
t	shell wall thickness
R/t	shell slenderness ratio
L	meridional length of the shell
x	running length parameter starting from bottom of shell, in axial direction
s	arc length in meridian direction
ξ	normalized meridional length parameter
X	meridional direction
θ	circumferential direction
r	running radius of shell middle surface, perpendicular to the axis of rotation
R_{10}	radius of curvature in meridional direction, located on the shell normal
R_{20}	radius of curvature in circumferential direction, located on the shell normal
U	meridional deformation
W	radial deformation
β_X	meridional rotation
σ_x	meridional normal membrane stress
σ_θ	circumferential normal membrane stress
N_x	meridional normal section force
N_θ	circumferential normal section force
Q_x	transverse shear section force
M_x	meridional bending section moment
M_θ	circumferential bending section moment
n_x	normalized meridional section force (= N_x/N_{pl})
n_θ	normalized circumferential section force (= N_θ/N_{pl})

m_x	normalized meridional section moment (= M_x/M_{pl})
m_θ	normalized circumferential section moment (= M_θ/M_{pl})
N_1	principal normal section force in “1”-direction
N_2	principal normal section force in “2”-direction
M_1	principal section moment in “1”-direction
M_2	principal section moment in “2”-direction
n_1	normalized principal section force in “1”-direction (= N_1/N_{pl})
n_2	normalized principal section force in “2”-direction (= N_2/N_{pl})
m_1	normalized principal section moment in “1”-direction (= M_1/M_{pl})
m_2	normalized principal section moment in “2”-direction (= M_2/M_{pl})
E	modulus of elasticity
f_y	yield strength
ν	Poisson’s ratio
G	shear modulus
p	internal pressure
$\sigma_{x,1}$	meridional normal membrane stress at bottom support
$\sigma_{\theta,1}$	circumferential normal membrane stress at bottom support
$\sigma_{x,Rcr}$	elastic critical buckling stress of an axially compressed cylinder (0.605 Et/R)

Conical shells:

h’	height of liquid surface level above base level ’1’
h	height of cone above base level ’1’
L	meridional length of the cone
r	running radius of cone middle surface, perpendicular to the axis of rotation
r_1	small radius at the base of the cone
r_2	large radius at the upper end of cone
r'_2	large radius at the liquid surface level
t	wall thickness of the conical shell
β	apex half angle of the cone
γ'	specific weight of the liquid filling
z	running height parameter above the base level ’1’
ζ	running geometry parameter, $(z.\tan\beta/r_1)$
ζ'	geometry parameter, $(h'.\tan\beta/r_1)$
ρ	running nondimensional coordinate parameter, (r/r_1)
ρ'	nondimensional coordinate parameter at the liquid surface level, (r'_2/r_1)
$\sigma_{x,1}$	meridional normal membrane stress at the cone support
$\sigma_{\theta,1}$	circumferential normal membrane stress at the cone support
$\sigma_{x,Rcr}$	elastic critical buckling stress of an axially compressed conical shell $(0.605.Et\cos\beta/r_1)$
$\overline{p}$	internal pressure parameter $(\sigma_{\theta,1}/\sigma_{x,Rcr})$
$\overline{\psi}$	ratio of meridonal to circumferential membrane stress at the cone support
R	radius of an equivalent cone at cone-base $(r_1/\cos\beta)$
p	pressure at cone-base $(\gamma'h')$

General & EN 1993-1-6:

$\overline{p}$	critical-stress-related internal pressure parameter (= $\sigma_{\theta,1}/\sigma_{x,Rcr}$)
μ	yield-related internal pressure parameter (= $\sigma_{\theta,1}/f_y$)
$\overline{\psi}$	ratio of meridional to circumferential membrane stress at the bottom support
α_x	unpressurized elastic imperfection reduction factor of EN 1993-1-6, Annex-D
α_{xpe}	pressurized elastic imperfection reduction factor of EN 1993-1-6, Annex-D
α_{xpp}	pressurized plastic imperfection reduction factor
FEM	finite element method using ABAQUS Version 6.7-1 (2007)
LA	Linear Analysis
LB	Linear Buckling
LBA	Linear Buckling Analysis
MNL	Materially Nonlinear
MNA	Material Nonlinear Analysis
GMNL	Geometrically and Materially Nonlinear
GMNA	Geometrically and Materially Nonlinear Analysis
GMNLI	Geometrically and Materially Nonlinear with Imperfections
GMNIA	Geometrically and Materially Nonlinear Analysis with Imperfections
l_b	Buckle length
L_{eff}	effective length
A_{eff}	effective area
σ_{cr}	elastic buckling stress
σ_k	characteristic buckling stress
$\overline{\lambda}$	relative buckling slenderness parameter
$\overline{\lambda}_o$	relative buckling slenderness parameter
$\overline{\lambda}_p$	relative buckling slenderness parameter
χ	buckling reduction factor
β	plastic range factor
η	elastic-plastic buckling interaction exponent

1

Introduction and state-of-the-art

1.1 Motivation

Cylindrical and conical shells have a wide range of applications in engineering, in general, and in structural engineering, in particular. To mention some, these shells are used as pressure vessels, pipes, tanks, silos, roof structures. In many of these practical engineering applications, cylindrical and conical shells are subjected to axisymmetric type of loading such as gravity (self-weight, snow), hydrostatic pressure, internal or external gas pressure. More specifically pipes, tanks and silo structures are mainly subjected to the simultaneous effects of meridional compression and internal pressurization coming from the contained material. Such types of loading cause bi-axial stress state: meridional membrane compression and circumferential (hoop) membrane tension.

The appropriate functioning of such structures requires a proper design that takes all possible failure conditions in to account. One of such possible and most dominant failure conditions for thin shells is failure by buckling (stability considerations). There have been buckling failure cases of civil engineering thin-walled metal cylindrical and conical shells under axial compressive loads with co-existent internal pressure. Many of the buckling failures in cylindrical shells happened forming outward bulges near the supported edge (elephant's-foot buckling phenomenon) resulting from earthquake induced effects. Figure 1.1 to Figure 1.4 show pictures of few of such failure cases.

The elephant's-foot type buckling phenomenon may generally occur in cylindrical and conical shells so long as they are subjected to meridional compression and circumferential tension near the boundary. More specifically, axisymmetric elastic-plastic buckling near a boundary may happen in thin-walled cylindrical and conical shells with constant/varying meridional compression and hydrostatic internal pressure. Since a liquid-filled conical shell falls into such a loading category, an axisymmetric elastic-plastic buckling near the boundary is possible and hence the buckling strength of conical shells associated to an elephant's-foot buckling phenomenon needs to be investigated in detail. Besides, there have been buckling failure cases of conical shells as in the cases of the Belgium water tower in 1972 and Canada water tower in 1991 for which the real causes need to be invetigated.

There, as well, have been a lot of research attempts, both theoretically and experimentally, to determine the exact buckling capacity of cylindrical and conical shells under axial compressive loads with co-existent internal pressure. Despite the number of research attempts so far, their prediction of the buckling strengths do have serious insupportable problems.

This work will mainly address the axisymmetric elastic-plastic buckling strength of isotropic unstiffened cylindrical and conical shells and re-investigates the numerous experimental results performed in Gent on the elastic and elastic-plastic buckling of conical shells.

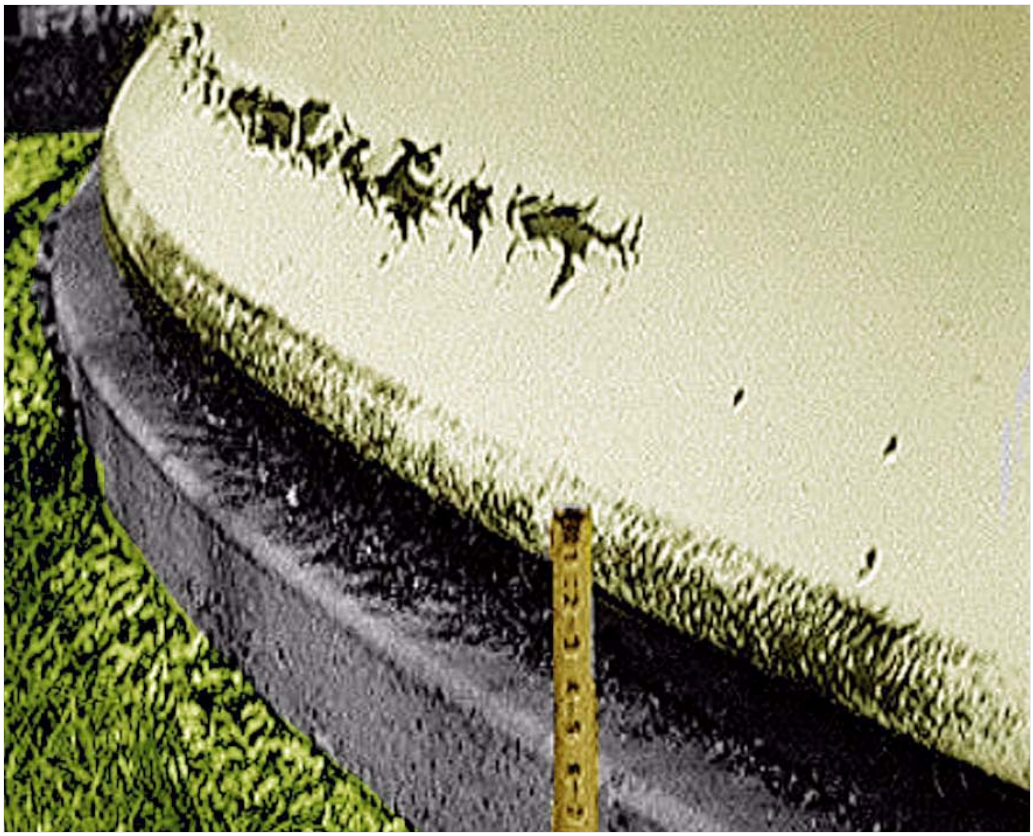

Figure 1.1 Elephant's foot buckling (JM Rotter)

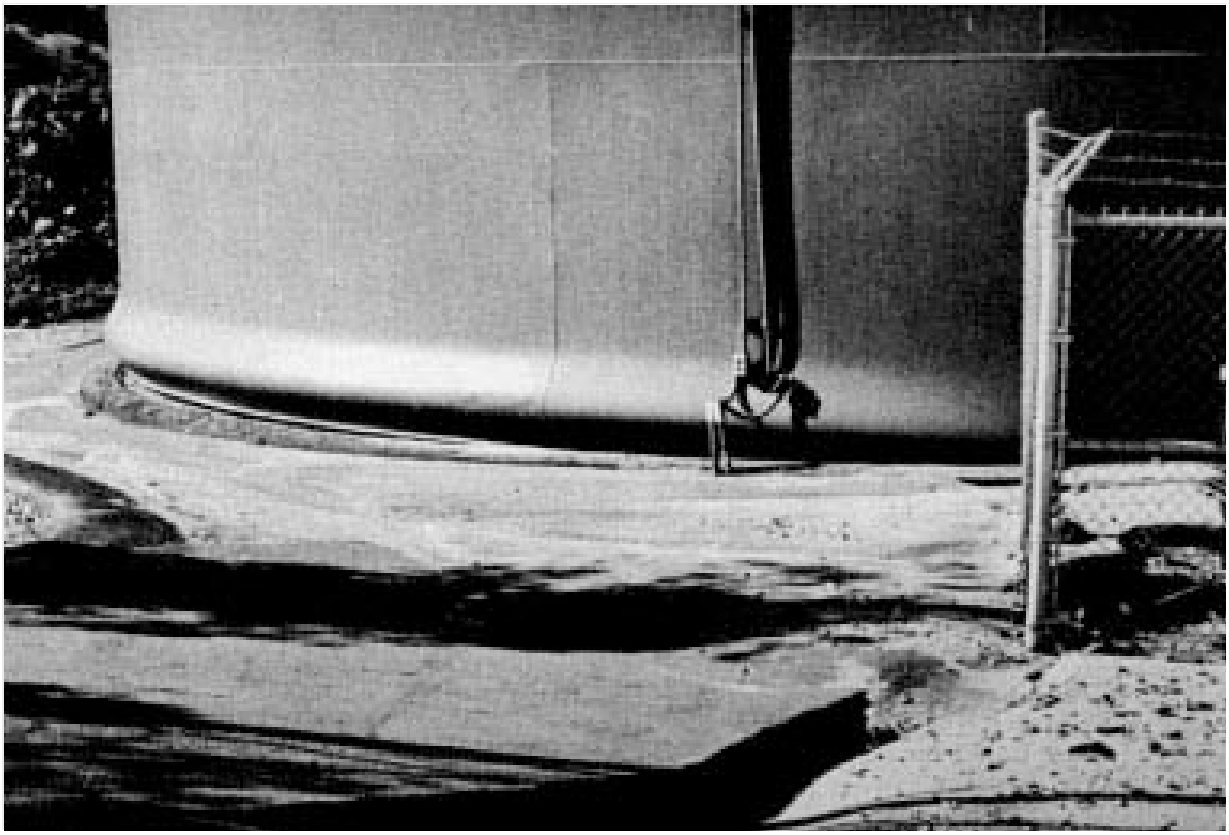

Figure 1.2 Elephant's foot buckling (JM Rotter)

Figure 1.3 Elephant's foot buckling (Gould)

Figure 1.4 Elephant's foot buckling above a column support (Guggenberger)

1.2 Overview

The general behaviour of cylindrical & conical shells under meridional compression and circumferential tension will be analyzed using analytical and numerical linear analysis techniques from which the pure membrane and edge-bending effects can be separately seen. These effects will later be used in reasoning out special buckling phenomenon. The results will be compared with a finite element linear analysis results for verification purposes. The small displacement linear buckling strengths of these shell types will then be computed approximately and investigated numerically. This strength will later be used as a reference to express other buckling strengths according to the frame work of EN 1993-1-6.

The effects of imperfections on the elastic buckling strength of thin-walled cylindrical and conical shells will be discussed in detail for different fabrication quality classes as recommended in EN 1993-1-6 and comparisons between the cylinder and cone will be made. Explanations will be given about the LFC-specific buckling phenomenon and corresponding strengths. Simplified expressions for the prediction of linear buckling strengths of liquid-filled general cones with pinned and fixed bottom boundary conditions will be obtained. In doing so, the numerous laboratory experiments made on liquid-filled conical shells will be re-examined. Comparisons of the perfect and imperfect linear buckling strengths of cylindrical and conical shells will be made.

Nonlinear buckling and plastic strengths of cylindrical and conical shells will be computed approximately using analytical models with second order effects included and numerically using a finite element package (ABAQUS). The pure plastic limit strengths of the shells will be computed approximately using von Mises membrane yield criterion taking the membrane stresses at the shell-base as references; and using stress resultant oriented approximate yield criteria. The effects of material nonlinearity, geometric nonlinearity and imperfections will be numerically investigated. Comparisons of the results obtained using the analytical model and numerical analysis will be made. Detailed comments and explanations on the results will be given.

The numerical simulation results will be used to derive a set of basic data that can be used in a straight forward buckling design by hand calculations in-line with the underlying structure of the European standard EN1993-1.6. Design recommendations will finally be proposed which will be compared with previous research results and code recommendations. Additional comments and explanations concerning the results will also be included.

Detailed investigation of Gent mercury test results along with detailed discussions, explanations, and conclusions will be done. Previous LFC-related research works on nonlinear simulation of liquid-filled conical shells with/out geometric imperfections will as well be discussed and few cases will be re-examined for confirmation and further studying purposes. Relevant explanations

and conclusions will be given to the outcomes of those works.

Moreover, the Belgium and Canada steel water tower failure cases will be re-examined to check for any possible roles played by plasticity effects during the collapse. Previous research works related to the collapse of the water towers will also be discussed.

A “corresponding” cylinder of a liquid-filled conical shell will be introduced which behaves in exactly the same way as the LFC. Detailed invetigation of the “corresponding” cylinder will then be made which will turn out to be that the liquid-filled cone is nothing but a “wet-cylinder”.

1.3 State-of-the-art

Many shell stability related research works have been done so far. The results of such research works have been included in design standards. The latest design standard which is believed to include many of the research results is discussed below. For this reason, in the discussions of the current study, references to and comparisons with this standard will be made.

In the buckling strength assessment of thin-walled general metal shells-of-revolution, the European Standard EN1993-1-6 recommends to use three different approaches (methods) which apply to all geometries, all loading conditions, and all material conditions. The hierarchy of these general buckling design procedures are summarized as follows:

method-1: buckling stress design or LA-based buckling design approach

method-2: LBA/MNA-based buckling design approach using simplified global numerical analysis

method-3: GMNIA-based buckling design approach using advanced global numerical analysis

The **buckling stress design approach** is based on a membrane theory or linear bending theory analysis. The elastic critical buckling stress is computed/estimated based on linear analysis. Thus, buckling stress design is usually performed by "hand calculation" using formulas and/or diagrams prepared for this purpose. In this method, the linear elastic stress field (meridional, circumferential, and shear) are computed at every point of the midsurface of the shell. The elastic critical buckling stresses of the perfect shell for each stress component are then determined on which imperfection reduction factors are applied to obtain the elastic buckling stresses of the imperfect shell. Using the elastic critical buckling stresses of the perfect shell and the uni-axial yield stress of the material, relative buckling slenderness parameters are computed for each stress component upon which the buckling strength reduction factors depend. These buckling strength reduction factors which account for plasticity effects are then each applied to the uni-axial yield stress to obtain the respective characteristic buckling stresses. Interaction formulas are used to account for any possible interaction between the effects of the different stress components. The design value of the buckling stress components are then computed by applying partial safety factors on the characteristic strengths.

Buckling strength assessment using design by **global numerical LBA/MNA procedure**, according to EN1993-1-6, is also a reduction factor approach. The steps involved in the LBA/ MNA procedure to predict the buckling strength of the shell have a similar format to those of the buckling stress design aproach. In the LBA/MNA approach, however, the elastic critical buckling stress and plastic collapse strength are evaluated accurately using the more rigorous global numerical analysis methods.

The **GMNIA procedure**, on the other hand, uses advanced global (geometrically and materially nonlinear) numerical analysis with the consideration of possible imperfections to accurately simulate the buckling strength of real shells and to directly obtain the characteristic elastic-plastic buckling strength of a practical shell.

2

Problem statement, goal & scope of the work

2.1 Problem statement

It has been repeatedly reported in many literatures that thin-walled cylindrical shells usually buckle elastically under pure axial compression. The respective buckling strength for such axially loaded cylindrical shells is usually lower than the theoretical elastic critical stress, the difference accounting for the decrease in buckling strength caused by the presence of various imperfections and geometric nonlinearity. The presence of an accompanying internal pressure, however, reduces this strength-weakening effect of the imperfections there by increasing the buckling strength of the shell. However, when the intensity of the internal pressure exceeds a certain value, the circumferential membrane stress becomes significant causing bi-axiality effect to come into play.

An unpressurized cylindrical shell under pure axial compressive load tends to radially expand due to Poisson's effect. An internally pressurized cylindrical shell under axial compressive load tends to radially expand due to the combined effects of both the internal pressurization and Poisson's effect. The presence of boundary conditions, however, constricts this expansion causing local bending under the action of the axial compressive load. Similar local bending effects may occur at locations of change in wall thicklness, ring stiffeners, or local axisymmetric imperfections causing immature buckling under a small meridional compression. Thus, the presence of significant internal pressure will have a destabilizing effect there by reducing the buckling strength of the shell. Such a buckling type, caused by local bending adjacent to the boundary, is termed as an "elephant's-foot" type buckling and the corresponding strength as elephant-foot buckling strength. Moreover, when combined with ill-natured axisymmetric imperfections, the weakening effect of the significant internal pressure along with the edge constriction effect, will be more pronounced that the cylinder buckles at a very low axial compressive load.

However, a question which still remains unanswered in many of the researches and studies done so far is the physically possible critical (worst) imperfection shape, wavelength, amplitude, orientation, and location along the meridian, each of which has an influence on the buckling behavior and buckling strength of the shell.

On the other hand, the meridional membrane section force distribution in liquid-filled conical shells is maximum at the lower supported edge and decreases nonlinearly and rapidly up the meridian. Such a distribution of the meridional compressive section force superimposed with the edge constriction effects of the bottom boundary conditions will restrict the elastic-plastic buckling phenomenon to a region very close to the supported lower edge causing elephant's-foot type buckling. Despite this fact, not much has been done to investigate the possible elephant's-foot buckling strength of conical shells. Such type of buckling in liquid-filled conical shells, may specially happen when there exist a global bending effect which may result, say, from geometric eccentricity (global tilting) of the cone. This geometric eccentricity, even upon filling may result in global

bending effect which shortens the life span of the structure with the formation of a possible elephant's-foot type buckling phenomenon. Apart from this, a perfect liquid-filled conical shell may buckle in such an axisymmetric elastic-plastic buckling mode near the supported edge so long as a bi-axial state of stress, similar to that of the cylindrical shell, exists.

2.2 Goal of the work

The true nature of buckling in real-world thin-walled shell structures is at most simulated, at least numerically, by analysis models that take the effect of geometric and material nonlinearity into account. For this reason, it is believed and has been applied in the buckling strength determination of thin-walled shells that the geometrically and materially nonlinear finite element analysis (GMNA) with physically possible imperfections (GMNIA) predicts closer results to the buckling strength of real-world thin-walled shells.

It is, therefore, the ultimate goal of this work to numerically simulate cylindrical and conical shell axisymmetric buckling and finally come up with a set of basic data that can be used in a straight forward buckling design by hand calculations. This work also aims to investigate the effects of axisymmetric imperfection shapes on the elastic-plastic buckling strengths of axisymmetric shells and finally recommend a physically possible worst axisymmetric local imperfection.

It is also the goal of this study to re-investigate the numerous laboratory tests performed in Gent using liquid-filled conical shells and propose a recommendation for future works and design purposes.

A comparison of the results with the previous research works and existing design recommendation, EN1993-1-6, will then be made.

2.3 Solution methods

In the course of investigating the axisymmetric elastic-plastic buckling phenomena and corresponding buckling strengths of thin-walled cylindrical and conical shells, a combination of both analytical and numerical (using finite element program) analysis methods will be used to assess the applied loads, depending on the nature and complexity of the problem type under consideration. For this reason, the mentioned shells will be analysed using membrane theory, linear shell bending theory (LA), linear buckling analysis (LBA), small displacement materially nonlinear analysis (MNA), perfect geometrically and materially nonlinear analysis (GMNA), and geometrically and materially nonlinear analysis with imperfections (GMNIA).

In all the analyses, no hardening of any kind (material or geometric) will be considered. The buckling failure criteria will be interpreted, more generally, relative to each analysis result but mainly, in-line with the underlying structure of the European standard EN1993-1.6, relative to the two reference strengths: small displacement linear buckling analysis (LBA) and small displacement materially nonlinear analysis (MNA).

The numerical study will be done computationally using the program ABAQUS, which is proven to be able to follow the post-buckling response of the complete phenomenon of shell buckling. The 3-node general-purpose axisymmetric shell element with axisymmetric deformation, SAX2, will be used throughout the study. Comprehensive parametric studies will be carried out for different shell slenderness ratios, shell lower bundary conditions, and the intensity of the internal pressurization. Linear and nonlinear numerical analyses will be made for different shell slenderness (R/t for the cylinder & $r_1/t\cos\beta$ for the cone) values which span from 100 to 1500 representing the practical range of cylindrical shells in civil engineering constructions. The lengths of the cylinders will be taken in such a way that no boundary-effect interactions are possible between the top and bottom boundary condtions. The material considered throughout the study will be mild steel with an ideal elastic-plastic von Mises yield criterion and a yield stress f_y = 240 MPa, elastic modulus E = 210 GPa, and Poisson's ratio ν = 0.3. The results will all be expressed interms of non-dimensional variables and hence can be used to address other practical sets of conditions as well.

2.4 Scope of the work

This work is mainly concerned with the axisymmetric elastic-plastic buckling of thin-walled cylindrical and conical metal shells. Detailed re-investigation of the numerous Gent laboratory test results of liquid-filled conical shells was the other concern of this study. A brief discussion on the general scope of the work is given below:

Chapter 3 - Axisymmetric elastic-plastic buckling of cylindrical shells under axial compression & internal pressure

3.1 - Introduction

A brief introduction about thin-walled cylindrical shells, the load types that they are usually subjected to, the resulting stresses and what this study is generally going to address.

3.2 - Problem statement

A brief discussion of the problem statement specific to thin-walled cylindrical shells will be discussed. Besides, the solution method that will be used to address the problem will be discussed along with the way how the results will be represented.

3.3 - Linear shell analysis (LA)

The pure membrane behavior and edge bending effects of meridionally compressed and internally pressurized cylindrical shells will be computed using considerations of static equilibrium for the pure membrane situation and using an effective-ring model analogy for the edge bending effects. The total results (membrane + edge bending) will be compared with the finite element linear analysis results for verification purposes.

3.4 - Linear elastic buckling strength of an ideally perfect cylinder

The linear buckling strengths of meridionally compressed and internally pressurized perfect cylindrical shells will be computed approximately and investigated numerically. An analytical model of a beam on an elastic foundation will also be used to simulate the elastic buckling behavior and strength of cylindrical shells.

3.5 - Elastic buckling strength of an imperfect cylinder

The effects of imperfections on the elastic buckling strength of cylindrical shells under meridional compression with/out internal pressurization will be discussed. The history about the treatment of imperfections in design considerations will be summarized. The effect of different imperfection amplitudes depending on the fabrication quality classes as recommended in EN 1993-1-6 will also be discussed.

3.6 - Pure plastic strength of cylindrical shells

The pure plastic limit strengths of meridionally compressed and internally pressurized cylindrical shells will be computed approximately using von Mises membrane yield criterion taking the pure membrane stresses. The plastic strength using stress resultant oriented approximate yield criteria will also be discussed. Moreover, small displacement materially nonlinear numerical simulations will be done to compute the exact plastic capacity of meridionally compressed and internally pressurized cylindrical shells.

3.7 - Elastic-plastic buckling phenomena, analysis, and strength

In this chapter, the general buckling phenomena of meridionally compressed with/out internally pressurized cylindrical shells will be discussed. The effects of plasticity and edge constriction on buckling strengths will also be discussed.

3.8 - Axisymmetric elastic-plastic buckling of imperfect cylindrical shells

The elephant's-foot buckling strengths of meridionally compressed and internally pressurized perfect cylinders will also be investigated in detail after which simplified expressions are obtained for the prediction of the axisymmetric elastic-plastic buckling strength of general thin-walled cylinders under such loading. Axisymmetric sinusoidal and local imperfections will be investigated in detail. A practically possible worst local imperfection will also be studied and explained. Different buckling modes and corresponding buckling strengths will be discussed and will be compared one another.

3.9 - New buckling design recommendation

This chapter discusses about a design recommendation which will be proposed for design purposes and future research works. Different possibilities for representing and interpreting the results will also be shown. Detailed explanations will as well be included.

3.10 - Comparison of the new buckling design recommendation with EN 1993-1-6 buckling design regulation

The new design recommendation obtained from the current work will be compared with the existing design regulation and other related research work results.

3.11 - Summary and conclusions

A brief summary of what has been done in the chapters and general conclusion of the results obtained will be given.

Chapter 4 - Axisymmetric elastic-plastic buckling of liquid-filled conical shells (LFC)

4.1 - Introduction

A brief introduction about thin-walled liquid-filled conical shells, the resulting stresses & distributions and how the elastic-plastic buckling investigation is addressed in this study.

4.2 - Problem statement

A brief discussion of the problem statement specific to the thin-walled liquid-filled conical shells will be discussed. Besides, the solution methods that will be used to address the problem will be discussed along with the way how the results will be represented.

4.3 - Linear shell analysis (LA)

The pure membrane behavior and edge bending effects of liquid-filled conical shells will be computed using considerations of static equilibrium for the pure membrane situation and using an effective-ring model analogy for the edge bending effects. The total results (membrane + edge bending) will be compared with the finite element linear analysis results for verification purposes.

4.4 - Loading procedure for numerical analysis purposes

The possible loading procedures in dealing with liquid-filled conical shells will be discussed. Besides, which loading procedure should be used in what circumstances and for what purposes will be pointed out.

4.5 - Linear buckling strength of an ideally perfect liquid-filled cone

The linear buckling strengths of liquid-filled perfect cones will be computed approximately and investigated numerically. Explanations will be given about the LFC-specific buckling phenomenon and corresponding strengths. Simplified expressions for the prediction of linear buckling strengths of liquid-filled general cones with pinned and fixed bottom boundary conditions will be obtained.

4.6 - Elastic buckling strength of an imperfect liquid-filled cone

The effects of imperfections on the elastic buckling strength of conical shells under meridional compression with/out internal pressurization will be discussed. The effect of different imperfection amplitudes depending on the fabrication quality classes as recommended in EN 1993-1-6 will also be discussed.

4.7 - Pure plastic strength of liquid-filled conical shells

The pure plastic limit strengths of liquid-filled conical shells will be computed approximately using von Mises membrane yield criterion taking the membrane stresses at the cone-base as references. The plastic strength using stress resultant oriented approximate yield criteria will also be discussed. Moreover, small displacement materially nonlinear numerical simulations will be done to compute the exact plastic capacity of liquid-filled cones. Simplified expressions along with detailed explanations will be obtained to predict the materially nonlinear limit strength of both pinned

and fixed bottom liquid-filled general cones.

4.8 - Elastic-plastic buckling phenomena, analysis and strength

The consideration of the effect of plasticity on elastic buckling with non-axisymmetric buckling failure mode will be discussed. The elephant's-foot buckling strengths of perfect cones due to liquid-loading will also be investigated in detail after which simplified expressions are obtained for the prediction of the axisymmetric elastic-plastic buckling strength of general thin-walled liquid-filled cones.

4.9 - Buckling design recommendation

This chapter discusses about a design recommendation which will be proposed for design purposes and future research works.

4.10 - Summary and conclusions

A brief summary of what has been done in the chapters and conclusion of the results obtained will will be given.

Chapter 5 - Re-investigation of Gent test results: Elastic buckling of liquid-filled cones

In this whole chapter, a detailed re-investigation and re-examination of the numerous laboratory tests performed using liquid-filled cones in Gent for more than a decade will be made. Detailed comparisons of results, representations and interpretations will be made. An overview of this particular chapter is given as follows:

5.1 - Introduction

A brief introduction about steel tower failure cases and Gent laboratory tests on buckling of liquid-filled conical shells.

5.2 - Problem statement

This chapter discusses how the test results were analyzed and interpreted. It also discusses the design proposal given by Vandepitte *et. al.* and what was missing while interpreting and what should have been included.

5.3 - Liquid-filled conical shell parameters and representation

The basic parameters which play the major role in interpreting and representing analysis and test results of liquid-filled conical shells will be listed.

5.4 - Fluid-filled conical shells: comparison of gas-filled vs. liquid-filled conical shells

This chapter discusses the difference in the stress distribution of a gas-filled cone and liquid-filled cone. The overall relative buckling strengths of a cone under the two loading situations will be discussed. The strength gains due to internal pressurization under the same state of meridional membrane compression at the cone-base will also be discussed in detail.

5.5 - Test results and Gent University design proposal

This chapter gives a detailed overview of the test set up. The liquid types used, boundary conditions and the overall procedure for data recording, analyzing and interpreting will be discussed. Besides, an overall tabular summary of the test data will be given.

5.6 - Comparison of parameter choices and representations

A comparative study of the LFC basic parameters of this study and Gent's basic parameters will be made. Both mathematical and graphical detailed comparisons of the corresponding representations will also be made.

5.7 - Detail re-investigation of test results

This chapter discusses a detailed re-investigation of the Gent laboratory test results by taking the shell slenderness ration in to account. Separation of the data into different groups will be made depending on their slenderness ratio, material type, bottom boundary conditions etc.

5.8 - Detailed comparison based on the LFC-elastic buckling limits

This chapter discusses the linear buckling behavior of perfect liquid-filled conical shells and compares the test results with the elastic buckling strengths of liquid-filled conical shells.

5.9 - LFC-imperfection reduction factor

This chapter confirms the imperfection reduction factor of cylindrical and conical shells to be similar and examines the Belgium and Canada steel water tower failure cases. Corresponding comments and conclusions will also be made.

5.10 - Summary and Conclusion

A brief summary of the works that have been done in the whole chapter will be given. Conclusions will also be included.

Chapter 6 - Re-investigation of Gent test results: Mercury-filled steel cones

Detailed investigation of Gent mercury test results along with detailed discussions, explanations, and conclusions will be made. Previous LFC-related research works on nonlinear simulation of liquid-filled conical shells with/out geometric imperfections will as well be discussed and few cases will be re-examined for confirmation and further studying purposes. Relevant explanations and conclusions will be given to the outcomes of those works.

Chapter 7 - Re-examination of two tank failure cases

In this chapter, the Belgium and Canada steel water tower failure cases will be re-examined to check for any possible roles played by plasticity effects during the collapse. Previous research works related to the collapse of the water towers will also be discussed.

Chapter 8 - The notion of the “corresponding” cylinder

A “corresponding cylinder” of a liquid-filled conical shell will be introduced which behaves in exactly the same way as the LFC. Detailed investigation of the “corresponding cylinder” will then be made which will turn out to be that the liquid-filled cone is nothing but a “wet-cylinder”.

Chapter 9 - General summary & conclusion

In this chapter, the general summary of the whole work and accompanying conclusions will be given. An outlook and possible future work will be proposed. Besides, modifications on the European Standard EN 1993-1-6 will be proposed.

Annex A - Ilyushin yield criterion and related approximations

This chapter discusses Ilyushin’s stress resultant oriented yield criterion and the approximations made to simplify the expression for Ilyushin’s yield surface. Different approximate yield criteria will be discussed and comparisons of one another will be made using illustrative meridionally compressed & internally pressurized cylindrical and conical shells. Comparisons of these stress resultant oriented approximate yield criteria will also be made with that of the pure membrane Mises yield criterion.

Annex B - Axisymmetric rigid plastic plate & shell analysis

In this chapter, Ilyushins yield criterion and the related approximations will be used to compute the rigid plastic strength of circular and annular plates uniform or ring lateral loads. Besides, the plastic strength of cylindrical shells under radial ring loads with and without axial loading and internal pressurization will be computed.

Annex C - Analytical elastic buckling analysis of cylindrical shells

In this chapter, the elastic buckling behaviour and strength of cylindrical shells will be computed analytically. Moreover, the analytical model along with the stress resultant oriented yield criteria a will be used to assess the approximate geometrically and materially nonlinear buckling strengths of cylindrical shells.

3

Axisymmetric elastic-plastic buckling of cylindrical shells under axial compression & internal pressur

3.1 Introduction

Cylindrical shells have a wide range of applications in engineering, in general, and in structural engineering, in particular. To mention some, cylindrical shells are used as pressure vessels, pipes, tanks, silos, roof structures. In many of these practical engineering applications, cylindrical shells are subjected to axisymmetric type of loading such as gravity (self-weight, snow), hydrostatic pressure, internal or external gas pressure. More specifically pipes, tanks and silo structures are mainly subjected to meridional compression simultaneously with internal pressure coming from the contained material. Such types of loading cause bi-axial stress state: meridional membrane compression and circumferential (hoop) membrane tension.

The appropriate functioning of such structures requires a proper design that takes all possible failure conditions in to account. One of such possible and most dominant failure conditions for thin shells is failure by buckling (stability considerations) and hence this work is much concerned with the considerations of failure by buckling. In the buckling strength assessment of thin-walled general metal shells-of-revolution, the European Standard EN1993-1-6 recommends to use three different approaches (methods) which apply to all geometries, all loading conditions, and all material conditions. The hierarchy of these general buckling design procedures have been summarized in the discussion on the state-of-the-art.

This study is concerned with thin-walled metal cylindrical shell structures with pinned or fixed bottom boundary conditions under the action of axisymmetric meridional compressive ring load and uniform internal pressure, Figure 3.1. The cylindrical shell will be analysed using membrane theory, linear shell bending theory (LA), linear bifurcation analysis (LBA), small displacement materially nonlinear analysis (MNA), perfect geometrically and materially nonlinear analysis (GMNA), and geometrically and materially nonlinear analysis with imperfections (GMNIA). A combination of both analytical and numerical (using finite element program) analysis methods will be used depending on the nature and complexity of the problem type in consideration. In all the analyses, no hardening of any kind (material or geometric) is considered. The buckling failure criteria will be interpreted, more generally, relative to each analysis result but mainly, in-line with the underlying structure of the European standard EN1993-1.6, relative to the two reference strengths: small displacement linear bifurcation analysis (LBA) and small displacement materially nonlinear analysis (MNA).

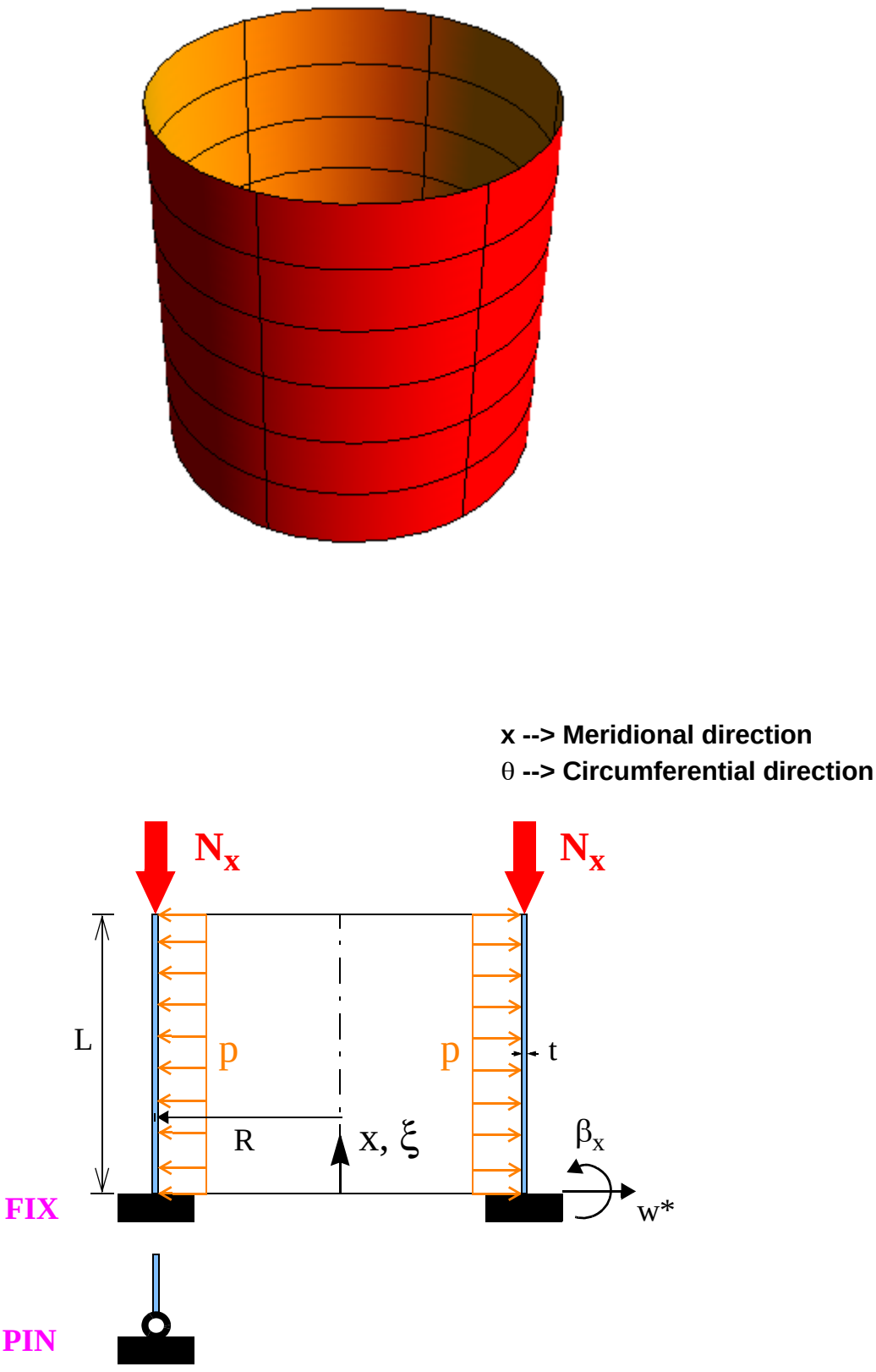

Figure 3.1 Geometry, loading, and boundary conditions

3.2 Problem statement

There have been buckling failure cases of civil engineering thin-walled metal cylindrical shells under axial compressive loads with co-existent internal pressure, many of which happened forming outward bulges near the supported edge (elephant's-foot buckling phenomenon) resulting from earthquake induced effects. There, as well, have been a lot of research attempts, both theoretically and experimentally, to determine the exact elastic-plastic buckling capacity of cylindrical shells under axial compressive loads with co-existent internal pressure. Despite the number of research attempts so far, their prediction of the elastic-plastic buckling strengths do have serious insupportable problems. This work addresses the axisymmetric elastic-plastic buckling strength of isotropic unstiffened cylindrical shells using numerical parametric simulations, with the ultimate goal of deriving a set of basic data that can be used in a straight forward buckling design by hand calculations. A comparison with the previous research works and existing design recommendation, EN1993-1-6, will then be made. Eventhough the effects of possible axisymmetric imperfections are investigated in detail, the design recommendation resulting from this work will be made based on the GMNA (perfect elephant's foot) numerical results of the perfect shell. This is because of the simple fact that there is no common agreement between the researchers about the "practical and worst" imperfection type and nature.

The study was done computationally using the program ABAQUS, which is proven to be able to follow the post-buckling response of the complete phenomenon of shell buckling. The 3-node general-purpose axisymmetric shell element with axisymmetric deformation, SAX2, is used throughout the study. Linear and nonlinear numerical analyses were made for different shell slenderness (R/t) values which span from 100 to 1500 representing the practical range of cylindrical shells in civil engineering constructions. The lengths of the cylinders are taken in such a way that no boundary-effect interactions are possible between the top and bottom boundary condtions. The material considered throughout the study is mild steel with an ideal elastic-plastic von Mises yield criterion and a yield stress f_y = 240 MPa, elastic modulus E = 210 GPa, and Poisson's ratio ν = 0.3. The results are all expressed interms of non-dimensional variables and hence can be used to address other practical sets of conditions. In many of the upcoming discussions, a cylindrical shell with the following set of conditions will be used for illustration purposes.

Geometry: R/t = 500; t = 1.0 cm; L/R = 1.0

Boundary conditions: pinned or fixed bottom and rotational restaraint at top

Loading: meridional ring tip-loading and uniform internal pressure p

Material properties: E = 21000 kN/cm^2; ν = 0.3; f_y = 24.0 kN/cm^2

3.3 Linear shell analysis (LA)

The basic problem of linear shell theory for general shells of revolution with symmetric conditions can be split into two effects: the axisymmetric membrane and axisymmetric edge-bending effects as shown below.

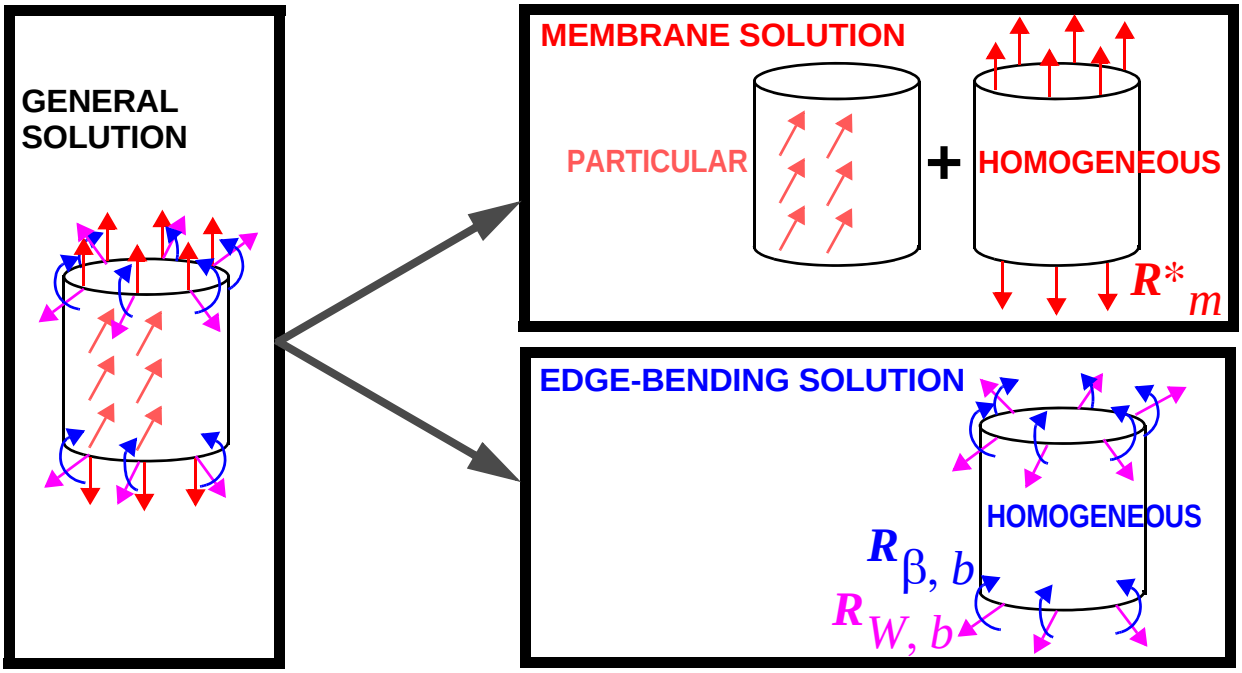

Figure 3.2 Decomposition of the general solution into particular and homogeneous parts

3.3.1 Pure membrane behavior

For Axisymmetric type of shells, with all axisymmetric conditions, the cross-sectional stress state of a shell segment is primarily governed by membrane action due to the continuously distributed loads which the shell is subjected to.

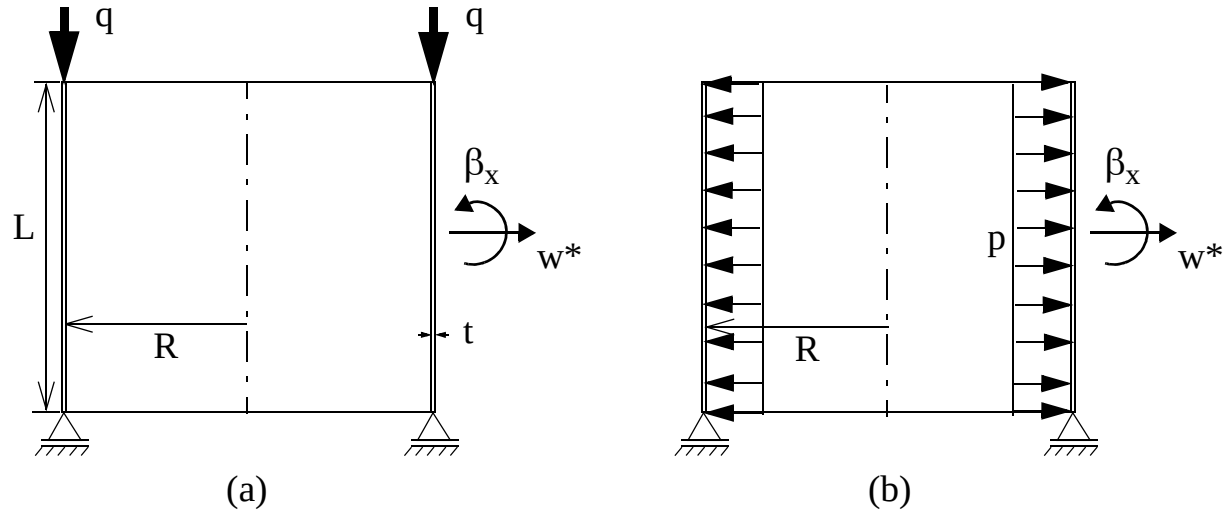

Figure 3.3 Loading and geometry: (a) vertical ring load; (b) internal uniform pressure

The pure membrane behavior can easily be computed and is given, interms of the deformations and section forces, as

Axial Ring (tip) load case:

$$N_x = q = -\sigma_x \cdot t = const$$
$$N_\theta = 0$$

. . . membrane section forces (Eq. 3.1)

$$w^* = -\nu \frac{q}{E \cdot t} R = \nu \frac{\sigma_x \cdot t}{E \cdot t} R = const$$
$$\beta_x = 0$$

. . . membrane deformations (Eq. 3.2)

Uniform Internal pressure case:

$$N_x = 0$$
$$N_\theta = p \cdot R = const$$

. . . membrane section forces (Eq. 3.3)

$$w^* = \frac{p \cdot R^2}{E \cdot t} \quad \text{. . . membrane deformations} \quad \text{(Eq. 3.4)}$$

$$\beta_x = 0$$

3.3.2 Edge-bending effects

Even though, the primary stresses are pure membrane stresses, additional secondary bending effects occur at shell discontinuities due to compatibility requirements. Shell discontinuity includes stepped wall thickness, cylinder-cone transition junction, heavy T-bar ring stiffener, lap-jointed bolted wall connection, and boundary supports, Guggenberger (2004a).

A general linear elastic stress analysis approach to analyze axisymmetric stress states at arbitrary shell junctions of thin-walled axisymmetric shell structures is presented by Linder (2001). This analysis method is based on a newly developed effective-ring analogy model and it is used, in this work, to compute the edge bending effects due to different support conditions. The basic edge bending solution-functions, Figure 3.4, used by the effective-ring analogy model are given by:

$$f_1 = e^{-\bar{\chi}\bar{\xi}} \cdot \sin\bar{\chi}\bar{\xi}$$
$$f_2 = e^{-\bar{\chi}\bar{\xi}} \cdot \cos\bar{\chi}\bar{\xi} \qquad \text{(Eq. 3.5)}$$

$$f_3 = f_2 - f_1 = e^{-\bar{\chi}\bar{\xi}}(\cos\bar{\chi}\bar{\xi} - \sin\bar{\chi}\bar{\xi})$$
$$f_4 = f_1 + f_2 = e^{-\bar{\chi}\bar{\xi}}(\cos\bar{\chi}\bar{\xi} + \sin\bar{\chi}\bar{\xi}) \qquad \text{(Eq. 3.6)}$$

Where

$$\bar{\chi} = \frac{L}{L_{eff}} = \sqrt{\sqrt{3(1-\nu^2)} \cdot \frac{1}{t \cdot R}} \cdot L$$
$$= \frac{L}{0.778\sqrt{R \cdot t}} \quad \text{... for } \nu = 0.3 \qquad \text{(Eq. 3.7)}$$

$$\bar{\xi} = \frac{x}{L}$$
$$\bar{\chi}\bar{\xi} = \frac{x}{L_{eff}} \qquad \text{(Eq. 3.8)}$$

$$L_{eff} = \sqrt{\frac{R \cdot t}{\sqrt{3(1-\nu^2)}}}$$
$$= 0.778\sqrt{R \cdot t} \quad \text{... for } \nu = 0.3 \qquad \text{(Eq. 3.9)}$$

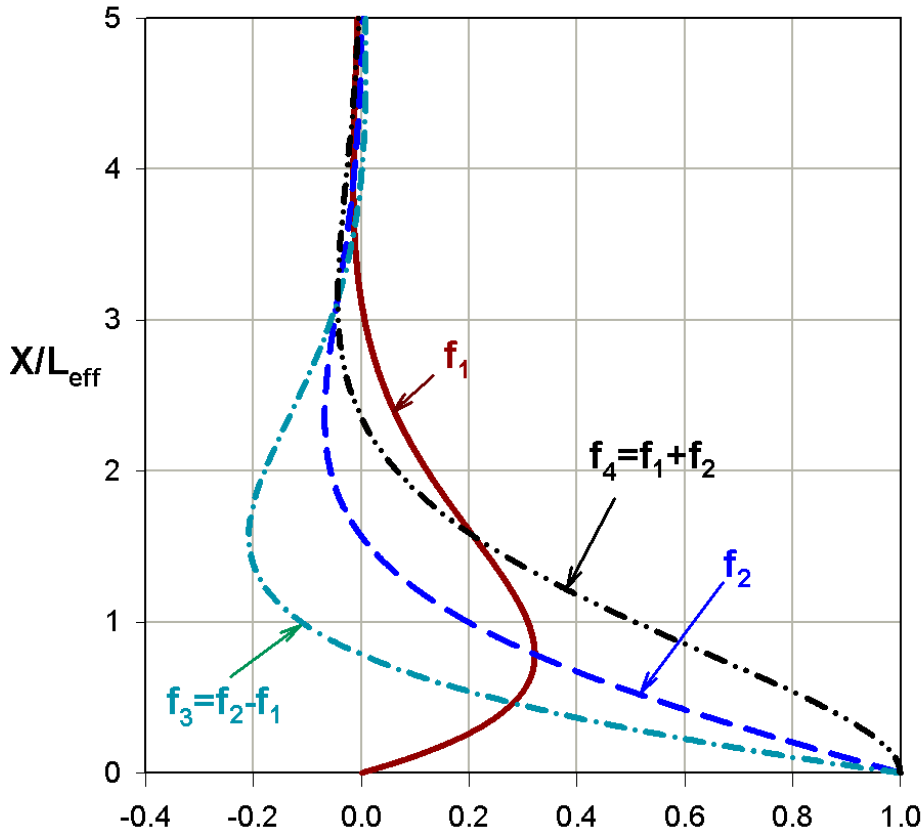

Figure 3.4 Basic solution functions of the ring model analogy

These basic solution functions and their linear combinations are used throughout the solution of the edge bending problem. Condensed mathematical expressions are also presented by Linder (2001) for the overall (membrane and edge bending) analysis of shell problems.

The stiffness of the equivalent ring model of the cylindrical shell for edge bending effects is given by:

$$\underline{\underline{K}} = \frac{EA_{eff}}{2R^2} \cdot \begin{bmatrix} 2 & -L_{eff} \\ -L_{eff} & L_{eff}^{\,2} \end{bmatrix} \qquad \text{(Eq. 3.10)}$$

For edge displacement disturbances w^*_A and $\beta_{x,A}$ at the bottom edge "A" of the shell, the restraining edge forces can be computed using the stiffness of the ring model as

$$\begin{bmatrix} R_{H,A} \\ R_{M,A} \end{bmatrix} = -\underline{\underline{K}} \cdot \begin{bmatrix} w_A^* \\ \beta_{x,A} \end{bmatrix} = -\frac{EA_{eff}}{2R^2} \cdot \begin{bmatrix} 2 & -L_{eff} \\ -L_{eff} & L_{eff}^{\,2} \end{bmatrix} \cdot \begin{bmatrix} w_A^* \\ \beta_{x,A} \end{bmatrix} \qquad \text{(Eq. 3.11)}$$

For a cylindrical shell, the total deformation and section forces (edge bending effects included) according to the effective-ring analogy model are genrally computed as follows. The actual ditributions along the meridian of the shell will depend on the type of bottom boundary condition considered.

Deformations:

$$\begin{bmatrix} w^* \\ \beta_x \end{bmatrix} = \begin{bmatrix} (f_1 + f_2) & -L_{eff} \cdot f_1 \\ \dfrac{2f_1}{L_{eff}} & (f_2 - f_1) \end{bmatrix} \cdot \left(\begin{bmatrix} w_A^* \\ \beta_{x,A} \end{bmatrix} - \begin{bmatrix} w_A^* \\ \beta_{x,A} \end{bmatrix}_{part} \right) + \begin{bmatrix} w^* \\ \beta_x \end{bmatrix}_{part} \qquad \text{(Eq. 3.12)}$$

Section forces:

$$Q_x = \begin{bmatrix} (f_2 - f_1) & \dfrac{2f_1}{L_{eff}} \end{bmatrix} \cdot \begin{bmatrix} R_{H,A} \\ R_{M,A} \end{bmatrix} \qquad \text{(Eq. 3.13)}$$

$$N_x = N_{x,part} \qquad \text{(Eq. 3.14)}$$

$$N_\theta = \frac{Et}{r_1} \cdot \begin{bmatrix} (f_1 + f_2) & -L_{eff} \cdot f_1 \end{bmatrix} \cdot \left(\begin{bmatrix} w_A^* \\ \beta_{x,A} \end{bmatrix} - \begin{bmatrix} w_A^* \\ \beta_{x,A} \end{bmatrix}_{part} \right) + N_{\theta,part} \qquad \text{(Eq. 3.15)}$$

$$M_x = -\left[L_{eff} \cdot f_1 \quad (f_1 + f_2)\right] \cdot \begin{bmatrix} R_{H,A} \\ R_{M,A} \end{bmatrix} \qquad \text{(Eq. 3.16)}$$

$$M_\theta = \nu \cdot M_x \qquad \text{(Eq. 3.17)}$$

The section moments are assumed positive when outer side of the shell is under compression.

For the particular shell and loading cases of this study, the total deformation and section forces according to this method are given as follows

Deformations:

$$w^* = -\frac{R}{E \cdot t \cdot h}(\nu \cdot \sigma_x \cdot t + p \cdot R) \cdot \begin{cases} (f_2 - 1) \cdot h & \text{for pinned bottom} \\ (f_1 + f_2 - 1) \cdot h & \text{for fixed bottom} \end{cases} \qquad \text{(Eq. 3.18)}$$

$$\beta_x = -\frac{R}{E \cdot t \cdot h}(\nu \cdot \sigma_x \cdot t + p \cdot R) \cdot \begin{cases} f_1 + f_2 & \text{for pinned bottom} \\ 2f_1 & \text{for fixed bottom} \end{cases}$$

Section forces:

$$N_x = N_{x,membrane} = -\sigma_x \cdot t \qquad \text{for both pinned and fixed bottoms}$$

$$N_\theta = p \cdot R - (\nu \cdot \sigma_x \cdot t + p \cdot R) \cdot \begin{cases} f_2 & \text{for pinned bottom} \\ f_1 + f_2 & \text{for fixed bottom} \end{cases} \qquad \text{(Eq. 3.19)}$$

$$Q_x = \frac{A_{eff}}{R \cdot t}(\nu \cdot \sigma_x \cdot t + p \cdot R) \cdot \begin{cases} 0.5(f_1 - f_2) & \text{for pinned bottom} \\ \left(1 - \dfrac{h}{L_{eff}}\right)(f_1 - f_2) & \text{for fixed bottom} \end{cases}$$

Section moments:

$$M_x = -\frac{A_{eff}}{2R \cdot t} h(\nu \cdot \sigma_x \cdot t + p \cdot R) \cdot \begin{cases} f_1 & \text{for pinned bottom} \\ f_1 - f_2 & \text{for fixed bottom} \end{cases} \qquad \text{(Eq. 3.20)}$$

$$M_\theta = \nu \cdot M_x \qquad \text{for both pinned and fixed bottoms}$$

Where

$$A_{eff} = L_{eff} \cdot t \qquad \text{(Eq. 3.21)}$$

For illustration purposes, consider the cylindrical shell stated above loaded with a tip-compressive ring load equal to the classical buckling stress σ_{xRcr} and a uniform internal pressure p of magnitude $0.5p_y$ (half of the pressure which causes uni-axial yielding in the circumferential direction), i.e.

$$\sigma_x = \sigma_{xRcr} = 0.605E\frac{t}{R}$$
$$p = 0.5p_y = 0.5f_y\frac{t}{R} \qquad \text{(Eq. 3.22)}$$

The deformations and section force results from the linear shell analysis method discussed above would then be as shown on the plots, Figure 3.5 to Figure 3.9. The normal section force and bending moments shown in these plots are normalized with respect to the corresponding un-axial yield section force, $N_{pl} = t.f_y$, and section moment, $M_{pl} = t^2.f_y/4$, respectively. The meridional section force N_x and the circumferential bending moment M_θ distributions along the meridian are not included as the first is constant through out the meridian and the later is the product of the poison's ratio ν and the meridional bending moment M_x.

3.3.3 Numerical finite element linear analysis (LA)

Numerical finite element small displacement linear analyses of the illustrative cylindrical shell under the aforementioned meridional tip-compressive ring loading with uniform internal pressure were made for verification purposes. The deformation and section force results obtained from ABAQUS finite element linear analysis are exactly the same as those obtained using the effective-ring-model analogy, Figure 3.5 to Figure 3.9.

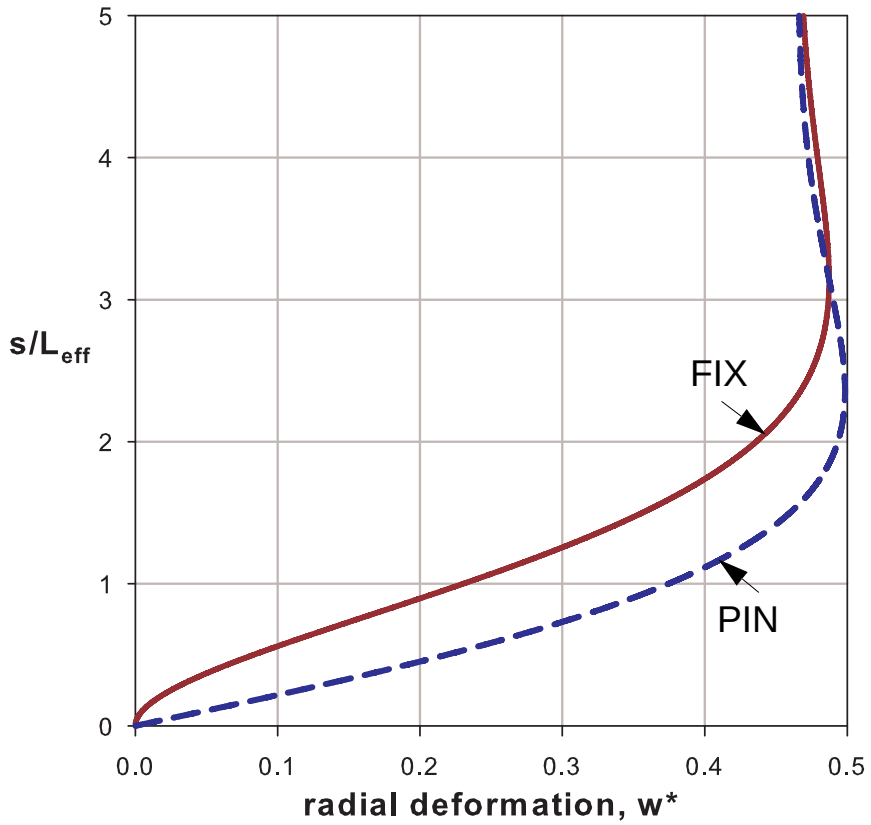

Figure 3.5 Radial deformation

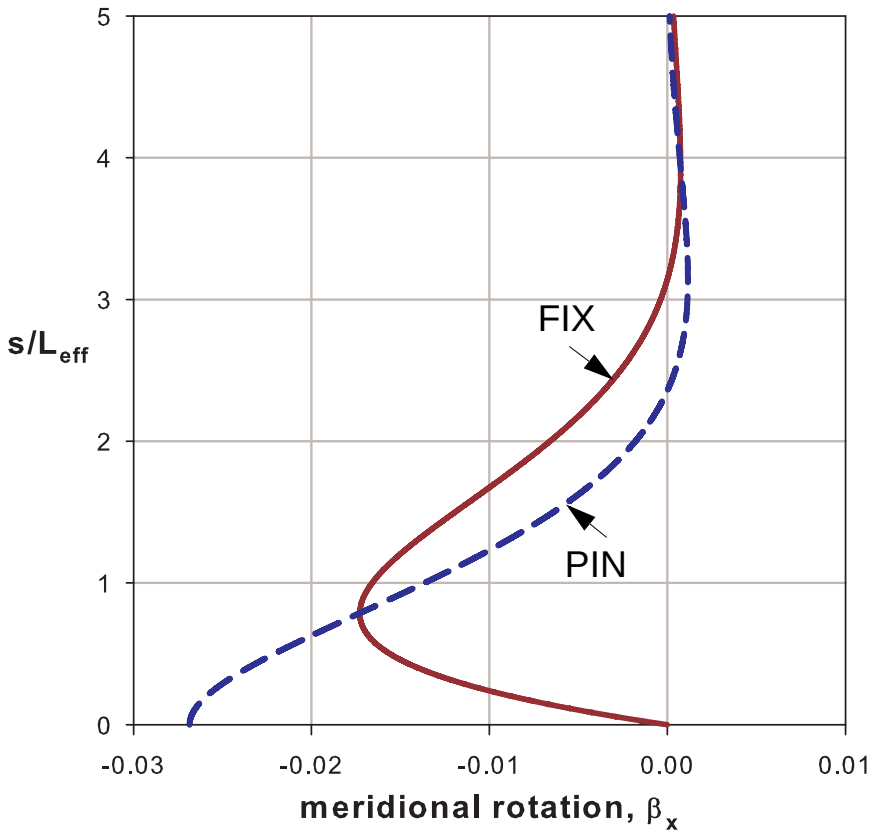

Figure 3.6 Meridional rotation

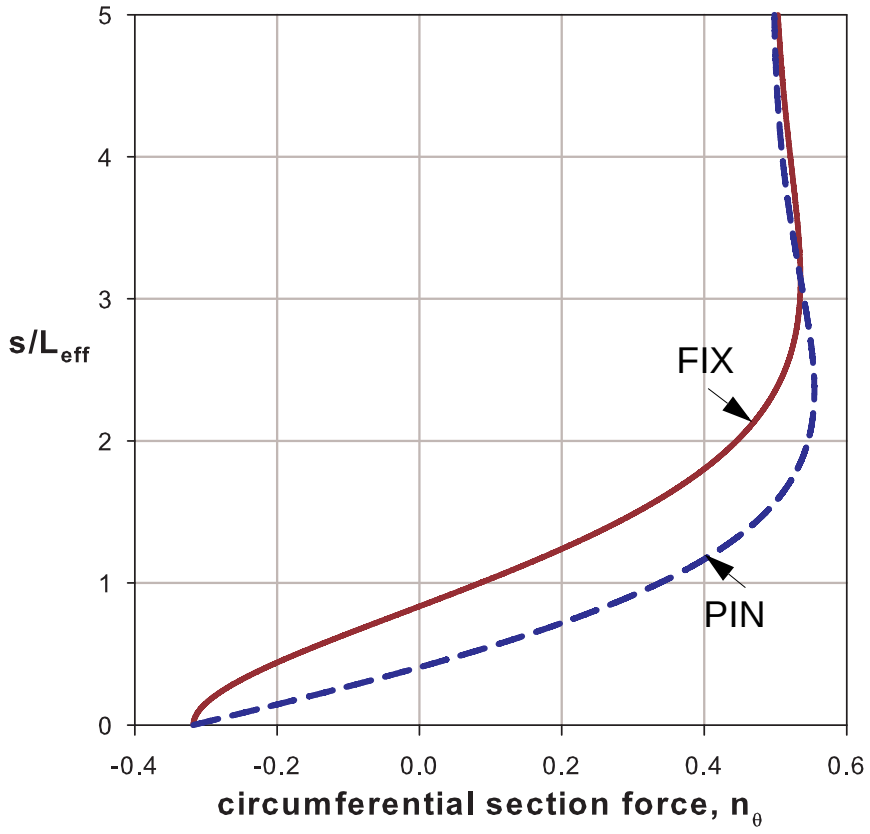

Figure 3.7 Circumferential section force

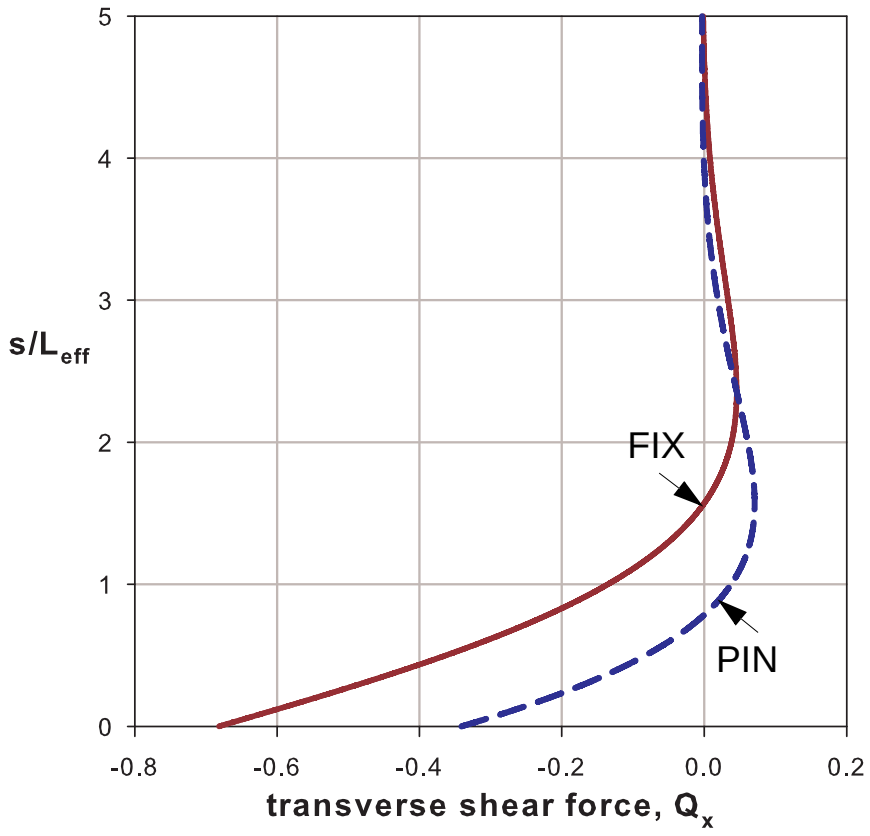

Figure 3.8 Transverse shear force

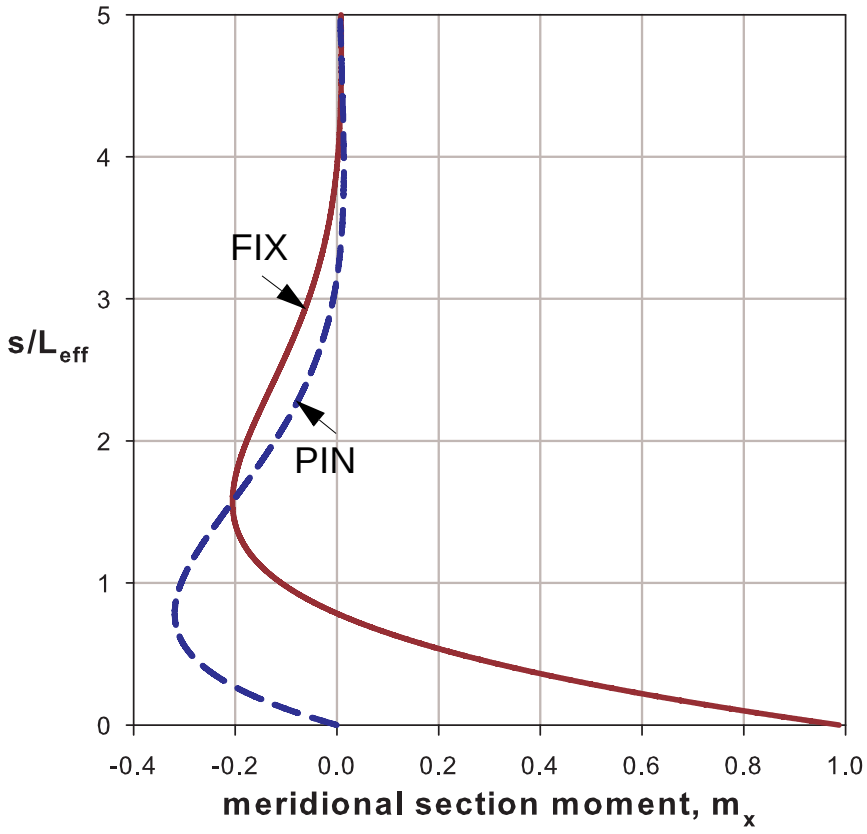

Figure 3.9 Meridional section moment

3.4 Linear elastic buckling strength of an ideally perfect cylinder

In elastic buckling design assessments according to EN1993-1-6, the characterstic buckling strength of an imperfect elastic shell, σ_k, is related to the elastic critical buckling stress of the perfect shell, σ_{cr}, using an elastic imperfection reduction (knock-down) factor α which quanitifies the combined effect of geometric nonlinearity and all types of possible imperfections. The relationship is generally given by

$$\sigma_k = \alpha \cdot \sigma_{cr} \qquad \text{(Eq. 3.23)}$$

Since the effect of geometric nonlinearities are included in the imperfection reduction factor α, the elastic critical buckling stress of the perfect shell, σ_{cr}, represents the small displacement linear elastic bifurcation stress of the perfect shell and not the snap-through buckling stress which is associated with geometric nonlinearity.

In line with the “stress-design” (LA-stress-based) approach, the elastic critical buckling stress of the perfect shell, σ_{cr}, is computed using linear elastic shell analysis. This stress will then be compared with the buckling stress from FE-based LBA only for verification purposes.

The pure elastic buckling strength of the perfect shell will later be used as a reference strength in evaluating the shell buckling relative slenderness parameter $\overline{\lambda}_x$.

3.4.1 Approximate linear buckling analysis based on linear shell analysis

In the general LBA sense, a shell subjected to an axial loading (no matter where the axial loading and related section forces come from) buckles at a section located a meridional distance "x" from the supported base, when the membrane meridional section stress $\sigma_x(x)$ due to the applied axial loading reaches the section's limiting value for elastic buckling, $\sigma_{xcr}(x)$, which is given by

$$\sigma_{xcr}(x) = \frac{1}{\sqrt{3(1-\nu^2)}} \cdot \frac{E \cdot t(x)}{r(x)} \qquad \text{(Eq. 3.24)}$$

Generally speaking, even though the stress at the supported base reaches its buckling limiting value, buckling will not take place at the base. Instead, it occurs at a small distance away from the base (along the meridian). This is because of the two facts that (i) it is restrained and (ii) there is no enough space for buckling to occur.

Buckling practically occurs when the stress at the location for the "center of buckle" reaches the critical stress for that particular section. In other words, the stress distribution should be increased, after reaching the critical stress at the base, by a load factor so that the stress at the center of buckle reaches its limiting value for buckling, thereby producing buckling.

The above discussion, however, will be more clear and applicable for elastic buckling of conical shells than the cylindrical shells. Hence, the same discussion would be repeated later when investigating the approximate elastic buckling strength of perfect conical shells.

For a cylindrical shell of constant thickness, the elastic critical section force is constant, since t(x) and r(x) are constant, throughout the height of the shell. Besides, the meridional stress at any point along the meridian is equal to the membrane meridional compression resulting from the applied tip-compressive loading. As a result, the approximate elastic buckling stress is equal to the theoretical elastic buckling stress given by

$$\begin{aligned} \sigma_{xcr}(x) &= \frac{1}{\sqrt{3(1-\nu^2)}} \cdot \frac{E \cdot t}{R} \\ &= 0.605\frac{E \cdot t}{R} \qquad \text{for } \nu = 0.3 \end{aligned} \qquad \text{(Eq. 3.25)}$$

3.4.2 Linear buckling analysis using an analytical model based on theory of second order

The linear elastic buckling load and the corresponding buckling mode of an axially ring-compressed cylindrical shell (which is independent of the internal pressure) can be analytically obtained using a stability analysis (Theory of second order) of an equivalent beam on an elastic foundation. The foundation modulus of the elastic beam will be obtained from the consideration of stiffness of the shell in the radial direction and is given by

$$C_f = (E \cdot t) / R^2 \qquad \text{(Eq. 3.26)}$$

See Annex-C for the full discussion.

3.4.3 Numerical finite element linear buckling analysis (LBA)

Only for verification purposes, numerical finite element linear buckling analyses (LBA) of cylindrical shells with a reference axial tip-compressive ring loading equal to the theoretical elastic critical buckling stress and varying the intensity of a uniform internal pressure were made. In this case, the critical load factor is taken as the lowest buckling load. The combined effect of the shell slenderness, bottom boundary conditions, and the intensity of internal pressurization is very small and hence is generally neglected. It should, however, be clear here that a high internal pressurization means a relatively bigger contribution to the axial compression due to poisson's effect. This fact can be observed from the somehow declining buckling load results as the internal pressurization increases. The results are plotted in the LBA/Rcr vs. μ representation as shown in Figure 3.10 and Figure 3.11 for fixed and pinned bottom boundary conditions, respectively.

The maximum deviation being for the relatively thick shell, 0.98% for the fixed bottom cylindrical shell and 0.2% for the pinned bottom case, one can see that the approximate linear buckling analysis result predicts well the FE LBA result. As a result, the LBA_approximate will be used instead of the FE LBA in the upcoming computations and discussions.

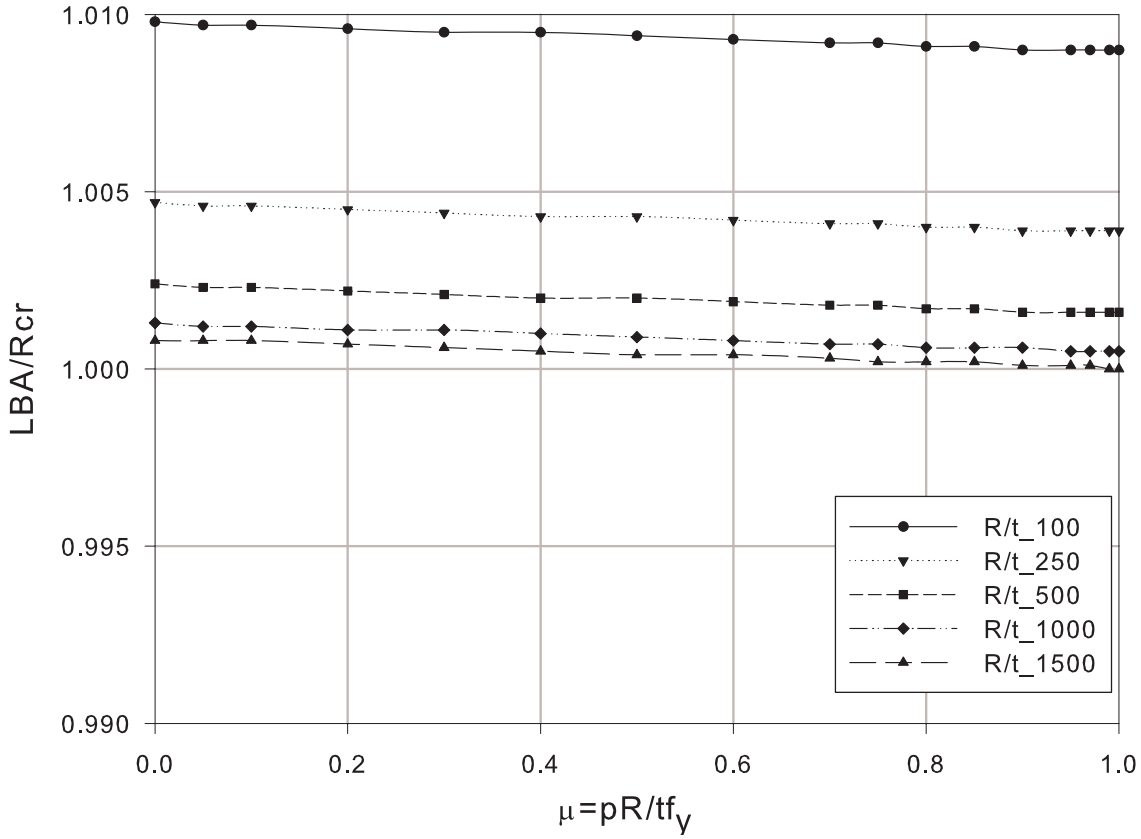

Figure 3.10 Finite element LBA analyses results: Fixed bottom

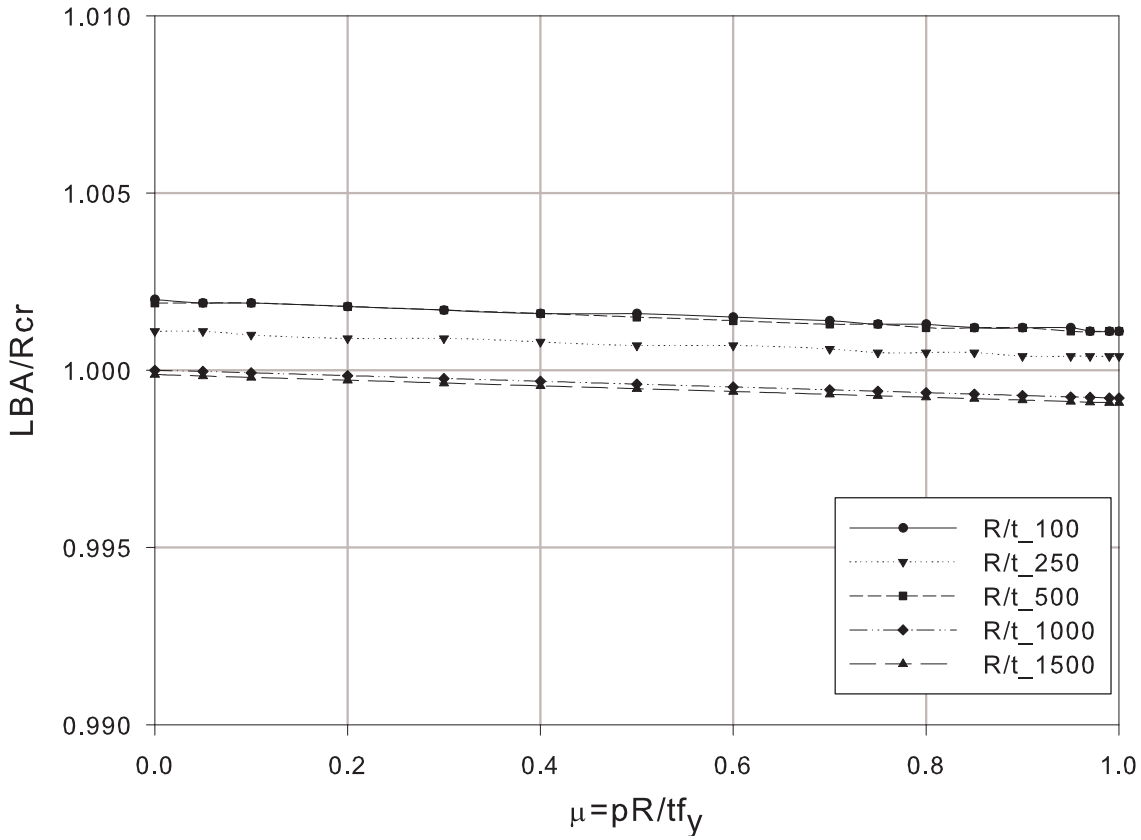

Figure 3.11 Finite element LBA analyses results: Pinned bottom

3.5 Elastic buckling strength of an imperfect cylinder

3.5.1 Elastic buckling strength: history

The elastic buckling load of cylindrical shells predicted by the classical stability theory is applicable only to an idealized mathematical model of the structure. The actual shell structure, however, is far from the perfect idealized model as it usually has initial imperfections of any type (geometric, loading, boundary conditions, and material.). This fact has been a secret for a long time during the past when buckling loads measured in experiments often were as small as a quarter (even smaller) of the theoretical critical buckling load showing high imperfection sensitivity.

Following a large number of laboratory experimental investigations on buckling loads, specifications concerning design loads with respect to stability were proposed for thin-walled cylindrical shells under simple types of loads and imperfections not exceeding certain limits. The experimental investigations made on axially loaded cylindrical shells included pure meridional compression (with no internal pressure) and combined loading of meridional compression and internal pressure. It has been shown that the elastic buckling strength of an axially compressed imperfect thin-walled cylindrical shell with co-existent internal pressure increases with internal pressurization as the circumferential membrane tensile stress smooths out the imperfections thereby reducing their negative effect. The specifications introduced an elastic buckling reduction factor α which is equal to the ratio of the experimental elastic buckling load to the theoretical critical buckling load of the perfect idealized shell and hence always less than unity. The magnitude of the reduction factor depends on the imperfection type & amplitude, internal pressure intensity, shell slenderness ratio R/t, and the type of loading.

In **1976**, a task group of the European Convention for Constructional Steelwork (ECCS 1976) recomended to use imperfection reduction factors (obtained from lower bounds of scatter bands of numerous laboratory test results) for both unpressurized (α_0) and pressurized (α_p) given by (Eq. 3.28) and (Eq. 3.29), respectively. This recommendation was limited to medium height cylindrical shells with imperfection amplitude, $\overline{w}$, not exceeding $0.01\ell_r$ (Eq. 3.27) measured from a straight rod of length $l_r = 4\sqrt{Rt}$ held anywhere against any meridian of the shell. It apparently prohibits shells with larger imperfection amplitudes. Moreover, nothing has been reported with respect to the nature of the imperfections of the laboratory tests on which the specification was based. Thus, it predicts a buckling strength of a shell irrespective of the fabrication methods used and resulting imperfection nature. The imperfections might, however, be random (therefore non-axisymmetric) as laboratory model cylinders are commonly fabricated by wrapping a single sheet of material around a form and making a longitudinal (meridional) joint, Teng & Rotter (1992). **On the other hand, the same recommendation shows the enormous influence of a small axisymmetric initial imperfection on the buckling strength of an axially loaded cylindrical shell. It,**

however, does not recommend to consider such imperfections believing that initial defects in real shell structures are not axisymmetric but randomly distributed.

$$\bar{w}_{max} = 0.01 l_r = 0.04\sqrt{Rt} \qquad \Rightarrow \frac{\bar{w}_{max}}{t} = \frac{1}{25}\sqrt{\frac{R}{t}} \tag{Eq. 3.27}$$

$$\alpha_0 = \begin{cases} \dfrac{0.83}{\sqrt{1 + 0.01R/t}} & \text{for R/t < 212} \\ \dfrac{0.70}{\sqrt{0.1 + 0.01R/t}} & \text{for R/t > 212} \end{cases} \tag{Eq. 3.28}$$

$$\alpha_p = \alpha_0 + (1 - \alpha_0)\frac{\rho}{\rho + 0.007} \tag{Eq. 3.29}$$

where

$$\rho = \frac{pR}{Et}\sqrt{\frac{R}{t}} = \frac{0.605 \cdot \bar{p}}{\sqrt{R/t}} \tag{Eq. 3.30}$$

$$\bar{p} = \frac{pR}{t \cdot \sigma_{Rcr}} \tag{Eq. 3.31}$$

In **1984**, the task group of the European Convention for Constructional Steelwork (ECCS 1984) recomended to use the same imperfection reduction factors as ECCS 1976. This recommendation, like ECCS-1976, was limited to medium height cylindrical shells with imperfection amplitudes not exceeding $0.01\ell_r$. Besides, it recommends to consider half of the imperfection reduction factors (α_0/ 2 for buckling under pure axial load and α_p/2 for buckling under axial load with internal pressure) when the imperfection amplitude is equal to 0.02 and to linearly interpolate for values of amplitudes lying in between. The imperfection amplitudes according to this recommendation are measured from a straight rod and a circular template of length $l_r = 4\sqrt{Rt}$ held anywhere against any meridian, Figure 3.12a, and against any parallel circle along the circumference, Figure 3.12b, respectively. In case of circular welds, the specification recommends to use a rod of length $l_r = 25t$, Figure 3.12c, for imperfection amplitude mesurements.

In the relatively latest recommendation, **ECCS 1988**, nothing has been changed from ECCS 1984 with respect to imperfection amplitude measurement, shell length limitation, imperfection amplitude restriction, and the strength prediction for buckling under axial loading with or without accompanying internal pressure.

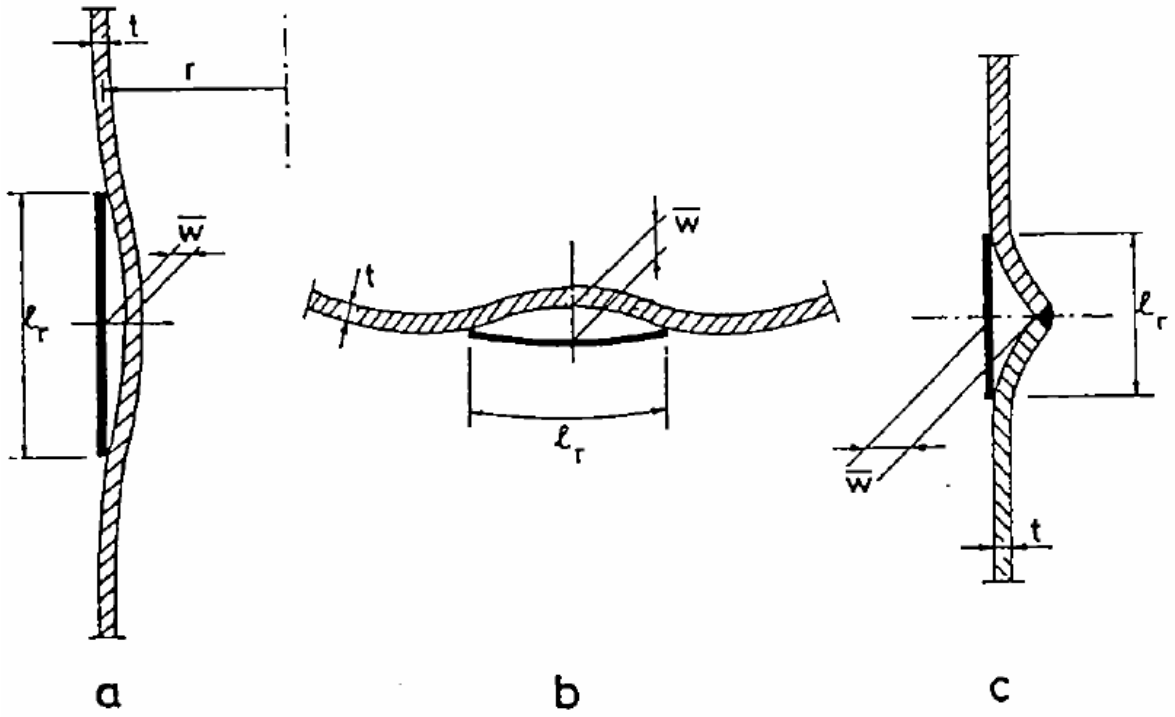

Figure 3.12 Measurements of imperfection amplitude $\overline{w}$ according to ECCS 1976, 1984, 1988

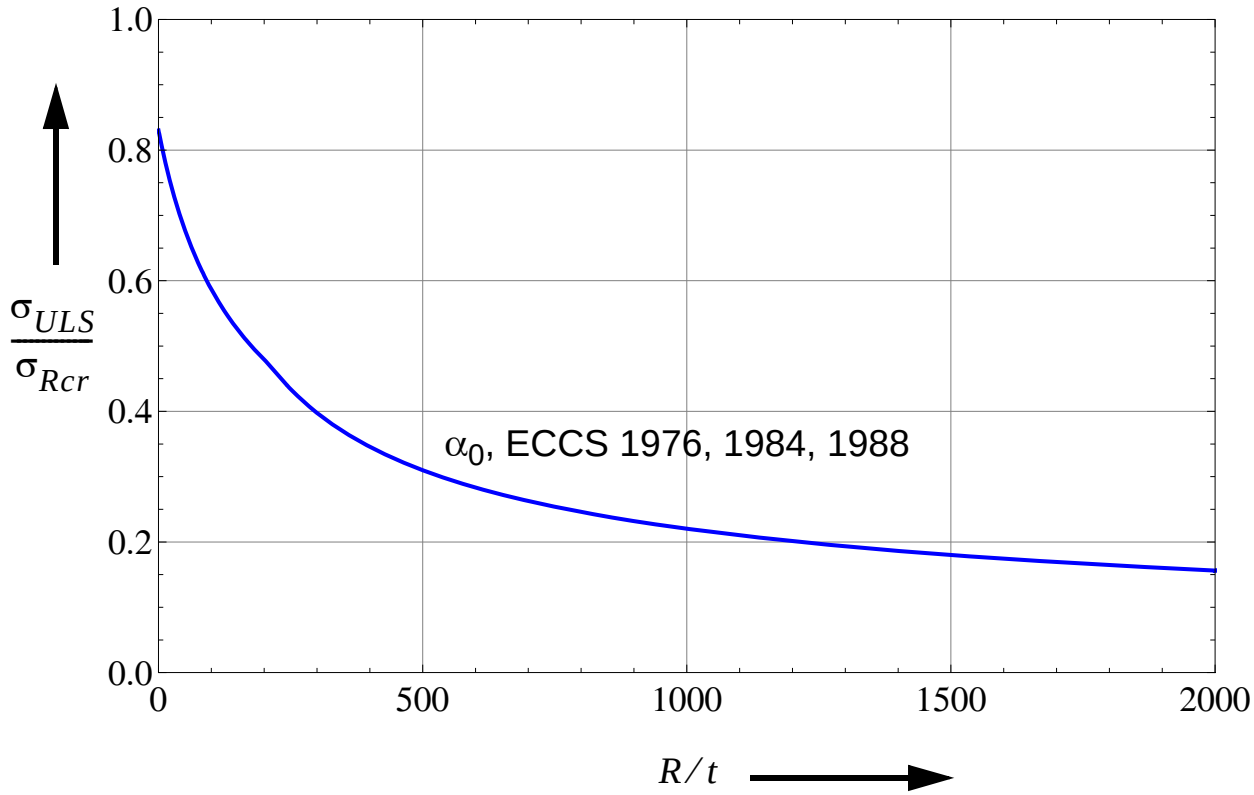

Figure 3.13 Unpressurized elastic buckling imperfection reduction factor

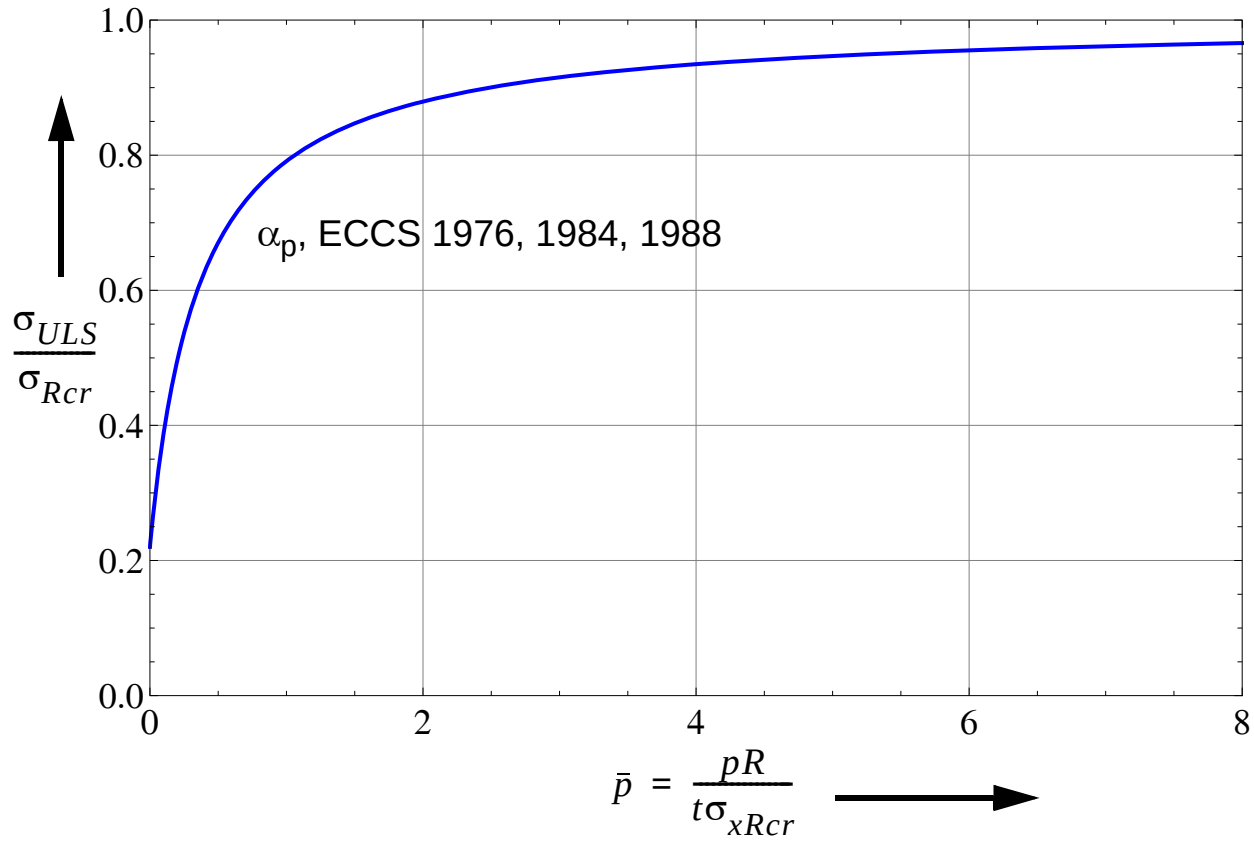

Figure 3.14 Pressurized elastic buckling imperfection reduction factor: R/t = 1000

On the other hand, **Hutchinson (1965)**, after mathematically investigating the imperfection sensitivity of axially compressed and internally pressurized cylindrical shells by considering axisymmetric, non-axisymmetric, and mixed imperfection modes indicated that different modes of initial geometric imperfections not only produce different unpressurized buckling strengths but are also affected differently by internal pressure. The buckling strength of an unpressurized cylindrical shell with pure axisymmetric imperfection is found to be lower and gains less strength with internal pressurization than that of a cylinder with pure non-axisymmetric or mixed modes of imperfections. The pressurized elastic imperfection reduction factor of a cylindrical shell with pure axisymmetric sinusoidal imperfection according to the mathematical model of Hutchinson is computed using (Eq. 3.32) for known values of the internal pressure parameter, $\bar{p}$, and the imperfection amplitude to shell thickness ratio, δ_0/t. The unpressurized elastic imperfection reduction factor is also computed from the same expression by setting $\bar{p} = 0$ (Eq. 3.33). An imperfection which has mixed modes of both axisymmetric and non-axisymmetric imperfections gives a strength higher than the pure axisymmetric but lower than the pure non-axisymmetric imperfections. In addition, Hutchinson compared his results with the lower bound result of the laboratory tests on which the aforementioned specifications were based and found out that the imperfections of the laboratory tests were close to his results of the non-axisymmetric type imperfections and hence confirmed the argument given above by Teng & Rotter (1992).

$$4(1 + \bar{p} - \alpha_{xpe})(1 - \alpha_{xpe}) - \sqrt{3(1 - \nu^2)}(2 + \alpha_{xpe})\frac{\delta_0}{t} = 0 \qquad \text{(Eq. 3.32)}$$

$$4(1 - \alpha_{xpe})^2 - \sqrt{3(1 - \nu^2)}(2 + \alpha_{xpe})\frac{\delta_0}{t} = 0 \qquad \text{(Eq. 3.33)}$$

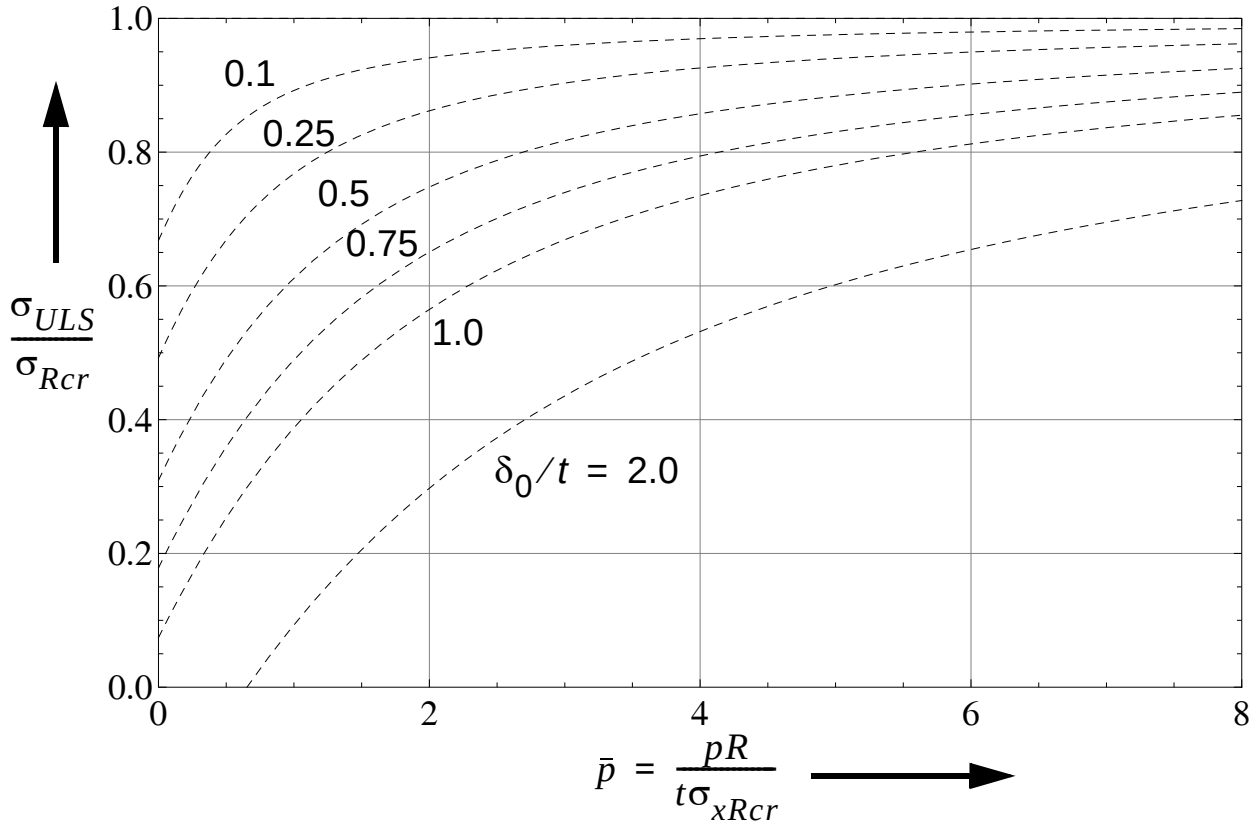

Figure 3.15 Hutchinson's pressurized elastic buckling strength for pure axisymmetric imperfections

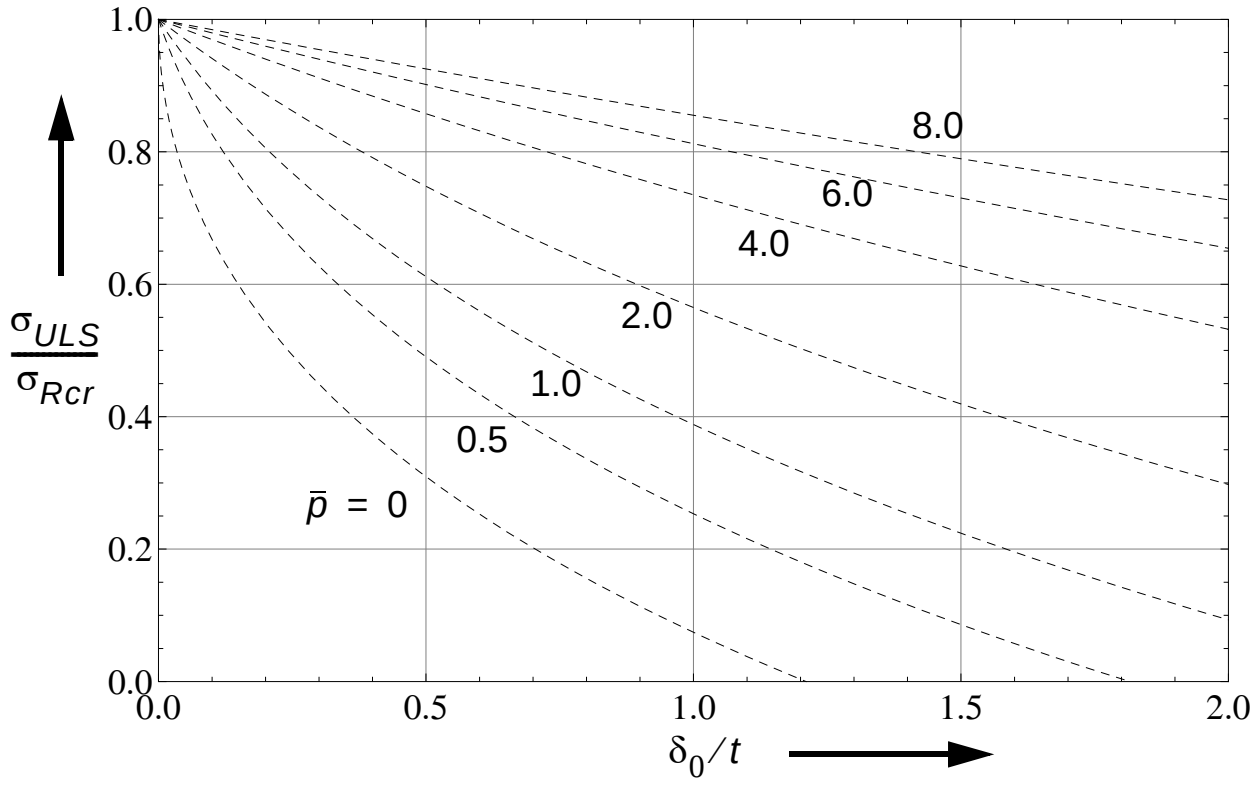

Figure 3.16 Hutchinson's pressurized elastic buckling strength for pure axisymmetric imperfections

Later, **Rotter & Teng (1989), Teng & Rotter (1992)** opposed the idea which says that initial defects in real shell structures are not axisymmetric but randomly distributed. They genuinely argued that civil engineering shell structures can have axisymmetric depresions resulting from circumferential welding and recommended the consideration of the effects of axisymmetric imperfections on buckling strength predictions of cylindrical shells. They studied the elastic buckling of thin-walled unstiffened cylindrical shells under axial load and internal pressure with sinusoidal, local inward, and local outward axisymmetric imperfections. Their results were compared with that of Hutchinson's sinusoidal imperfection and ECCS recommendation. **Here it has to be noted, however, that Teng & Rotter (1992) used an incorrect Hutchinson's strength curve when comparing their results with and led them to incorrect conclusions. In the comparison, they took Hutchinson's buckling strength curve with an imperfection amplitude equal to half of the wall thickness (instead of one wall thickness, Figure 3.15) and compared it with their results where the imperfection amplitude was equal to one wall thickness. The corrected comparison of the results is shown in Figure 3.21.** Eventhough all such imperfections were found to be worst in the sense that they lead to lower results than the ECCS recommendations, the sinusoidal and outward local axisymmetric imperfections were then dropped as they are not practically relevant. The inward local axisymmetric weld depression was then considered practical and further studies has been done to determine the worst possible shape of weld depressions, Rotter & Teng (1989). The introduction of the effects of these axisymmetric weld depressions into the specifications was then recommended. Besides, the elastic imperfection reduction factors for both unpressurized and pressurized buckling are recommended to be modified in such a way that they take care of different fabrication qualities. These recommendations are included in EN1993-1-6.

According to **EN1993-1-6**, the elastic pressurized buckling strength of cylindrical shells is given interms of elastic pressurized imperfection reduction factor which depends on the shell slenderness, loading condition, and imperfection amplitude which in turn depends on the fabrication quality class. The imperfection amplitudes are measured at every position in both the meridional and circumferential directions using the same guages as in ECCS 1988. In addition, this specification recommends to use guages of lengths $l_{gx} = 4\sqrt{Rt}$ and $l_{gw} = 25t_{min} \leq 500mm$ separately across welds, Figure 3.17. The expression for computing the imperfection reduction factor as given in EN1993-1-6, (Eq. 3.34) to (Eq. 3.37), will be used throughout the upcoming discussions.

A comparison of both the unpressurized and pressurized imperfection reduction factors according to the different recommendations and study results discussed above have been made in the current work. Figure 3.18 shows a comparative plot of the unpresssurized elastic buckling imperfection reduction factors according to the different specifications versus the shell slenderness ratio, R/t.

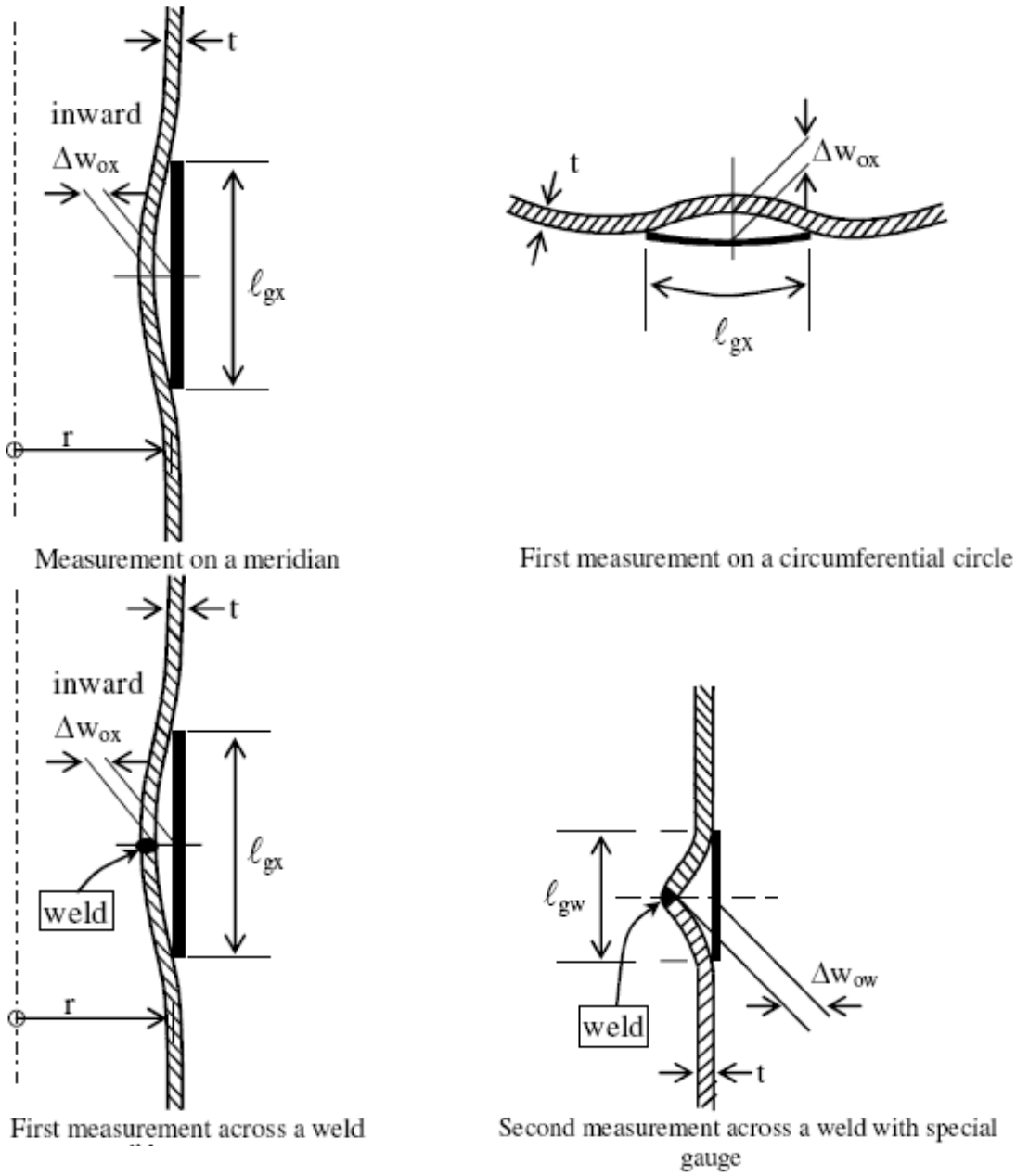

Figure 3.17 Measurements of depths Δw_0 of initial dimples according to EN1993-1-6

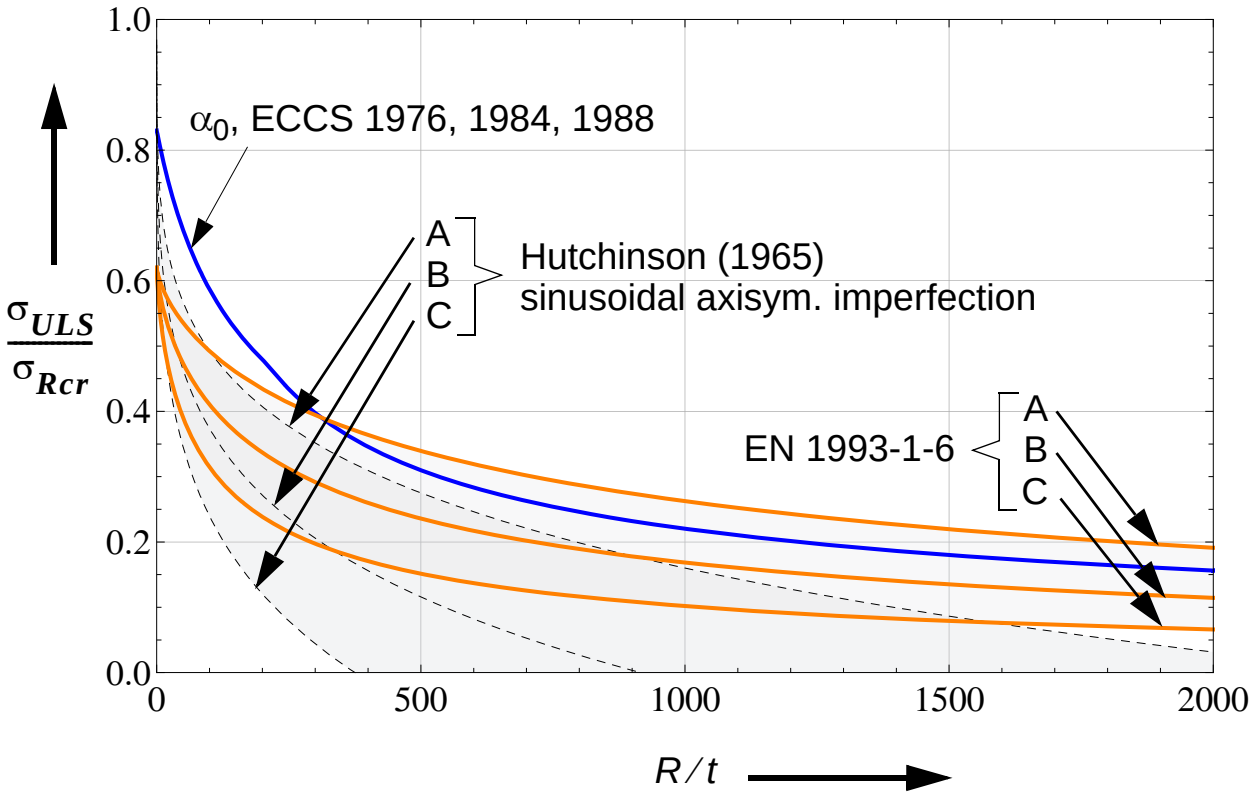

Figure 3.18 Unpressurized elastic buckling imperfection reduction factors

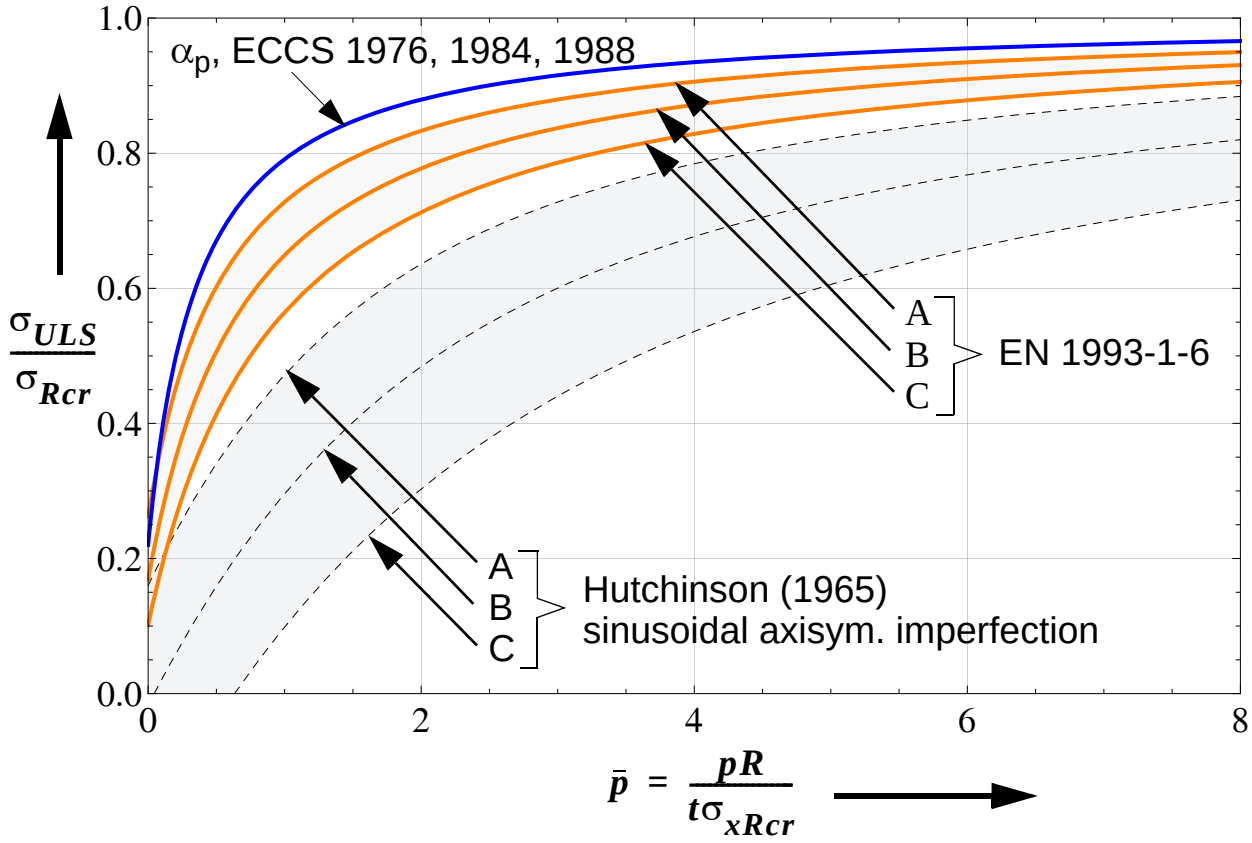

Figure 3.19 Pressurized elastic buckling imperfection reduction factors: R/t = 1000

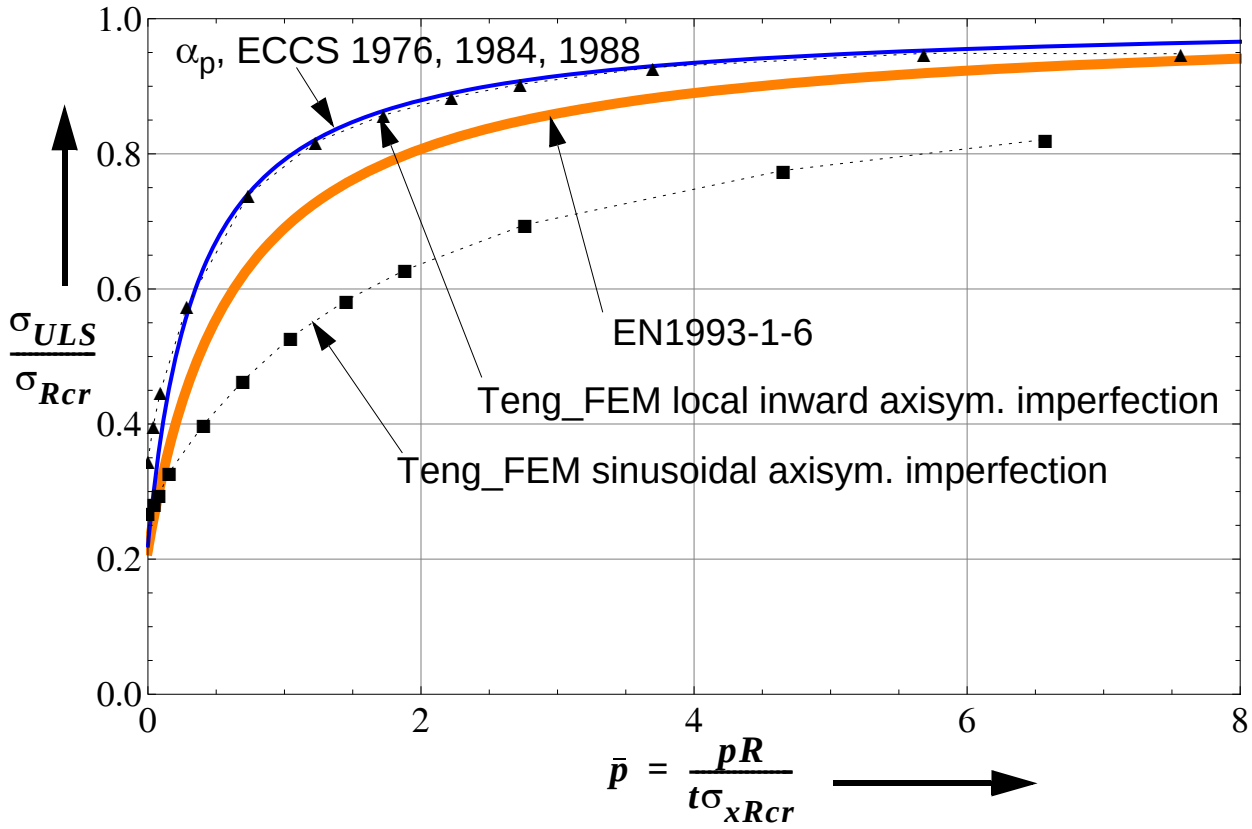

Figure 3.20 Pressurized elastic buckling imperfection reduction factors: R/t = 1000, δ_0/t = 1.0

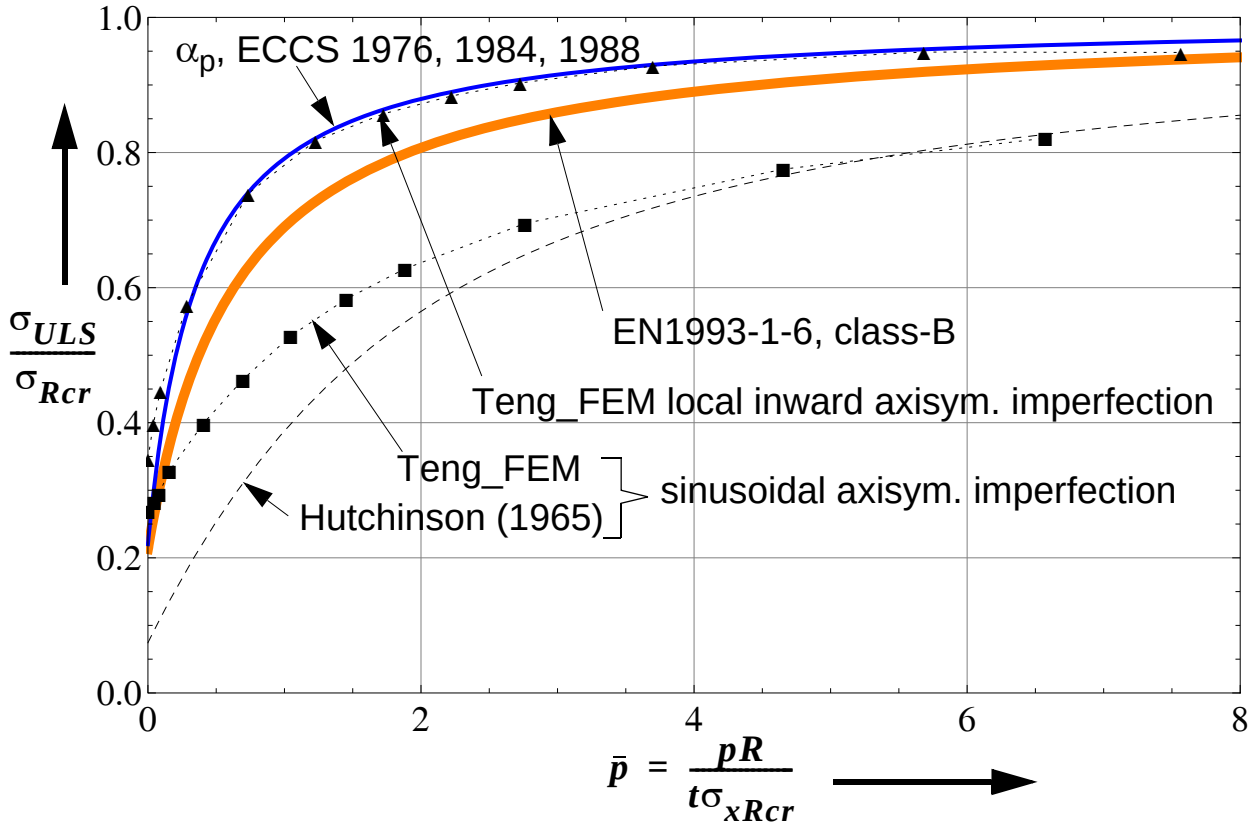

Figure 3.21 Pressurized elastic buckling imperfection reduction factors: R/t = 1000

3.5.2 Elastic imperfection reduction factor, EN1993-1-6

In accordance to the frame work of the European standard EN1993-1-6, the elastic imperfection reduction factor is a factor applied to the small displacement linear bifurcation buckling strength of a perfect shell, Figure 3.24, to account for geometric imperfections and the effect of geometric nonlinearity, Figure 3.25. It depends on the shell geometry, loading condition, and imperfection amplitude. The linear bifurcation buckling strength of a perfect cylindrical shell is independent of the internal pressure intensity. The elastic imperfection reduction factor of cylindrical (and conical shells, for that matter) subjected to meridional compression with/without co-existent internal pressure is given as follows:

- **elastic imperfection reduction for pressurized cases**

$$\alpha_{xpe} = \alpha_x + (1 - \alpha_x)\frac{\bar{p}}{\bar{p} + 0.3/\sqrt{\alpha_x}} \qquad \text{(Eq. 3.34)}$$

- **elastic imperfection reduction for unpressurized cases**

$$\alpha_x = \frac{0.62}{1 + 1.91(\Delta w_k/t)^{1.44}} \qquad \text{(Eq. 3.35)}$$

with the characteristic imperfection amplitude parameter, Δw_k given as

$$\Delta w_k = \frac{1}{Q} \cdot \sqrt{\frac{R}{t}} \cdot t \qquad \text{(Eq. 3.36)}$$

where

$$\bar{p} = \frac{\sigma_\theta}{\sigma_{xRcr}} = \frac{pR/t}{\sigma_{xRcr}} = \mu \cdot \bar{\lambda}_x^2 \qquad \text{(Eq. 3.37)}$$

Q is fabrication quality parameter and should be taken, depending on the fabrication tolerance quality class, from

Fabrication tolerance quality class	Description	Q
Class A	Excellent	40
Class B	High	25
Class C	Normal	16

Table 3.1 Values of fabrication quality parameter Q

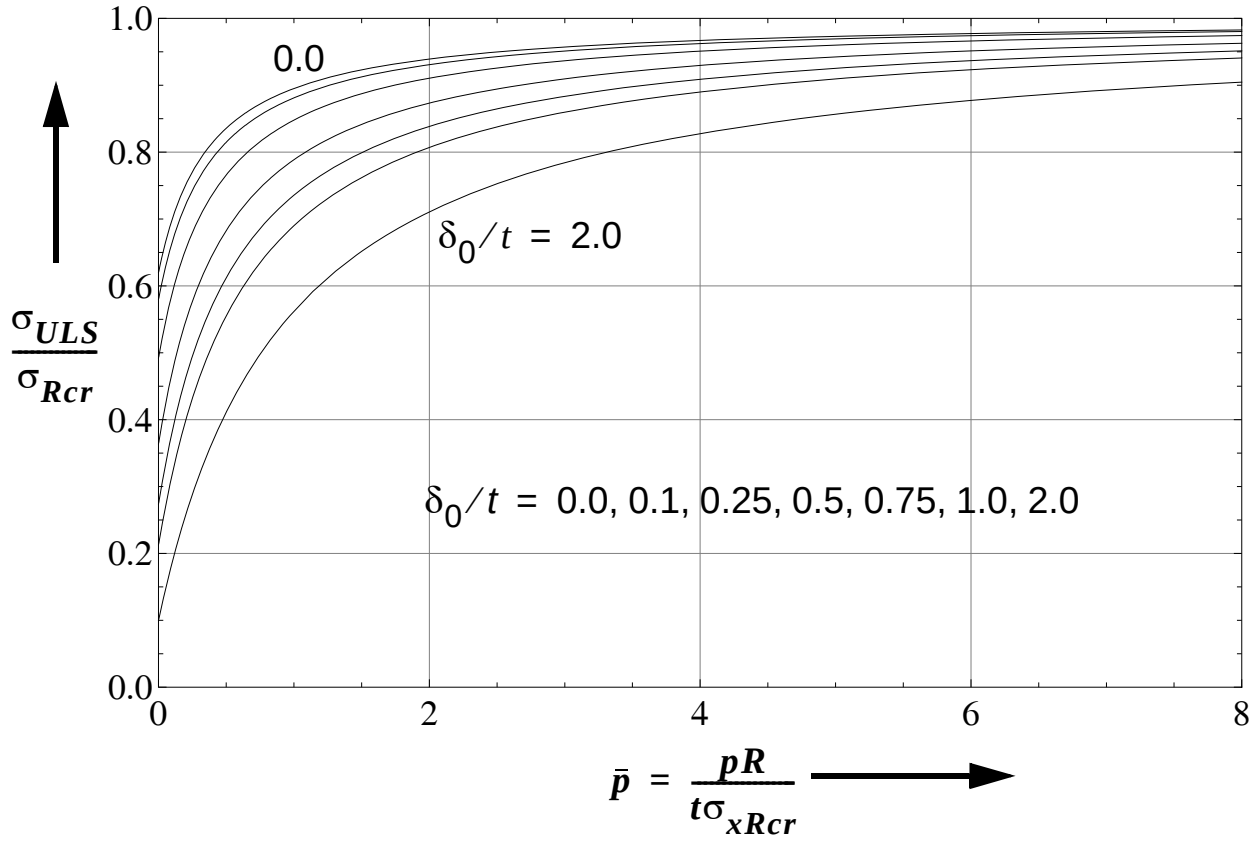

Figure 3.22 EN1993-1-6 pressurized elastic buckling imperfection reduction factor

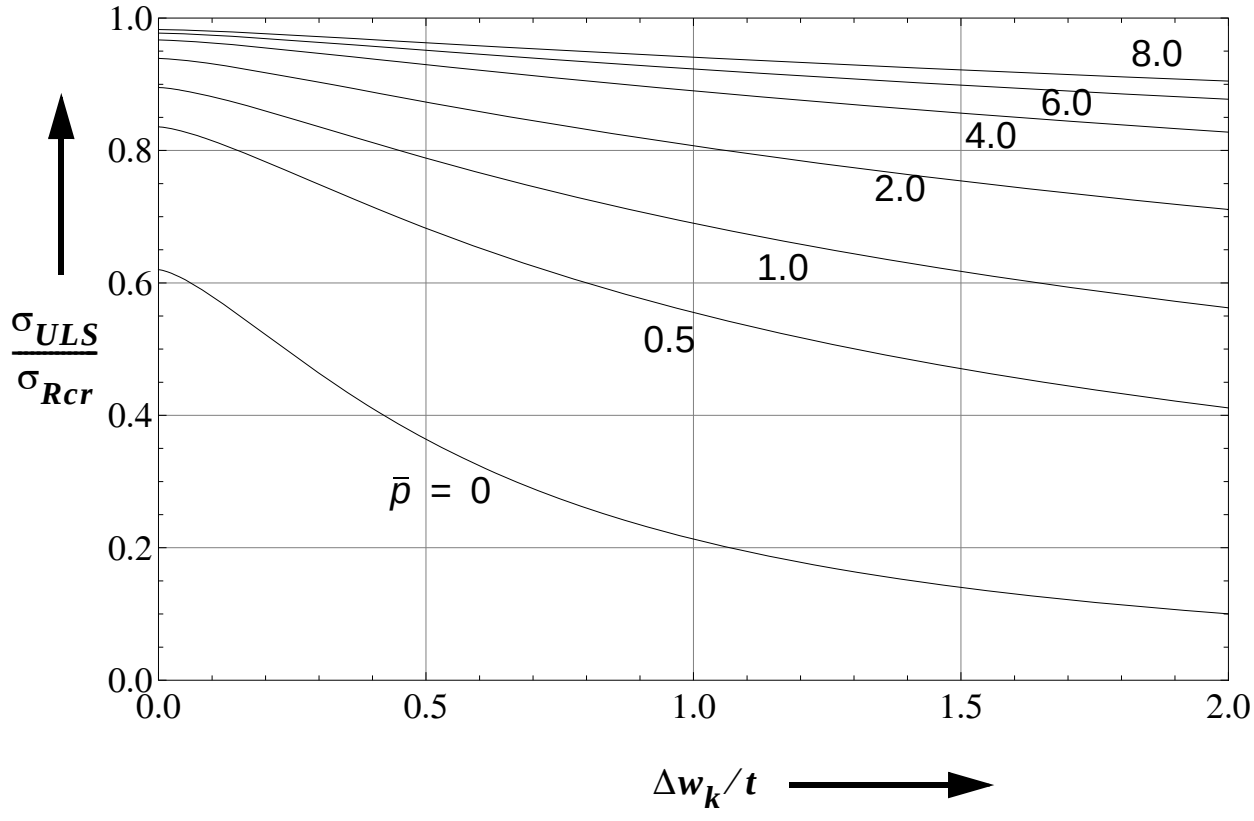

Figure 3.23 EN1993-1-6 pressurized elastic buckling imperfection reduction factor

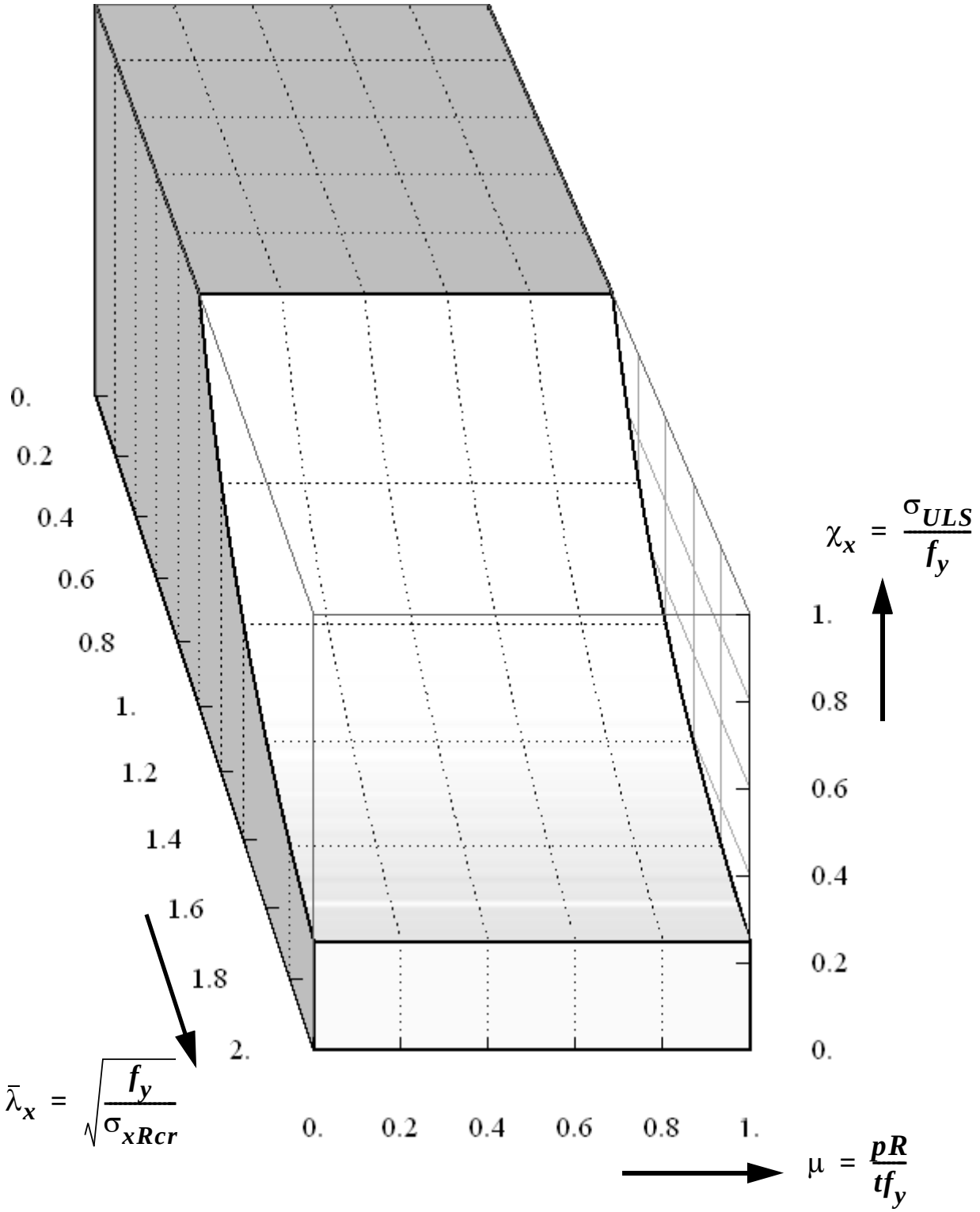

Figure 3.24 Perfect elastic buckling strength depending on shell slenderness ratio (independent of internal pressure)

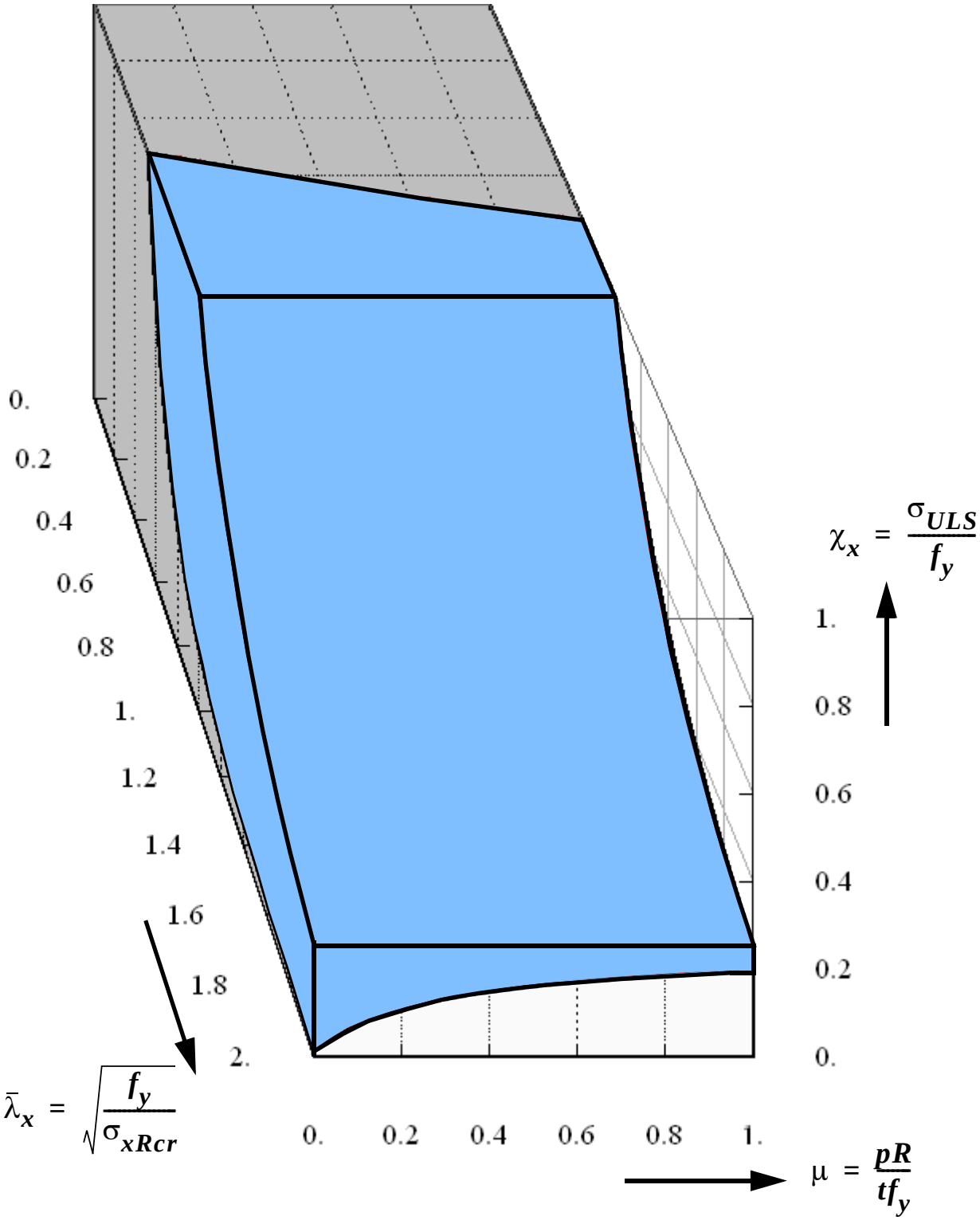

Figure 3.25 Effect of imperfections on elastic buckling strength: perfect and imperfect elastic buckling strengths

3.6 Pure plastic strength of cylindrical shells

The pure plastic (yield) strength represents the load (stress) which, with no stability phenomena intervening, causes an unacceptably large plastic deformation. The plastic strength of shells can be computed using membrane stresses approximately, using finite element small displacement theory (MNA) analysis, or using yield functions based on stress resultants which will be discussed later in detail.

3.6.1 Plastic strength according to von Mises membrane criteria

For axisymmetric shells under axisymmetric loading and boundary conditions where 2D principal membrane stresses exist, the von Mises membrane yield criteria is given by

$$\sigma_x^2 + \sigma_\theta^2 - \sigma_x \sigma_\theta \leq f_y^2 \qquad \text{(Eq. 3.38)}$$

with an upper limiting (yield) curve given by

$$\sigma_x^2 + \sigma_\theta^2 - \sigma_x \sigma_\theta = f_y^2 \qquad \text{(Eq. 3.39)}$$

For a cylindrical shell under the actions of uniform axial compression with co-existent uniform internal pressure, the limiting plasticity curve can be obtained using the following two different ways depending on the load aplication procedure. Different loading parameters are used to represent the two procedures. This separation will be more useful later in the finite element numerical analysis.

1 ***Pre-specified pressure load:*** For a specified intensity of internal pressure (Eq. 3.40), compute the meridional membrane stress (Eq. 3.41) which will cause yielding and the corresponding plastic load factor (Eq. 3.42).

$$\mu = \frac{p}{p_{yield}} = \frac{\sigma_\theta}{f_y} = \frac{p \cdot R}{t \cdot f_y} \qquad \text{(Eq. 3.40)}$$

$$\sigma_{x,\,pl} = \frac{\sqrt{4 - 3\mu^2} - \mu}{2} \cdot f_y \qquad \text{(Eq. 3.41)}$$

$$\Lambda_{Mises} = \frac{\sigma_{x,\,pl}}{\sigma_{x,\,Rcr}} = \frac{\sqrt{4 - 3\mu^2} - \mu}{2} \cdot \bar{\lambda}_x^2 \qquad \text{(Eq. 3.42)}$$

2 ***Proportional load increase:*** For a specified ratio of the two membrane section forces/ stresses (Eq. 3.43), compute the meridional membrane stress (Eq. 3.45) which will cause yielding and the corresponding plastic load factor (Eq. 3.46).

$$\bar{\psi} = \frac{N_x}{N_\theta} = \frac{\sigma_x}{\sigma_\theta} \qquad \text{(Eq. 3.43)}$$

$$\sigma_{x,\,pl} = \frac{\bar{\psi}}{\sqrt{1 + \bar{\psi} + \bar{\psi}^2}} \cdot f_y \qquad \text{(Eq. 3.44)}$$

$$\Lambda_{Mises} = \frac{\sigma_{x,\,pl}}{\sigma_{x,\,Rcr}} = \frac{\bar{\psi}}{\sqrt{1 + \bar{\psi} + \bar{\psi}^2}} \cdot \bar{\lambda}_x^2 \qquad \text{(Eq. 3.45)}$$

where

$$\bar{\lambda}_x = \sqrt{\frac{f_y}{\sigma_{xRcr}}} \qquad \text{relative buckling slenderness parameter} \qquad \text{(Eq. 3.46)}$$

Whichever way is used the plastic strength is same and is represented by the curve in Figure 3.28.

3.6.2 Stress resultant oriented approximate yield criteria

The plastic capacity of cylindrical shells can be estimated approximately using the section forces (membrane & edge bending effects) obtained from linear analysis (LA). In the current study, the section forces (stress resultants) computed using the effective ring model analogy, Chapter 3.3, along with the different approximate yield criteria, Annex-A, will be used to estimate the plastic strength of axially loaded and internally pressurized cylinders.

For an illustrative cylindrical shell with R/t = 500, t = 1.0 cm, E = 21000 kN/cm^2, f_y = 24.0 kN/ cm^2 and ν = 0.3, the estimated plastic capacity according to the different yield criteria for a fixed and pinned boundary conditions are plotted in a pressure representation as shown in Figure 3.26 and Figure 3.27, respectively. Comparison of the plastic strengths according to the stress resultant oriented yield criteria with that of membrane Mises yield criterion can be made from these strength plots.

The plastic load factors estimated using all the approximate yield criteria are generally smaller than the load factors obtained using membrane Mises yield criterion because of the edge bending effects, i.e. the edge bending effects result in an increased circumferential section force and additional bending moments (both meridional and circumferential) at a meridional location that result in the fulfilment of the stress resultant oriented yield criteria at a relatively smaller load factor than the membrane Mises.

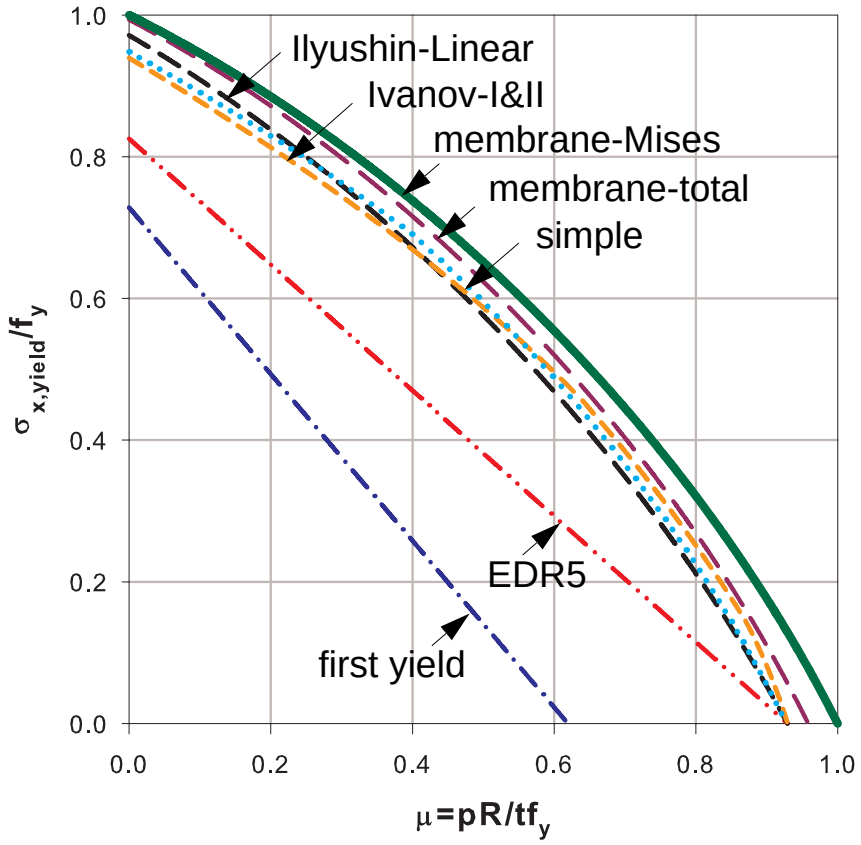

Figure 3.26 Approximate yield criteria R/t = 500: fixed bottom

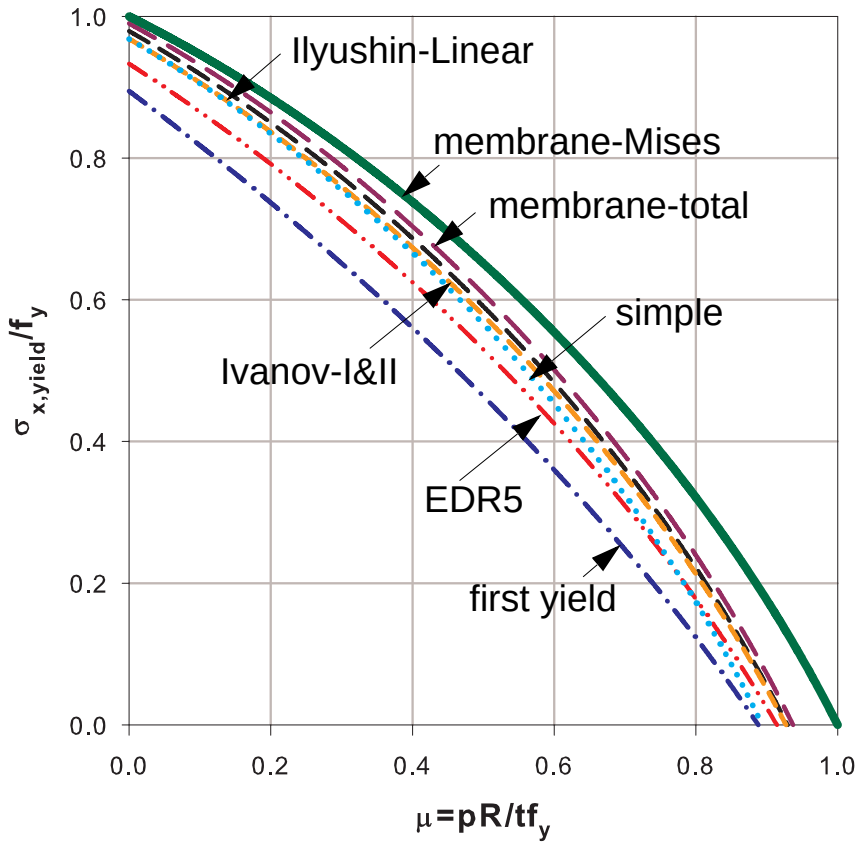

Figure 3.27 Approximate of yield criteria R/t = 500: pinned bottom

3.6.3 Small displacement materially nonlinear finite element analysis (MNA)

Numerical finite element small displacement materially non-linear analyses of cylindrical shells with a reference meridional tip-compressive ring loading equal to theoretical elastic critical buckling stress and varying the intesnisty of the internal uniform pressure were made. The results are plotted in the pressure representation (MNA/f_y vs. μ) representation as shown Figure 3.28.

It can be seen from the results that there is no difference between the materially nonlinear finite element analysis results and the results according to Von Mises pure membrane yield criterion. Hence, the results from the membrane Mises yield criterion will be used instead of the small displacement FE MNA results in the upcoming computations and discussions.

The fact that the finite element LBA and MNA for the cylindrical shell under consideration are equal with the membrane-based approximateb-LBA and Mises yield condition, respectively, makes the upcoming numerical analysis studies adaptable to the simple and straight forward stress design procedure as outlined in EN1993-1-6.

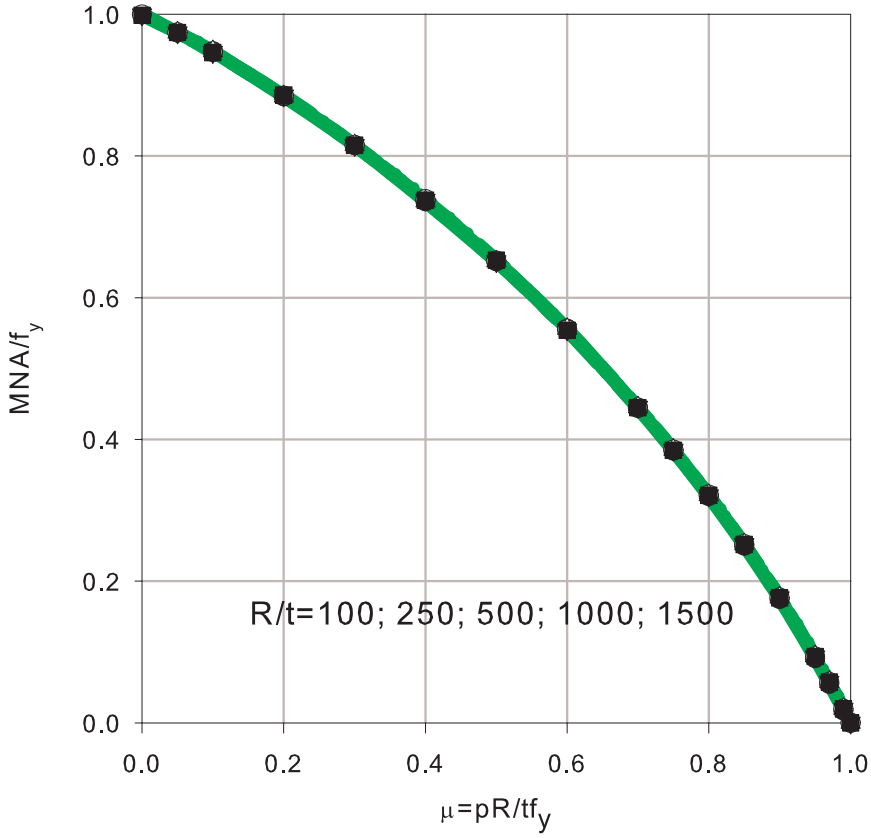

Figure 3.28 FE MNA for both fixed & pinned bottom; and bi-axial membrane Mises yield strength

3.7 Elastic-plastic buckling phenomena, analysis and strength

3.7.1 General concept of buckling phenomena

It has been repeatedly reported in many literatures that thin-walled cylindrical shells usually buckle elastically under pure axial compression. The respective buckling strength for such axially loaded cylindrical shells is usually lower than the theoretical elastic critical stress, the difference accounting for the decrease in buckling strength caused by the presence of various imperfections and geometric nonlinearity. The presence of an accompanying internal pressure, however, reduces this strength-weakening effect of the imperfections there by increasing the buckling strength of the shell. However, when the intensity of the internal pressure exceeds a certain value, the circumferential membrane stress becomes significant causing bi-axiality effect to come into play.

An unpressurized thin-walled cylindrical shell under an axial load buckles elastically forming a diamond type buckling mode, Esslinger & Geier (1975). Generally speaking, the diamond type elastic buckling phenomenon of an unpressurized cylindrical shell happens at locations of geometric imperfections in the shell interior (where there exist no edge constriction effects) forming two or three layers of buckles, Figure 3.29a.

As the internal pressurization increases, the weakening effect of the geometric imperfections will be reduced due to the stretching (strengthening effect) resulting from internal pressurization; and at the same time, the edge constriction (boundary condition) effects become stronger when compared with the unpressurized cylinder case. This edge constriction effect produces a decaying wave type prebuckling radial deformation leading to buckling phenomenon in a region close to the boundary. For this reason, at low internal pressure levels, the elastcic buckling mode will have a tendency of shifting towards the boundary condition resulting in an intermediate zigzag type buckling mode, Figure 3.29b. At medium internal pressure levels, the effect of imperfections is highly weakend and the effect of boundary condition becomes responsible for buckling, restricting the elastic buckling phenomenon to happen in a region close to the boundary, Figure 3.29c. On the other hand, as the internal pressurization further increases the buckles will become shorter in the meridonal direction and longer in the circumferential direction thereby producing localized buckle mode.

At very high internal pressure level, the localized prebuckling radial deformation which results from the very high edge constriction effect may suffer local yielding due to bending leading to elastic-plastic buckling near the boundary condition under very small axial load. This type of elastic-plastic buckling is known as elephant’s foot type buckling. Figure 3.30 shows buckling modes at different internal pressure levels and the evolution (as the intensity of the internal pressure increases) and happening of the elephant’s foot type buckling phenomenon under the

action of a very high internal pressure and bending moment.

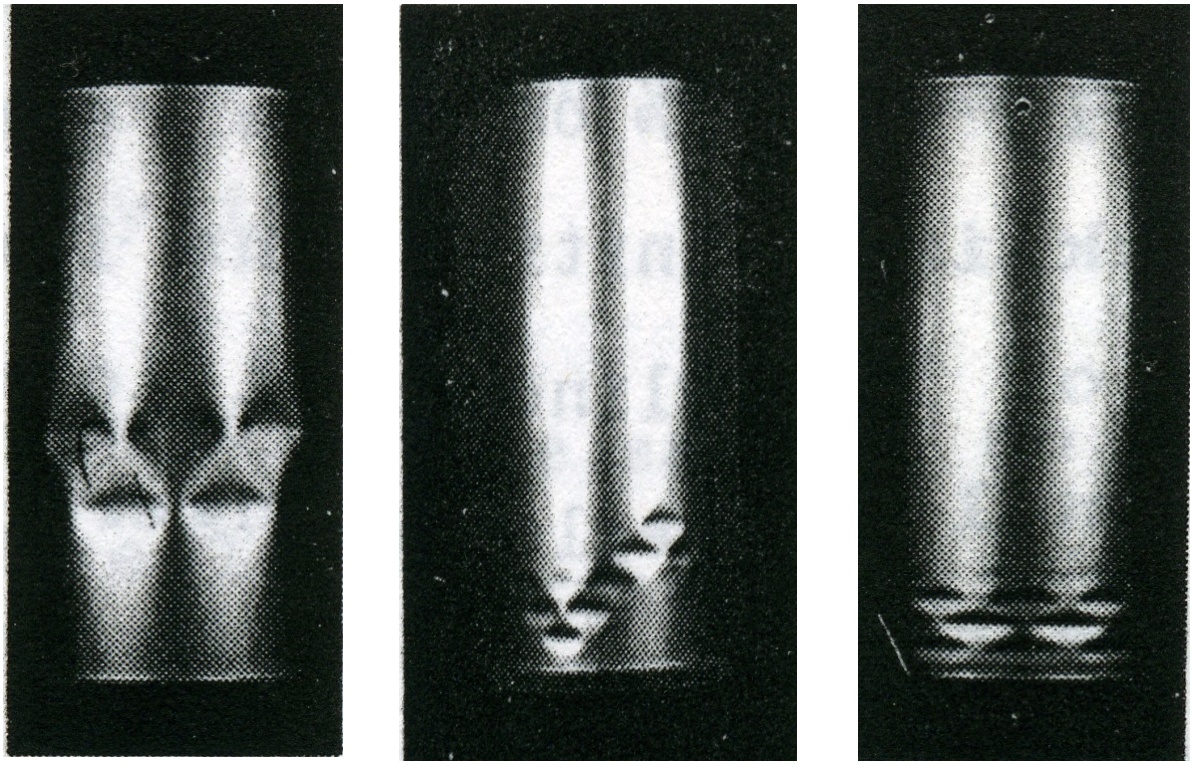

(a) zero pressure (b) low pressure (c) medium pressure

Figure 3.29 Elastic buckling modes (Esslinger): axial load and internal pressure

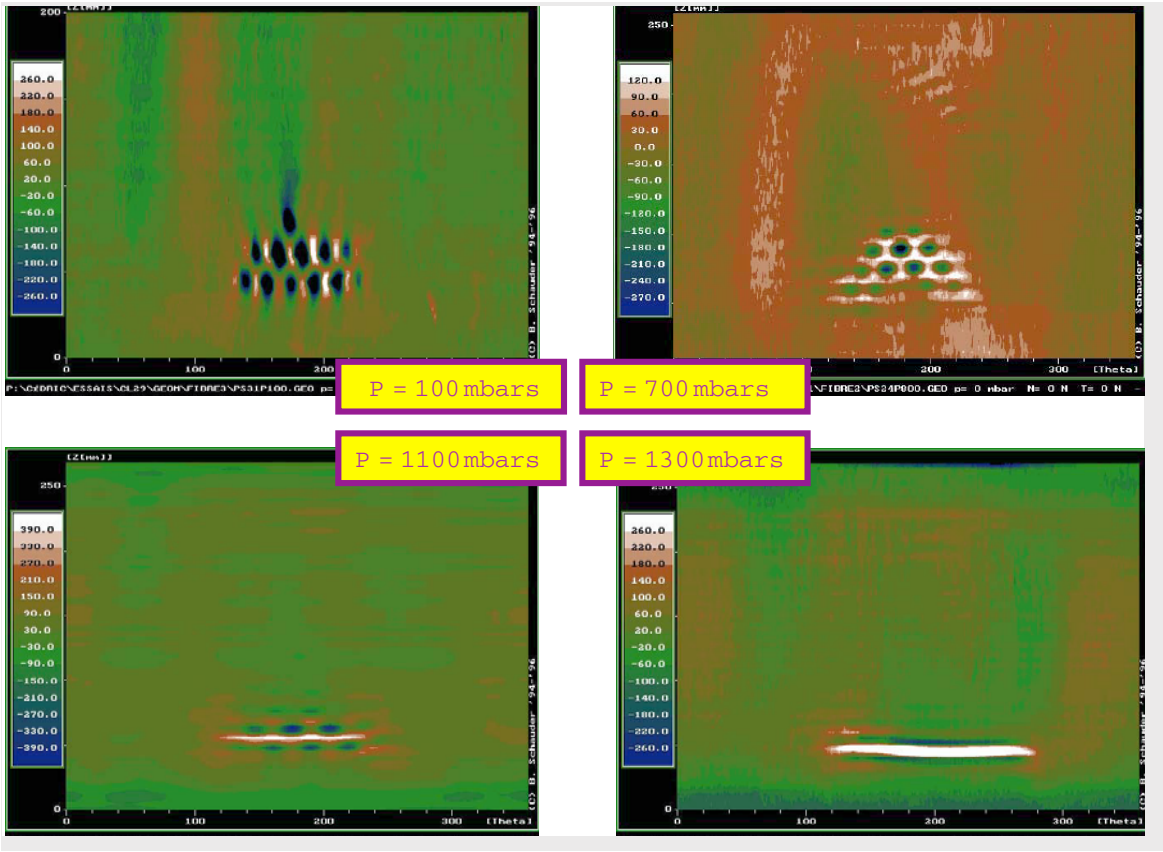

Figure 3.30 Elastic-plastic buckling mode evolution (INSA Lyon): bending and internal pressure

3.7.2 Elastic buckling strength

The pure elastic pressurized buckling strength of a cylindrical shell, computed using α_{xpe}, are plotted in the pressure representation (χ_x vs μ plot), Figure 3.31, for different shell slenderness, R/t, values of 250, 500, 750, 1000, and 1500 for fabrication tolerance quality class-A and for internal pressure intensity, μ = 0 to 1. The buckling strength for relatively thick shells are much greater than the uni-axial yield strength, f_y, and can not be seen in this plot where a maximum buckling strength equal to f_y is plotted. The strength values corresponding to the intersections of each of those curves and the ordinate of the graph represent the elastic-unpressurized buckling strengths of the respective clyinders. The bi-axial membrane Mises plasticity is also shown with uni-axial yield strengths at μ values of 0 and 1 corresponding to uni-axial meridional and uni-axial circumferential yielding, respectively. At other values of μ bi-axial membrane plasticity takes place. The same information is shown, Figure 3.32, in the capacity representation (χ_x vs $\bar{\lambda}_x$ plot) for different values of the internal pressure parameter μ. Both the pressure and capacity representations are combined to give the 3D plot, Figure 3.33, of the pure elastic imperfect characterstic buckling strength.

When there exist no elastic-plastic buckling interaction, the ultimate strength of the cylinder will be governed either by pure elastic imperfect buckling or pure plastic collapse depending on the internal pressure level and shell slenderness ratio. The envelope of these two strengths is shown in Figure 3.34.

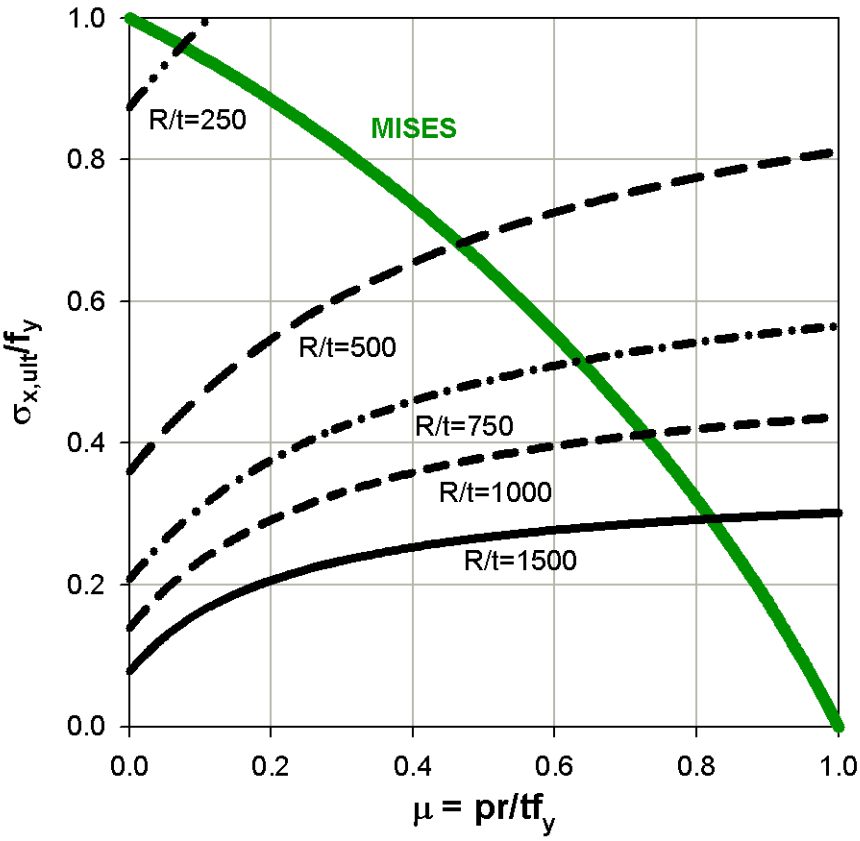

Figure 3.31 Pressurized pure elastic buckling strength for class-A & bi-axial membrane Mises

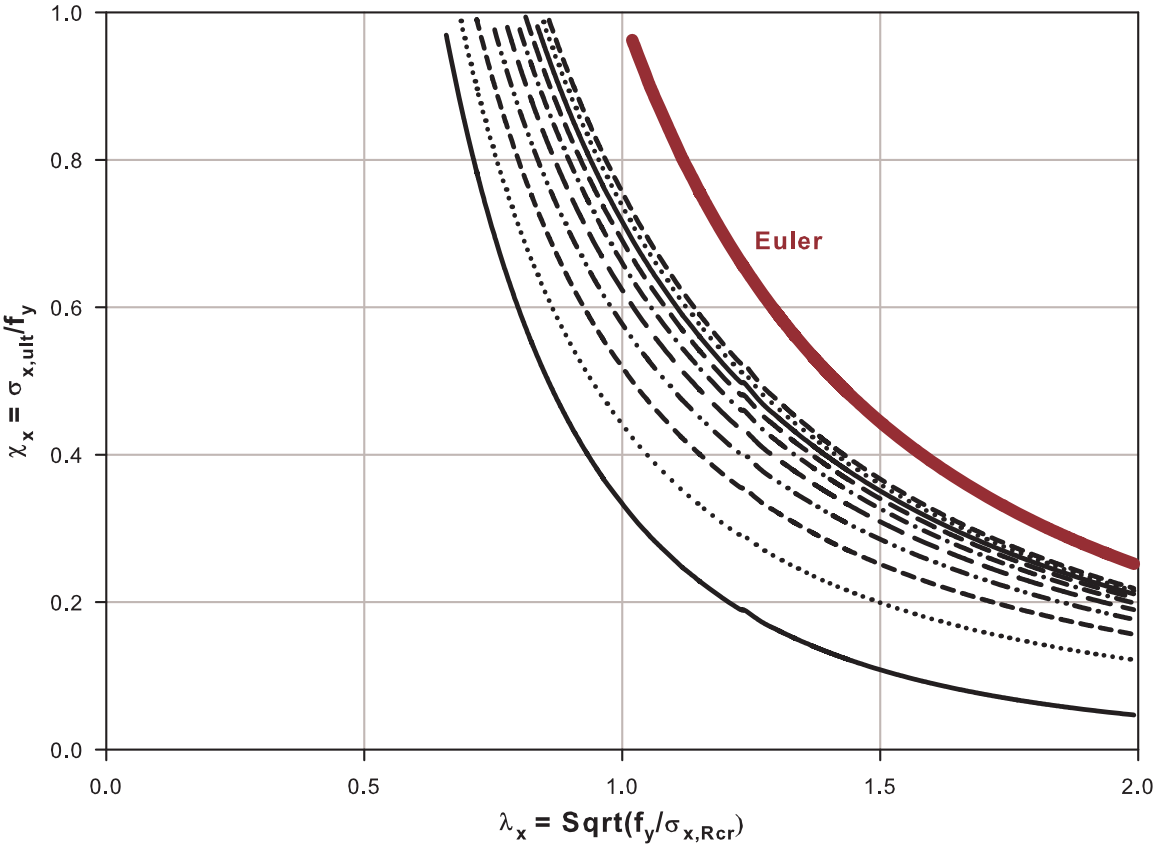

Figure 3.32 Pressurized pure elastic buckling strength for class-A & Euler's curve

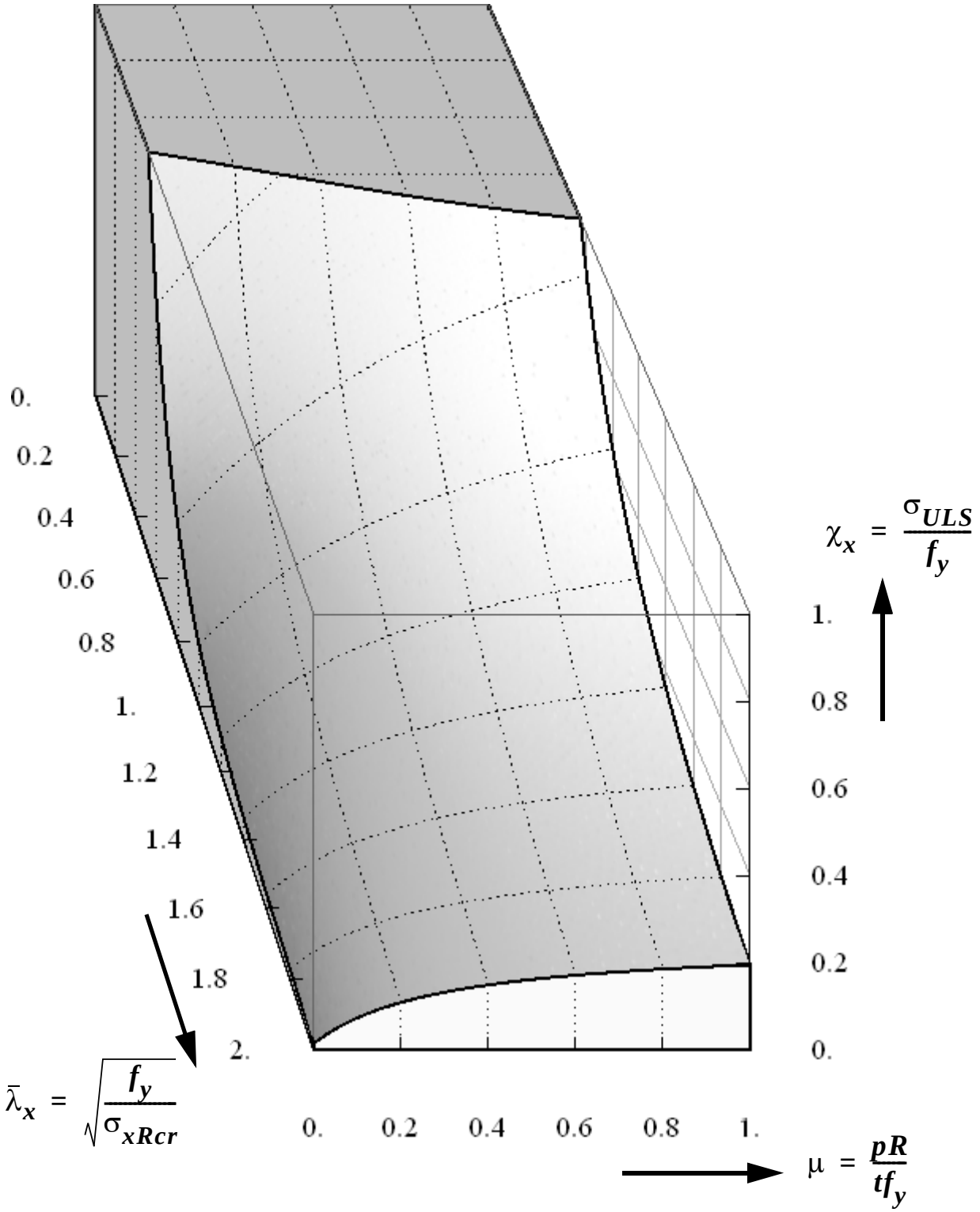

Figure 3.33 Imperfect elastic buckling strength for quality class-C (depends on pressure, shell slenderness ratio, and fabrication quality class)

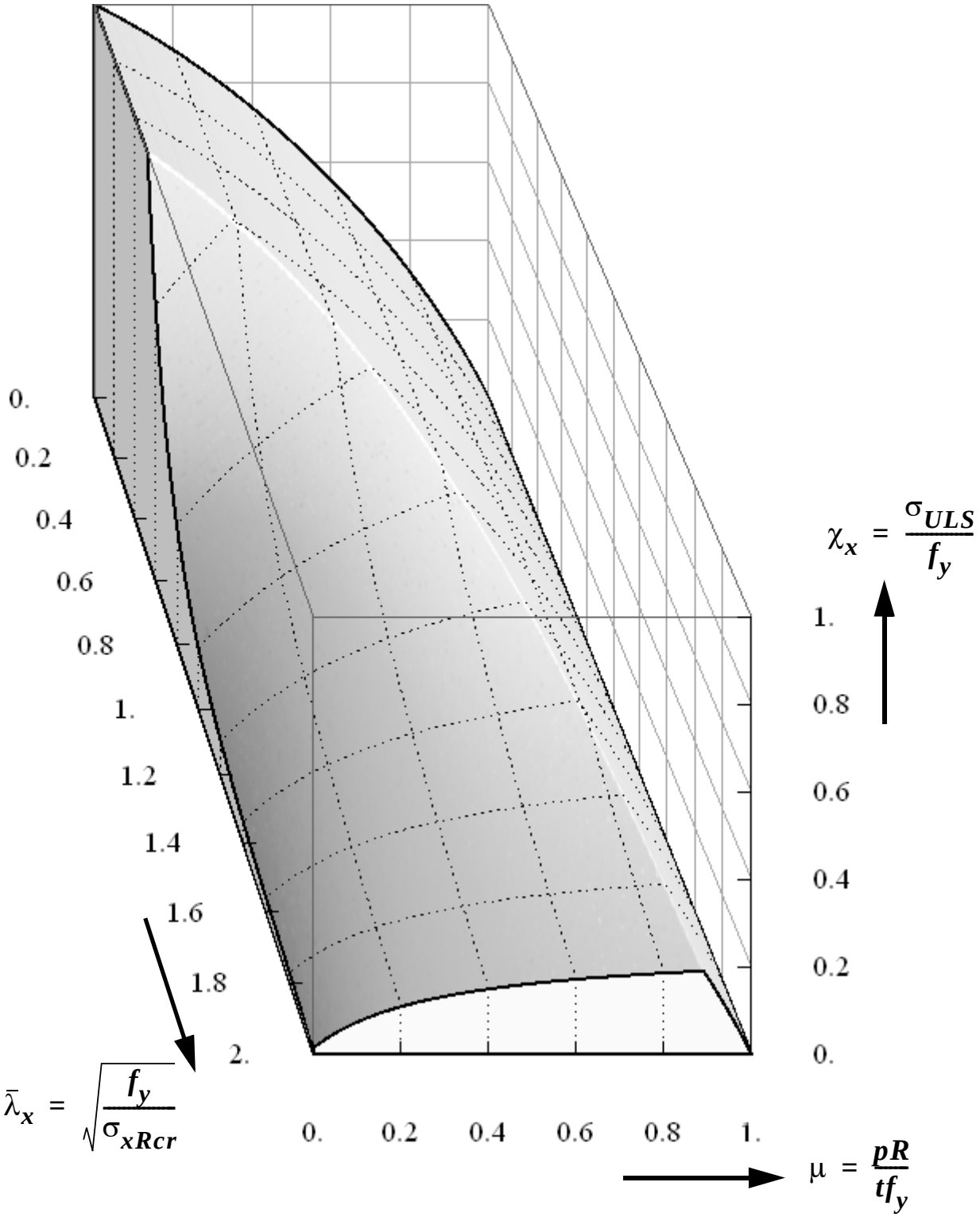

Figure 3.34 Envelope of imperfect elastic buckling strength and perfect bi-axial membrane Mises yield strength

3.7.3 Elastic-plastic buckling in the free shell interior

For relatively big shell slenderness values (thin shells) and low internal pressure cases, pure elastic buckling behaviour governs causing diamond-shaped buckles to form. As the internal pressure increases, the corresponding circumferential membrane stress becomes significant implying that the effect of biaxiality comes into play and an interaction between the elastic buckling and plasticity begins. At relatively very high internal pressure levels where the uni-axial circumferential yield condition is approached and if there is no edge bending disturbance, the failure will be governed by pure plastic collapse. This condition is represented by the plastic-plateau in the capacity representation.

The existence of two dimensional state of stress shows that yielding is represented by the von Mises plasticity criterion. As a result any possible elastic-plastic buckling phenomena will be governed by this yield criterion and not the uni-axial yield condition. This elastic-plastic interaction with membrane Mises plasticity guarantees that no elastic-plastic buckling strength will exceed the plastic capacity for a given loading state.

The characterstic strengths (pure plastic collapse, elastic-plastic buckling, and pure elastic buckling) of the shell, accounting for imperfections and bi-axial plasticity, in accordance with the stress design principle of EN1993-1-6 is predicted from the elastic-membrane Mises plastic interaction expressions (Eq. 3.47) to (Eq. 3.52) and is plotted in the capacity representation (χ_{Mises} vs $\bar{\lambda}_{\text{Mises}}$), Figure 3.36, depending on the value of the relative buckling slenderness parameter $\bar{\lambda}_{\text{Mises}}$. The relative buckling slenderness parameter $\bar{\lambda}_{\text{Mises}}$ implicitly includes the internal pressure, shell slenderness, modulus of elasticty, and yield stress values. The same curve is plotted in the pressure representation (χ_x vs μ), Figure 3.35, for different shell slenderness ratio values. A combined 3D plot of both the pressure and capacity representations is shown in Figure 3.37. The reduction in strength due to elstic-plastic buckling interaction is shown shaded in Figure 3.38.

$$\chi_{Mises} = \frac{\sigma_{x,\,Rk}}{\sigma_{x,\,Mises}} = \begin{cases} 1 & \text{for} \quad \bar{\lambda}_{Mises} \le \bar{\lambda}_o \\ 1 - \beta \cdot \left(\dfrac{\bar{\lambda}_{Mises} - \bar{\lambda}_o}{\bar{\lambda}_p - \bar{\lambda}_o} \right)^{\eta} & \text{for} \quad \bar{\lambda}_o < \bar{\lambda}_{Mises} < \bar{\lambda}_p \\ \dfrac{\alpha_{xpe}}{\bar{\lambda}^2_{Mises}} & \text{for} \quad \bar{\lambda}_p \le \bar{\lambda}_{Mises} \end{cases} \qquad \text{(Eq. 3.47)}$$

where

$$\bar{\lambda}_{Mises} = \sqrt{\frac{\sigma_{x,\,Mises}}{\sigma_{xRcr}}} \qquad \text{(Eq. 3.48)}$$

$$\bar{\lambda}_p = \sqrt{\frac{\alpha_{xpe}}{1-\beta}} \qquad \text{(Eq. 3.49)}$$

the elastic-plastic buckling parameters η, $\bar{\lambda}_o$, and β are given as

Interaction exponent:

$$\eta = 1.0 \qquad \text{(Eq. 3.50)}$$

Squash limit relative slenderness:

$$\bar{\lambda}_o = 0.2 \qquad \text{(Eq. 3.51)}$$

Plastic range factor:

$$\beta = 0.6 \qquad \text{(Eq. 3.52)}$$

Since no geometrically and materially nonlinear analysis of imperfect cylindrical shells and tests were undertaken to investigate the actual elastic-plastic buckling interaction in the free shell interior of an axially compressed internally pressurized cylindrical shell, the plastic buckling parameters of an axially compressed unpressurized cylinder are adopted in the elastic-plastic interaction procedure to predict the elastic-plastic buckling strengths for buckling in the free shell interior. As will be seen later in this work, however, few GMNLI analyses were made to check the validity of the mentioned strength prediction procedure for imperfection-led elastic-plastic buckling in the shell interior where no edge consticion exists. Despite these few geometrically and materially nonlinear analysis results for imperfection-led elastic-plastic buckling in the shell interior, the aforementioned procedure with the basic plastic interaction parameters will be referred to whenever buckling in the free shell interior is involved. This is because of the open question about the choice of a worst possible imperfection nature.

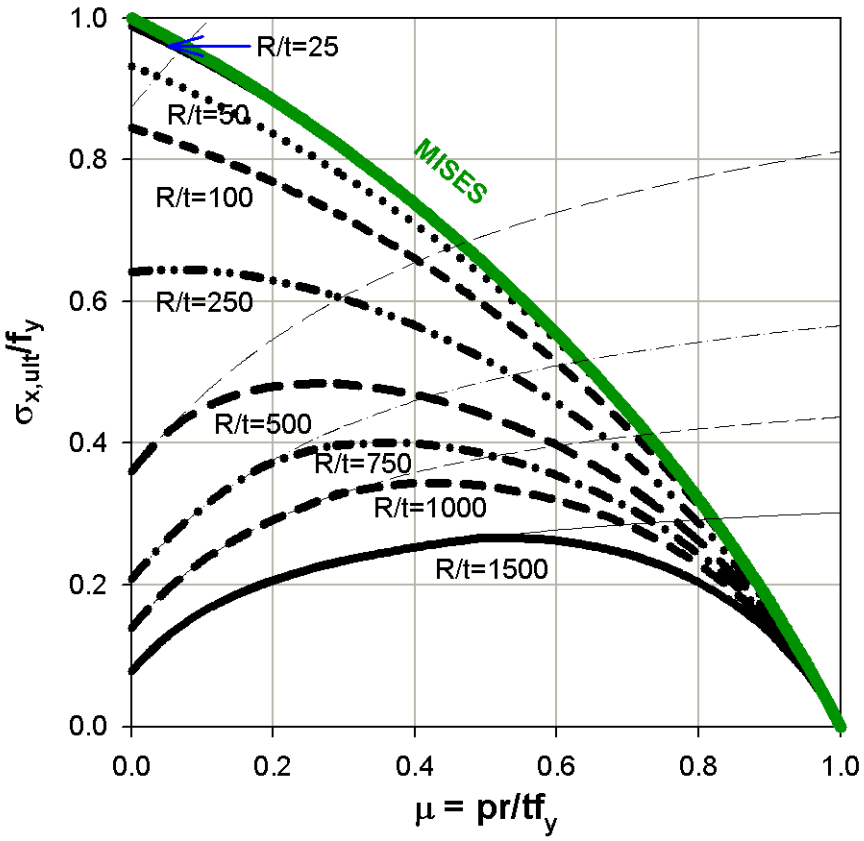

Figure 3.35 E-P interaction using bi-axial membrane Mises & basic plastic parameters

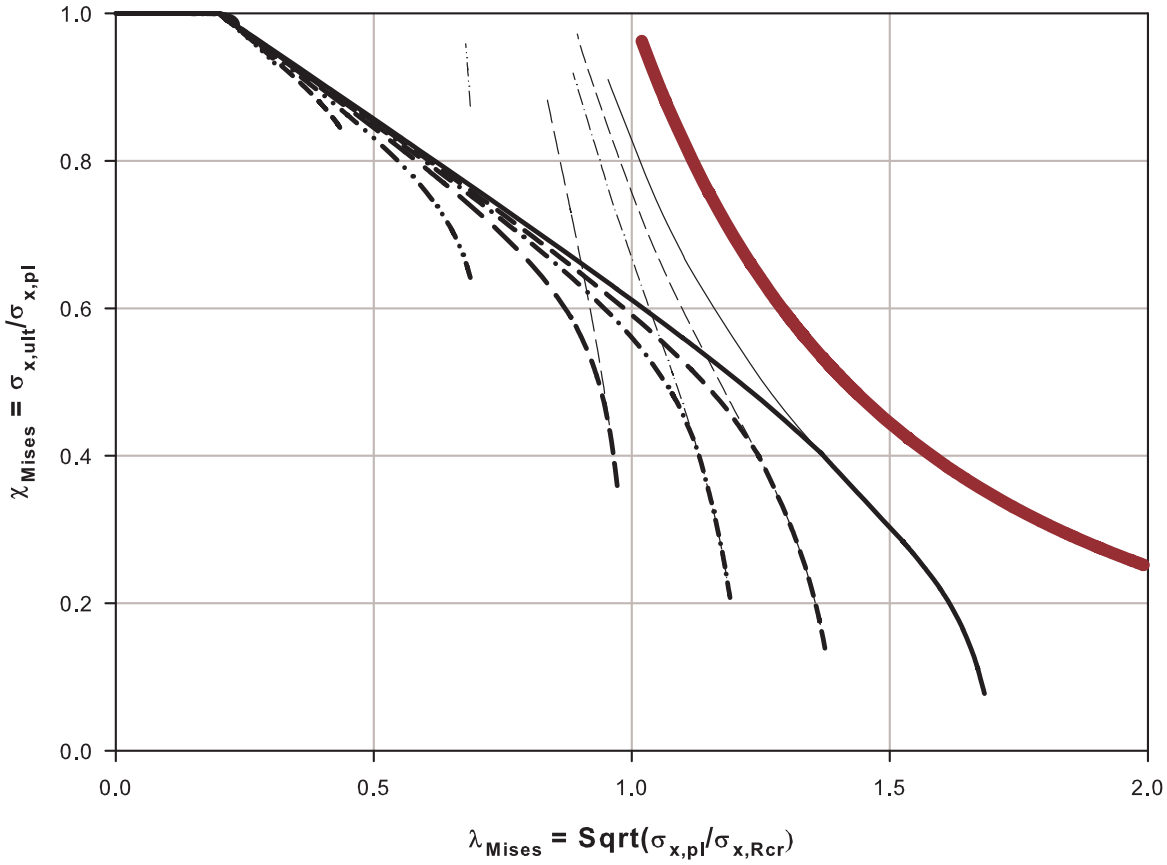

Figure 3.36 E-P interaction using membrane Mises & basic plastic parameters

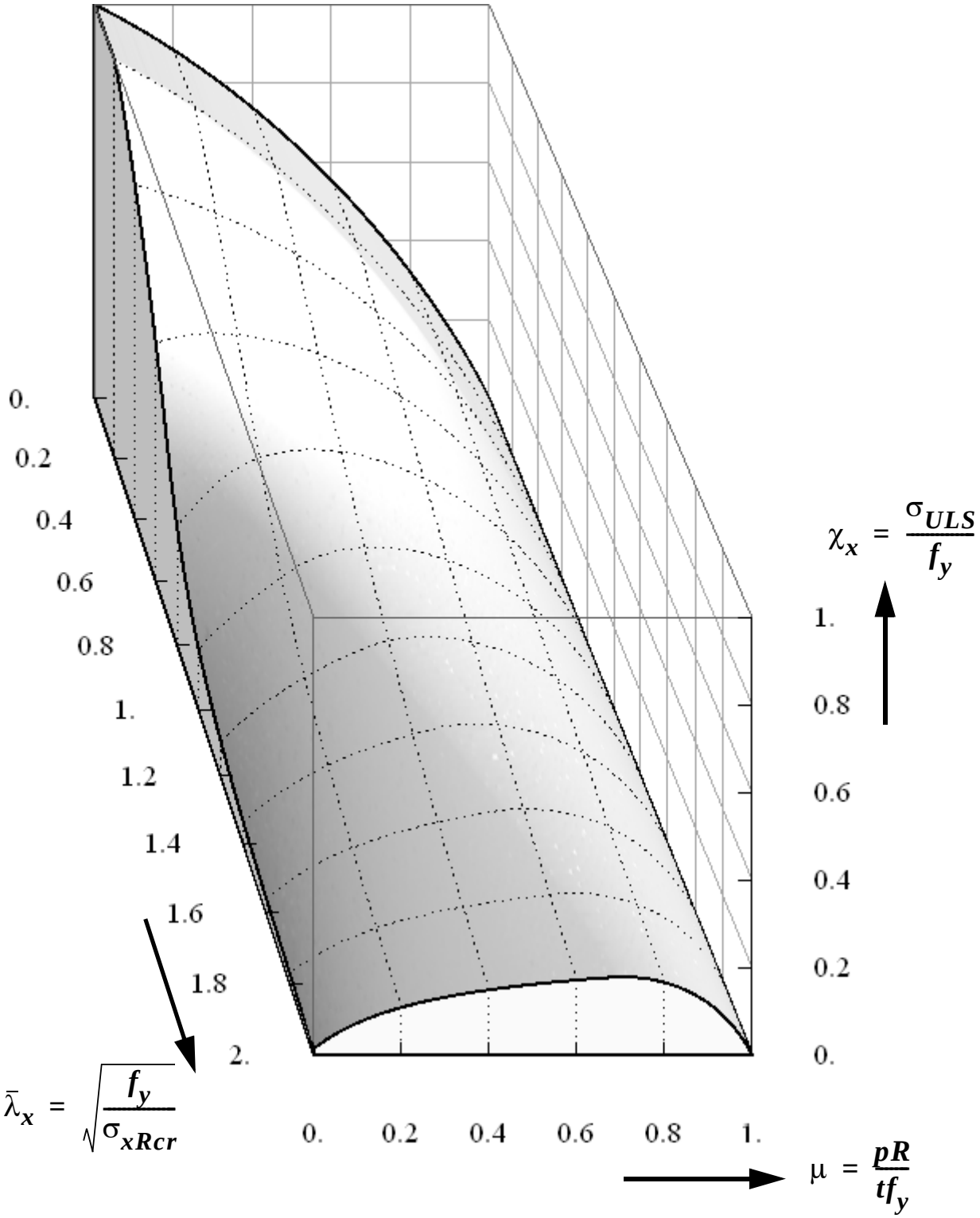

Figure 3.37 Elastic-plastic buckling interaction using bi-axial membrane Mises yield condition & basic plastic buckling parameters

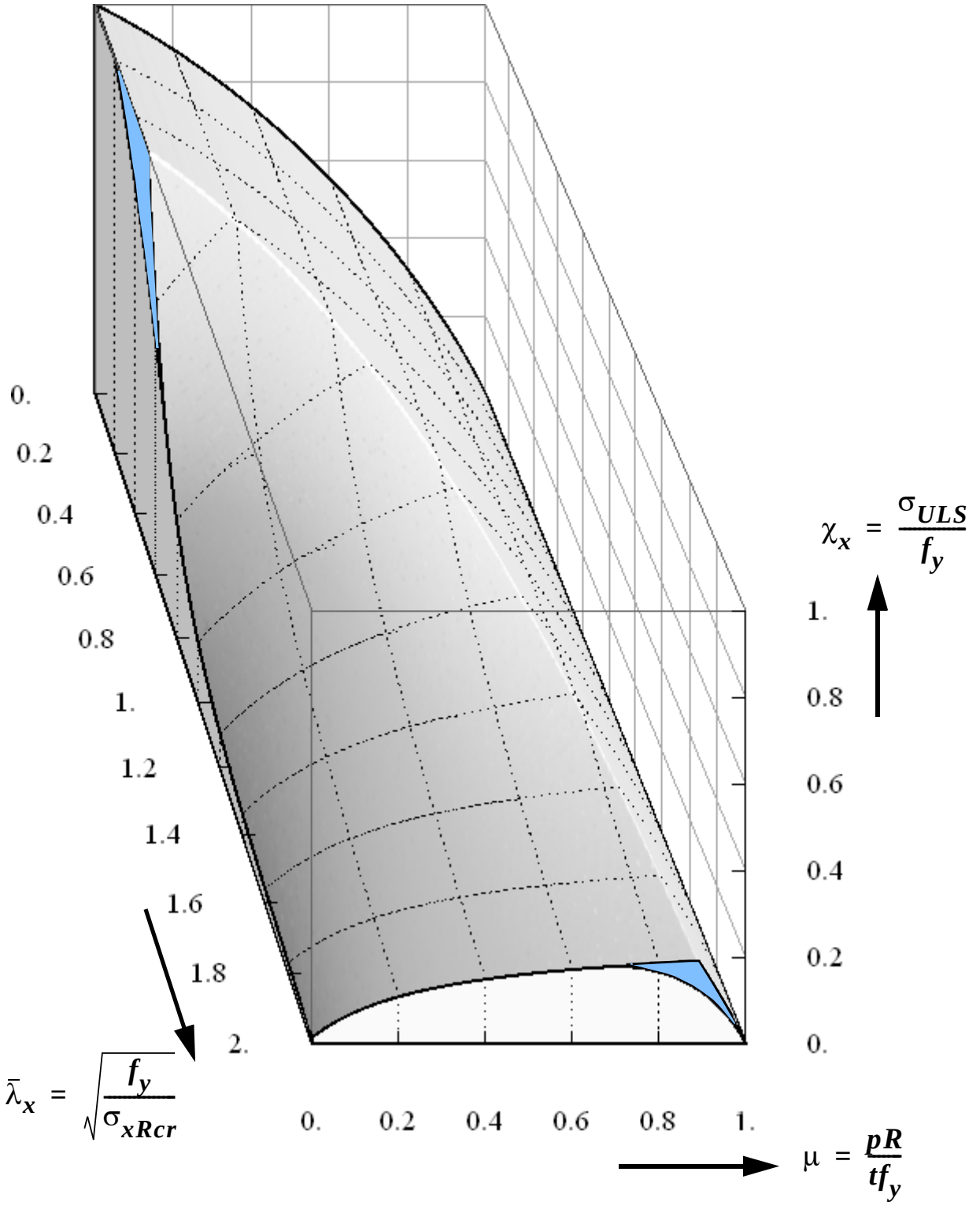

Figure 3.38 Comparison of elastic-plastic buckling interaction using basic plastic buckling parameters with the envelope of imperfect elastic buckling strength & perfect bi-axial membrane Mises yield strength

3.7.4 Axisymmetric elastic-plastic buckling of perfect cylindrical shells

3.7.4.1 Geometrically and materially nonlinear finite element analysis (GMNA)

As discussed in the previous section, an unpressurized cylindrical shell under pure axial compressive load tends to radially expand due to Poisson's effect. An internally pressurized cylindrical shell under axial compressive load tends to radially expand due to the combined effects of both the internal pressurization and Poisson's effect. The presence of boundary conditions, however, constricts this expansion causing local bending under the action of the axial compressive load. Similar local bending effects can be observed at locations of change in wall thicklness, ring stiffeners, or local axisymmetric imperfections causing immature buckling under a small meridional compression. Thus, the presence of significant internal pressure will have a destabilizing effect there by reducing the buckling strength of the shell. Such a buckling type, caused by local bending adjacent to the boundary, is termed as an "elephant's-foot" type buckling and the corresponding strength as elephant-foot buckling strength. The main focus of the current study is to investigate the elastic-plastic buckling phenomenon and corresponding buckling strength close to the lower supported shell boundary where local edge bending disturbances play a leading role.

Comprehensive parametric studies are carried out varying the shell slenderness, shell lower bundary conditions, and the intensity of the internal pressurization. More specifically, geometrically and materially nonlinear finite element analyses which resulted in localized axisymmetric buckling modes were made on cylindrical shells with R/t = 100, 250, 500, 1000, 1500 by varying the internal pressure value from zero-pressure (pure axial loading case) to a pressure value that produces circumferential uni-axial yielding, i.e. a circumferential membrane stress equal to the yield stress of the material. Boundary conditions of PIN or FIX at bottom and rotational restraint at top were examined for each R/t and varying the internal pressure value. Small displacement linear buckling analysis (LBA) and small displacement materially nonlinear analysis (MNA) results are used for reference purposes. Those reference strengths are given (see discussion above) by the classical elastic critical buckling stress and bi-axial membrane Mises yield condition, respectively. All the results are plotted in both the pressure (χ_x vs. μ) and capacity curve (χ vs. $\overline{\lambda}_{pl}$) representations.

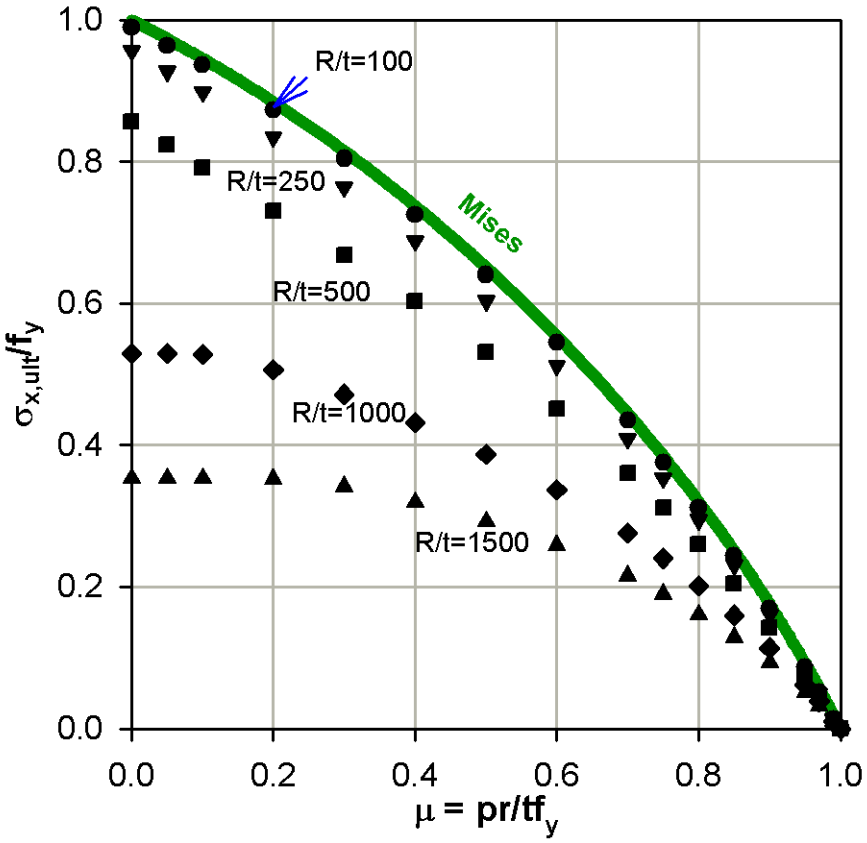

Figure 3.39 Geometrically & materially nonlinear (elephant's-foot) strength: fixed

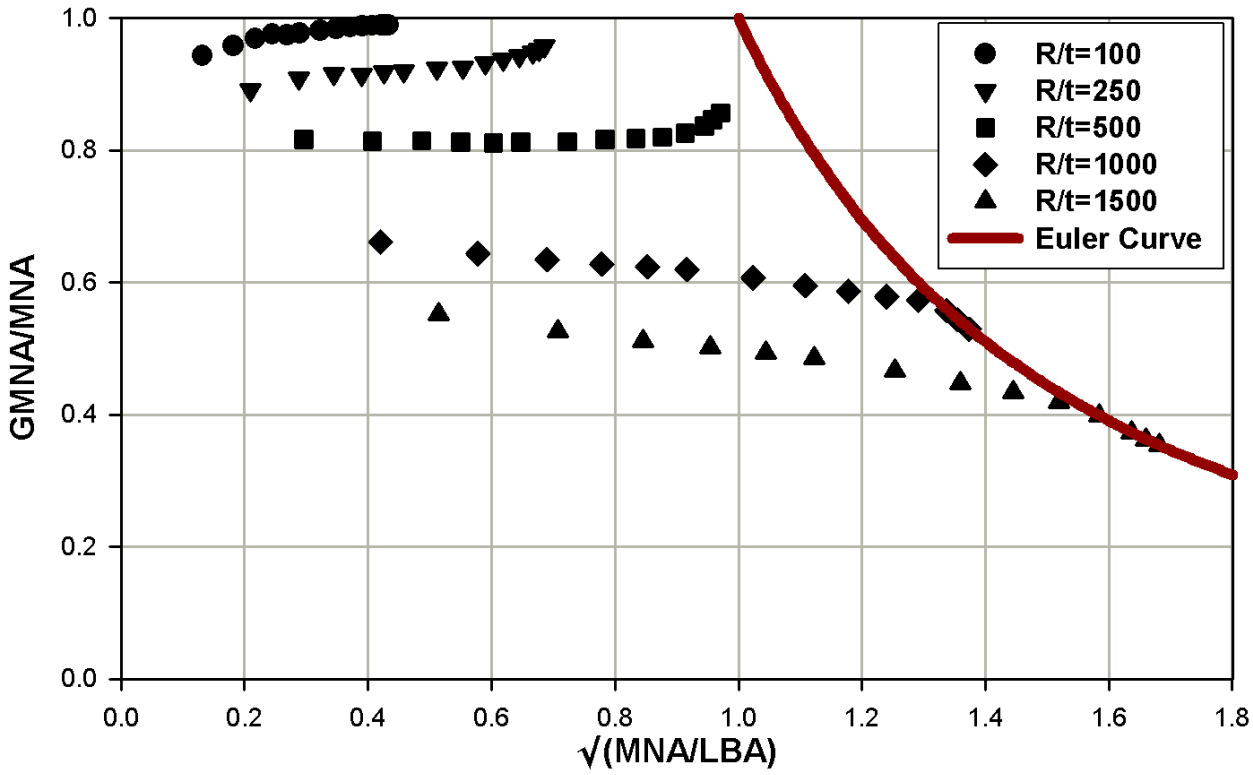

Figure 3.40 Geometrically & materially nonlinear (elephant's-foot) strength: fixed

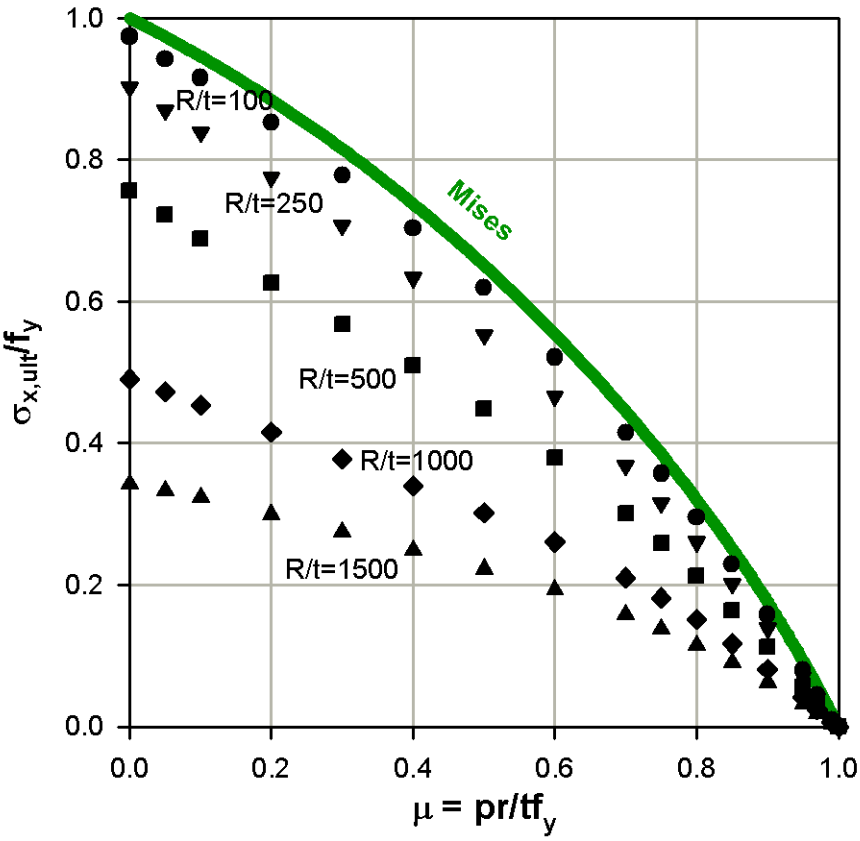

Figure 3.41 Geometrically & materially nonlinear (elephant's-foot) strength: pinned

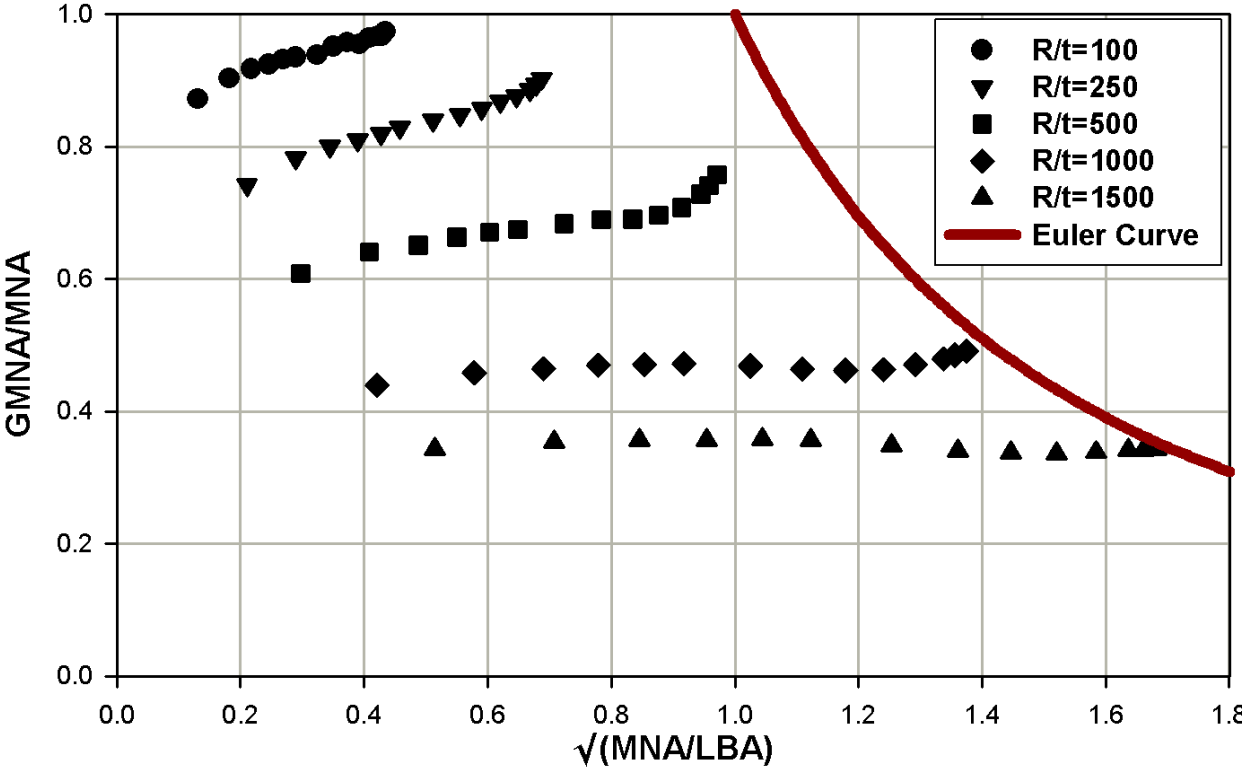

Figure 3.42 Geometrically & materially nonlinear (elephant's-foot) strength: pinned

The geometrically and materially nonlinear effects in the GMNA results are responsible for the localized axisymmetric buckling at the pinned (or fixed) cylindrical shell boundaries and for the lower capacity when compared with the geometrically linear but materially nonlinear MNA counterpart. When the geometric nonlinearity effects are very small as in the case of relatively thick-walled cylindrical shells, the GMNL buckling strengths will be closer (or atmost equal) to the pure plastic strength of the shell. On the other hand, when both the geometric and material nonlinearity effects are very small as in the case of relatively thin-walled cylindrical shells and lower internal pressure values, the GMNL buckling strengths will be closer (or atmost equal) to the pure elastic buckling strength of the perfect shell. These facts can be observed from the plots of the GMNA results shown in Figure 3.39 to Figure 3.42 for both the fixed and pinned bottom boundary conditions.

It can be deduced from the above discussion (with the help of Figure 3.39 to Figure 3.42) that the geometric and material nonlinear (GMNL) load carrying capacity, which is upper-bounded by the fulfillment of either the membrane Mises yield condition or the elastic critical buckling stress (whichever is smaller), can be put into direct relationship with the small displacement materially nonlinear (MNL) counterpart which corresponds to the pure bi-axial membrane Mises load carrying capacity. This relationship between the geometrically and materially nonlinear buckling strength and pure plastic carrying capacity of the shell, accounting for the large displacement (geometric nonlinearity) effects which is relevant for localized axisymmetric buckling at the pin-ended or fix-ended cylindrical shell boundaries, depends on the shell slenderness ratio and can be dealt with in two different ways depending on the curve fitting to be used and representation procedure to be followed. These are:

- **depending on both the shell slenderness and the intensity of the internal pressure**
- **depending on the shell slenderness alone (i.e. independent of internal pressurization)**

These two different ways are discussed in detail in the following section. It has to, however, be emphasized that in both procedures the same GMNA numerical results are at the background. The question, therefore, has to be put after the right choice of the reference parameters for non-dimensional representation purposes and the best but suitable choice of fitting curve type.

GMNA versus MNA strength: internal pressure dependent relationship

The effects of internal pressurization varation on the perfect elephant's-foot buckling strength can be seen from the capacity representations. One way of expressing this strength with respect to the pure plastic capacity of the shell is obtained using straight-line fitting of the GMNL strengths from the capacity representation. The resulting linear relationship, for a given R/t, between the GMNL to MNL strength ratio and the shell buckling slenderness value, $\bar{\lambda}_{\text{Mises}}$, results in a nonlinear relationship of the strength ratio and the internal pressure parameter μ. This nonlinear relationship is written as follows:

$$\frac{GMNA}{Mises} = 1 - \beta_{EFoot} = d_{var} + k \cdot \bar{\lambda}_x \cdot \sqrt{\sqrt{4 - 3\mu^2} - \mu} \qquad \text{(Eq. 3.53)}$$

$$d_{var} = \begin{cases} 0.2 \cdot e^{\left(\frac{1.75}{1.15 + \rho}\right)} & \text{for pinned bottom} \\ 0.3 \cdot e^{\left(\frac{2.75}{2.3 + \rho}\right)} & \text{for fixed bottom} \end{cases} \qquad \text{(Eq. 3.54)}$$

$$k = \begin{cases} 0.25 - 0.35\rho + 0.11\rho^2 & \text{for pinned bottom} \\ 0.1 - 0.25\rho + 0.08\rho^2 & \text{for fixed bottom} \end{cases} \qquad \text{(Eq. 3.55)}$$

$$\rho = \frac{R/t}{1000} \qquad \text{(Eq. 3.56)}$$

These approximate perfect elephant's-foot strength according to the pressure-dependent reduction of the plastic strength is plotted in the pressure representation, Figure 3.43 and Figure 3.44, for fixed and pinned bottom boundary conditions, respectively, and for the different shell slenderness ratio values, where the corresponding numerical GMNL strength results are also shown for comparison purposes. There is a good fit between the approximate expression and the numerical analyses results for the entire pressure range. At very low internal pressure levels, however, the approximate expressions result in strength values somehow higher than the pure elastic buckling strength of the perfect shell which should not generally be the case. In such cases the fitting curve should always be cut-off by the pure elastic buckling strength of the perfect shell. However, the elephant-foot type buckling, as previously discussed, is relevant only for very high internal pressure values. For this reason it is better to use a somewhat simpler expression to relate the two strengths and at the same time fitting the numerical GMNA results in the high pressure range where the elephant's-foot buckling phenomenon governs failure.

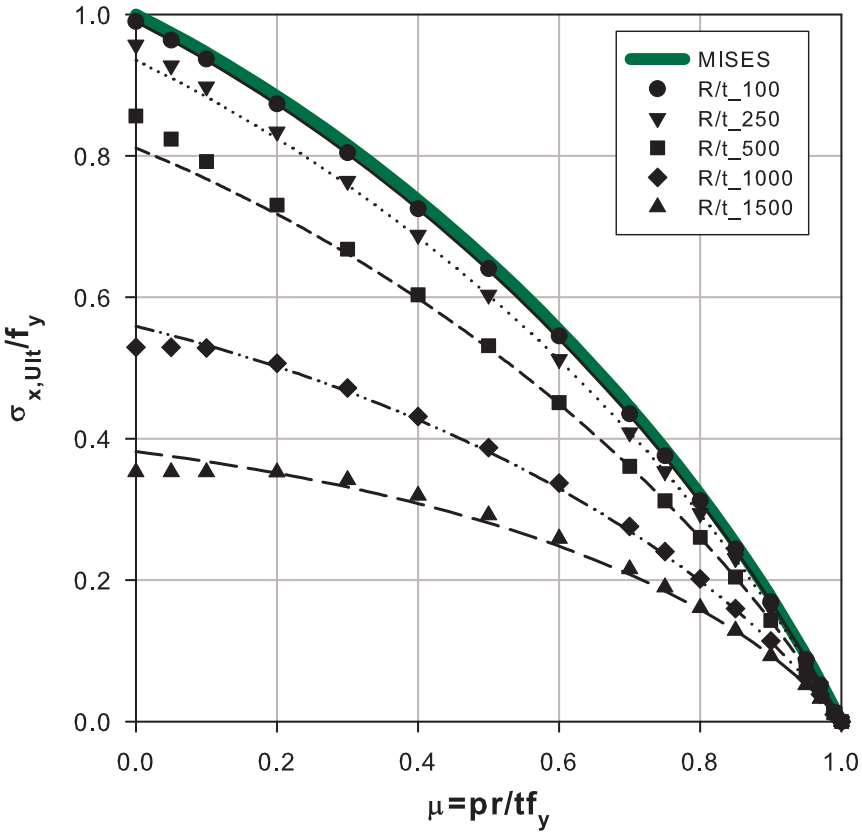

Figure 3.43 GMNL strength as μ & R/t dependent reduction of MNL strength: fixed

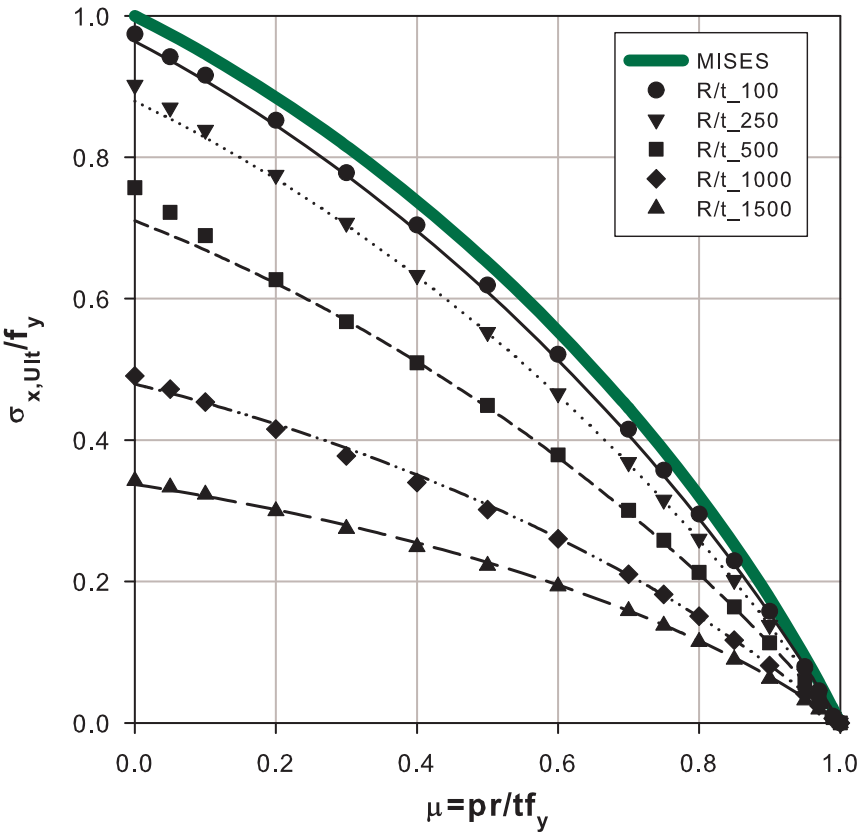

Figure 3.44 GMNL strength as μ & R/t dependent reduction of MNL strength: pinned

GMNA versus MNA strength: internal pressure independent relationship

In this case, the reduction in buckling strength due to geometric nonlinearity is taken to be constant for a given shell slenderness ratio independent of the internal pressure intensity in such a way that there will be a good conservative fit for relatively high internal pressure levels ($\mu > 0.5$ about) where the elephant's-foot type buckling becomes deterministic.

For all the pressure levels, the geometric and material noninear buckling strength can be expressed as a constant reduction of the plastic (MNL or membrane Mises) strength. This constant reduction of the plastic strength depends only on the shell slenderness, R/t, and fits well to the GMNL strengths at relatively high internal pressure levels ($\mu > 0.5$ about) for all R/t ratio, where the elephant's-foot buckling becomes deterministic. Once again, for very low internal pressure levels, the fitting curve results in strength values higher than the pure elastic buckling strength of the perfect shell which should not be the case and therefore should always be cut-off by the later strength curve. The constant reduction factor relating the perfect elephant's-foot buckling strength with the pure bi-axial plastic strength is given by

$$d_c = 1 - \beta_{EFoot} = \frac{GMNA}{Mises} \qquad \text{(Eq. 3.57)}$$

$$\beta_{EFoot} = \begin{cases} 0.8(1 - e^{-1.15\rho}) & \text{for pinned-bottom} \\ 0.75(1 - e^{-0.75\rho}) & \text{for fixed-bottom} \end{cases} \qquad \text{(Eq. 3.58)}$$

$$\rho = \frac{R/t}{1000} \qquad \text{(Eq. 3.59)}$$

The perfect elephant-foot strengths according to the pressure-independent constant reduction of the plastic strength are plotted in the pressure representation, Figure 3.45 and Figure 3.46, for fixed and pinned bottom boundary conditions respectively and for the different shell slenderness values, where the GMNA results from finite element numerical analysis are also shown for comparison purposes. It can be seen from the plots that there is a good conservative fit between the approximate expression and the numerical analysis results for the relatively high internal pressure intensity range as it should be.

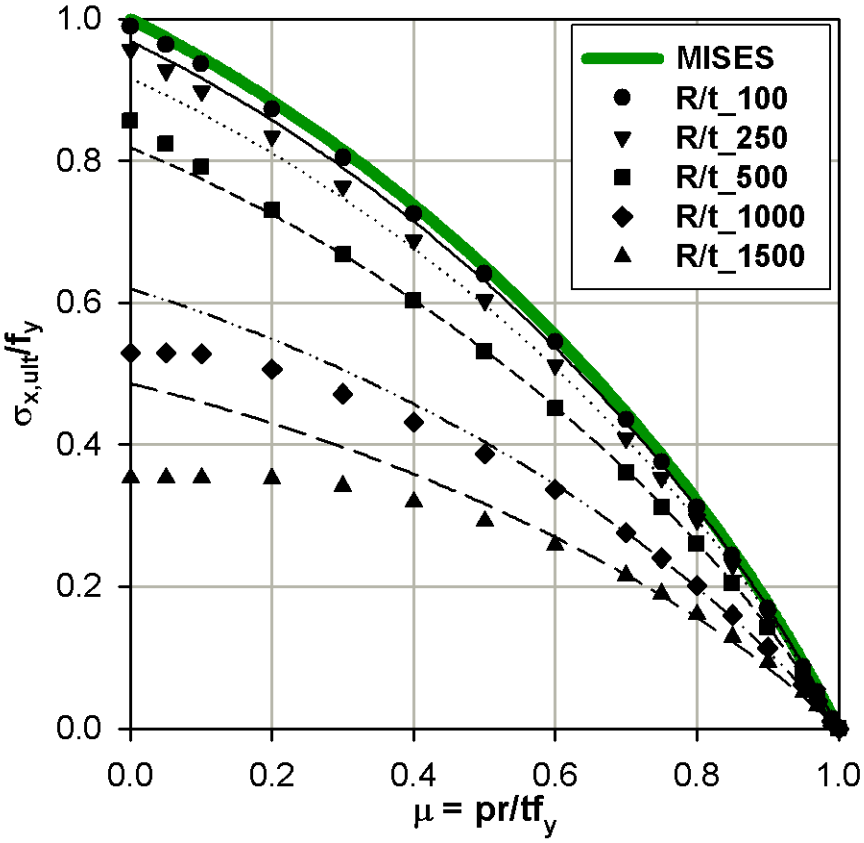

Figure 3.45 GMNL strength as R/t dependent reduction of MNL strength: fixed

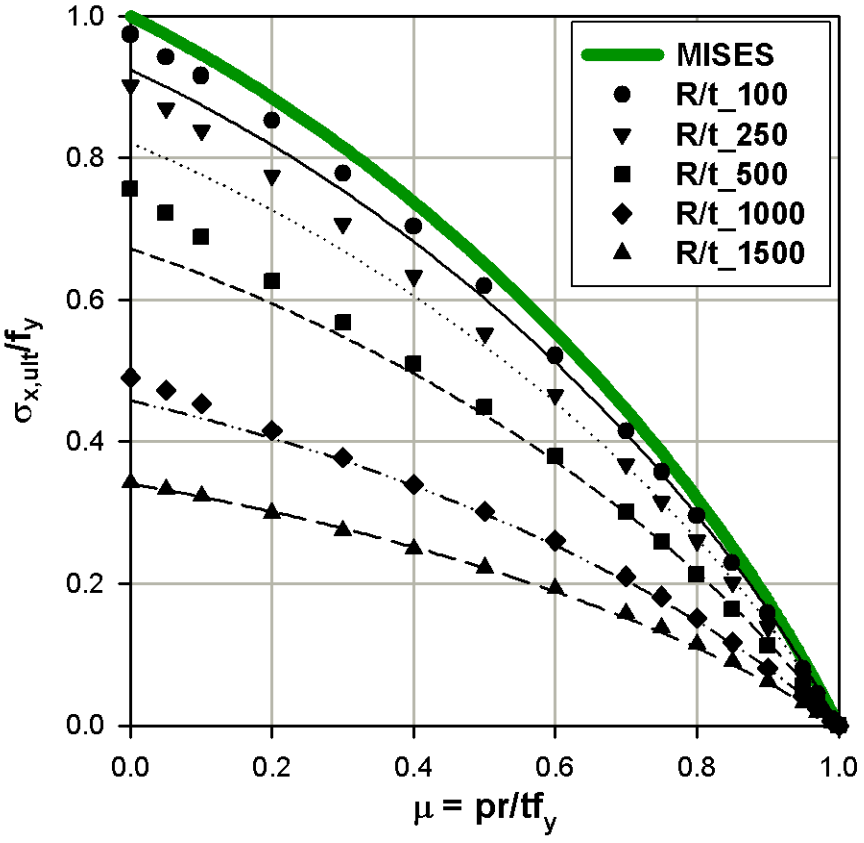

Figure 3.46 GMNL strength as R/t dependent reduction of MNL strength: pinned

3.7.4.2 Analytical model based on theory of second order with material nonlinear effects

The geometric and material nonlinear effects of a cylindrical shell can be analytically modelled approximately using a combination of theory of second order (Th.2.o.) and the stress resultant oriented approximate yield criteria. In doing so, the beam on an elastic foundation model of a cylindrical shell has been used, see Annex.

In the analytical model, the elastic-plastic buckling loads are computed in an iterative manner as discussed below. Once the second order effect due to an axial compression is considered in the force equilibrium equation (in the transverse direction), a trial load factor is applied with which the section force distributions along the meridian are computed. Using these section forces (stress resultants), a check is made for possible yield at each point along the meridian using one of the approximate yield criteria already discussed, Chapter 3.6. If yield criteria is not fulfilled, apply another load factor depending on the result obtained, i.e. if the yield surface defined by the approximate yield function is exceeded, apply a smaller load factor; if the result lies with in the yield surface, apply a larger load factor. This procedure is repeatedly used until the yield criterion is exactly fulfilled. The fulfilment of the yield criterion shows through-thickness yielding; and therefore, when combined with Th.2.o, represents an approximate elastic-plastic buckling.

Such analysis using Ivanov's approximate yield criterion has been made in the current study for both fixed & pinned-bottom cylindrical shells of slenderness ratio R/t = 500 & 1000 with t = 1.0 cm, E = 21000 kN/cm^2, f_y = 24.0 kN/cm^2 and ν = 0.3. The results obtained from the analytical model along with the geometrically and materially nonlinear analysis results obtained using ABAQUS are shown in Figure 3.47 & Figure 3.48 for R/t = 500; and Figure 3.49 & Figure 3.50 for R/t = 1000.

A second analysis using the "first-yield" approximate yield criterion has been done for the cylinder with shell slenderness ratio R/t = 1000 and the results are shown in Figure 3.51 & Figure 3.52, along with Ivanov's yield criterion and ABAQUS results, for the fixed and pinned bottom boundary conditions, respectively.

At very high internal pressure levels where the axial compression needed to cause elastic-plastic buckling is very small, the strength results from theory of second order are close to the approximate plastic strength of the shell. As it has been already discussed, at relatively high internal pressure levels, the edge bending effects cause approximate yield at relatively low load factors. Apart from this, an overall assessment of the results obtained from the analytical model tells that such analysis gives relatively bigger load factors than the ABAQUS results when compared relative to the corresponding plastic strengths. One possible reason for this effect can be the fact that in the case of a finite element numerical analysis, the stiffness of the shell is updated at each load increment thus any effects of plasticity are automatically applied thereby reducing the stiffness and hence, needs a relatively smaller load factor to cause elastic-plastic buckling. Whereas in the combined consideration of the Th.2.o. and approximate yield criterion, the shell remains elastic which is relatively stiff and hence, needs a relatively higher load factor to fulfil approximate elastic-plastic buckling.

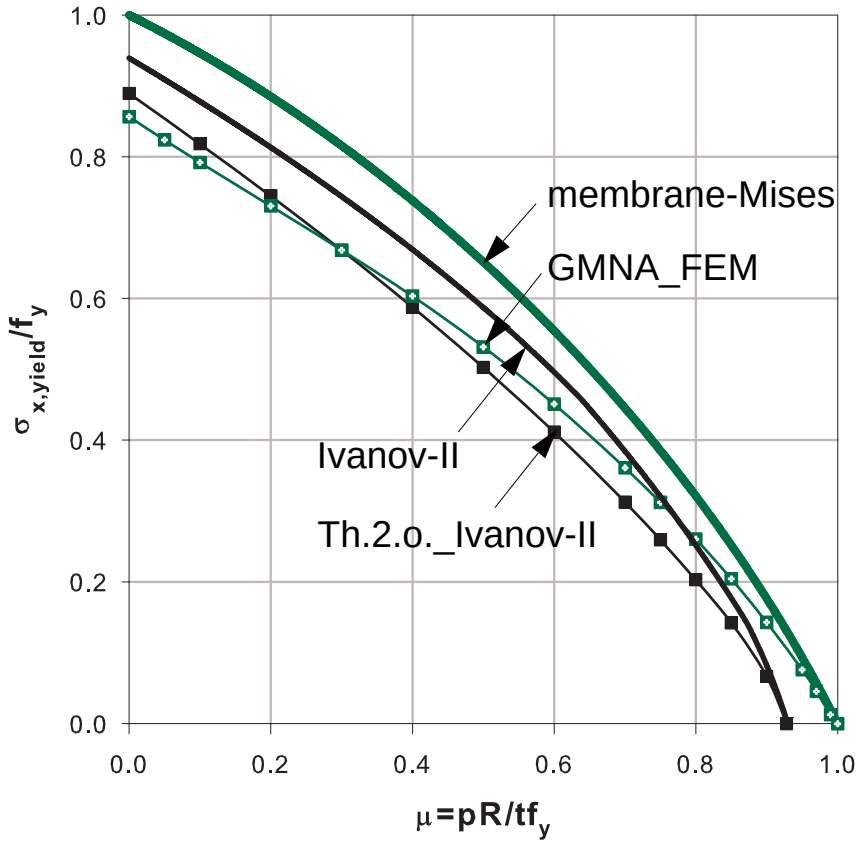

Figure 3.47 Elephant's-foot buckling strength, R/t = 500: fixed bottom

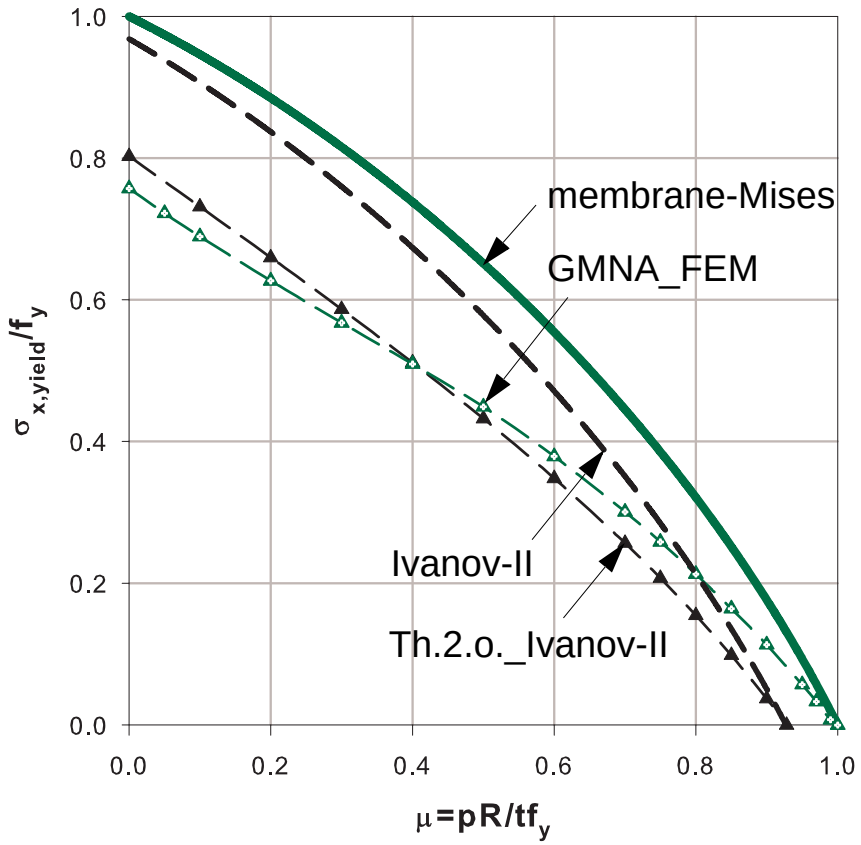

Figure 3.48 Elephant's-foot buckling strength, R/t = 500: pinned bottom

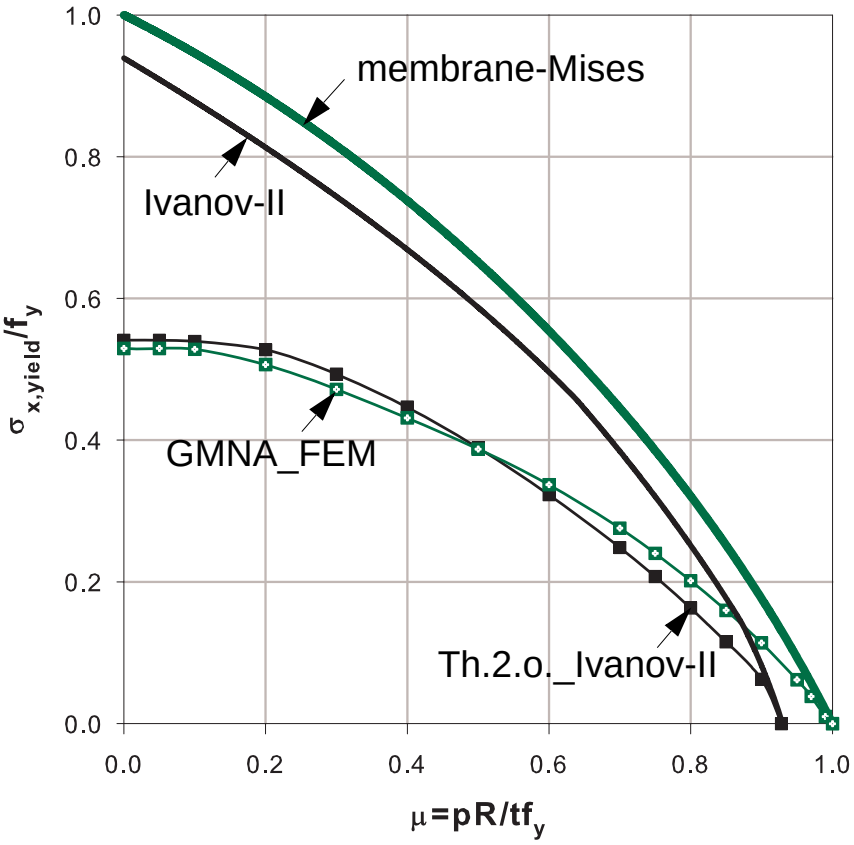

Figure 3.49 Elephant's-foot buckling strength, R/t = 1000: fixed bottom

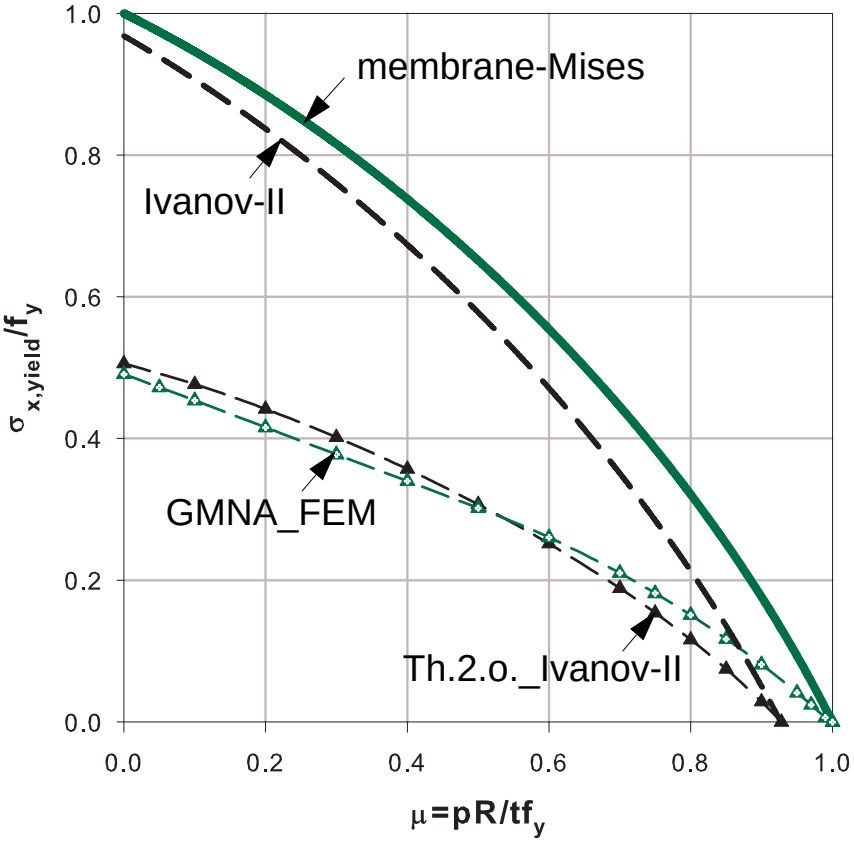

Figure 3.50 Elephant's-foot buckling strength, R/t = 1000: pinned bottom

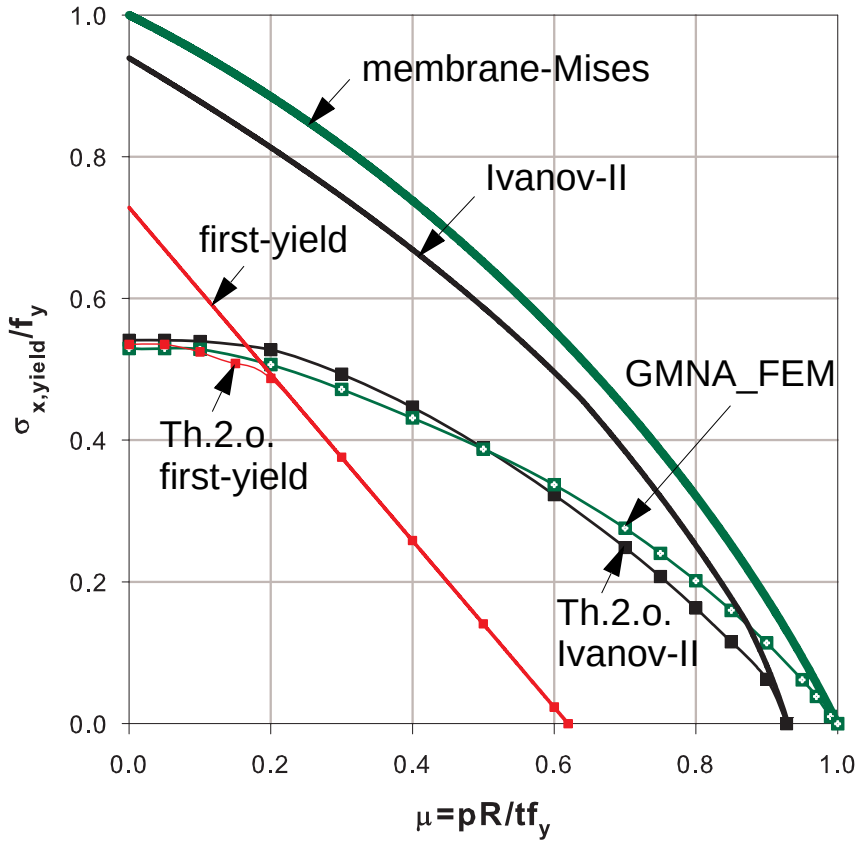

Figure 3.51 Elephant's-foot buckling strength, R/t = 1000: fixed bottom

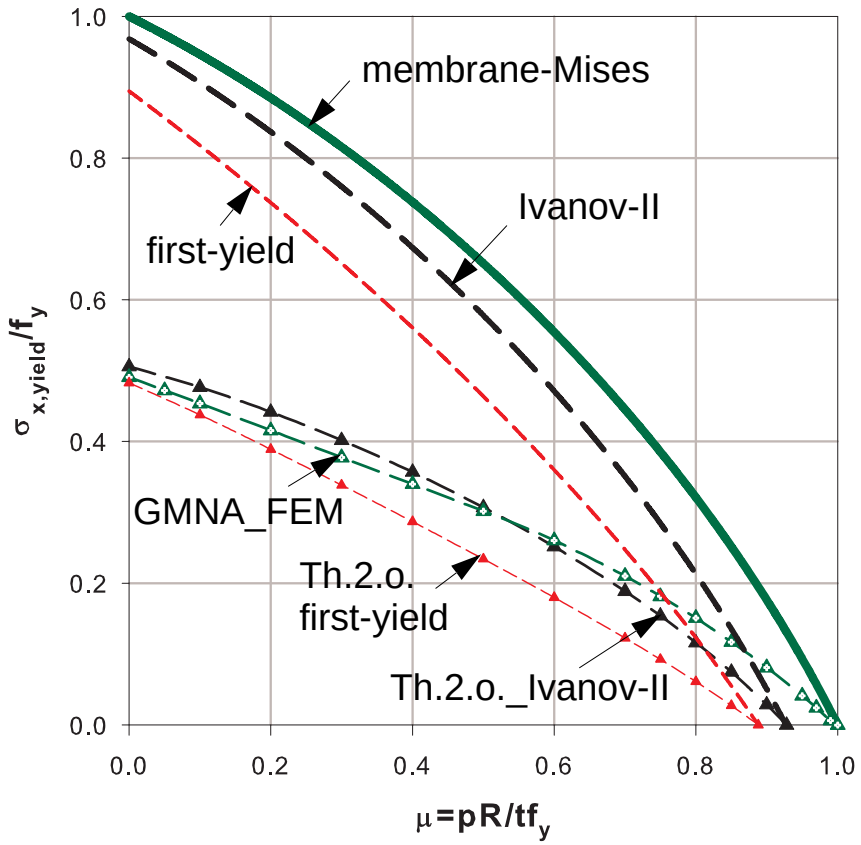

Figure 3.52 Elephant's-foot buckling strength, R/t = 1000: pinned bottom

3.8 Axisymmetric elastic-plastic buckling of imperfect cylindrical shells

3.8.1 Geometrically and materially nonlinear finite element analyses with axisymmetric imperfections (GMNIA)

3.8.1.1 Introduction

It is known that the major factor which plays a great role in the reduction of the buckling strength of thin-walled shells is the presence of various types of imperfections such as loading, boundary conditions, geometry, and material. Loading imperfections include non-uniformity of the load distribution and load eccentricities. Boundary condition imperfections include non-uniformity of support conditions, for example, causing unintended edge moments. Geometrical imperfections include out-of-straightness, out-of-roundness (ovality), deviations from nominal thickness. Material imperfections include material inhomogeneity and residual stresses. For structural modelling and analysis purposes, all imperfections are equivalently expressed in terms of the geometric imperfection with specific imperfection shape, imperfection wave length, imperfection amplitude, imperfection orientation (inward or depression vs. outward or bulge), and imperfection location along the meridian of the shell. Each of these properties of an equivalent geometric imperfection has an influence on the buckling behavior and buckling strength of the shell. In order to clearly show the influence of geometric imperfections on the axisymmetric elastic-plastic buckling strength of shells, an imperfection sensitivity study using axisymmetric LBA eigenmode-affine, nonlinear eigenmode-affine, and local imperfection shapes has been made numerically on a cylindrical shell with the following set of geometry, boundary, loading, and shell material conditions. The results will all be expressed interms of dimensionless quanitities and therefore can be interpreted in such a way that they are applicable to other sets of conditions as well.

Geometry: shell slenderness ratio, R/t = 500; meridional length to radius ratio, L/R = 1.0

Boundary conditions: pinned or fixed (clamped) bottom and rotationally restrained top

Loading: uniform meridional (axial) tip compression with co-existent uniform internal pressure

Material properties:

Modulus of elasticity, E = 21000 kN/cm^2;

Mises yield criterion with uni-axial yield strength, f_y = 24 kN/cm^2;

Poisson's ratio, ν = 0.3

3.8.1.2 Linear elastic buckling (LB) eigenmode-affine imperfection

In cases where a different unfavourable imperfection pattern can not be justified, EN1993-1-6 recommends to use a linear elastic critical eigenmode based on an LBA of the perfect shell. For the illustrative fixed-bottom cylindrical shell discussed above, a typical LBA basic eigenmode is shown in Figure 3.53. A typical LBA basic eigenmode of the pinned-bottom cylinder is also shown in Figure 3.55. Despite the fact that such imperfection shapes are very far from existing in real shells, imperfection sensitivity studies have been done considering the LBA eigenmodes (first half-wave oriented outward in both boundary conditions) as an imperfection shape and varying the imperfection amplitude for both bottom boundary conditions. The materially and geometrically nonlinear elastic-plastic buckling strength of the imperfect cylinder (GMNIA), normalized with respect to the perfect (GMNA) shell strength, versus the imperfection amplitude for the fixed and pinned bottom boundary condition are shown in Figure 3.54 & Figure 3.56, respectively, for different values of meridional to circumferential membrane stresses ratio given by $\overline{\psi} = \sigma_x / \sigma_\theta$ according to the proportional load increase procedure. The value of $\overline{\psi}$ is indirectly proportional to the internal pressure level, i.e. a bigger value of $\overline{\psi}$ indicates a smaller internal pressurization. Thus, the LBA eigenmode-affine imperfection led to very low buckling strengths.

It should, however, be noted here that if the cylinder is ideally perfect or if the strength-reducing effect of imperfections are negligible, the effect of edge constriction alone will be responsible for instability resulting in a bulge type buckling mode near the edge. If there exist a worst imperfection at the same location as the edge constriction; or when both are closely located and able to interact, it is clear that the two effects help each other in destabilizing the shell. On the other hand, in cases when both exist on a shell but at different locations along the meridian with no interaction of any kind among them, an imperfection-led buckling phenomenon may happen at the imperfection location depending on the imperfection-nature.

An imperfection-led buckling phenomenon is what is exactly happening in the fixed-bottom cylinder where the LBA eigenmode-affine imperfection considered has its peak value at the other (top) end of the shell. With such imperfection shape but low internal pressure levels, the edge constriction effect is relatively small and hence an imperfection-led buckling will happen at the top edge of the shell even for small amplitudes of the imperfection. For high internal pressure levels, however, the edge constriction effect becomes larger and the cylinder buckles near the edge for relatively small amplitudes of the LBA eigenmode-affine imperfection. As the imperfection amplitude increases, irrespective of the internal peressure level, buckling happens at the top edge of the cylinder where the LBA eigenmode has its peak value.

On the other hand, for a pinned-bottom cylinder where the LBA eigenmode has the same amplitude at top-end of the shell and close to the bottom boundary, such an LBA eigenmode-affine imperfection along with the edge-constriction effect will restrict the axisymmetric elastic-plastic buckling phenomenon to happen close to the bottom boundary unless it is oriented in such a way that it opposes the edge bending effect. In cases when the imperfection-orientation opposes the edge-constriction effect, the shell may get strengthened at bottom and the buckling phenomenon will be shifted up and happens somewhere along the meridian.

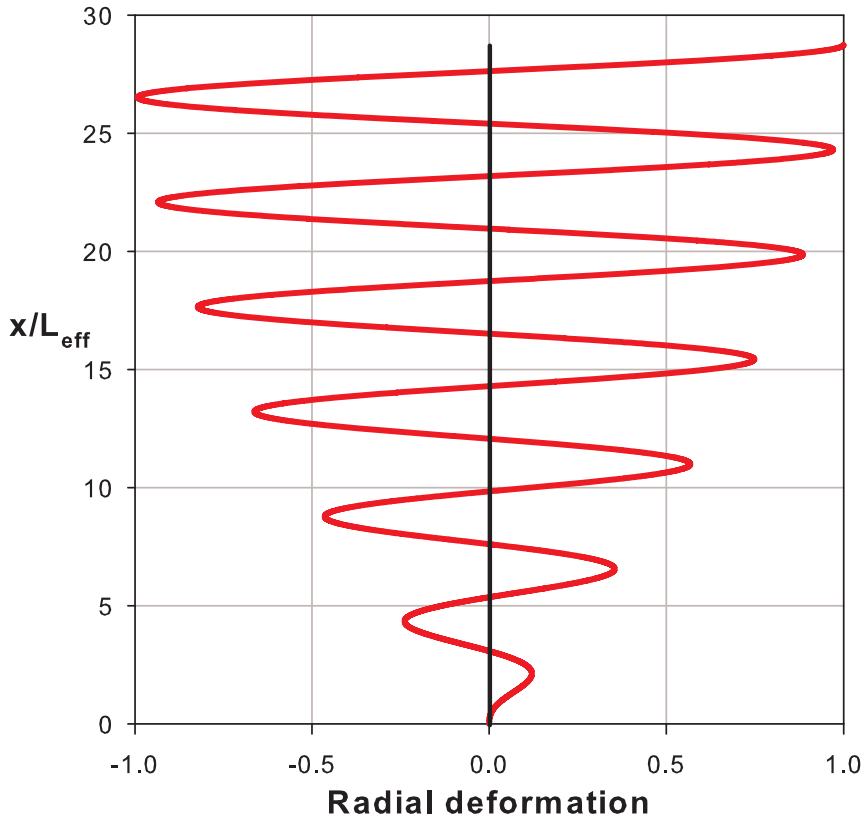

Figure 3.53 LBA basic eigenmode: fixed bottom

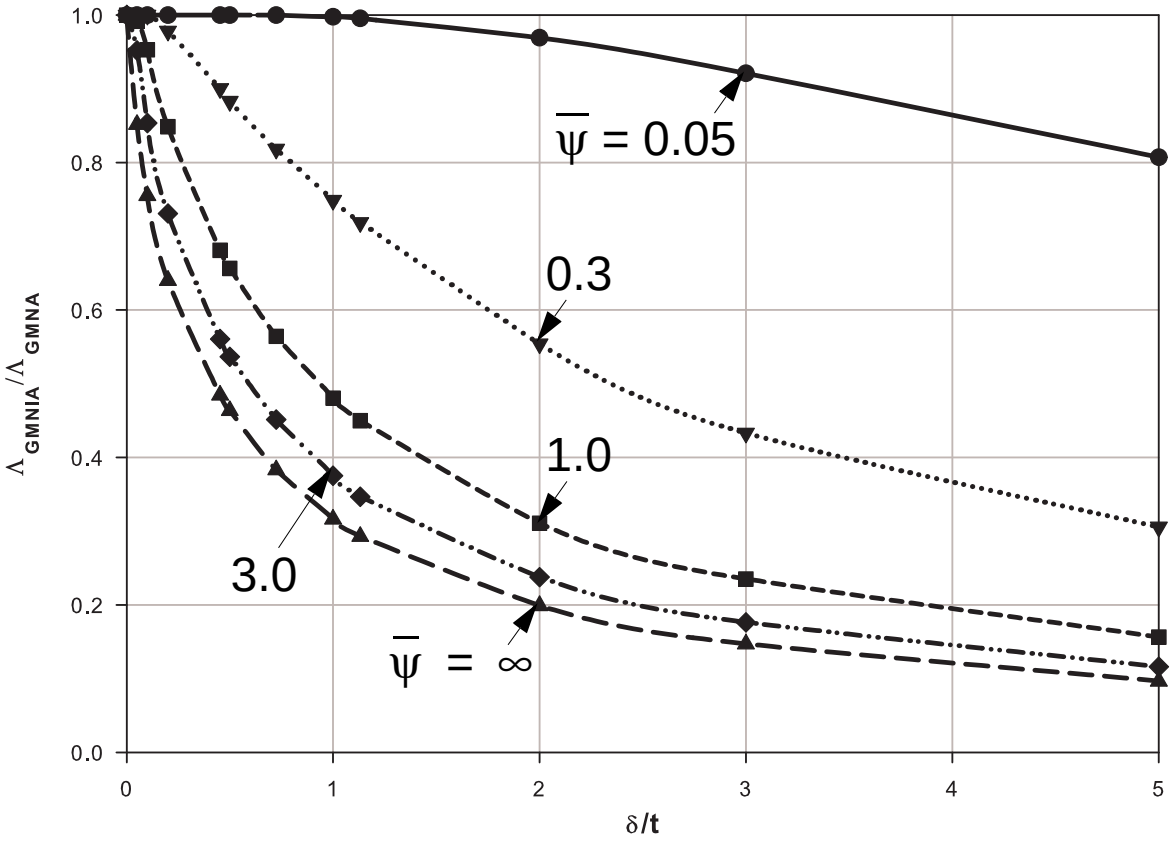

Figure 3.54 Imperfection amplitude sensitivity, LBA eigenmode-affine imperfection: fixed

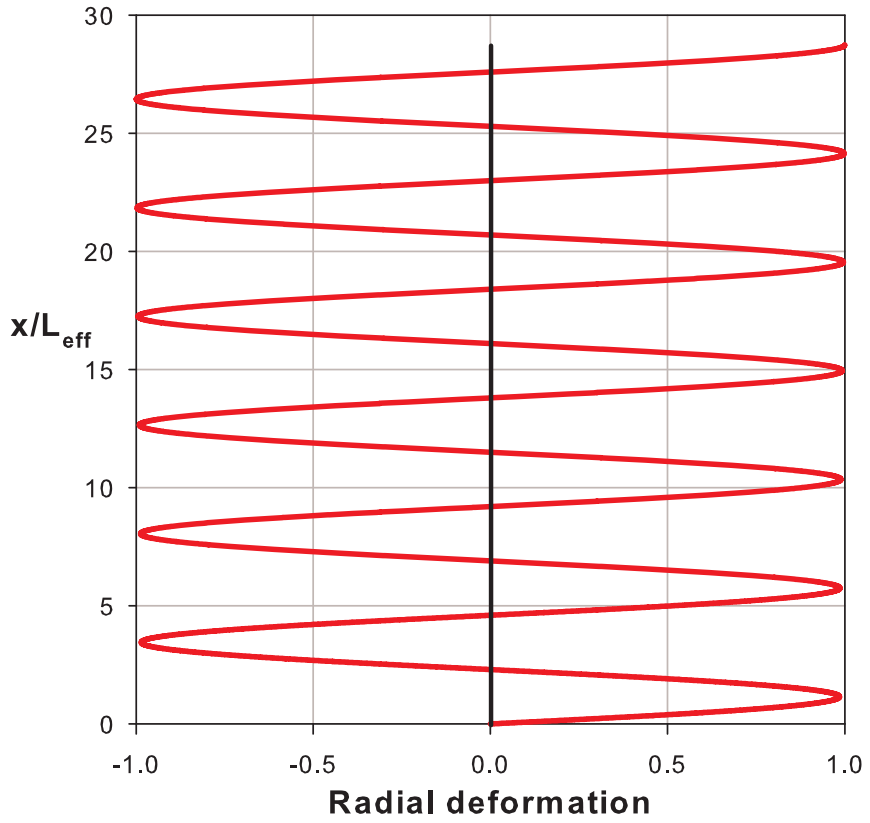

Figure 3.55 LBA basic eigenmode: pinned bottom

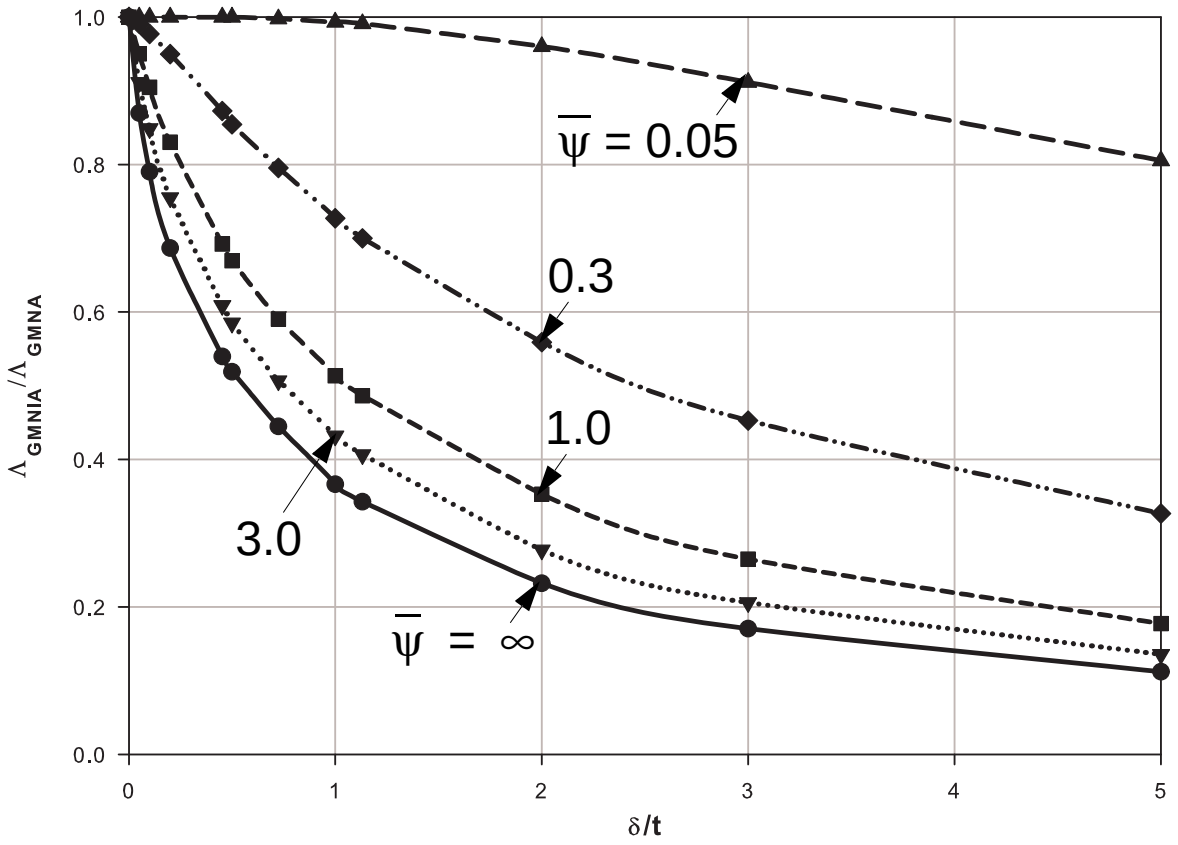

Figure 3.56 Imperfection amplitude sensitivity, LBA eigenmode affine imperfection: pinned

3.8.1.3 Understanding axisymmetric elastic-plastic buckling phenomenon of thin-walled shells

The true nature of buckling in real-world thin-walled shell structures is at most simulated, at least numerically, by analysis models that take the effect of geometric and material nonlinearity into account. For this reason, it is believed and has been applied in the buckling strength determination of thin-walled shells that the geometrically and materially nonlinear finite element analysis (GMNA) with physically possible imperfections (GMNIA) predicts closer results to the buckling strength of real-world thin-walled shells. The question which still remains unanswered in many of the researches and studies done so far is the physically possible critical (worst) imperfection shape, wavelength, amplitude, orientation, and location along the meridian. The following discussion will address the investigation made in the current work to asses a physically possible worst imperfection resulting in reduced buckling strengths of cylindrical shells.

Small imperfection amplitudes

In this case, great attention and careful observation of the geometrically and materially nonlinear perfect buckling behaviour under the action of the loads that the shell is subjected to, will be needed. Imperfections with small amplitudes will have worst deteriorating effects on the buckling strength of the shell when they are shaped, located, and oriented in such a way that they follow the increased nonlinear prebuckling radial deformations and thereby shortening the life span of the buckling phenomenon and leading to a very low buckling load. The nonlinear prebuckling radial deformation leads to the ultimate nonlinear (snap-through) buckling mode that the shell will finally fail in. This is the buckling eigenmode which represents the actual incremental deformation pattern between two equilibrium states (pre- and post-) in infinitesimal neighborhood of the critical nonlinear load level, Guggenberger (2005a).

From the above discussion, one can conclude that the worst imperfection shape, location and orientation can be well explained in terms of the nonlinear (snap-through) buckling mode. In this regard, the snap-through type buckling mode of the perfect cylinder and the possible worst imperfections will be investigated in this part of the study. Comparison of the results will be made later with the results obtained using an LBA eigenmode-affine imperfection according to EN1993-1-6 recommendations.

The illustrative cylindrical shell loaded with a uniform axial ring compressive load and a uniform pre-specified internal pressure, $p = 0.8p_y = 0.8t \cdot f_y / R$ was numerically investigated using ABAQUS and thoroughly examined. The reason for choosing a pressure value of 80% of the yield pressure (for uni-axial circumferential yielding) is purely a matter of picking an illustrative value on the range of pressure levels where elephant's-foot type buckling is prominent. The ratio of meridional to circumferential membrane stresses, according to the proportional load increase procedure, which results in an equal ultimate buckling load as the pre-specified pressure procedure is when $\overline{\psi} = \sigma_x / \sigma_\theta = 0.326$.

Figure 3.57 and Figure 3.59 show the load-radial displacement of a node close to the boundary and the nonlinear eigenmode, respectively, obtained from a perfect geometrically and materially

nonlinear numerical analysis (GMNA) using the two different ways of load application, the nonlinear eigenmode bieng exactly the same for both load application procedures. Figure 3.58 graphically explains the procedure used in getting the snap-through eigenmode of the perfect structure, with w* representing the radial deformation. The two-step procedure (i.e. with pre-specified internal pressure level) will be used in the remaining parts of this study.

A plot of the nonlinear eigenmode curvature is shown in Figure 3.60. With the help of the nonlinear eigenmode and its curvature, the nonlinear defomation and curvature tendency of the cylindrical shell can be observed. The point now is, **if the possible imperfection shapes are in line with this tendency of nonlinear radial deformation and curvature, thereby increasing the prebuckling nonlinear deformation and speeding up collapse, the ultimate buckling strength of the shell decreases drastically**. If, on the other hand, an imperfection exists but oriented opposite to the nonlinear prebuckling deformation (some sort of “pre-cambering“ effect), the buckling strength of the shell may even increase as will be seen later.

Big Imperfection Amplitudes

For imperfections with big amplitudes, the above discussion on small imperfection amplitudes may not apply for the clear reason that if the imperfection amplitude is big, no matter how the imperfection shape looks like, it means that the imperfection is forcing the nonlinear buckling phenomenon to happen in a completely different manner depending on the imperfection nature. In other words, the nonlinear buckling behaviour will be dictated by the imperfection, thereby, the shell will have forced nonlinear deformation behaviour. In this case, the nonlinear buckling mode and buckling strength may be difficult to predict. Such imperfection amplitudes may change the complete shape and behaviour of the shell and may even be far from the behaviour of cylindrical shells, which in this case needs different treatment depending on the shape. For this reason, cylindrical shells with such imperfection amplitudes should either be discarded in practical shell design and construction or treated as shells of another shape depending on the nature of the imperfection involved. The effects of relatively big imperfection amplitudes on the buckling phenomena and strength will be discussed in the following section.

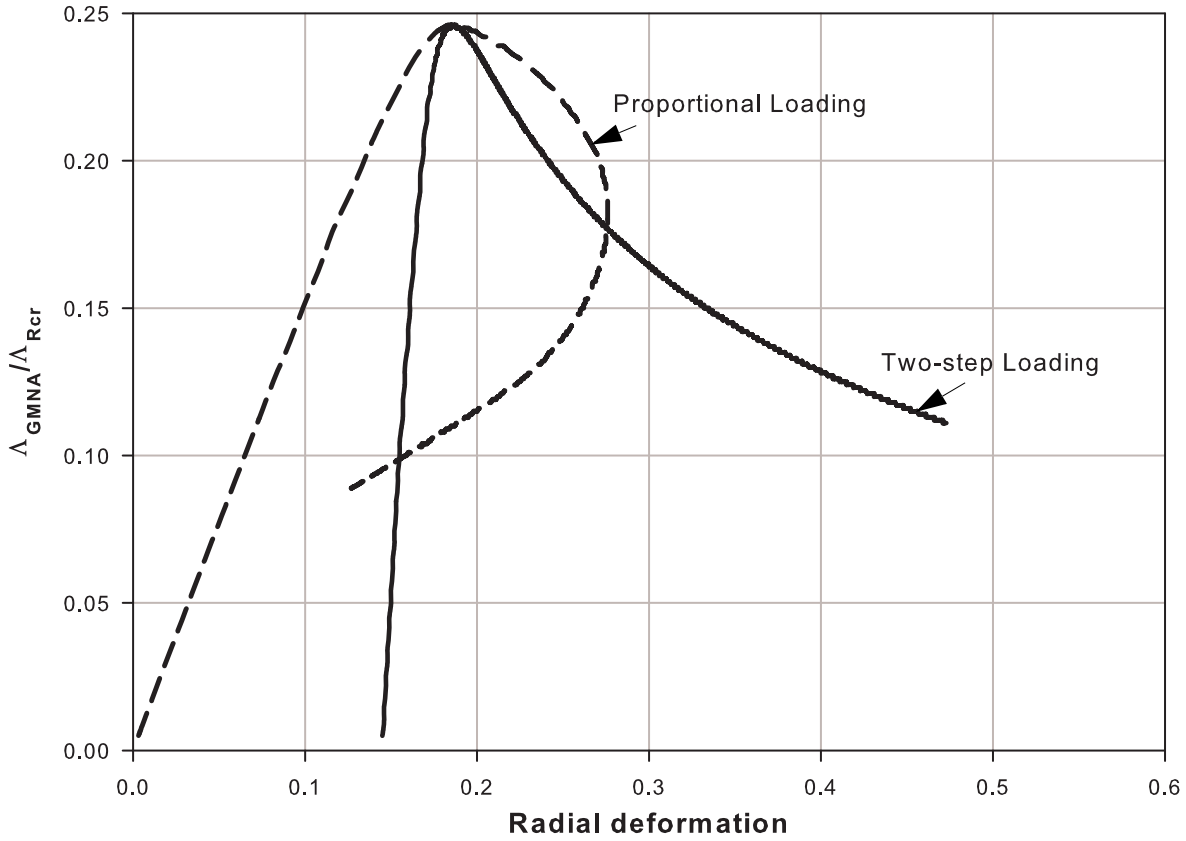

Figure 3.57 Load-radial displacement curve

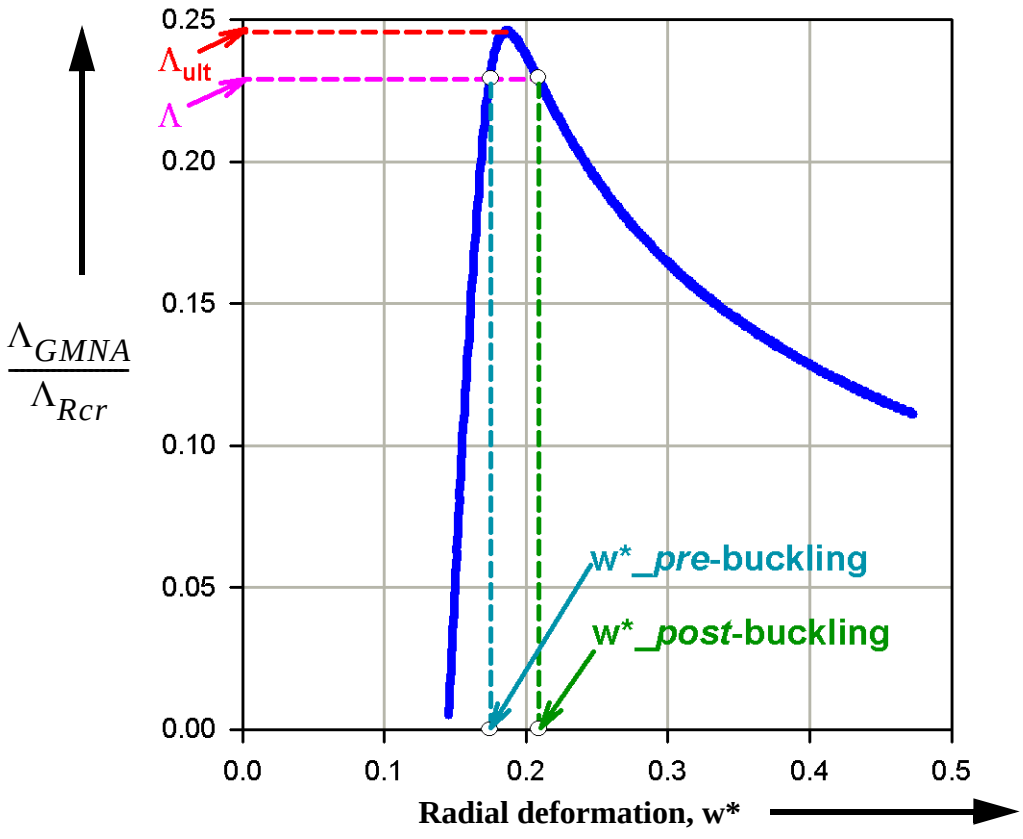

Figure 3.58 Load-radial displacement curve: snap-through eigenmode explanation

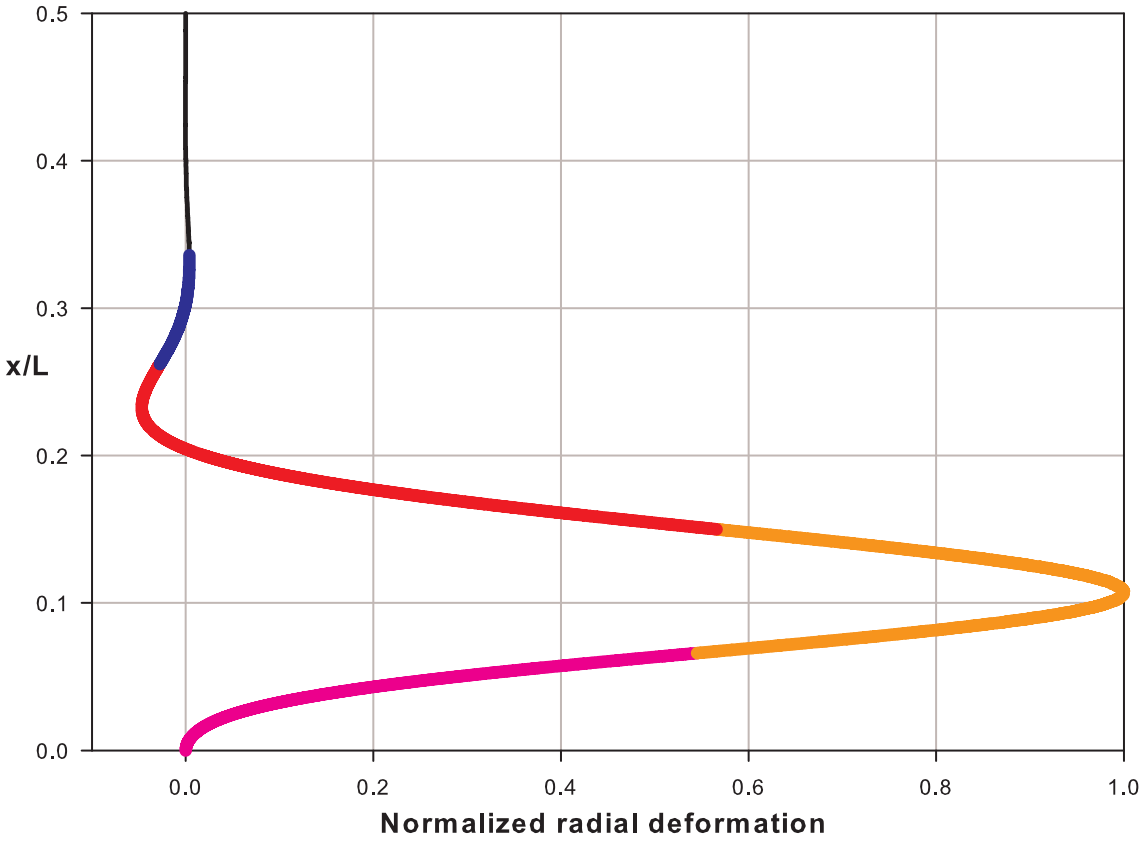

Figure 3.59 Nonlinear (snap-through) eigenmode of the perfect cylinder (elephant's foot buckling)

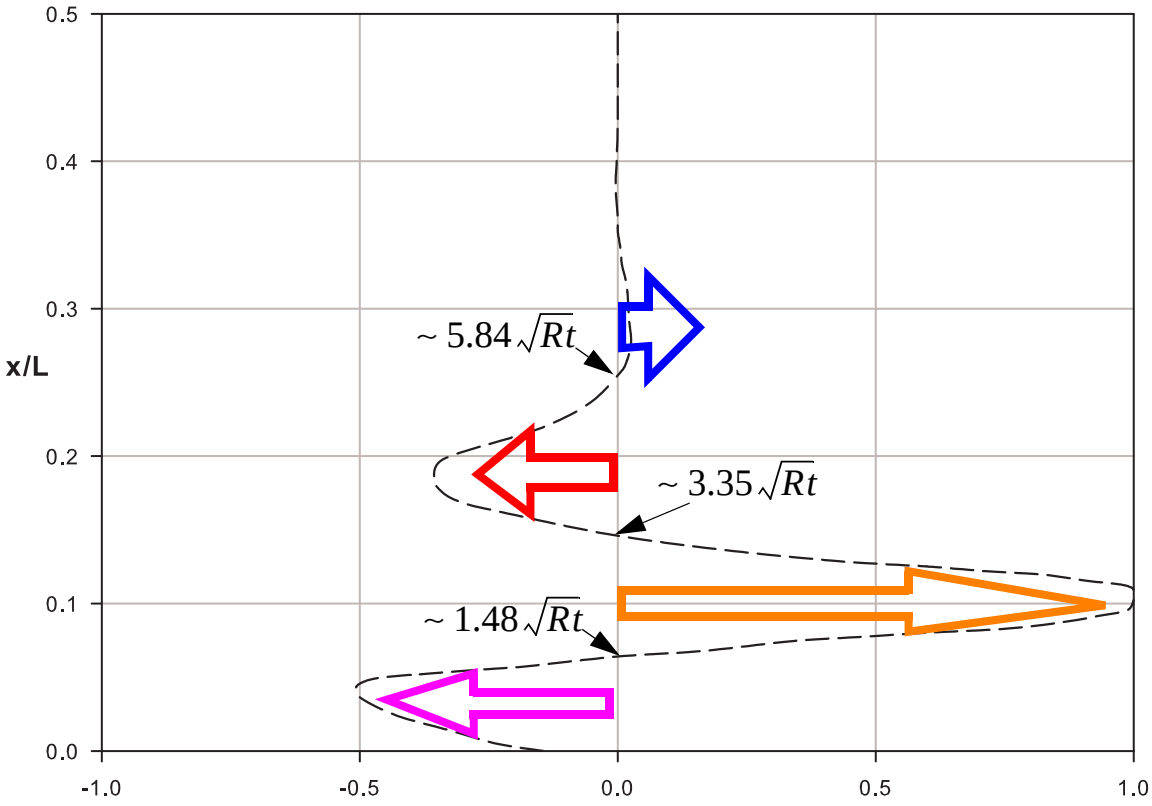

Figure 3.60 Nonlinear (snap-through) eigenmode curvature: possible tendency

The snap-through eigenmode

To elaborate the above discussion, geometrically and materially nonlinear finite element analyses with imperfections (GMNIA) have been made to compute the buckling strength of the thin-walled cylindrical shell. First the nonlinear eigenmode has been used as an imperfection shape to study the sensitivity of the cylindrical shell to this mode. It should be clear at this stage that a nonlinear eigenmode-affine imperfection shape will well be in-phase with the edge constriction effects (since the shape resulted from the edge effect) leading to a very low buckling strength with an imperfect elephant's foot bulge near the edge. A graphical comparison of the buckling strengths resulting from the LBA and snap-through buckling eigenmode-affine imperfections has been made, Figure 3.61. This comparison, however, shows only the buckling strengths (hence only numbers) and not the buckling phenomena since each happen at different locations along the meridian and each caused by different primary agents (imperfection shapes) as already discussed. For the relatively larger imperfection amplitudes, an imperfection-led buckling phenomenon occurs (for the LBA eigenmode-affine imperfection buckling will occur at the top-end of the shell) and therefore comparative conclusions can not be drawn.

Eventhough the snap-through eigenmode affine imperfection leads to relatively lower buckling strengths for small imperfection amplitudes than the LBA eigenmode-affine imperfection, a question needs to be raised about the practicability of both imperfection shapes. Studies, Rotter & Teng (1989), Teng & Rotter (1992), show that the most probable axisymmetric type imperfections on civil engineering cylindrical shells being local-type shapes and not sinusoidal as in the eigenmodes discussed previously. For this reason, the upcoming discussion is fully devoted to the detailed investigation made on "practically possible" local-type axisymmetric imperfection shapes with the help of the snap-through buckling eigenmode discussed above. For common understanding (see Figure 3.60), the bottom region is called the "bottom-inward-worst" zone; the next upper region is called the "bottom-outward-worst" zone; the next upper region is called the "second-inward-worst" zone; and it goes on like that. The approximate lengths of these regions are obtained by subtracting the ordinate values of the plot in Figure 3.60.

3.8.1.4 Local axisymmetric imperfection shapes near the boundary

Figure 3.62 shows half-wave local axisymmetric imperfection shapes expected in practice. For the present study, however, the effects of the local shapes shown in (a) and (e) of Figure 3.62 will be investigated. These shapes represent a general-type and a weld-type imperfections, respectively. The "hinge" on the shapes only means a sharp edge (kink) on the shape. The effects of wavelength, location along the meridian, orientation, and amplitude of these imperfections are examined.

Effect of imperfection wavelength

As a first step in the investigation of imperfection sensitivity of the cylindrical shell to the general-type and weld-type local imperfections, the effect of imperfection wavelength has been studied for an imperfection amplitude equal to the wall thickness. The imperfection shapes start at the bottom of the cylinder and stretches upwards depending on the wavelength, expressed as a constant multiple of $\sqrt{R.t}$. Outward and inward-oriented imperfections are considered. The results obtained are shown in Figure 3.63 and Figure 3.64 for imperfection shape types (a) and (e), respectively. In both cases an outward-oriented imperfection with an imperfection wavelength of about $4.0\sqrt{Rt}$ resulted in the lowest buckling strength. The inward-oriented imperfection (in both imperfection shape cases) leads to lower buckling strengths than the outward-oriented imperfections for all wavelengths not exeeding $2.0\sqrt{Rt}$. Besides, an inward-oriented imperfection with about $2.0\sqrt{Rt}$ wavelength leads to the relative lowest buckling strength when compared to other wavelengths of the same orientation. Thus, the results found are well in line with the snap-through eigenmode concept discussed previously. For the larger wavelengths, no clear conclusion can be drawn as they include combinations of the inward-worst and outward-worst regions discussed in the snap-through eigenmode. This ambguity will be cleared when the imperfections are shifted up along the meridian leading to the upcoming study. Comparisons will then be made within the no-shift and up-shifted imperfections.

Effect of imperfection location along the meridian

The next step in the investigation of imperfection sensitivity of the cylindrical shell to the general-type & weld-type local imperfections is to pre-specify the imperfection wavelength & imperfection amplitude and vary the location of the imperfection along the meridian. The vertical shifts of the imperfections are expressed as a constant multiple of $\sqrt{Rt}$. Following the results from the above study on wavelength effects, general type imperfections with wavelengths of $4.0\sqrt{Rt}$ and $2.0\sqrt{Rt}$ and a weld type imerfection with wavelength equal to 25t are investigated. The $4.0\sqrt{Rt}$ and 25t lengths are the EN1993-1-6 gauge-lengths for measuring amplitudes across general shape deviations and welds, respectively. The imperfection amplitude is kept equal to the wall thickness in all the cases. Figure 3.65 and Figure 3.67 show the effect of vertical shifts for the general type imperfections with $4.0\sqrt{Rt}$ and $2.0\sqrt{Rt}$ wavelengths, respectively. Figure 3.69 shows a similar plot for the weld type imperfection with 25t wavelength. It can be seen from the plots that the lowest buckling strengths result at vertical shifts of $0.5\sqrt{Rt}$ and $1.5\sqrt{Rt}$ for the $4.0\sqrt{Rt}$ and $2.0\sqrt{Rt}$ wavelengths of the general type imperfection shapes, respectively. Those shifts bring the peak point of the imperfection shapes considered close to the peak point of the outward-worst region of

the nonlinear eigenmode. This fact leads to the investigation of imperfection shapes having coinciding peak points as the snap-through eigenmode and will be discussed at the end of this section. For the $4.0\sqrt{Rt}$ wavelength imperfection, the outward-orientation leads to lower buckling strengths for all the locations considered than the inward-orientation. The inward-oriented $2.0\sqrt{Rt}$ wavelength imperfection leads to lower buckling load only when there is no upward shift. A similar observation on the weld imperfection shows an outward-oriented imperfection leads to the lowest buckling load when it is located at about $1.2\sqrt{Rt}$. The inward-oriented weld imperfection leads to lower results when the upward shift is not exeeding $0.6\sqrt{Rt}$. Once again, the results found from this investigation are all in line with the snap-through eigenmode concept already discussed.

Effect of imperfection amplitude

Imperfection amplitude-sensitivity of the aforementioned wavelengths and locations along the meridian has been then made to verify the conclusions drawn so far. Figure 3.66 and Figure 3.68 show the effect of imperfection amplitudes for different imperfection locations of the general type imperfections with $4.0\sqrt{Rt}$ and $2.0\sqrt{Rt}$ wavelengths, respectively. Figure 3.70 shows a similar plot for the weld type imperfection with 25t wavelength. All the results coincide with the snap-through eigenmode concept.

Outward-oriented worst local imperfection

As a final step in the investigation, imperfection wavelengths were varied in such a way that the peak points of the imperfection shapes remain at the peak point of the outward-worst region of the nonlinear eigenmode. The imperfection amplitude was kept the same for all shapes and equal to the wall thickness. The results are shown in Figure 3.71. Once again, one can see that the worst imperfection orientation is outwards and its length is approximately $2.0\sqrt{R.t}$ which again is approximately equal to the length of the outward-worst region, as expected. To further highlight this behaviour, imperfection amplitude-sensitivity analyses were made for the $2.0\sqrt{R.t}$ and $4.0\sqrt{R.t}$ wavelength general-type local imperfections and both outward and inward orientations. These results along with the results obtained using the nonlinear eigenmode-affine imperfection are shown in Figure 3.72.

The following question can be raised here: why did the outward-oriented local imperfections lead to relatively lower buckling loads than the nonlinear eigenmode-affine imperfection? It is because the nonlinear eigenmode-affine imperfection, even though it has the same curvature as the nonlinear eigenmode itself, its shape-deviations are not exactly in-phase with the worst shape-deviation discussed in the curvature of the nonlinear eigenmode, Figure 3.60.

Figure 3.73 to Figure 3.76 show the effects of imperfection orientations on the ultimate radial deformations corresponding to the ultimate buckling load factors. Comparisons of these ultimate buckling loads and their corresponding radial deformations for the perfect cylinder, imperfect cylinder with outward-oriented imperfection, and imperfect cylinder with inward-oriented imperfection can be easily made for the different imperfection shapes. These comparisons will strengthen the concept of using the nonlinear eigenmode oriented local imperfections as the worst possible imperfections. Besides, it contributes much to the basic understanding of worst axisymmetric imperfections.

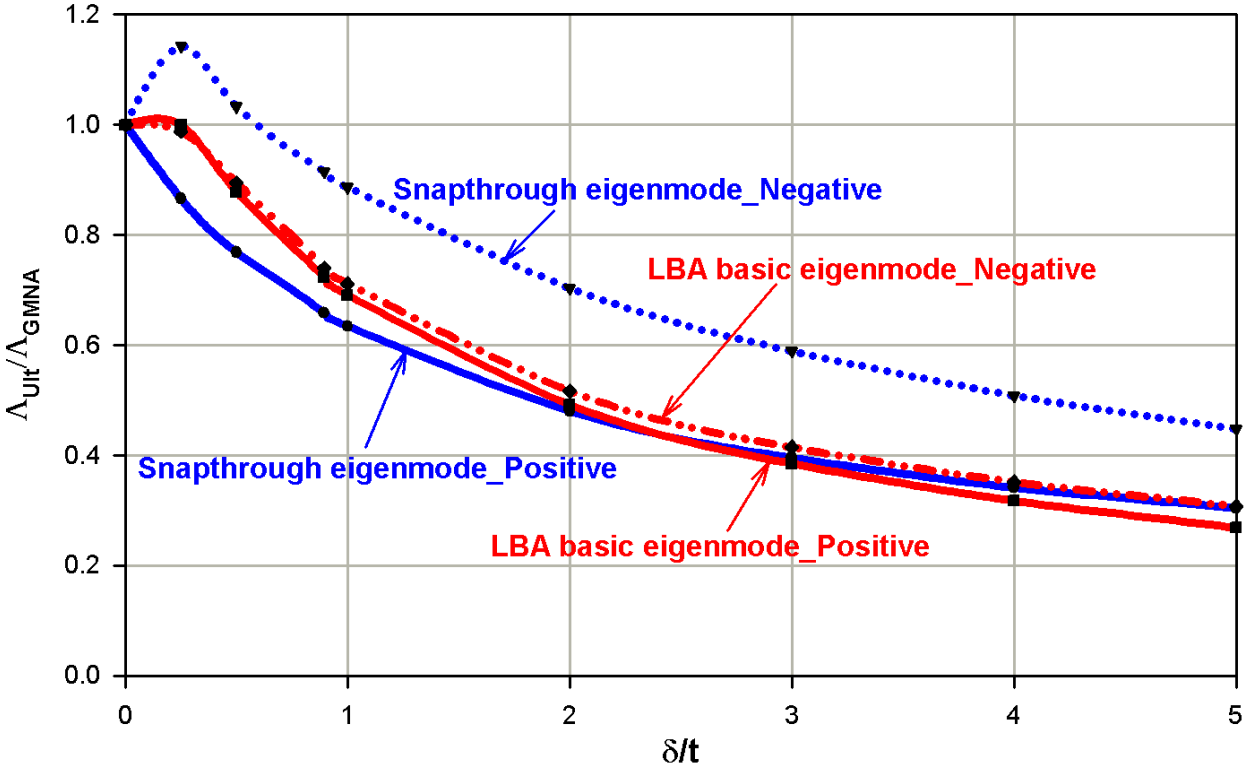

Figure 3.61 Imperfection sensitivity comparison to LBA and snap-through eigenmode shapes

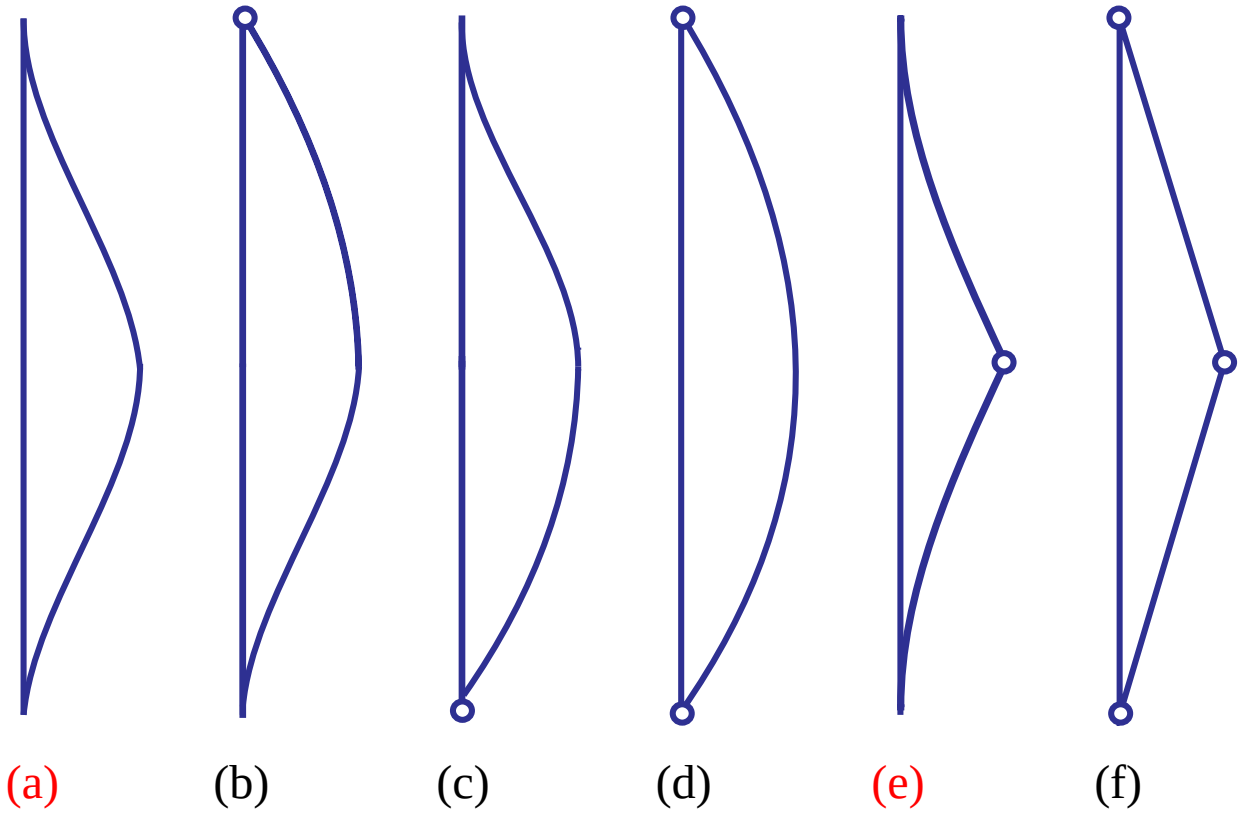

Figure 3.62 Possible local axisymmetric imperfection shapes

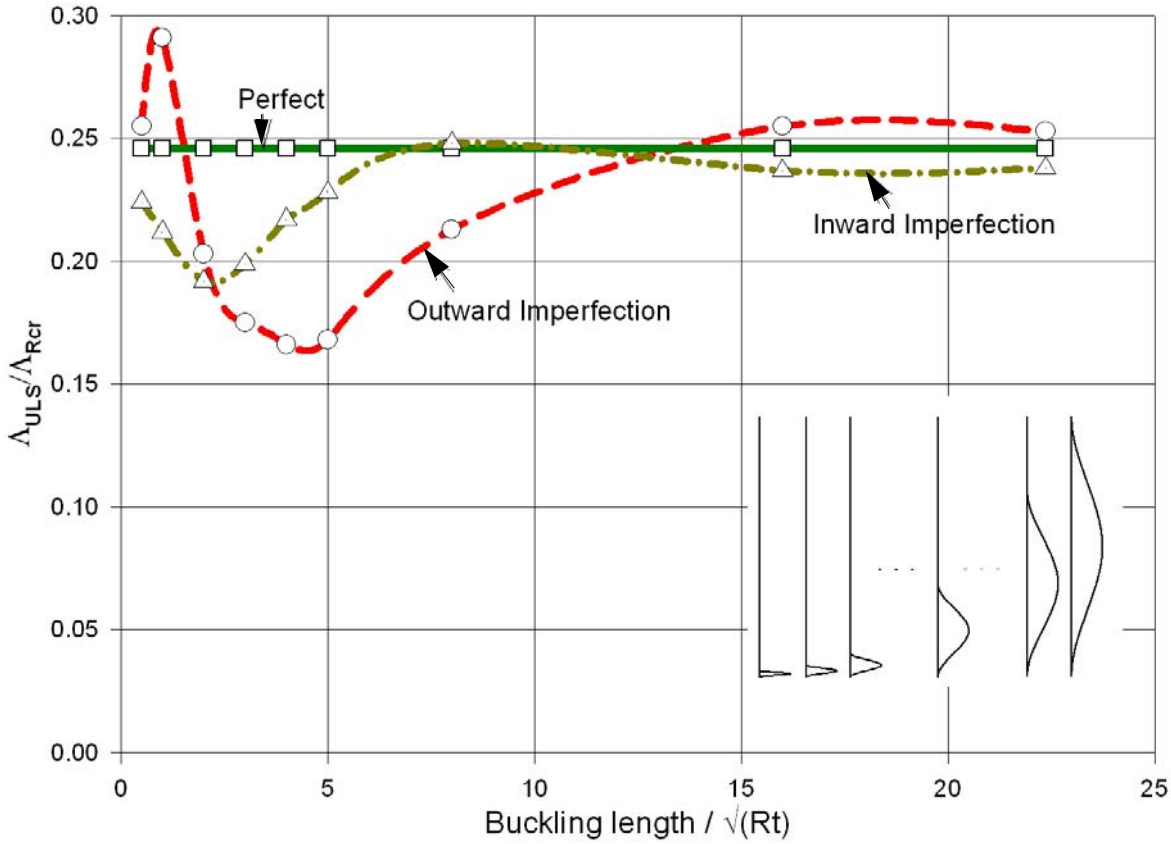

Figure 3.63 Effect of imperfection wavelength: type-(a) imperfection

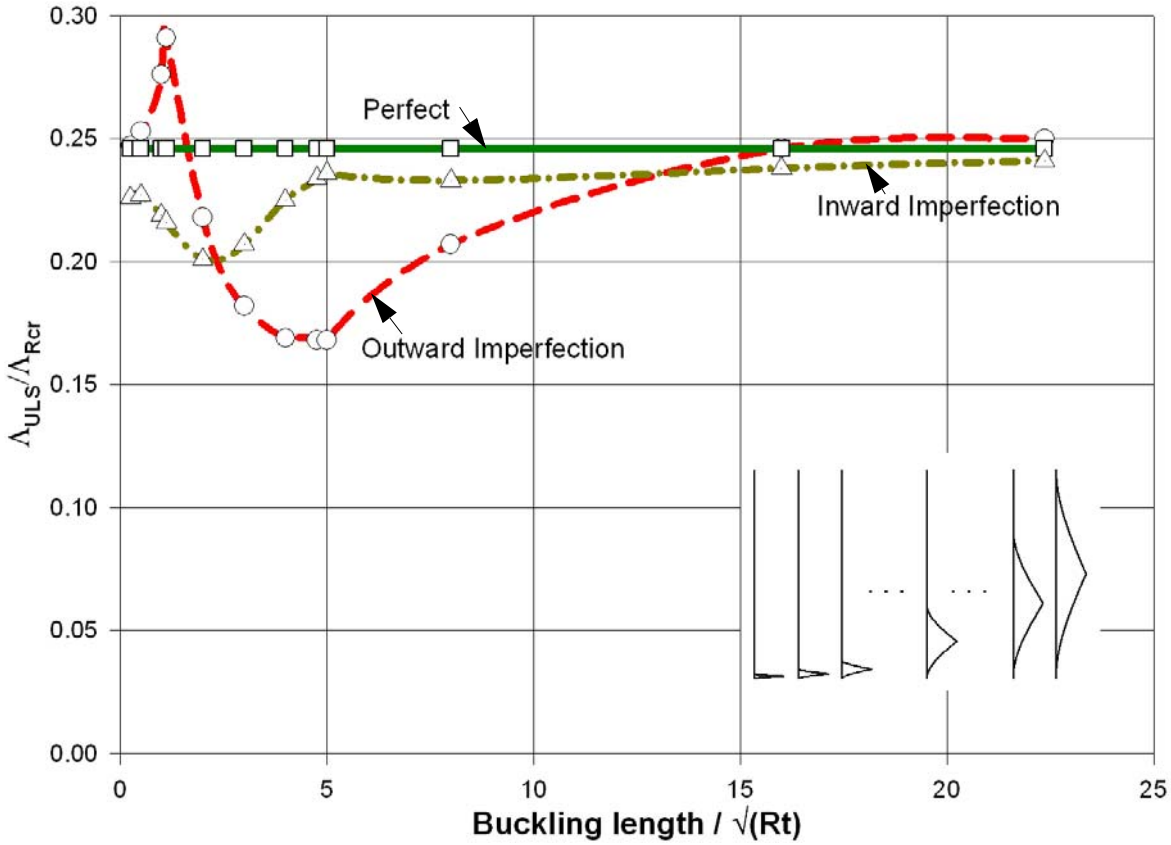

Figure 3.64 Effect of imperfection wavelength: type-(e) imperfection

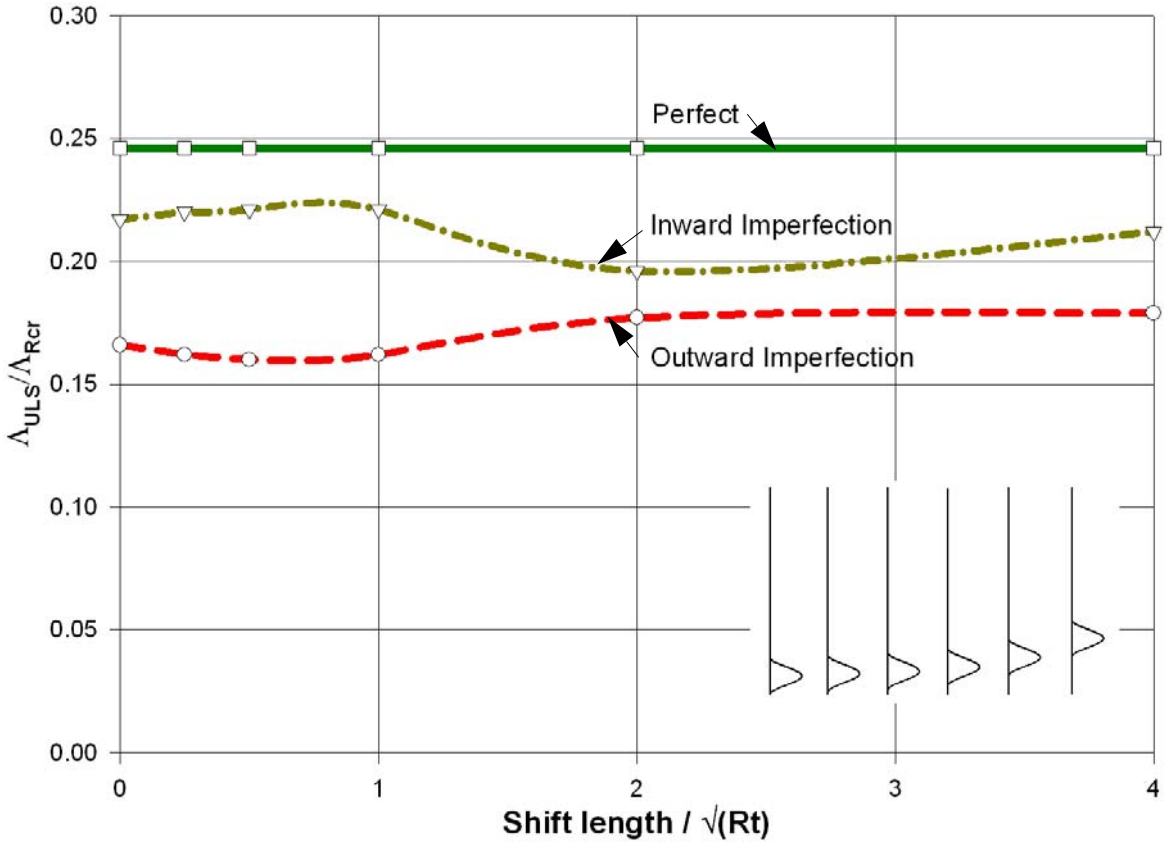

Figure 3.65 Effect of imperfection location: type-(a) imperfection & wavelength = $4.0\sqrt{Rt}$

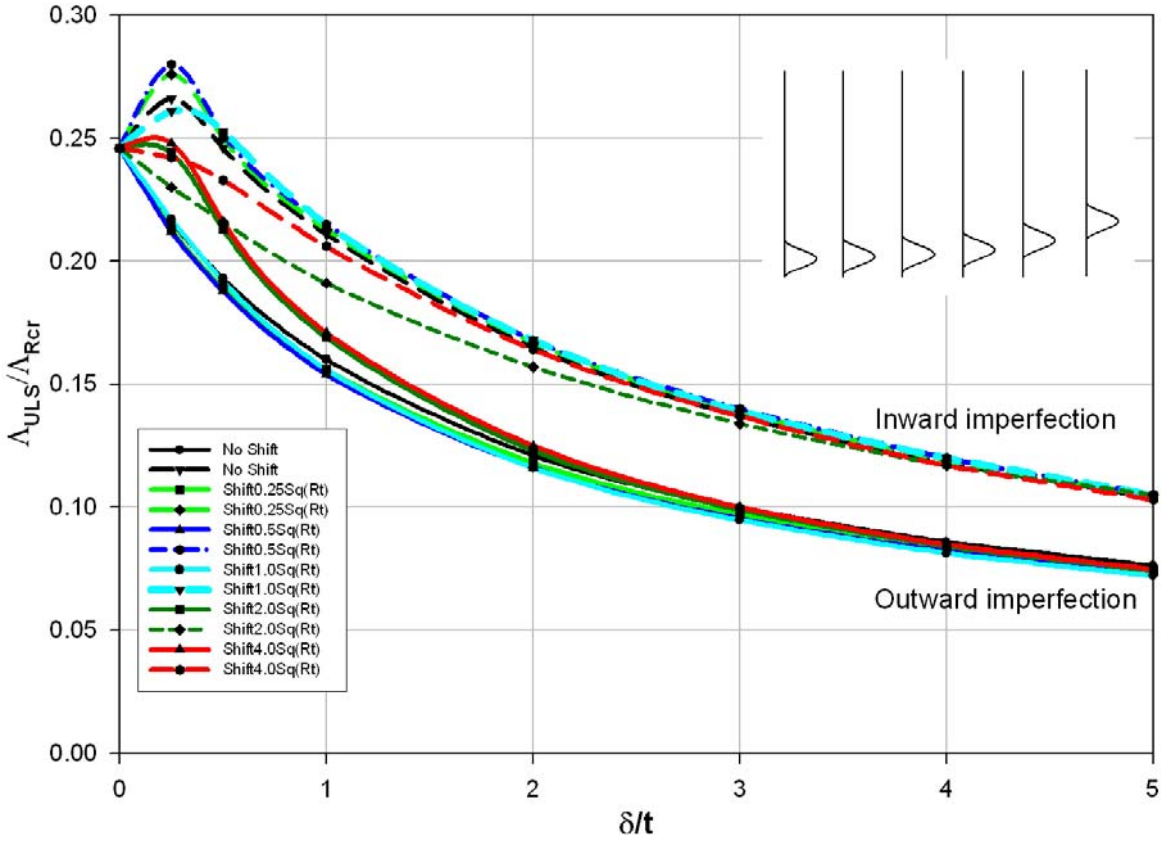

Figure 3.66 Imperfection sensitivity for different up-shifts: type-(a) imperfection & wavelength $4.0\sqrt{Rt}$

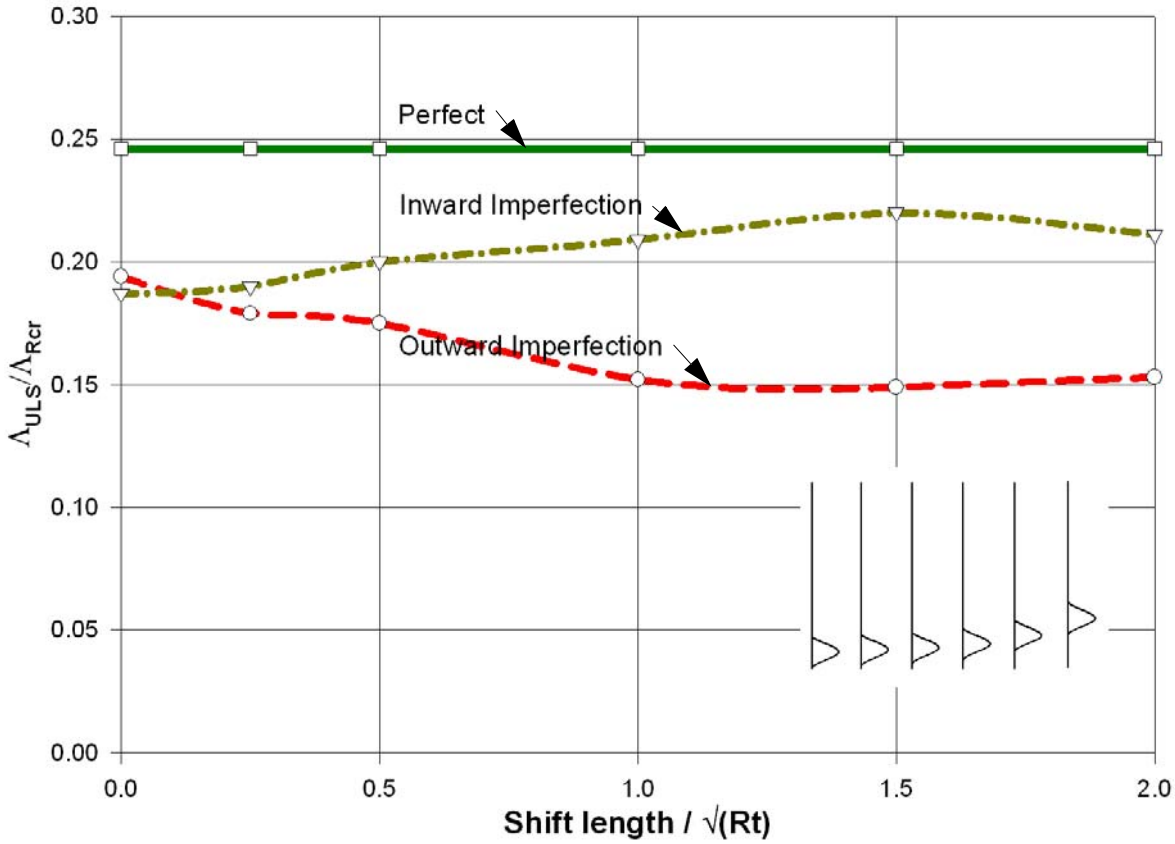

Figure 3.67 Effect of imperfection location: type-(a) imperfection & wavelength = $2.0\sqrt{Rt}$

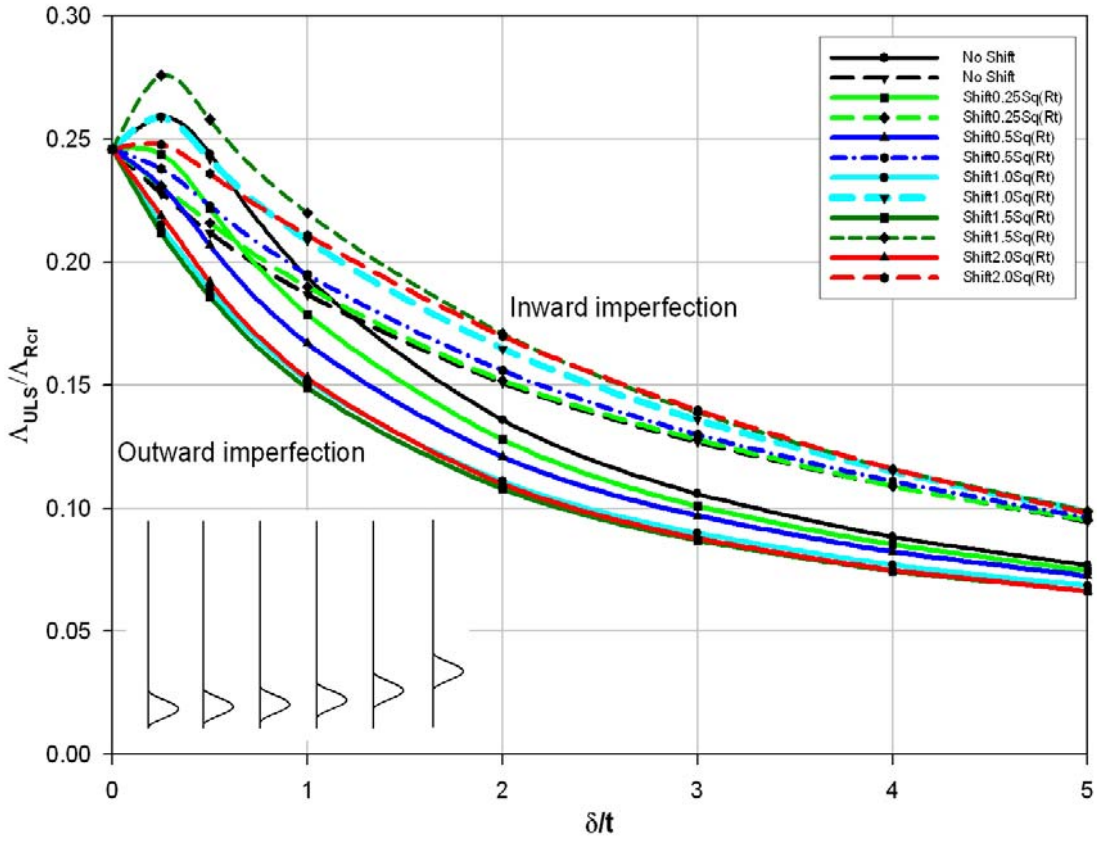

Figure 3.68 Imperfection sensitivity for different up-shifts: type-(a) imperfection & wavelength $2.0\sqrt{Rt}$

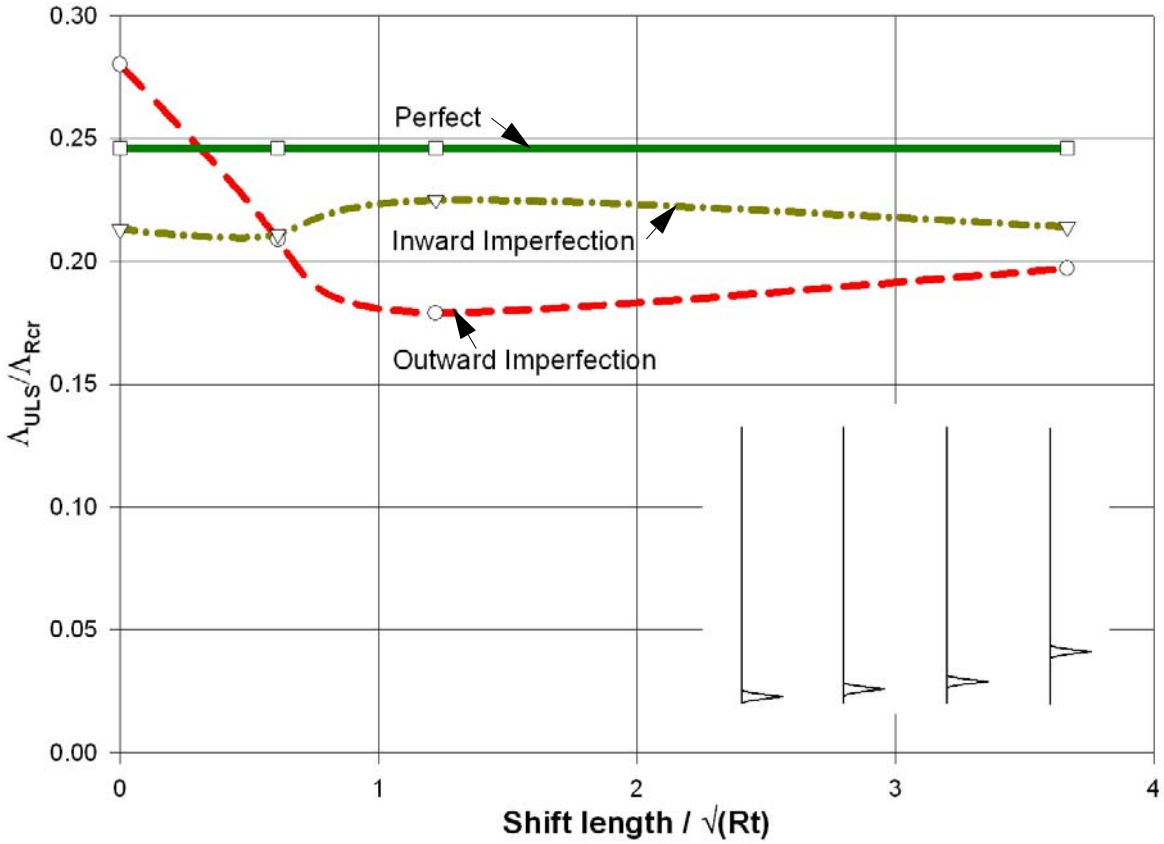

Figure 3.69 Effect of imperfection location: type-(e) imperfection & wavelength = 25t

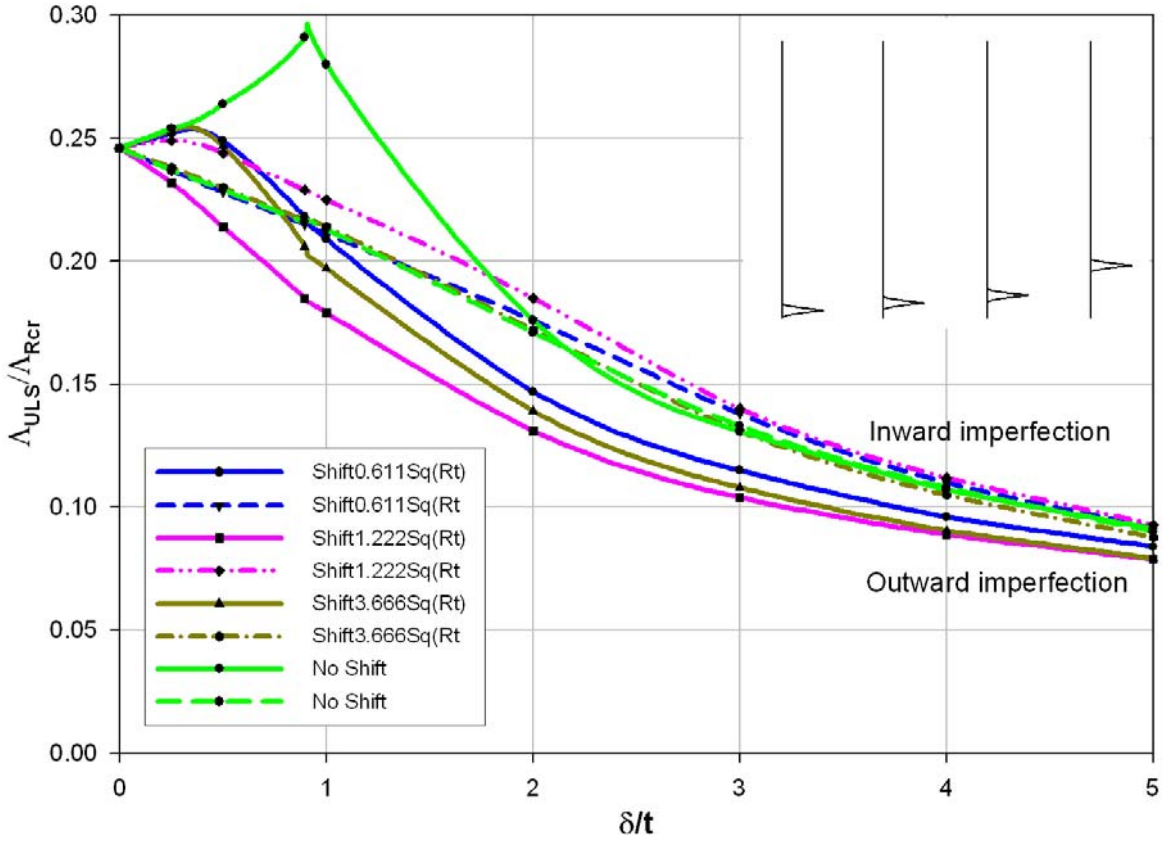

Figure 3.70 Imperfection sensitivity for different up-shifts: type-(e) imperfection & wavelength = 25t

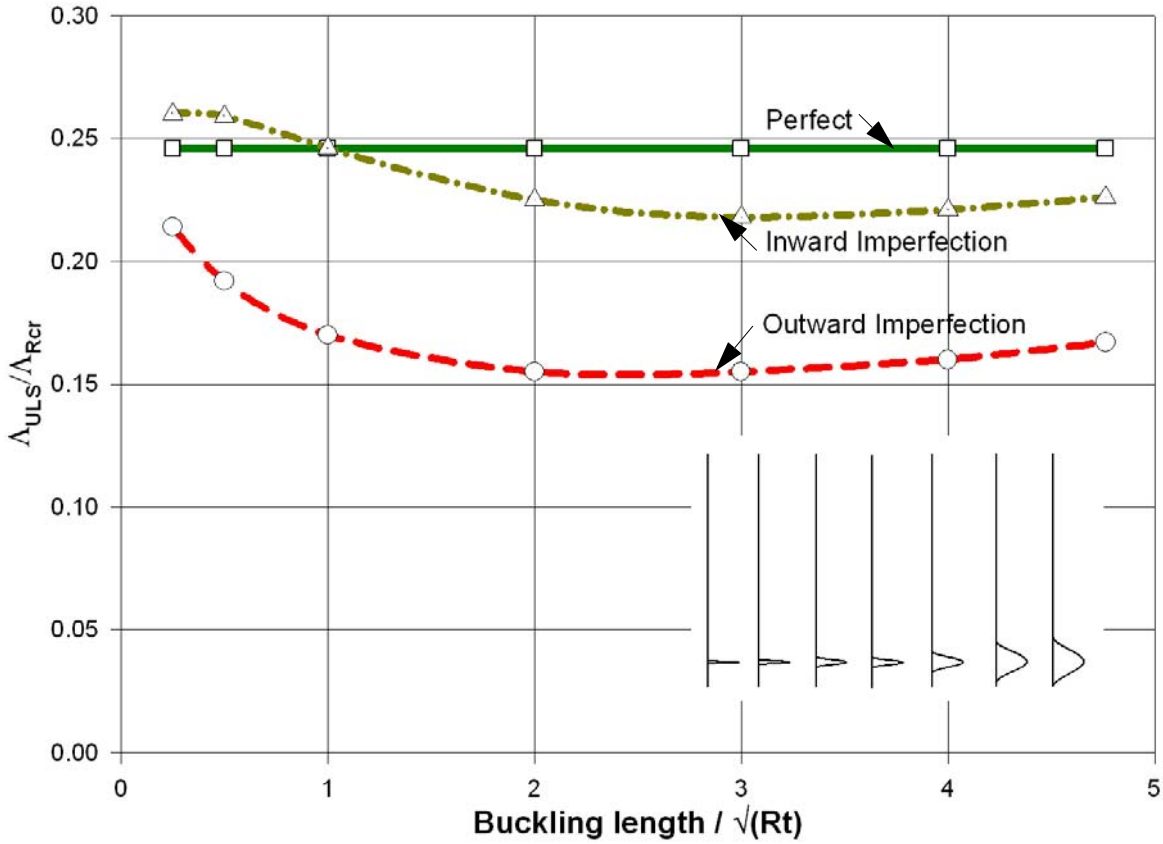

Figure 3.71 Effect of imperfection wavelength: type-(a) imperfection & amplitude = wall thickness

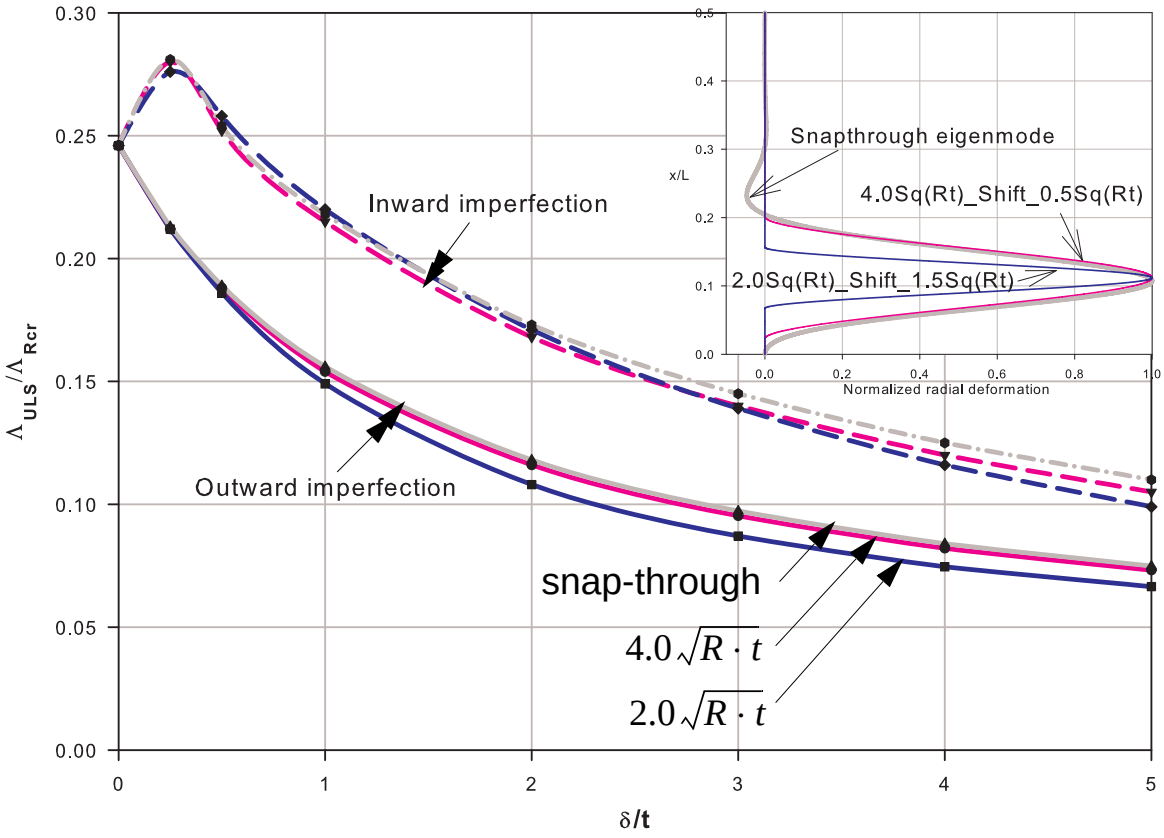

Figure 3.72 Imperfection sensitivity: snap-through eigenmode & type-(e) imperfection

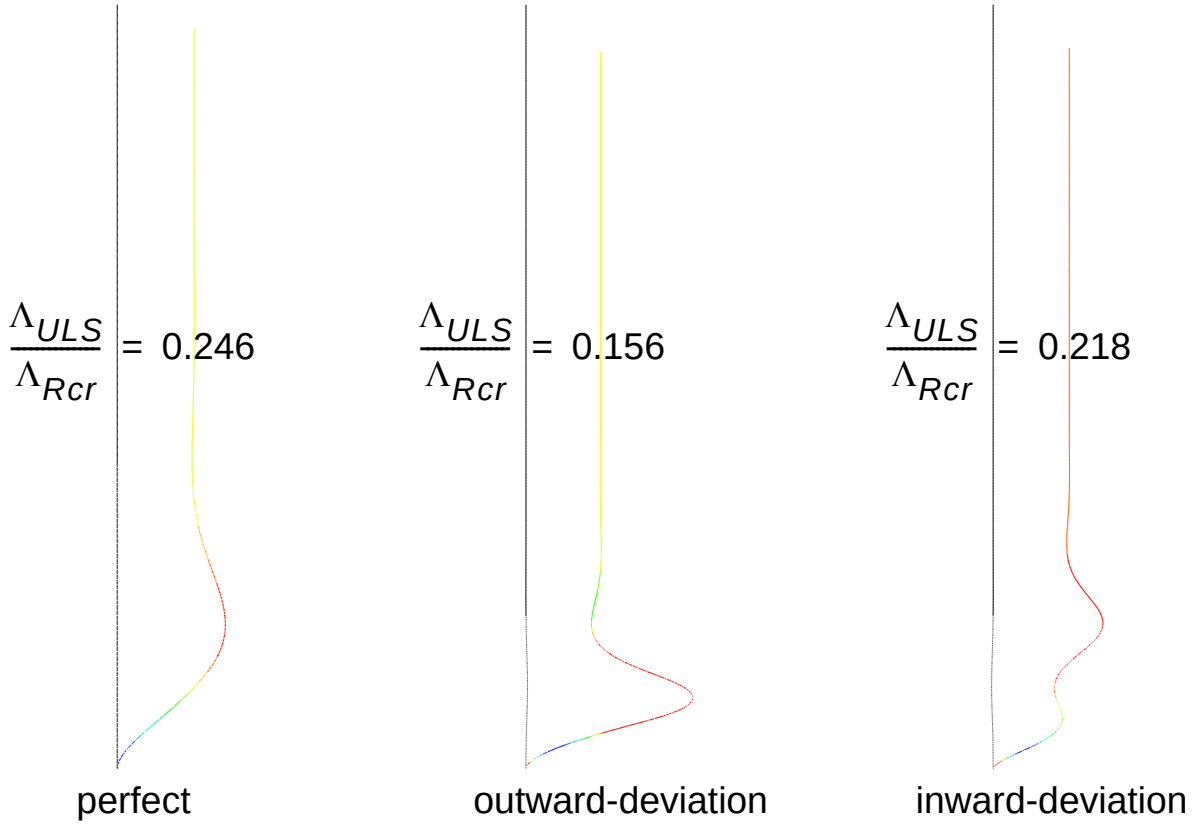

Figure 3.73 Radial deformation: snap-through eigenmode-affine imperfection

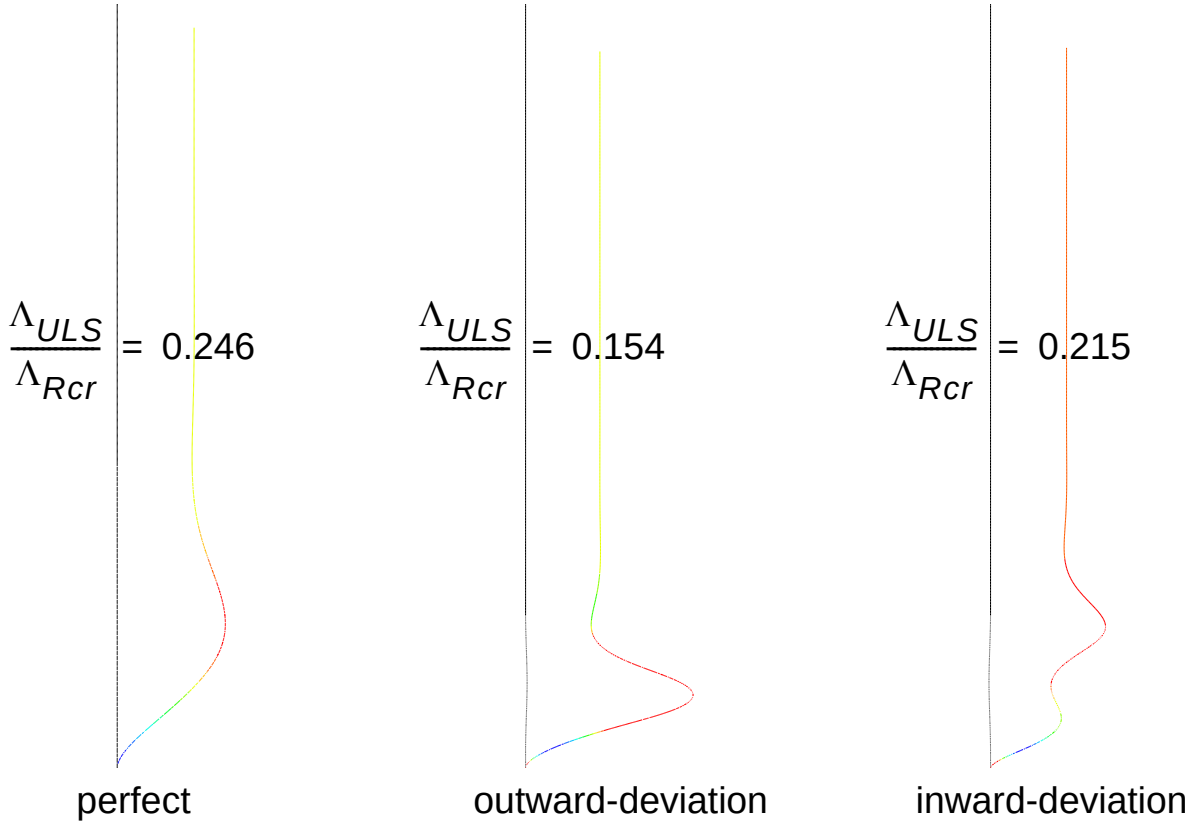

Figure 3.74 Radial deformation: type-(a) imperfection, wavelength $4.0\sqrt{Rt}$ and up-shift $0.5\sqrt{Rt}$

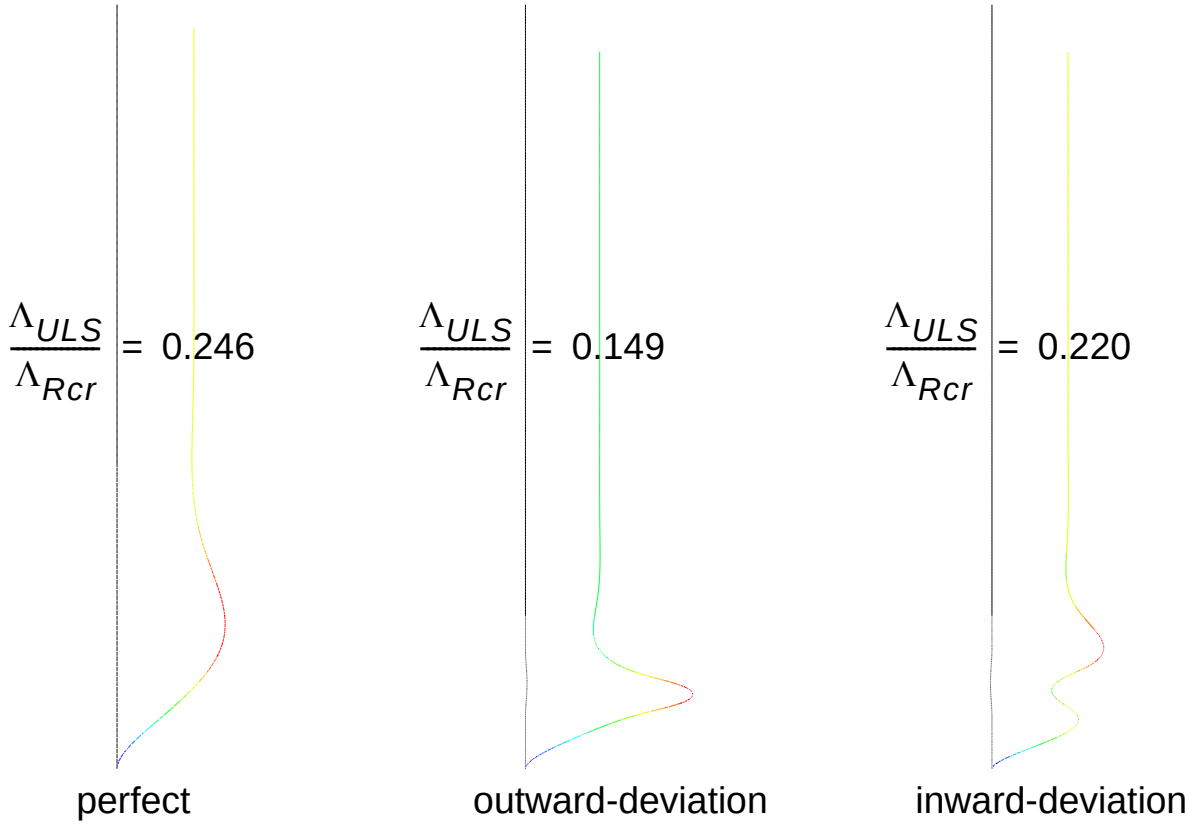

Figure 3.75 Radial deformation: type-(a) imperfection, wavelength $2.0\sqrt{Rt}$ and up-shift $1.5\sqrt{Rt}$

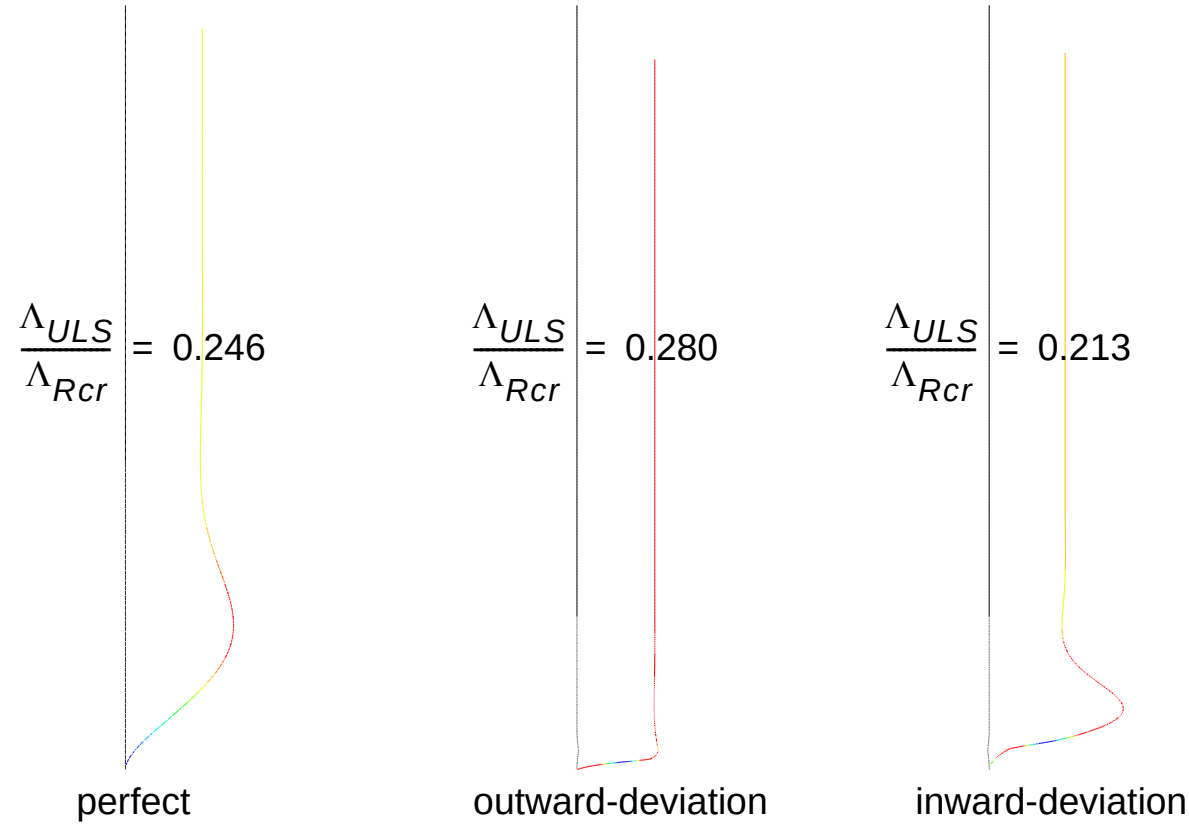

Figure 3.76 Radial deformation: type-(e) imperfection, wavelength = 25t and no up-shift

3.8.1.5 Local axisymmetric imperfection in the free shell interior

As it has already been discussed, when the internal pressure level acting on a thin-walled cylindrical shell is medium-to-high, it weakens the elastic-plastic buckling strength of the shell by raising the circumferential membrane stress to such an extent where bi-axial plasticty effect leads to buckling at a relatively low axial compressive load. Generally speaking, the elastic-plastic buckling behavior and buckling strength of an axially compressed and internally pressurized thin-walled metal cylindrical shells depend on the imperfection nature (shape, wavelength, amplitude, orientation, and location along the meridian), edge constriction effects, and resulting buckling modes. For an ideally perfect cylinder or if the strength-reducing effect of imperfections are negligible, the effect of edge constriction comes into play resulting in a bulge type buckling mode near the edge. The effect of pure edge constriction on the buckling phenomenon and buckling strength of a perfect cylinder has already been discussed. On the other hand, when combined with ill-natured axisymmetric imperfections, the weakening effect of the medium-to-high internal pressure, will be more pronounced that the cylinder buckles at a very low axial compressive load. Such imperfection-led buckling phenomenon happens at the location of the imperfection. In cases where there exist a worst imperfection at locations of edge constriction or when both are closely located and able to interact, it is clear that the two effects help each other in destabilizing the shell. The worst possible combined effect of an edge constriction and an imperfection in destabilizing the cylindrical shell has also been already discussed.

It is, however, not clearly understood so far that when both exist on a shell but at different locations along the meridian with no interaction of any kind among them, a very closer look and comparison need to be made on the resulting buckling modes and buckling strengths. This study addresses an imperfection-led axisymmetric elastic-plastic buckling caused by an axisymmetric local imperfections. This will be done by applying a local axisymmetric imperfection up the meridian on a location where there exist no edge constriction effects (free shell interior). To investigate this type of buckling phenomenon and the corresponding buckling strength, materially and geometrically nonlinear analyses of the illustrative cylindrical shell with local axisymmetric imperfection types (a) and (e), Figure 3.62, have been made with wavelengths of $4.0\sqrt{Rt}$ and 25t, respectively, and imperfection amplitudes allowed for fabrication quality classes A, B, and C as given in EN1993-1-6. Both outward and inward orientations of the imperfections and their effects are considered in the investigation.

The results of the GMNLI analyses and their comparisons with the buckling strengths obtained from the elastic-plastic interaction using the basic plastic interaction parameters, pure effects of edge constriction (perfect elephant’s-foot buckling strength), and combined effects of edge constriction and imperfection (imperfect elephant’s-foot buckling strength) are discussed as follows.

Surprisingly, an inward-oriented class-A general-type (type-(a)) local axisymmetric imperfection with wavelength of $4.0\sqrt{Rt}$ in the free shell interior (no edge constriction effects) has the same reduction effect in the elastic-plastic buckling strength as the edge constriction of the perfect shell (perfect elephant’s-foot buckling), Figure 3.78. For the lower quality classes of the inward-oriented

imperfection and all quality classes of the outward-oriented imperfection, an imperfection-led buckling in the free shell interior governs the buckling phenomena when compared to the edge constriction effect. The results obtained tell the that the effect of edge constriction is not as unfavorable as one may think when compared with an imperfection-led buckling in the free shell interior. The buckling strengths obtained from the elastic-plastic interaction using the basic plastic interaction parameters are generally unconservative when compared with the GMNIA results obtained using the aforementioned imperfection.

When a weld-type imperfection with wavelength of 25t is used, irrespective of the imperfection-orientation and fabrication quality class, the effect of edge constriction governs the buckling phenomena and the buckling strengths obtained from elastic-plastic interaction using the basic plastic interaction parameters are generally conservative to use, Figure 3.79.

Moreover, the imperfection-led elastic-plastic buckling strengths were compared with the buckling strength obtained using the combined effects of imperfection and edge constriction for the general-type (type-(a)) imperfection with wavelength of $4.0\sqrt{Rt}$ as shown in Figure 3.80. In the consideration of the combined effects of imperfection and edge constriction, the imperfection was shifted up by $0.5\sqrt{Rt}$ where its relative effect is worst. The results obtained tell the fact that the effect of edge constriction, once again, is not as unfavorable as one may think when compared with an imperfection-led buckling in the free shell interior.

It can be seen from the already investigated imperfection-led elastic-plastic buckling in the free shell interior that the buckling strength depends on the shape, orientation, and amplitude of the imperfection under consideration. Thus, there remains a challenge to decide on the form and amplitude of the imperfection. For this reason, the buckling strengths obtained from elastic-plastic interaction using the basic plastic interaction parameters are refered to, in the remaining discussions, as the elastic-plastic buckling strengths in the free shell interior, Figure 3.77.

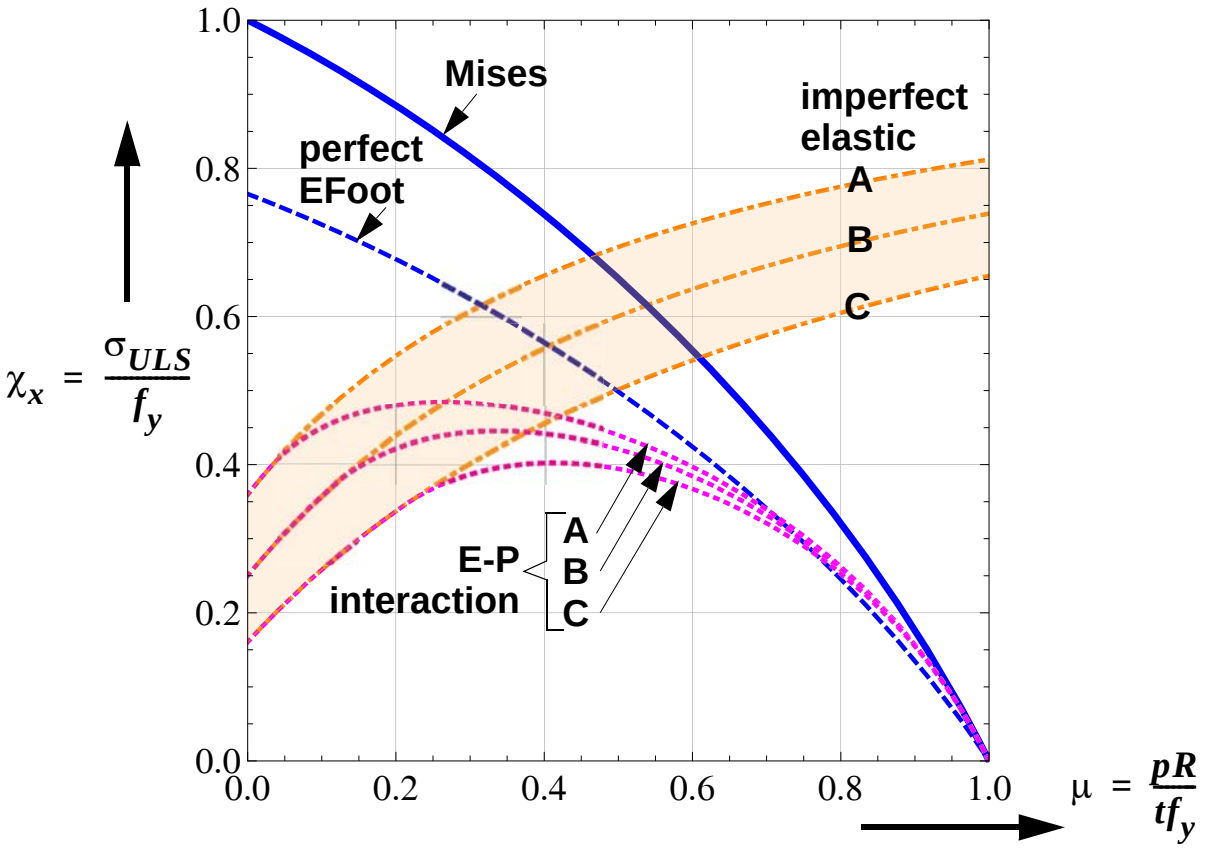

Figure 3.77 Buckling strength: R/t = 500, fixed bottom

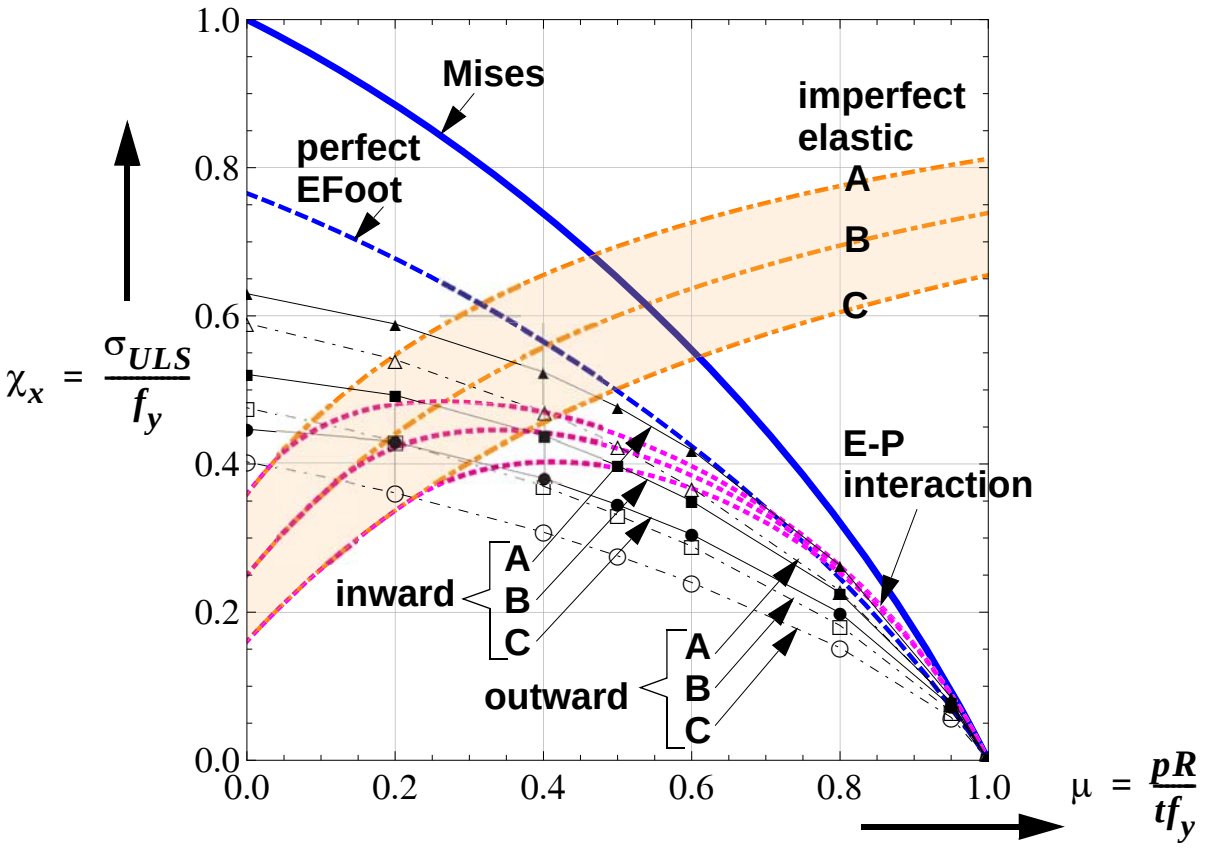

Figure 3.78 Buckling strength: R/t = 500, type-(a) imperfection, fixed bottom

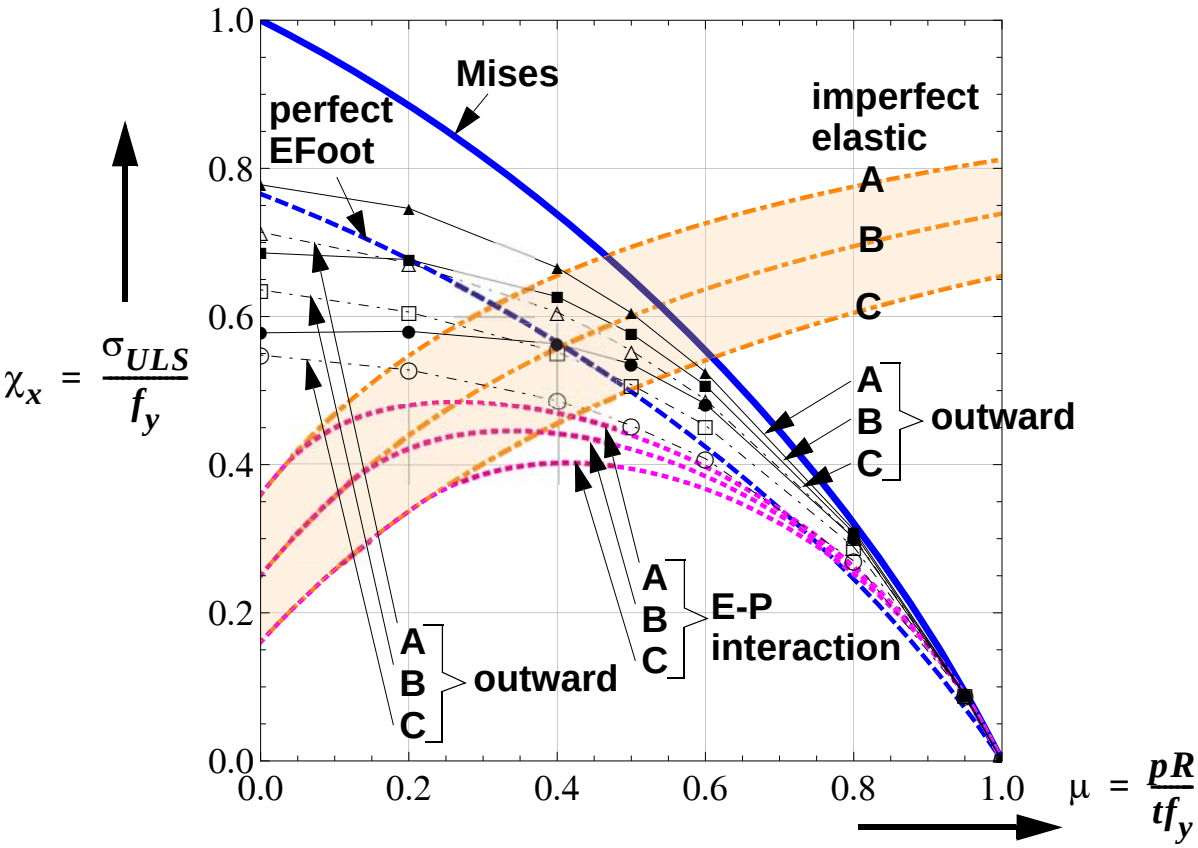

Figure 3.79 Buckling strength: R/t = 500, weld-type imperfection, fixed bottom

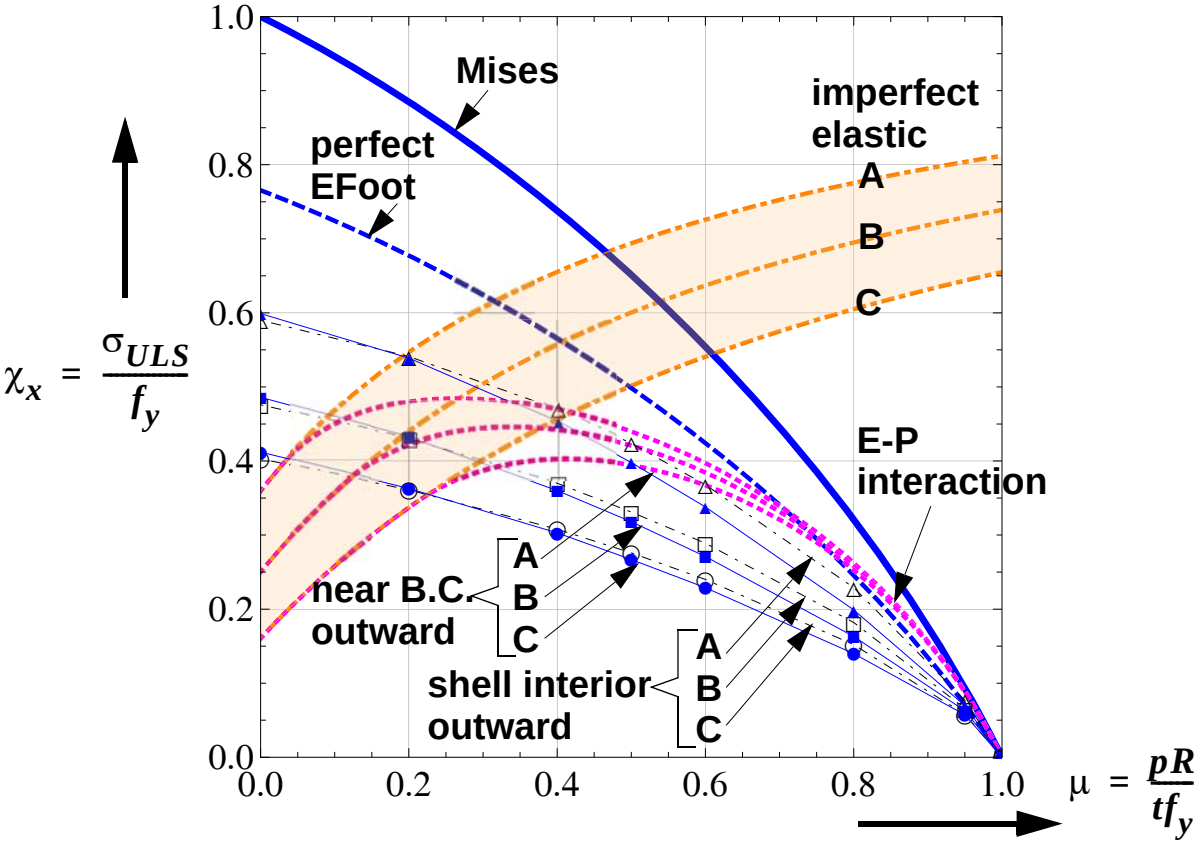

Figure 3.80 Buckling strength: R/t = 500, type-(a) imperfection, fixed bottom

3.9 New buckling design recommendation

3.9.1 General characteristic buckling strength

Figure 3.81 and Figure 3.82 (for fixed and pinned bottom boundary conditions, respectively) show the combined plots of pure elastic imperfect buckling strength, shell interior elastic-plastic imperfect buckling strength, and near boundary perfect elastic-plastic (perfect elephant-foot) buckling strength in the pressure representation.

Figure 3.83 shows a 3D plot of the elastic-plastic buckling interaction using the basic plastic buckling parameters and the elephan's-foot buckling strength. Both modes are dominated and limited by the bi-axial Mises membrane yield condition. The minimum strength (envelope) of the two strengths is shown in Figure 3.84. Figure 3.85 shows the reduction in strength due to edge constriction of a pinned bottom cylinder causing elephant's-foot buckling when compared with the elastic-plastic buckling in the free shell interior as computed by using the basic plastic interaction parameters. This reduction is even smaller when the bottom boundary condition of the cylinder is clamped (fixed). From this comparison, it turns out that the boundary elastic-plastic buckling mode is not significantly more unfavourable than the related free-shell-interior elastic-plastic buckling mode. This is in contrast to some of the existing interpretations and explanations that compare the edge constriction effects with the small displacment elastic and platic strengths as shown in Figure 3.86. The combined effects of imperfection and edge bending disturbance in destablizing the shell have already been discussed in the GMNIA investigation.

Explanatory plots of all characteristic buckling strengths corresponding to the different buckling phenomena are shown in Figure 3.87 to Figure 3.90. For a clear understanding of the different representations, the same characteritsic buckling strengths are shown in pressure representation (Figure 3.87), capacity representation (Figure 3.88), membrane Mises-related interaction representation (Figure 3.89), and perfect elephant's-foot-related interaction representation (Figure 3.90). Basic understanding of these different representations will help in easy manipulation of the buckling strength results and ultimately leading to the best representation where simple expressions can be formulated that are able to accurately predict the characteristic buckling strength of the cylinder.

It should again be noted that as far as elastic-plastic buckling of the imperfect cylindrical shells is concerned, there should be a well defined (at least for numerical simulation purposes), practically possible (both from safety and economic considerations), and worst (in that it leads to lower buckling strength of the shell) imperfection. Once such imperfections are known and agreed upon by the research and practical engineers community, a unified and simplified design proposals can be made. In spite of this fact, different possible proposals are discussed in the following section, out of which the simplest yet best approach will be recommended for design and future researchs.

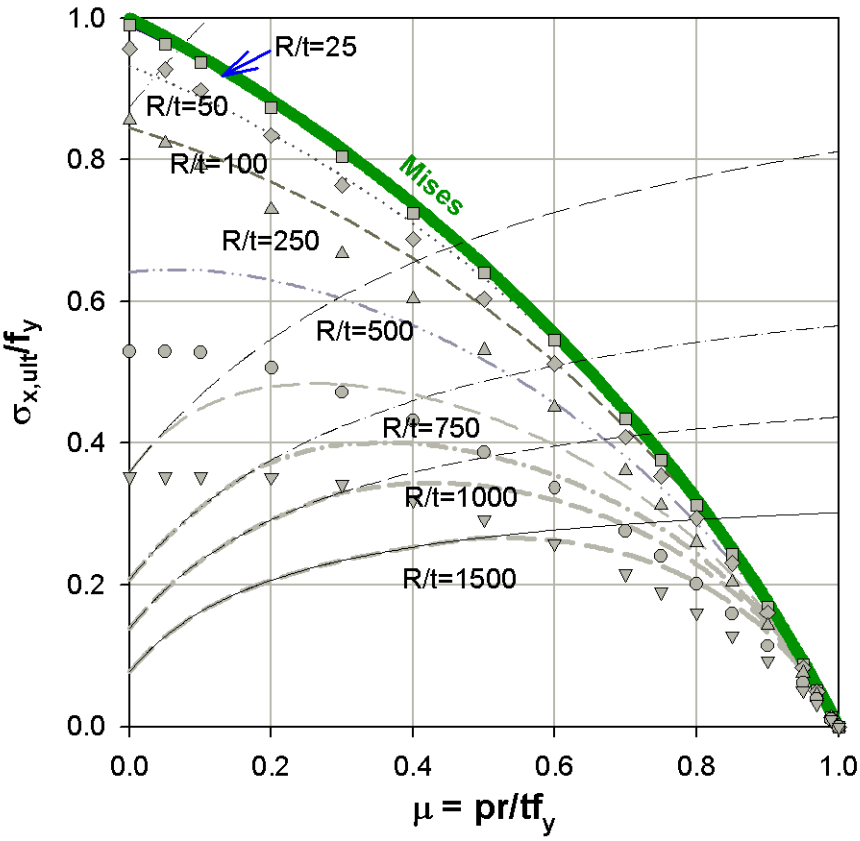

Figure 3.81 Perfect elephant's-foot buckling strength: fixed bottom

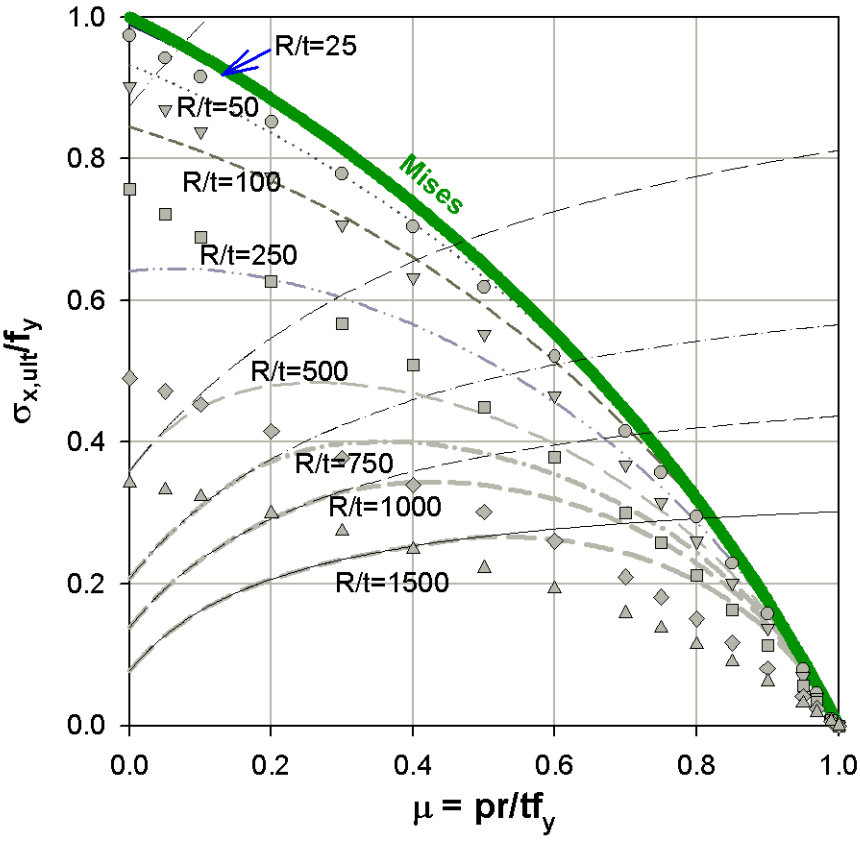

Figure 3.82 Perfect elephant's-foot buckling strength: pinned bottom

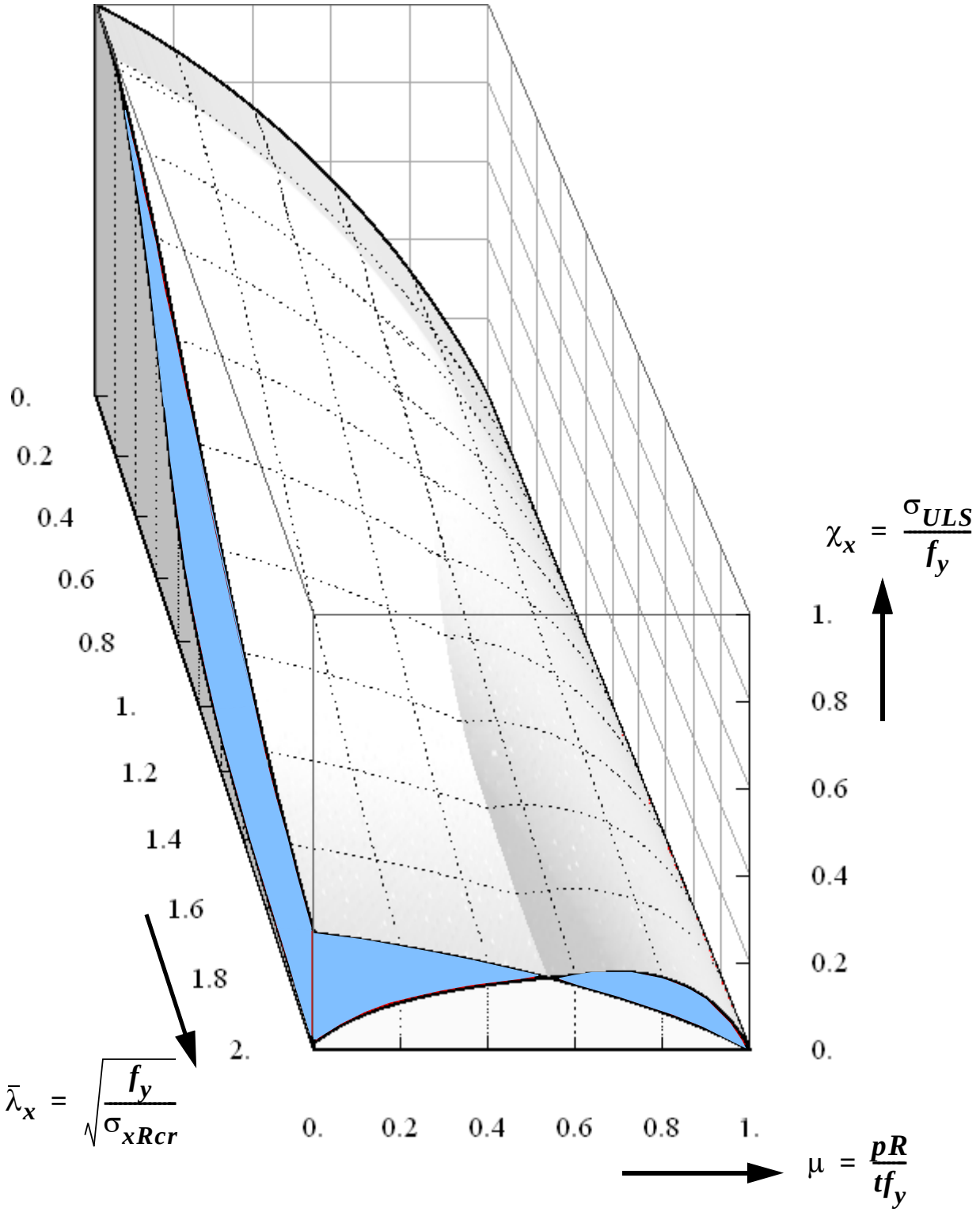

Figure 3.83 Comparison of elastic-plastic buckling interaction using basic plastic buckling parameters with elephant's-foot strength

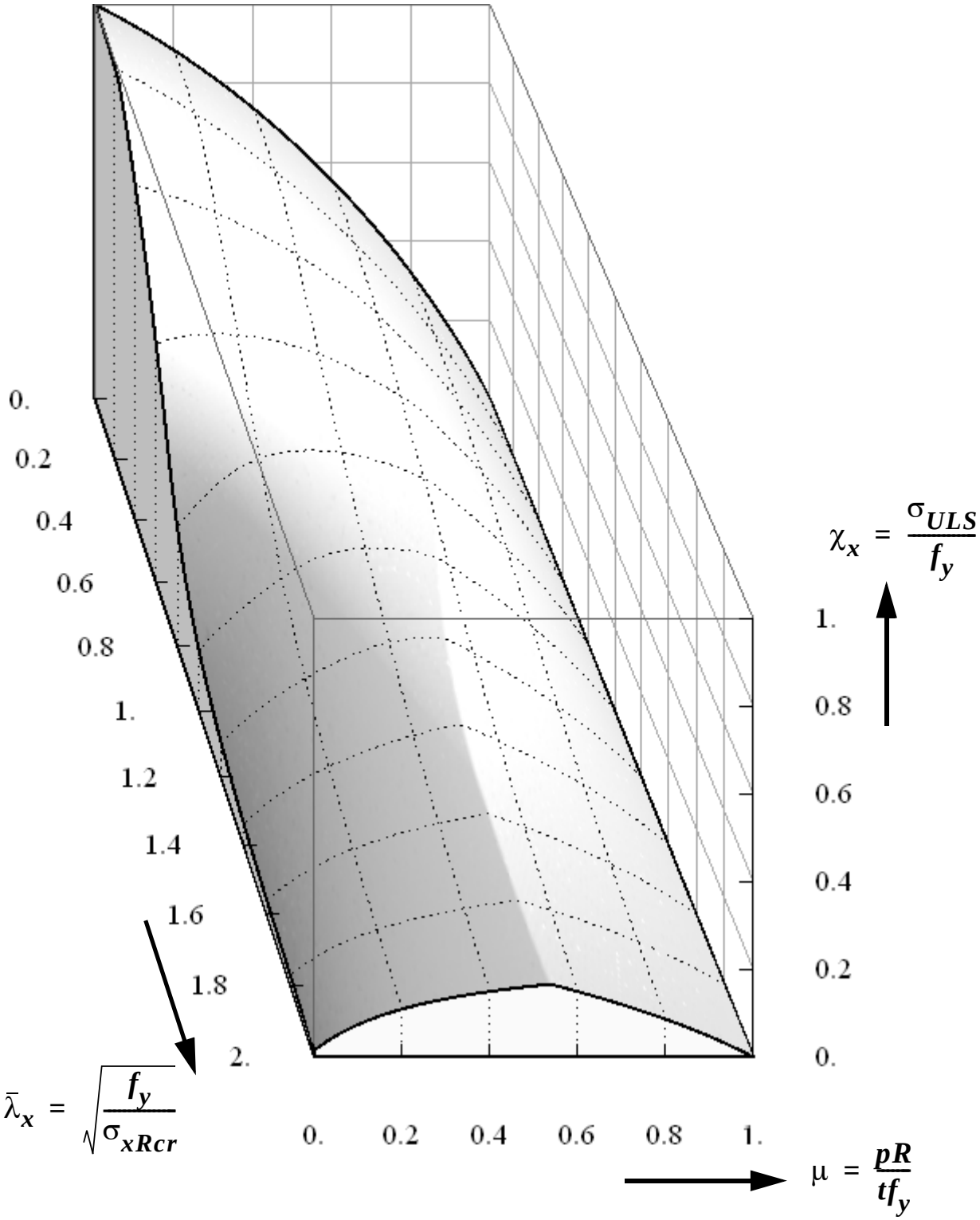

Figure 3.84 Envelope of elastic-plastic buckling interaction using basic plastic buckling parameters and elephant's-foot strength

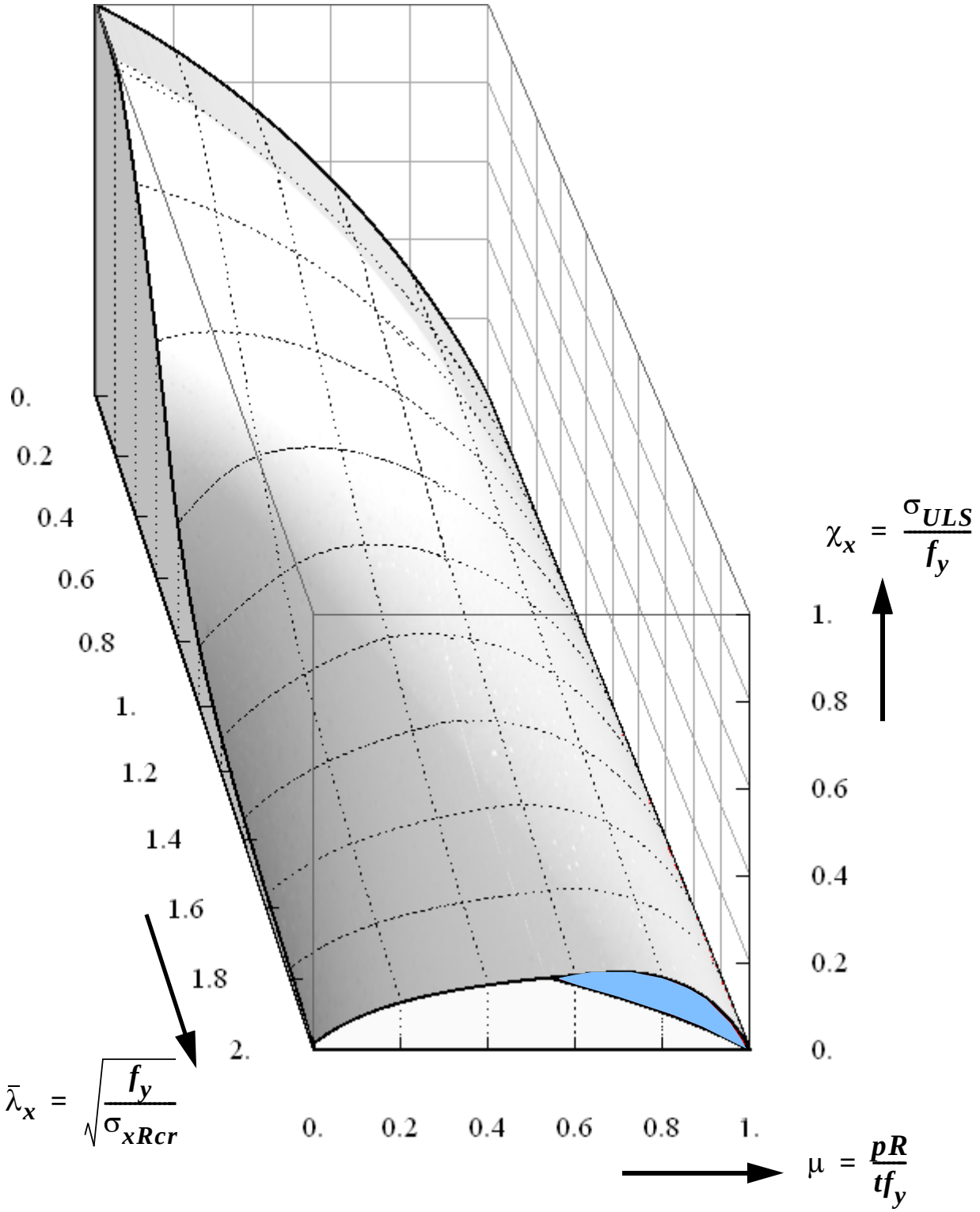

Figure 3.85 Buckling strength reduction due to edge constriction effects causing elephant's-foot buckling when compared with elastic-plastic buckling in the free shell interior

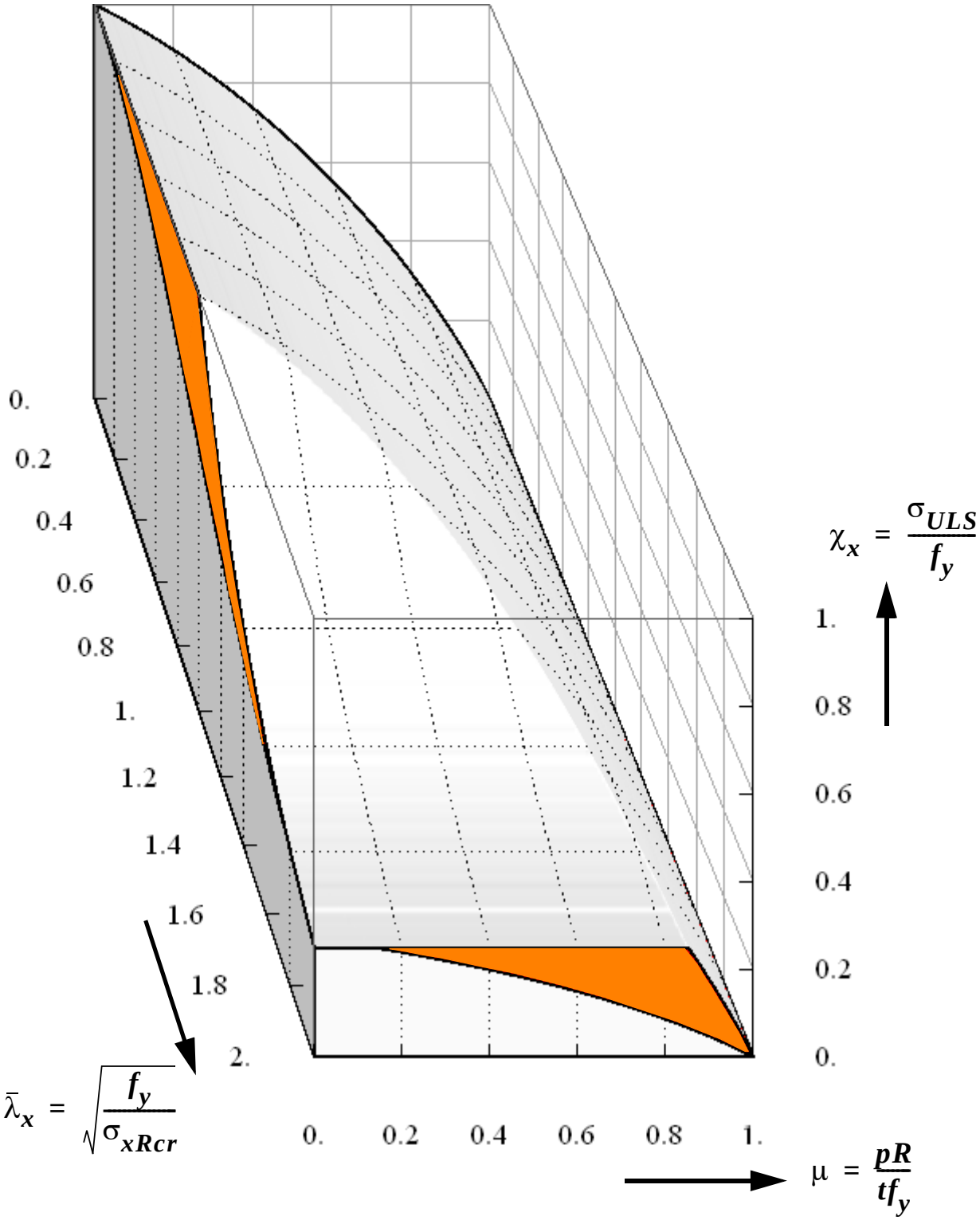

Figure 3.86 Buckling strength reduction due to edge constriction effects causing elephant's-foot buckling when compared with pure elastic and pure plastic strengths of the perfect shell

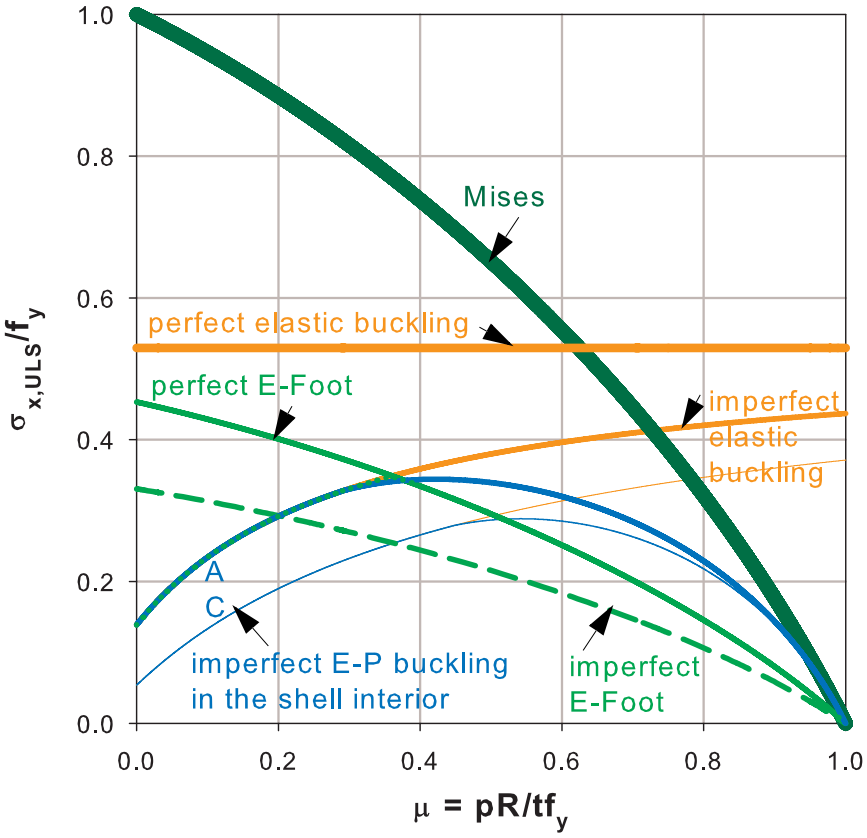

Figure 3.87 Comparison of different buckling strengths in pressure representation

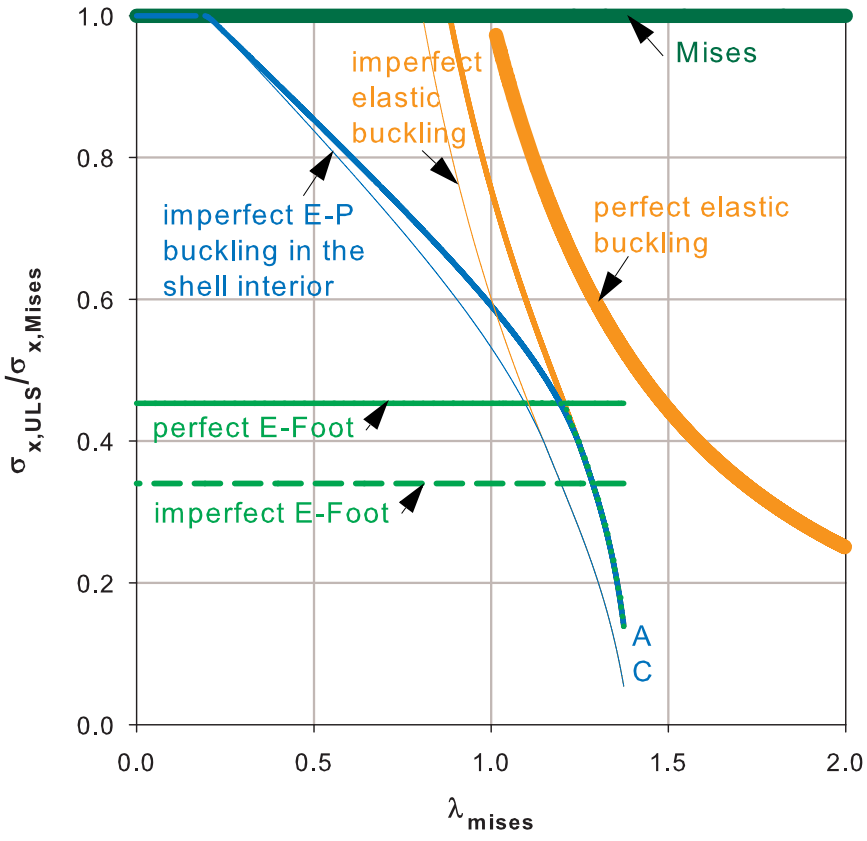

Figure 3.88 Comparison of different buckling strengths in capacity representation

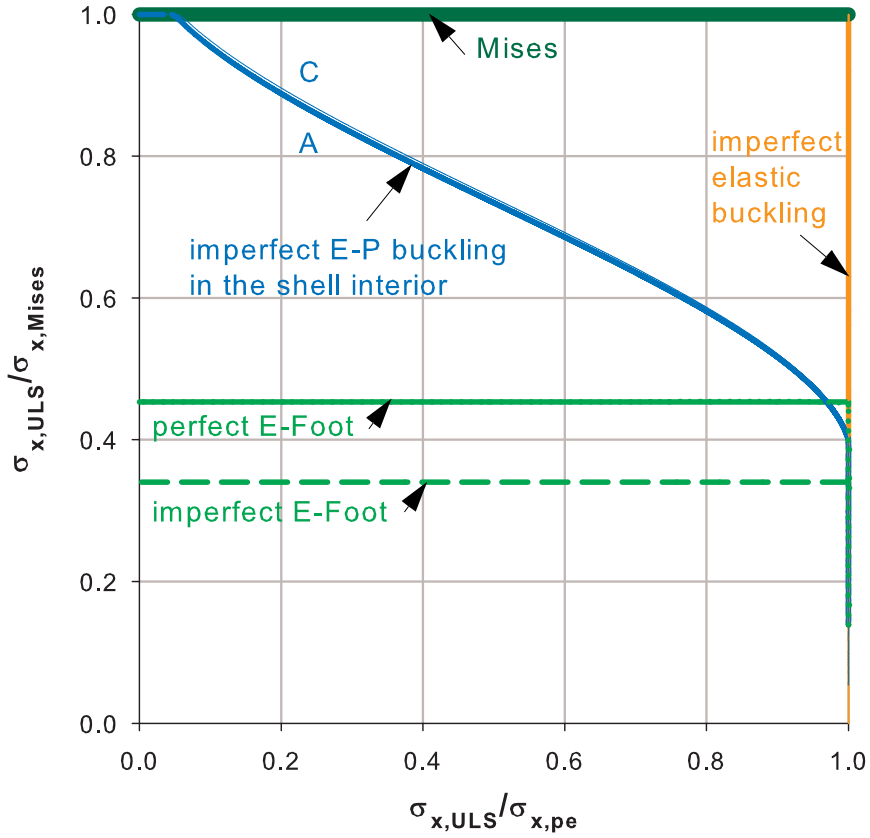

Figure 3.89 Different buckling strengths in Mises-related interaction representation

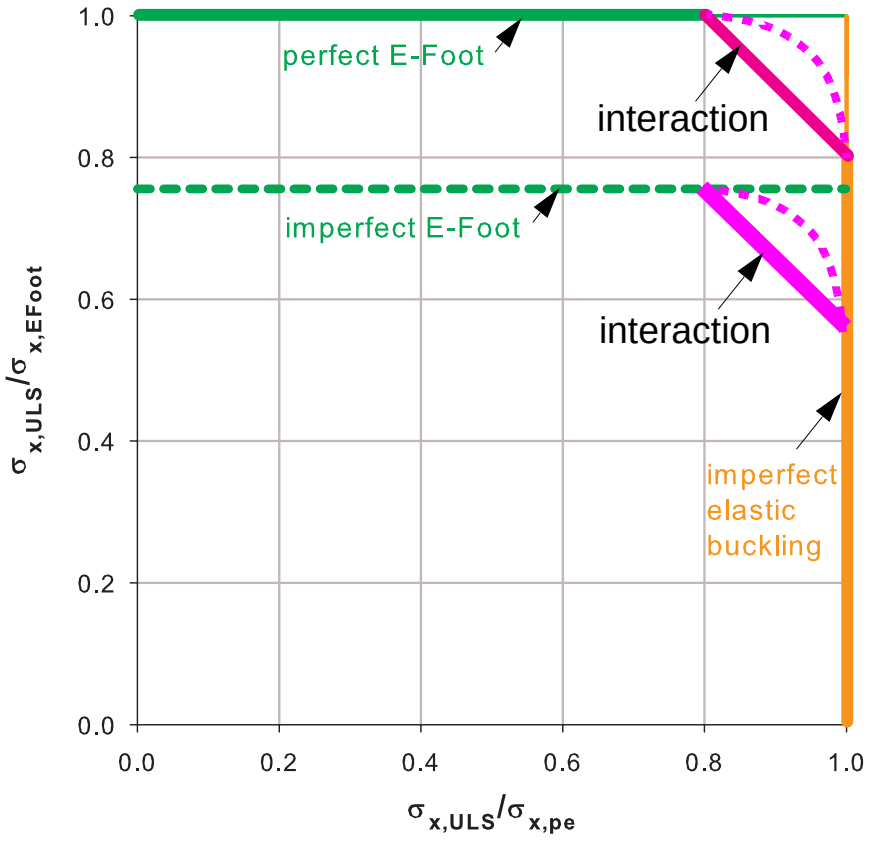

Figure 3.90 Different buckling strengths in EFoot-related interaction representation

3.9.2 Characteristic buckling strength prediction recommendation

Based on the results obtained so far for the different buckling phenomena and their corresponding buckling strengths, five different methods can be applied in the prediction of the characterstic buckling strength of thin-walled cylindrical shells under uniform axial compression and internal pressure loading. In all the methods separation is made for the different types of bottom boundary condtions (fixed versus pinned).

An overview of the five possible options for predicting the characterstic buckling strengths of cylindrical shells is given below. Detailed discussion on each approach will then follow.

Method -1. elastic-plastic interaction with the bi-axial membrane Mises to directly catch the pure elastic, elastic-plastic buckling in the shell interior, and elephant's-foot buckling strengths using a new set of plastic buckling interaction parameters (see Figure 3.91).

Method - 2a. envelope of the pure elastic and elephant's-foot strengths with no interaction of any kind. This method results in somehow unconservative buckling strength prediction when compared to the other methods. The left part in the envelope (see Figure 3.92) represents pure elastic buckling strength of the imperfect shell and the right part for elastic-plastic buckling near the boundary of the perfect shell.

Method - 2b. envelope of the pure elastic, elastic-plastic interaction with bi-axial membrane Mises using the basic plastic buckling parameters, and the perfect elephant's foot buckling strength. The first (left) part in the envelope (see Figure 3.93) represents pure elastic buckling strength of the imperfect shell; the second (middle) part represents the elastic-plastic buckling strength in the free shell interior; and the third (right) for elastic-plastic buckling near the boundary.

Method - 3. elastic-plastic buckling interaction of the pure elastic strength curve with the elephant's foot strength curve using the basic plastic buckling parameters $\beta = 0.6$; $\overline{\lambda}_0 = 0.2$; and $\eta = 1.0$. This approach leads to very big interaction and too conservative strength predictions (see Figure 3.94).

Method - 4. elastic-plastic buckling interaction of the pure elastic strength curve with the elephant's-foot strength curve using a completely new single buckling parameter $\Delta\beta_{EFoot}$. This method, depending on the value of $\Delta\beta_{EFoot}$, predicts the separate characteristic buckling strengths: pure elastic, elephant's-foot near the boundary, and a possible interaction in between (see Figure 3.95 for $\Delta\beta_{EFoot} = 0.1$). This method, as it will be seen later, is the simplest, easy to understand, easy to apply, easy to modify, straight forward, and yet accurate (specially when compared to method-1). Hence, it is the best approach of all the methods discussed so far.

All the above procedures (except method-3) predict same or very close strength results in the pure elastic (low pressure level) and elastic-plastic elephant's-foot buckling near the boundary (high pressure level). They, however, differ in the strength prediction of the elastic-plastic buckling in the free shell interior. These differences are left open till test or GMNIA results are performed for elastic-plastic buckling in the free shell interior. Since the bi-axial membrane Mises yield condition

is on the background, all the methods by default guarantee that no buckling strength exceeds the pure plastic capacity. An illustrative comparison of the different methods (a combination of Figure 3.91 to Figure 3.95) has been done for a cylinder with fixed bottom boundary condition and shell slenderness ratio R/t = 1000 and is shown in the pressure representation, Figure 3.96. For very thin shells the characteristic buckling strength prediction using method-1 is equal to that of method-2, i.e the elastic-plastic buckling interaction according to method-1 diminishes as the shell gets thinner.

A detailed discussion on the above methods is given below. Method-3 will be skipped in the discussion as it predicts buckling strengths much too low when compared to the other methods. It is upto the designer's choice which one of the above procedures to use for the prediction of the characterstic buckling strength. It should, however, be noted here that the elephant's-foot type buckling near the bounadary for the imperfect cylinder is not included and hence that of a perfect cylinder is used in all the methods as there is no common agreement on the "practical and worst" imperfection shape, wavelength, amplitude, location along the meridian of the shell, and the orientation of the imperfection in the inward-outward sense. Once a common agreement is reached on the imperfection type, the geometrically and materially nonlinear analysis results of the imperfect shell can directly be applied to method-2 (the envelope method) and easily be adopted to all other methods.

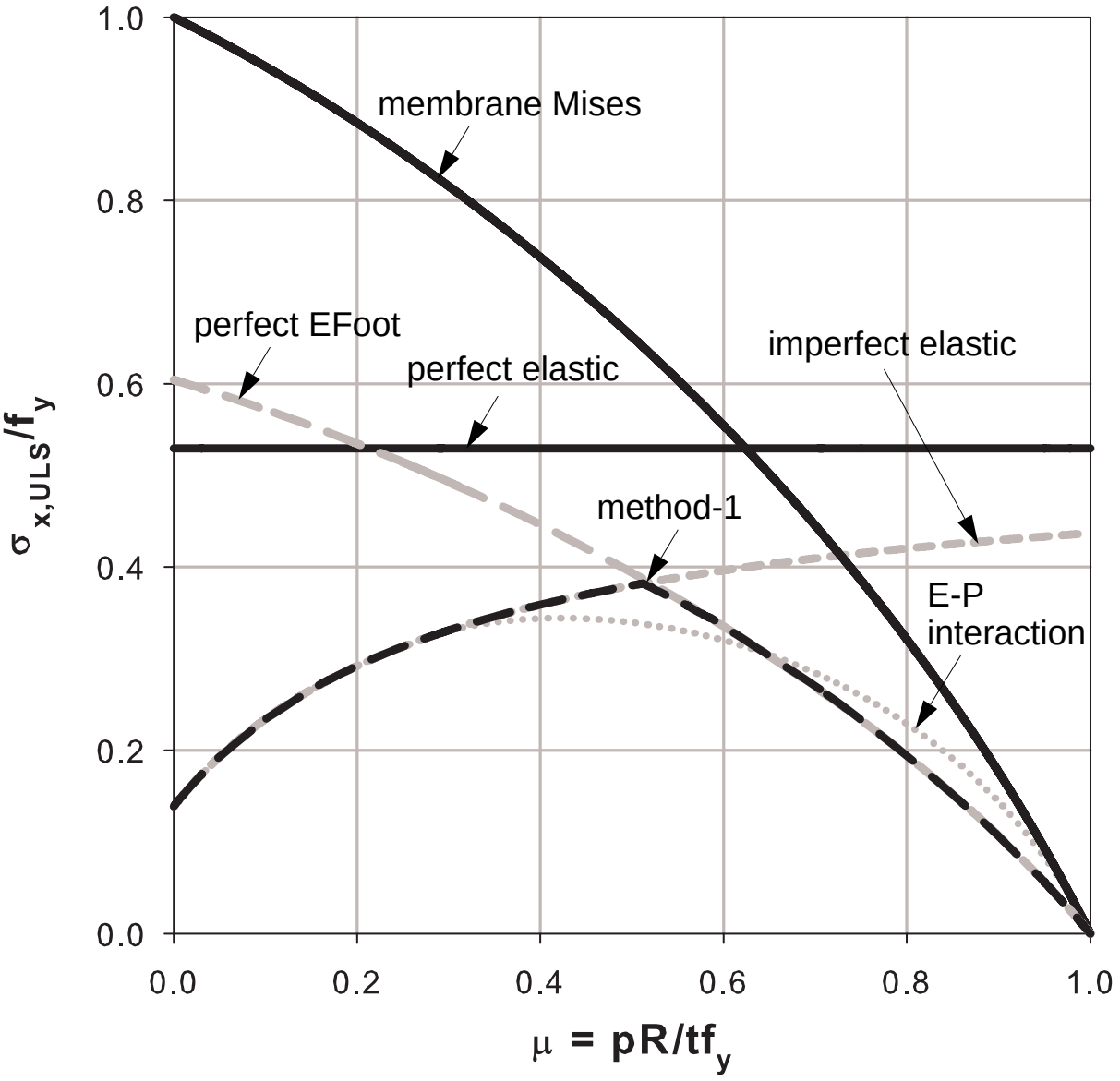

Figure 3.91 Characteristic buckling strength prediction: R/t = 1000, method-1

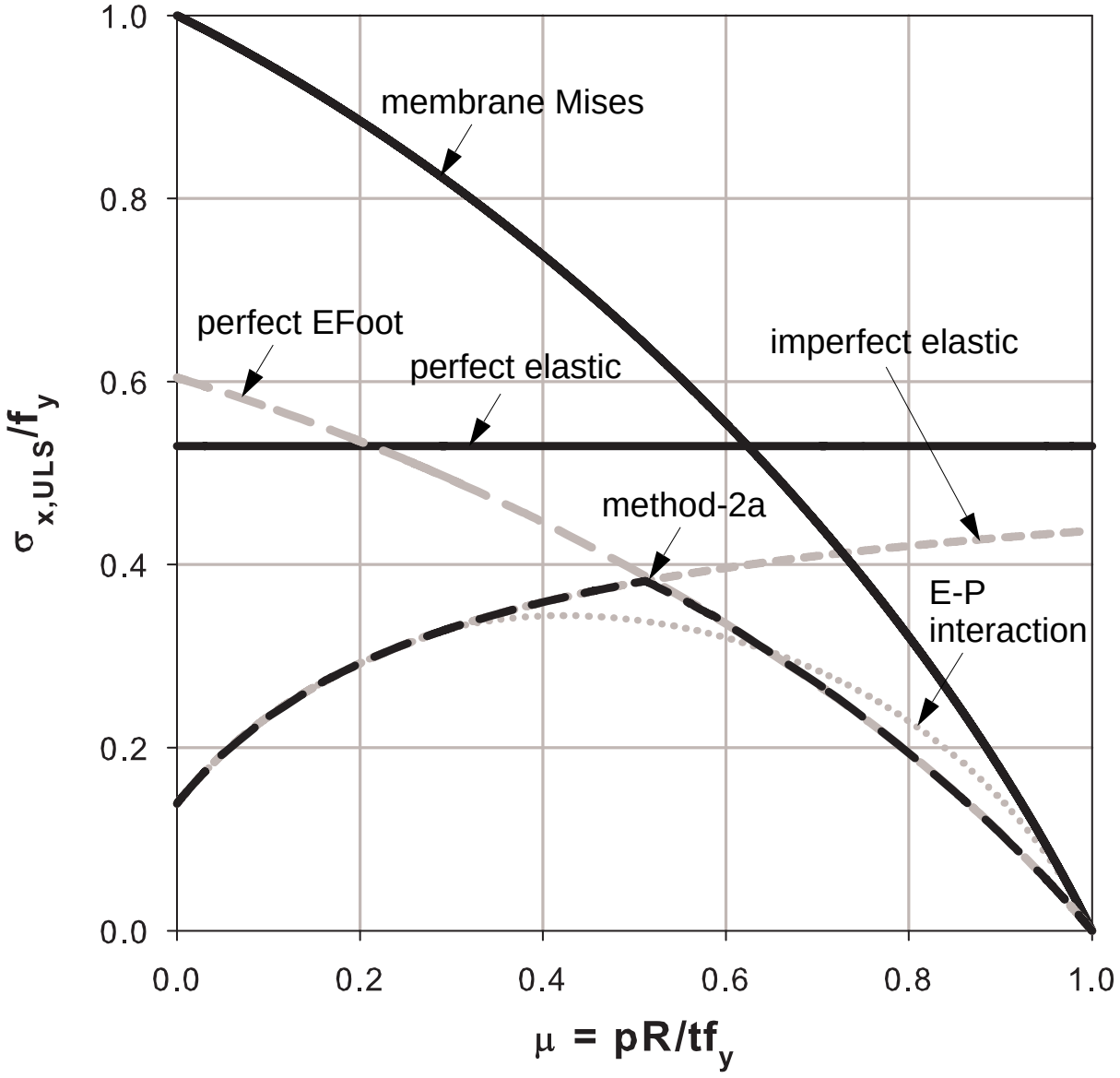

Figure 3.92 Characteristic buckling strength prediction: R/t = 1000, method-2a

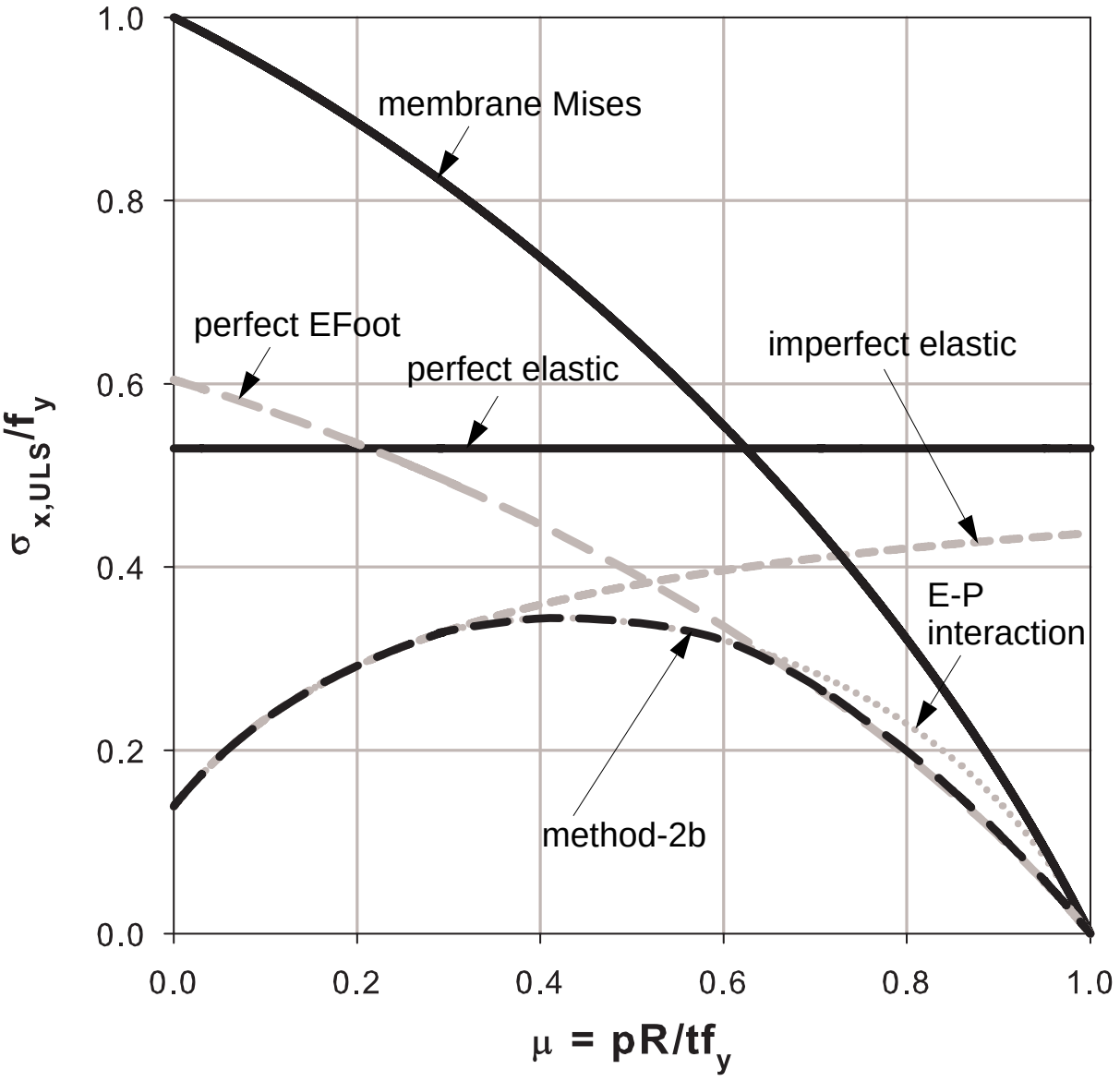

Figure 3.93 Characteristic buckling strength prediction: R/t = 1000, method-2b

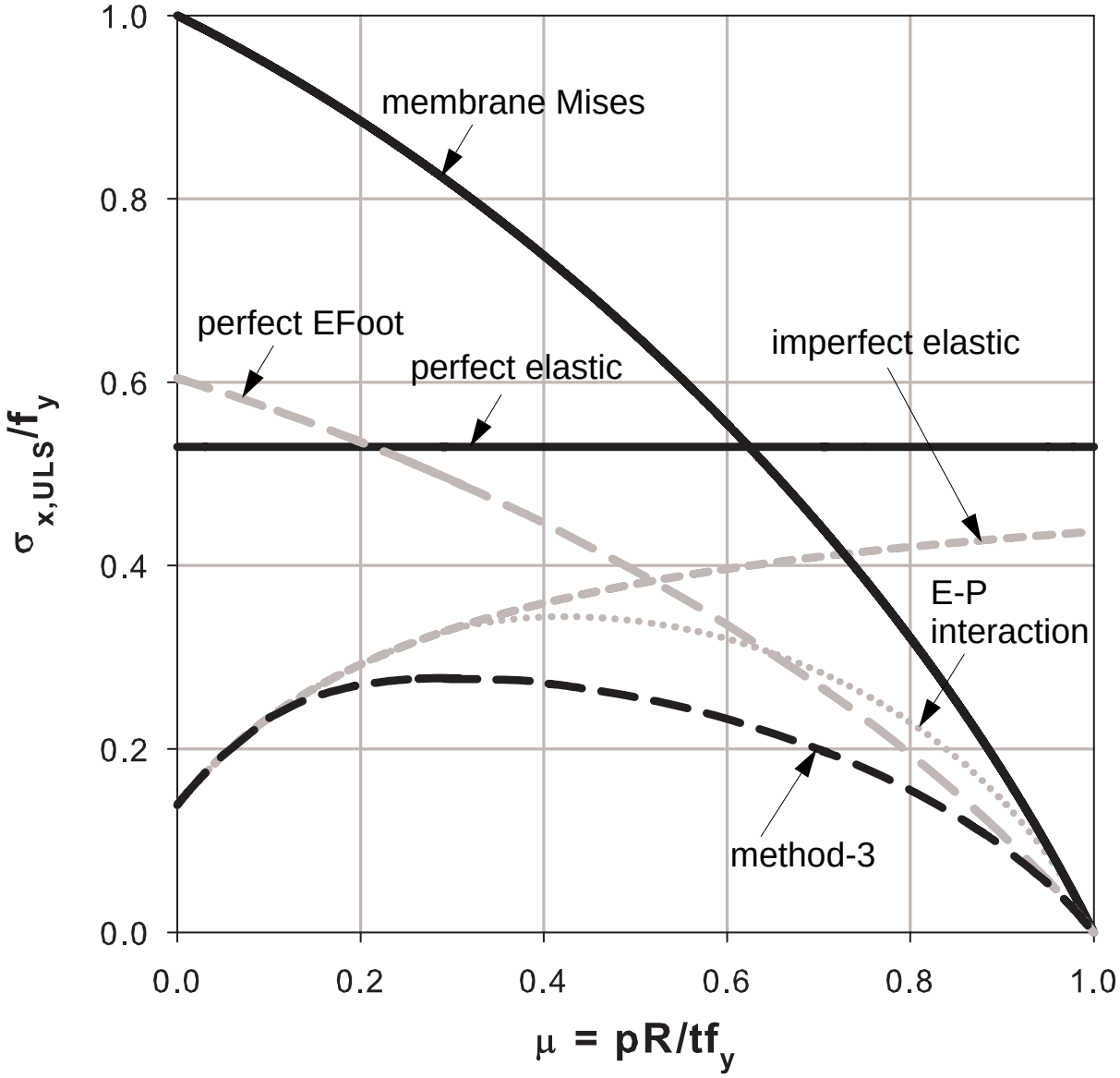

Figure 3.94 Characteristic buckling strength prediction: R/t = 1000, method-3

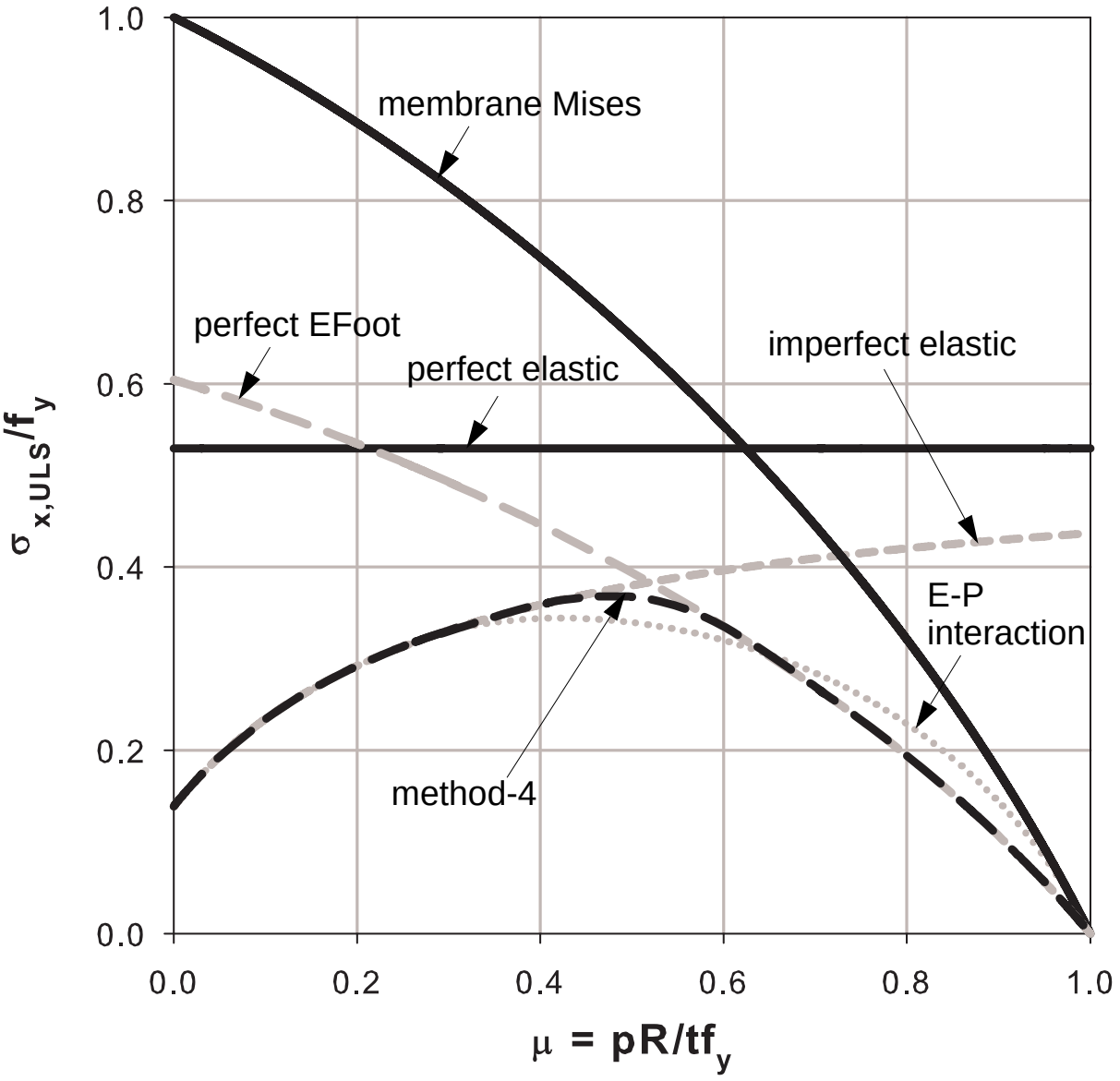

Figure 3.95 Characteristic buckling strength prediction: R/t = 1000, method-4

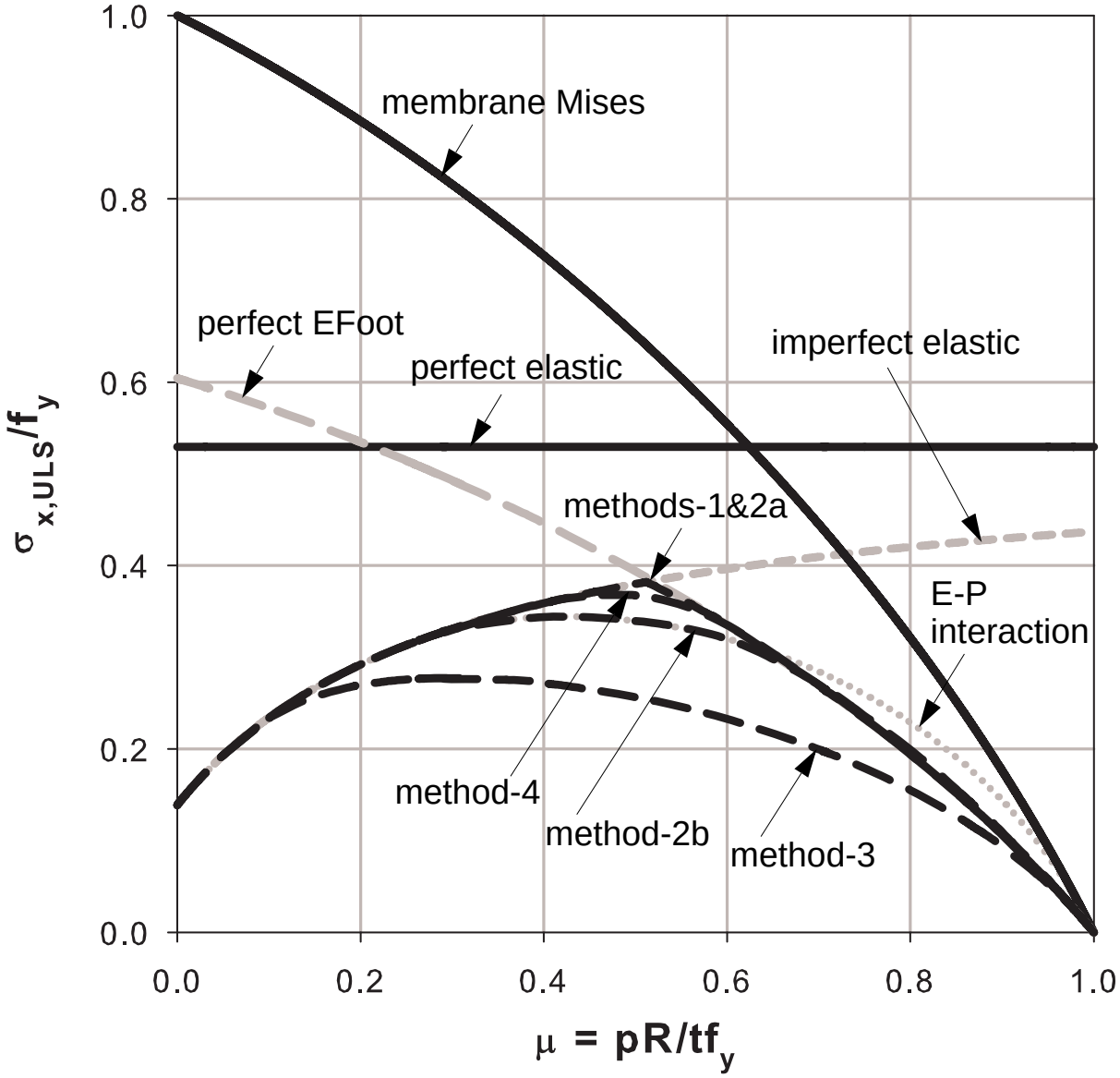

Figure 3.96 Characteristic buckling strength prediction: R/t = 1000, comparison of methods

3.9.2.1 Method-1: Elastic-plastic interaction using pressure dependent interaction parameters in such a way that EFoot strength is directly included

In this method the elastic-plastic interaction for the prediction of characteristic buckling strengths using membrane Mises yield condition will be extended and made in such a way that it directly includes the pure elastic buckling, elastic-plastic buckling in the free shell interior, and elephant-foot type buckling near boundary conditions. This will be achieved with the help of the geometrically and materially nonlinear numerical analysis results (for both the fixed and pinned bottom boundary conditions) using internal pressure dependent plastic buckling parameters $\bar{\lambda}_o(\mu)$, $\eta(\mu)$, and $\beta(\mu)$ instead of the basic constant values of an axially compressed and internally unpressurized cylinder. These new set of plastic buckling parameters do have the same values for unpressurized buckling conditions as those of the basic ones.

The pressurized elastic buckling strength of the imperfect thin-walled cylindrical shell, which have already been discussed, will be used in the following discussion on the new elastic-plastic buckling interaction formulation.

Plastic Buckling:

Pressure dependent plastic buckling parameters

Interaction exponent:

$$\eta = \eta_o \cdot f_0(\mu) \qquad \text{(Eq. 3.60)}$$

Squash limit relative slenderness:

$$\bar{\lambda}_o = \bar{\lambda}_{o,o} \cdot f_0(\mu) \qquad \text{(Eq. 3.61)}$$

Plastic range factor:

$$\beta = \beta_o + (\beta_{EFoot} - \beta_o) \cdot (1 - f_\beta(\mu)) \qquad \text{(Eq. 3.62)}$$

where η_o, $\bar{\lambda}_{o,o}$, and β_o are the basic plastic buckling parameters and stay valid for the unpressurized cylinder condition.

$$\eta_o = \eta(\mu = 0) = 1.0 \qquad \text{(Eq. 3.63)}$$

$$\bar{\lambda}_{o,o} = \bar{\lambda}_o(\mu = 0) = 0.2 \qquad \text{(Eq. 3.64)}$$

$$\beta_o = \beta(\mu = 0) = 0.6 \qquad \text{(Eq. 3.65)}$$

and the β_{EFoot} factor which takes care of the pressure-independent reduction in strength (when compared with the pure plastic capacity of the perfect shell) due to geometric nonlinearity (large deformation) effects is repeated here as follows

$$\beta_{EFoot} = \begin{cases} 0.8(1 - e^{-1.15\rho}) & \text{for pinned bottom} \\ 0.75(1 - e^{-0.75\rho}) & \text{for fixed bottom} \end{cases} \quad \text{(Eq. 3.66)}$$

in which

$$\rho = \frac{R/t}{1000} \quad \text{(Eq. 3.67)}$$

$$f_0(\mu) = (1 - \mu^2)^a \quad \text{(Eq. 3.68)}$$

$$f_\beta(\mu) = \left(1 - \mu^{1.5\sqrt{\bar{\lambda}_x}}\right)^a \quad \text{(Eq. 3.69)}$$

The value of the exponent “a” in the expressions for the f_0 and f_β is equal to 4 for the fixed-bottom cylinder and 8 for the pinned-bottom case. The variations of β_{EFoot} as a function of the shell slenderness parameter ρ; and f_0 & f_β for R/t = 1000 as a function of the internal pressure parameter μ are shown in Figure 3.97 and Figure 3.98, respectively, for both fixed and pinned bottom boundary conditions.

The characterstic buckling strength plots according to this method are shown using the pressure representation in Figure 3.99 and Figure 3.100 for both the fixed and pinned bottom boundary conditions, respectively. For a better view and comparison, the same plots are shown in Figure 3.101 and Figure 3.102 using the capacity representation, respectively. The difference in the characteristic buckling strength caused by the two types of bottom boundary conditions can be clearly seen from the plots. Figure 3.103 shows the 3D plot of the characteristic buckling strength of a cylindrical shell with fabrication quality class-C and pinned bottom boundary condition.

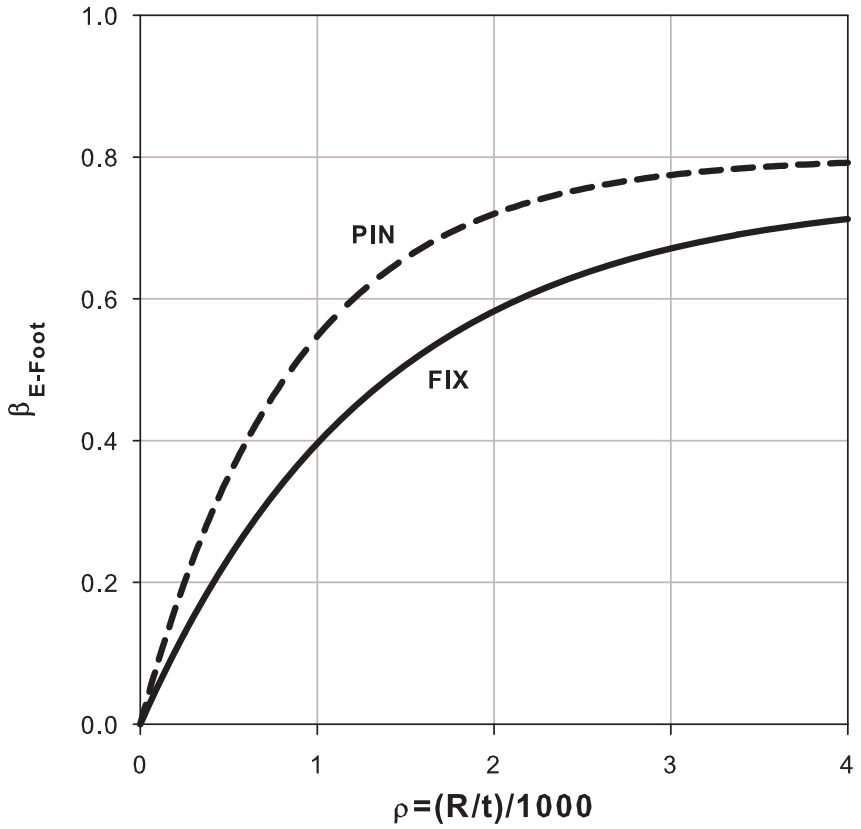

Figure 3.97 Comparison of β_{EFoot} values: pinned and fixed

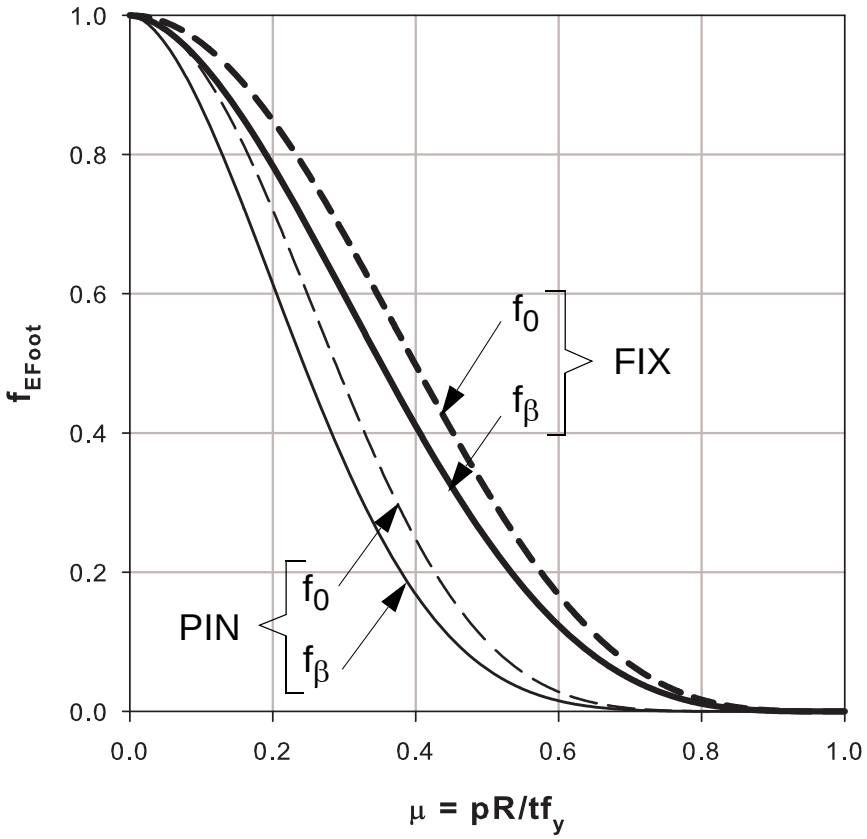

Figure 3.98 Comparison of f_0 & f_β values: pinned and fixed

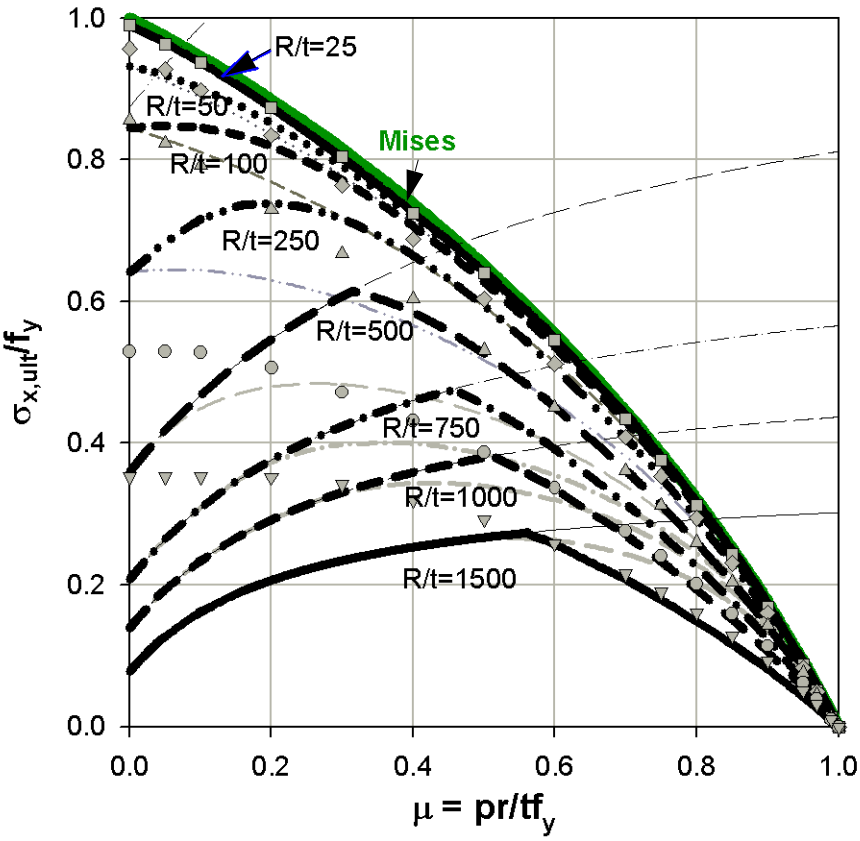

Figure 3.99 characteristic buckling strength according to method-1: fixed bottom

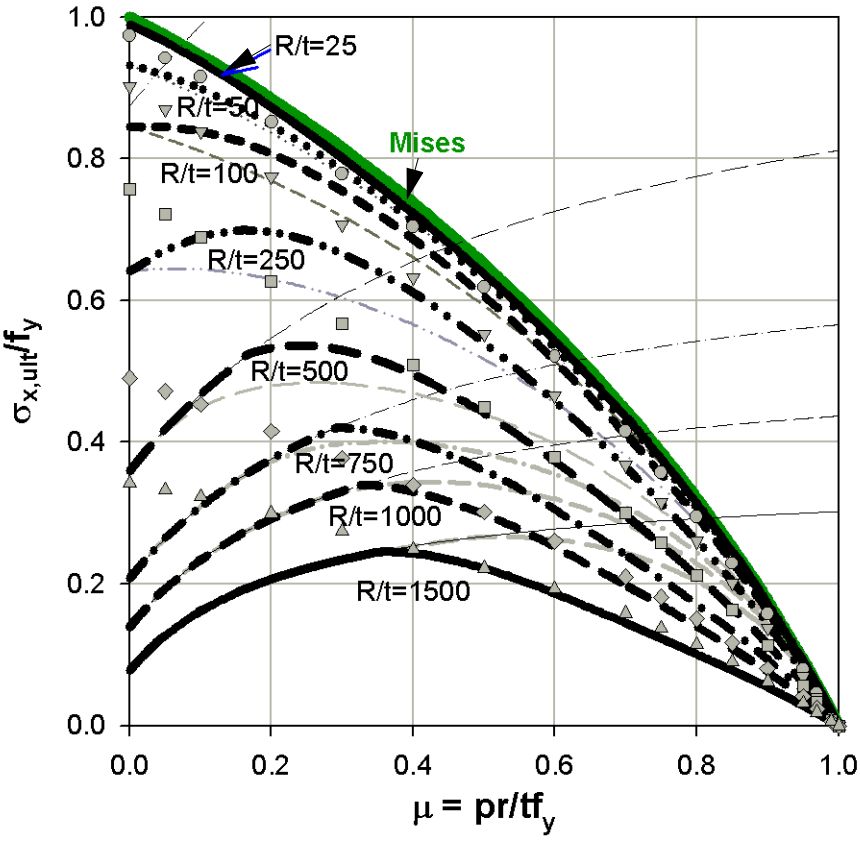

Figure 3.100 characteristic buckling strength according to method-1: pinned bottom

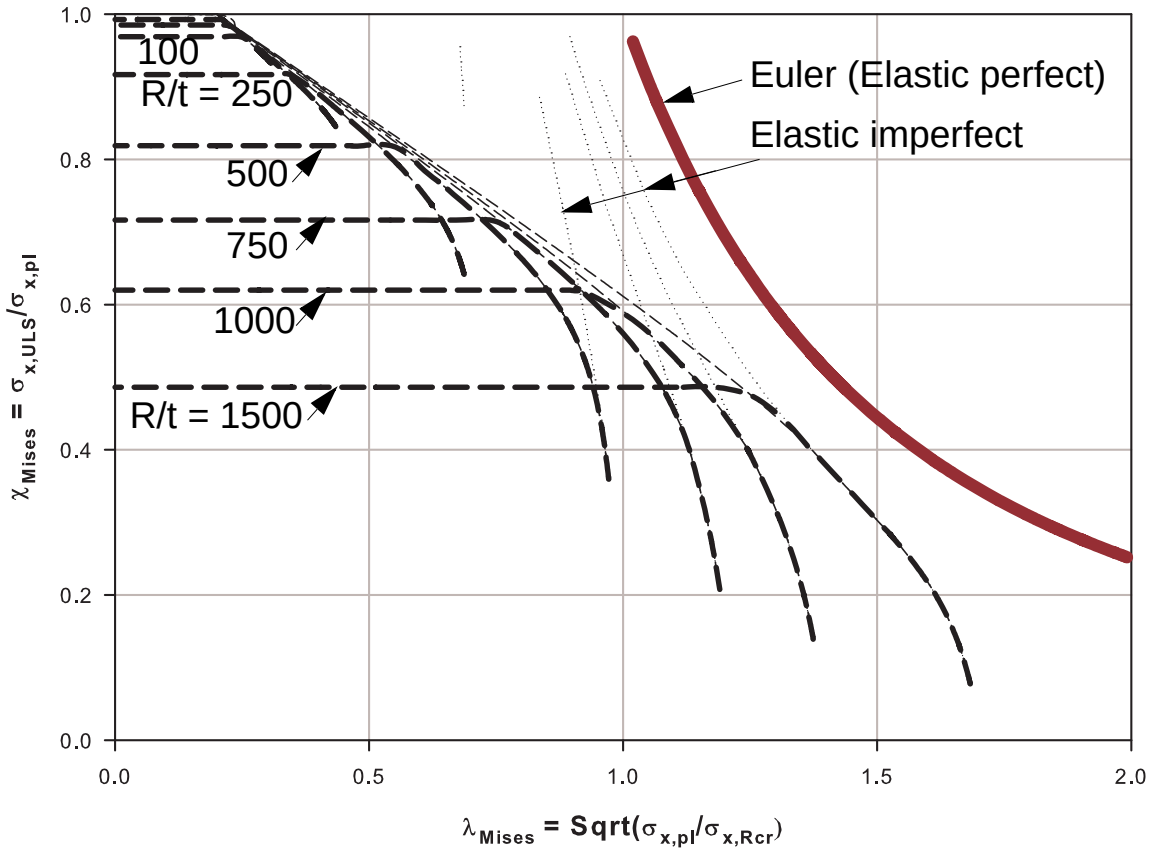

Figure 3.101 characteristic buckling strength according to method-1: fixed bottom

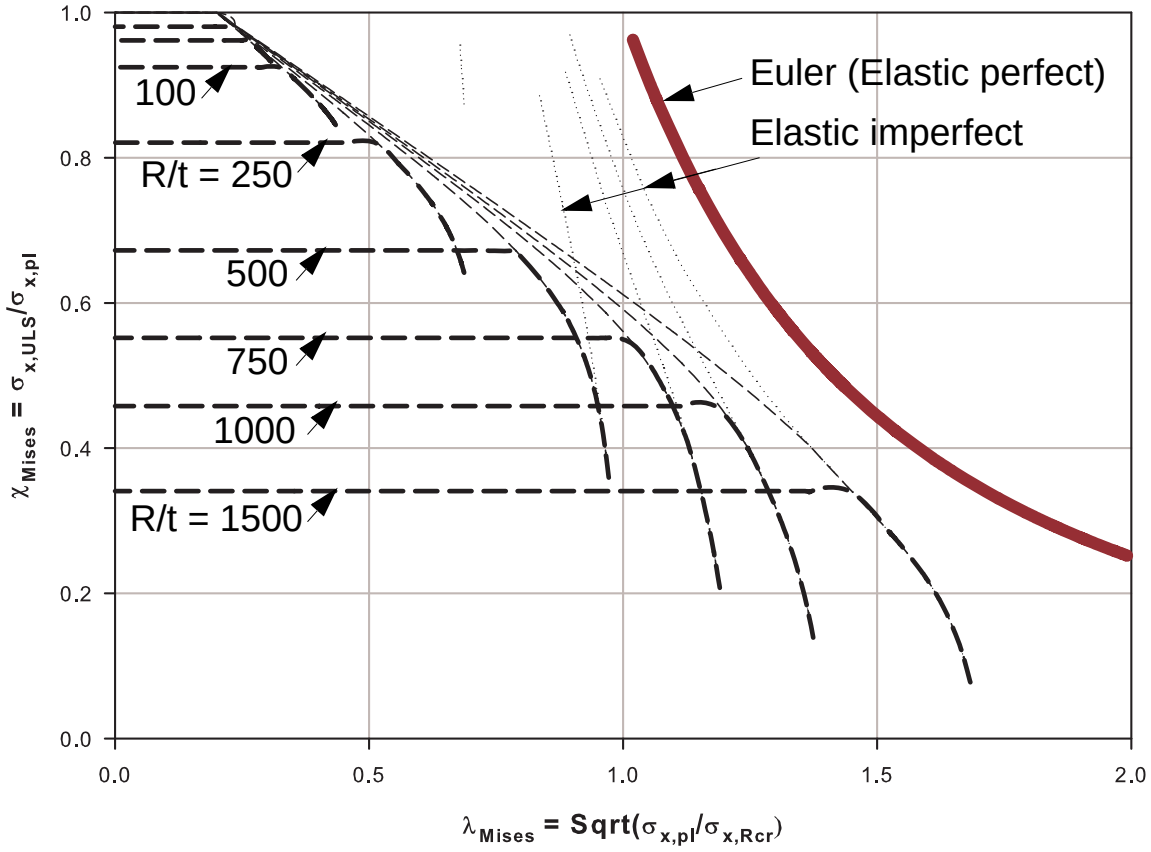

Figure 3.102 characteristic buckling strength according to method-1: pinned bottom

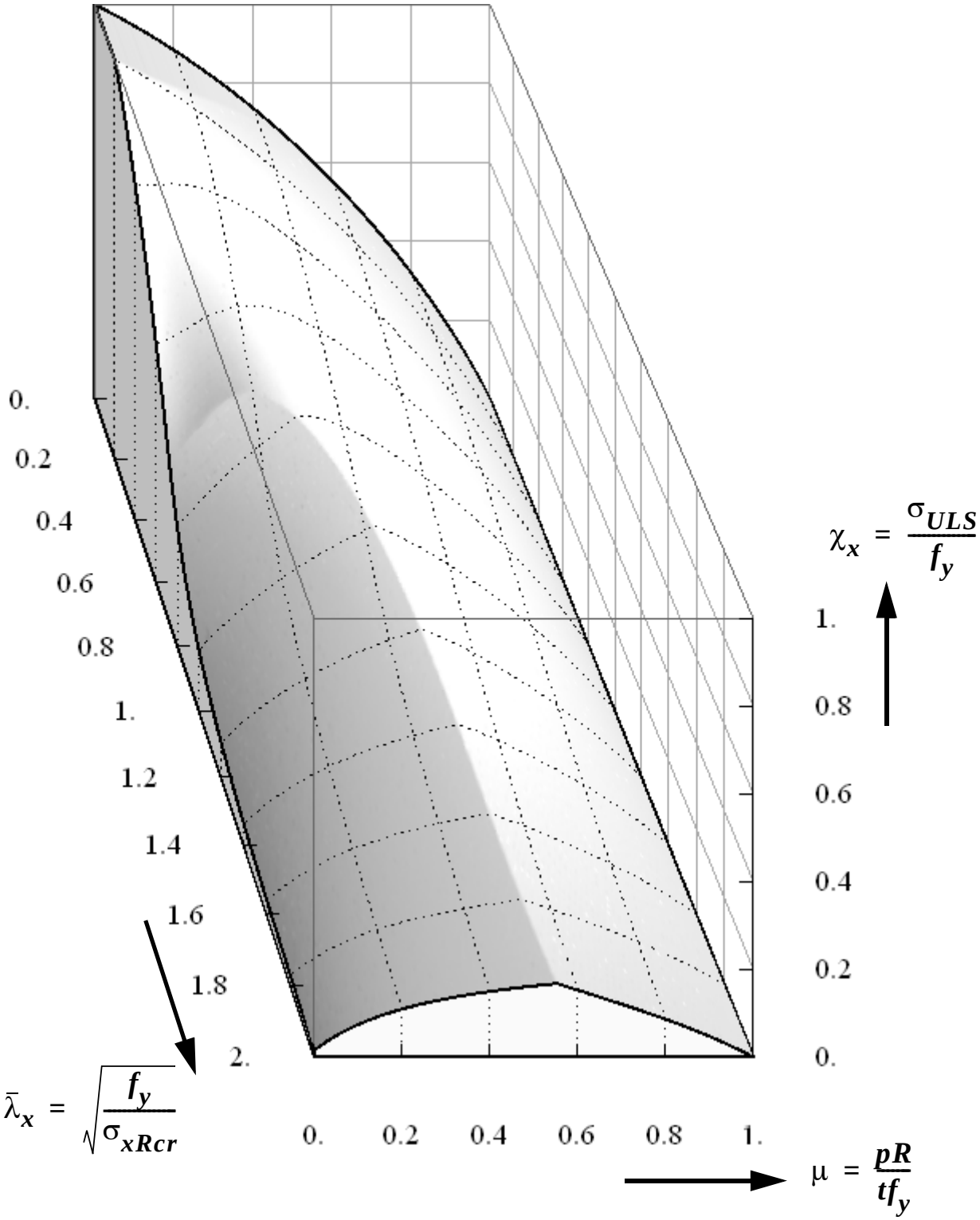

Figure 3.103 3D representation of the characteristic buckling strength of axially compressed and internally pressurized cylindrical shells according to method-1: pinned bottom

3.9.2.2 Method-2: Envelope of the different buckling strengths

This method introduces no new plastic buckling parameters but instead recommends to take the envelope of the separate strengths, i.e. the minimum of the buckling strengths under consideration depending on the choice as discussed below. In comparison with the first method, this method on one hand, clearly represents the different buckling phenomena and on the other hand, gives more room for direct inclusion of future test or GMNIA results representing the imperfect elastic-plastic buckling phenomena in the free shell interior and near the boundary.

Method-2a: **Envelope of pure elastic and elephant's-foot buckling strengths**

This method results in the minimum of the pure elastic buckling strength of the imperfect cylinder and the elastic-plastic buckling near the boundary (elephant's-foot buckling) strengths. Hence, only two distinct buckling phenomena can be represented by this method namely:

- pure elastic buckling of the imperfect cylinder at relatively low-to-medium internal pressure levels
- perfect elastic-plastic buckling near the boundary (perfect elephant's-foot buckling) at relatively medium-to-high internal pressure levels

This method, though it is the easiest and straight forward of all, gives higher (hence unconservative) buckling strengths than the remaining methods. Illustrative plots of the buckling strength according to this method are shown in Figure 3.92 and Figure 3.96.

Method-2b: **Envelope of pure elastic, elastic-plastic in the free shell interior, and elephant's-foot buckling strengths**

This method results in the minimum of the pure elastic buckling strength of the imperfect cylinder, elastic-plastic interaction using bi-axial membrane Mises yield condition (adopting the plastic buckling parameters of an axially compressed internally unpressurized cylinder), and the elastic-plastic buckling near the boundary (elephant's-foot buckling) strengths. In this case the buckling strength obtained from the elastic-plastic interaction using the bi-axial membrane Mises yield condition represents the strength of an imperfection-led elastic-plastic buckling in the free shell interior where edge constrcition effects do not exist. Hence, three distinct buckling phenomena can be represented by this method namely:

- pure elastic buckling of the imperfect cylinder at relatively low internal pressure levels
- imperfection-led elastic-plastic buckling in the free shell interior of the cylinder at medium internal pressure levels
- edge constriction-led elastic-plastic buckling near the boundary conditions of the perfect cylinder (perfect elephant's-foot buckling) at relatively high internal pressure levels

This method, when compared to method-2a, results in somehow conservative results at medium pressure levels. The characteristic buckling strength according to this method are shown in Figure

3.104 and Figure 3.105 using the pressure representation for the fixed and pinned bottom cases, respectively. A 3D plot of the characterstic buckling strength of a pinned bottom cylindrical shell obtained using this method has been shown in Figure 3.84.

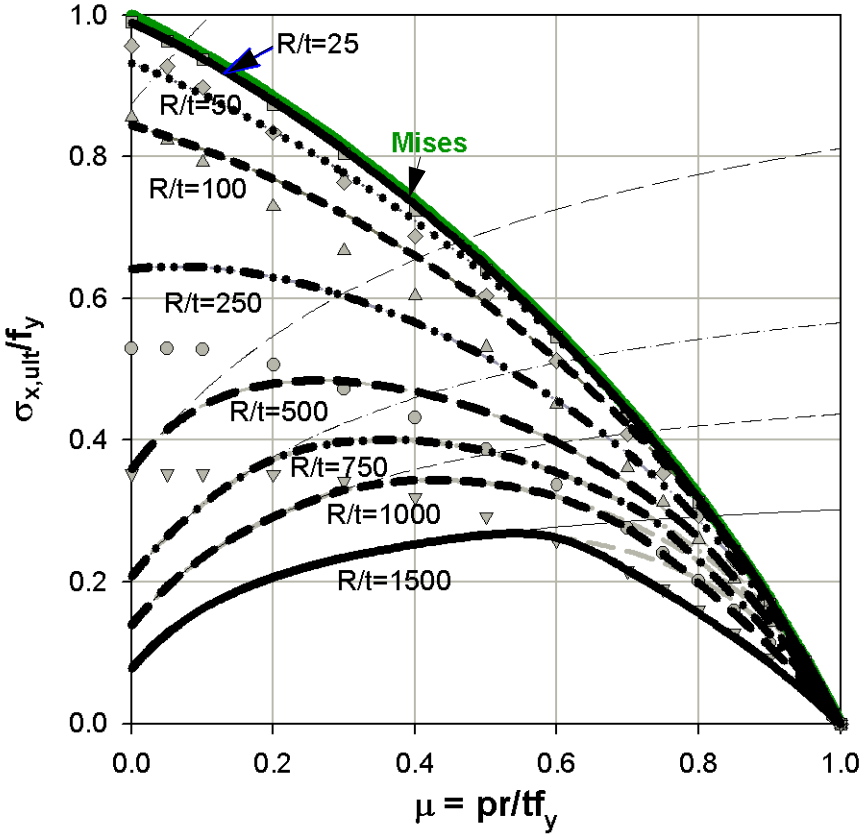

Figure 3.104 characteristic buckling strength according to method-2b: fixed bottom

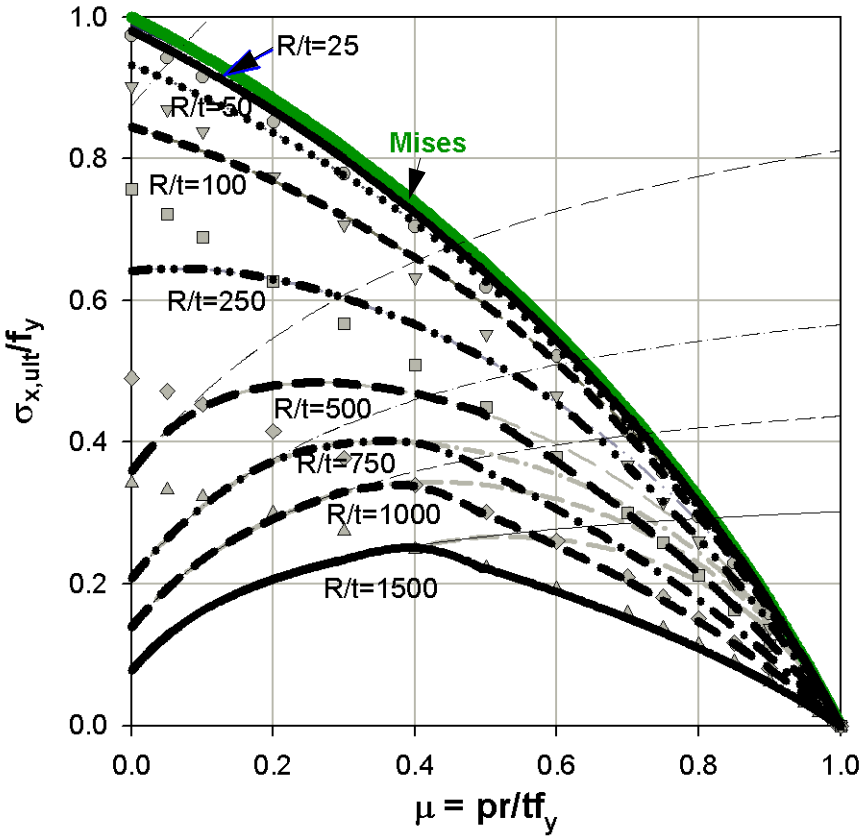

Figure 3.105 characteristic buckling strength according to method-2b: pinned bottom

3.9.2.3 Method-4: Elastic-plastic interaction using a completely new interaction parameter

This method introduces a completely new plastic buckling parameter $\Delta\beta_{EFoot}$. By the introduction of this single plastic interaction parameter, the different buckling phenomena can be explicitly expressed namely:

- pure elastic buckling of the imperfect cylinder at relatively low internal pressure levels
- imperfection-led elastic-plastic buckling in the free shell interior of the cylinder at medium internal pressure levels
- edge constriction-led elastic-plastic buckling near the boundary conditions of the perfect cylinder (perfect elephant's-foot buckling) at relatively high internal pressure levels

Illustrative characteristic buckling strength curves that will fully explain about this particular method are, once gain, shown in the membrane Mises-related interaction representation (Figure 3.106), perfect elephant's-foot-related interaction representation (Figure 3.107), and pressure representation (Figure 3.108).

Elephant's-foot-related interaction expression

With the help of the characteristic buckling strengths shown in Figure 3.107, the following interaction expression can easily be formulated.

$$\chi_{EFoot} = \frac{\sigma_{x,\,Rk}}{\sigma_{x,\,EFoot}} = \begin{cases} 1.0 & \text{for} \quad \bar{\lambda}_{EFoot} \le \bar{\lambda}_o \\ (2 - \Delta\beta_{EFoot}) \cdot \left(\dfrac{1}{1 + \dfrac{\bar{\lambda}_{EFoot}^2}{\alpha_{xpe}}} \right) \cdot f & \text{for} \quad \bar{\lambda}_o < \bar{\lambda}_{EFoot} < \bar{\lambda}_p \\ \dfrac{\alpha_{xpe}}{\bar{\lambda}_{EFoot}^2} & \text{for} \quad \bar{\lambda}_p \le \bar{\lambda}_{EFoot} \end{cases} \qquad \text{(Eq. 3.70)}$$

where

$$\bar{\lambda}_{EFoot} = \sqrt{\frac{\sigma_{x,\,EFoot}}{\sigma_{xRcr}}} = \bar{\lambda}_{Mises}\sqrt{1 - \beta_{EFoot}} \quad \text{... shell buckling relative slenderness} \qquad \text{(Eq. 3.71)}$$

$$\bar{\lambda}_p = \sqrt{\frac{\alpha_{xpe}}{(1 - \Delta\beta_{EFoot})}} \quad \text{... elastic limit relative slenderness} \qquad \text{(Eq. 3.72)}$$

$$\bar{\lambda}_0 = \sqrt{\alpha_{xpe} \cdot (1 - \Delta\beta_{EFoot})} \quad \text{... EFoot limit relative slenderness} \qquad \text{(Eq. 3.73)}$$

Membrane Mises-related interaction expression

The elephant's-foot-related expression (Eq. 3.70) for the prediction of characteristic buckling strengths can be rewritten in the usual membrane Mises-related expression as

$$\chi_{Mises} = \frac{\sigma_{x,\,Rk}}{\sigma_{x,\,Mises}} = \begin{cases} (1-\beta_{EFoot}) & \text{for} \quad \bar{\lambda}_{Mises} \le \bar{\lambda}_o \\ (2-\Delta\beta_{EFoot}) \cdot \left(\dfrac{1}{\dfrac{1}{(1-\beta_{EFoot})} + \dfrac{\bar{\lambda}^2_{Mises}}{\alpha_{xpe}}} \right) \cdot f & \text{for} \quad \bar{\lambda}_o < \bar{\lambda}_{Mises} < \bar{\lambda}_p \\ \dfrac{\alpha_{xpe}}{\bar{\lambda}^2_{Mises}} & \text{for} \quad \bar{\lambda}_p \le \bar{\lambda}_{Mises} \end{cases}$$

(Eq. 3.74)

where

$$\bar{\lambda}_{Mises} = \sqrt{\frac{\sigma_{x,\,Mises}}{\sigma_{xRcr}}} \quad \text{... shell buckling relative slenderness} \quad \text{(Eq. 3.75)}$$

$$\bar{\lambda}_p = \sqrt{\frac{\alpha_{xpe}}{(1-\Delta\beta_{EFoot}) \cdot (1-\beta_{EFoot})}} \quad \text{... elastic limit relative slenderness} \quad \text{(Eq. 3.76)}$$

$$\bar{\lambda}_0 = \sqrt{\frac{\alpha_{xpe} \cdot (1-\Delta\beta_{EFoot})}{(1-\beta_{EFoot})}} \quad \text{... EFoot limit relative slenderness} \quad \text{(Eq. 3.77)}$$

and f is a general shape function which controls the nature of buckling interaction. In cases of no known accurate results a linear interaction can be considered and hence $f = 1.0$.

The effects of varying the interaction parameter $\Delta\beta_{EFoot}$ can be seen from the elephant's-foot-related representation shown in Figure 3.109 and the corresponding pressure representation shown in Figure 3.110. It can be seen that a linear interaction in the elephant's-foot-related representation does not mean a linear interaction in the pressure representation.

Additional comments

As it can be seen from the representation used and formulation reached at, this method is the simplest, easy to understand, easy to apply, easy to modify, and straight forward method of all the other methods discussed and is, therefore, highly recommended for design and future research applications because of the following facts:

- **it includes the good features of both methods - 1&2, i.e. it is a one-way go to predict the buckling strength like method-1 and it strictly differentiates between different buckling phenomena and strengths like method - 2**
- **the elastic-plastic buckling interaction is fully controlled (when f = 1) by a single interaction parameter, $\Delta\beta_{EFoot}$, which has a very clear and straight forward meaning.**
- **it can easily be adjusted to give a room for inclusion of future test or GMNIA numerical analysis results representing elastic-plastic buckling phenomena in the free shell interior and near the boundary of an imperfect thin-walled cylindrical shell.**
- **when separate interaction levels are needed on the imperfect elastic and perfect EFoot strength curves, the slope of the "interaction" line, Figure 3.107, can be easily adjusted.**

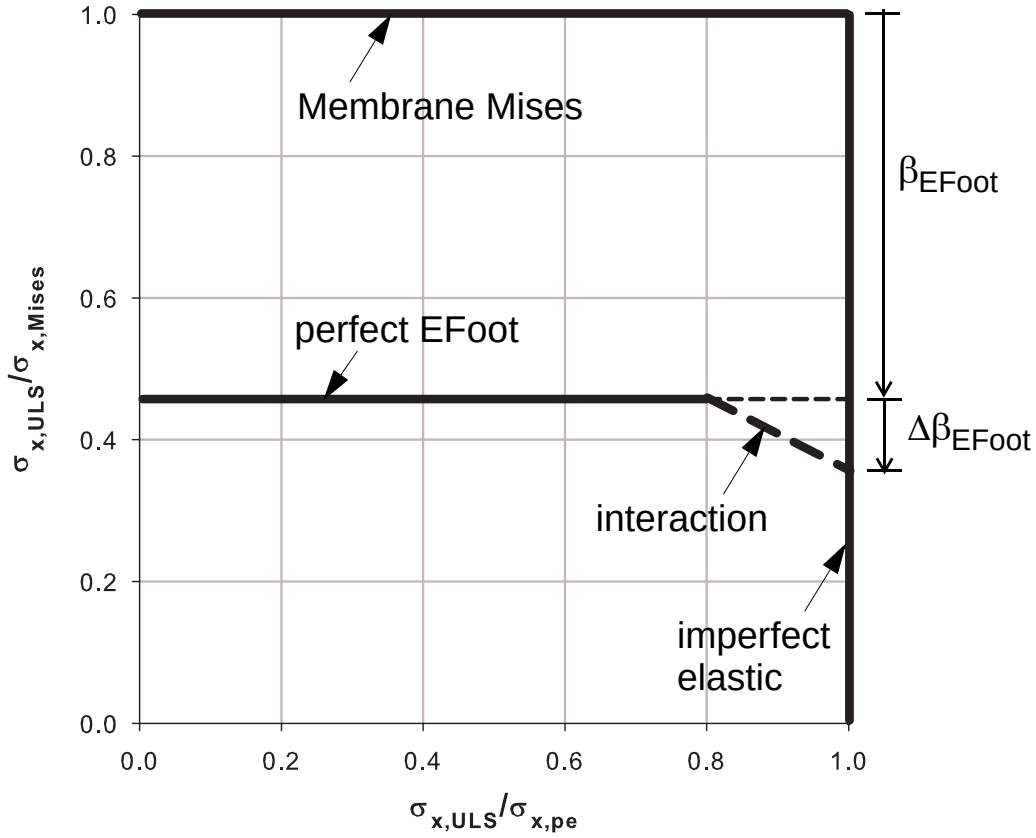

Figure 3.106 Buckling strength in Mises-related interaction representation: method-4

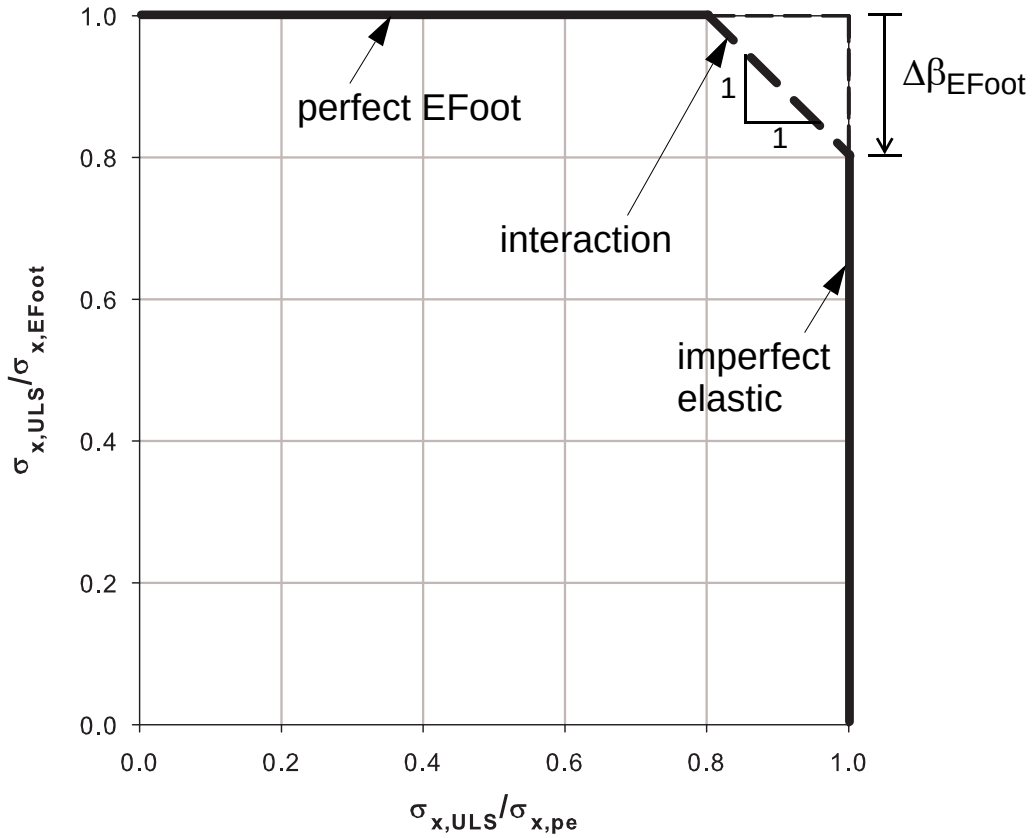

Figure 3.107 Buckling strength in EFoot-related interaction representation: method-4

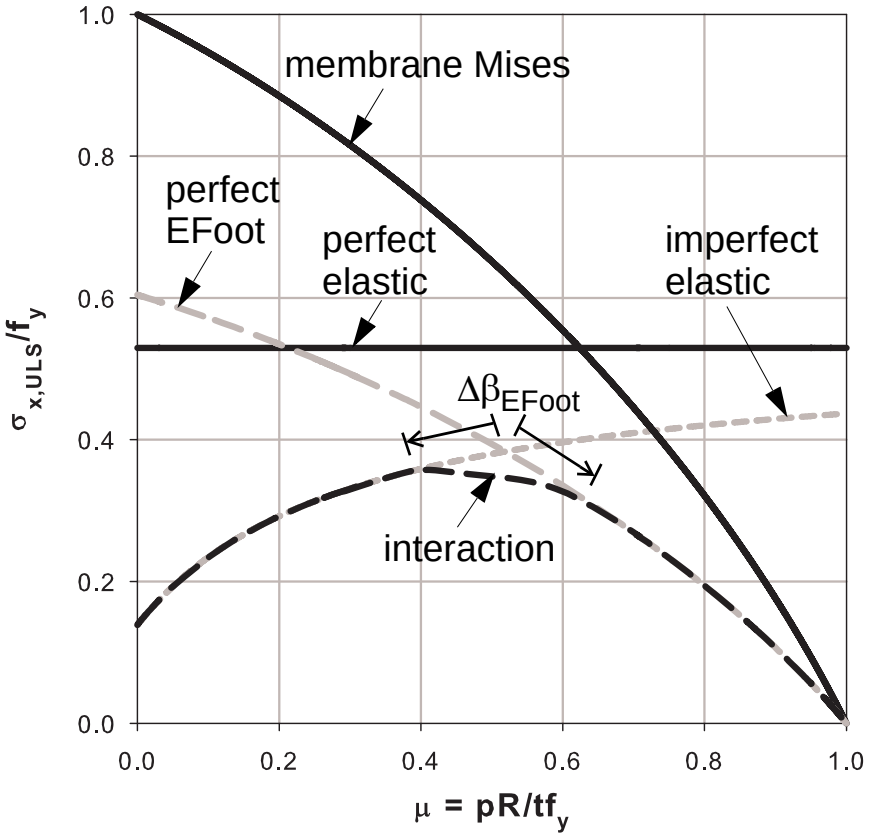

Figure 3.108 Characteristic buckling strength in pressure representation: method-4

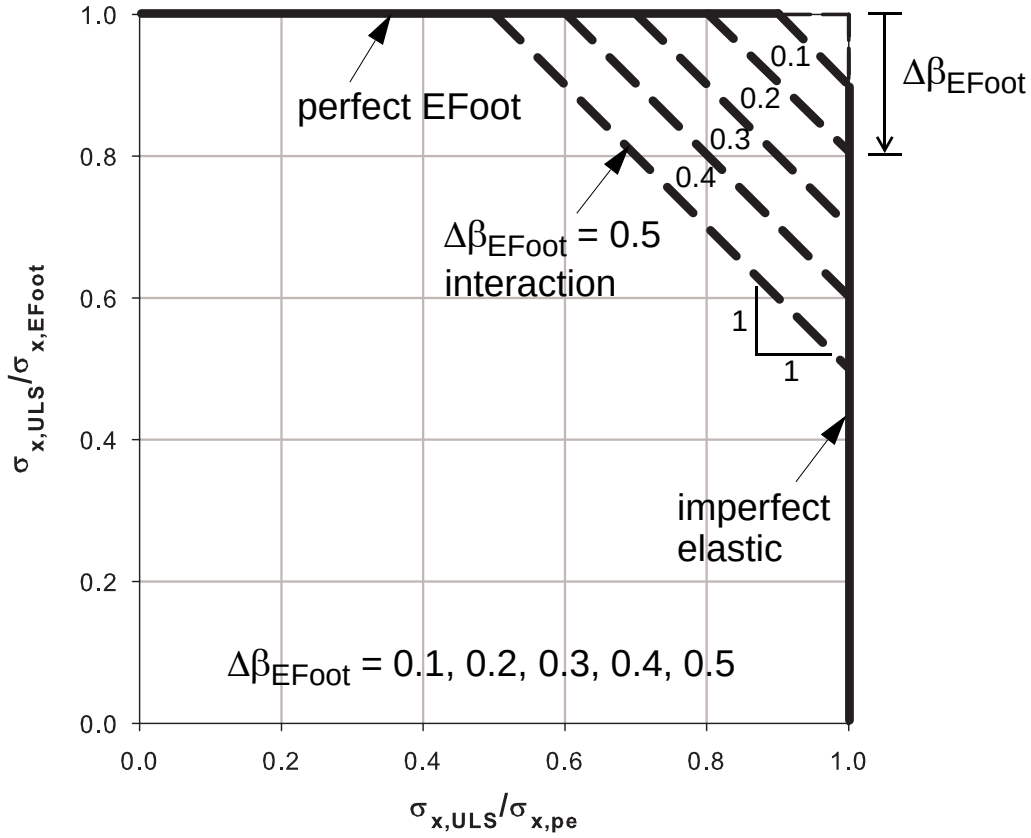

Figure 3.109 Effect of varying $\Delta\beta_{EFoot}$: EFoot-related interaction representation

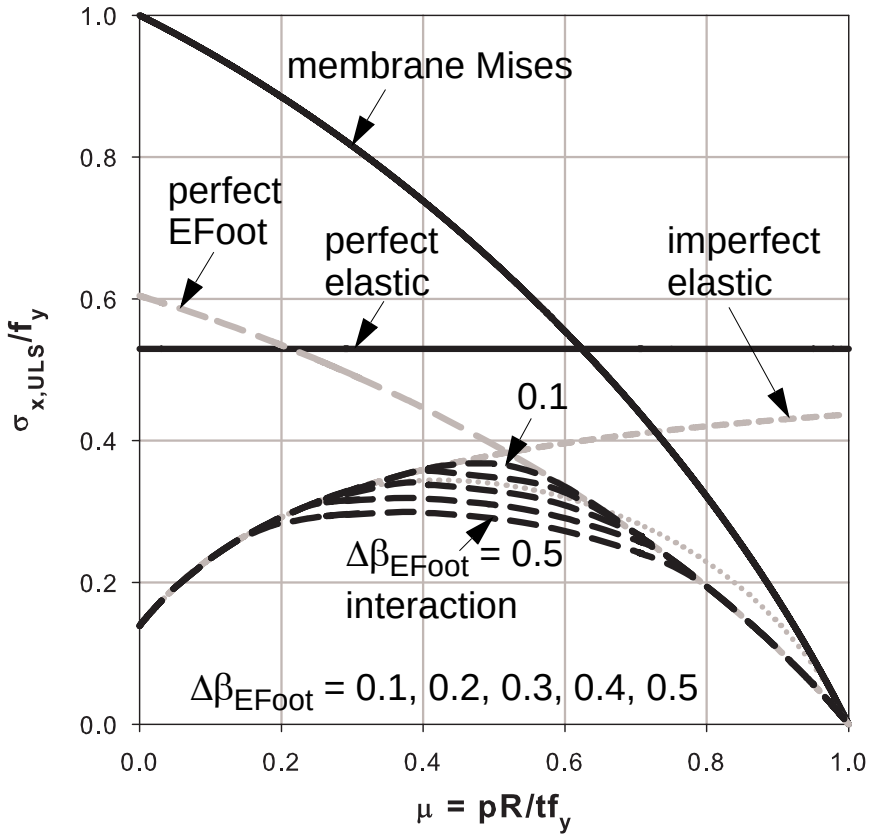

Figure 3.110 Effect of varying $\Delta\beta_{EFoot}$: pressure representation

3.10 Comparison of the new buckling design recommendation with EN 1993-1-6 buckling design regulation

This section first discusses the buckling design recommendation according to EN 1993-1-6 design regulation and then compares it with the new buckling design recommendation of this work. The overall difference between the two recommendations lie only on the elastic-plastic buckling strength prediction and not on the pure elastic buckling strength as both recommendations use the same unpressurized and pressurized elastic imperfection reduction factors. Hence, the discussions on the unpressurized and pressurized, perfect and imperfect pure elastic buckling strengths made previously apply to both recommendations. The EN 1993-1-6 procedure for computing characteristic buckling strengths of cylindrical shells is discussed below.

3.10.1 Perfect elephant's foot buckling strength using EN 1993-1-6

Following geometrically and materially nonlinear numerical analyses, the elastic-plastic buckling strength of a perfect cylindrical shell for buckling near the boundary (perfect elephant's-foot buckling strength) is given interms of a fitting curve of the analyses results. The fitting curve is expressed as a reduction factor, α_{xpp}, called plastic pressurized imperfection reduction factor which is a ratio of the elastic-plastic buckling load to the elastic classical buckling load of the shell.

The name given to this factor is quite confusing as it has nothing to do with imperfections. This name might have been given as it, like that of the pressurized elastic imperfection reduction factor, is a ratio of the buckling load to the classical critical load. It should, however, be noted here that this factor is not an imperfection reduction factor as the name implies but instead a reduction factor, when referred to the classical elastic buckling strength, accounts for material and geometric nonlinearities. It can also be interpreted as a reduction factor, when referred to the pure plastic capacity of the shell, accounts for geometric nonlinearities. Despite this fact, it will still be called plastic pressurized imperfection reduction factor in the remaining parts of the discussion so that it will not be confused whenever reference to EN 1993-1-6 is made.

The elephant's foot buckling strength obtained using α_{xpp} for different shell slenderness ratios are shown in the pressure representation, Figure 3.111, where a quantitative comparison can be made with the pure bi-axial plastic strength of the shell. The same buckling strength is shown in Figure 3.112 using the capacity represnetation. A combined 3D plot of the same strength is shown in Figure 3.113. For shell slenderness ratio $R/t \leq 145$, the elephant foot buckling strength prediction using the α_{xpp} expression is higher than the pure bi-axial plastic strength of the cylinder as can be seen from Figure 3.111 and more clearly from Figure 3.114.

Why EN 1993-1-6 elephant's-foot strength prediction is higher than the pure plastic capacity of the cylinder?

This problem arises because, upon fitting, the expression for α_{xpp} (Eq. 3.78) bases on a pressure dependent quadratic curve $(1-\mu^2)$ which has nothing to do with bi-axial plasticity and applying two separate pressure independent correction factors as follows:

$$\alpha_{xpp} = \{1-\mu^2\} \cdot f_g \cdot f_m \qquad \text{(Eq. 3.78)}$$

with

a geometry correction factor, f_g (Eq. 3.79):

$$f_g = \left(1 - \frac{1}{1.12 + s^{3/2}}\right) \qquad \text{(Eq. 3.79)}$$

and a material correction factor, f_m (Eq. 3.80).

$$f_m = \left(\frac{s^2 + 1.21\bar{\lambda}_x^2}{s(s+1)}\right) \qquad \text{(Eq. 3.80)}$$

where

$$\mu = \frac{\sigma_\theta}{f_y} = \frac{pR/t}{f_y} \qquad \text{(Eq. 3.81)}$$

$$s = \frac{R/t}{400} \qquad \text{(Eq. 3.82)}$$

$$\bar{\lambda}_x^2 = \frac{f_y}{\sigma_{xRcr}} \qquad \text{(Eq. 3.83)}$$

An illustrative plot for R/t = 1000, f_y = 24 kN/cm^2, E =21000 kN/cm^2, and ν = 0.3 is shown in Figure 3.115. The geometry correction factor depends purely on the shell slenderness ratio R/t while the material correction factor depends on the combined effects of the material properties (uni-axial yield strength f_y, modulus of elasticity E, and Poisson's ratio ν) and the shell slenderness ratio R/t. A close look at the material correction factor reveals that it is very close to unity for the standard steel properties and varies little with varying R/t values.

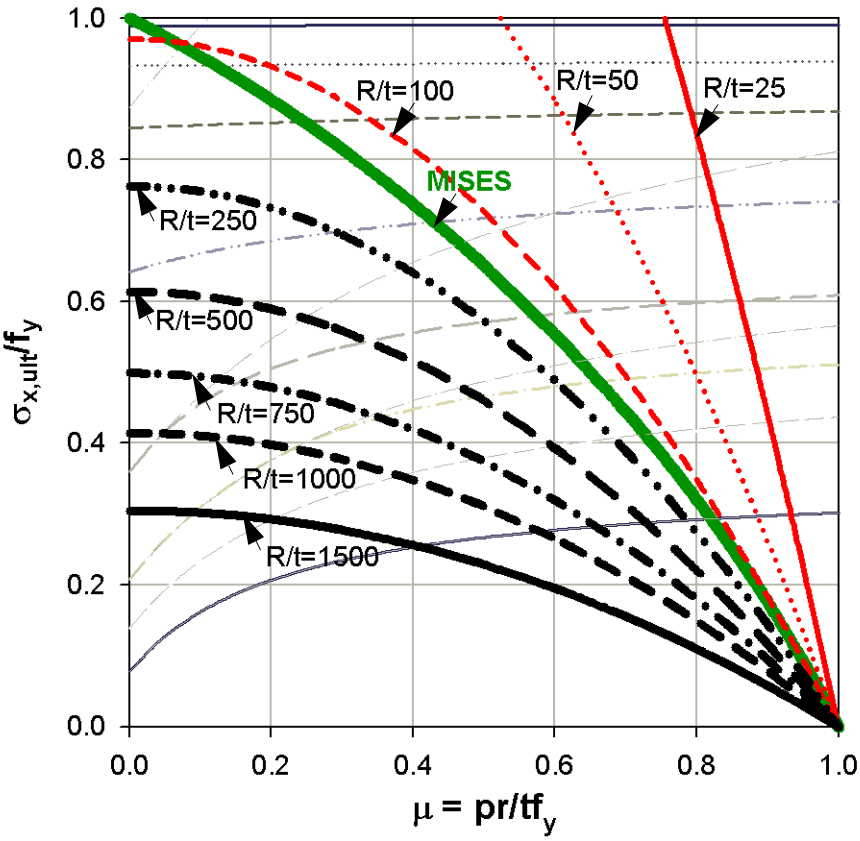

Figure 3.111 Elephant's-foot buckling strength of the perfect cylinder: pinned bottom

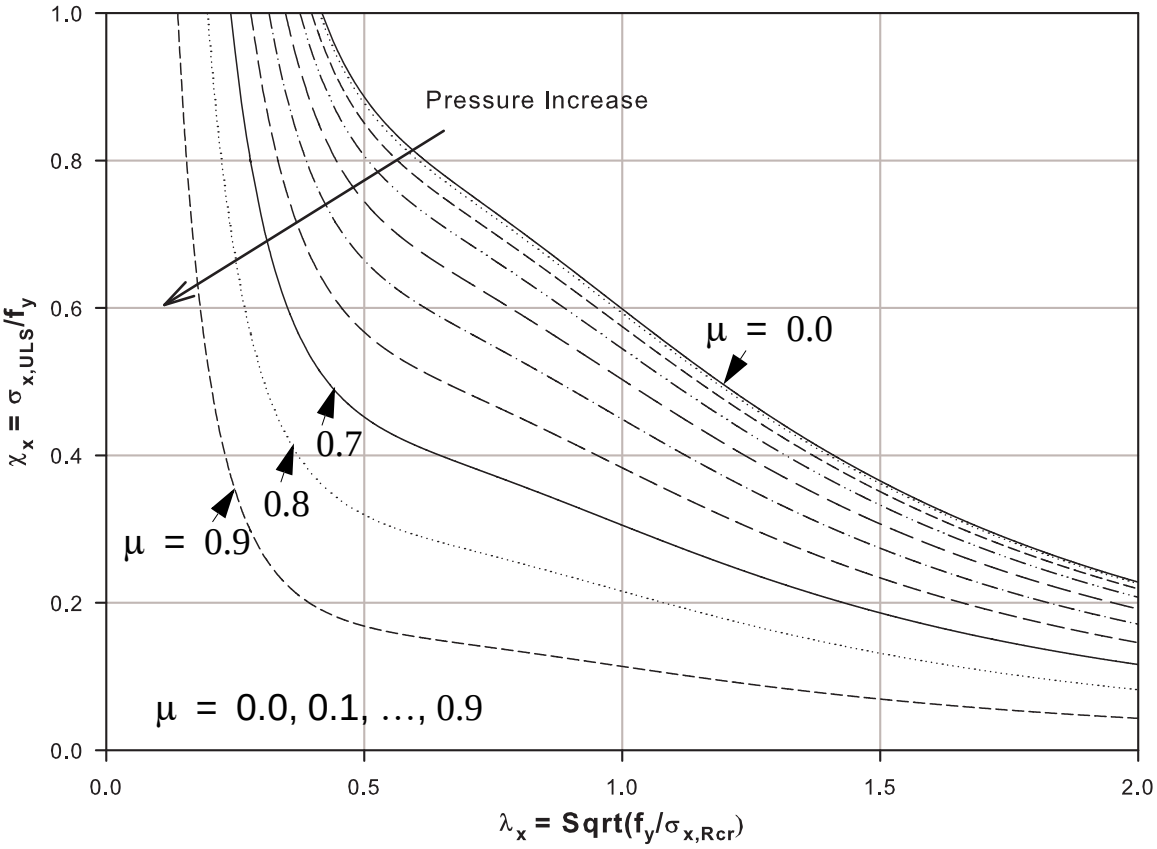

Figure 3.112 Elephant's-foot buckling strength of the perfect cylinder: pinned bottom

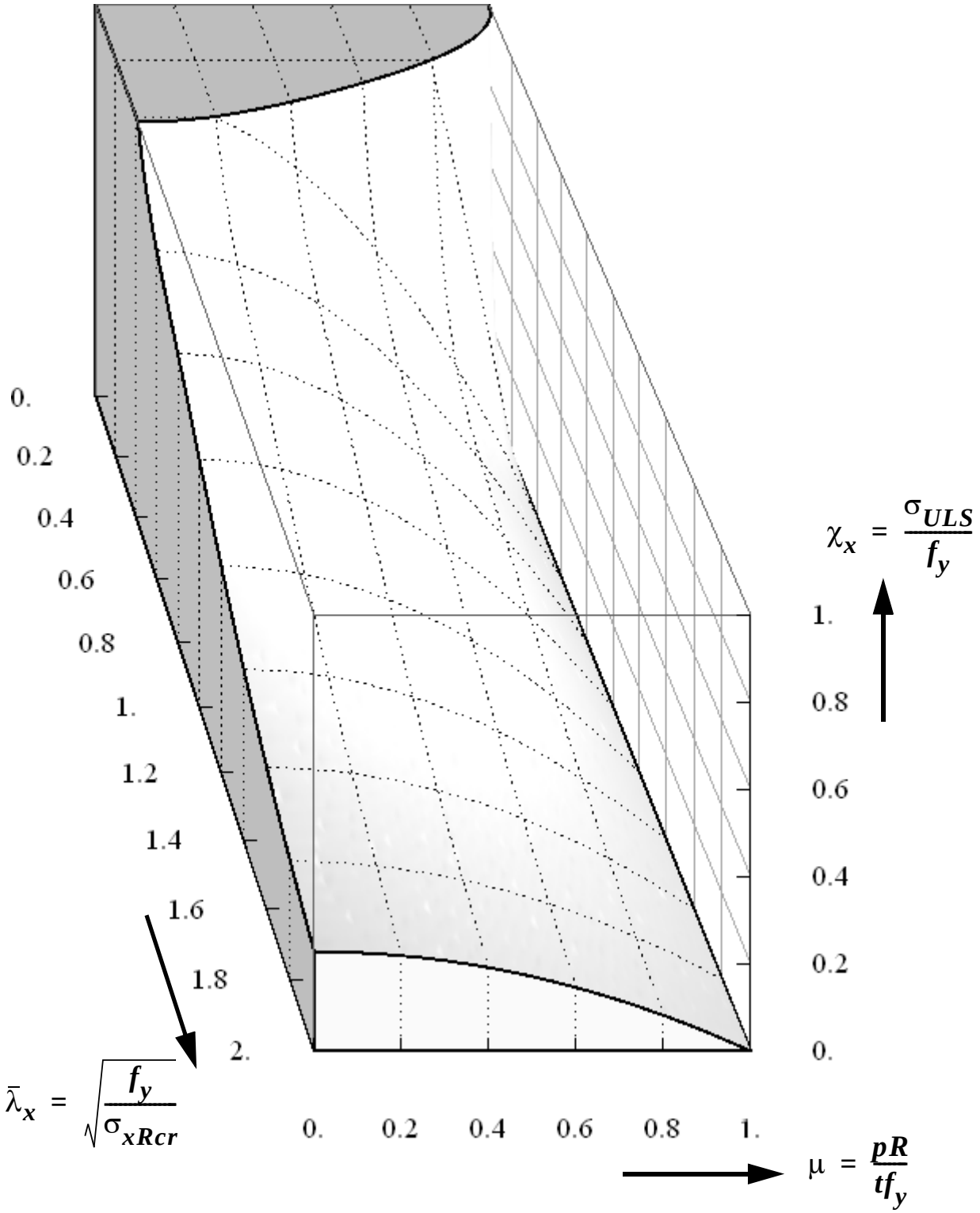

Figure 3.113 Elephant's-foot buckling strength of the perfect cylindrical shell according to EN 1993-1-6: pinned bottom

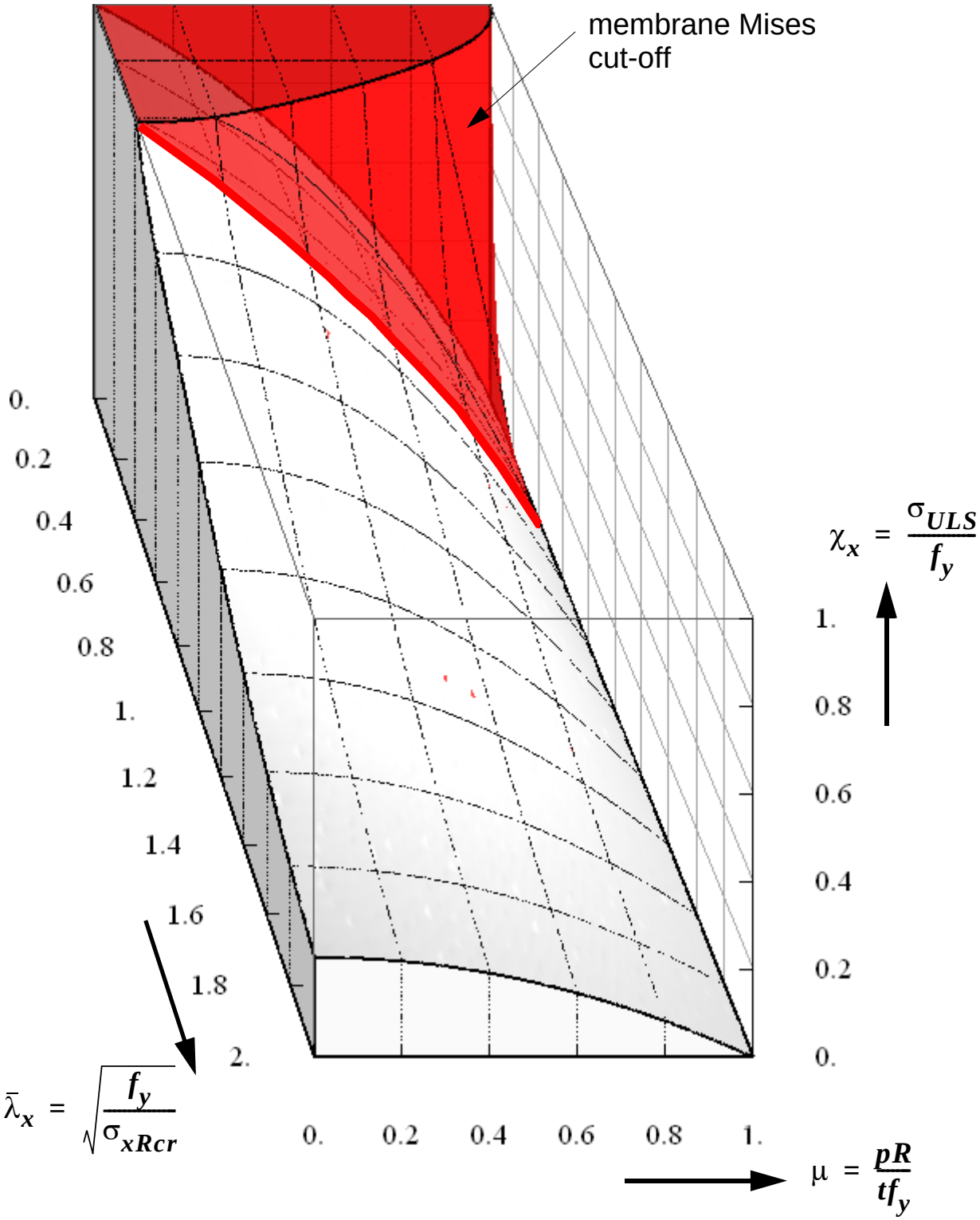

Figure 3.114 Elephant's-foot buckling strength of the perfect cylindrical shell according to EN 1993-1-6 and bi-axial membrane Mises cut-off: pinned bottom

Elephant's-foot buckling strength prediction comparison

In this section, the elephant's-foot buckling strength according to EN 1993-1-6 will be compared with the same strength obtained from the current study. The geometrically and materially nonlinear numerical anlysis results (which are exactly the same as those results where the EN1993-1-6 recommendation were based) will be used as benchmarks in the comparison.

As a first step, comparison of the overall reduction factors applied to the base curve $(1-\mu^2)$ as in EN 1993-1-6; and to the MNA strength as in the new recommendation of the current work to obtain the perfect elephant's-foot buckling strength are shown, depending on R/t, in Figure 3.116. It has to, however, again be emphasized here that coinciding GMNA numerical results are at the basis in obtaining the approximate expression for α_{xpp} according to EN1993-1-6 and the direct relationship between GMNL and MNL carrying capacities according to the new recommendation of this work. This fact is shown in Figure 3.117 for R/t = 500 and Figure 3.118 for R/t = 1000 where overlying data points of the pinned and fixed boundary conditions are shown for the GMNA results. The difference lies on the choice of the reference parameter for non-dimensional representation purposes and the choice of fitting curve type.

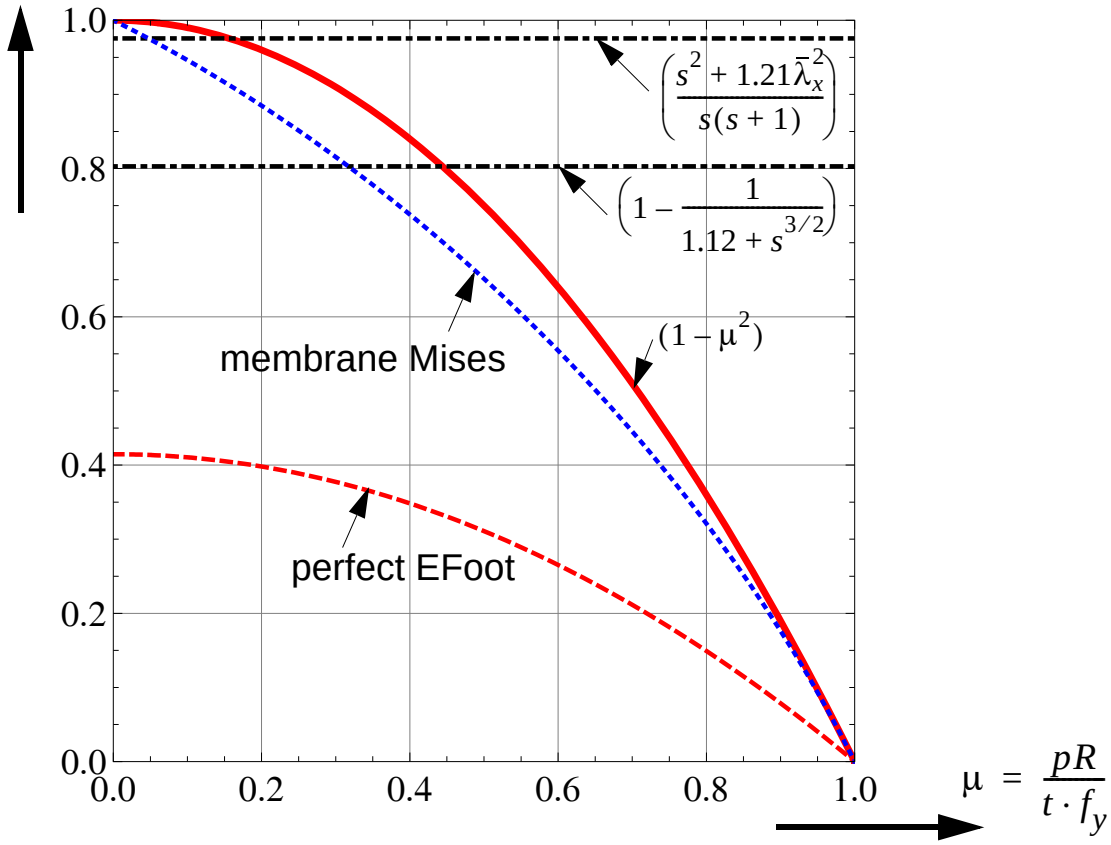

Figure 3.115 EN1993-1-6 elephant's-foot buckling strength of the perfect cylinder: R/t = 1000

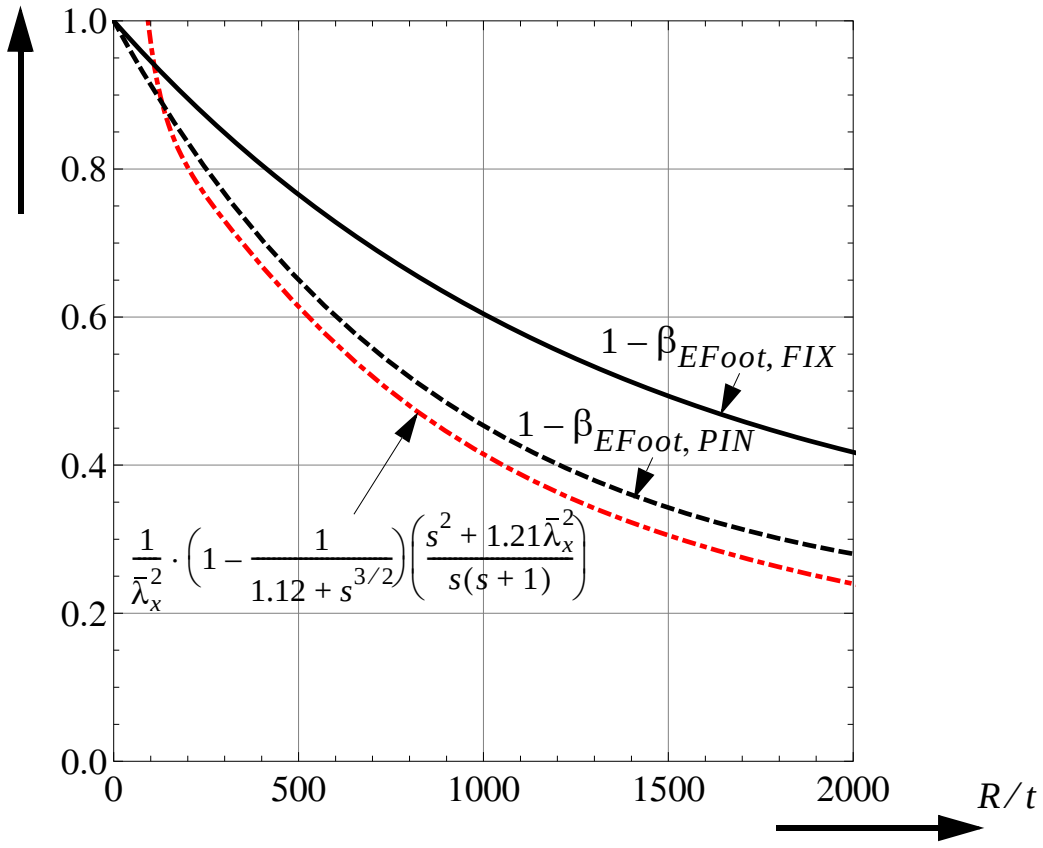

Figure 3.116 Comparison of elephant's-foot buckling strengths of the perfect cylinder

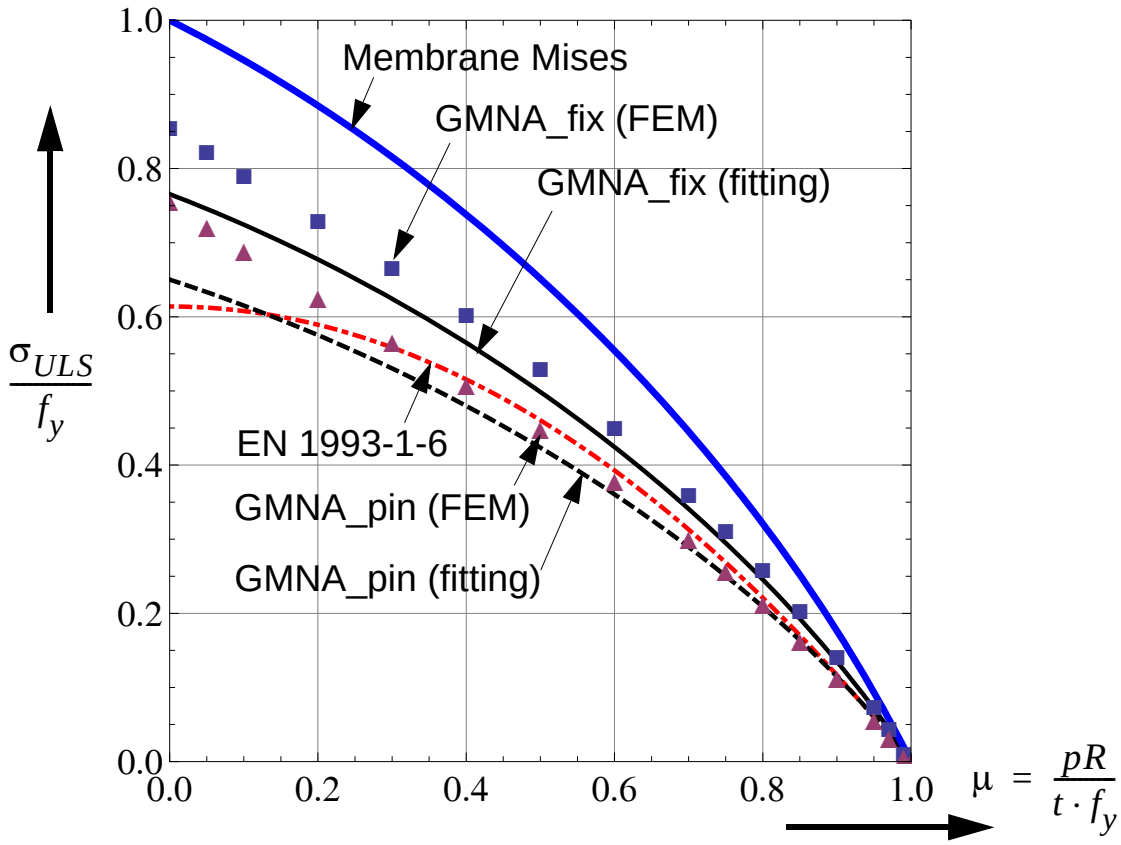

Figure 3.117 Elephant's-foot buckling strengths of the perfect cylinder: R/t = 500

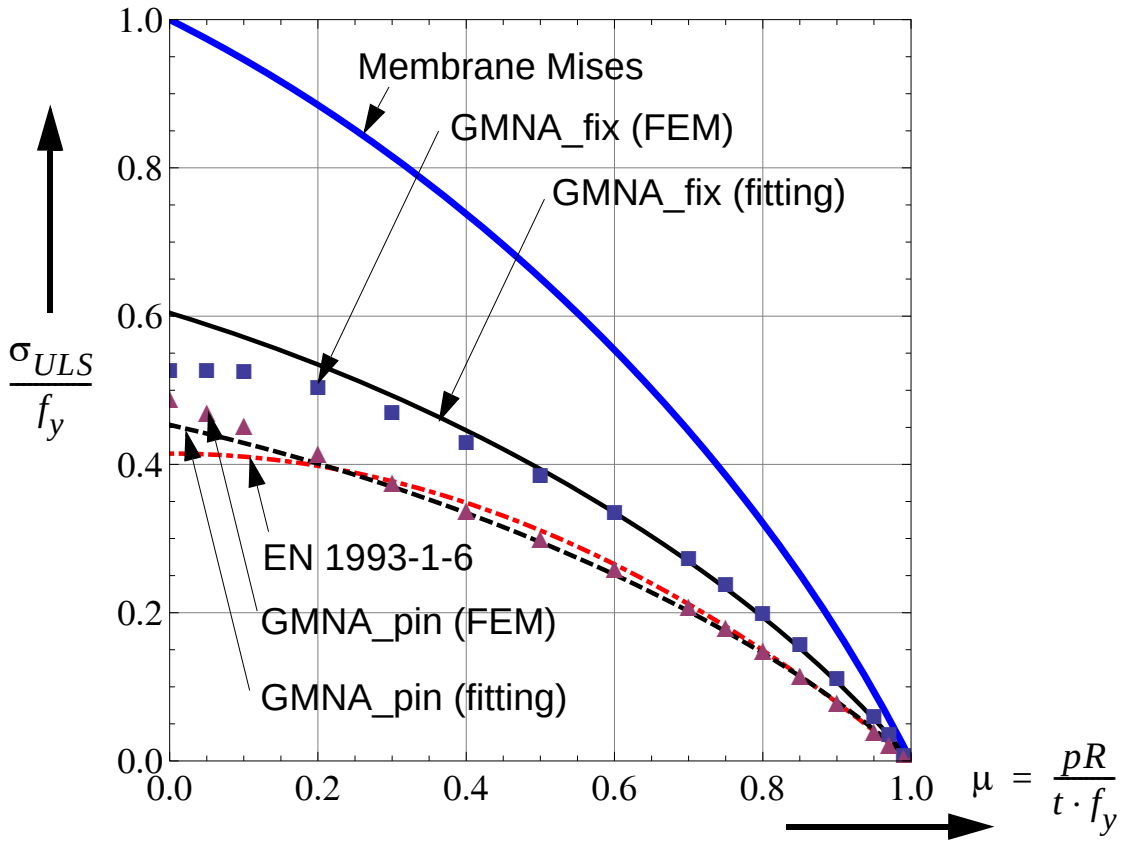

Figure 3.118 Elephant-foot buckling strengths of the perfect cylinder: R/t = 1000

3.10.2 EN 1993-1-6 buckling design regulation

The steps involved in the stress design procedure, according to EN 1993-1-6, for the prediction of the characteristic buckling strength of axially compressed and internally pressurized cylindrical shells are summarized below.

- compute the elastic pressurized imperfection reduction factor, α_{xpe}, at the location of the point being assessed from, see (Eq. 3.34) to (Eq. 3.37) and Figure 3.31 to Figure 3.33,

$$\alpha_{xpe} = \alpha_x + (1-\alpha_x)\frac{\bar{p}}{\bar{p} + 0.3/\alpha_x^{0.5}} \qquad \text{(Eq. 3.84)}$$

- compute the plastic pressurized imperfection reduction factor, α_{xpp}, at the location of the point being assessed from, see (Eq. 3.81) to (Eq. 3.83) and Figure 3.111 to Figure 3.118,

$$\alpha_{xpp} = \left\{1 - \left(\frac{\bar{p}}{\bar{\lambda}_x^2}\right)^2\right\}\left(1 - \frac{1}{1.12 + s^{3/2}}\right)\left(\frac{s^2 + 1.21\bar{\lambda}_x^2}{s(s+1)}\right) \qquad \text{(Eq. 3.85)}$$

where

$$\bar{p} = \frac{\sigma_\theta}{\sigma_{xRcr}} = \frac{pR/t}{\sigma_{xRcr}} = \mu \cdot \bar{\lambda}_x^2 \qquad \text{(Eq. 3.86)}$$

- compute the value of the pressurized imperfection reduction factor, α_{xp}, which is taken as the smaller of α_{xpe} and α_{xpp}.

$$\alpha_p = Min(\alpha_{xpe}, \alpha_{xpp}) \qquad \text{(Eq. 3.87)}$$

- compute the bucking strength reduction factor of the cylinder from

$$\chi_x = \frac{\sigma_{x,Rk}}{f_y} = \begin{cases} 1 & \text{for } \bar{\lambda}_x \le \bar{\lambda}_o \\ 1 - \beta \cdot \left(\dfrac{\bar{\lambda}_x - \bar{\lambda}_o}{\bar{\lambda}_p - \bar{\lambda}_o}\right)^\eta & \text{for } \bar{\lambda}_o < \bar{\lambda}_x < \bar{\lambda}_p \\ \dfrac{\alpha_{xp}}{\bar{\lambda}_x^2} & \text{for } \bar{\lambda}_p \le \bar{\lambda}_x \end{cases} \qquad \text{(Eq. 3.88)}$$

where

$$\bar{\lambda}_x = \sqrt{\frac{f_y}{\sigma_{xRcr}}} \quad \text{relative shell buckling slenderness parameter} \qquad \text{(Eq. 3.89)}$$

$\bar{\lambda}_p = \sqrt{\frac{\alpha_{xp}}{1-\beta}}$ plastic limit buckling slenderness (Eq. 3.90)

$\eta = 1.0$ interaction exponent (Eq. 3.91)

$\bar{\lambda}_o = 0.2$ squash limit relative slenderness (Eq. 3.92)

$\beta = 0.6$ plastic range factor (Eq. 3.93)

- the characteristic buckling strength will then be computed from

$$\sigma_{x,Rk} = \chi_x \cdot f_y \quad \text{(Eq. 3.94)}$$

The characteristic buckling strengths obtained from the separate use of the elastic α_{xpe} and plastic α_{xpp} imperfection reduction factors have been shown in Figure 3.31 to Figure 3.33 for the elastic and Figure 3.111 to Figure 3.113 for the plastic. The envelope of these two strengths (with no elastic-plastic interaction) is shown in Figure 3.119 and will be used for later comparisons.

Figure 3.120 and Figure 3.121 (χ_x vs μ plot for different shell slendernesses and χ_x vs $\bar{\lambda}_x$ plot for different internal pressures, respectively) show the elastic-plastic buckling strength resulting from the interaction expression (Eq. 3.88) with $\alpha_{xp} = \alpha_{xpe}$. This interaction guarantees that no elastic-plastic buckling strength exceeds the uni-axial yield strength f_y. This situation, without considering the elastic-plastic buckling adjacent to the boundary (i.e. not taking α_{xpp} into account), represents the elastic-plastic buckling in the shell interior. A 3D combination of the pressure and capacity representations is also shown in Figure 3.122. On the other hand, an elastic-plastic buckling strength resulting from the interaction expression (Eq. 3.88) with $\alpha_{xp} = \alpha_{xpp}$ is shown in Figure 3.123

The characteristic buckling strength according to EN 1993-1-6 (from the interaction expression (Eq. 3.88) with $\alpha_{xp} = \text{Min}(\alpha_{xpe},\alpha_{xpp})$) is shown in Figure 3.124. The same characteristic buckling strength will be obtained from a separate interaction of the the pressurized elastic buckling strength and pressurized plastic buckling strength with the uni-axial yield strength (as has already been done and shown in Figure 3.122 and Figure 3.123, respectively) and then taking the minimum of the two results.

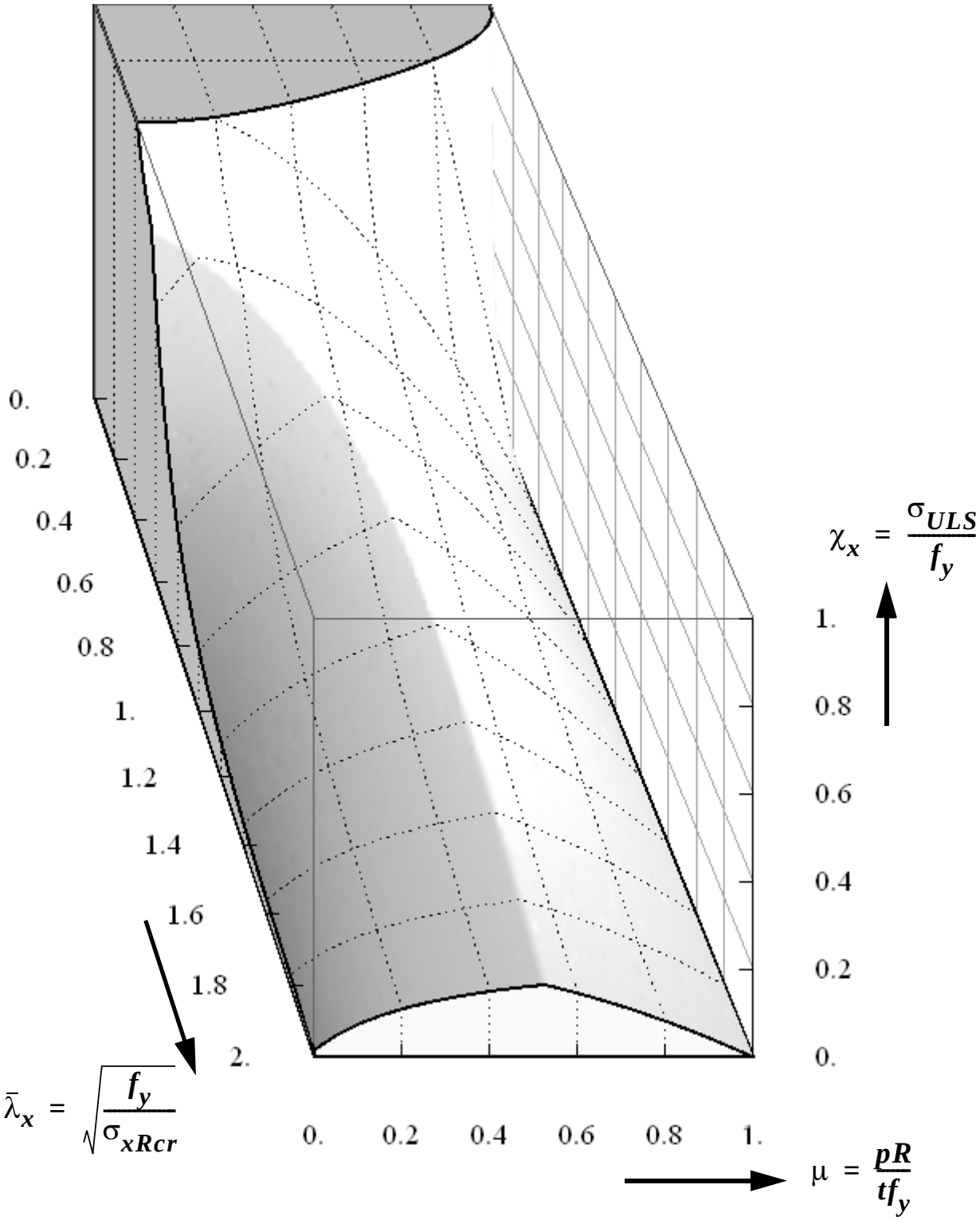

Figure 3.119 Envelope of α_{xpe} and α_{xpp} with no elastic-plastic interaction

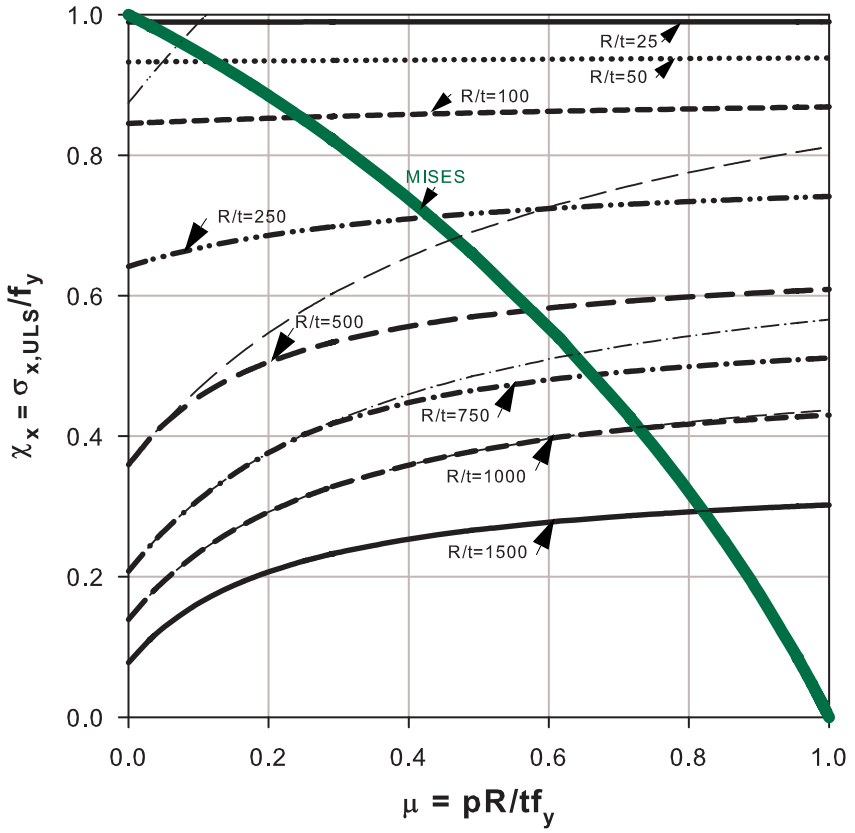

Figure 3.120 Elastic-plastic interaction with uni-axial yield for class-A and bi-axial membrane Mises

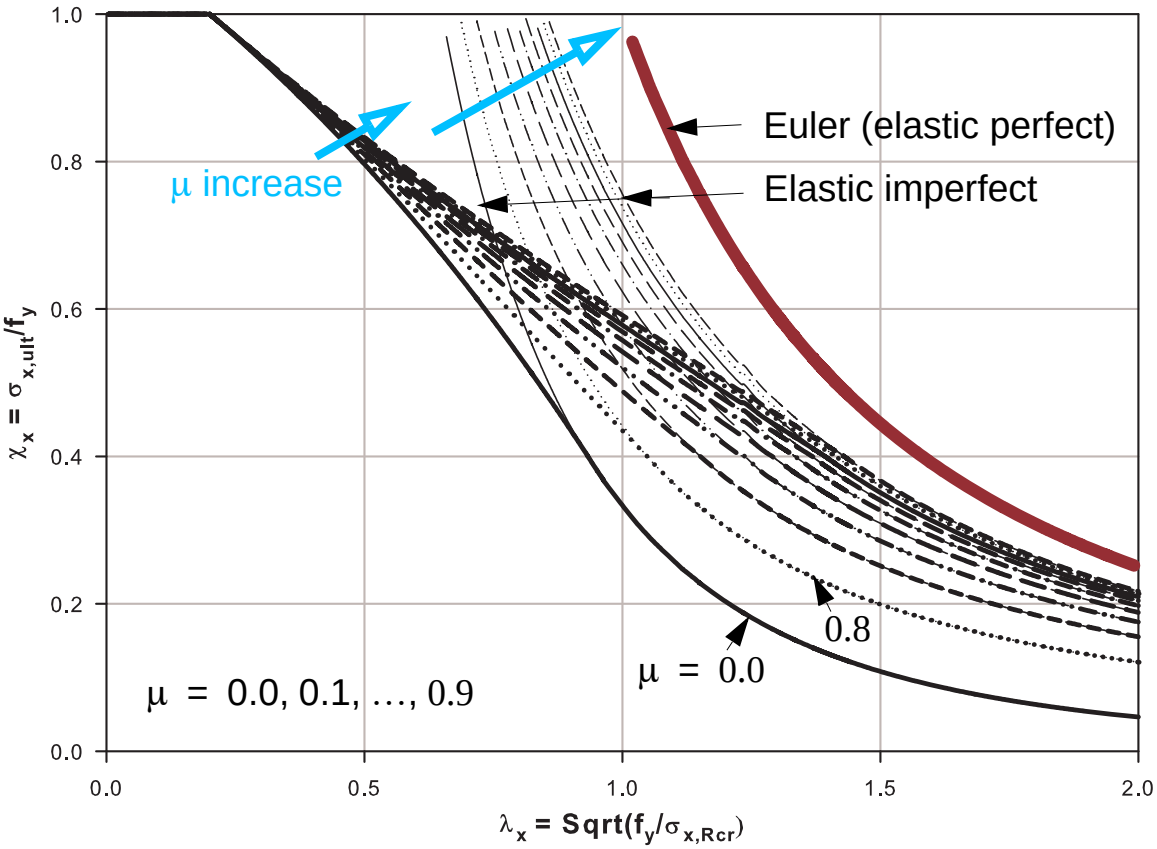

Figure 3.121 Elastic-plastic interaction with uni-axial yield for class-A and Euler's curve

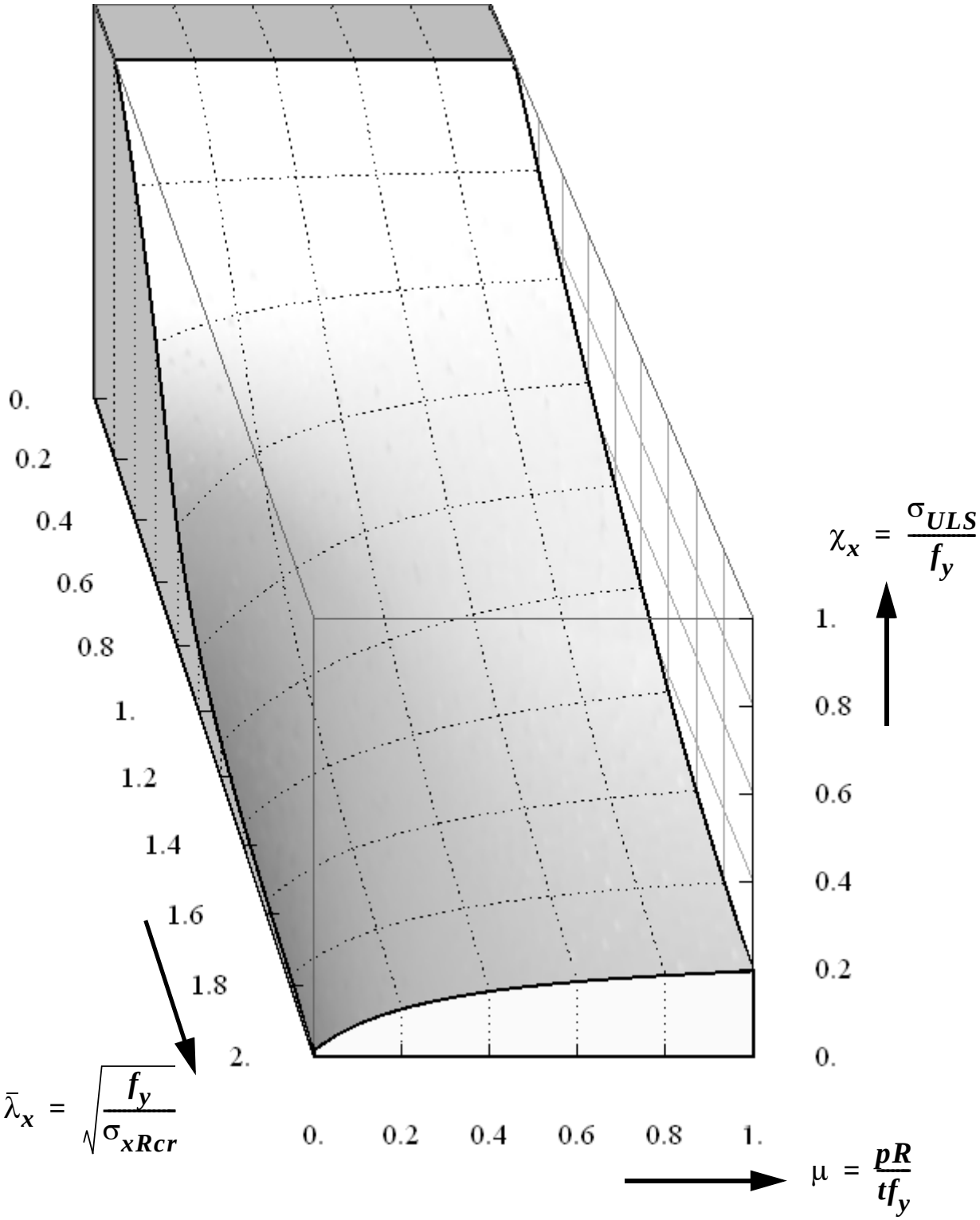

Figure 3.122 Elastic-plastic interaction of $\alpha_{xp} = \alpha_{xpe}$ with uni-axial yield

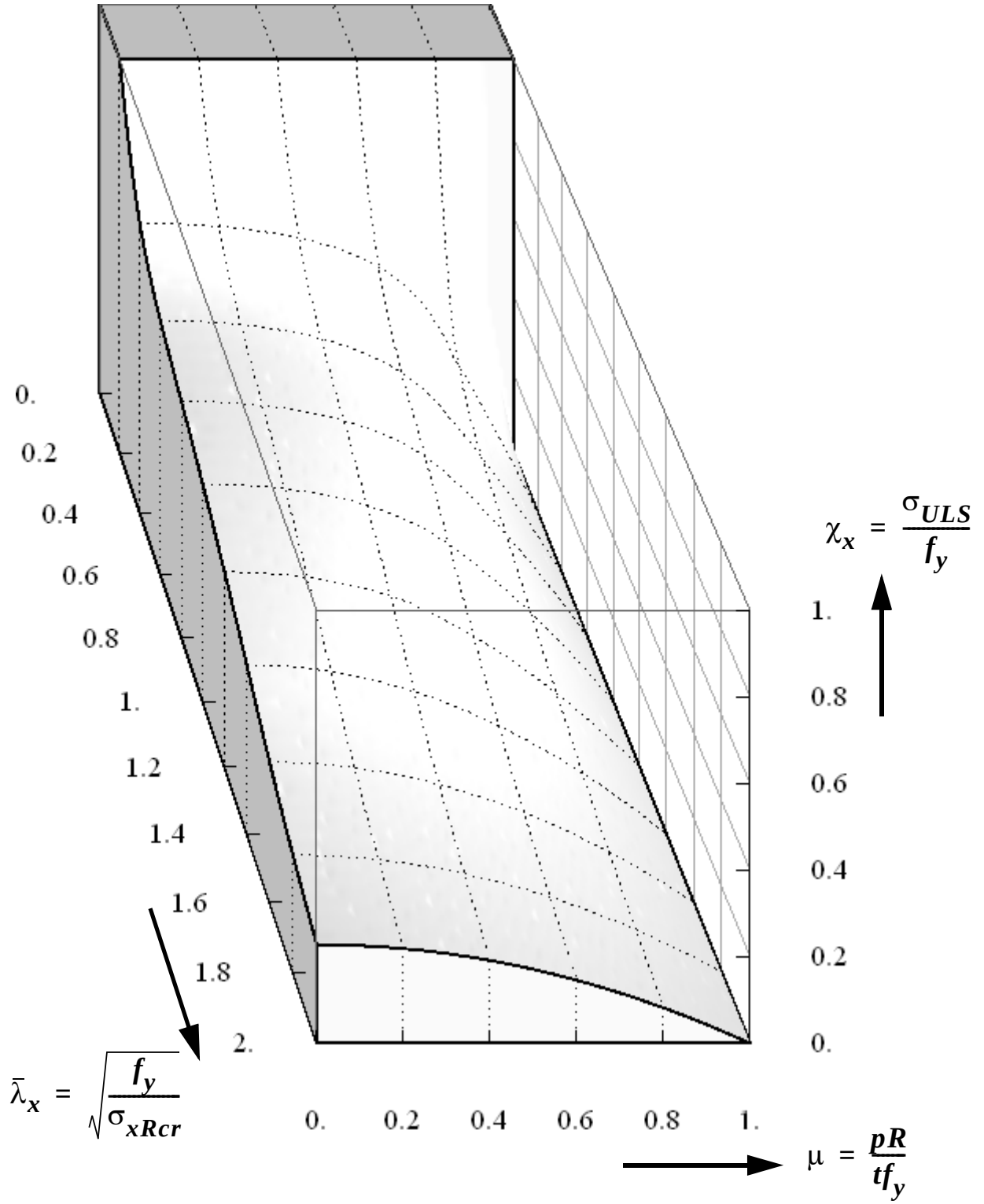

Figure 3.123 Elastic-plastic interaction of $\alpha_{xp} = \alpha_{xpp}$ with uni-axial yield

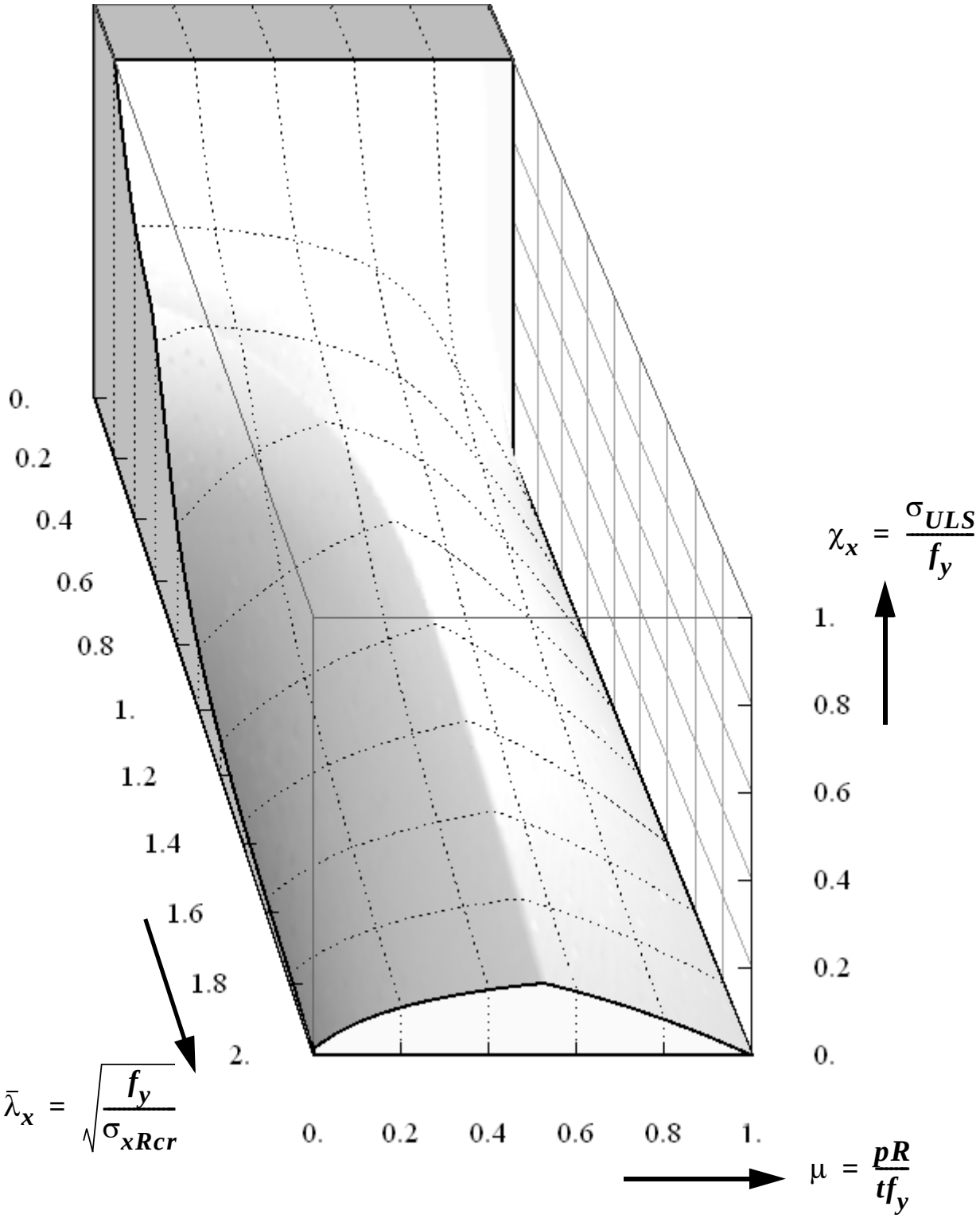

Figure 3.124 Characteristic buckling strength according to EN 1993-1-6: pinned bottom

3.10.3 Summary of EN 1993-1-6 design regulation

The elastic-plastic buckling strength according to EN 1993-1-6 for buckling phenomenon in the shell interior where there exist no edge constriction effects is predicted using an interaction formula which considers uni-axial yield conditions. This procedure results in elastic-plastic buckling strengths higher than the pure bi-axial plastic capacity of the shell, Figure 3.120 and Figure 3.122.

The geometrically and materially nonlinear (GMNL) buckling strength prediction of the perfect cylindrical shell using the pressurized imperfection reduction factor, α_{xpp}, may predict strengths higher than the bi-axial plastic capacity (MNL strength) of the shell. This situation is mainly seen in relatively thick cylindrical shells ($R/t \leq 145$) and hence the pressurized imperfection reduction factor can not be applied to all shell slendernesses, Figure 3.111 and Figure 3.114.

In using the interaction expression to predict the characteristic elastic-plastic buckling strength of a cylindrical shell, the imperfection reduction factor, α_{xp}, is taken as the smaller of the pressurized elastic, α_{xpe}, and the pressurized plastic, α_{xpp}, imperfection reduction factor values; and plastic interaction is applied using the basic plastic interaction parameters $\overline{\lambda}_o$, η, and β. This procedure results in the same buckling strength as making a separate use of the pressurized elastic and presurized plastic imperfection reduction factors in the interaction expression and taking the smaller of the final results obtained. However, in cases of smaller α_{xpp} values than α_{xpe}, applying the interaction means that applying the effect plasticity for the second time since α_{xpp} (obtained from geometric and material nonlinear numerical analyses) itself includes such effect from the beginning; a procedure which makes no logical sense.

Besides, when using the procedure, the resulting characteristic buckling strength may even be higher than not only the bi-axial plastic capacity of the cylindrical shell but also the already higher elephant's foot strength values obtained using α_{xpp} (see Figure 3.125 and Figure 3.127). A third plasticity condition should therefore be applied to garantee that no elastic-plastic buckling strength exceeds the bi-axial plastic capacity of the shell.

Evenif a third separate plasticity condition (cut-off by membrane Mises yield condition, Figure 3.128) is applied to it, the strength results are inconsistent with those computed numerically, except for the relatively very thin cylindrical shells.

Moreover, this procedure produces an inconsistency in strength prediction at very low pressure level thereby producing a jump between a very small pressure level and a non-pressurized (Zero pressure level) cases. This effect is shown in Figure 3.126 and Figure 3.127.

The α_{xpp} factor is not an imperfection reduction factor as it is used in EN1993-1-6 and has nothing to do with imperfections but instead a reduction factor, when referred to the classical elastic buckling strength, accounts for material and geometric nonlinearities; or when referred to the pure plastic capacity of the shell, accounts for geometric nonlinearities.

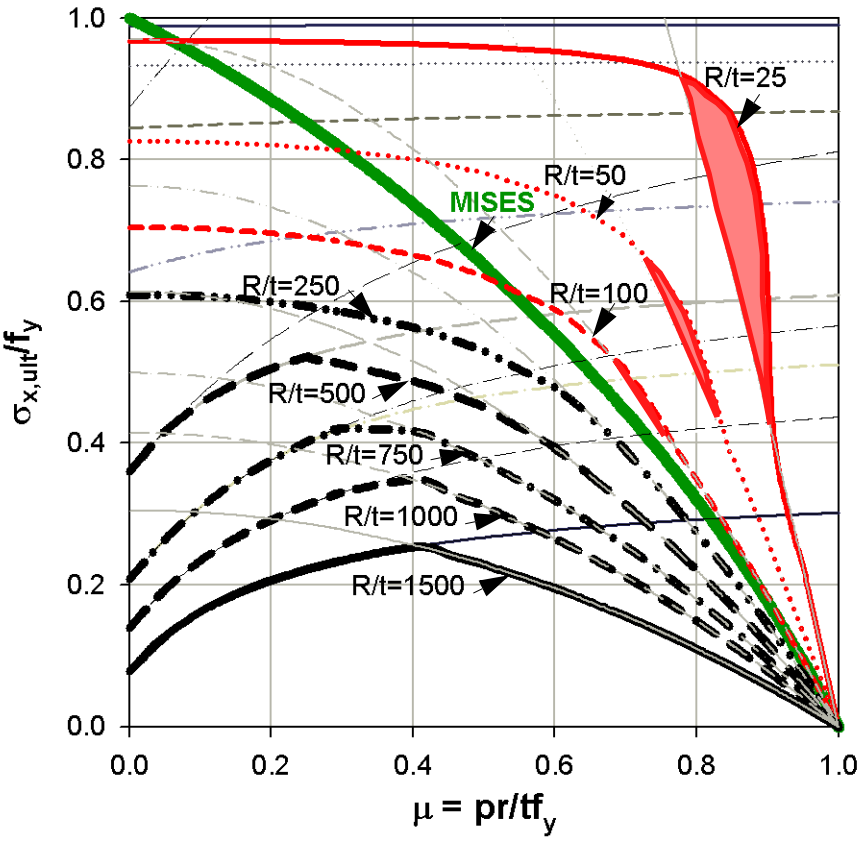

Figure 3.125 Characteristic buckling strength according to EN 1993-1-6: pinned bottom

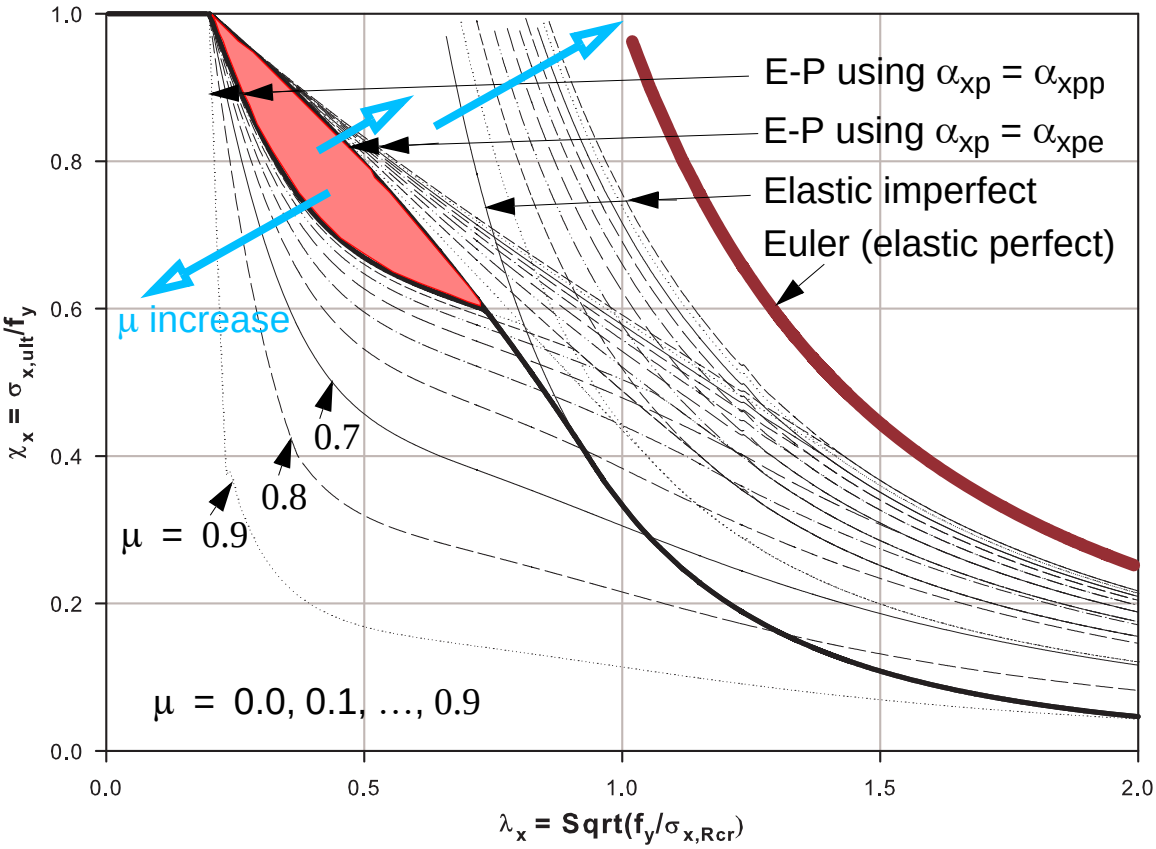

Figure 3.126 A jump in characteristic buckling strength: EN 1993-1-6, pinned bottom

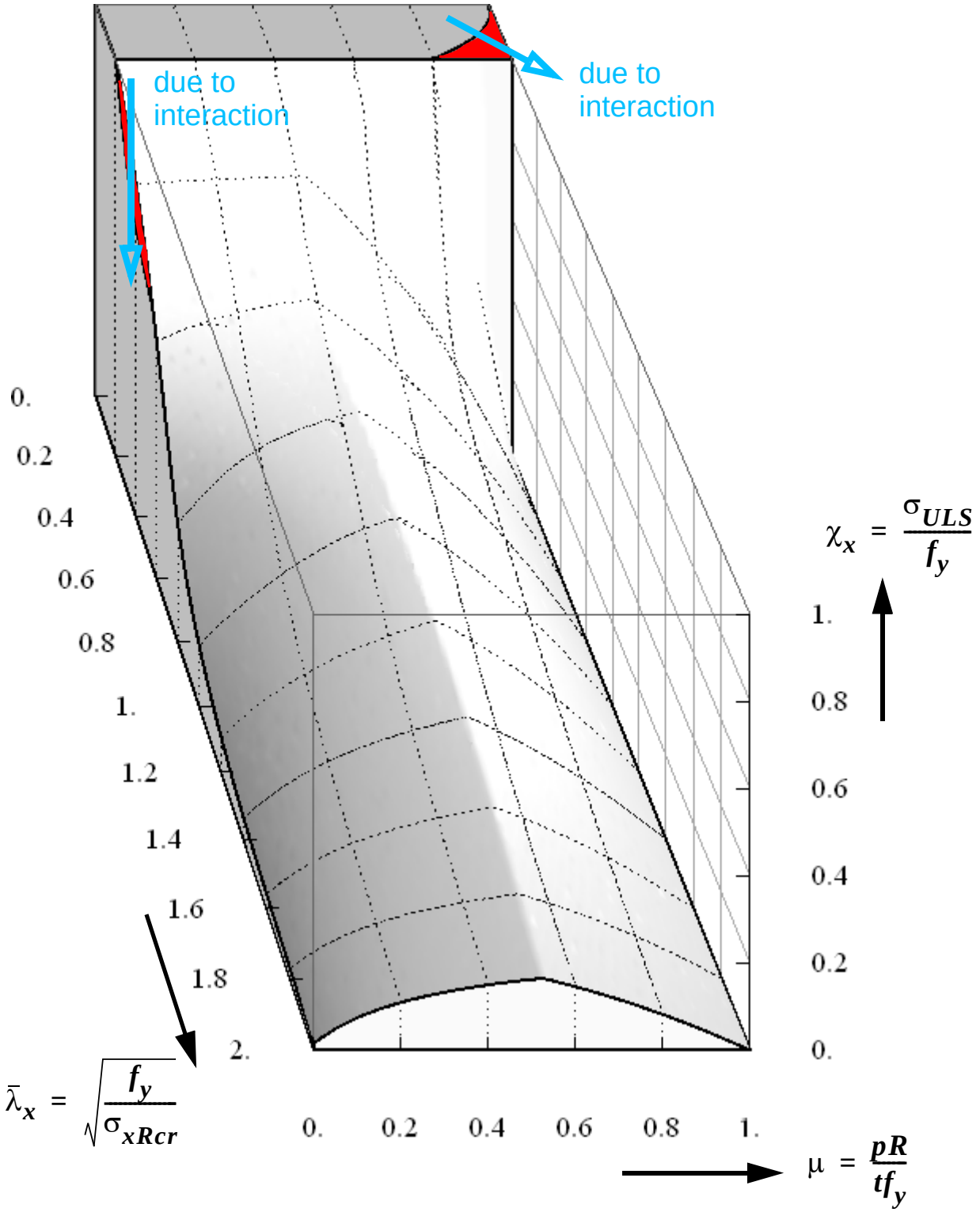

Figure 3.127 Characteristic buckling strength according to EN 1993-1-6: pinned bottom

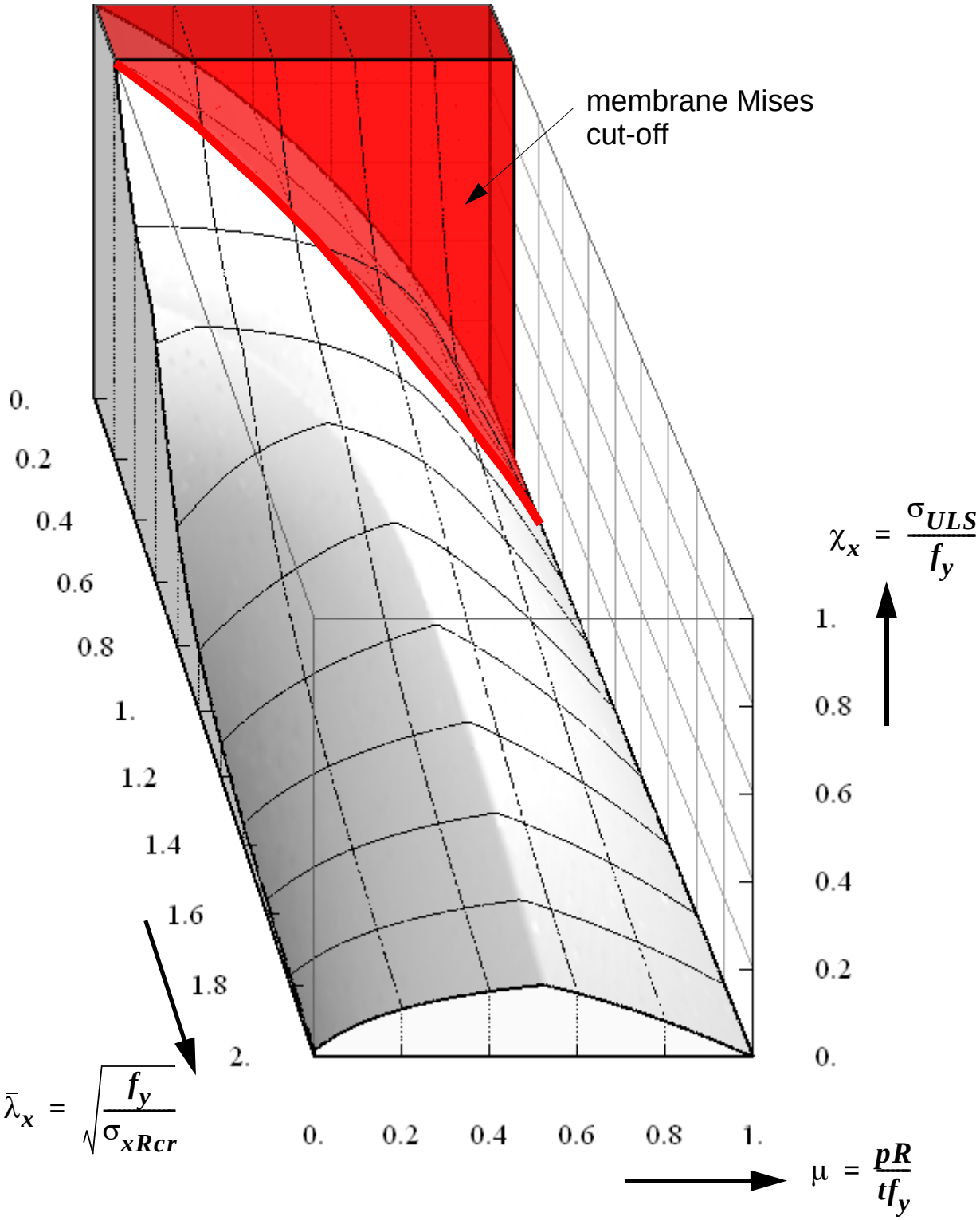

Figure 3.128 Characteristic buckling strength according to EN1993-1-6 and bi-axial membrane Mises cut-off

3.10.4 Related previous study and results

Leaving everything the same (except the plastic buckling parameters) as it was discussed in EN 1993-1-6 buckling design recommendation, Rotter (2006a) presented a way to directly and precisely extract the plastic buckling interaction parameters to be used in the buckling interaction expression (instead of the constant values $\bar{\lambda}_o = 0.2$, $\beta = 0.6$, and $\eta = 1.0$) from an interaction representation (GMN(i)A/MNA versus GMN(i)A/LBA plot). Using his procedure, Rotter extracted the follwoing plastic buckling parameters:

$$\bar{\lambda}_o = 0 \qquad \text{(Eq. 3.95)}$$

$$\beta = 0.25(\alpha_{xpe} + 2\alpha_{xpe}^2) \qquad \text{(Eq. 3.96)}$$

$$\eta = \frac{\ln(1-k) - \ln(\beta)}{\ln(1-\beta)} \qquad \text{(Eq. 3.97)}$$

with

$$k = \left(\frac{1 + \alpha_{xpe}/4}{\alpha_{xpe}^2}\right) \cdot \left[\left(1 + \frac{2\alpha_{xpe}^2}{(1 + \alpha_{xpe}/4)^2}\right)^{1/2} - 1\right] \qquad \text{(Eq. 3.98)}$$

The characteristic buckling strength of the cylindrical shell using these plastic interaction parameters and the procedure discussed in the EN1993-1-6 buckling design recommendation are shown in the pressure representation, Figure 3.129, and capacity representation, Figure 3.130.

The results obtained using this procedure, when compared to EN1993-1-6, results in somewhat lesser interaction between the elastic and plastic buckling which means higher buckling strength for medium internal pressure level. Besides, this procedure avoids the problem of getting an increased buckling strength due to interaction. However, since the same α_{xpp} strength factor, like in EN 1993-1-6, is on the foundation the problem of predicting higher strengths than the bi-axial plastic capacity of the shell and inconsistency with the nonlinear numerical analyis results remain unchanged.

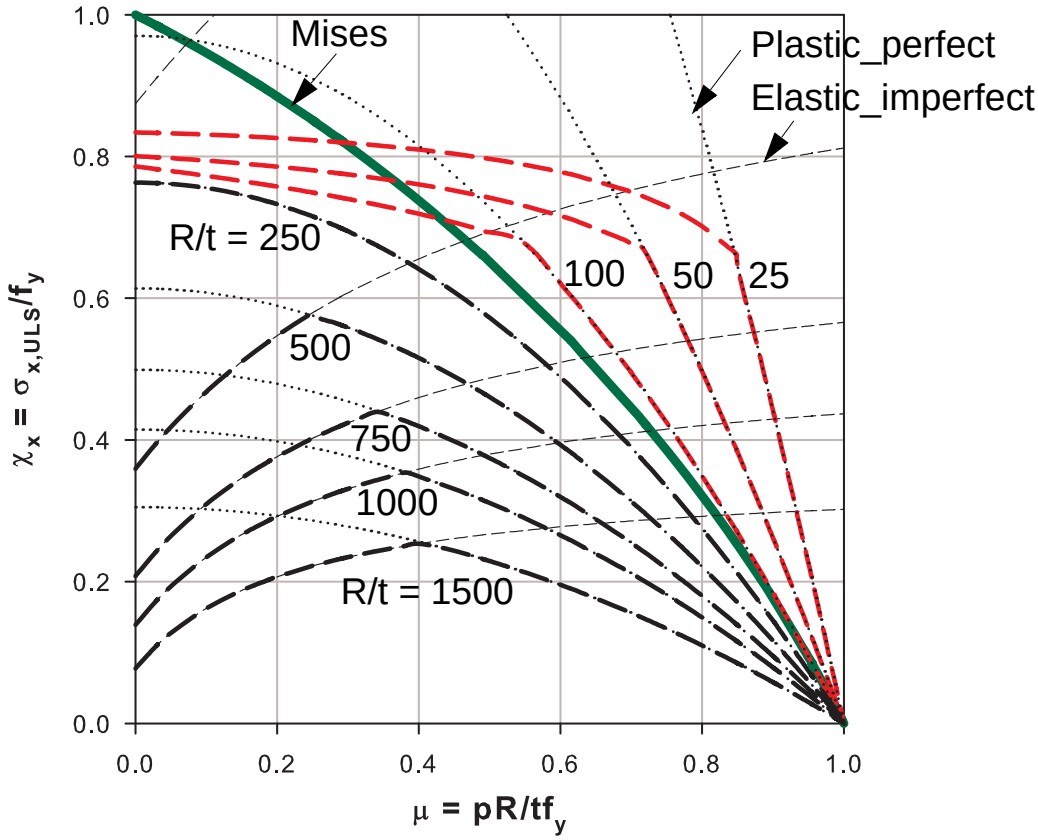

Figure 3.129 Characteristic buckling strength according to Rotter (2006a): pinned

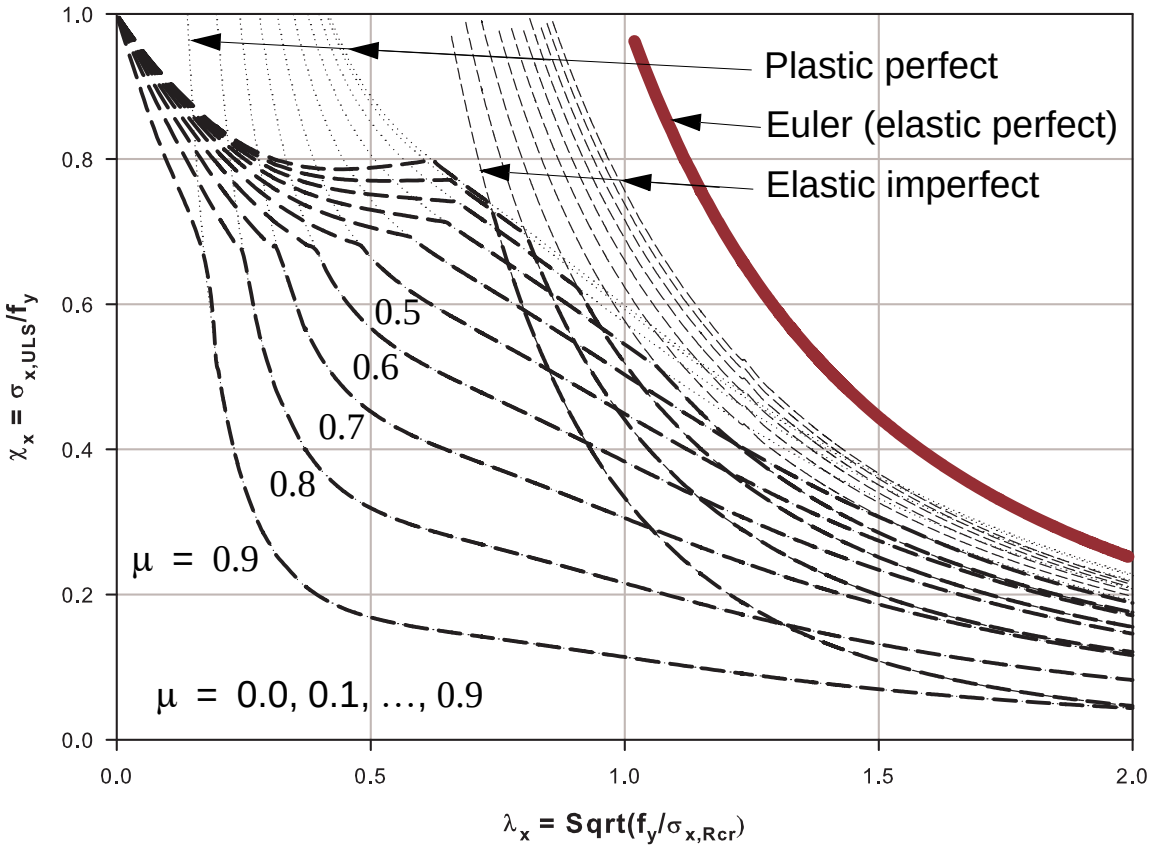

Figure 3.130 Characteristic buckling strength according to Rotter (2006a): pinned

3.11 Summary and conclusions

EN1993-1-6 buckling design recommendation:

- the overall procedure in predicting the characteristic buckling strength of cylindrical shell involves many steps
- the reduction factor α_{xpp}, which really is a plastic buckling reduction factor, is being treated as if it is an elastic reduction factor. Besides, it is referred to as an imperfection reduction factor while it has nothing to do with imperfections.
- applies plasticity conditions twice, first in α_{xpp} itself as it basically includes material and geometric nonlinear effects and a second elastic-plastic buckling interaction of α_{xpp} with the uni-axial yield condition
- predicts elastic-plastic buckling strengths higher than the pure bi-axial plastic resistance of the cylinder
- needs additional separate plasticity check against bi-axial yielding
- even if separate plasticity condition is applied to it, the strength results are inconsistent with those computed numerically
- inconsistency in buckling strength predictions at very low pressure level and zero-pressure level resulting in a jump of strength
- applies only for pinned bottom cases (with more safety for fixed cases?)

Buckling design recommendation of the current work:

- considers bi-axial plasticity from the very beginning
- strictly differentiates typical buckling failure modes: buckling in the free shell interior and buckling adjacent to the boundary (elephant’s-foot buckling mode)
- it is easy to follow and apply; straight forward approach
- differentiates pinned and fixed bottom boundary condition cases

4

Axisymmetric elastic-plastic buckling of liquid-filled conical shells (LFC)

4.1 Introduction

The axisymmetric elastic-plastic (elephant's-foot) buckling phenomenon and strength of axially ring-compressed and internally uniformly pressurized thin-walled cylindrical shells have already been investigated in detail. The elephant's-foot type buckling phenomenon, however, is not only restricted to uniformly (meridionally and internally) loaded cylinders but to general cylindrical and conical shells so long as they are subjected to meridional compression and circumferential tension near the boundary. More specifically, axisymmetric elastic-plastic buckling near a boundary may happen in thin-walled cylindrical and conical shells with constant/varying meridional compression and hydrostatic internal pressure. Since a liquid-filled conical shell falls into such a loading category, an axisymmetric elastic-plastic buckling near the boundary is possible and hence the buckling strength of conical shells associated to an elephant's-foot buckling phenomenon needs to be investigated in detail.

Unlike that of a uniformly loaded cylindrical shell which results in uniform meridional and circumferential membrane section force ditributions, the meridional membrane section force distribution in the liquid-filled conical shell is maximum at the lower supported edge and decreases nonlinearly and rapidly up the meridian. Such a distribution of the meridional compressive section force superimposed with the edge constriction effects of the bottom boundary conditions will restrict the elastic-plastic buckling phenomenon to a region very close to the supported lower edge causing elephant's-foot type buckling.

This study is concerned with thin-walled metal liquid-filled conical shell structures with pinned or fixed bottom boundary conditions, Figure 4.1. In the course of investigating the elastic-plastic buckling strength, liquid-filled conical shells will be analysed using membrane theory, linear shell bending theory (LA), linear bifurcation analysis (LBA), small displacement materially nonlinear analysis (MNA), perfect geometrically and materially nonlinear analysis (GMNA), and geometrically and materially nonlinear analysis with imperfections (GMNIA). A combination of both analytical and numerical (using finite element program) analysis methods will be used depending on the nature and complexity of the problem type in consideration. In all the analyses, no hardening of any kind (material or geometric) is considered. The buckling failure criteria will be interpreted, more generally, relative to each analysis result but mainly, in-line with the underlying structure of the European standard EN1993-1.6, relative to the two reference strengths: small displacement linear bifurcation analysis (LBA) and small displacement materially nonlinear analysis (MNA).

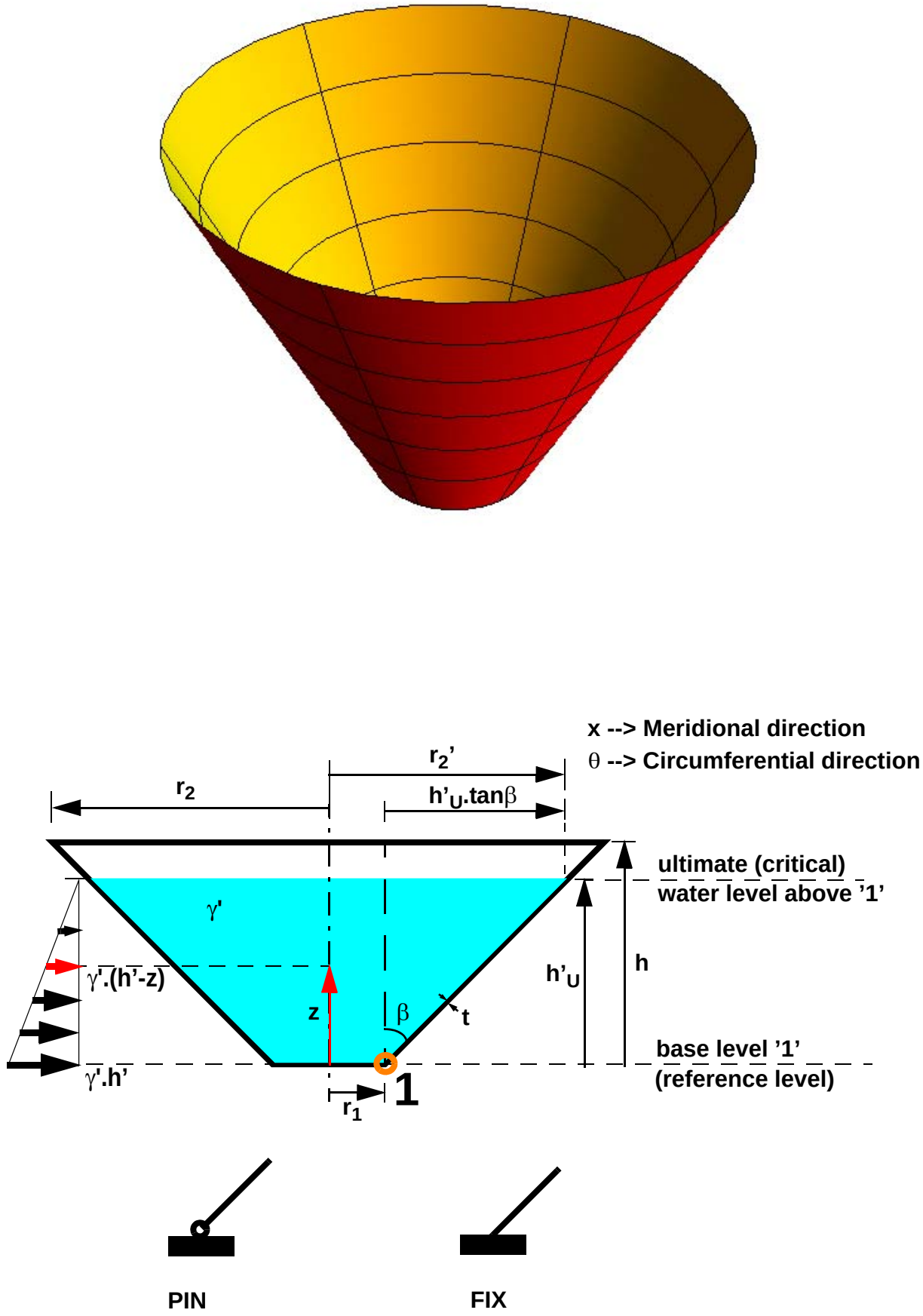

Figure 4.1 Geometry, loading, and boundary conditions

4.2 Problem statement

Despite the fact that there have been conical steel water tower collapse cases, of which the real causes are not surely known yet, not much has been done to investigate the possible elephant's-foot buckling strength of conical shells. Such type of buckling may happen in liquid-filled conical shells, specially when there exist a global bending effect which may result, say, from geometric eccentricity (global tilting) of the cone. This geometric eccentricity, even upon filling may result in global bending effect which shortens the life span of the structure with the formation of a possible elephant's-foot type buckling phenomenon. Apart from this, a perfect liquid-filled conical shell may buckle in such an axisymmetric elastic-plastic buckling mode near the supported edge so long as a bi-axial state of stress, similar to that of the cylindrical shell, exists.

This work, therefore, addresses the axisymmetric elastic-plastic buckling strength of isotropic unstiffened liquid-filled conical shells using numerical parametric simulations, with the ultimate goal of deriving a set of basic data that can be used in a straight forward buckling design approach by hand calculations.

Once again, the study was done computationally using ABAQUS and using the 3-node general-purpose axisymmetric shell element with axisymmetric deformation, SAX2. Linear and nonlinear numerical analyses were made for different shell slenderness (r_1/t) values which span from 100 to 1500 and an apex-half angle $\beta = 45°$, representing the practical range of conical shells in civil engineering constructions. The lengths of the cones are taken in such a way that no boundary-effect interactions are possible between the top and bottom boundary conditions. The material considered throughout the study is mild steel with an ideal elastic-plastic von Mises yield criterion and a yield stress $f_y = 240$ MPa, elastic modulus $E = 210$ GPa, and Poisson's ratio $\nu = 0.3$. The results are all expressed interms of non-dimensional variables and hence can be used to address other practical sets of conditions. In many of the upcoming discussions, a conical shell with the following set of conditions will be used for illustration purposes.

Geometry: $r_1/t = 500$ cm and $t = 1.0$ cm

Boundary conditions: pinned or fixed bottom and rotational restaraint at top

Loading: liquid-filling with specific weight γ'

Material properties: $E = 21000$ kN/cm^2; $\nu = 0.3$; $f_y = 24.0$ kN/cm^2

4.3 Linear shell analysis (LA)

4.3.1 Pure membrane behavior

Generally speaking, for axisymmetric shells with axisymmetric loading and boundary conditions, the cross-sectional stress state of a shell segment is primarily governed by pure membrane action due to the continuously distributed loads which the shell is subjected to.

The pure membrane behavior of a liquid-filled conical shell can easily be computed and is given, interms of the deformations and section forces, as

$$N_x = \frac{\gamma' h' r}{\cos\beta} \cdot \left(1 + \frac{r_1 - r}{\tan\beta}\right) \cdot \frac{1}{6}\left(\frac{r_1}{r}\right)^2 \cdot \left(\frac{r}{r_1} - 1 - \frac{h'\tan\beta}{r_1}\right) \cdot \left(2\frac{r}{r_1} + 1 + \frac{h'\tan\beta}{r_1}\right)$$

$$N_\theta = \frac{\gamma' h' r}{\cos\beta} \cdot \left(1 + \frac{r_1 - r}{\tan\beta}\right)$$

. . . membrane section forces (Eq. 4.1)

$$w^* = \frac{\gamma' r^3}{6Et\sin\beta} \cdot \left[2(\nu - 3) - 3(\nu - 2)\frac{r_1}{r} \cdot \left(1 + \frac{h'\tan\beta}{r_1}\right) + \nu\left(\frac{r_1}{r}\right)^3\left(1 + \frac{h'\tan\beta}{r_1}\right)^3\right]$$

$$\beta_x = \frac{\gamma' r^2}{6Et\cos\beta} \cdot \left[16 - 9\frac{r_1}{r} \cdot \left(1 + \frac{h'\tan\beta}{r_1}\right) - \left(\frac{r_1}{r}\right)^3\left(1 + \frac{h'\tan\beta}{r_1}\right)^3\right]$$

. . . membrane deformations (Eq. 4.2)

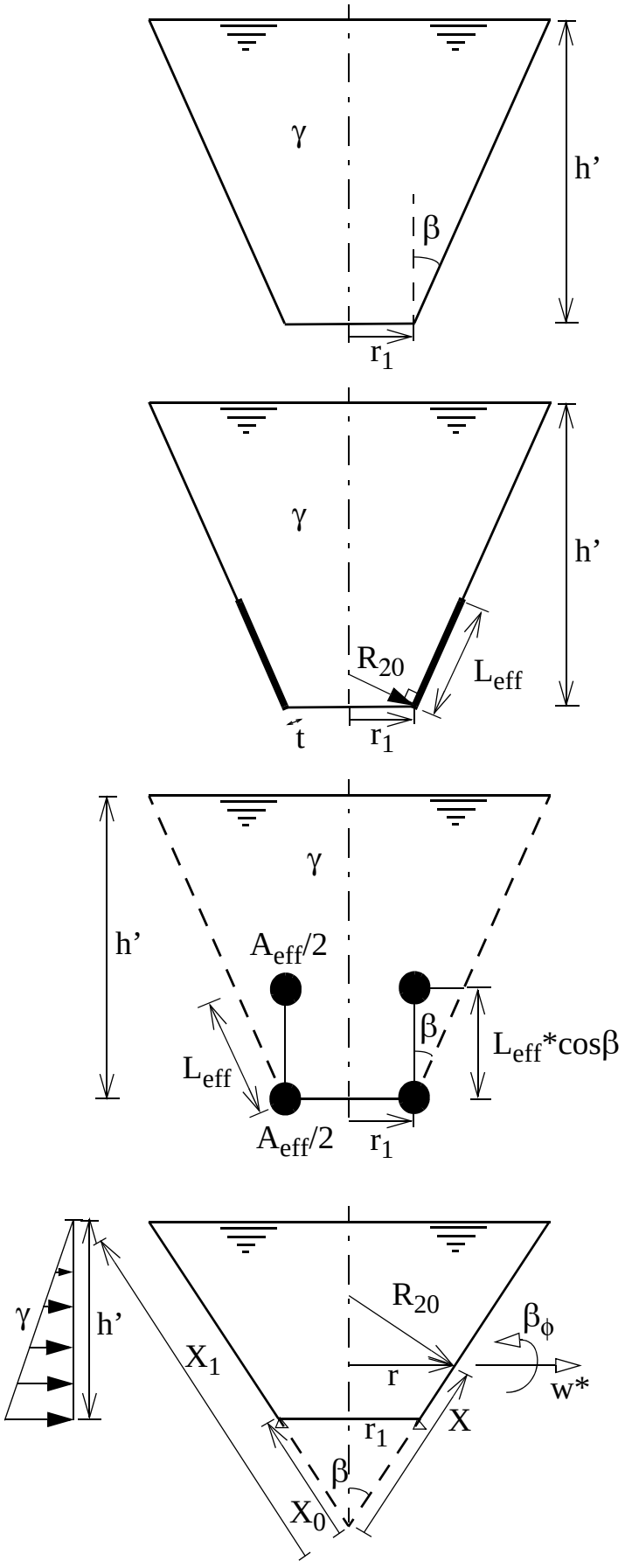

Figure 4.2 Ring model analogy, loading and geometry

4.3.2 Edge-bending effects

The stiffness of the equivalent ring model of the conical shell for edge bending effects, Linder (2001), is given by:

$$\underline{\underline{K}} = \frac{EA_{eff}}{2r_1^2} \cdot \begin{bmatrix} 2 & -L_{eff} \cdot \cos\beta \\ -L_{eff} \cdot \cos\beta & (L_{eff} \cdot \cos\beta)^2 \end{bmatrix} \qquad \text{(Eq. 4.3)}$$

for edge displacement disturbances w^*_A and $\beta_{x,A}$ at the bottom edge "A" of the cone, the restraining edge forces can be computed using the stiffness of the equivalent ring model as

$$\begin{bmatrix} R_{H,A} \\ R_{M,A} \end{bmatrix} = -\underline{\underline{K}} \cdot \begin{bmatrix} w_A^* \\ \beta_{x,A} \end{bmatrix} = -\frac{EA_{eff}}{2r_1^2} \cdot \begin{bmatrix} 2 & -L_{eff} \cdot \cos\beta \\ -L_{eff} \cdot \cos\beta & (L_{eff} \cdot \cos\beta)^2 \end{bmatrix} \cdot \begin{bmatrix} w_A^* \\ \beta_{x,A} \end{bmatrix} \qquad \text{(Eq. 4.4)}$$

For a liquid-filled conical shell, the total deformation and section forces (edge bending effects included) according to the effective-ring analogy model are generally computed as given below. The actual distributions along the meridian of the cone will depend on the type of bottom boundary condition considered.

Deformations:

$$\begin{bmatrix} w^* \\ \beta_x \end{bmatrix} = \begin{bmatrix} (f_1 + f_2) & -(L_{eff}\cos\beta) \cdot f_1 \\ \dfrac{2f_1}{(L_{eff}\cos\beta)} & (f_2 - f_1) \end{bmatrix} \cdot \left(\begin{bmatrix} w_A^* \\ \beta_{x,A} \end{bmatrix} - \begin{bmatrix} w_A^* \\ \beta_{x,A} \end{bmatrix}_{part} \right) + \begin{bmatrix} w^* \\ \beta_x \end{bmatrix}_{part} \qquad \text{(Eq. 4.5)}$$

Section forces:

$$Q_x = \begin{bmatrix} (f_2 - f_1)\cos\beta & \dfrac{2f_1}{L_{eff}} \end{bmatrix} \cdot \begin{bmatrix} R_{H,A} \\ R_{M,A} \end{bmatrix} \qquad \text{(Eq. 4.6)}$$

$$N_x = -Q_x \cdot \tan\beta + N_{x,part} \qquad \text{(Eq. 4.7)}$$

$$N_\theta = \frac{Et}{r_1} \cdot \begin{bmatrix} (f_1 + f_2) & -(L_{eff}\cos\beta) \cdot f_1 \end{bmatrix} \cdot \left(\begin{bmatrix} w_A^* \\ \beta_{x,A} \end{bmatrix} - \begin{bmatrix} w_A^* \\ \beta_{x,A} \end{bmatrix}_{part} \right) + N_{\theta,part} \qquad \text{(Eq. 4.8)}$$

$$M_x = -\left[(L_{eff}\cos\beta)\cdot f_1 \quad (f_1 + f_2)\right] \cdot \begin{bmatrix} R_{H,A} \\ R_{M,A} \end{bmatrix} \qquad \text{(Eq. 4.9)}$$

$$M_\theta = \nu \cdot M_x \qquad \text{(Eq. 4.10)}$$

The section moments are assumed positive when outer side of the shell is under compression.

For the conical shell of this study, pinned- or fixed-bottom boundary conditions are considered where the distributions of the deformations and section forces under the action of liquid-loading can easily be computed.

Where

$$L_{eff} = 0.778\sqrt{\frac{r_1 \cdot t}{\cos\beta}} \qquad \text{(Eq. 4.11)}$$
$$A_{eff} = L_{eff} \cdot t$$

For illustration purposes, consider a conical shell with the following geometry, material, loading, and boundary conditions:

Geometry: r_1 = 500 cm; t = 1.0 cm; β = 45°; h'/r_1 = 3.0

Boundary conditions: pinned- and fixed-bottom

Loading: liquid filling γ' = 5.64669 .10^{-6} kN/cm^3

Material properties: E = 21000 kN/cm^2; ν = 0.3; f_y = 24 kN/cm^2

The liquid density is chosen in such a way that the meridional membrane compressive stress at the cone-base is equal to the classical elastic critical buckling stress of the cone. The deformations and section force results obtained from the linear shell analysis using the ring model analogy discussed above would then be as shown on the plots in Figure 4.3 to Figure 4.8. The normal section force and bending moments shown in these plots are normalized with respect to the corresponding uni-axial yield section force, $N_{pl} = t.f_y$, and section moment, $M_{pl} = t^2.f_y/4$. The circumferential bending moment M_θ distribution along the meridian is not plotted as it is the product of the poison's ratio ν and the meridional bending moment M_x.

4.3.3 Numerical finite element linear analysis (LA)

Numerical finite element small displacement linear analyses of liquid-filled conical shells were made for verification purposes. The deformation and section force results obtained from ABAQUS finite element linear analysis are exactly the same as those obtained using the effective-ring-model analogy, Figure 4.3 to Figure 4.8.

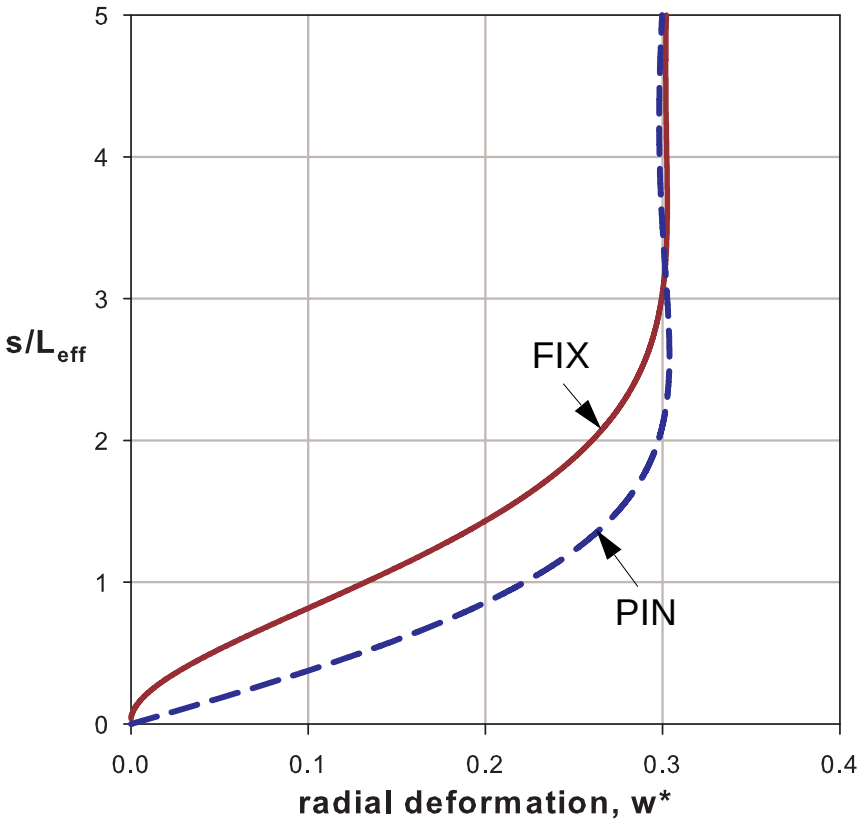

Figure 4.3 Radial deformation

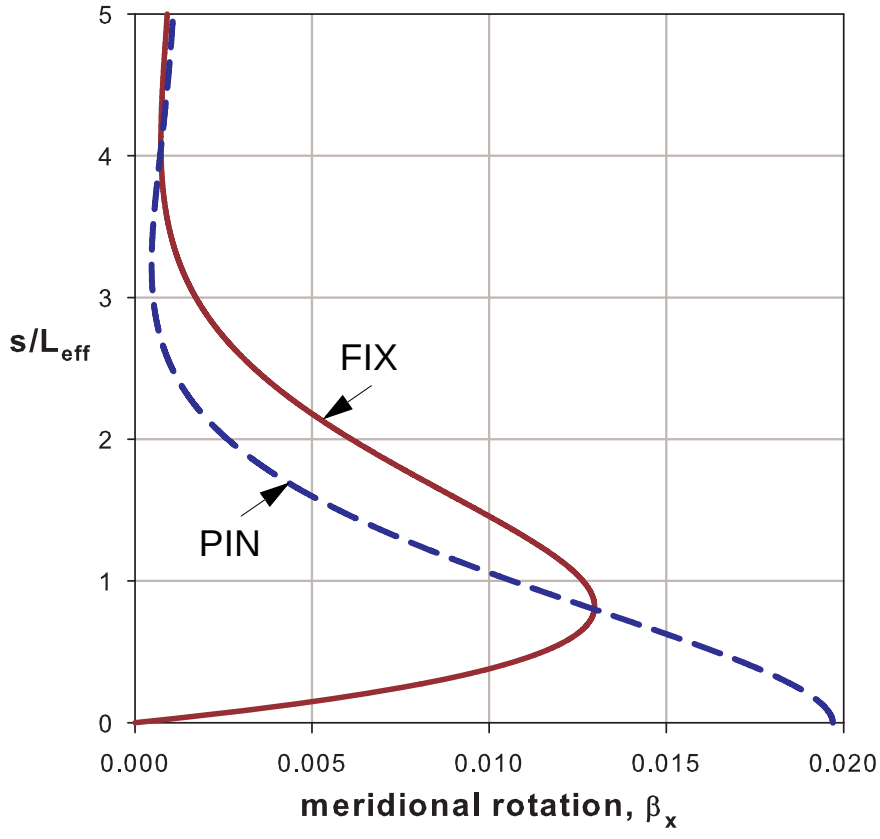

Figure 4.4 Meridional rotation

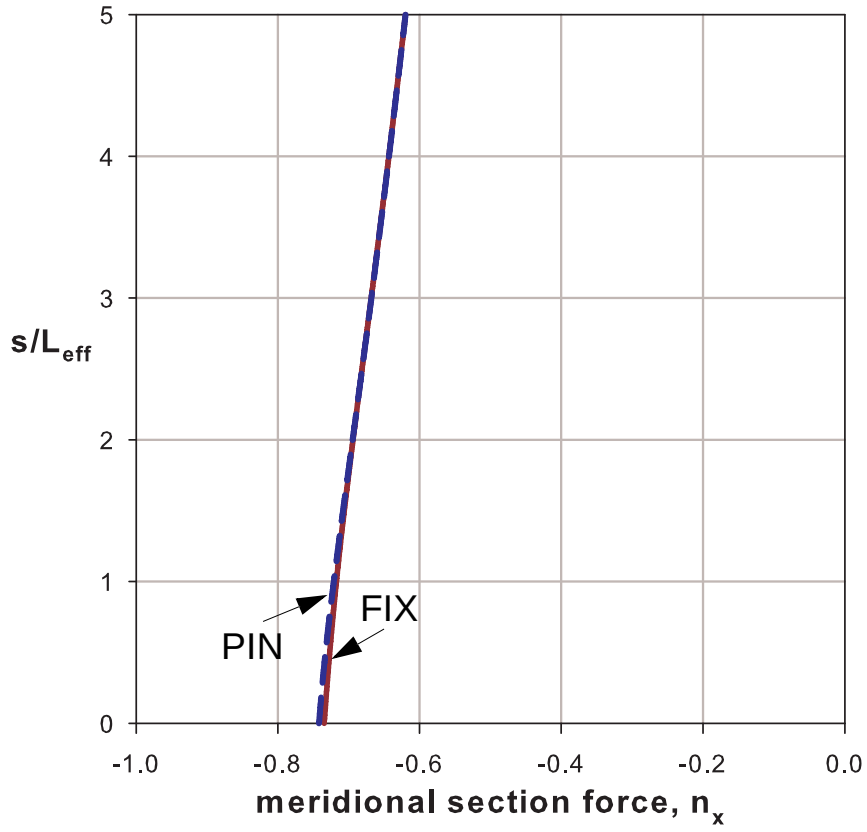

Figure 4.5 Meridional section force

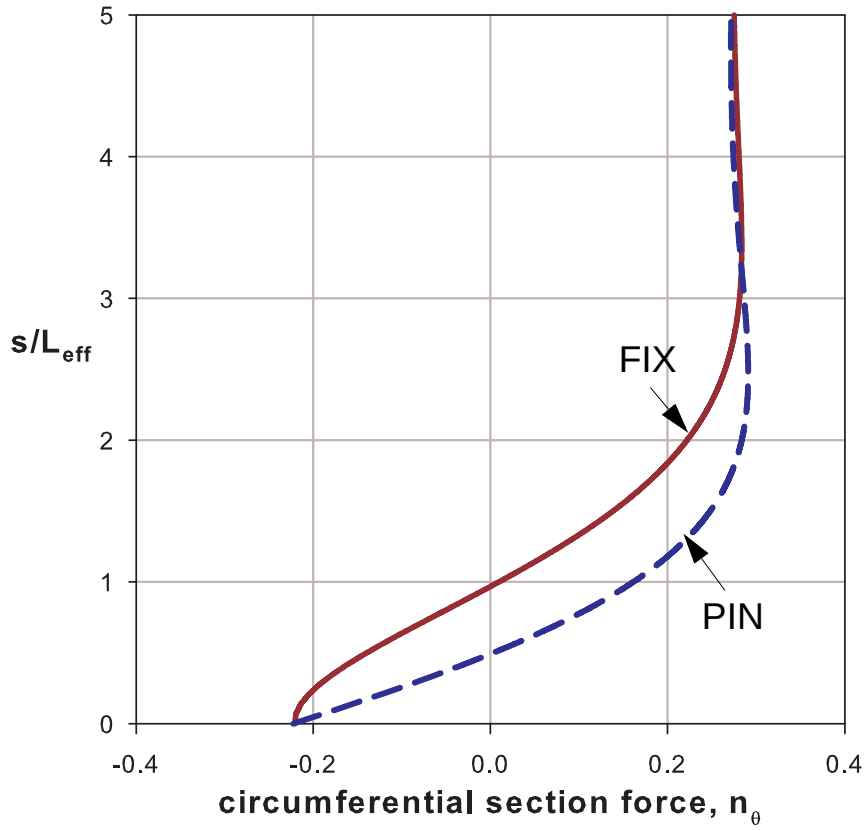

Figure 4.6 Circumferential section force

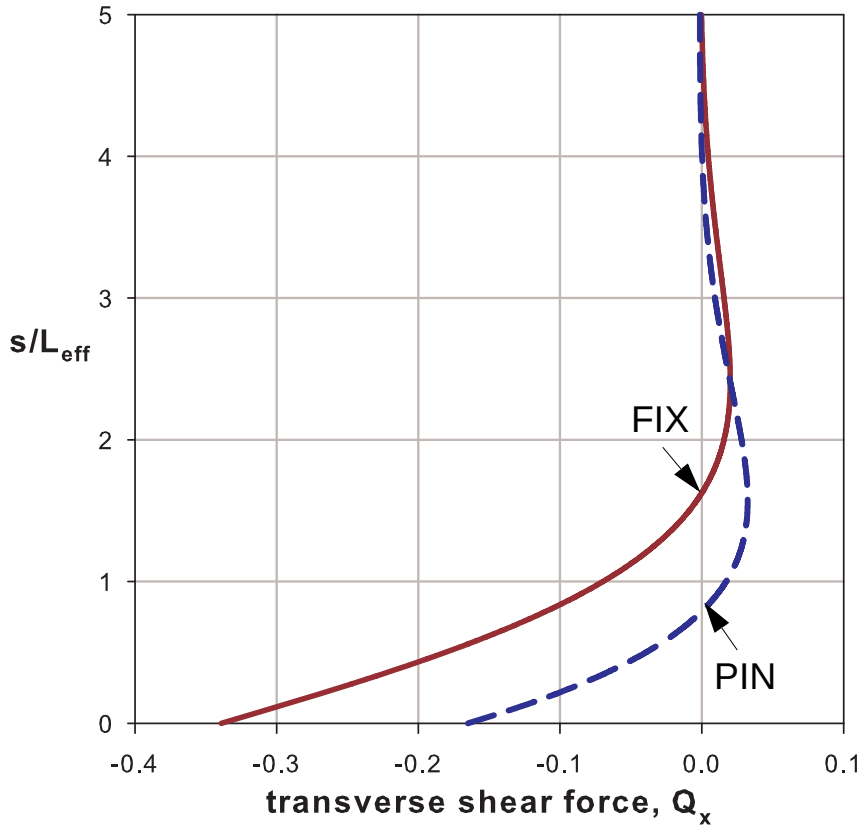

Figure 4.7 Transverse shear force

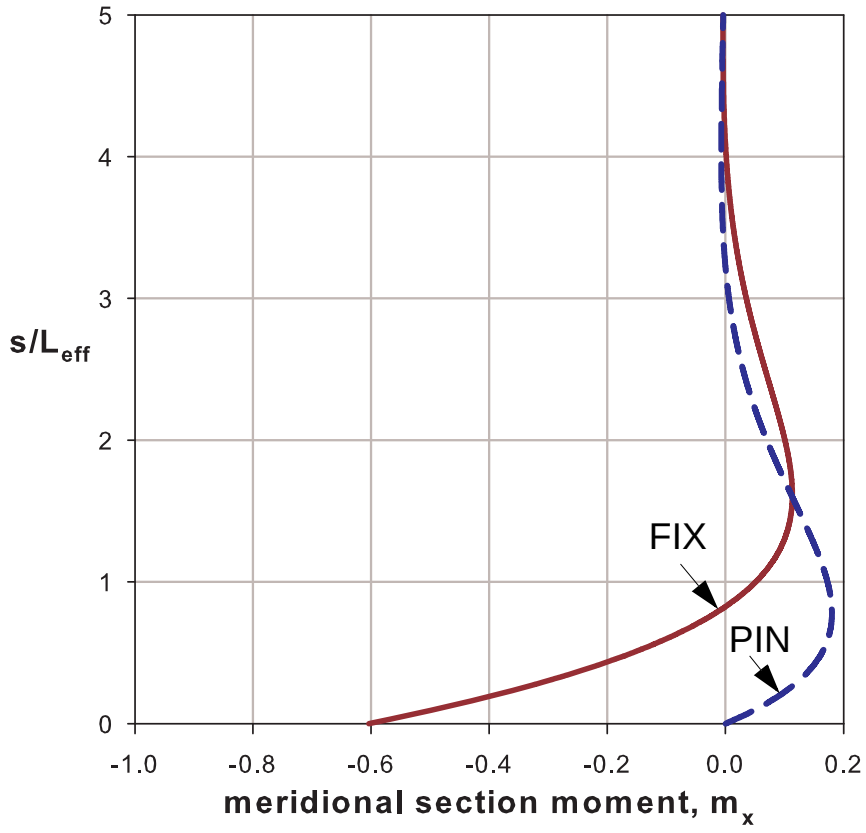

Figure 4.8 Meridional section moment

4.4 Loading procedure for numerical analysis purposes

In liquid-filled conical shells the resulting meridional and circumferential membrane section forces will depend on both the specific weight (or density) of the liquid and depth of the filling. In the practical cone loading sense, the specific weight of the liquid is known hence pre-specified and loading is applied by increasing the depth of the liquid-filling. On the other hand, when checking the safety of an already constructed water tower, the height of the shell is known implying that the maximum liquid-depth is pre-specified (otherwise overflow) and the specific weight of the liquid should be varied to determine the strength of the shell and compare it with the acting liquid load. However, in dealing with numerical analysis of conical shells solely loaded by liquid-filling, the following two separate loading procedures can be employed, i.e.

- increasing the liquid-depth for a pre-specified specific weight, Figure 4.9
- increasing the specific weight of the liquid for a pre-specified liquid depth, Figure 4.11

The first loading procedure, which is similar to the way it is done in the practical world (e.g. when filling for the first time), leads to an iterative procedure to obtain the ultimate liquid-depth at which buckling occurs. The iteration steps (see Figure 4.10) that needs to be followed when using this loading procedure are explained as follows:

1 Assume a starting liquid-depth

2 Using the pre-specified density of the liquid, perform a numerical analysis to obtain a buckling load factor.

3 The load factor, even though it is a factor which should directly be applied to the liquid density, can be applied to the liquid-depth in such a way that the meridional membrane compressive stresses at the base of the cone obtained using the factored liquid-depth and the factored liquid-density are equal to each other.

4 With the factored liquid-depth but an unfactored (or the pre-specified) liquid-density, perform a second numerical analysis to obtain a new buckling load factor.

5 Repeat the above steps until the load factor is equal to 1.0

6 The liquid-depth, along with the pre-specified liquid-density, which will result in a buckling load factor of 1.0 will be the ultimate liquid-depth.

The second loading procedure, which is similar to the way used when checking the safety of an already constructed water tower or when analyzing water tower collapses, is a direct and shortest way to obtain a buckling load factor. This means, for every pre-specified liquid-depth the buckling

load factor which should only be applied to the liquid-density is computed. Hence, only the first two steps of the first loading procedure are used here. In the general invetigation of buckling strengths of liquid-filled conical shells, these two steps are repeatedly used for different pre-specified liquid-depths.

Comparing the two separate loading procedures, the first procedure is limited to a specific liquid-filled cone situation and the important buckling parameter is the ultimate liquid-depth hence the intermediate iterative results are not needed. Whereas the second procedure can be applied for general cases specially when extraction of useful data for general buckling design purposes is required. The second method, in other words, when performed repeatedly by varying the liquid-depth is similar to the first procedure without dropping the load factors at each iteration step.

On the other hand, the first method, when used in numerical studies, needs separate iterations for each analysis type (e.g. LBA, MNA, GMNA, GMNIA etc.) making it a very expensive method interms computational costs. The second method is useful in numerical studies because each anaylsis type is performed with no iterations for a pre-specified liquid-depth (or $\overline{\psi}$) and hence a direct comparison can be made for a given $\overline{\psi}$ value. Since the main purpose of this study is to extract useful data for general buckling purposes, the second loading procedure will be used throughout the study.

Ultimate liquid-filling load level parameters, using membrane theory

$$\zeta'_U = \frac{h'_U \tan\beta}{r_1}$$

$$\bar{\psi} = \frac{\sigma_{x,U,1}}{\sigma_{\theta,U,1}} = \frac{\zeta'_U}{6}\cdot(3+\zeta'_U)$$

$$\alpha_{xpe} = \frac{\sigma_{x,U,1}}{\sigma_{x,Rcr}}$$

$$\bar{p} = \frac{\sigma_{\theta,U,1}}{\sigma_{x,Rcr}}$$

$$\bar{\psi} = \frac{\alpha_{xpe}}{\bar{p}}$$

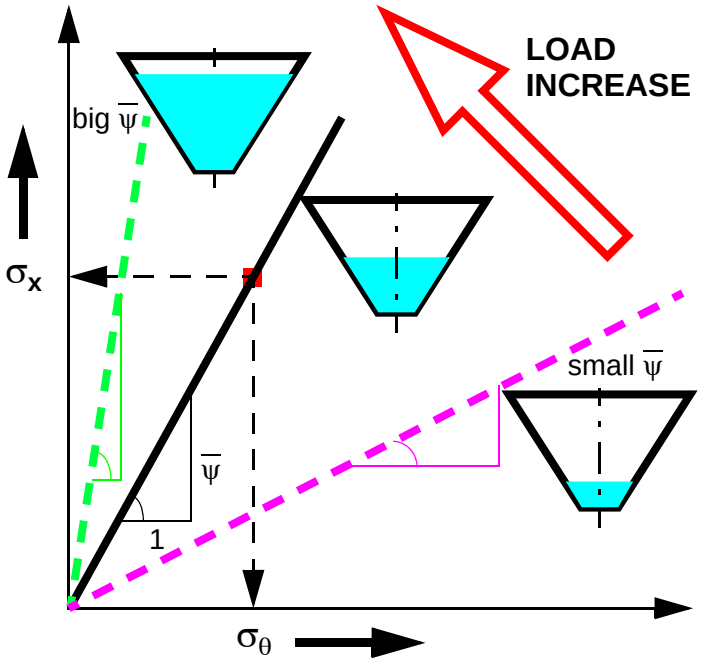

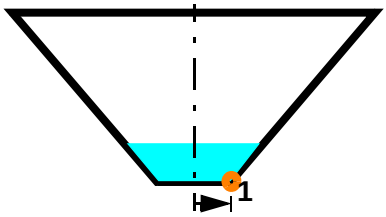

$\bar{\psi} = 0.5$

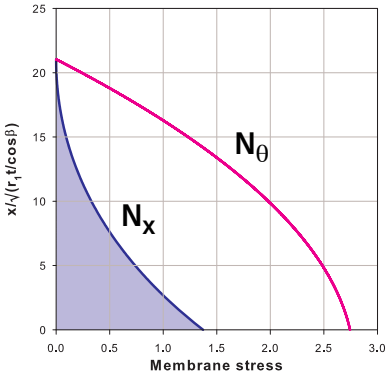

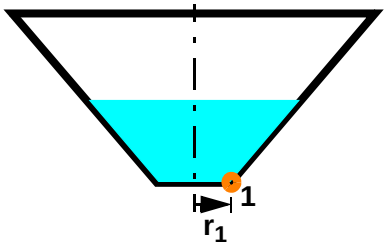

$\bar{\psi} = 1.5$

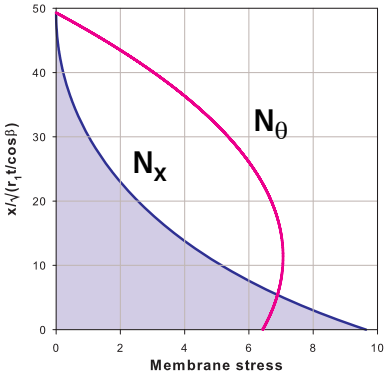

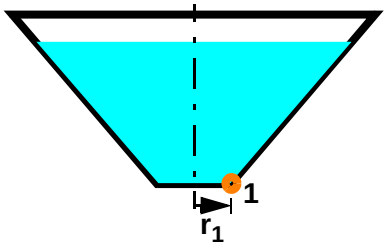

$\bar{\psi} = 3.0$

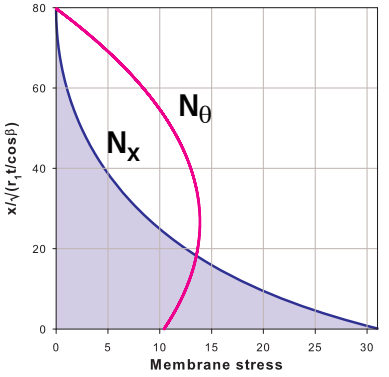

Figure 4.9 Loading by increasing liquid-depth for a pre-specified liquid-density

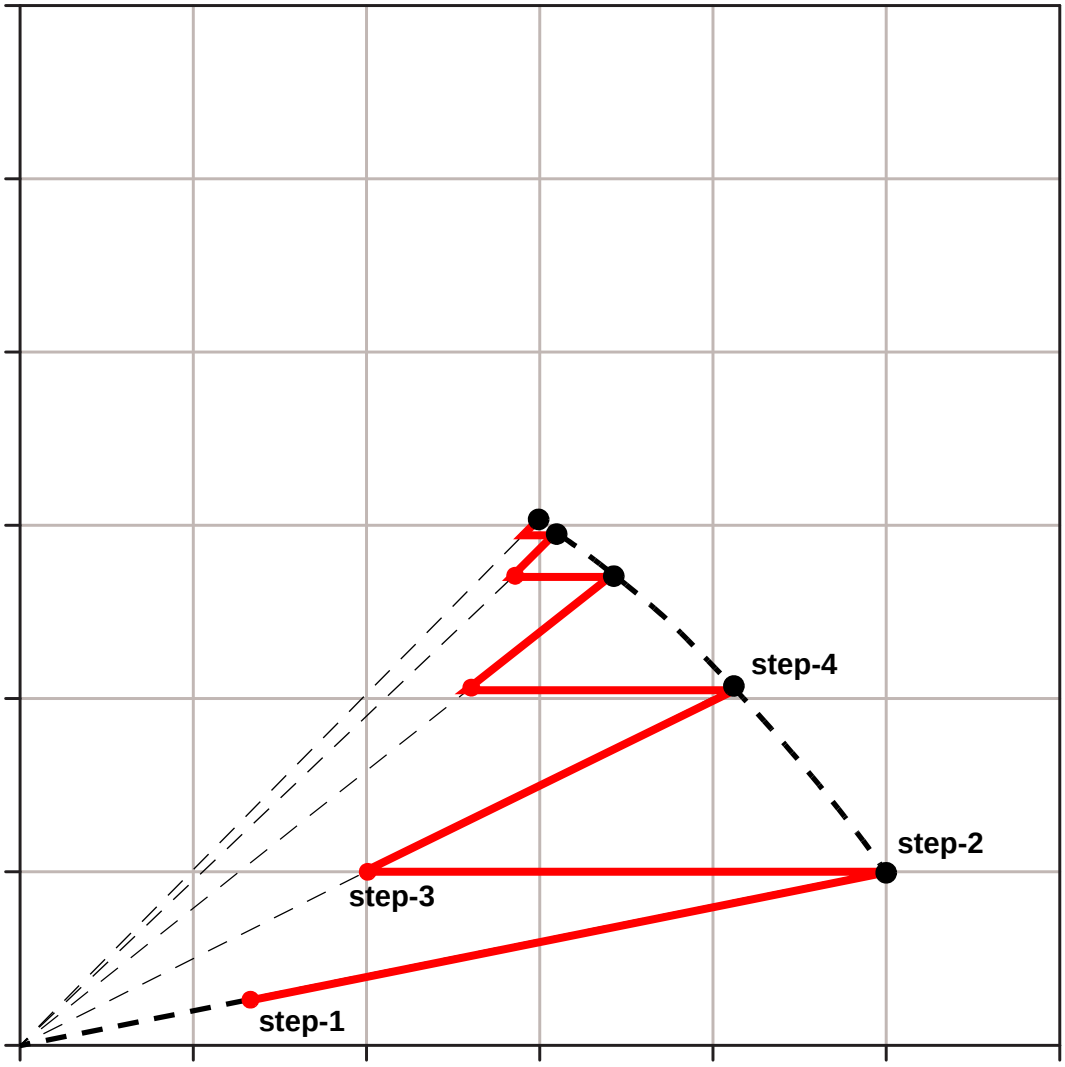

Figure 4.10 Iterative computation of critical buckling liquid-depth for a pre-specified liquid density

Ultimate load level parameters, using membrane theory

$$\zeta' = \frac{h' \tan\beta}{r_1}$$

$$\bar{\psi} = \frac{\sigma_{x,U,1}}{\sigma_{\theta,U,1}} = \frac{\zeta'}{6} \cdot (3 + \zeta')$$

$$\alpha_{xpe} = \frac{\sigma_{x,U,1}}{\sigma_{x,Rcr}}$$

$$\bar{p} = \frac{\sigma_{\theta,U,1}}{\sigma_{x,Rcr}}$$

$$\bar{\psi} = \frac{\alpha_{xpe}}{\bar{p}}$$

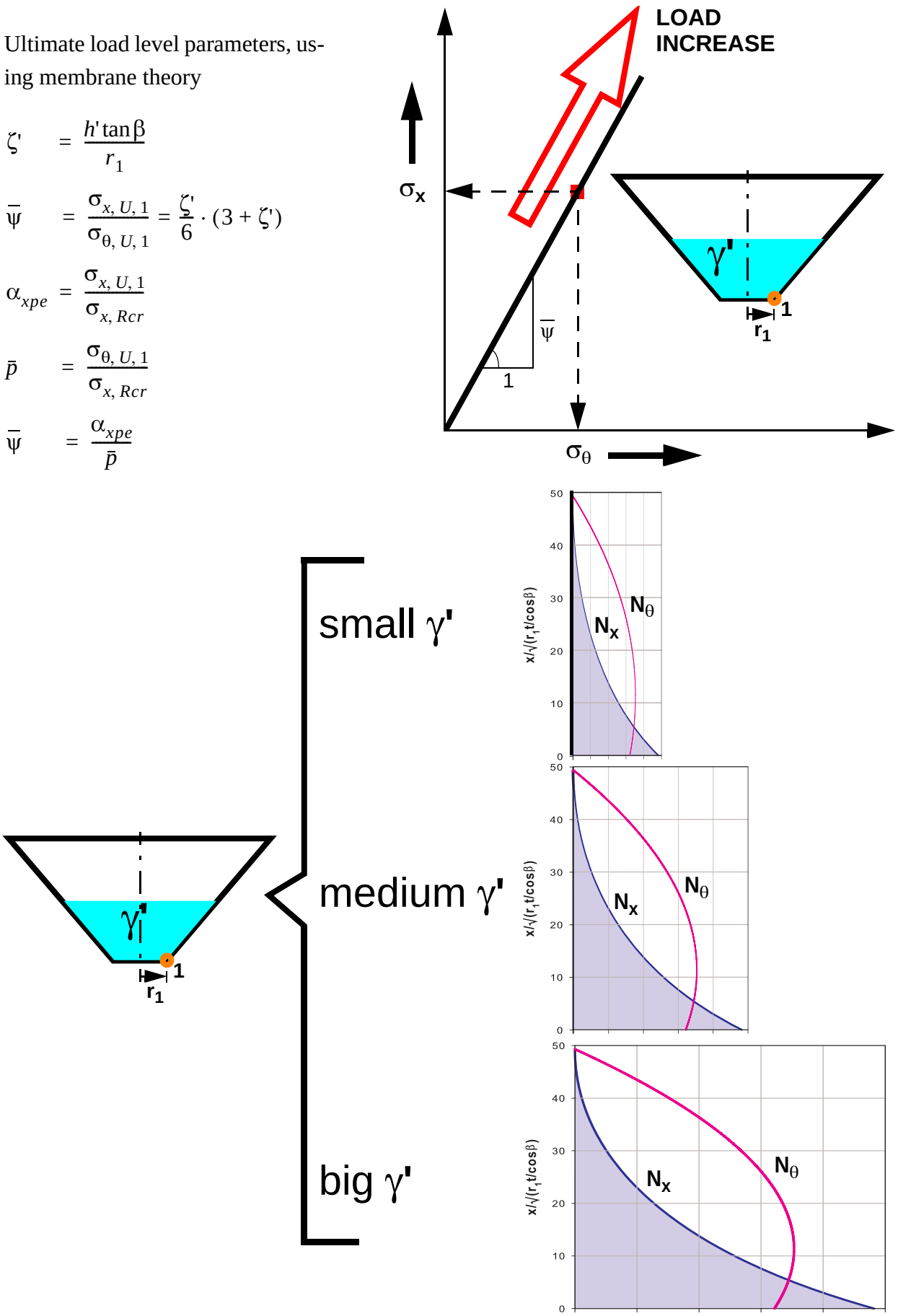

Figure 4.11 Loading by increasing the liquid-density for a pre-specified filling-depth

4.5 Linear buckling strength of an ideally perfect liquid-filled cone

4.5.1 Approximate linear buckling analysis

In the LBA sense, a conical shell subjected to axial loading (no matter where the axial loading and related section forces come from) buckles at a section located a meridional distance "x" from the supported base, when the membrane meridional section stress $\sigma_x(x)$ due to the applied axial loading reaches the critical value, $\sigma_{xCr}(x)$, which is given by

$$\sigma_{xCr}(x) = \frac{E}{\sqrt{3(1-\nu^2)}} \cdot \frac{1}{r(x)/(t\cos\beta)} \quad \text{... from theory!} \qquad \text{(Eq. 4.12)}$$

For steel conical shells, where the poisson's ratio $\nu = 0.3$, the critical buckling stress is given by

$$\sigma_{xCr}(x) = 0.605 \cdot \frac{E \cdot t\cos\beta}{r(x)} \qquad \text{(Eθ. 4.13)}$$

The critical buckling stress at the base of the cone will then be

$$\sigma_{xRCr} = \sigma_{xCr}(x = 0) = 0.605 \cdot \frac{E \cdot t\cos\beta}{r_1} \qquad \text{(Eθ. 4.14)}$$

In bottom-supported conical shells, even though the stress at the supported base reaches its buckling limiting value, buckling will not take place at the base. Instead, it occurs at a small distance away from the base (along the meridian). This is because of the two facts that (i) it is restrained & hence stiffer and (ii) there is no enough space for buckling to occur.

Buckling practically occurs when the stress at the location for potential "center of buckle" reaches the critical stress for that particular section. In other words, the meridional membrane compressive stress distribution with a critical stress at the base and fast decaying up the meridian, should be increased by a load factor higher than 1.0 so that the stress at the center of potential buckle reaches its limiting value thereby producing buckling.

Mathematically, for buckling to occur at the potential center of buckle, the respective stress should be equal to

$$\sigma_{x,b} = \sigma_{xCr,b} = 0.605 \cdot \frac{E \cdot t\cos\beta}{r_b} \qquad \text{(Eq. 4.15)}$$

Besides, the ratio of the meridional membrane stress at any location along the meridian to the circumferential membrane stress at the base of the cone is given by

$$\frac{\sigma_x(x)}{\sigma_{\theta,1}} = \frac{1}{6} \cdot \frac{(\rho' - \rho)^2}{\rho' - 1} \cdot \left(3 + \frac{\rho' - \rho}{\rho}\right) \qquad \text{(Eq. 4.16)}$$

whic can be re-worked to obtain a relationship between the acting meridional membrane stress at any location along the meridian and the corresponding critical meridional membrane stress of the cone at the same location as follows

$$\frac{\sigma_x(x)}{\sigma_{\theta,1}} = \frac{\sigma_x(x)/\sigma_{xCr}(x)}{\frac{\sigma_{\theta,1}}{\sigma_{xRCr}} \cdot \frac{\sigma_{xRCr}}{\sigma_{xCr}(x)}} = \frac{\sigma_x(x)/\sigma_{xCr}(x)}{\bar{p} \cdot \rho} \qquad \text{(Eq. 4.17)}$$

$$\Rightarrow \frac{\sigma_x(x)}{\sigma_{xCr}(x)} = \frac{1}{6}\bar{p} \cdot \frac{(\rho' - \rho)^2}{\rho' - 1} \cdot (\rho' + 2\rho) \qquad \text{(Eq. 4.18)}$$

The previous statement about the occurrence of buckling can now be mathematically explained, using (Eq. 4.18), as

$$\frac{\sigma_x(x)}{\sigma_{xCr}(x)} = 1$$
$$\Rightarrow \bar{p} = \frac{6}{(\rho' + 2\rho)} \cdot \frac{\rho' - 1}{(\rho' - \rho)^2} \qquad \text{(Eq. 4.19)}$$

On the other hand, the ratio of the meridional membrane compressive stress at any location along the meridian to the meridional membrane compressive stress at the base of the cone is given by

$$\frac{\sigma_x(x)}{\sigma_{x,1}} = \left(\frac{\rho' - \rho}{\rho' - 1}\right)^2 \cdot \frac{\rho' + 2\rho}{\rho(\rho' + 2)} \qquad \text{(Eq. 4.20)}$$

At the buckling load level, (Eq. 4.20) will be written as

$$\frac{\sigma_{x,U}(x)}{\sigma_{x,1,U}} = \frac{\sigma_{xCr}(x)}{\sigma_{x,1,LBA}} = \left(\frac{\rho' - \rho}{\rho' - 1}\right)^2 \cdot \frac{\rho' + 2\rho}{\rho(\rho' + 2)} \qquad \text{(Eq. 4.21)}$$

where $\sigma_{x,1,LBA}$ is the corresponding meridional membrane stress at the base of the cone when the stress at the potential buckle center reaches its critical value.

The buckling load factor, $\alpha_{LBA} = \sigma_{xCr}(x)/\sigma_x(x)$, when written in terms of the membrane stresses at the cone base will then be given by

$$\alpha_{LBA} = \frac{\sigma_{x,1,LBA}}{\sigma_{xRCr}} = \frac{\sigma_{xCr}(x)}{\sigma_{xRCr}} \cdot \left(\frac{\rho' - 1}{\rho' - \rho}\right)^2 \cdot \frac{\rho(\rho' + 2)}{\rho' + 2\rho} \quad \text{(Eq. 4.22)}$$

$$\Rightarrow \alpha_{LBA} = \left(\frac{\rho' - 1}{\rho' - \rho}\right)^2 \cdot \frac{(\rho' + 2)}{\rho' + 2\rho} \quad \text{(Eq. 4.23)}$$

using (Eq. 4.19), (Eq. 4.23) can be re-written as

$$\alpha_{LBA} = 1 + \frac{3\rho'(\rho^2 - 1) - 2(\rho^3 - 1)}{6(\rho' - 1)} \cdot \bar{p} \quad \text{(Eq. 4.24)}$$

Since for liquid-filled conical shells, where the meridional membrane compressive stress decays rapidly up the meridian, buckling occurs somewhere close to the base of the cone and hence for relatively longer conical shells the value of the running parameter ρ is very close to 1.0. For such a situation, (Eq. 4.24) can be approximately re-written (applying linearization) as

$$\alpha_{LBA} = 1 + (\rho - 1) \cdot \bar{p} \quad \text{(Eq. 4.25)}$$

Let the length of buckle be l_b which, generally, is given as a function of the shell slenderness ratio by

$$l_b = k \cdot \sqrt{\frac{r_1 t}{\cos\beta}} \quad \text{(Eq. 4.26)}$$

the buckle center is then located at $l_b/2$ and the corresponding $\rho = \rho_b$ is given by

$$\rho_b = \frac{r_b}{r_1} = 1 + \frac{l_b}{2r_1}\sin\beta = 1 + \frac{k}{2}\frac{\tan\beta}{\sqrt{r_1/(t\cos\beta)}} \quad \text{(Eq. 4.27)}$$

Letting $b = k/2$ and $\varepsilon_b = \dfrac{\tan\beta}{\sqrt{r_1/(t\cos\beta)}}$,

$$\rho_b - 1 = b\varepsilon_b \quad \text{(Eq. 4.28)}$$

Substituting (Eq. 4.28) into (Eq. 4.25), one gets

$$\alpha_{LBA} = 1 + b\varepsilon_b \cdot \bar{p} \quad \text{(Eq. 4.29)}$$

For an axisymmetric buckling type, the buckle length factor $k \approx 1.72 \approx 2.0$. This axisymmetric buckle starts at the base of the cone for simply supported (pinned-) bottom boundary condition and has a shift of $\approx 1.0\sqrt{r_1 t/\cos\beta}$ for a fixed bottom boundary condition. As a result, the approximate LBA buckling load for “FIX” and “PIN” bottom support types is given by

$$\alpha_{LBA,\,approx} = \frac{\sigma_{LBA,\,approx}}{\sigma_{Rcr}} = 1.0 + b\left(\frac{\tan\beta}{\sqrt{\frac{r_1}{t\cos\beta}}} \cdot \bar{p}\right) \qquad \text{(Eq. 4.30)}$$

with $b = \begin{cases} 2.0 \ldots\ldots FIX \\ 1.0 \ldots\ldots PIN \end{cases}$

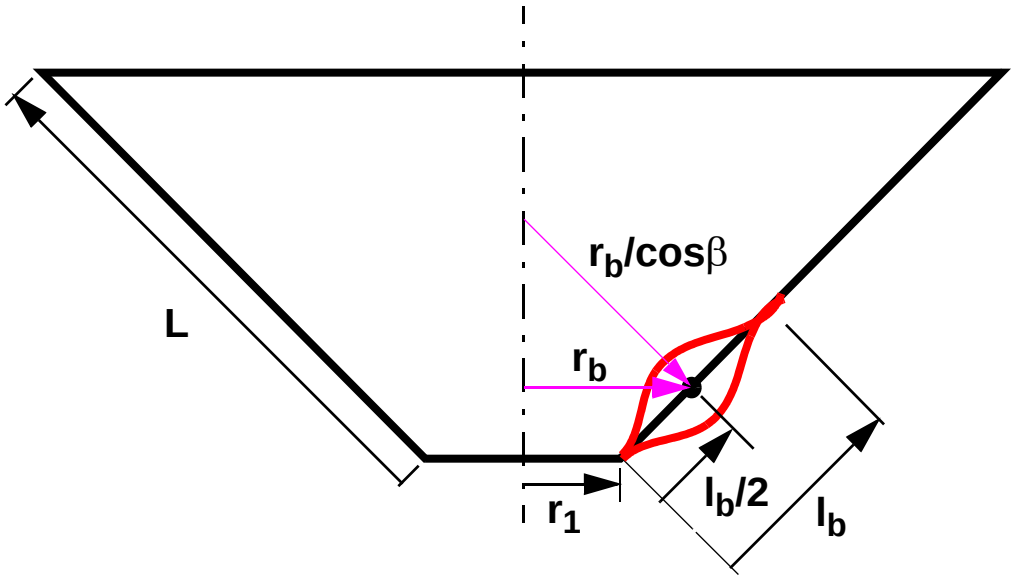

Figure 4.12 Approximate buckle center

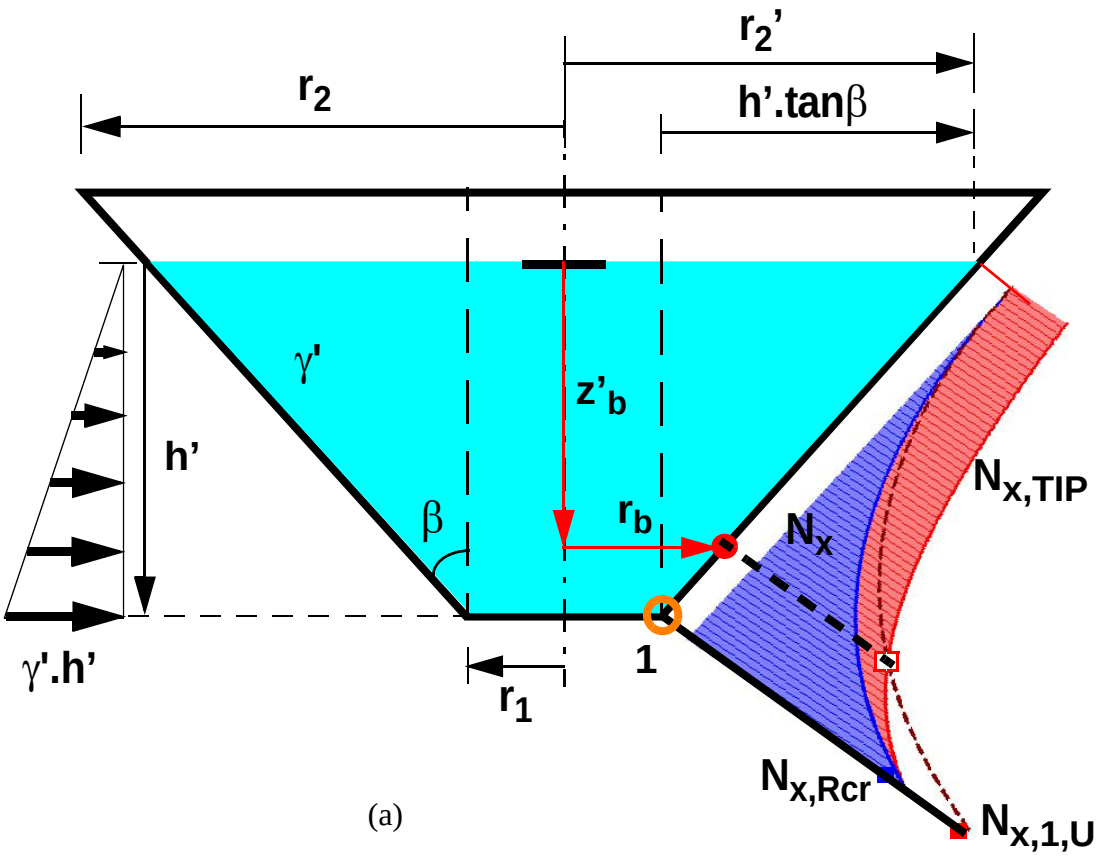

(a)

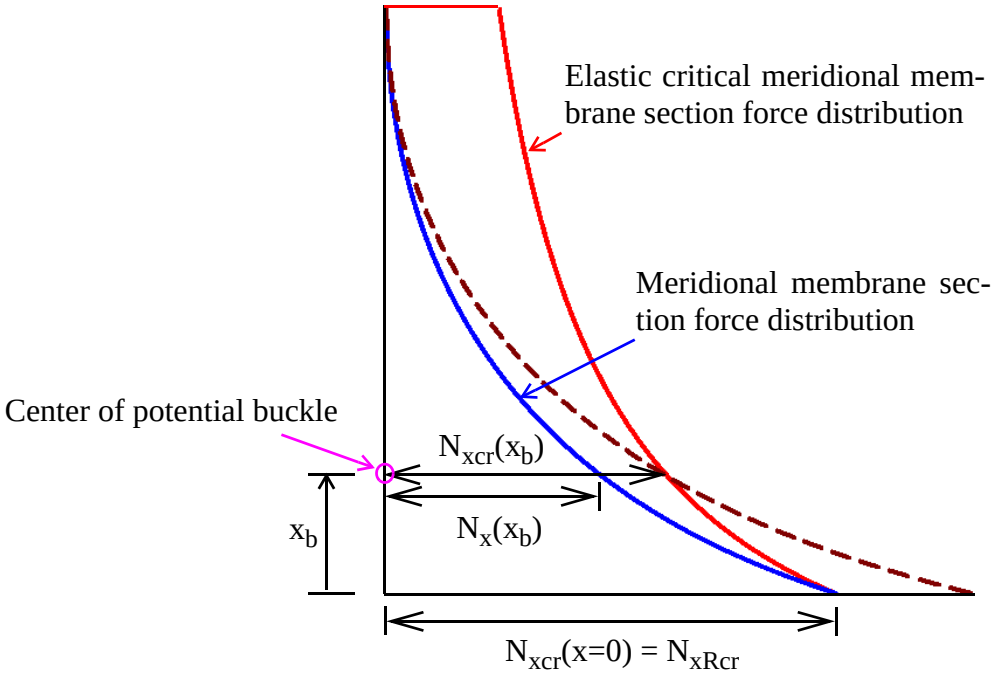

(b)

Figure 4.13 Meridional membrane section force distribution & approximate buckling load

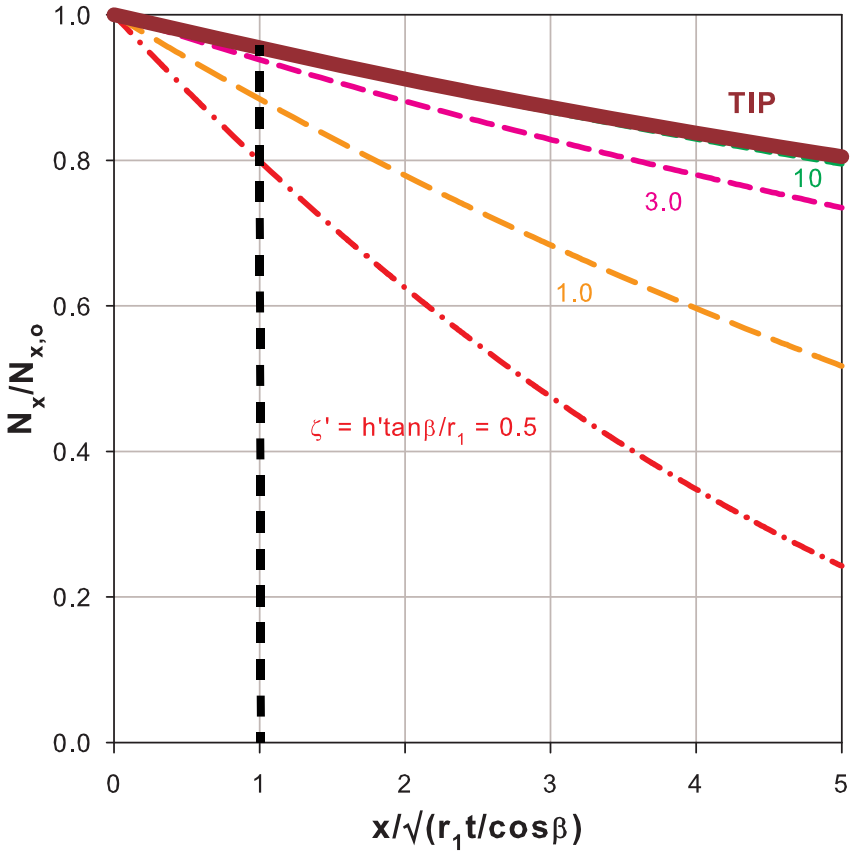

Figure 4.14 Normalized meridional membrane section force distribution

4.5.2 Linear buckling analysis using numerical finite element method

Linear finite element buckling analyses were made using ABAQUS for different shell slenderness ratios, ranging from $r_1/t\cos\beta$ = 140 to 2100 (or r_1/t = 100 to 1500 for an apex-half angle of 45°), and varying the liquid depth which in other words means varying the internal pressure parameter, $\bar{p}$ value.

Basic buckle mode shapes of liquid-filled conical shells with $h'\tan\beta/r_1$ values of 0.5, 1.0, and 3.0 are shown in Figure 4.15 and Figure 4.16 for both the "fixed" and "pinned" bottom boundary conditions, respectively. In doing so, the lengths of the cones were kept constant so that an easy qualitative comparison can be made from the eigenmodes. Moreover, a fourth plot showing the buckle mode shape of a meridional "tip" loaded conical shell case is included in each of the aforementioned figures. The effects of the meridional "tip" loading case, when compared at the potential critical location (cone bottom zone), is equivalent to the effects of a very big liquid-depth ($h'\tan\beta/r_1$ value).

Comparison of the radial deviations from the unbuckled perfect shape of the shell has been done for the different $h'\tan\beta/r_1$ values already mentioned and for a unit normalized maximum reference amplitude along the meridian. These comparisons, in the lower critical part of the cone, are shown in Figure 4.17 and Figure 4.18 for both bottom boundary condition types with positive values showing outward deviations, away from the axis of revolution.

Curve-fitting of the numerical analysis results from α_{LBA} vs. $\bar{p}$ plot, see Figure 4.19 and Figure 4.20, were then done for both "fixed" and "pinned" bottom boundary conditions, respectively. The resulting linear buckling loads can then be calculated from

$$\alpha_{LBA} = \frac{\sigma_{LBA}}{\sigma_{Rcr}} = 1.0 + a\left(\frac{\tan\beta}{\sqrt{\frac{r_1}{t\cos\beta}}}\cdot\bar{p}\right)^{0.6} \quad \text{with} \quad a = \begin{cases} 1.55\ldots\ldots FIX \\ 0.76\ldots\ldots PIN \end{cases} \qquad \text{(Eq. 4.31)}$$

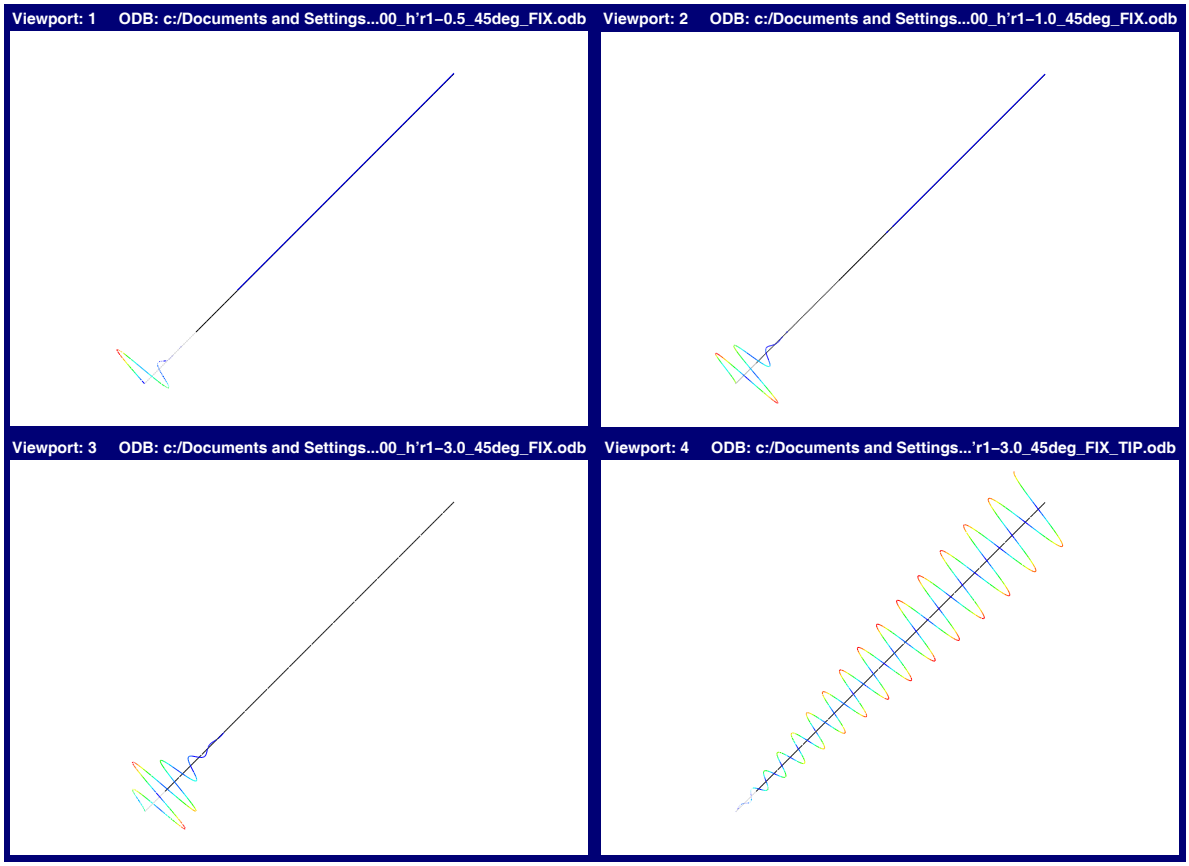

Figure 4.15 Linear buckling eigenmodes: h'tanβ/r_1 = 0.5, 1.0, 3.0, tip: **fixed** bottom

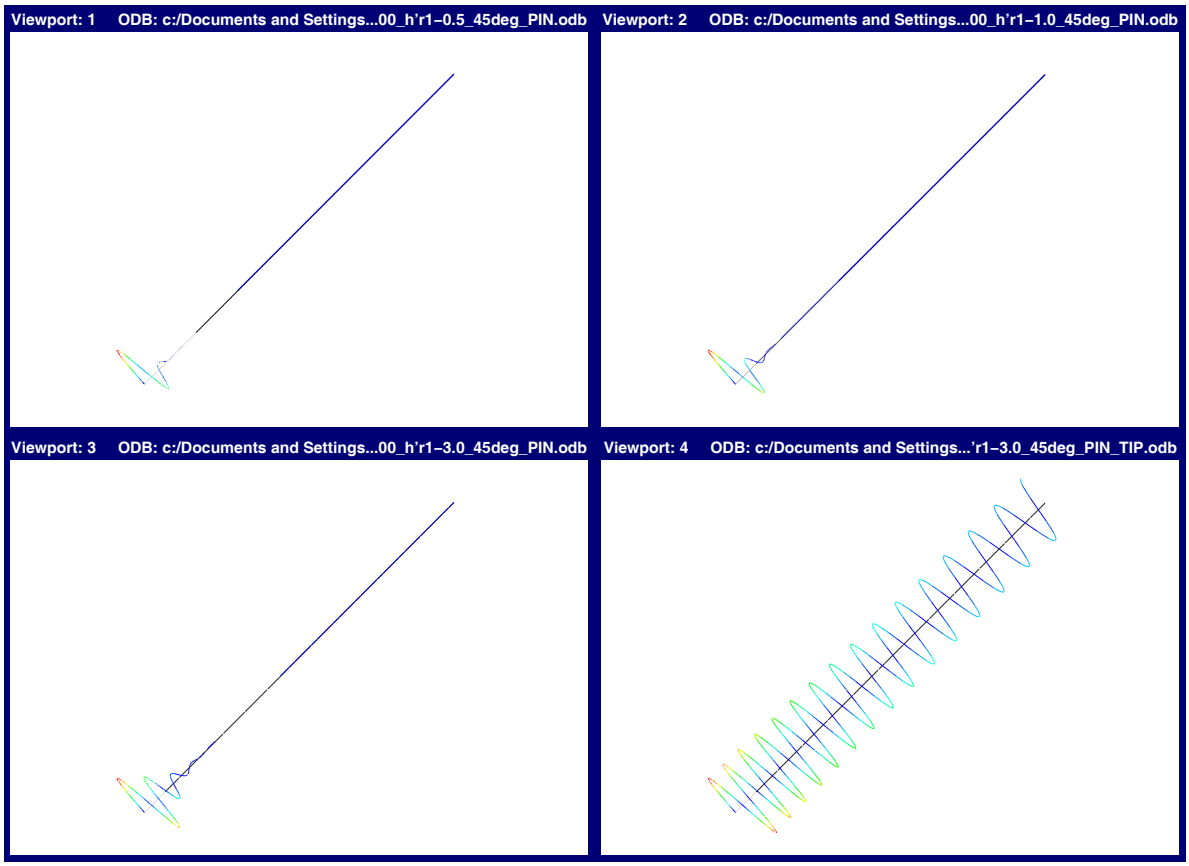

Figure 4.16 Linear buckling eigenmodes: h'tanβ/r_1 = 0.5, 1.0, 3.0, tip; **pinned** bottom

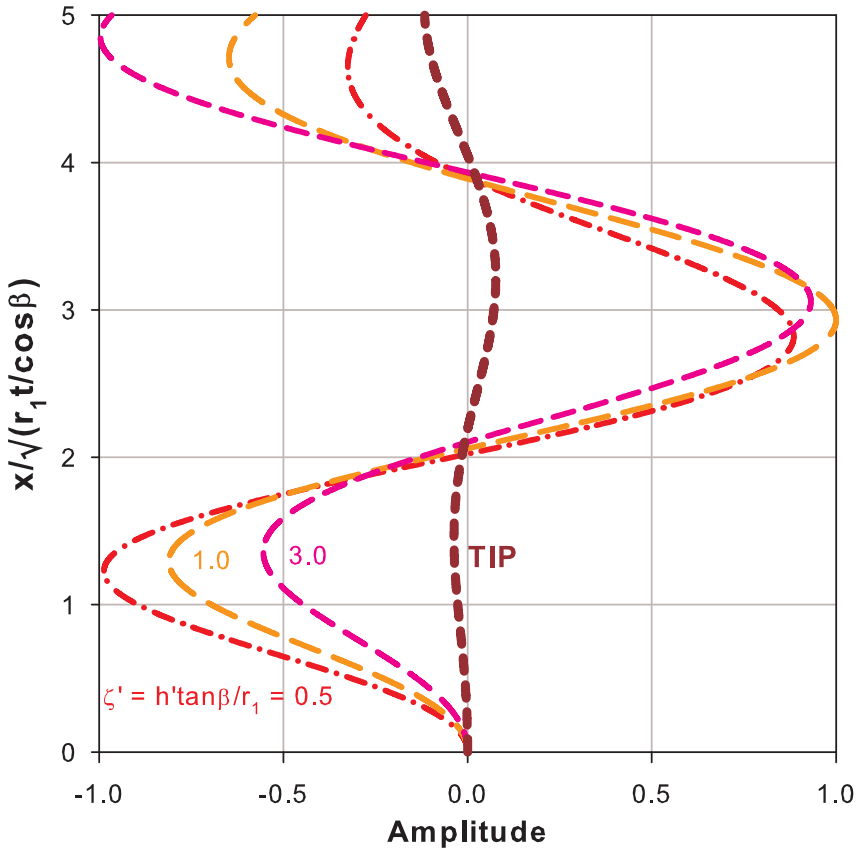

Figure 4.17 Eigenmode amplitude in the critical zone: **fixed** bottom

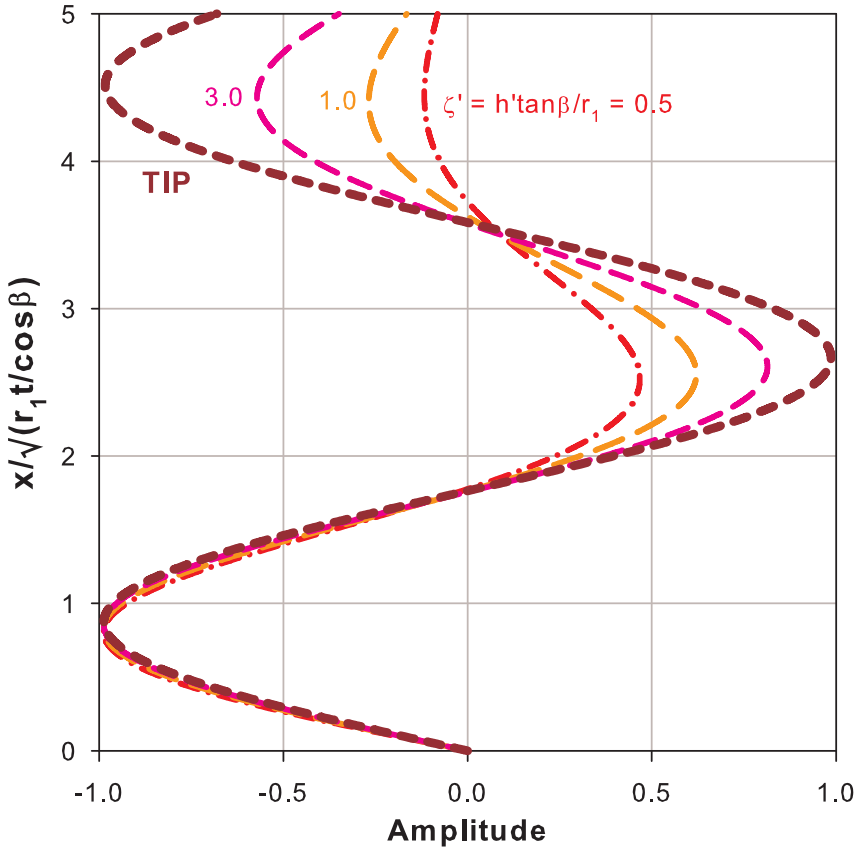

Figure 4.18 Eigenmode amplitude in the critical zone: **pinned** bottom

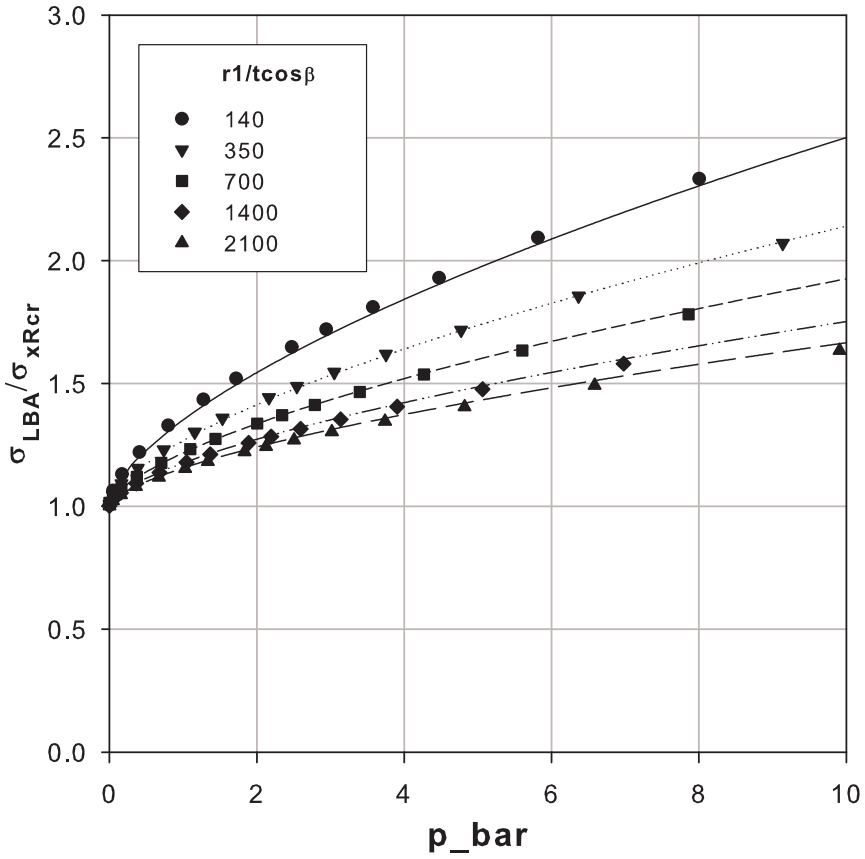

Figure 4.19 FEM LBA: **fixed** bottom

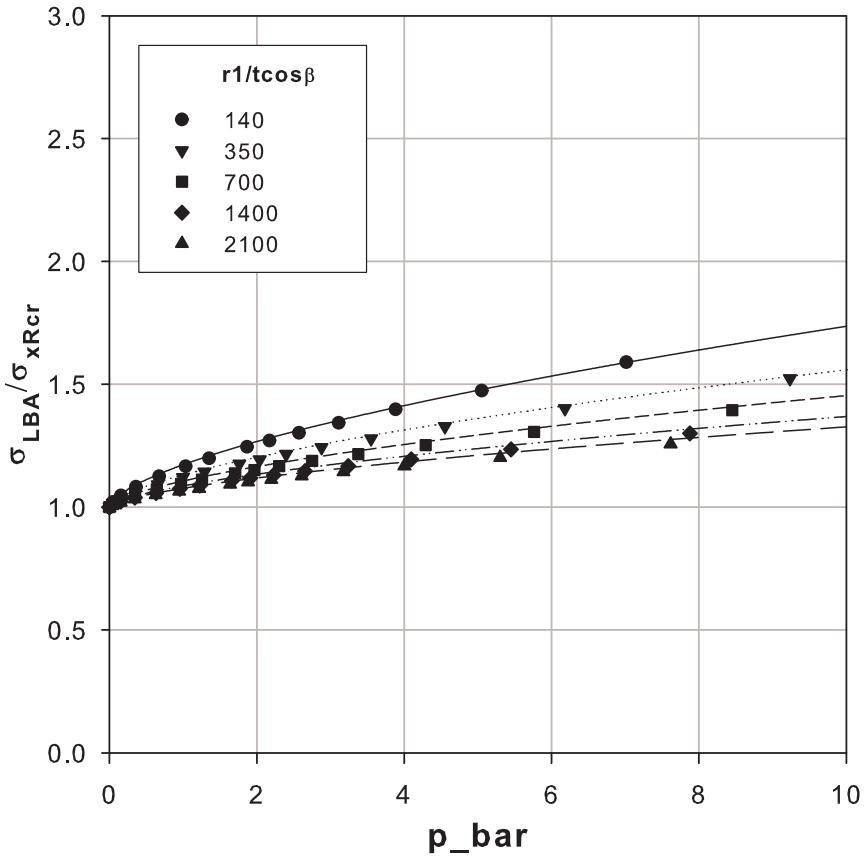

Figure 4.20 FEM LBA: **pinned** bottom

4.6 Elastic buckling strength of an imperfect liquid-filled cone

4.6.1 Elastic imperfection reduction factor, EN1993-1-6

In accordance to the frame work of the European standard EN1993-1-6, the elastic imperfection reduction factor of conical (and cylindrical) shells subjected to meridional compression (α_x for unpressurized or α_{xpe} for pressurized cases) is a factor applied to the linear bifurcation (LB) buckling strength of a perfect shell to account for the strength reducing effects of geometric imperfections and geometric nonlinearities. This factor depends on the shell geometry, loading condition, and imperfection amplitude. The elastic imperfection reduction factor of cylindrical and conical shells subjected to meridional compression with/without co-existent internal pressure is given as follows:

- **elastic imperfection reduction for pressurized cases**

$$\alpha_{xpe} = \frac{\sigma_{x,\,ULS,\,elastic}}{\sigma_{x,\,LBA}} = \alpha_x + (1-\alpha_x)\frac{\bar{p}}{\bar{p} + 0.3/\sqrt{\alpha_x}} \qquad \text{(Eq. 4.32)}$$

- **elastic imperfection reduction for unpressurized (tip loading) cases**

$$\alpha_x = \frac{0.62}{1 + 1.91(\Delta w_k/t)^{1.44}} \qquad \text{(Eq. 4.33)}$$

with the characteristic imperfection amplitude parameter, Δw_k given as

$$\Delta w_k = \frac{1}{Q}\cdot\sqrt{\frac{r_1}{t\cos\beta}}\cdot t \qquad \text{(Eq. 4.34)}$$

where

$$\bar{p} = \frac{\sigma_\theta}{\sigma_{xRcr}} = \frac{pr_1/(t\cos\beta)}{\sigma_{xRcr}} = \mu\cdot\bar{\lambda}_x^2 \qquad \text{(Eq. 4.35)}$$

where Q is fabrication quality parameter depending on the fabrication tolerance quality class.

4.6.2 Elastic buckling strength

For relatively big shell slenderness ratio values (thin shells) and low internal pressurization (very high liquid depths), pure elastic buckling behaviour governs the failure phenomena causing diamond-shaped buckling mode close to the boundary because of the relatively big meridional compressive stress at this zone and its fast decaying distribution. As the internal pressure increases and the corresponding circumferential membrane stress becomes significant, the effect of bi-axiality comes into play and an interaction between the elastic buckling and plasticity begins. In liquid-filled conical shells with a pre-specified liquid-density, the circumferential tension becomes relatively big (when compared to the meridional compression) as the liquid-depth gets smaller.

For the case of an axially uniformly compressed and internally pressurized cylindrical shell, the linear bifurcation load of the perfect shell is independent of internal pressurization and is equal to the classical critical buckling load and therefore the elastic characteristic buckling strength is computed from:

$$\alpha_{xpe,\,CYL} = \frac{\sigma_{x,\,ULS,\,elastic}}{\sigma_{x,\,LBA}} = \frac{\sigma_{x,\,ULS,\,elastic}}{\sigma_{x,\,Rcr}} \qquad \text{(Eq. 4.36)}$$

$$\sigma_{x,\,ULS,\,elastic} = \alpha_{xpe,\,CYL} \cdot \sigma_{x,\,LBA} = \alpha_{xpe,\,CYL} \cdot \sigma_{x,\,Rcr} \qquad \text{(Eq. 4.37)}$$

However, for a liquid-filled conical shell, the fast decaying meridional compression (when compared to the tip-loaded cone stress, which itself is decaying as well) is interlinked with the internal pressurization, i.e. at the region where buckling occurs, the acting meridional compression is lower than the corresponding classical critical buckling load and hence needs a load factor higher than 1.0 to bring it to the buckled state. The value of the linear buckling load factor, therefore, depends on the liquid-depth and hence the internal pressurization. For conical shells the linear bifurcation load is equal to the classical critical buckling load only for tip-loaded cases because under this load every point on the meridian of the shell is loaded to its critical value. Therefore, the elastic characteristic buckling strength of a liquid-filled conical shell is computed from:

$$\begin{aligned} \alpha_{xpe,\,LFC} = \frac{\sigma_{x,\,ULS,\,elastic}}{\sigma_{x,\,LBA}} &= \frac{\sigma_{x,\,ULS,\,elastic}}{\sigma_{x,\,Rcr}} \cdot \underbrace{\frac{\sigma_{x,\,LBA}}{\sigma_{x,\,Rcr}}} \\ &= \frac{\sigma_{x,\,ULS,\,elastic}}{\sigma_{x,\,Rcr}} \cdot \alpha_{LBA} \end{aligned} \qquad \text{(Eq. 4.38)}$$

$$\sigma_{x,\,ULS,\,elastic} = \alpha_{xpe,\,LFC} \cdot \sigma_{x,\,LBA} = \alpha_{xpe,\,LFC} \cdot \alpha_{LBA} \cdot \sigma_{x,\,Rcr} \qquad \text{(Eq. 4.39)}$$

In other words, when dealing with liquid-filled conical shells, the following relationships should be kept in mind so as to easily differentiate between elastic buckling strength of conical and cylindrical shells:

$$\frac{\sigma_{x,\,ULS,\,elastic}}{\sigma_{x,\,LBA}} = \alpha_{xpe,\,LFC} \qquad \text{(Eq. 4.40)}$$

$$\frac{\sigma_{x,\,ULS,\,elastic}}{\sigma_{x,\,Rcr}} = \alpha_{xpe,\,LFC} \cdot \alpha_{LBA} \qquad \text{(Eq. 4.41)}$$

4.6.3 Re-investigation of Gent's experimental test results

Following the collapse of the conical steel water tower in belgium, a huge amount of laboratory tests (over 800) on liquid-filled cones and numerical (using BOSOR) studies were made for more than a decade (1977-1987) at Gent university by D. Vandepitte *et. al.* The results of the study were reported in many papers. A detailed re-investigation of the test results has been done in the current work in line with the discussions so far. The full discussion is covered in next chapter.

4.7 Pure plastic strength of liquid-filled conical shells

Once again, the pure plastic (yield) strength represents the load (stress) which, with no stability phenomena intervening, causes an unacceptably large plastic deformation. The plastic strength of conical shells can be computed approximately using membrane Mises yield criterion or using yield criteria based on LA-based stress resultants; or accurately using finite element small displacement materially nonlinear analysis.

4.7.1 Plastic strength according to von Mises membrane criterion

For axisymmetric shells under axisymmetric loading and boundary conditions where bi-axial principal membrane stresses exist, the von Mises membrane yield criteria is given by

$$\sigma_x^2 + \sigma_\theta^2 - \sigma_x \sigma_\theta \leq f_y^2 \qquad \text{(Eq. 4.42)}$$

with an upper limiting (yield) curve given by

$$\sigma_x^2 + \sigma_\theta^2 - \sigma_x \sigma_\theta = f_y^2 \qquad \text{(Eq. 4.43)}$$

For a liquid-filled conical shell, the limiting plasticity curve should be obtained using the method of proportional load increase as follows: for a specified liquid-depth or specified ratio of the two membrane section forces/stresses at the base of the cone (Eq. 4.44), compute the meridional membrane stress (Eq. 4.46) which will cause yielding according to the von Mises yield criterion and the corresponding plastic load factor (Eq. 4.47).

$$\bar{\psi} = \frac{N_{x,1}}{N_{\theta,1}} = \frac{\sigma_{x,1}}{\sigma_{\theta,1}} \qquad \text{(Eq. 4.44)}$$

$$\sigma_{x,pl} = \frac{\bar{\psi}}{\sqrt{1 + \bar{\psi} + \bar{\psi}^2}} \cdot f_y \qquad \text{(Eq. 4.45)}$$

$$\Lambda_{Mises} = \frac{\sigma_{x,pl}}{\sigma_{x,Rcr}} = \frac{\bar{\psi}}{\sqrt{1 + \bar{\psi} + \bar{\psi}^2}} \cdot \bar{\lambda}_x^2 \qquad \text{(Eq. 4.46)}$$

where

$$\bar{\lambda}_x = \sqrt{\frac{f_y}{\sigma_{xRcr}}} \qquad \text{(Eq. 4.47)}$$

4.7.2 Stress resultant oriented approximate yield criteria

The plastic capacity of conical shells can be estimated approximately using the section forces (membrane & edge bending effects) obtained from linear analysis (LA). In the current study, the section forces (stress resultants) computed using the effective ring model analogy, Chapter 4.3, along with the different approximate yield criteria, Annex-A , will be used to estimate the plastic strength of the liquid-filled conical shell.

For an illustrative liquid-filled conical shell with $r_1/t = 500$, $t = 1.0$ cm, $\beta = 45°$, $E = 21000$ kN/cm^2, $f_y = 24.0$ kN/cm^2 and $\nu = 0.3$, the estimated plastic capacity according to the different yield criteria for a fixed and pinned boundary conditions are plotted in the pressure representation as shown in Figure 4.21 and Figure 4.22, respectively. Comparison of the plastic strengths according to the stress resultant oriented yield criteria with that of membrane Mises yield criterion can be made from these strength plots.

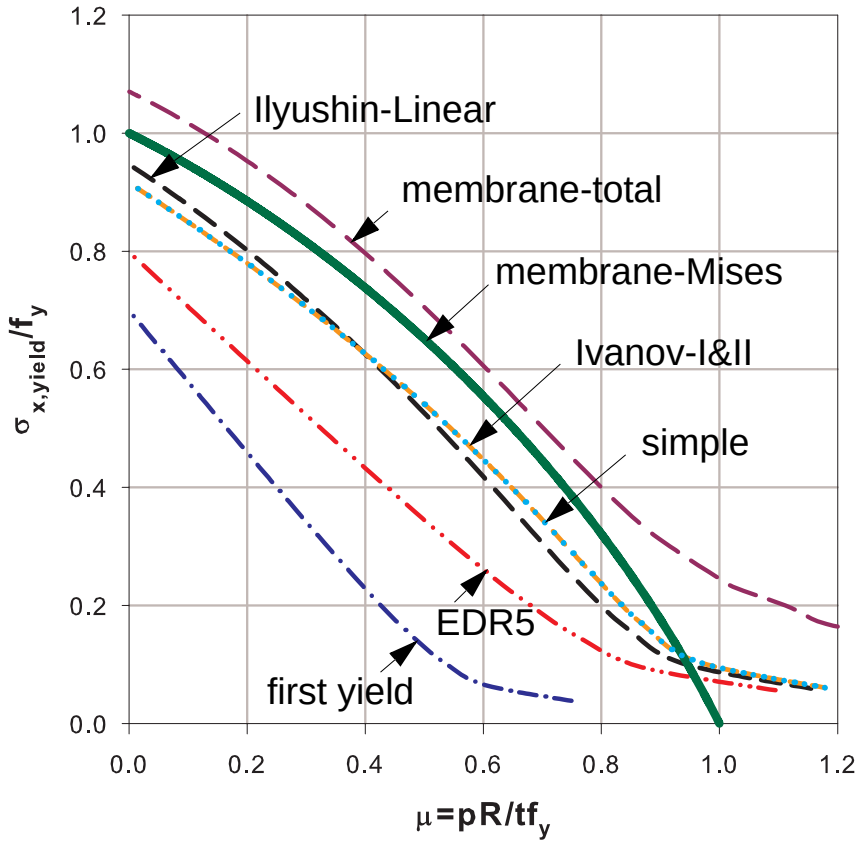

Figure 4.21 Approximate yield criteria, $r_1/t = 500$, $\beta = 45°$: fixed bottom

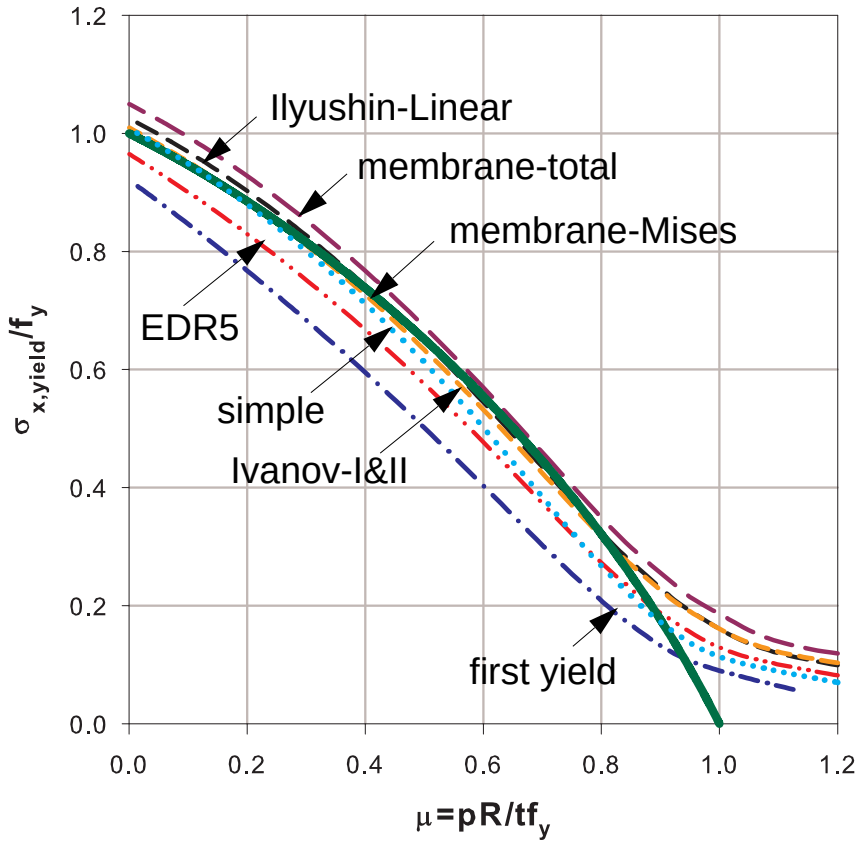

Figure 4.22 Approximate yield criteria, $r_1/t = 500$, $\beta = 45°$: pinned bottom

4.7.3 Small displacement materially nonlinear finite element analysis (MNA)

In order to obtain the exact plastic limit capacities of liquid-filled conical shells, numerical FE small displacement materially non-linear analyses, with a reference liquid-density chosen in such a way that the meridional membrane compressive stress at the base of the cone is equal to the theoretical elastic critical stress and varying the liquid-depth (and therefore the liquid-density), were made. The results are plotted in different representations as shown in Figure 4.23 to Figure 4.32. An MNA/fy vs. ζ' (= h'tanβ/r_1) plots are shown in Figure 4.23 and Figure 4.24 for the fixed and pinned bottom cases, respectively. The same plastic strengths are plotted using the pressure representation (MNA/fy vs. μ) in Figure 4.29 and Figure 4.31 for the fixed and pinned bottom cases, respectively.

As can be seen from the results, unlike that of a cylindrical shell under axial ring-compression and uniform internal pressure, the pure plastic strength of liquid-filled conical shells is not governed by the pure bi-axial membrane Mises plasticity condition at the cone-base. This is because: (i) the reference stresses are taken at the supported base of the cone and hence pure membrane plasticity condition will not occur at boundary conditions; and (ii) at the locations where edge bending effects are negligble (and hence pure membrane stresses act), the effective bi-axial stress state is smaller as the membrane stresses rapidly decay away from the cone-base. The second reason is somehow similar to the reason given for the "potential elastic-buckle center". The exact locations where perfect elastic buckling and pure plastic yielding may be slightly different but very close to each other. This fact can be examined through the comparison of the exact MNA/LBA with the ratio of the corresponding reference values taken at the base, i.e. Mises/Rcr. It turns out that the two ratios are apparently equal and hence both locations are close to each other, Figure 4.25 and Figure 4.26.

Moreover, the apparent equality of the two ratios, MNA/LBA and Mises/Rcr, makes the relative buckling slenderness parameter $\bar{\lambda}_{MNA} = \sqrt{MNA/LBA}$, Figure 4.27 and Figure 4.28, to be computed using either of the two ratios, i.e.

$$\bar{\lambda}_{MNA} = \sqrt{\frac{MNA}{LBA}} = \sqrt{\frac{Mises}{Rcr}} = \bar{\lambda}_{Mises} \qquad \text{(Eq. 4.48)}$$

Therefore, the membrane stresses-related expression for the relative buckling slenderness parameter will be used in the upcoming discussions. The plastic strengths are re-plotted using the capacity representation (MNA/Mises vs. $\bar{\lambda}_{\text{Mises}}$) in Figure 4.30 and Figure 4.32 for the fixed and pinned bottom cases, respectively.

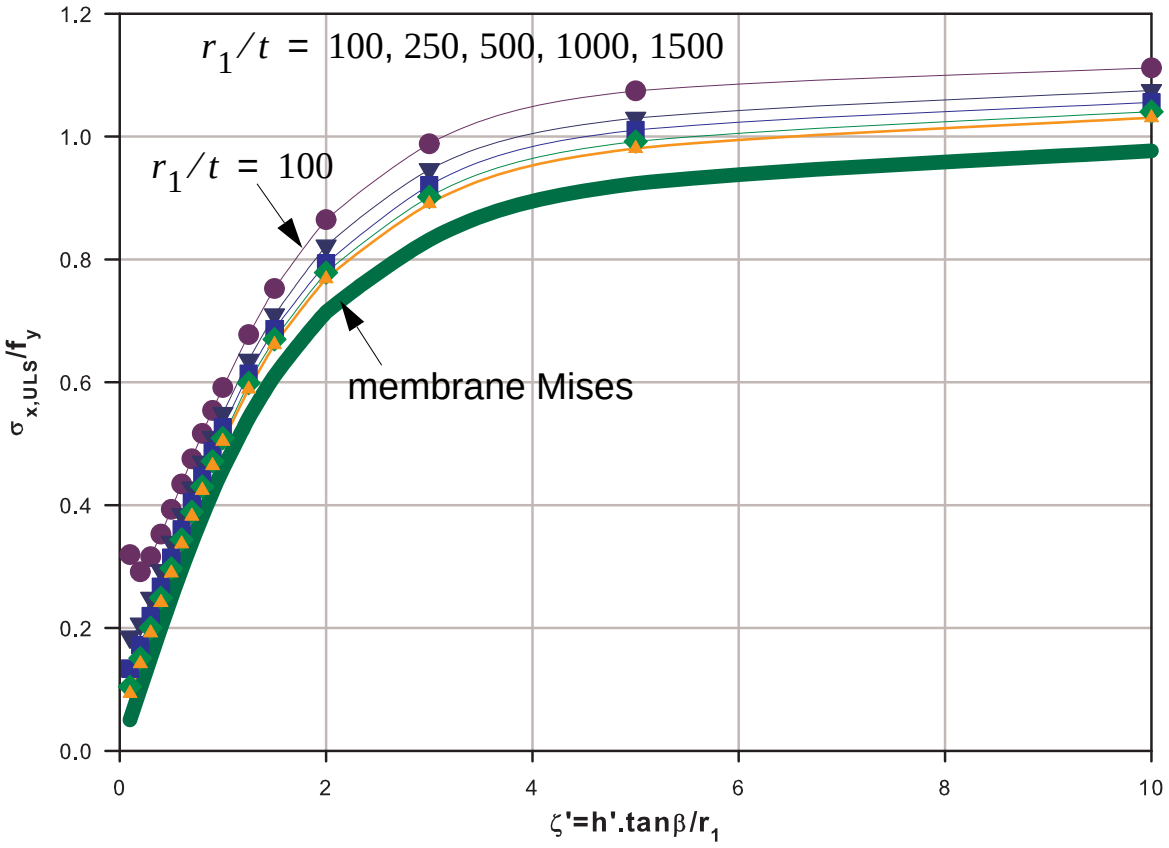

Figure 4.23 Small displacement materially nonlinear analysis: fixed bottom

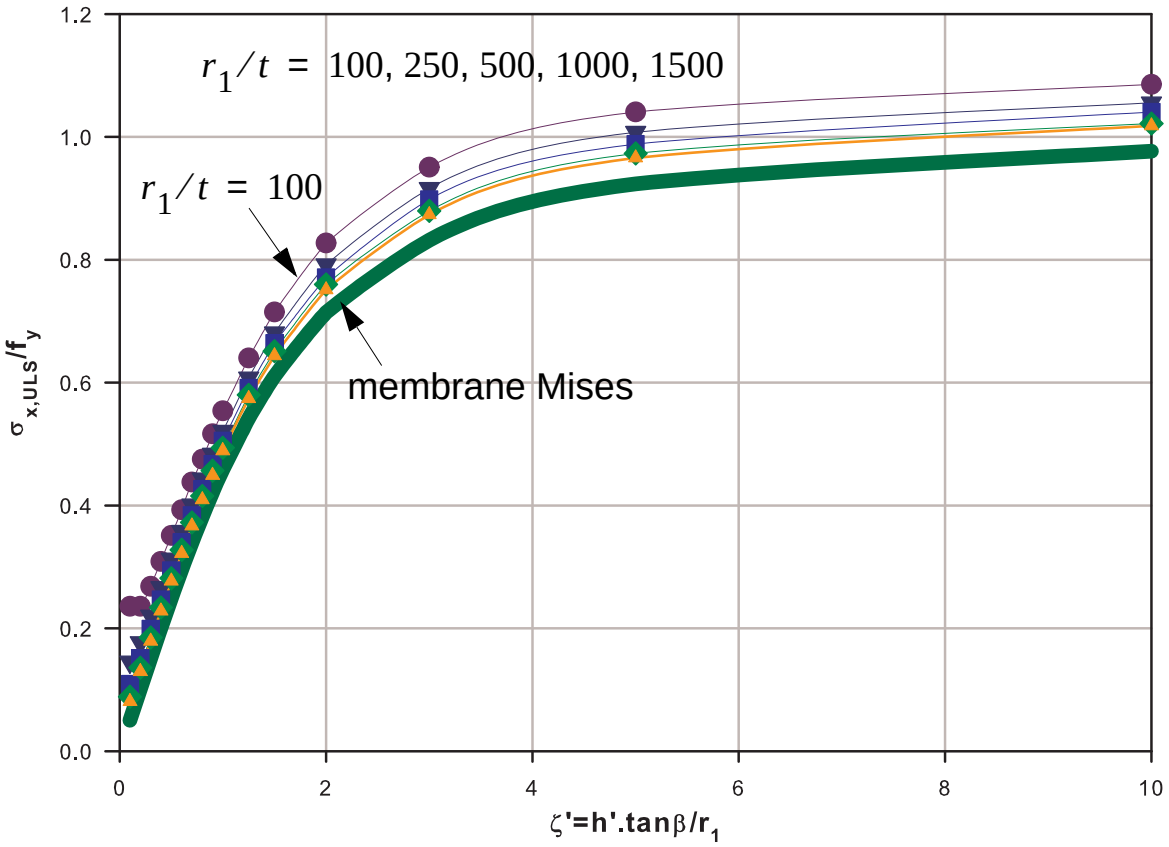

Figure 4.24 Small displacement materially nonlinear analysis: pinned bottom

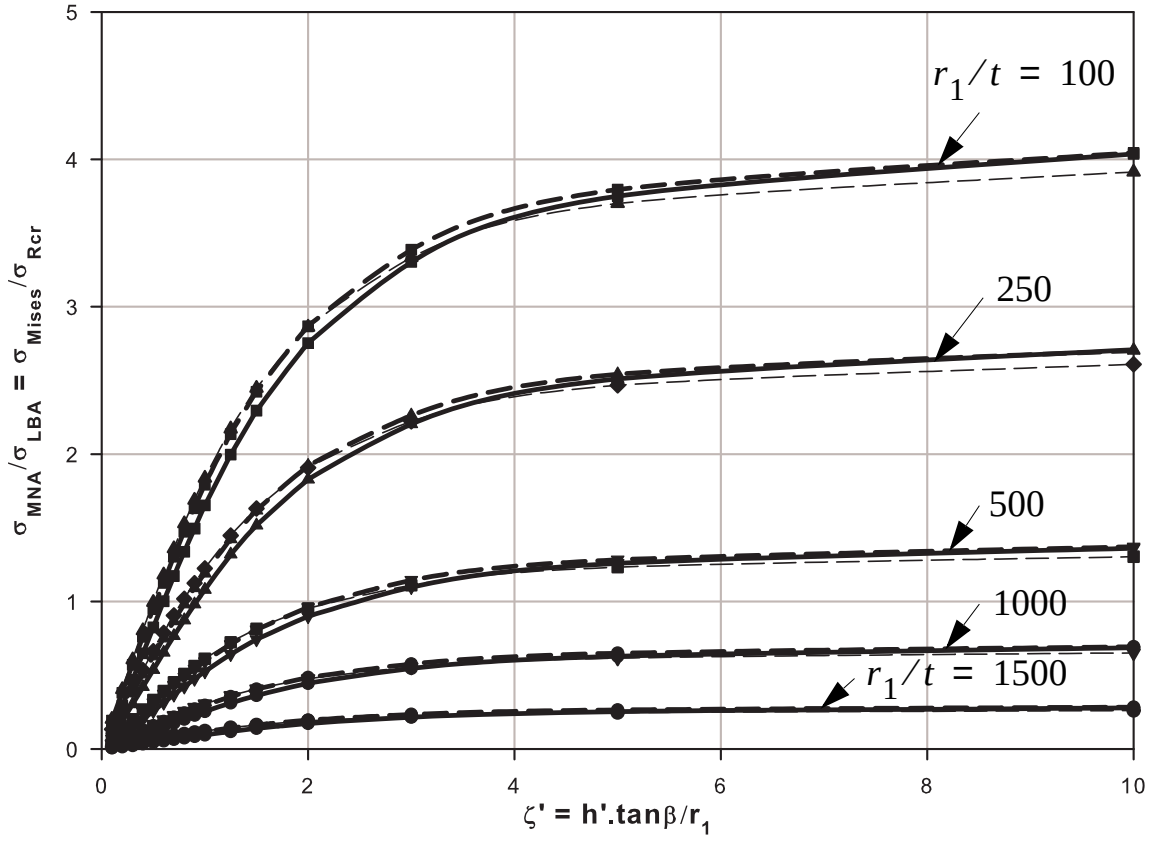

Figure 4.25 Reference strengths ratio: Fix &Pin

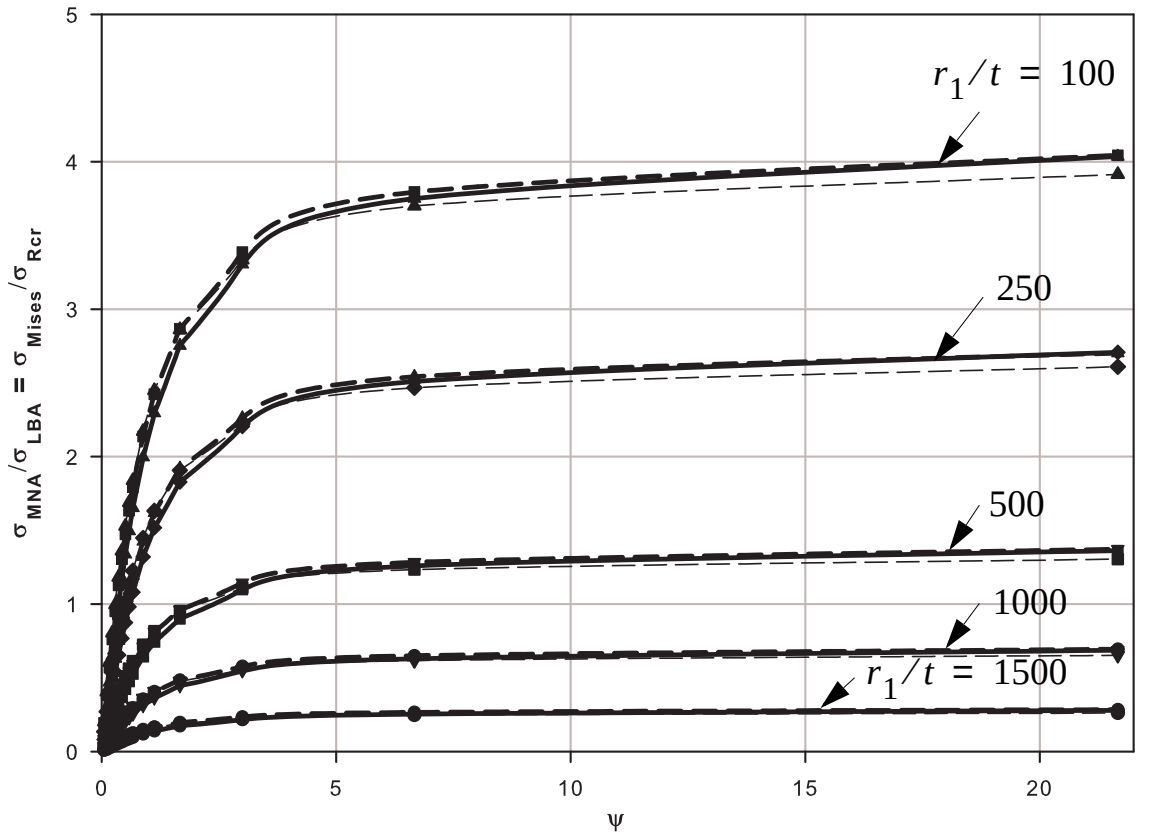

Figure 4.26 Reference strengths ratio: Fix &Pin

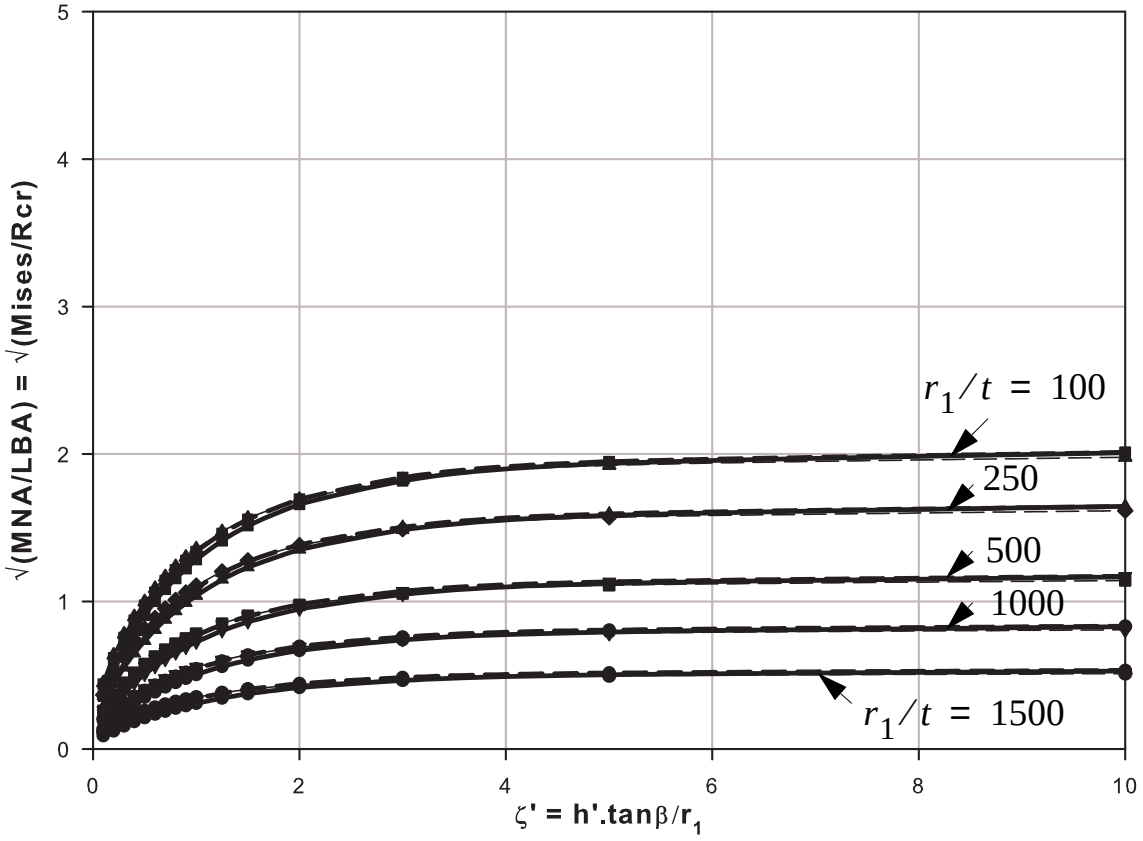

Figure 4.27 Relative buckling slenderness parameter: Fix &Pin

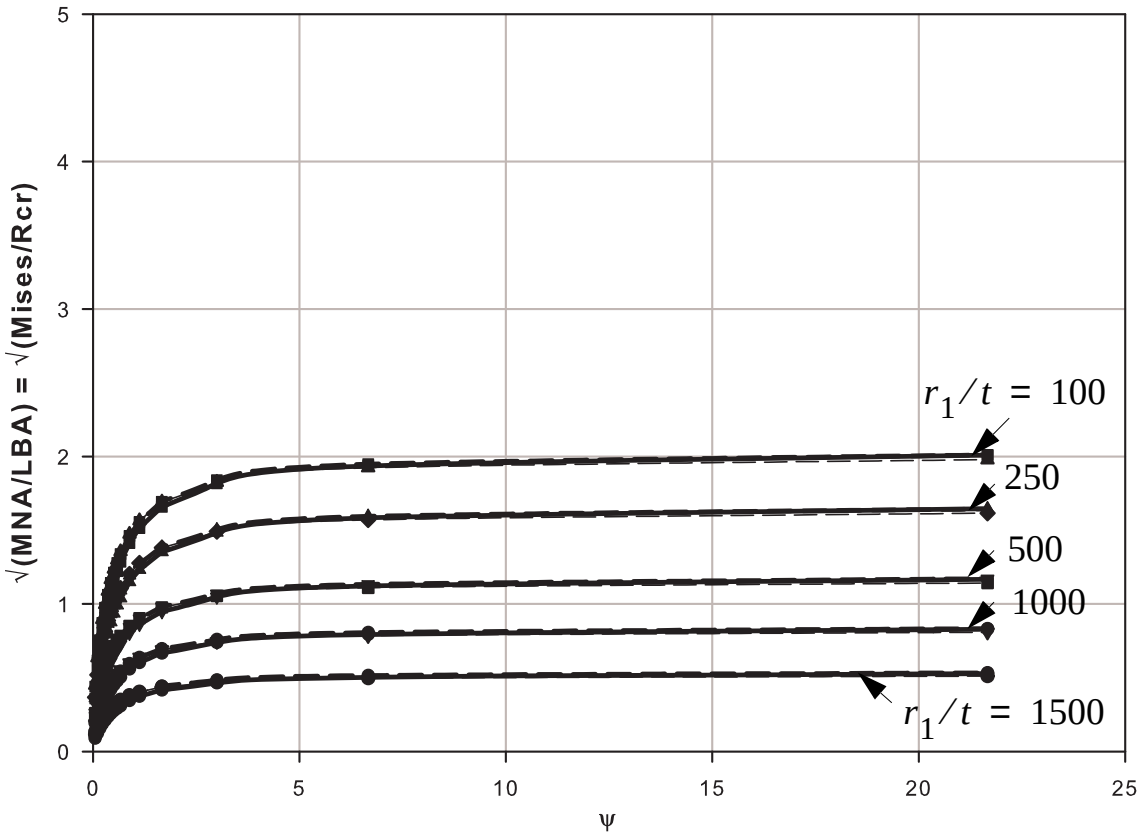

Figure 4.28 Relative buckling slenderness parameter: Fix &Pin

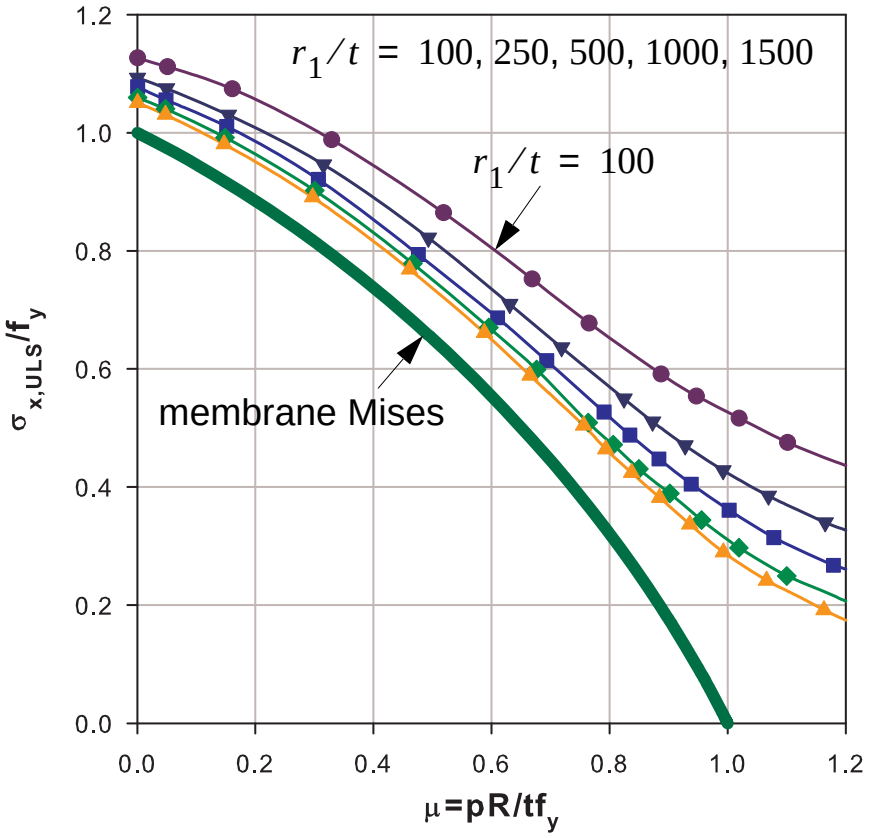

Figure 4.29 Small displacement materially nonlinear analyses: fixed bottom

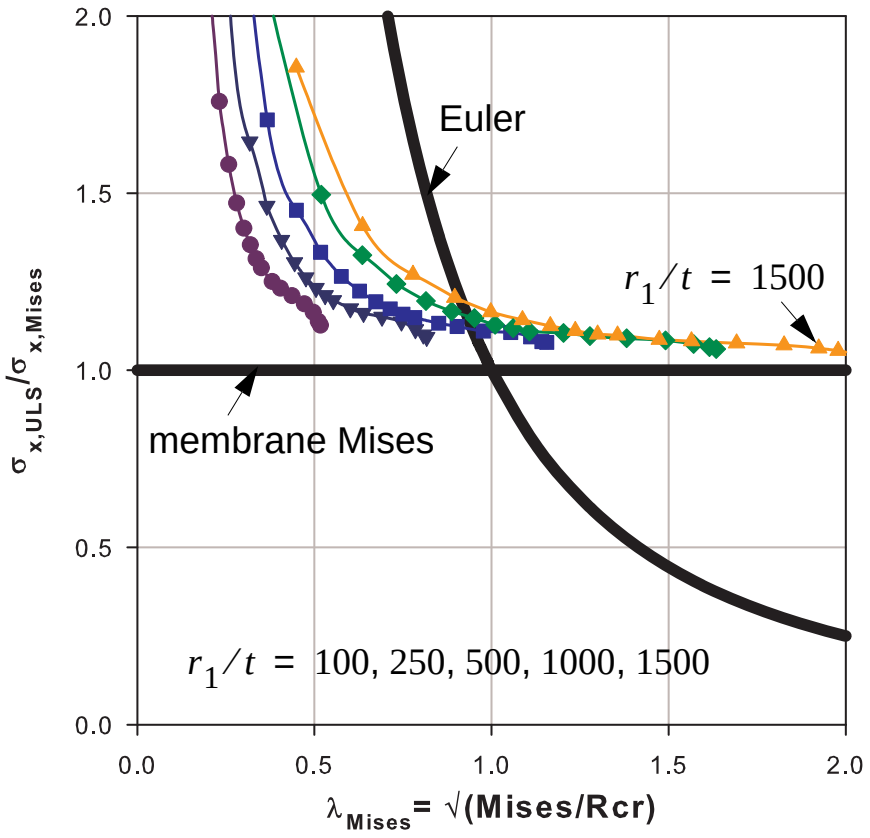

Figure 4.30 Small displacement materially nonlinear analyses: fixed bottom

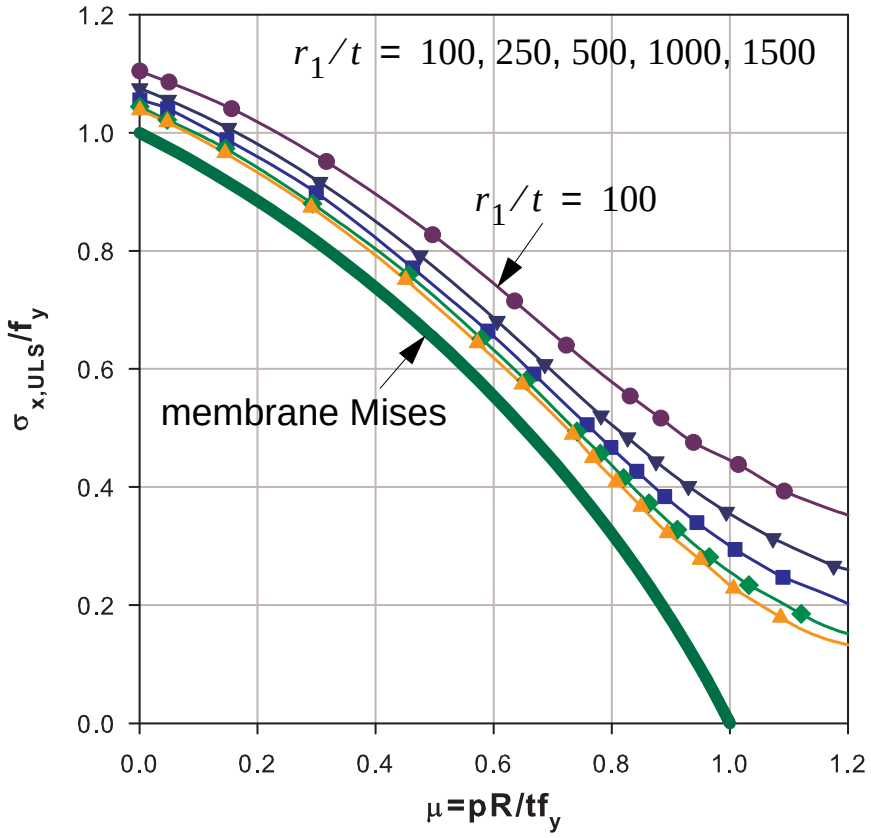

Figure 4.31 Small displacement materially nonlinear analyses: pinned bottom

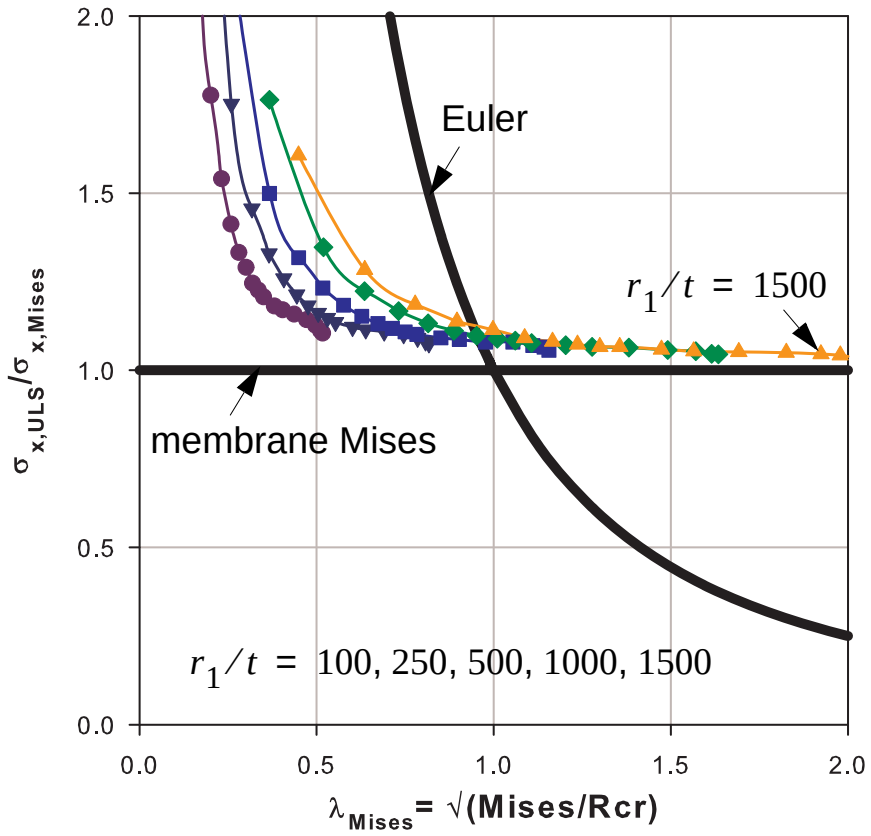

Figure 4.32 Small displacement materially nonlinear analyses: pinned bottom

The pure plastic capacities for liquid-filled conical shells, as can be seen from the plots discussed above, are higher than the pure membrane Mises yield strength at the base of the cone depending on the shell slenderness ratio and intensity of internal pressurization. For the smaller liquid-depth cases, the liquid-density should be extra high to cause yielding of the cone. Even with such extra high liquid-densities, which were chosen in such a way that the resulting membrane compressive stress at the base of the cone equals the classical critical buckling stress, the load factors needed to cause yielding are relatively higher forming a “tail” of the curves for higher internal pressures. These “tailes” can be seen in on the right-hand sides of the plots in Figure 4.29 & Figure 4.31 and left-hand side of the plots shown in Figure 4.30 & Figure 4.32.

In the practical sense, however, for thin-walled conical shells solely loaded by liquid, yielding under shallow liquid depths is far from happening because the specific-weights of the commonly contained liquids are relatively very low. For this reason, in the process of extracting useful informations for practical design purposes the impractical range is somehow cut-off and approximated by simpler buckling strength prediction expressions (partial fitting of the MNA reults) as shown in Figure 4.33 and Figure 4.35. The expressions for those simpler approximate expressions are given as follows:

$$\frac{MNA}{Mises} = 1 + \frac{a_1}{1 + \sqrt{Mises/Rcr}} = 1 + \frac{a_1}{1 + \bar{\lambda}_{Mises}} \qquad \text{(Eq. 4.49)}$$

where “a_1” is a constant equal to 0.2 for fixed bottom and 0.15 for pinned bottom boundary conditions.

With this approximate expression for the materially nonlinear strength of the shell interms of the membrane Mises yield strength at the bottom edge, the pressure representation of the MNA FEM results along with the partial-fitting are re-plotted in Figure 4.34 and Figure 4.36.

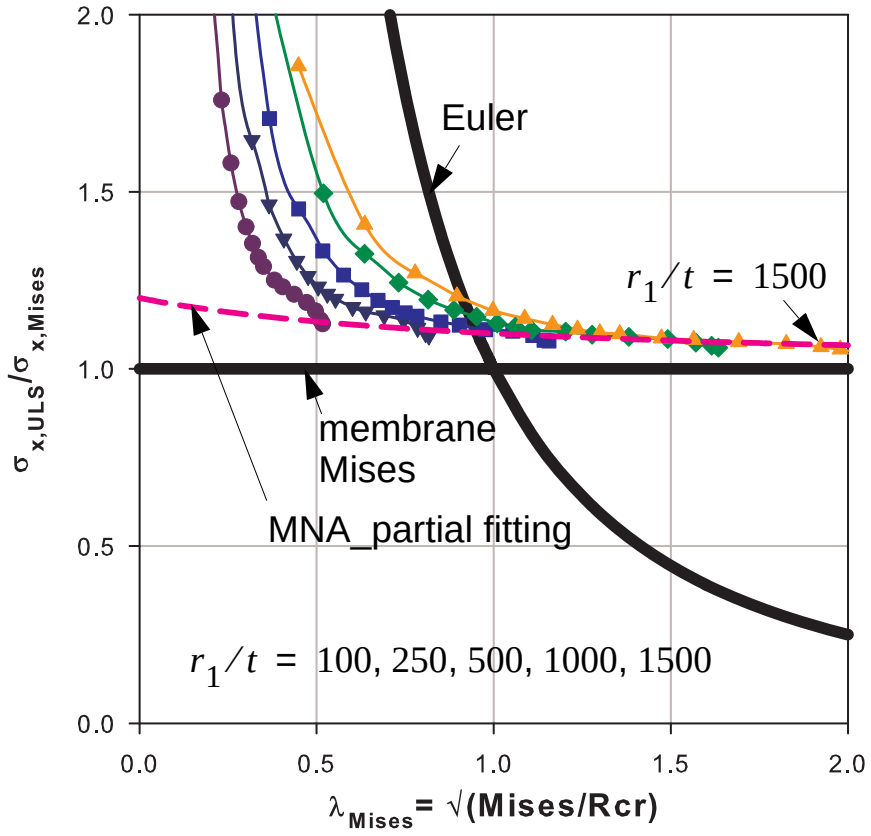

Figure 4.33 Small displacement materially nonlinear analyses: fixed bottom

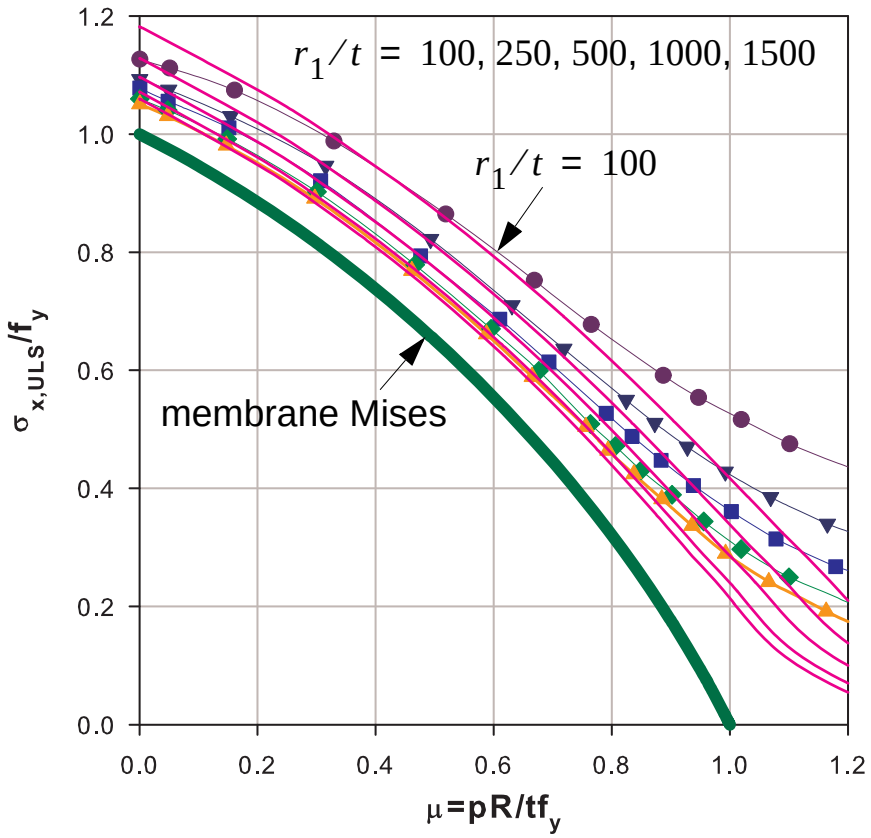

Figure 4.34 Small displacement materially nonlinear analyses: fixed bottom

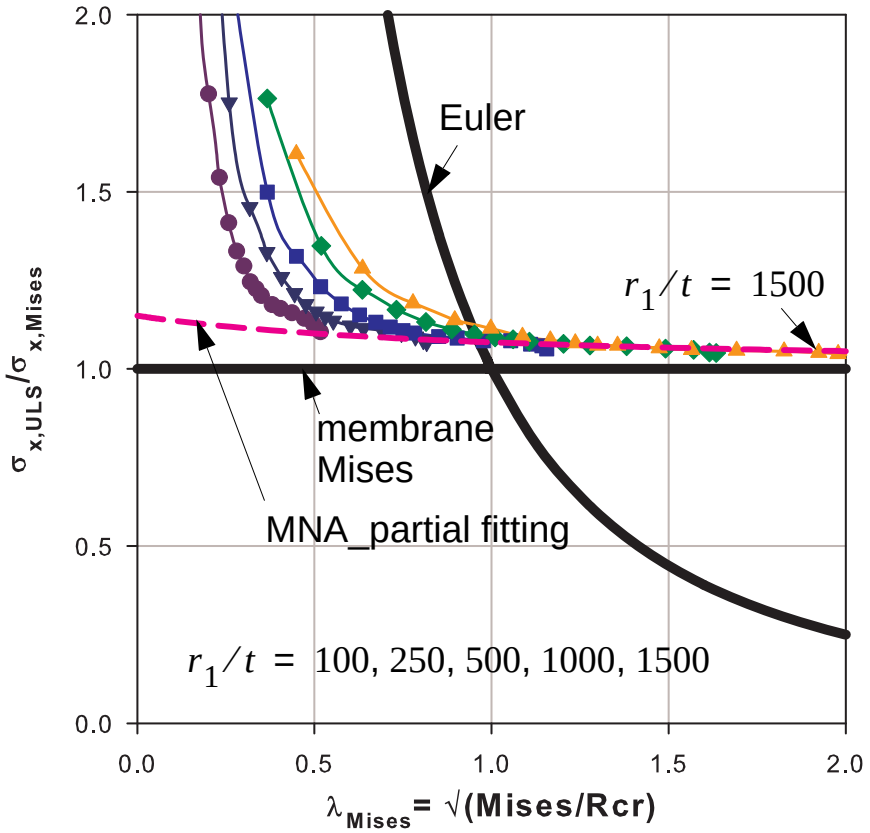

Figure 4.35 Small displacement materially nonlinear analyses: pinned bottom

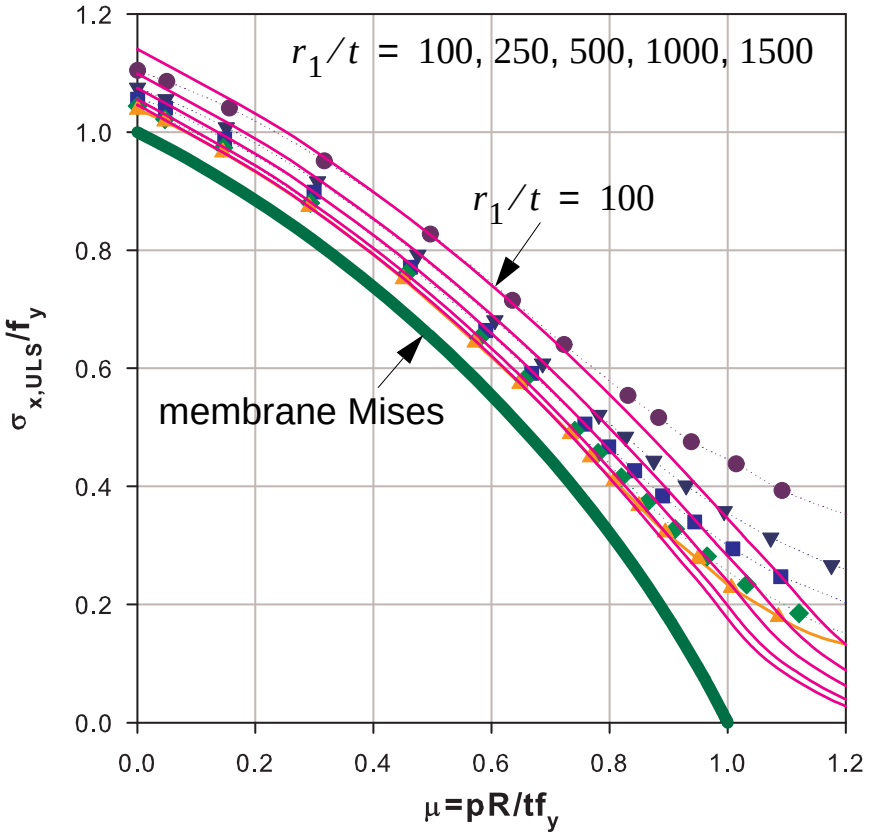

Figure 4.36 Small displacement materially nonlinear analyses: pinned bottom

4.8 Elastic-plastic buckling phenomena, analysis and strength

4.8.1 Elastic-plastic non-axisymmetric buckling

A tip-loaded perfect cone behaves the same way as that of a cylindrical shell under pure axial tip-load and elastic buckling phenomenon equally happens everywhere along the meridian of the shell. However, if there exists an imperfection, the buckling phenomenon will happen at the location of the imperfection under a lower buckling load. For a given fabrication quality class of a cone, the imperfection amplitude to wall-thickness ratio, $\Delta w_k/t = 1/Q \cdot (\sqrt{r/t\cos\beta})$, will be higher at every point (and gets even higher up the meridian) than that of the base (because of the widening geometry of the cone) implying that for a tip-loaded cone the most probable location for elastic buckling will be somewhere up the meridian depending on the boundary condition at the top end of the cone. Moreover, an imperfection of quality class-A at the shell interior of a tip-loaded cone may govern the buckling phenomenon eventhough there exists an imperfection of qulaity class-C at the cone-base depending on the ratio of the radii at the respective locations. On the other hand, as long as plasticity of a given material is concerned, the relative buckling slenderness of the cone, $\bar{\lambda}_x = \sqrt{f_y/\sigma_{xcr}}$, (where $\sigma_{xcr}(r) = 0.605Et\cos\beta/r$) will be smaller at the cone base and hence plasticity effect will play a greater role in buckling near the cone-base than in the shell interior.

Unlike that of a tip-compressed cone, in liquid-filled conical shells both elastic and elastic-plastic buckling phenomena occur at a region near the bottom boundary. The elastic-plastic buckling phenomenon may happen at relatively low or high internal pressurization depending on the geometric and material properties of the shell. For the elastic-plastic buckling phenomenon, which happens at relatively high internal pressurization, the edge constriction effect, in addition to the decaying meridional compressive stress, plays a great role results in axisymmetric buckling mode near the boundary. This type of buckling phenomenon along with the corresponding buckling strength will be investigated later in detail. For an elastic-plastic buckling at relatively low internal pressurization, a non-axisymmetric buckling mode near the boundary occurs the characterstic buckling strength of which may be computed using an interaction expression where elastic buckling interacts with bi-axial plasticity of the liquid-filled conical shell. The plastic buckling parameters of that of a tip-loaded cone (or an unpressurized cylindrical shell under pure axial compression) are used to assess such strengths. The bi-axial plastic capacity of liquid-filled conical shells will be taken as the partial fitting of the plastic capacity obtained using the MNA results and expressed as a function of the mebrane Mises yield capacity at the base of the cone (has already been discussed above) and will be named as $\sigma_{x,Mises}+$, the "+" sign showing that the material nonlinear limit strength of the cone is expressed as an "up-scaled" membrane Mises strength.

$$\chi_{Mises+} = \frac{\sigma_{x,\,ULS}}{\sigma_{x,\,Mises+}} = \begin{cases} 1 & \text{for } \bar{\lambda}_{Mises+} \le \bar{\lambda}_o \\ 1 - \beta_0 \cdot \left(\dfrac{\bar{\lambda}_{Mises+} - \bar{\lambda}_o}{\bar{\lambda}_p - \bar{\lambda}_o} \right)^{\eta} & \text{for } \bar{\lambda}_o < \bar{\lambda}_{Mises+} < \bar{\lambda}_p \\ \dfrac{\alpha_{xpe}}{\bar{\lambda}^2_{Mises+}} & \text{for } \bar{\lambda}_p \le \bar{\lambda}_{Mises+} \end{cases} \quad \text{(Eq. 4.50)}$$

where

$$\bar{\lambda}_{Mises+} = \sqrt{\frac{\sigma_{x,\,Mises+}}{\sigma_{x,\,LBA}}} \quad \text{(Eq. 4.51)}$$

$$\bar{\lambda}_p = \sqrt{\frac{\alpha_{xpe}}{1 - \beta_0}} \quad \text{(Eq. 4.52)}$$

and the plastic buckling parameters $\eta = 1.0$, $\bar{\lambda}_o = 0.2$, and $\beta = 0.6$.

The characterstic buckling strength related to the bi-axial membrane Mises yield strength can then be computed as follows:

$$\begin{aligned} \chi_{Mises} = \frac{\sigma_{x,\,ULS}}{\sigma_{x,\,Mises}} &= \frac{\sigma_{x,\,ULS}}{\sigma_{x,\,Mises+}} \cdot \frac{\sigma_{x,\,Mises+}}{\sigma_{x,\,Mises}} \\ &= \chi_{Mises+} \cdot \left(1 + \frac{a_1}{1 + \bar{\lambda}_{Mises}} \right) \end{aligned} \quad \text{(Eq. 4.53)}$$

where "a_1" is a constant equal to 0.2 for fixed bottom and 0.15 for pinned bottom boundary conditions.

4.8.2 Axisymmetric elastic-plastic buckling

4.8.2.1 Geometrically and materially nonlinear finite element analysis of perfect conical shells (GMNA)

Unlike that of an axially loaded and internally pressurized cylindrical shell where the loading procedure can be done in two different ways, the loading in liquid-filled conical shells can not be splitted into a part which causes meridional compression and another part causing circumferential tension. The resulting meridional compression and circumferential tension section forces of a liquid-filled conical shell are therefore interlinked to each other. Apart from this fact, the elastic-plastic buckling phenomenon already discussed in the buckling investigation of the cylindrical shell applies to the case of liquid-filled conical shells as well. It should, however, be clear that the elastic-plastic buckling strengths of liquid-filled conical shells will be somehow different from the uniformly loaded cylindrical shells because of the following possible reasons:

- the difference in geometry of the shell
- the difference in along-meridian distribution of each component of the section force/stress and the overall distribution of the bi-axial stress state

In other words, when a one-to-one comparison of the cylinder and cone is sought, an equivalency in geometry and loading conditions along with boundary conditions needs to be met. The detailed investigation of such equivalency has been made in this work and will be discussed later.

On the other hand, unlike that of a uniformly loaded cylindrical shell which results in uniform meridional and circumferential membrane section force ditributions, the meridional membrane section force ditribution in the liquid-filled conical shell is maximum at the lower supported edge and decreases nonlinearly and rapidly up the meridian. Such a distribution of the meridional compressive section force superimposed with the edge constriction effects of the bottom boundary conditions will restrict the elastic-plastic buckling phenomenon to a region very close to the supported lower edge causing elephant's-foot type buckling. This study, therefore, addresses this type of elastic-plastic buckling phenomenon and strengths of liquid-filled conical shells.

Comprehensive parametric studies are carried out varying the shell slenderness ($r_1/t\cos\beta$), shell lower bundary conditions (fixed versus pinned), and the liquid depth parameter ($\zeta' = h'\tan\beta/r_1$) which indirectly determines the intensity of the internal pressurization. The membrane section forces ratio ($\overline{\psi} = N_{x,1}/N_{\theta,1}$) at the base level of the conical shell which directly depends on the liquid depth parameter ($\zeta' = h'\tan\beta/r_1$) is used as a measure of the reference loading. Geometrically and materially nonlinear finite element analyses which resulted in localized axisymmetric buckling modes were made on liquid-filled conical shells with an apex-half angle $\beta = 45$ degrees and $r_1/t =$ 100, 250, 500, 1000, 1500 by varying the liquid depth parameter ($\zeta' = h'\tan\beta/r_1$) from very small (or very high internal pressurization compared to meridional compression) to very high (or very high meridional compression compared with internal pressurization). Boundary conditions of PIN or FIX at bottom and rotational restraint at top were examined for each $r_1/t\cos\beta$. Small

displacement linear bifurcation analysis (LBA) and small displacement materially nonlinear analysis (MNA) results are used for reference purposes.

In an exactly similar loading procedure as in the investigation of the material nonlinear strength, geometrically and materially nonlinear analyses (GMNA) of liquid-filled perfect cones have been made to compute the elephant's-foot buckling strength. The results obtained are plotted in different representations as shown in Figure 4.37 to Figure 4.50. A GMNA/fy vs. ζ' (= h'tanβ/r_1) plots are shown in Figure 4.37 and Figure 4.38 for the fixed and pinned bottom cases, respectively. The same elastic-plastic buckling strengths are re-plotted using the pressure representation (GMNA/fy vs. μ) in Figure 4.39 & Figure 4.41 and in the capacity representation (GMNA/Mises vs. $\overline{\lambda}_{Mises}$) in Figure 4.40 and Figure 4.42 for the fixed and pinned bottom cases, respectively.

For the shallow liquid-depth cases, the same "tail" effect with the same explanations as in the MNA case can be seen from the elephant's-foot buckling strengths.

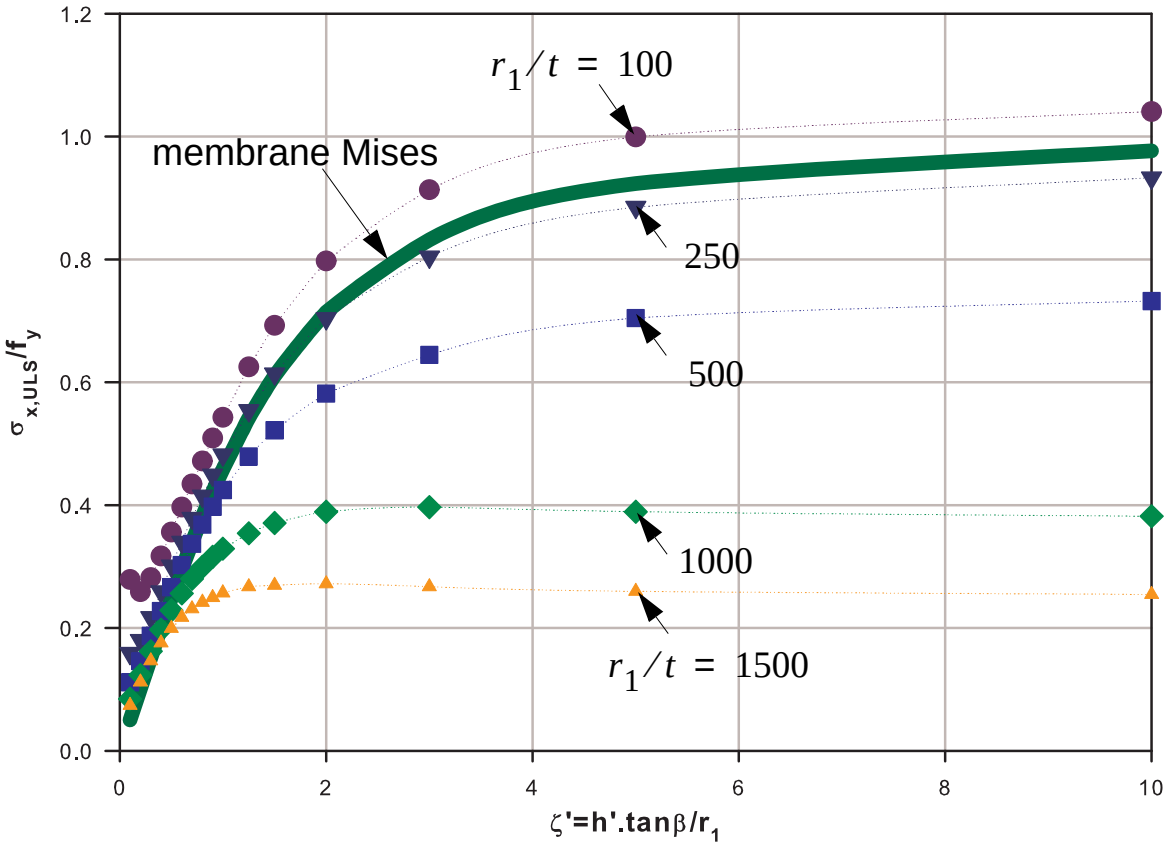

Figure 4.37 Geometrically and materially nonlinear analysis: fixed bottom

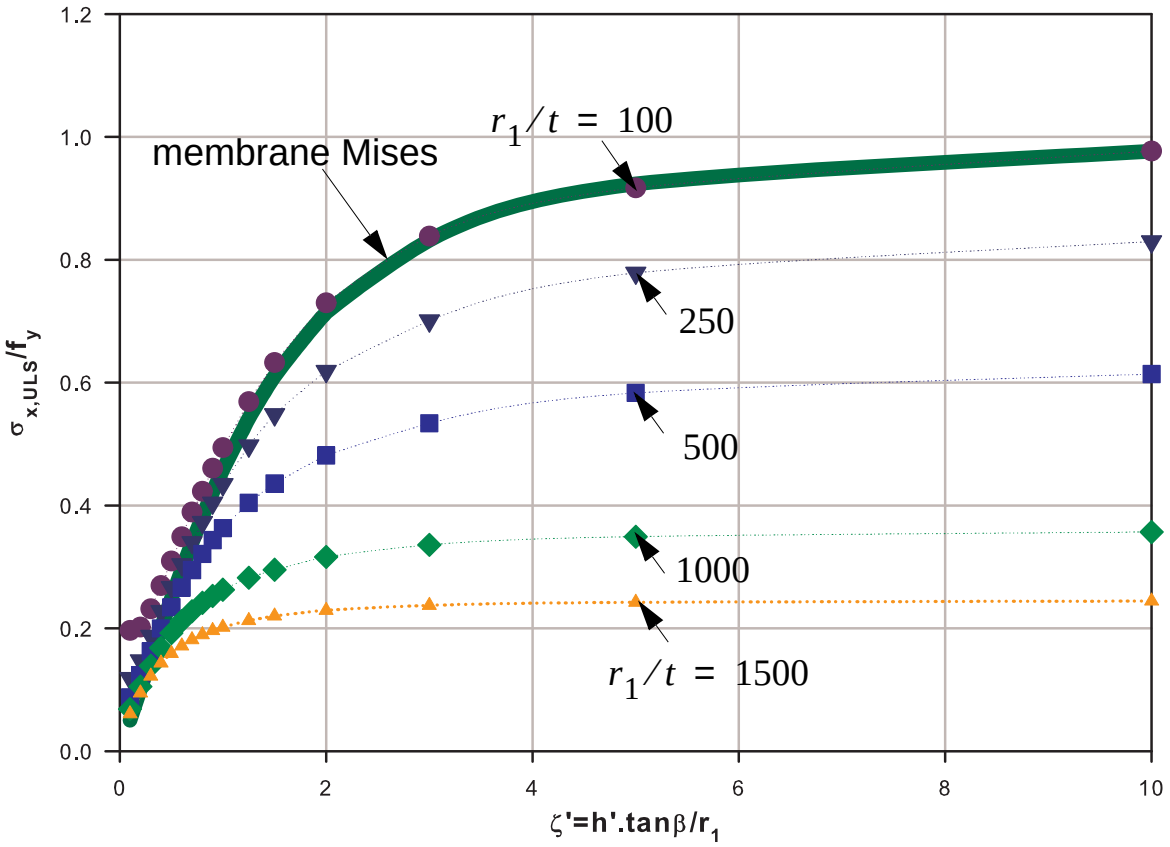

Figure 4.38 Geometrically and materially nonlinear analysis: pinned bottom

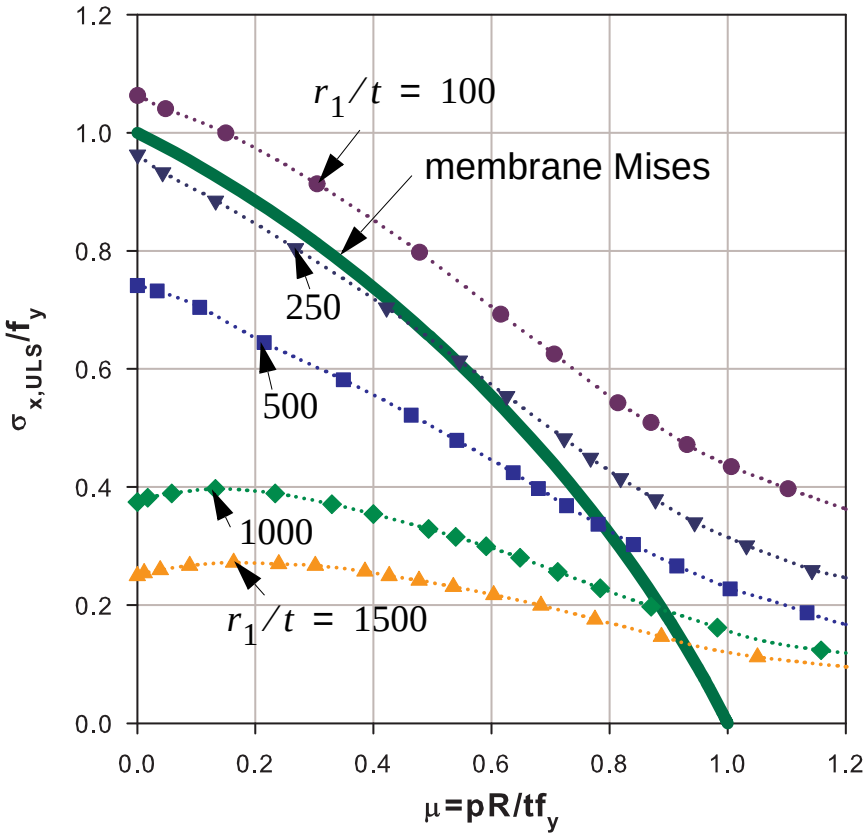

Figure 4.39 GMNA results (elephant's-foot strength): fixed bottom

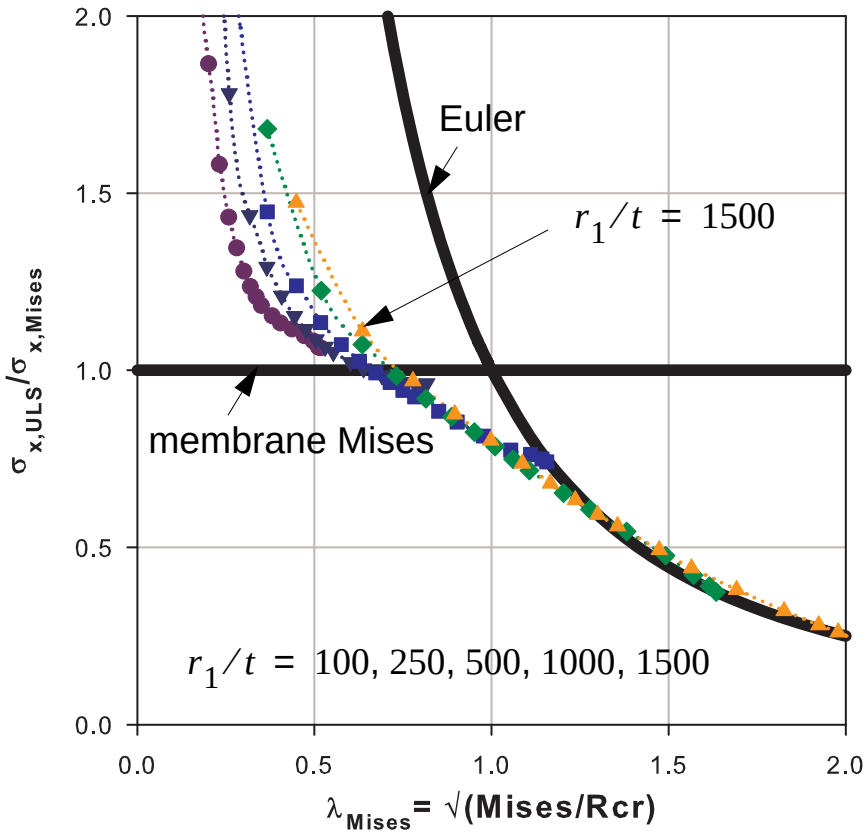

Figure 4.40 GMNA results (elephant's-foot strength): fixed bottom

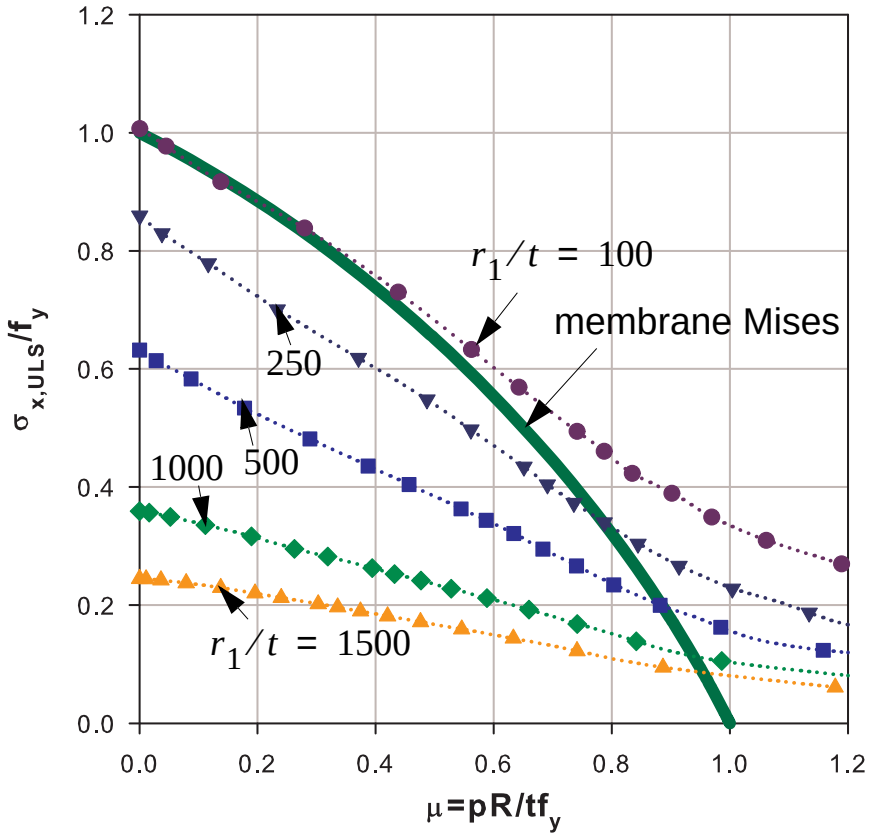

Figure 4.41 GMNA results (elephant's-foot strength): pinned bottom

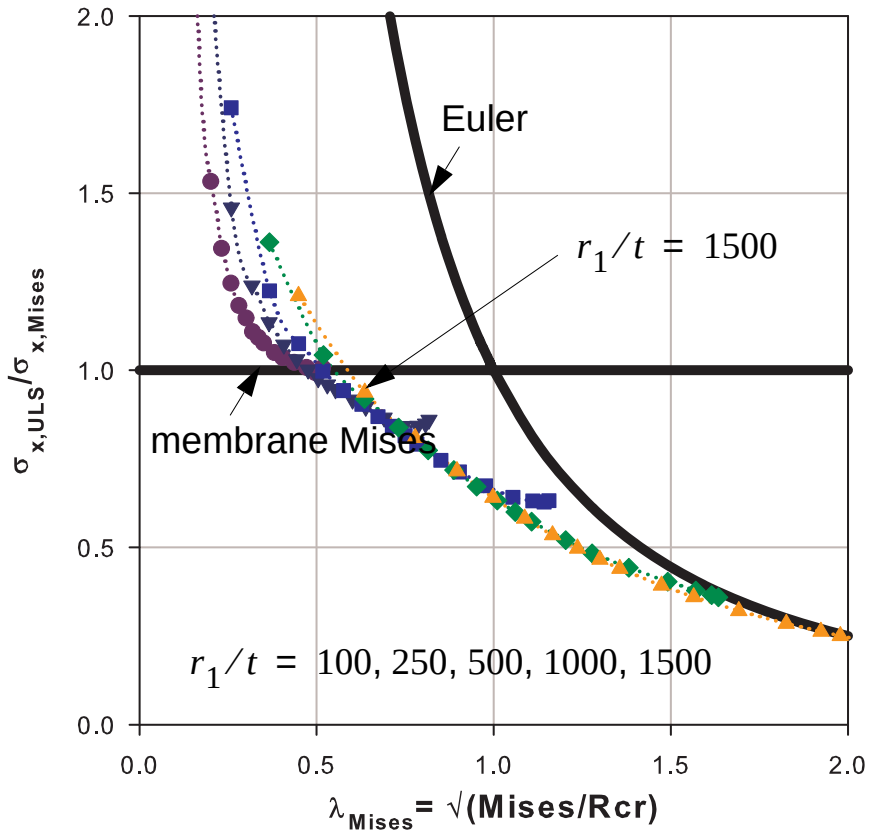

Figure 4.42 GMNA results (elephant's-foot strength): pinned bottom

The geometric nonlinearity effects in reducing the buckling strength of conical shells can be seen from the GMNA results when compared to the geometrically linear but materially nonlinear (MNL) strength. This relative strength (GMNL/MNL), where one can directly see the effects of geometric nonlinearities for different shell slenderness ratios, is shown in Figure 4.43 for the fixed bottom cone and Figure 4.44 for the pinned bottom.

When the geometric nonlinearity effects are very small as in the case of relatively thick-walled concal shells, the GMNL buckling strengths will be closer (or atmost equal) to the pure plastic (MNL) strength of the shell. On the other hand, when both the geometric and material nonlinearity effects are very small as in the case of relatively thin-walled cylindrical shells and lower internal pressure values, the GMNL buckling strengths will be closer (or atmost equal) to the pure elastic buckling (LB) strength of the perfect shell. These facts can be observed from the plots of the GMNL results shown in Figure 4.43 to Figure 4.44 for both the fixed and pinned bottom boundary conditions.

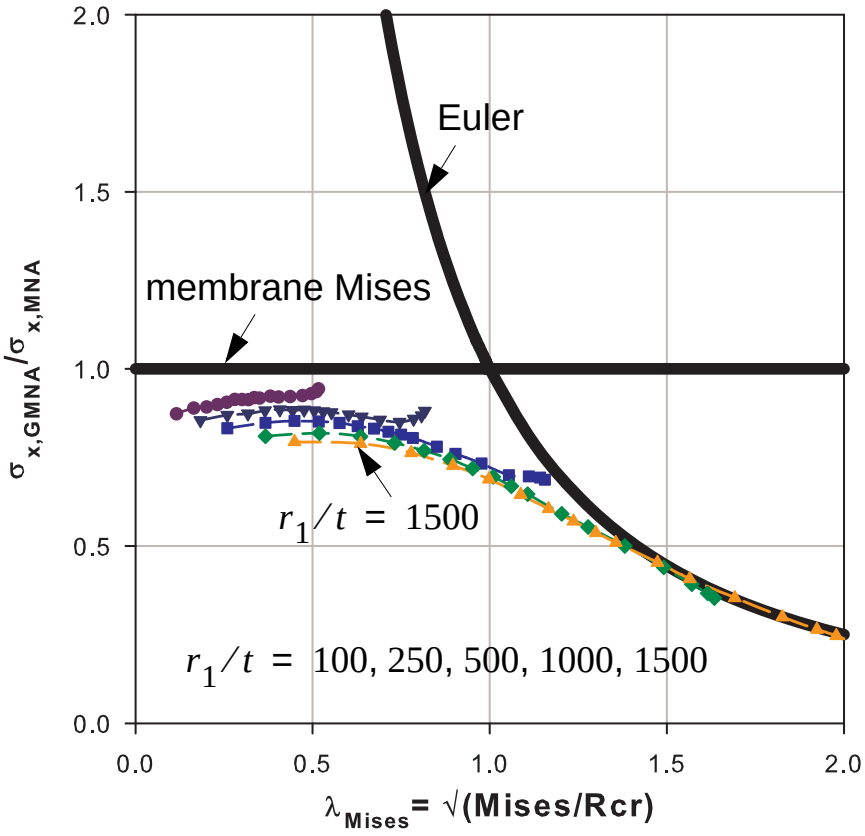

Figure 4.43 Elephant's-foot strength: fixed bottom

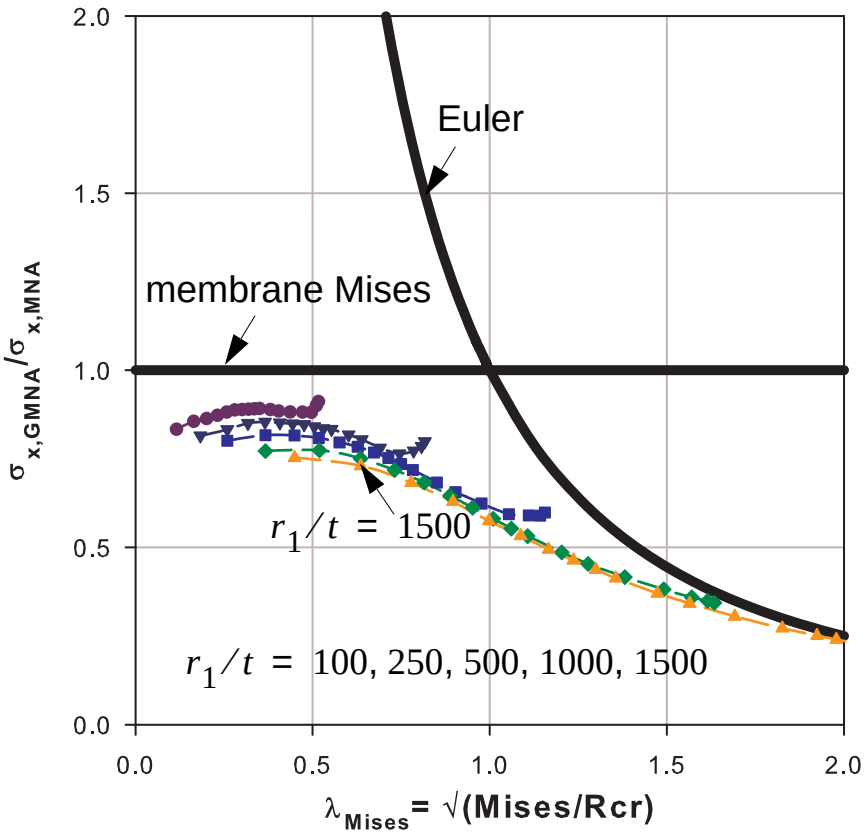

Figure 4.44 Elephant's-foot strength: pinned bottom

Since the meridional and circumferential membrane section forces in liquid-filled conical shells are always interlinked to each other through the membrane stress ratio parameter $\overline{\psi}$, the intensity of internal pressurization is expressed interms of this parameter which inturn depends on the liquid-depth parameter ζ'. Since the intensity of the internal pressurization is indirectly proportional to $\overline{\psi}$ (or ζ'), a high internal pressurization causing higher circumferential tension will be obtained at smaller values of $\overline{\psi}$ (or ζ'), i.e. at relatively shallow liquid-depths. This, however, needs a liquid loading with very high specific weight (as high as $10*\gamma_{mercury}$ or even more) to cause a very high circumferential tension somehow closer to the uni-axial yield strength of the shell and when superimposed with the edge constriction effect causes local bending which ultimately leads to an elastic-plastic buckling under the small acting meridional compression near the boundary. Even for such a liquid loading with very high specific weight, the characterstic elastic-plastic buckling load factor is relatively high because of the rapid decay leading to an even smaller meridional compression at the buckle center when compared with the existing small meridional compression at the supported base.

Once again, as alreday explained in the discussion of LFC MNL strengths, for thin-walled conical shells solely loaded by liquid, such a buckling phenomenon under shallow liquid depths is far from happening because the specific weights of the commonly contained liquids are relatively very low. For this reason, in the process of extracting useful informations for practical design purposes the impractical range is cut-off and approximated by simpler buckling strength prediction expressions (partial fitting of the GMNA reults) as will be discussed below. In the course of doing this, the ratios of the MNL and GMNL strengths with respect to the partial-fit of the MNL strengths (i.e. MNL/MNA_partial-fit and GMNL/MNA_partial-fit) are computed and shown in Figure 4.45 and Figure 4.46 for both the fixed and pinned bottom boundary conditions, respectively. Using these plots and a cut-off with the MNL-partial-fitting curve (the 1.0 line curves in the plots), final expressions for the characteristic buckling strengths of liquid-filled conical shells can be easily drawn as discussed below.

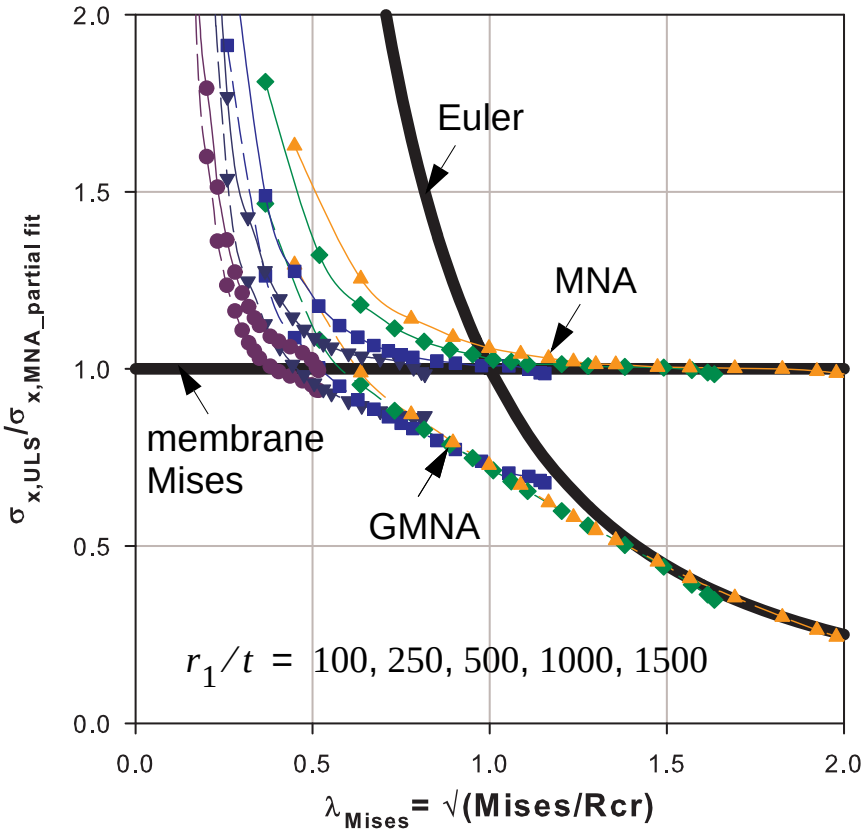

Figure 4.45 Nonlinear analysis results: fixed bottom

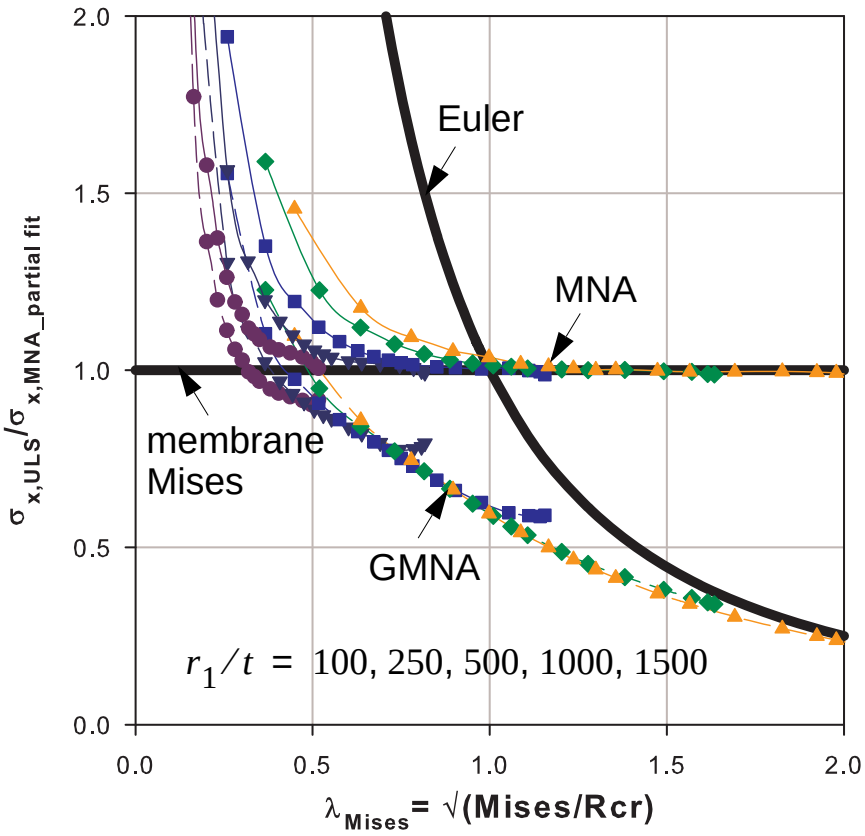

Figure 4.46 Nonlinear analysis results: pinned bottom

From the capacity representations of the geometrically and materially nonlinear analyses results (see Figure 4.47 & Figure 4.49), the values of the squash limit relative buckling slenderness parameter $\overline{\lambda}_0$ (below which stability effects are neglected and hence full plastic collapse is assumed to occur) and the plastic limit relative buckling slenderness parameter $\overline{\lambda}_p$ (at which material nonlinearity effect starts to come into play and interact with stability effects) can be directly extracted. For shell cases with $\overline{\lambda}_{\text{Mises}}$ values which are greater than $\overline{\lambda}_p$, pure elastic buckling will govern the design as far as buckling is concerned. For values of $\overline{\lambda}_{\text{Mises}}$ greater than $\overline{\lambda}_0$ but less than $\overline{\lambda}_p$, an elastic-plastic buckling phenomenon governs the design for which the characterstic buckling strengths should be obtained, generally speaking, either from tests or from geometrically and materially nonlinear analyses. In cases where such results do not exist a linear interpolation can be used as is recommended in EN1993-1-6. In cases where such results exist, shape functions are used which accurately represent the elastic-plastic buckling strengths of the shell under consideration. In the current study, since geometric and material nonlinear analyses are performed from which the best fit shape functions are chosen to represent the computed values in the elastic-plastic range (i.e. $\overline{\lambda}_0 < \overline{\lambda}_{Mises} < \overline{\lambda}_p$) for the different bottom boundary conditions as will be discussed below.

$$\chi_{Mises} = \frac{\sigma_{x,\,ULS}}{\sigma_{x,\,Mises}} = \left(1 + \frac{a_1}{1 + \overline{\lambda}_{Mises}}\right) \cdot \begin{cases} 1 & \text{for} \quad \overline{\lambda}_{Mises} \le \overline{\lambda}_o \\ 1 - \beta_0 \cdot f(\xi) & \text{for} \quad \overline{\lambda}_o < \overline{\lambda}_{Mises} < \overline{\lambda}_p \\ \dfrac{1}{\overline{\lambda}^2_{Mises}} & \text{for} \quad \overline{\lambda}_p \le \overline{\lambda}_{Mises} \end{cases} \qquad \text{(Eq. 4.54)}$$

where

$$\xi = \frac{\overline{\lambda}_{Mises} - \overline{\lambda}_o}{\overline{\lambda}_p - \overline{\lambda}_o} \qquad \text{(Eq. 4.55)}$$

$$f(\xi) = \xi^{\eta} \cdot (1 + a_2 \cdot (1 - \xi)^{\eta}) \qquad \text{(Eq. 4.56)}$$

$$\overline{\lambda}_{Mises} = \sqrt{\frac{\sigma_{x,\,Mises}}{\sigma_{xRcr}}} \qquad \text{(Eq. 4.57)}$$

$$\overline{\lambda}_p = \sqrt{\frac{1}{1 - \beta_0}} \qquad \text{(Eq. 4.58)}$$

the elastic-plastic buckling parameters: interaction exponent η, squash limit relative slenderness $\overline{\lambda}_o$, and plastic range factor β are given as follows depending on the type of bottom boundary condition.

	$\mathbf{a_1}$	$\mathbf{a_2}$	η	$\bar{\lambda}_{\mathbf{o}}$	β
Fixed bottom	0.20	0.00	1.0	0.45	0.6
Pinned bottom	0.15	0.75	1.0	0.35	0.8

Table 4.1 Values of plastic buckling parameters

Alternatively, for a liquid-filled conical shell with pinned bottom boundary condition the values $a_2 = 1.0$ and $\eta = 1.1$ can be used instead.

With this approximate expression for the geometrically and materially nonlinear strength of the shell interms of the membrane Mises yield strength at the bottom edge, the pressure representation of the GMNA FEM results along with the GMNA partial-fitting are re-plotted in Figure 4.48 and Figure 4.50.

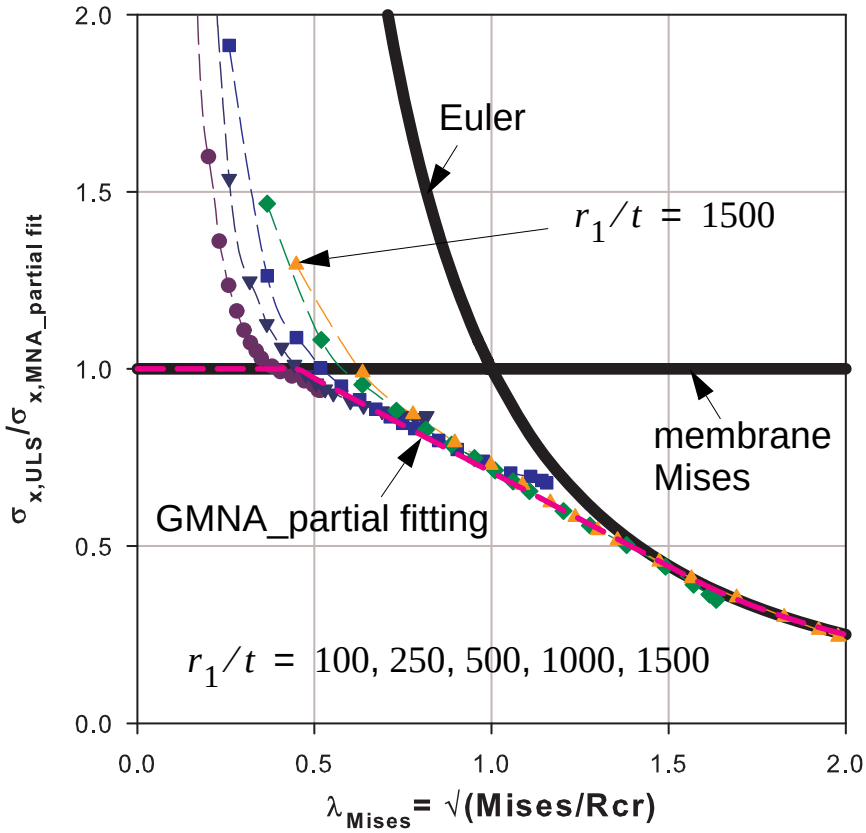

Figure 4.47 GMNA results (elephant's-foot strength): fixed bottom

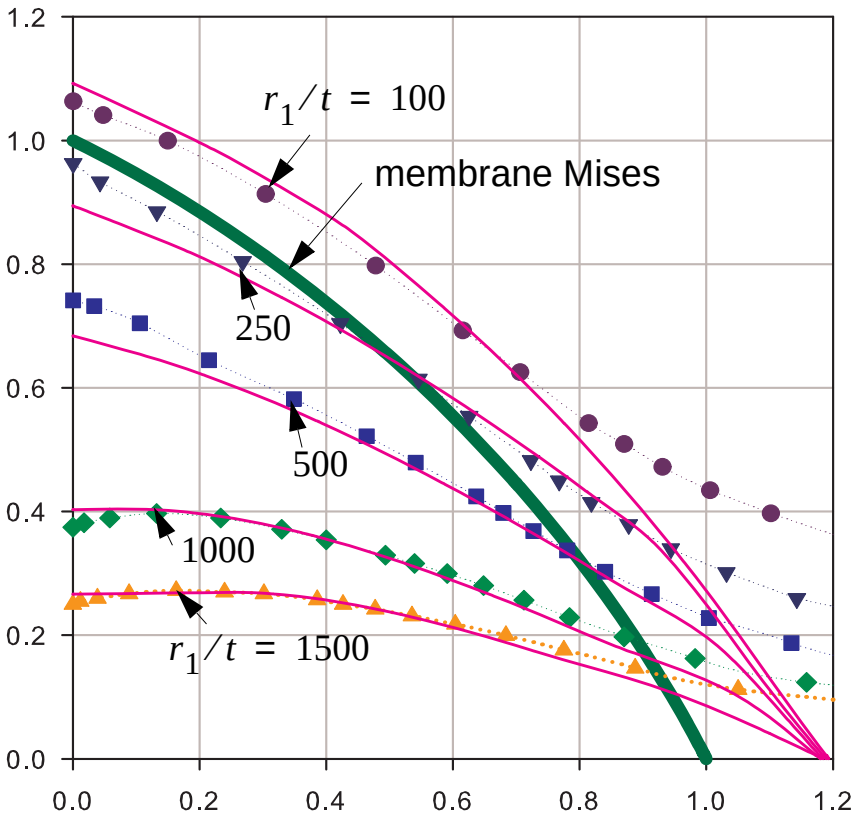

Figure 4.48 GMNA results (elephant's-foot strength): fixed bottom

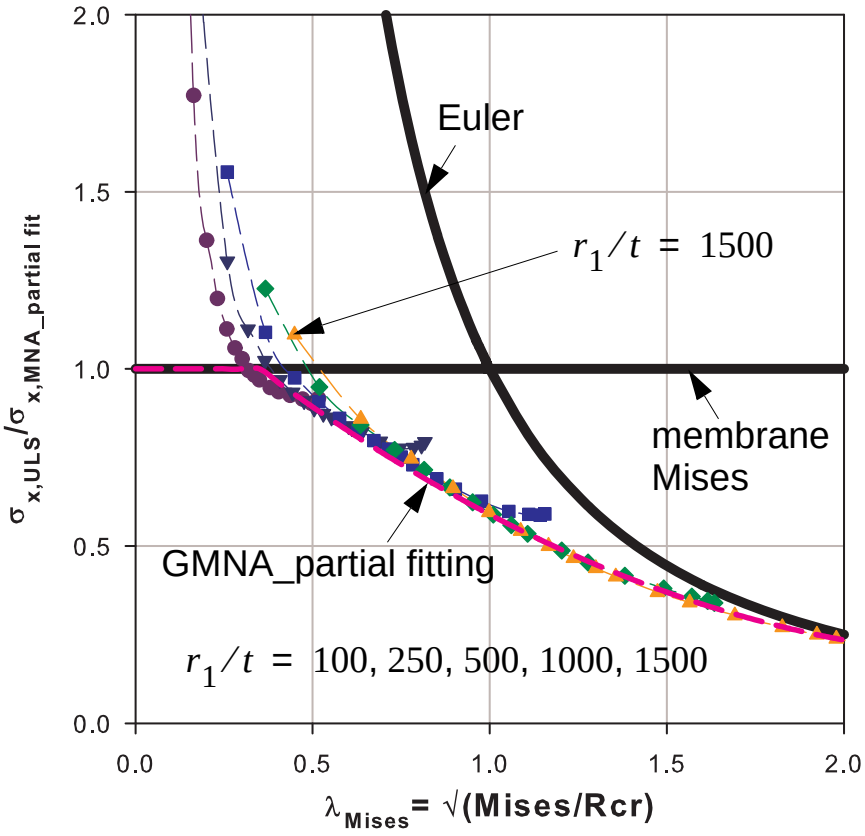

Figure 4.49 GMNA results (elephant's-foot strength): pinned bottom

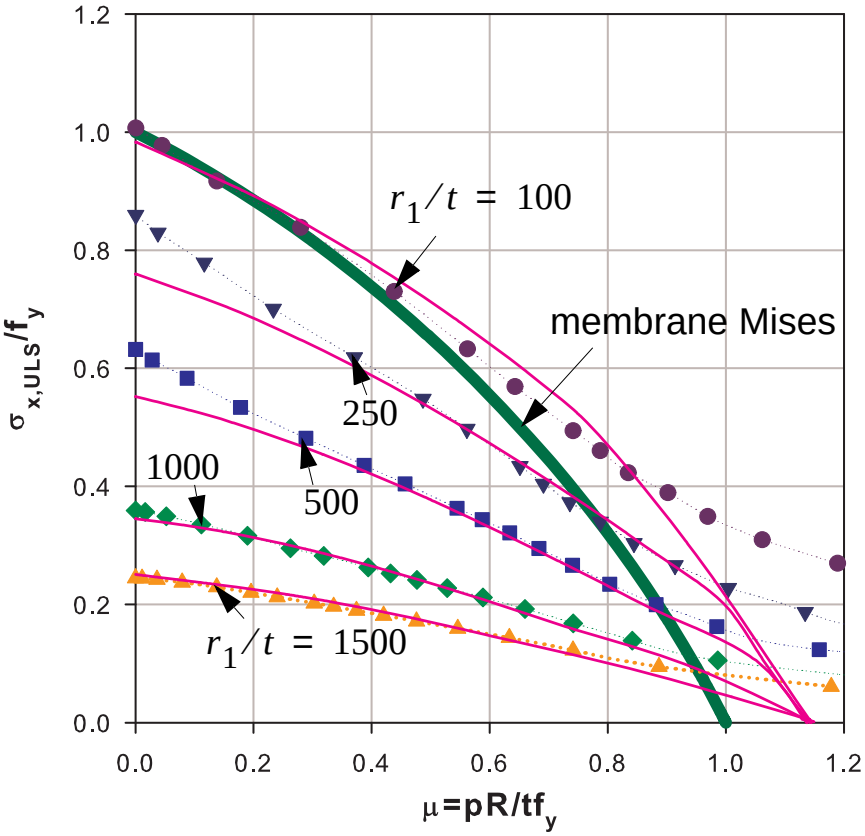

Figure 4.50 GMNA results (elephant's-foot strength): pinned bottom

4.8.2.2 Analytical model based on theory of second order with material nonlinear effects

The same basic idea, as used in the discussion on an anlytical model of cylindrical shells, can be applied to conical shells. In other words, the geometric and material nonlinear effects of a a liquid-filled conical shell can be analytically modelled approximately using a combination of theory of second order and the stress resultant oriented approximate yield criteria. However, this has not been covered in the current study.

4.9 Buckling design recommendation

Once the pure elastic buckling strength of an imperfect liquid-filled conical shell, which is related to a non-axisymmetric failure mode, and the elastic-plastic buckling strength of the perfect (or imperfect, for that matter, when a worst practical imperfection nature is agreed upon) liquid-filled conical shell, which is related to an axisymmetric buckling mode can be predicted using simpler expressions, exactly the same methods as those discussed in the buckling investigation of the cylindrical shell can be used. More specifically, method-4 is the best of all the methods discussed and is, therefore, highly recommended for design and future research applications because of the facts already stated during the discussion, chapter-3.

4.10 Summary and conclusions

The pure membrane behavior and edge bending effects of a liquid-filled conical shell have been computed using considerations of static equilibrium for the pure membrane situation and using an effective-ring model analogy for the edge bending effects. The total results (membrane + edge bending) have been compared with the finite element linear analysis results for verification purposes.

The possible loading procedures in dealing with liquid-filled conical shells have been discussed. Besides, which loading procedure should be used in what circumstances and for what purposes has been pointed out.

The linear buckling strengths of liquid-filled perfect cones have been computed approximately and investigated numerically. Explanations have been given about the LFC-specific buckling phenomenon and corresponding strengths. Simplified expressions for the prediction of linear buckling strengths of liquid-filled general cones with pinned and fixed bottom boundary conditions have been obtained. The effect of imperfections on the elastic buckling strength have been discussed as well for different fabrication quality classes as recommended in EN 1993-1-6.

The pure plastic limit strengths of liquid-filled conical shells have been computed approximately using von Mises membrane yield criterion taking the membrane stresses at the cone-base as references. The plastic strength using stress resultant oriented approximate yield criteria have also been included. Moreover, small displacement materially nonlinear numerical simulations have been done to compute the exact plastic capacity of liquid-filled cones. Simplified expressions along with detailed explanations have been obtained to predict the materially nonlinear limit strength of both pinned and fixed bottom liquid-filled general cones.

The consideration of the effect of plasticity on elastic buckling with non-axisymmetric buckling failure mode have been discussed. This type of elastic-plastic interaction happens for relatively smaller internal pressurization situations. The elephant's-foot buckling strengths of perfect cones due to liquid-loading have also been investigated in detail after which simplified expressions are obtained for the prediction of the axisymmetric elastic-plastic buckling strength of general thin-walled liquid-filled cones.

Elephant's-foot type buckling in liquid-filled conical shells, where the only loading is liquid-filling, may not be probable unless there exist a worst imperfection or a global bending moment resulting from, say, earthquake causing one-sided buldge. A very little global bending effect, in the general case of cones supported from bottom (i.e. on the smaller radius), will have a very big meridional compression on one side of the cone due to the shorter lever-arm at the smaller radius. It is this big meridional compression along with the existing circumferential stretching which results in bi-axial state of stress causing local yielding and hence elephant's-foot buckling.

On the other hand, if there exists an additional, say, roof loading on top of the existing liquid-loading, an additional meridional compression will result. This higher meridional commpression along with the existing circumferential tension (plus small addition due to poisonn’s effect) may therefore lead to the possibility of elephant’s-foot type buckling.

5

Re-investigation of Gent test results:

Elastic buckling of liquid-filled cones

5.1 Introduction

The term liquid-filled conical shells, in the context of this work, refers to truncated conical shells used as liquid storage tanks with a vertical axis of rotation and supported from below at their smaller radius edge. Apart from tanks, conical shells can also be found on the lower portion of silo structures. In cases where they are used as liquid containment vessels, as in steel water towers, the contained liquid exerts an internal hydrostatic pressure which results in meridional compression and tension in the hoop (circumferential) direction.

Though metal shells are the main interest of this study, such structures can also be constructed using reinforced concrete. The bottom edge of the LFC shells are mainly supported in two ways:

- the lower part is welded to an upper part of a short stiff conical or cylindrical shell where it in turn is welded to a rigid plate (e.g. the steel water tower failed in 1990, Fredericton, Canada)
- the lower part is welded directly to the rigid plate (e.g. the steel water tower failed in 1972, Belgium)

In the first type of supports, even though there is some rotational stiffness coming from the weld, the shell can conservatively be treated as “pin” supported. Where as in the second case the shell can be treated as “fixed” as long as the rigid plate helps the shell keep its conicity. For this reason, the “pin” and “fix” type of supports are the main concerns in this shell buckling study.

In 1972, a time when there were no buckling design regulations to refer to and even no enough buckling knowledge to rely to, a 1500 m^3 capacity steel water tower suddenly collapsed in Belgium upon filling for the first time, right before (1.74m below) the overflow level is reached. The failure occurred by buckling which started somewhere on the bottom region (i.e. close to the boundary). The bottom region comprised of two cone segments with the lower cone relatively thicker and shorter.

Following the collapse, a huge amount of experimental researches and numerical (using BOSOR) studies were made for more than a decade (1977-1987) at Gent university by D. Vandepitte *et. al.* The results of the study were reported in many papers (see Figure 5.1) and a design recommendation was then proposed based on straight line bounds of all the test results from a doubly logarithmic ψ - ω plot.

Figure 5.2 and Figure 5.3 show photos taken of the collapsed steel water tower from two different viewing angles. A laboratory experimental setup used in Gent and an explanatory sketch showing the geometry, loading, and boundary conditions are shown in Figure 5.4 and Figure 4.1, respectively.

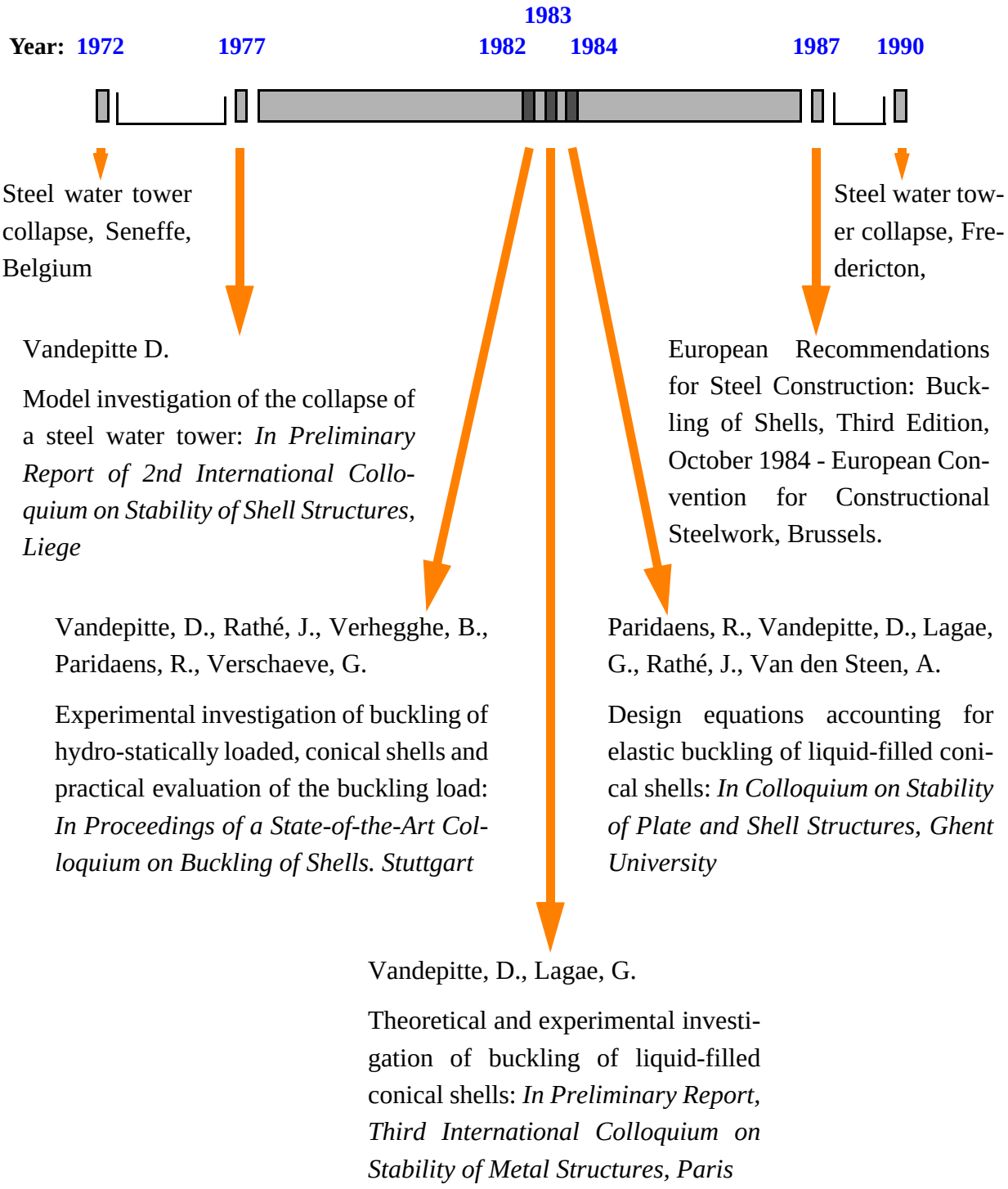

Figure 5.1 Summary of previous works related to the Gent experiments

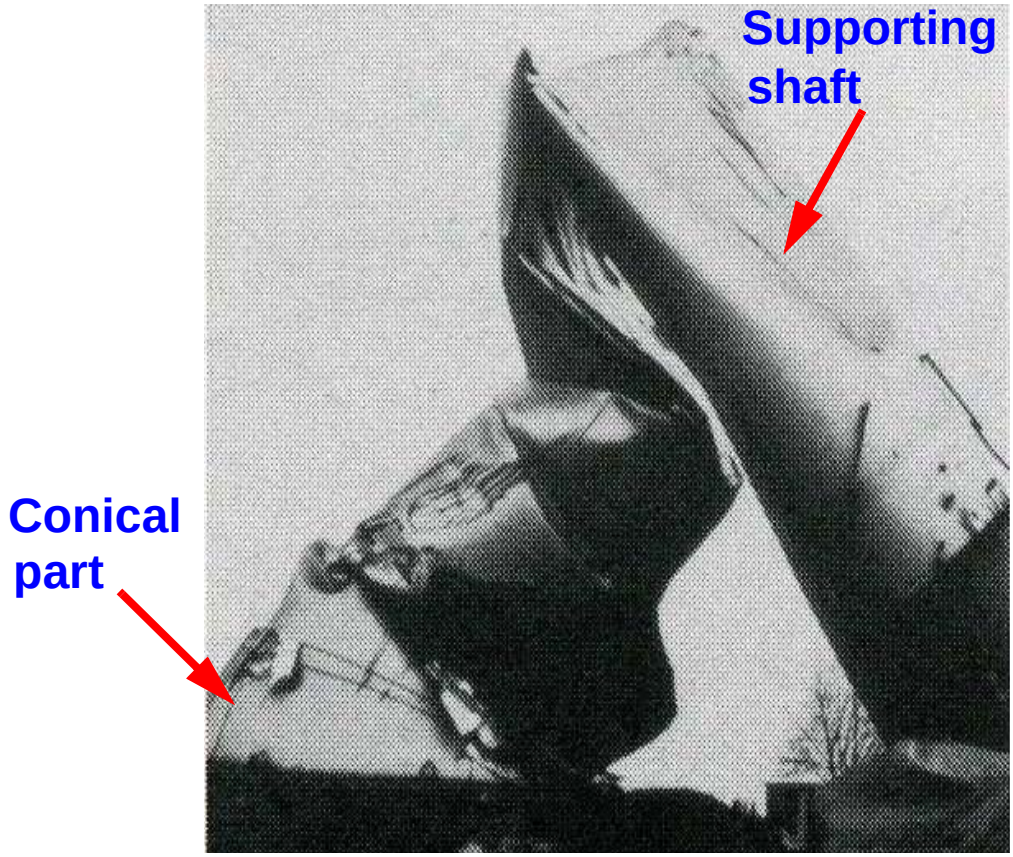

Figure 5.2 Collapsed steel water tower, 1972, Belgium

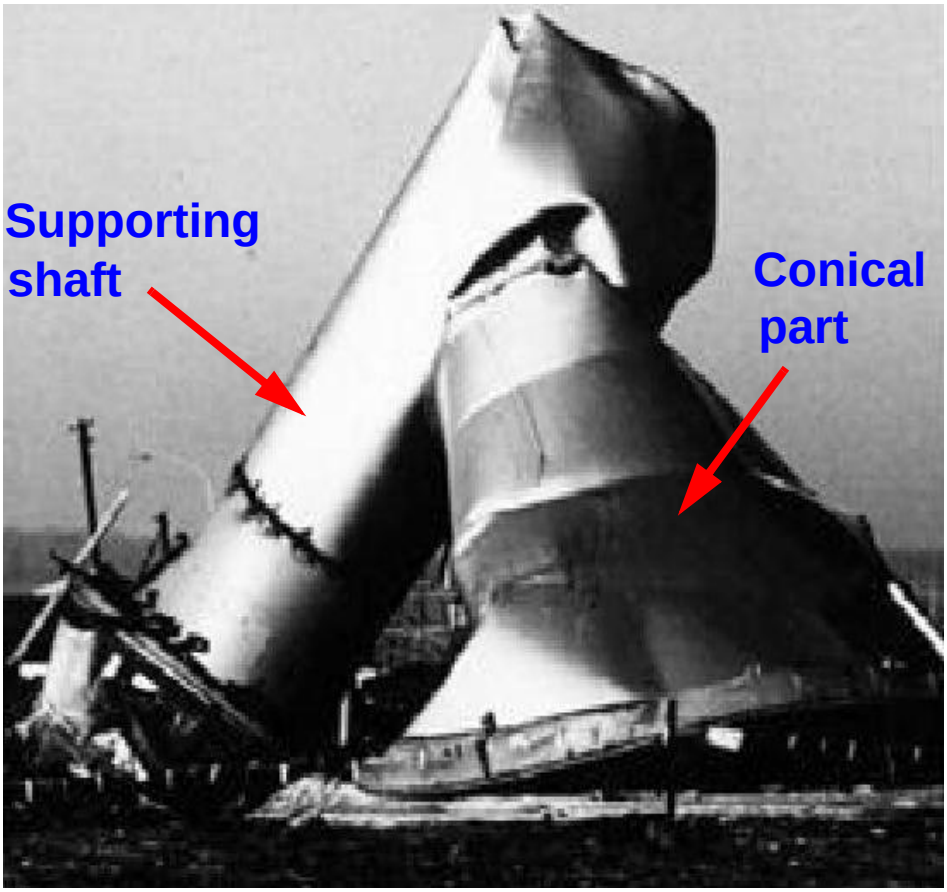

Figure 5.3 Collapsed steel water tower, 1972, Belgium

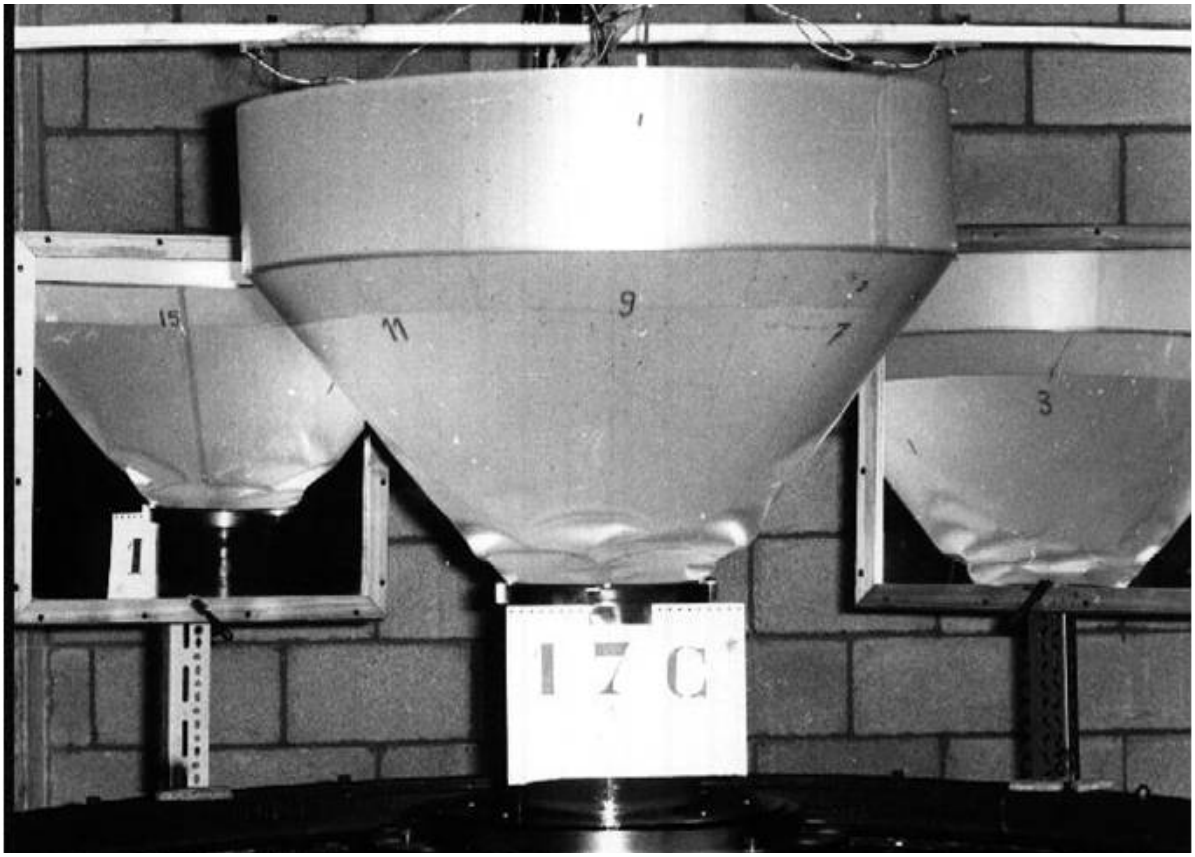

Figure 5.4 Gent laboratory experimental setup

5.2 Problem statement

With the help of the numerous Gent laboratory tests and numerical (using BOSOR) verifications D. Vandepitte *et. al.* proposed a design recommendation for the prediction of elastic buckling strengths of liquid-filled conical shells based on straight line bounds of all the test results from a doubly logarithmic ψ - ω plot.

The Gent proposal for the elastic carrying capacity of liquid-filled perfect and imperfect conical shells is given in terms of three equations of straight bounding lines. In a log-log representation of the Gent non-dimensional basic parameters ψ and ω, those straight lines are bounds for all (over 800) test data points irrespective of the very wide range of shell slenderness ratios, $r_1/t\cos\beta = 77 - 3760$. A series of researches have been made afterwards but most of them based on the straight line bounds already proposed. The same design proposal has also been used as a reference to compare other independent research results and failure cases with.

The shell slenderness, $r_1/t\cos\beta$ is a basic parameter that greatly affects the buckling strength of shells and plays the most important and decisive role in describing the load carrying behavior of shells.

It is, therefore, the primary purpose of this study to re-investigate and re-interpret the Gent test results in such a way that the resulting LFC-imperfection reduction factor, which directly is used in the prediction of the load carrying capacity of liquid-filled conical shells, takes the shell slenderness into account. A different set of LFC dimensionless parameters, including the shell slenderness parameter, will also be used in the investigation. Finally, a new elastic buckling design recommendation for liquid-filled conical shells will be proposed.

5.3 Liquid-filled conical shell parameters and representation

Basic non-dimensional system parameters

Parameter No. 1:

$$\frac{h'}{r_1}$$ liquid depth parameter

Parameter No. 2:

$$\tan\beta$$ cone apex angle parameter

Parameter No. 3:

$$\frac{r_1}{t\cos\beta}$$ shell slenderness parameter

Parameter No. 4:

$$\bar{p} = \frac{\sigma_{\theta,1}}{\sigma_{x,Rcr}} = 1.65\frac{\gamma' \cdot h'}{E} \cdot \left(\frac{r_1}{t\cos\beta}\right)^2$$ internal pressure parameter

Liquid surface level dimensionless variables

$$\zeta' = \frac{r_2' - r_1}{r_1} = \frac{h' \tan\beta}{r_1}$$

$$\rho' = \frac{r_2'}{r_1} = 1 + \zeta'$$

Running dimensionless variables

$$\zeta = \frac{r - r_1}{r_1} = \frac{z \tan\beta}{r_1}$$

$$\rho = \frac{r}{r_1} = 1 + \zeta$$

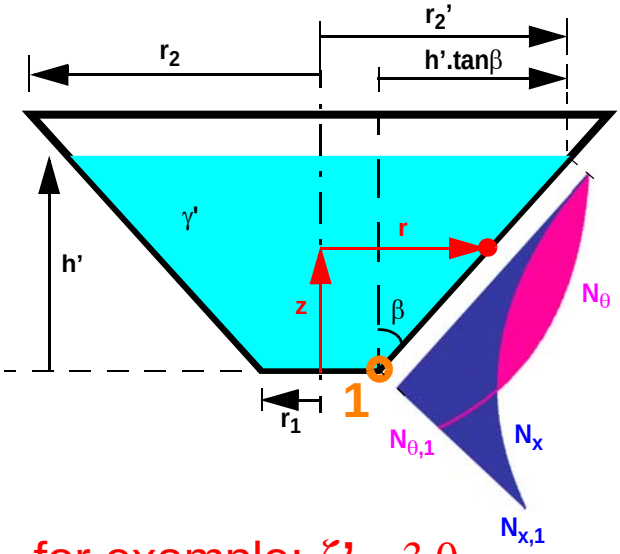

for example: $\zeta' = 3.0$

Membrane section forces

N_x ... Meridional membrane section force

N_θ ... Circumferential membrane section force

$N_{x,1}$ ... Meridional membrane section force at cone support

$N_{\theta,1}$ ... Circumferential membrane section force at cone support

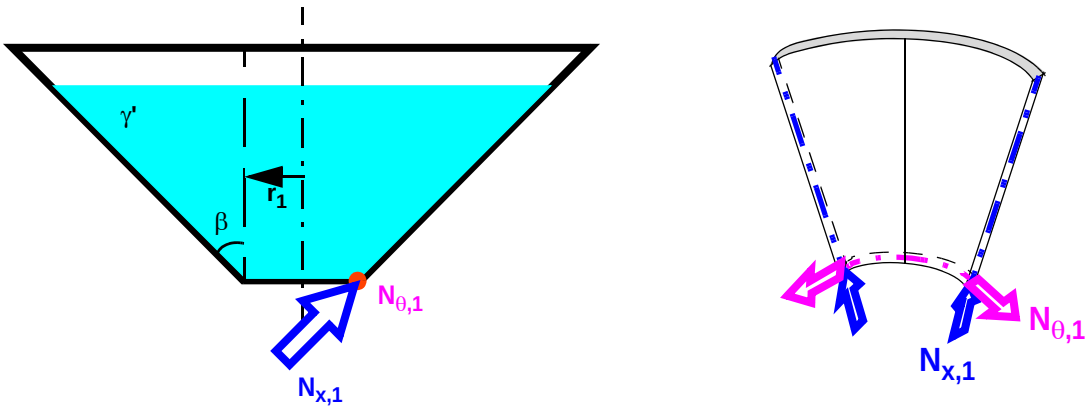

Figure 5.5 Demonstration of LFC variables and membrane section forces

Membrane section stress distributions

The meridional and circumferential membrane stresses along the meridian are given

- **as functions of the ρ and ρ' parameters**

$$\sigma_x = \frac{\gamma' h' r_1}{t\cos\beta} \cdot \frac{1}{6} \cdot \frac{(\rho' - \rho)^2}{\rho' - 1} \cdot \left(3 + \frac{\rho' - \rho}{\rho}\right) \quad \text{(Eq. 5.1)}$$

$$\sigma_\theta = \frac{\gamma' h' r_1}{t\cos\beta} \cdot \rho \cdot \left(\frac{\rho' - \rho}{\rho' - 1}\right) \quad \text{(Eq. 5.2)}$$

- **as functions of the ζ and ζ' parameters**

$$\sigma_x = \frac{\gamma' h' r_1}{t\cos\beta} \cdot \frac{1}{6} \cdot \frac{(\zeta' - \zeta)^2}{\zeta'} \cdot \left(3 + \frac{\zeta' - \zeta}{1 + \zeta}\right) \quad \text{(Eq. 5.3)}$$

$$\sigma_\theta = \frac{\gamma' h' r_1}{t\cos\beta} \cdot (1 + \zeta) \cdot \left(\frac{\zeta' - \zeta}{\zeta'}\right) \quad \text{(Eq. 5.4)}$$

Membrane section stresses at cone support

$$r = r_1 \qquad \Rightarrow \rho = 1; \qquad \zeta = 0 \quad \text{(Eq. 5.5)}$$

$$\sigma_{x,1} = \frac{\gamma' h' r_1}{t\cos\beta} \cdot \frac{1}{6} \cdot \zeta' \cdot (3 + \zeta') \quad \text{(Eq. 5.6)}$$

$$\sigma_{\theta,1} = \frac{\gamma' h' r_1}{t\cos\beta} \quad \text{(Eq. 5.7)}$$

The membrane section forces can be computed from the product of the thickness of the shell and the respective membrane stress, i.e.

$$N_x = t \cdot \sigma_x; \qquad N_\theta = t \cdot \sigma_\theta \quad \text{(Eq. 5.8)}$$

Figure 5.6 and Figure 5.7 show the meridional and circumferential membrane section force distributions, respectively, along the meridian normalized with respect to the circumferential membrane section force at the cone support, $N_{\theta,1}$. In each plot the liquid depth variable, ρ' is varied to produce a set of curves. For better understanding of different liquid-filling depths and corresponding parameters, see Figure 4.9.

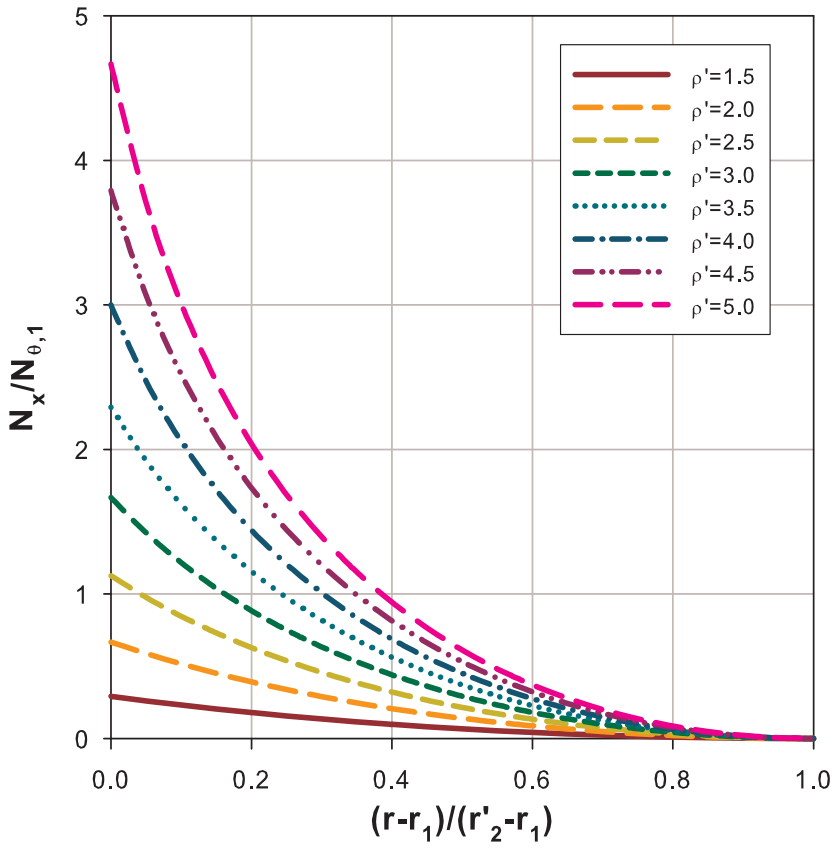

Figure 5.6 Meridional membrane section force distribution along the meridian

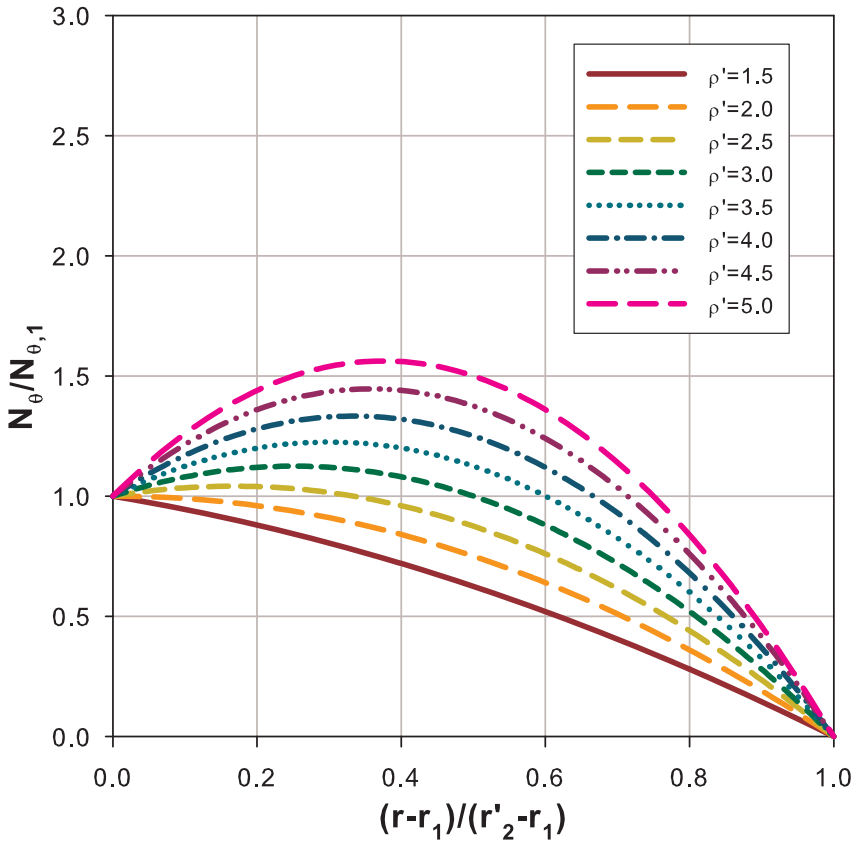

Figure 5.7 Circumferential membrane section force distribution along the meridian

Elastic imperfection reduction factors

In accordance to the frame work of the European standard EN 1993-1-6, the elastic imperfection reduction factor (a factor applied to the linear bifurcation buckling strength of a perfect shell to account for geometric imperfections and the effect of geometric nonlinearity) of cylindrical and conical shells subjected to meridional compression with/without co-existent internal pressure has been discussed in chapter-3 and chapter-4.

Figure 5.8 shows cylindrical and conical shells with different loading situations where the discussion on the pressurized or unpressurized elastic imperfection reduction factor can be applied. Figure 5.9 shows a plot of α_{xpe} vs. $\overline{p}$ for different shell slenderness, $r_1/t\cos\beta$, values ranging from 100 (upper most curve) to 3500 (lower most curve) and assuming fabrication tolerance quality class C.

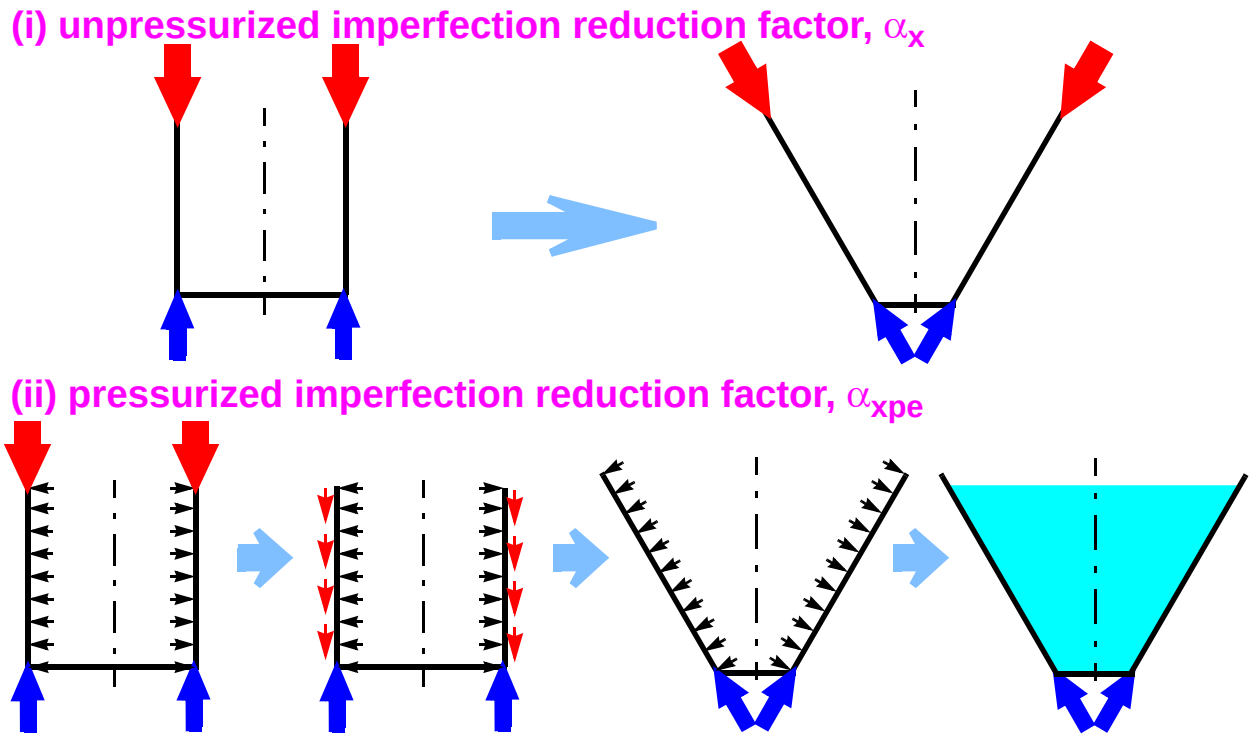

Figure 5.8 Cylindrical and conical shells with and without co-existent internal pressure

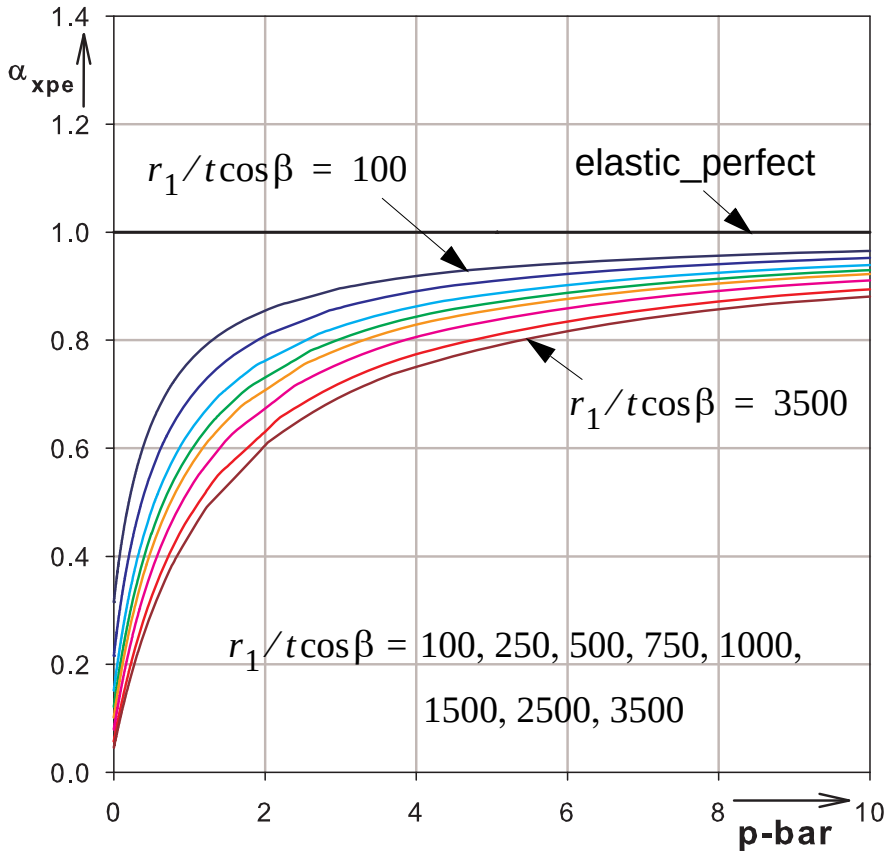

Figure 5.9 Elastic-imperfect characteristic buckling strengths of conical shells

5.4 Fluid-filled conical shells: comparison of gas-filled vs. liquid-filled conical shells

The susceptibility of fluid-filled conical (FFC) shells to buckling depends on the magnitude of the stabilizing effect of the circumferential tensioning as a result of internal pressurization. The internal pressurization may be uniform along the meridional length of the shell as in the gas-filled conical (GFC) shells or may vary linearly as in the hydrostatic pressure distribution of liquid-filled conical (LFC) shells. A comparison between the GFC and LFC shells has been made as follows.

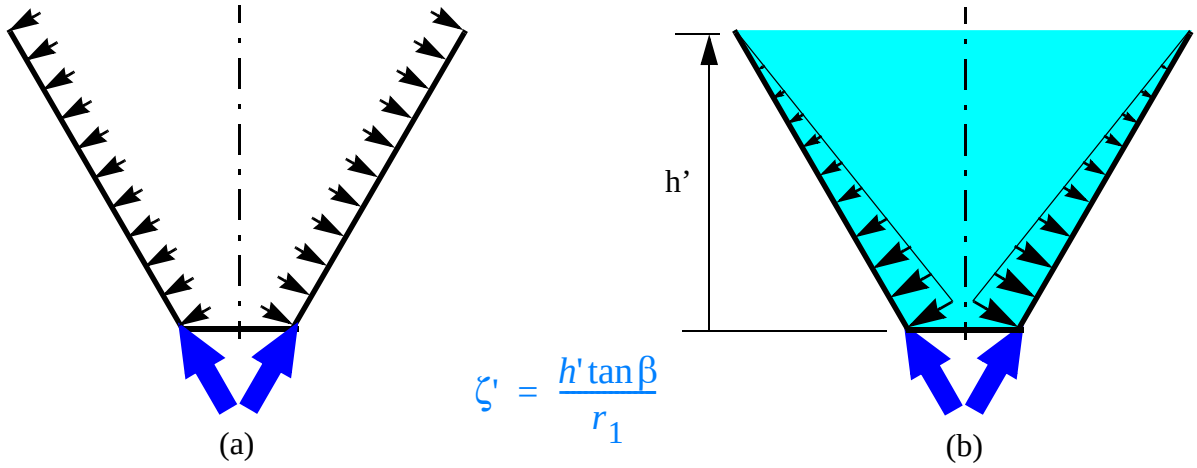

Figure 5.10 (a) GFC; (b) LFC

The membrane circumferential, $\sigma_{\theta,1}$ and meridional, $\sigma_{x,1}$ stresses at the bases of the cones can easily be calculated from membrane theory and are given by

- **LFC (hydrostatic internal pressure) case**

$$\sigma_{\theta,\,1,\,LFC} = \frac{\gamma' h' r_1}{t\cos\beta} \qquad \text{(Eq. 5.9)}$$

$$\sigma_{x,\,1,\,LFC} = \sigma_{\theta,\,1} \cdot \bar{\psi}_{LFC} \qquad \text{(Eq. 5.10)}$$

$$\bar{\psi}_{LFC} = \frac{\zeta'}{6}(3 + \zeta') \qquad \text{(Eq. 5.11)}$$

- **GFC (gas/uniform internal pressure) case**

$$\sigma_{\theta,\,1,\,GFC} = \frac{p r_1}{t\cos\beta} \qquad \text{(Eq. 5.12)}$$

$$\sigma_{x,\,1,\,GFC} = \sigma_{\theta,\,1} \cdot \bar{\psi}_{GFC} \qquad \text{(Eq. 5.13)}$$

$$\bar{\psi}_{GFC} = \frac{\zeta'}{2}(2 + \zeta') \qquad \text{(Eq. 5.14)}$$

The comparison between the above two cone loading situations can be done in two different ways as discussed below.

1. For a reference meridional membrane stress at cone-base:

To produce the same meridional membrane stress, $\sigma_{x,1}$ at the base of the cone, the relationship between the intensities of the internal pressure at the cone-base for the two loading situations will be given as follows:

$$\sigma_{x,\,1} = \sigma_{x,\,1,\,LFC} = \sigma_{x,\,1,\,GFC}$$

$$\Rightarrow \quad \frac{\gamma' h' r_1}{t\cos\beta} \cdot \frac{\zeta'}{6}(3 + \zeta') = \frac{p r_1}{t\cos\beta} \cdot \frac{\zeta'}{2}(2 + \zeta') \qquad \text{(Eq. 5.15)}$$

$$\Rightarrow p = \frac{1}{3}\left(\frac{3 + \zeta'}{2 + \zeta'}\right) \cdot \gamma' h' \qquad \begin{matrix} \rightarrow \lim\limits_{\zeta' \to 0} p = \dfrac{\gamma' h'}{2} \\ \rightarrow \lim\limits_{\zeta' \to \infty} p = \dfrac{\gamma' h'}{3} \end{matrix} \qquad \text{(Eq. 5.16)}$$

This means, when compared at the cone base, a lesser uniform internal pressure, p is required to produce the same meridional stress than the corresponding hydrostatic pressure, γ'h' showing that a lesser stabilizing effect in the GFC case due to a lesser circumferential tensioning than in the LFC case (see Figure 5.11a).

2. For a reference circumferential membrane stress at cone-base:

To produce the same circumferential membrane stress, $\sigma_{\theta,1}$ at the base of the cone, the relationship between the intensities of the internal pressure at the cone-base for the two loading situations will be given as follows:

$$\sigma_{\theta,\,1} = \sigma_{\theta,\,1,\,LFC} = \sigma_{\theta,\,1,\,GFC}$$

$$\Rightarrow \quad \frac{\gamma' h' r_1}{t\cos\beta} = \frac{p r_1}{t\cos\beta} \qquad \text{(Eq. 5.17)}$$

$$\Rightarrow p = \gamma' h' \qquad \text{(Eq. 5.18)}$$

When compared at the cone base, they both have the same stabilizing effect due to circumferential tension but, at the same time, the GFC case produces a higher meridional compressive stress which

makes the conical shell prone to buckling failure (see Figure 5.11b).

In both the above cases, one can see that under similar conditions of material properties, boundary conditions, imperfection types and amplitudes, and low to medium internal pressure magnitudes the GFC case is the favorable loading situation for buckling to happen.

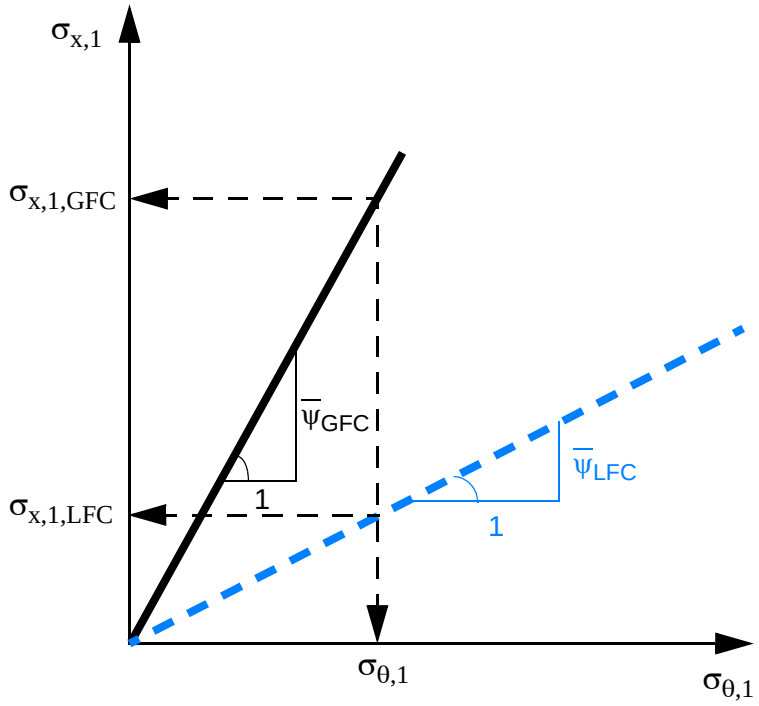

(a)

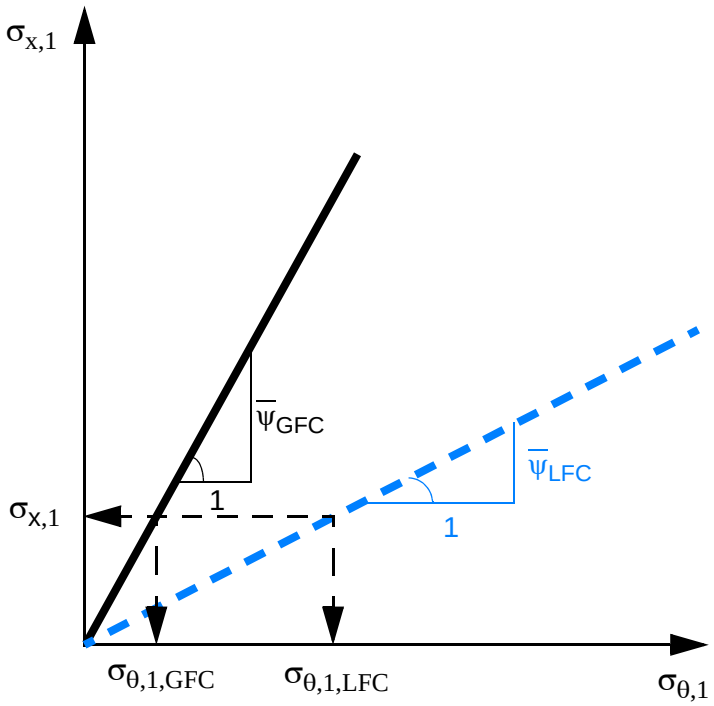

(b)

Figure 5.11 $\sigma_{x,1}$ vs. $\sigma_{\theta,1}$ plots: (a) same stabilizing effect; (b) same meridional compression at cone-base

5.5 Test results and Gent University design proposal

Hundreds of model cones have been tested at Gent university with the following general setup. All models were loaded by increasing the liquid depth until they collapsed. A detailed summary of all the tests performed, including the rejected ones, is presented in Table 5.1. A complete information, in addition to the summary in Table 5.1, of all the tests (i.e. material properties, loading situations, and boundary conditions) are given below:

- **Materials used**
  Aluminium, Steel, Brass, and Mylar
- **Liquid loading**
  Water, water with molasses (1.333 to 1.362 times heavier than water), water with barium sulfate suspension (1.950 to 2.075 times heavier than water), and mercury
- **Bottom boundary conditions**
  Simple sliding, Simple support, and clamped

Test procedure, test data recording, test data analysis and interpretation

The overall step-by-step procedure that has been followed during testing, test data recording, test data analysis and interpretation of the Gent laboratory tests can be put as follows:

- What was known before testing?

  cone geometry, liquid property, boundary condition, cone material properties, and imperfection amplitudes

- What types of imperfection shapes were considered, how were they produced, and how were the amplitudes measured?

  The imperfections considered were of arbitrary shapes as the imperfect cones used for testing were the already tested (collapsed) cones by straightening out the buckles from previous tests. The imperfection amplitudes were measured as the largest inward depression of the unloaded test cone from a straight rod of length $l = 3.6\sqrt{r_1 t / \cos\beta}$ placed against the generatrices in the lower $20\sqrt{r_1 t / \cos\beta}$ part of the cone.

- How was the liquid-loading applied and what was measured during testing?

  the liquid-depth was gradually increased until collapse occurs and the ultimate liquid depth, h'_U at which collapse happens was recorded

- What was computed after testing?

  the meridional membrane normal stress at the base of the cone corresponding to the ultimate liquid depth, h'$_U$

$$\sigma_{x,\,1,\,U} = \frac{\gamma' h'^2_U \tan\beta}{6t\cos\beta} \cdot \left(3 + \frac{h'_U \tan\beta}{r_1}\right) \qquad \text{(Eq. 5.19)}$$

- How were the test data analyzed?

  A big scatter of test data was obtained for which non-dimensional analyses were done and finally two non-dimensional basic parameters, ω and ψ were used for representing each test data. The ω parameter for each test, however, depends purely on the geometric, liquid, and cone material properties and therefore it was known before performing the test. The ψ parameter, on the other hand, was computed using the data obtained from the test, (Eq. 5.21).

$$\omega = \frac{1000 \cdot r_1}{t \cdot \cos\beta} \cdot \sqrt{\frac{\gamma' \cdot r_1}{E}\sqrt{1-\nu^2}} = \sqrt{\frac{\sigma_{\theta,\,1,\,U}}{\sigma_{x,\,Rcr}} \cdot \frac{1}{\sqrt{3}\cdot 10^{-6}} \cdot \left(\frac{r_1}{h'_U}\right)} \qquad \text{(Eq. 5.20)}$$

$$\psi = \sigma_{x,\,1,\,U} \cdot \frac{t \cdot \cos\beta}{\gamma' \cdot r_1^2} = \frac{\sigma_{x,\,1,\,U}}{\sigma_{\theta,\,1,\,U}} \cdot \left(\frac{h'_U}{r_1}\right) \qquad \text{(Eq. 5.21)}$$

- How were the scatter of the test data interpreted and what was deduced?

  All the test data, which were approved to be with no setup faults, were plotted together on a log-log scale of ψ vs. ω plot so that the scatter band is reasonably narrow for bounding curves to be applied (see Figure 5.12). Three straight bounding lines were chosen, two lower straight-line bounds for two different imperfection amplitude ranges, poor and good cones, and an upper straight-line bound for perfect cones (see Figure 5.13). The general mathematical expressions for these bounding lines are given in the linear-linear and log-log writing, respectively, by

$$\psi = b \cdot \omega^{-d} \qquad \text{(Eq. 5.22)}$$

$$\log\psi = \log b - d \cdot \log\omega \qquad \text{(Eq. 5.23)}$$

No.	Classification based on	types used	number of tests made	total	Remark
1	material type	Aluminium	45	811	
		Steel	132		
		Brass	77		
		Mylar	557		
2	bottom boundary condition	simple	627	811	
		simple sliding	146		all with in 20° - 60°
		clamped	37		
		?	1		
3	apex half angle, β	10°	39	811	(1) Mylar only (2) very big imperfection amplitudes
		20° - 60°	727		
		75°	45		(1) Mylar only (2) very small imperfection amplitudes
4	test evaluation by Gent	accepted	768	811	
		rejected	43		
5	reason for test refusal (for the rejected tests)	cone failed sideways (out of conicity)	22	43	(i) 16 have sliding bottom boundary condition (ii) relatively narrow base and high $h'\tan\beta/r_1$
		cone failed within the supporting device	10		
		cone with overlapping meridional seam in the critical zone	4		
		faulty test setup	7		

Table 5.1 Summary of Gent test data

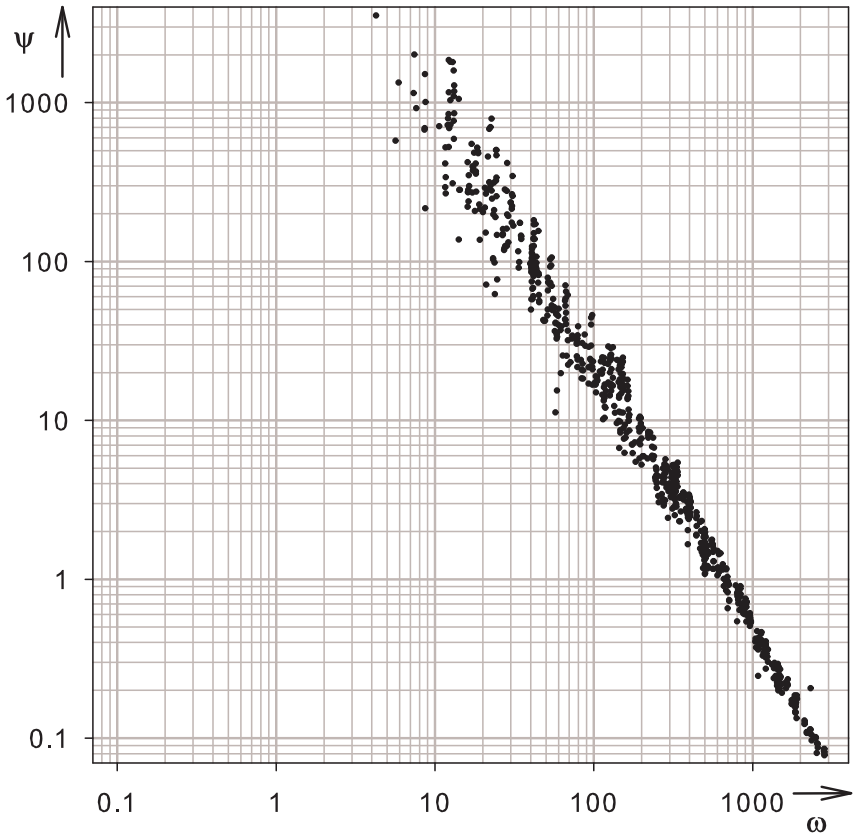

Figure 5.12 Log-Log plot of the test data points

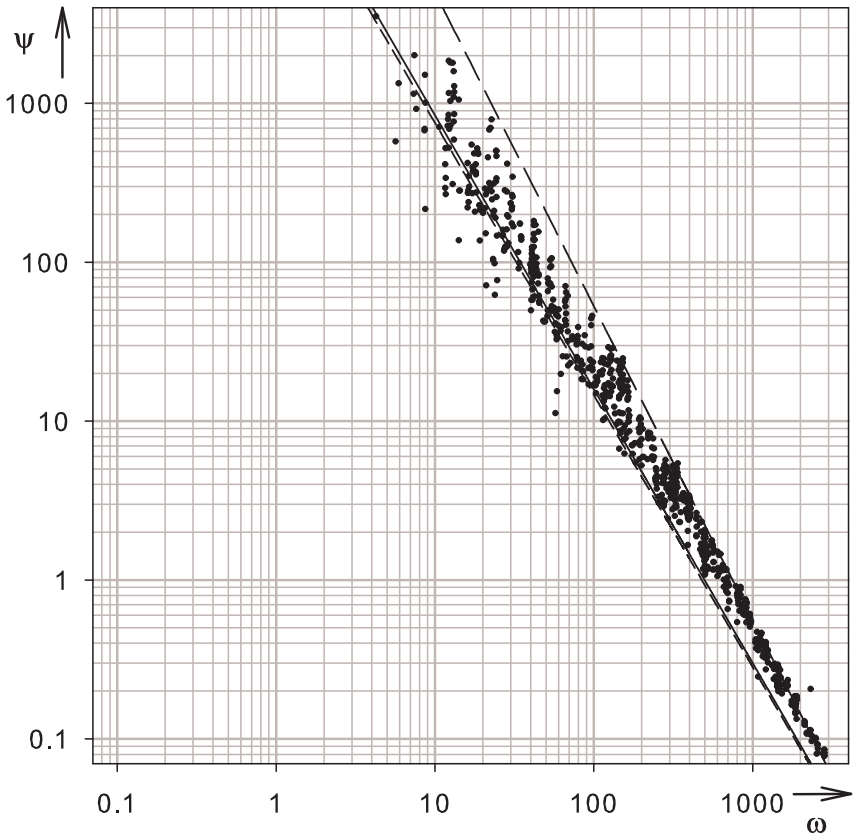

Figure 5.13 Log-Log plot of the test data points and Gent-bounding straight lines

Imperfection amplitudes and quality classes

The three straight bounding lines which represent the three quality classes (perfect, good, and poor) according to Gent nomenclature depends on the Gent imperfection amplitude parameter, $\overline{w}$ of the conical shell as given in Table 5.2.

The Gent imperfection amplitude parameter, $\overline{w}$, is the largest inward depression of the unloaded test cone from a straight rod of length $l = 3.6\sqrt{r_1 t / \cos\beta}$ placed against the generatrices in the lower $20\sqrt{r_1 t / \cos\beta}$ part of the cone. It is given in terms of another recorded parameter, "IMP" in %, which is related to the length of the straight rod as follows:

$$\overline{w} = \frac{l \cdot IMP}{100} \qquad \text{(Eq. 5.24)}$$

Quality class name	Imperfection amplitude parameter, $\overline{w}$
Perfect cones	0
Good cones	$\overline{w} \le 0.008 l$
Poor cones	$0.008\ \ l < \overline{w} \le 0.02 l$

Table 5.2 Gent quality class naming & imperfection amplitude values

Gent design proposal

The final design proposal by Vandepitte *et. al.* based on the scatter band of the test results from the doubly logarithmic plot, Figure 5.13, is expressed in terms equations of the bounding straight lines. These equations, for the different quality classes can be re-written in the doubly linear and doubly logarithmic way of writing as follows:

In a linear - linear representation, the equations of the three straight bounding lines are given by

$\psi = 471250 \cdot \omega^{-1.974}$ for '**perfect**' cones (Eq. 5.25)

$\psi = 44620 \cdot \omega^{-1.724}$ for ' **good**' cones (Eq. 5.26)

$\psi = 39030 \cdot \omega^{-1.713}$ for '**poor**' cones (Eq. 5.27)

In a log - log representation, the equations of the three straight bounding lines are given by

$\log\psi = 5.673 - 1.974 \cdot \log\omega$ for '**perfect**' cones (Eq. 5.28)

$\log\psi = 4.650 - 1.724 \cdot \log\omega$ for ' **good**' cones (Eq. 5.29)

$\log\psi = 4.591 - 1.713 \cdot \log\omega$ for '**poor**' cones (Eq. 5.30)

The test data points and Gent bounding straight-lines are re-plotted on a linear-linear scale (see Figure 5.14) to show the role of the scale type used on the graphical representation. For comparison purposes, the same bounding curves are plotted for h'/r_1 values of 2.0 and 8.0 (see Figure 5.15) in the α_{xpe} vs. $\overline{p}$ representation, together with the family of LFC curves (slenderness ratios of 100-3500).

Before going to the detailed investigation of the test results, a rough look at the data points in the different representations is important. For example, the following basic questions can be raised only from a qualitative look at the plot in Figure 5.15:

- **What is really going on at the very small pressure values?**
- **Why is there a wide gap between the LFC curves and the Gent curves for medium pressure values?**
- **What happens at high pressure values where an elastic-plastic interaction is expected?**

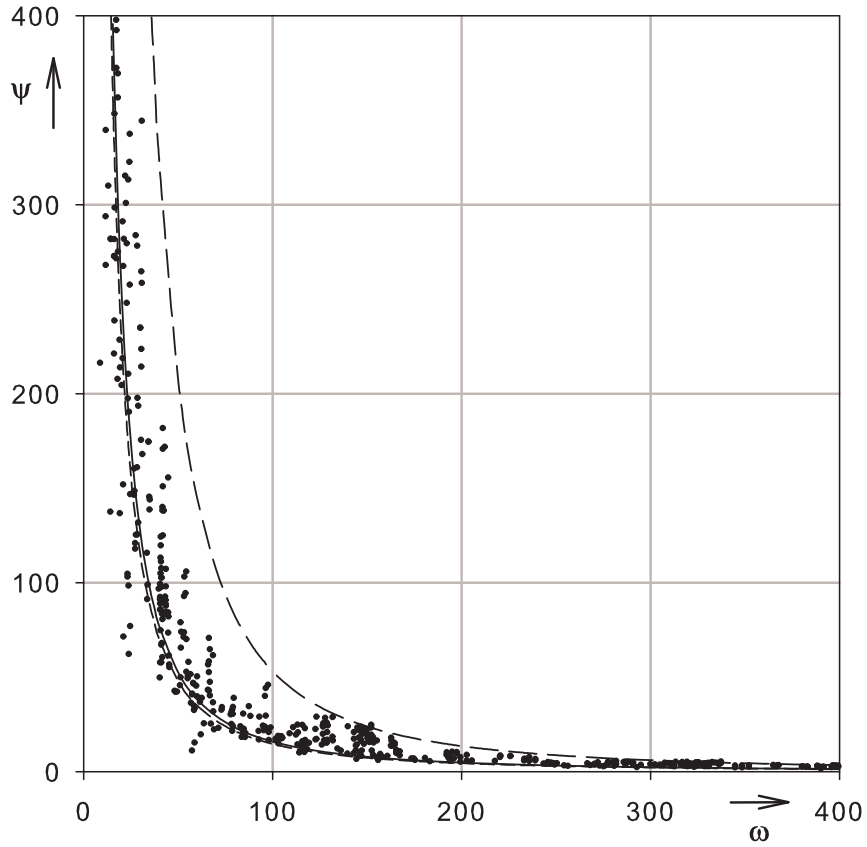

Figure 5.14 Linear-Linear plot of the test data points and Gent-bounding straight lines

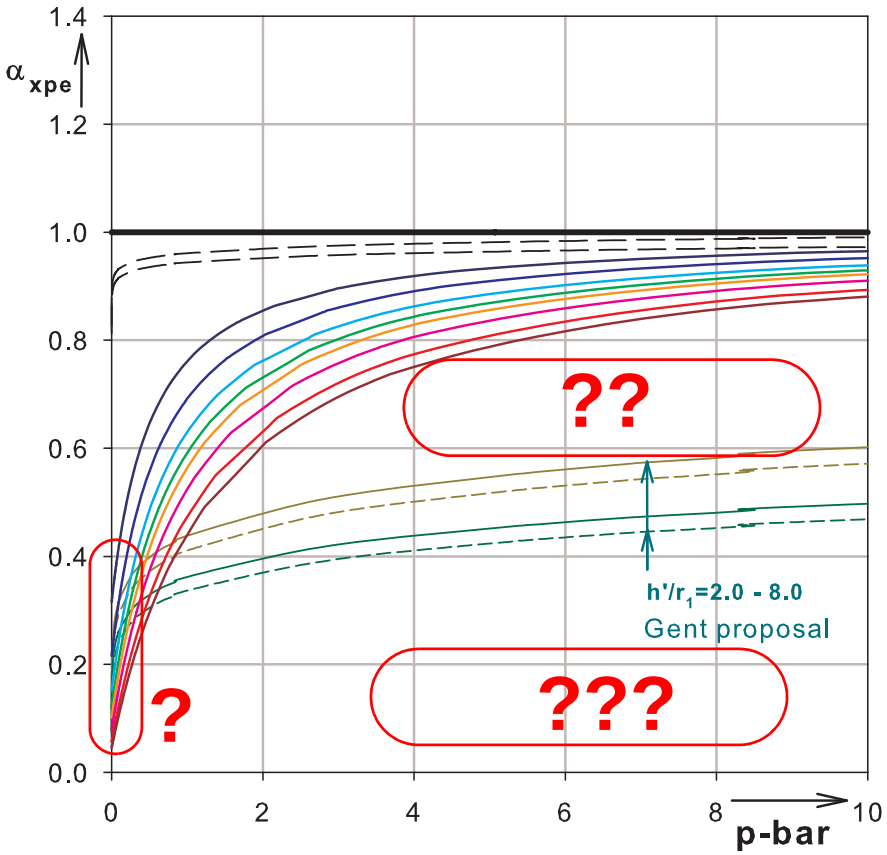

Figure 5.15 Qualitative comparison of LFC and Gent curves

5.6 Comparison of parameter choices and representations

A comparison of the parameters chosen in the two different representations, namely α_{xpe} vs. $\bar{p}$ and ψ vs. ω, has been made in the current work. Both qualitative and quantitative (mathematical) comparisons were made. The qualitative similarities and exact relationships between these parameters are explained below.

- **Proportionality relationships (for a given h'/r_1)**

$$\bar{\psi} \propto \psi \quad \text{(Eq. 5.31)}$$

$$\alpha_{xpe} \propto \psi \cdot \omega^2 \quad \text{(Eq. 5.32)}$$

$$\bar{p} \propto \omega^2 \quad \text{(Eq. 5.33)}$$

which show that the LFC $\bar{\psi}$ and Gent ψ parameters are linearly related to each other; whereas the LFC parameters α_{xpe} & $\bar{p}$ are nonlinearly related to the Gent parameters ψ & ω, respectively.

- **Mathematical relationships between the different scaling and parameters used**

The mathematical relationships between the LFC $\bar{\psi}$, α_{xpe} & $\bar{p}$ parameters and Gent ψ & ω parameters are discussed below. These relationships will later be used for the transfer of comparative curves from the Gent log-log plot to the LFC α_{xpe} - $\bar{p}$ log-log and linear-linear plots and vise versa.

Linear-linear relationship:

$$\bar{\psi} = \frac{\psi}{(h'_U / r_1)} \quad \text{(Eq. 5.34)}$$

$$\alpha_{xpe} = \sqrt{3} \cdot 10^{-6} \psi \omega^2 \quad \text{(Eq. 5.35)}$$

$$\bar{p} = \frac{\alpha_{xpe}}{\bar{\psi}} = \frac{\sqrt{3} \cdot 10^{-6} \psi \omega^2}{\psi / (h'_U / r_1)} = \sqrt{3} \cdot 10^{-6} \frac{h'_U}{r_1} \omega^2 \quad \text{(Eq. 5.36)}$$

Log-log relationship:

$$\begin{bmatrix} \log\alpha_{xpe} \\ \log\bar{p} \end{bmatrix} = \begin{bmatrix} 1 & 1 \\ 0 & 1 \end{bmatrix} \begin{bmatrix} \log\psi \\ 2\log\omega \end{bmatrix} + \log\left(\frac{h'_U}{r_1}\right) \cdot \begin{bmatrix} 0 \\ 1 \end{bmatrix} - 5.761 \begin{bmatrix} 1 \\ 1 \end{bmatrix} \qquad \text{(Eq. 5.37)}$$

Showing a non-linear relationship between the corresponding linear-linear representations and a linear relationship between the corresponding log-log representations. It can be seen from the linear-linear relationship that a pre-specified value for h'_U/r_1 is needed to directly compare two corresponding parameters from the different representations.

What are not OK with the Gent proposal & what should be re-investigated?

Figure 5.16 shows a plot of the LFC family of curves, all test data points, and Gent bounding curves in the α_{xpe} - $\bar{p}$ representation. The following list of questions can be raised by just having a rough look at this plot, see Figure 5.17. Brief remarks are also included for each question on how each issue has been addressed and re-investigated in this study.

- **What is happening at the zero-pressure (tip-loading) or small-pressure (very high liquid depth) situation?**

  a closer look at the small pressure levels has been done.

- **Why are there NO data points in the central α_{xpe} - $\bar{p}$ region, between the LFC family of curves and Gent bounding curves? BIG SURPRISE!!**

  a detailed investigation on the Gent original data, their parameter representation, and scaling applied has been done

- **What will happen at higher pressure values where elastic-plastic type buckling phenomenon is expected?**

  a detailed study on elephant's-foot type buckling has been done

- **Why are there so many data points above the α_{xpe} = 1.0 line?**

  a detailed study on buckling nature of LFC shells has been done

- **Why are the very wide shell-slenderness ranges mixed all up in one?**

  detailed view at the data by considering the $r_1/t\cos\beta$ - dependency has been done, i.e. a check if slenderness ratio related data points are really above their corresponding buckling curves was done

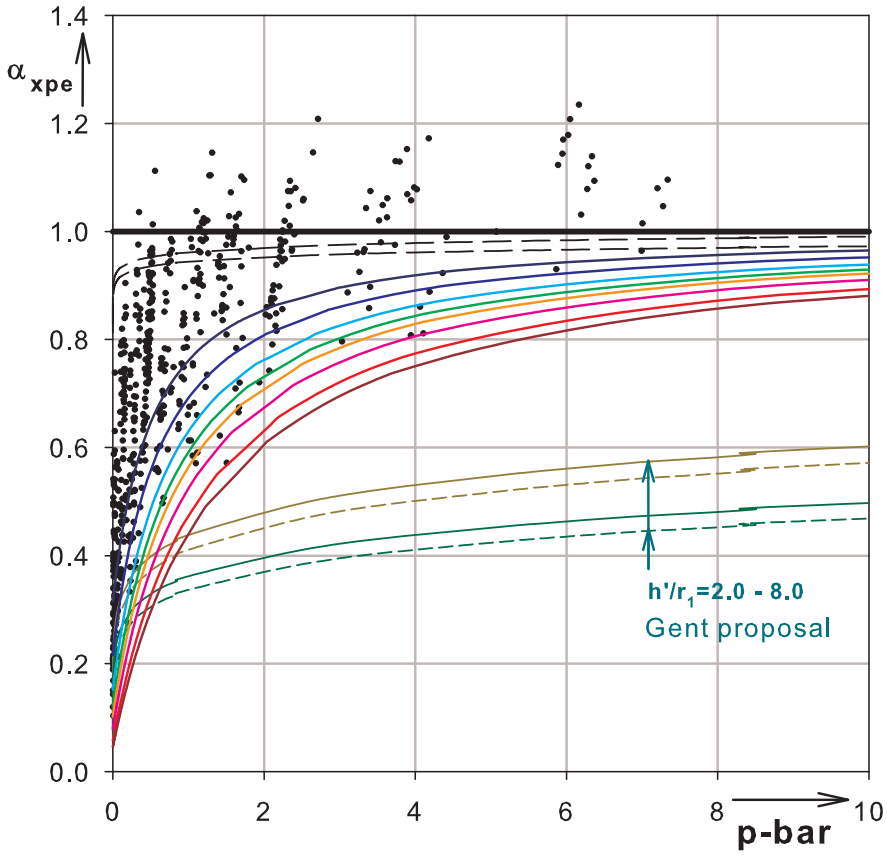

Figure 5.16 LFC curves, test data points and Gent bounding curves

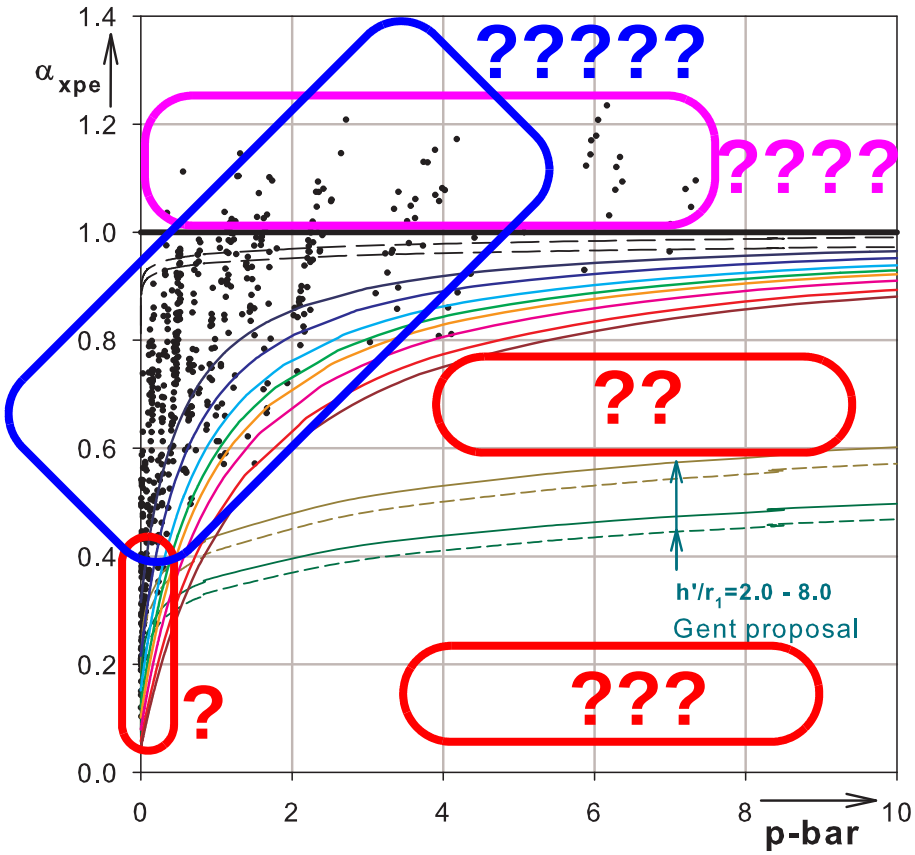

Figure 5.17 Comparison of LFC curves, test data points & Gent bounding curves

Basic demonstration: same curves in different representations

For basic demonstration and easy comparison purposes of the α_{xpe} - $\bar{p}$ linear-linear and ψ - ω log-log representations, a step-by-step procedure has been followed. The overall idea here is to see and compare how curves and data points are represented in the two different plot types. Following is an overview of what has been done:

1 The α_{xpe} - $\bar{p}$ plot of the LFC curves, all test data points, and Gent bounding curves is, once again, shown in Figure 5.18. The same curves and test data points are also shown on ψ - ω log-log plot, Figure 5.19.

2 A single curve (with a slenderness ratio of 2500), out of the family of LFC curves (see Figure 5.20 and Figure 5.21), is considered for detailed comparison of the two different representations (see Figure 5.22 and Figure 5.23) for $h'/r_1 = 2.0$

3 Analytic derivation of different illustrative curve types and their slopes in the two different representations are shown in (Eq. 5.38) to (Eq. 5.65). More details about the curve types illustrative curve types considered will come later.

4 Step-by-step plots of the different curves considered and their explanations are listed below. The Gent bounding curves are plotted for $h'/r_1 = 2.0$

Figure 5.24 & Figure 5.25 show the curve for $r_1/t\cos\beta = 2500$ and its lower limit line

Figure 5.26 & Figure 5.27 include an upper limit line

Figure 5.28 & Figure 5.29 include a tangent line, line-1, to the $r_1/t\cos\beta = 2500$ curve at $\bar{p} = 0$

Figure 5.30 & Figure 5.31 include a second tangent line, line-2

Figure 5.32 & Figure 5.33 include a third tangent line, line-3

Figure 5.34 is same as Figure 5.32 but on a log-log scale and Figure 5.35 same as Figure 5.33

Figure 5.36 & Figure 5.37 include $r_1/t\cos\beta = 100$ curve and show log-log representations of both α_{xpe} - $\bar{p}$ and ψ - ω

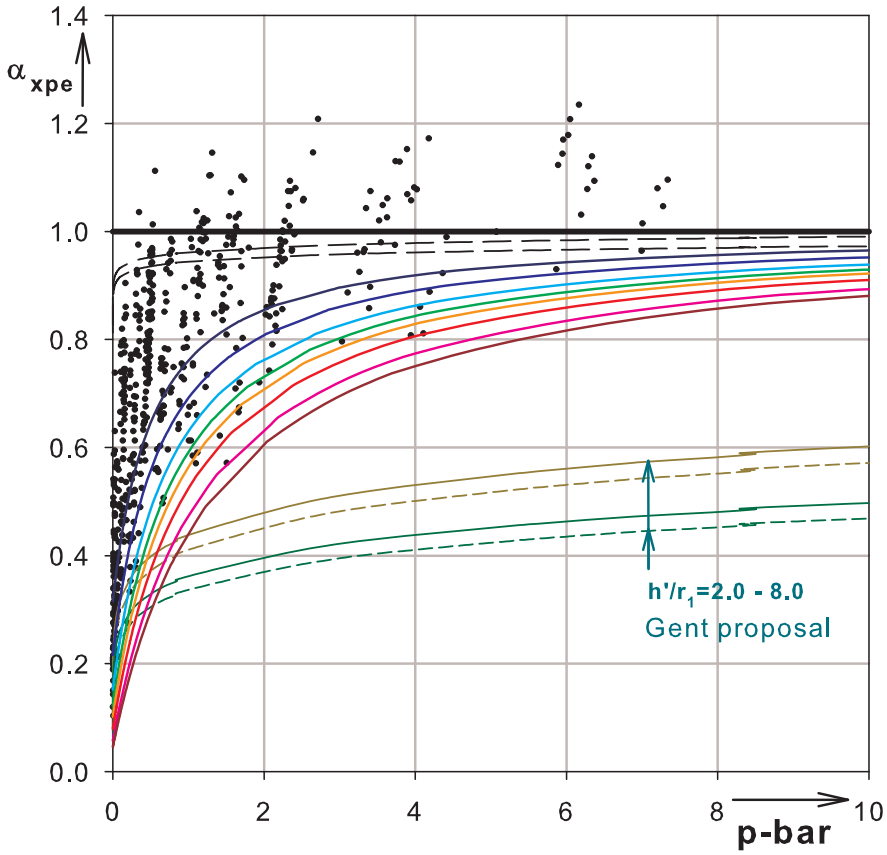

Figure 5.18 Linear-linear plot: LFC curves, test data points and Gent bounding curves

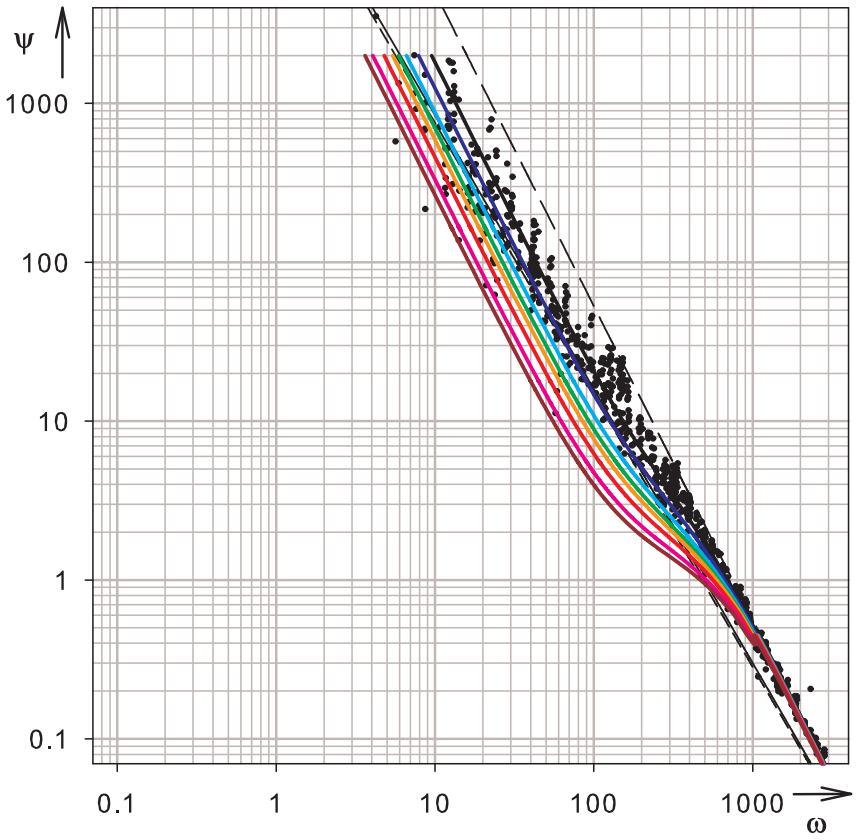

Figure 5.19 Log-log plot: LFC curves, test data points and Gent bounding curves

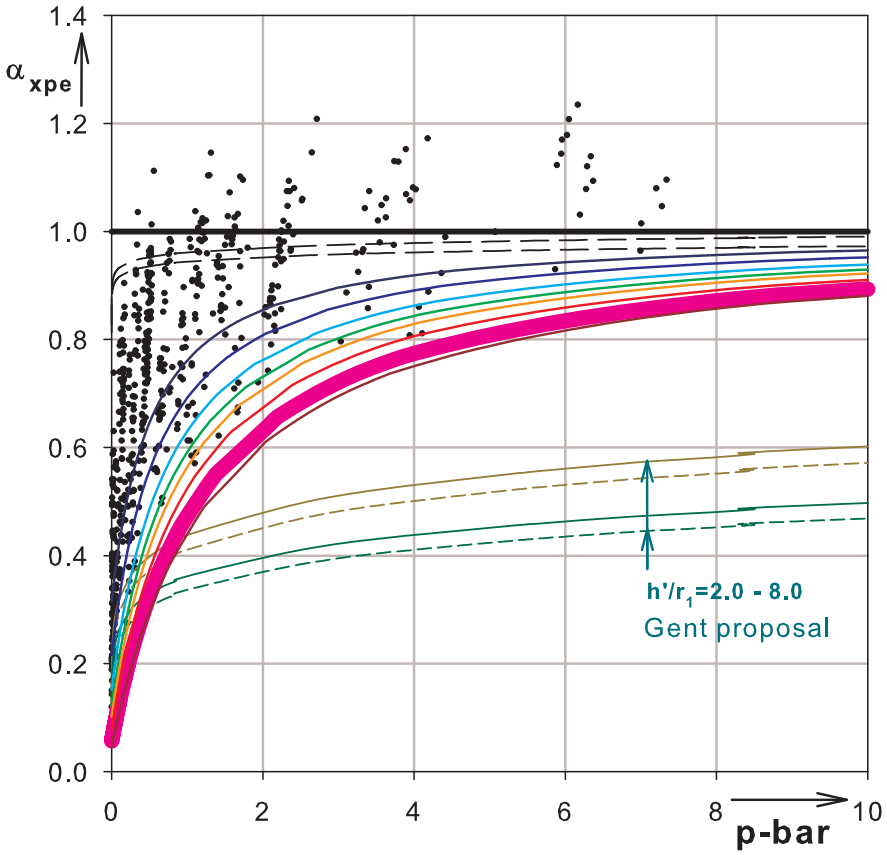

Figure 5.20 Linear-linear plot: picking out a single curve for comparison purposes

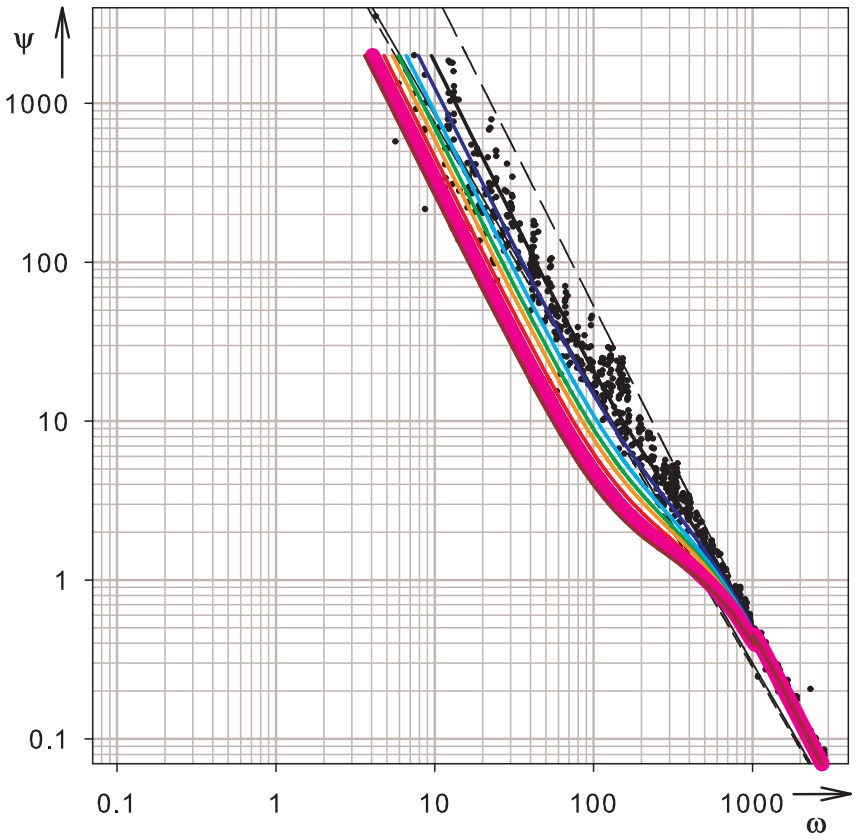

Figure 5.21 Log-log plot: picking out a single curve for comparison purposes

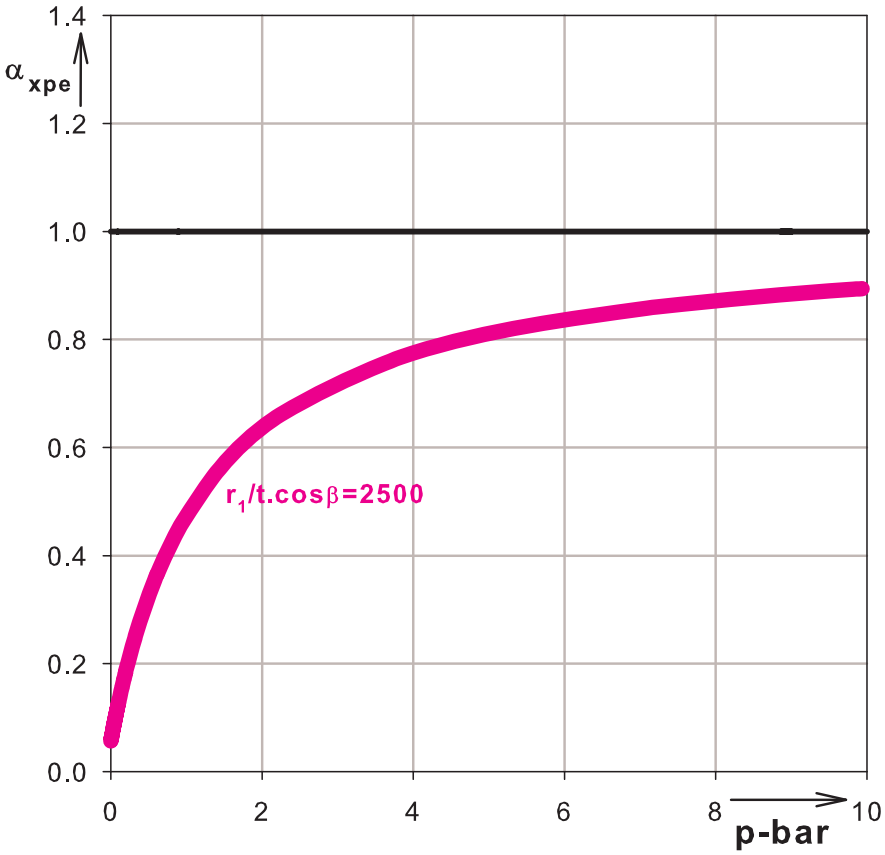

Figure 5.22 LFC linear-linear plot: curve selected for comparison

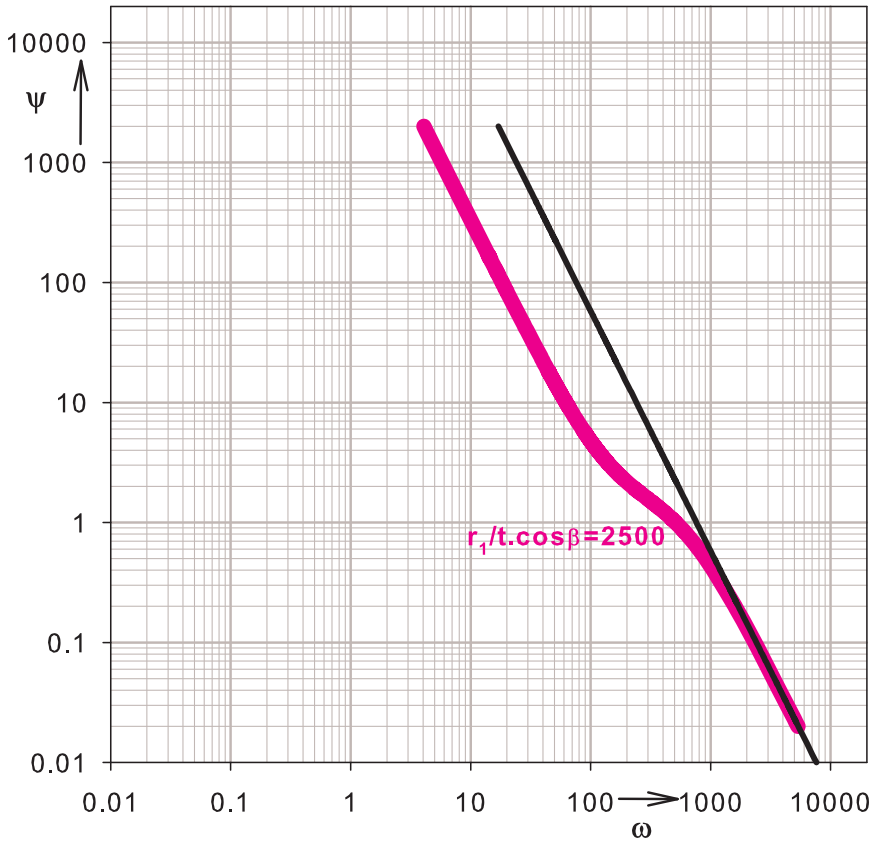

Figure 5.23 Gent log-log plot: curve selected for comparison

Analytic derivation of curves and slopes in different representations

As it has already been explained previously, for a better understanding and easy comparison of the LFC and Gent representations, different types of illustrative curves and corresponding slopes are considered. Both analytic and graphical representations of the curves and their slopes are shown below.

1. **Curve type-1:** $\alpha_{xpe} = C$ = constant ... independent of the internal pressure parameter, $\bar{p}$

α_{xpe} vs $\bar{p}$ in linear - linear representation:

$$\alpha_{xpe} = C = constant \quad \text{(Eq. 5.38)}$$

$$slope = \frac{\partial \alpha_{xpe}}{\partial \bar{p}} = 0 \quad \text{(Eq. 5.39)}$$

α_{xpe} vs $\bar{p}$ in log - log representation:

$$\log \alpha_{xpe} = \log C = constant \quad \text{(Eq. 5.40)}$$

$$slope = \frac{\partial \log \alpha_{xpe}}{\partial \log \bar{p}} = 0 \quad \text{(Eq. 5.41)}$$

ψ vs ω in log - log representation:

$$\log \psi = \log\left(\frac{C}{\sqrt{3} \cdot 10^{-6}}\right) - 2 \cdot \log \omega \quad \text{(Eq. 5.42)}$$

$$slope = \frac{\partial}{\partial \log \omega} \log \psi = -2 \quad \text{(Eq. 5.43)}$$

2. **Curve type-2:** $\alpha_{xpe} = \alpha_o + k \cdot \bar{p}$ ... linear function of the internal pressure parameter, $\bar{p}$

α_{xpe} vs $\bar{p}$ in linear - linear representation:

$$\alpha_{xpe} = \alpha_o + k \cdot \bar{p} \qquad \text{(Eq. 5.44)}$$

$$slope = \frac{\partial \alpha_{xpe}}{\partial \bar{p}} = k \qquad \text{(Eq. 5.45)}$$

α_{xpe} vs $\bar{p}$ in log - log representation:

$$\log \alpha_{xpe} = \log(\alpha_o + k \cdot \bar{p}) \qquad \text{(Eq. 5.46)}$$

$$slope = \frac{\partial \log \alpha_{xpe}}{\partial \log \bar{p}} = \frac{1}{1 + \dfrac{\alpha_o}{k \cdot \bar{p}}} \qquad \text{(Eq. 5.47)}$$

$$\lim_{\log \bar{p} \to -\infty} slope = \lim_{\bar{p} \to 0} slope = 0 \qquad \text{(Eq. 5.48)}$$

$$\lim_{\log \bar{p} \to \infty} slope = \lim_{\bar{p} \to \infty} slope = 1.0 \qquad \text{(Eq. 5.49)}$$

ψ vs ω in log - log representation:

$$\log \psi = \log\left(k \cdot \frac{h'}{r_1} + \frac{\alpha_o}{\sqrt{3} \cdot 10^{-6} \cdot \omega^2} \right) \qquad \text{(Eq. 5.50)}$$

$$slope = \frac{\partial}{\partial \log \omega} \log \psi = \frac{-2 \cdot \alpha_o}{\alpha_o + \sqrt{3} \cdot 10^{-6} \cdot k \cdot \dfrac{h'}{r_1} \cdot \omega^2} \qquad \text{(Eq. 5.51)}$$

$$\lim_{\log \omega \to -\infty} slope = \lim_{\omega \to 0} slope = -2 \qquad \text{(Eq. 5.52)}$$

$$\lim_{\log \omega \to \infty} slope = \lim_{\omega \to \infty} slope = 0 \qquad \text{(Eq. 5.53)}$$

3. **Curve type-3:** $\alpha_{xpe} = \alpha_x + (1-\alpha_x)\dfrac{\bar{p}}{\bar{p} + 0.3/\sqrt{\alpha_x}}$ ... hyperbolic function of, $\bar{p}$

α_{xpe} vs $\bar{p}$ in linear - linear representation:

$$\alpha_{xpe} = \alpha_x + (1-\alpha_x)\frac{\bar{p}}{\bar{p} + 0.3/\sqrt{\alpha_x}} \qquad \text{(Eq. 5.54)}$$

$$slope = \frac{\partial \alpha_{xpe}}{\partial \bar{p}} = (1-\alpha_x)\cdot\left(\frac{0.3/\sqrt{\alpha_x}}{(\bar{p} + 0.3/\sqrt{\alpha_x})^2}\right) \qquad \text{(Eq. 5.55)}$$

$$\lim_{\bar{p}\to 0} slope = \frac{(1-\alpha_x)}{(0.3/\sqrt{\alpha_x})} \qquad \text{(Eq. 5.56)}$$

$$\lim_{\bar{p}\to \infty} slope = 0 \qquad \text{(Eq. 5.57)}$$

α_{xpe} vs $\bar{p}$ in log - log representation:

$$\log\alpha_{xpe} = \log\left(\alpha_x + (1-\alpha_x)\frac{\bar{p}}{\bar{p} + 0.3/\sqrt{\alpha_x}}\right) \qquad \text{(Eq. 5.58)}$$

$$slope = \frac{\partial \log\alpha_{xpe}}{\partial \log\bar{p}} = \frac{(1-\alpha_x)\cdot(0.3/\sqrt{\alpha_x})}{\alpha_x\cdot\left(\sqrt{\bar{p}} + \dfrac{0.3}{\sqrt{\bar{p}}\cdot\sqrt{\alpha_x}}\right)^2 + (1-\alpha_x)\cdot\left(\bar{p} + \dfrac{0.3}{\sqrt{\alpha_x}}\right)} \qquad \text{(Eq. 5.59)}$$

$$\lim_{\log\bar{p}\to -\infty} slope = \lim_{\bar{p}\to 0} slope = 0 \qquad \text{(Eq. 5.60)}$$

$$\lim_{\log\bar{p}\to \infty} slope = \lim_{\bar{p}\to \infty} slope = 0 \qquad \text{(Eq. 5.61)}$$

ψ vs ω in log - log representation:

$$\log\psi = -\log C - 2\log\omega + \log\left(\alpha_x + (1-\alpha_x)\frac{1}{1+\dfrac{0.3}{C\cdot\dfrac{h'}{r_1}\omega^2\cdot\sqrt{\alpha_x}}}\right) \qquad \text{(Eq. 5.62)}$$

$$slope = \frac{\partial}{\partial\log\omega}\log\psi = -2 + \frac{1}{1+\dfrac{0.3}{C\cdot\dfrac{h'}{r_1}\omega^2\cdot\sqrt{\alpha_x}}}\cdot\frac{0.6(1-\alpha_x)}{0.3\alpha_x + C\cdot\dfrac{h'}{r_1}\omega^2\cdot\sqrt{\alpha_x}} \qquad \text{(Eq. 5.63)}$$

$$\lim_{\log\omega\to-\infty} slope = \lim_{\omega\to 0} slope = -2 \qquad \text{(Eq. 5.64)}$$

$$\lim_{\log\omega\to\infty} slope = \lim_{\omega\to\infty} slope = -2 \qquad \text{(Eq. 5.65)}$$

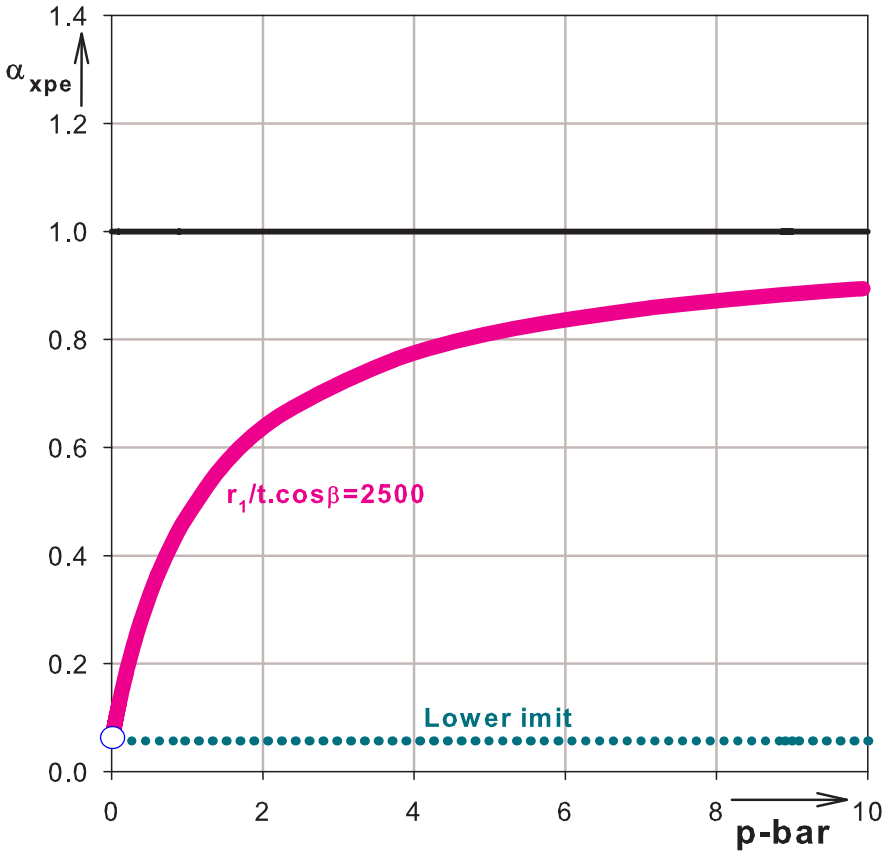

Figure 5.24 LFC linear-linear plot: lower limit line

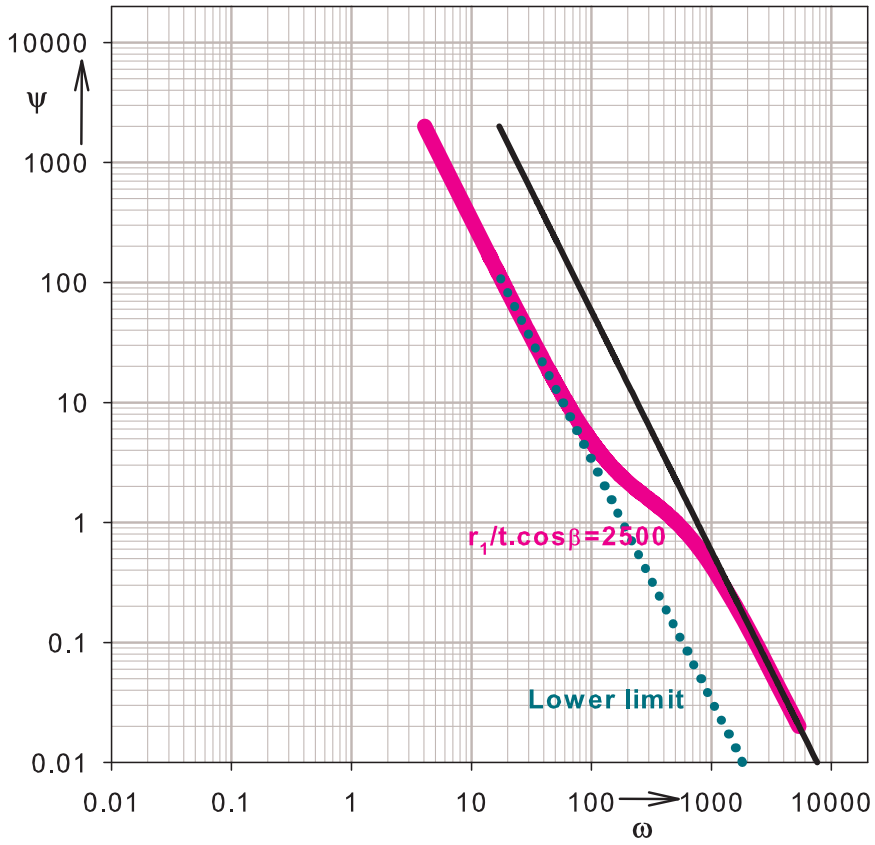

Figure 5.25 Gent log-log plot: lower limit line

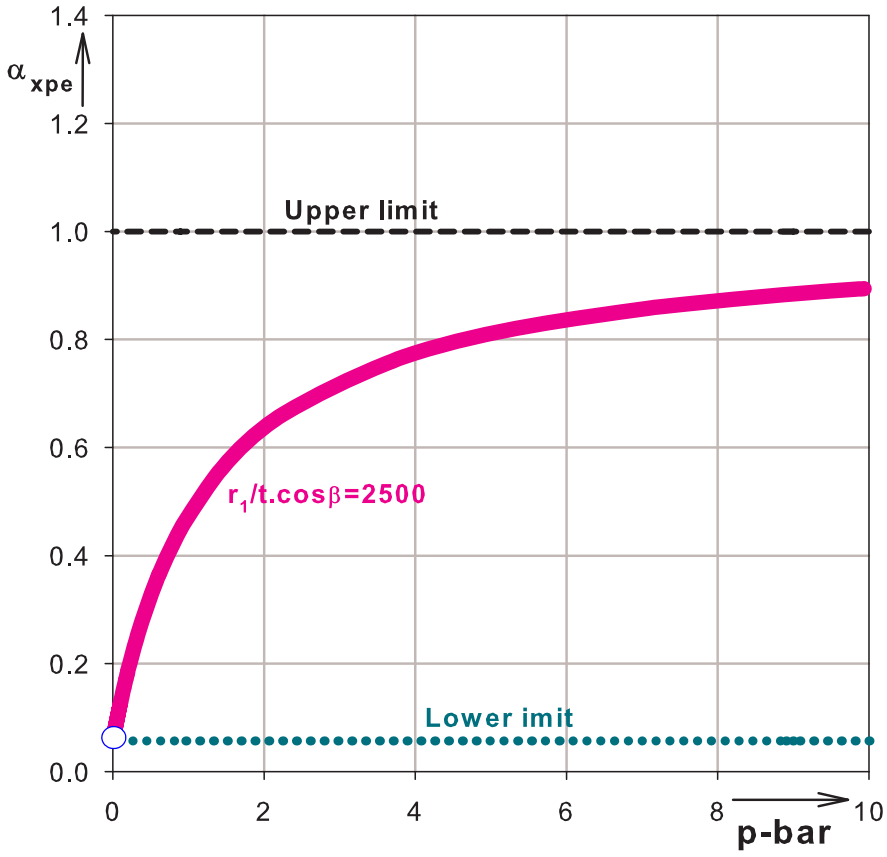

Figure 5.26 LFC linear-linear plot: upper limit line

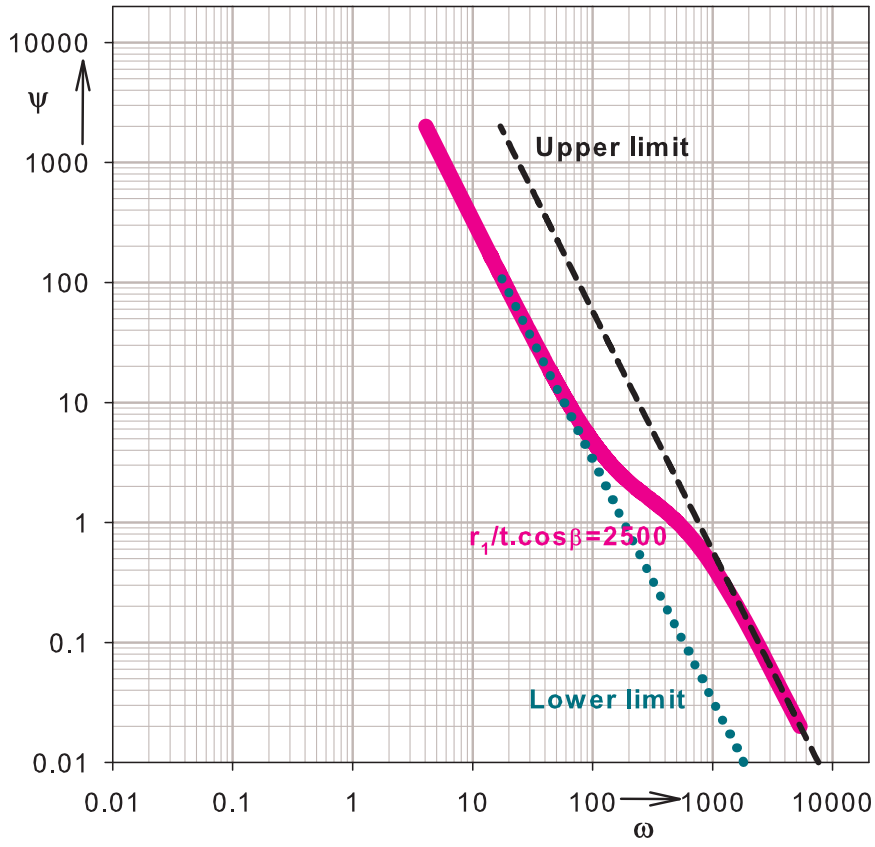

Figure 5.27 Gent log-log plot: upper limit line

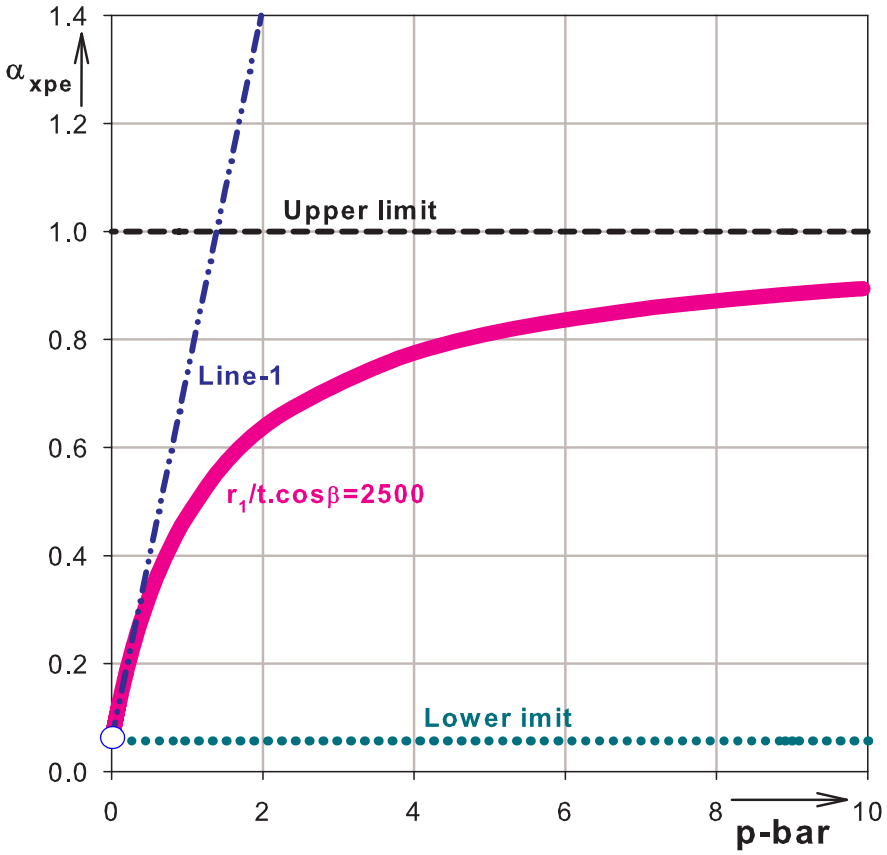

Figure 5.28 LFC linear-linear plot: tangent line-1

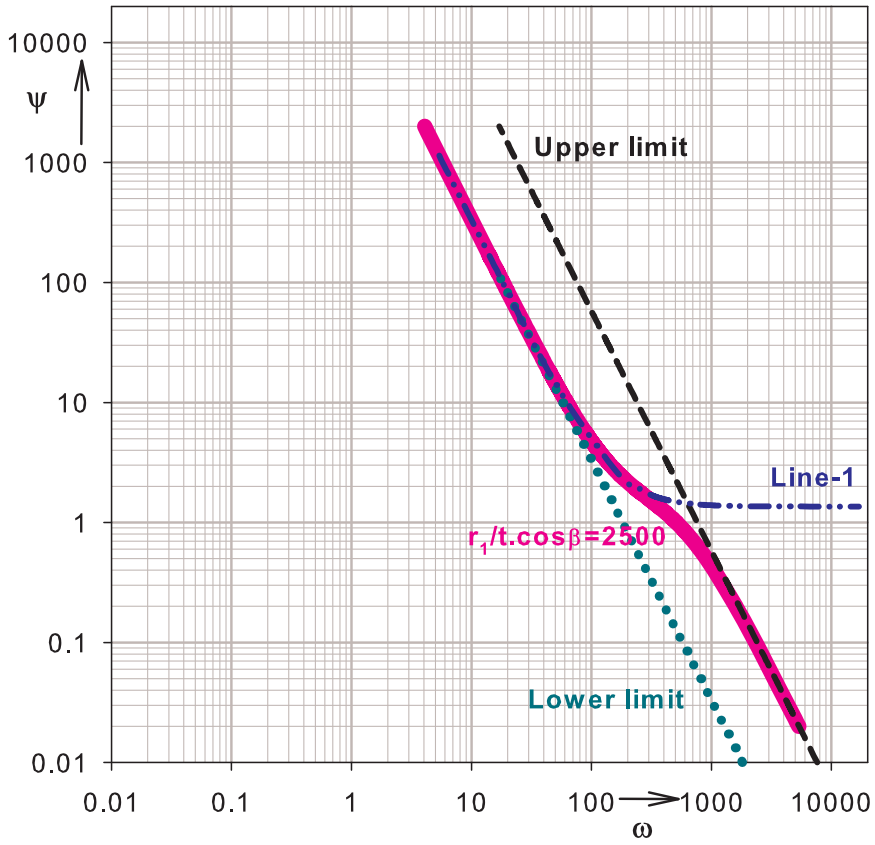

Figure 5.29 Gent log-log plot: tangent line-1

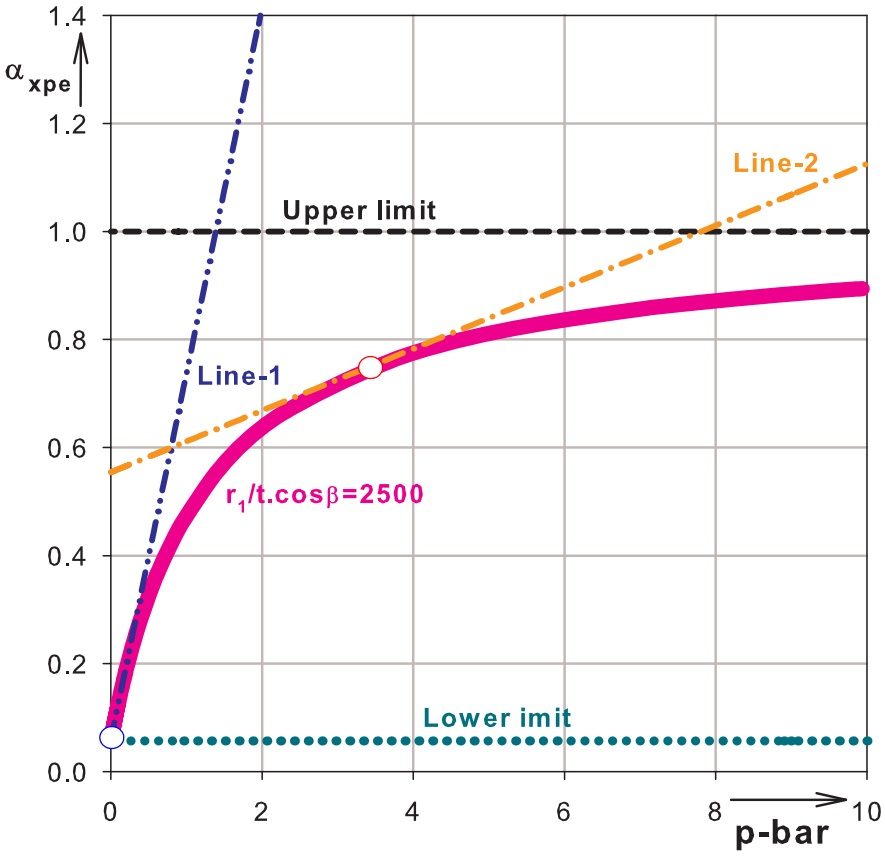

Figure 5.30 LFC linear-linear plot: tangent line-2

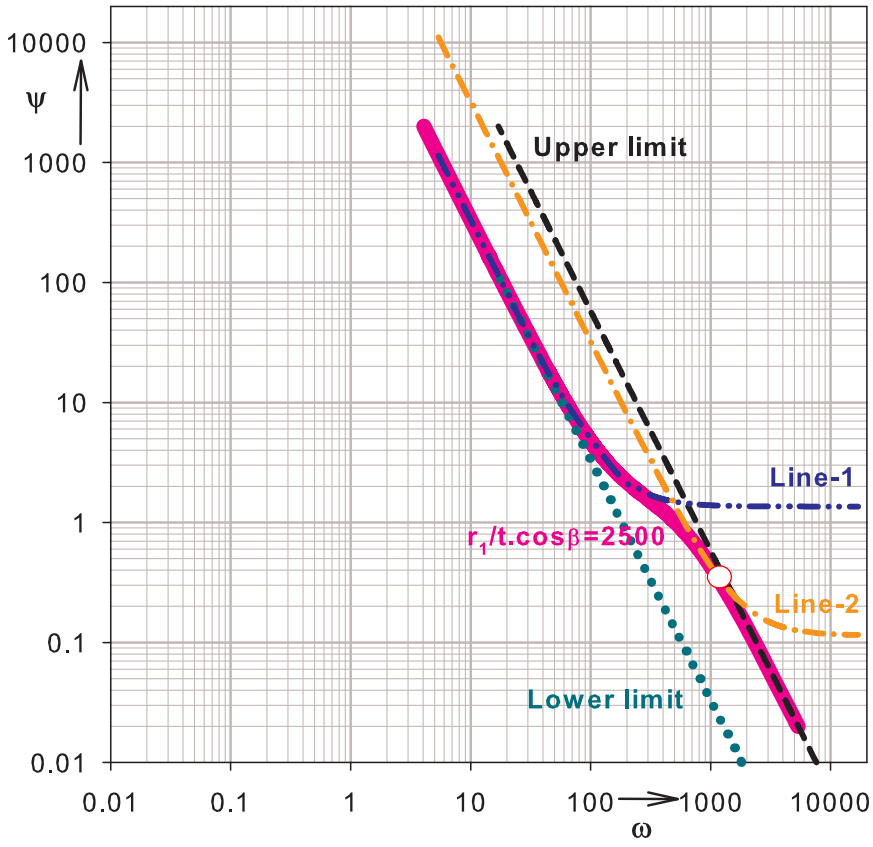

Figure 5.31 Gent log-log plot: tangent line-2

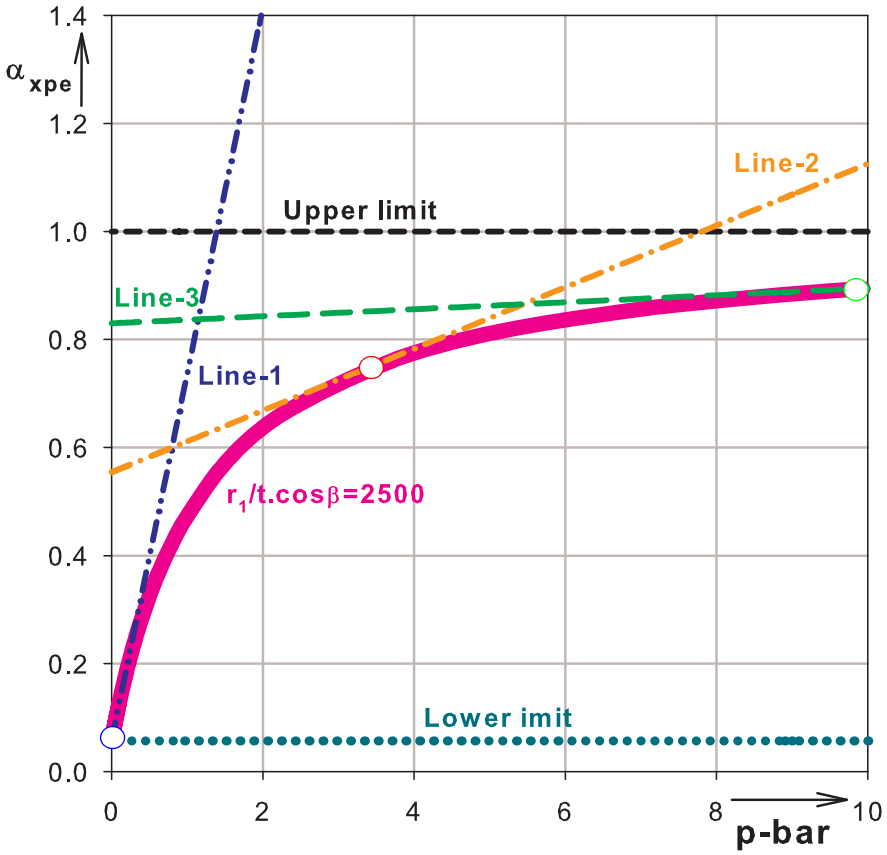

Figure 5.32 LFC linear-linear plot: tangent line-3

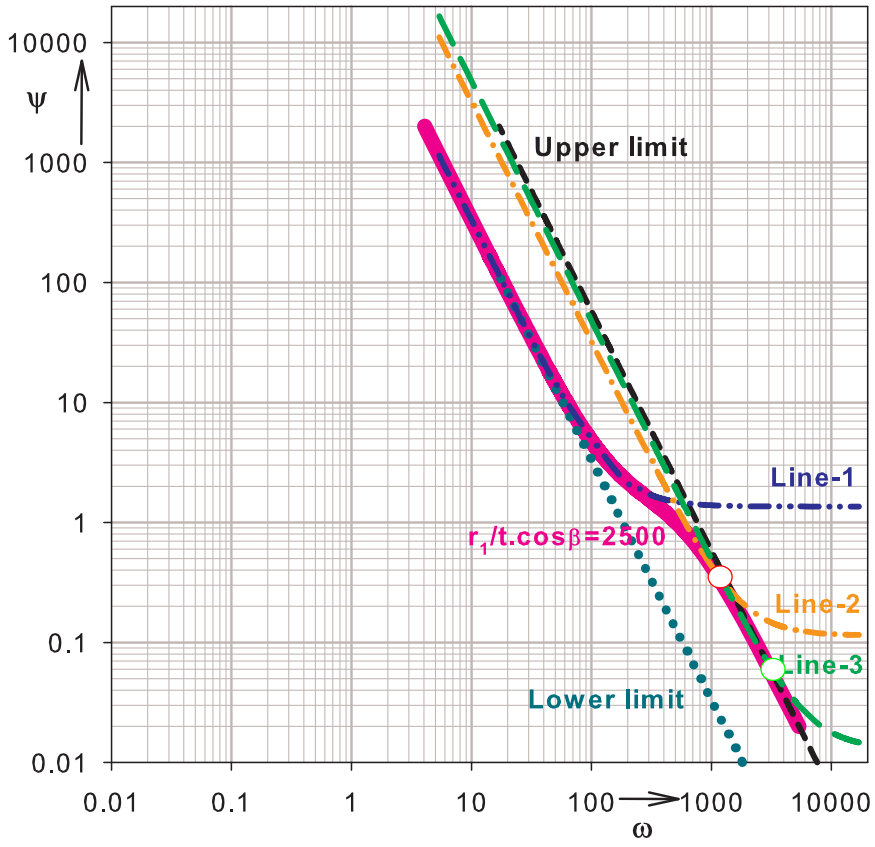

Figure 5.33 Gent log-log plot: tangent line-3

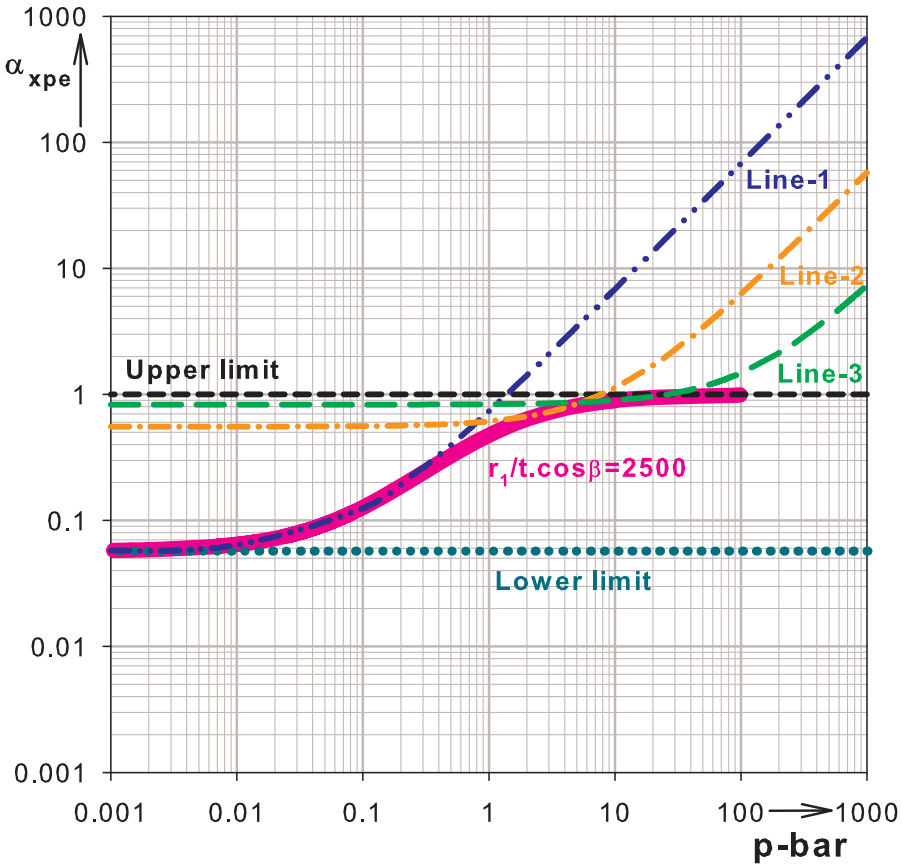

Figure 5.34 LFC log-log plot: all curves

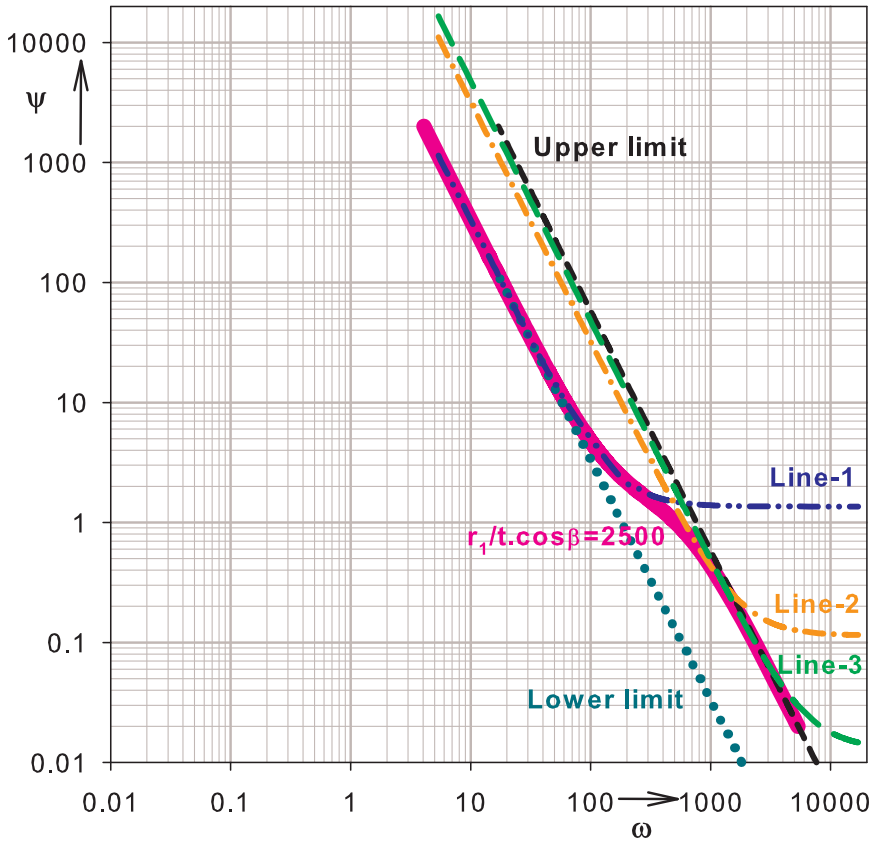

Figure 5.35 Gent log-log plot: all curves

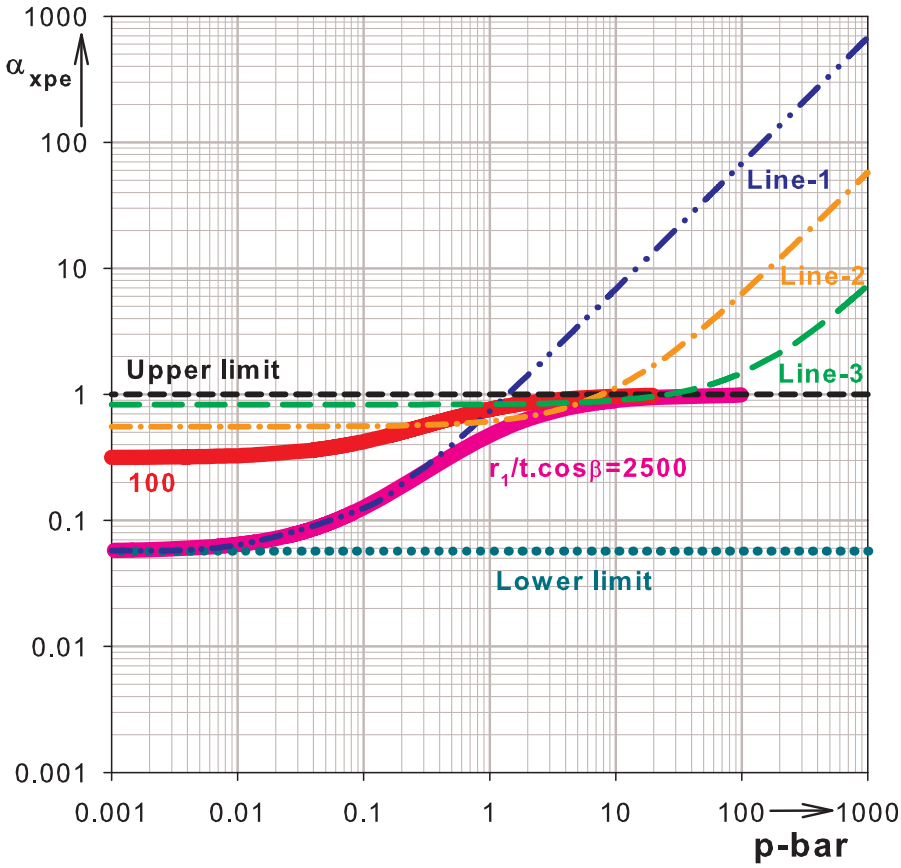

Figure 5.36 LFC log-log plot: inclusion of LFC curve with slenderness value of 100

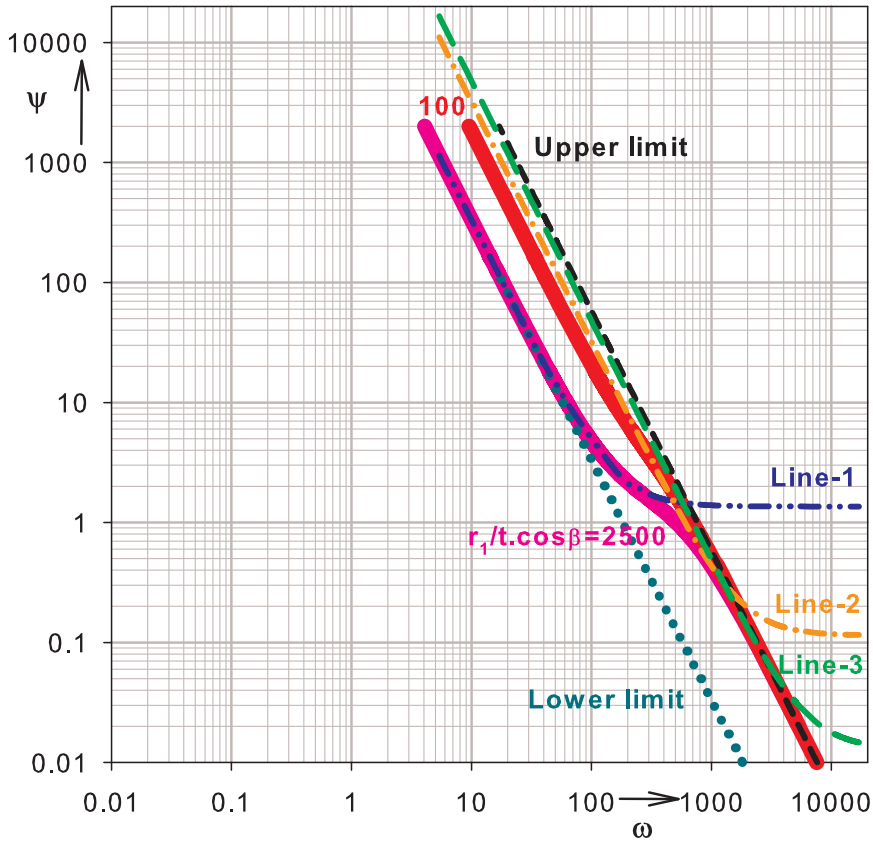

Figure 5.37 Gent log-log plot: inclusion of LFC curve with slenderness value of 100

5.7 Detail re-investigation of test results

Starting the Gent test results anew, a detailed analysis of all the test data, both rejected and accepted (see Table 5.1), has been made taking the slenderness ratio parameter, $\mathbf{r_1/tcos}\beta$ into account. A separation is made between the different material types and different slenderness ratio values. In subsequent plots, different solid shapes have been used to represent the type of materials and different coloring was used to differentiate between slenderness ratio values. Figure 5.38 and Figure 5.39 show the use of the different shapes and colors for the different materials and slenderness ratio values in α_{xpe} - $\bar{p}$ linear-linear and Gent ψ - ω log-log representations, respectively.

5.7.1 Cleaning the test data

By cleaning, it means that dropping those test data that are either not practical in civil engineering construction or having any kind of defect. Cleaning of the test data has been made in a step-by-step procedure. Figure 5.40 and Figure 5.41 show a comparison between α_{xpe} - $\bar{p}$ linear-linear and α_{xpe} - $\bar{p}$ log-log representations, respectively, of the curves and all test data points including those to be cleaned out.

extreme β angle ranges

the lower and upper extreme β values have been dropped since they are not practical apex-half angles for civil engineering liquid-filled conical shells. This means that only the $\beta = 20° - 60°$ range has only be considered, the remaining being all 10° or 75°. See Figure 5.42 and Figure 5.43.

global tilting failures

this is a different buckling phenomenon where a global bending type loading is included, resulting in non uniform meridional compression (may even be compression on one side and tension on the other side) on the base of the cone. This type of failure happened mostly for the cones with relatively narrow bases and/or high $h'\tan\beta/r_1$ values. A very small deviation from the upright position of the cone may lead to such type of failures in narrow cone-bases and relatively high liquid depths. See Figure 5.44 and Figure 5.45.

'bad' test configurations

this group includes test data points which had faulty experimental setup, cones with overlapping meridional seam in the critical zone of buckling, and cones failed with in the supporting device. See Figure 5.46 and Figure 5.47.

sliding bottom boundary condition

these are the cones where their bottom edges were allowed to deform freely perpendicular to the meridian and are dropped because they are not practical. See Figure 5.48 and Figure 5.49.

clamped bottom boundary condition

these are the tests which were completely clamped at their bottom edge. They are dropped because they are few in number and they need different treatment. See Figure 5.50 and Figure 5.51. However, they will be re-considered later when discussing the effect of fixed bottom boundary conditions, Figure 5.67 to Figure 5.73.

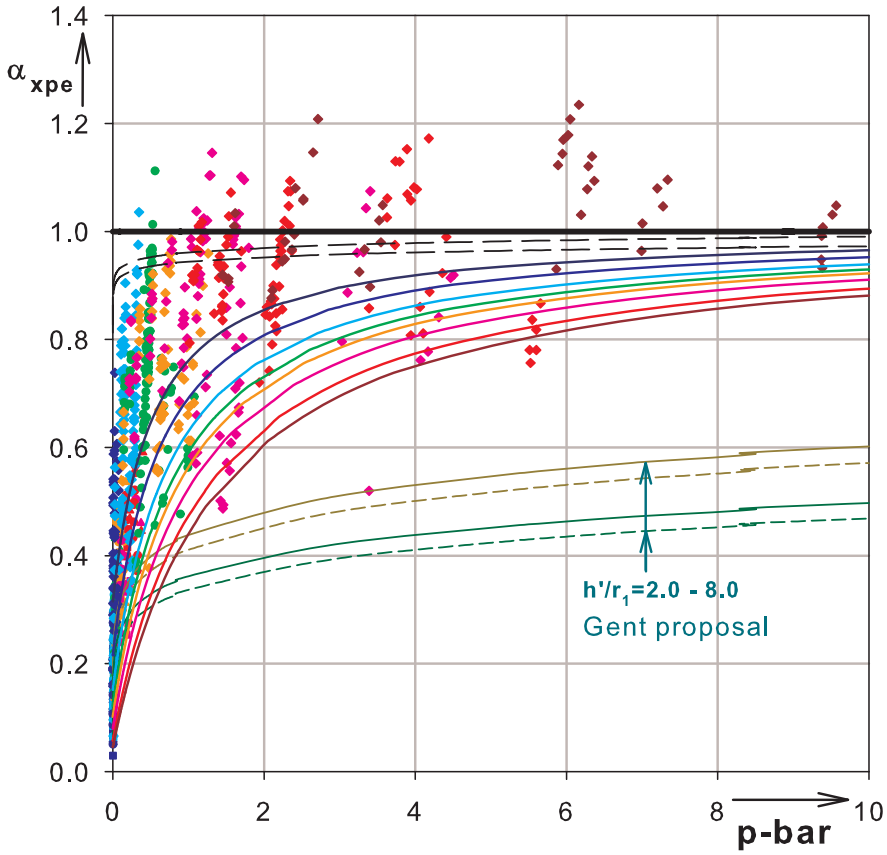

Figure 5.38 Linear-linear plot: different material types and different slenderness values

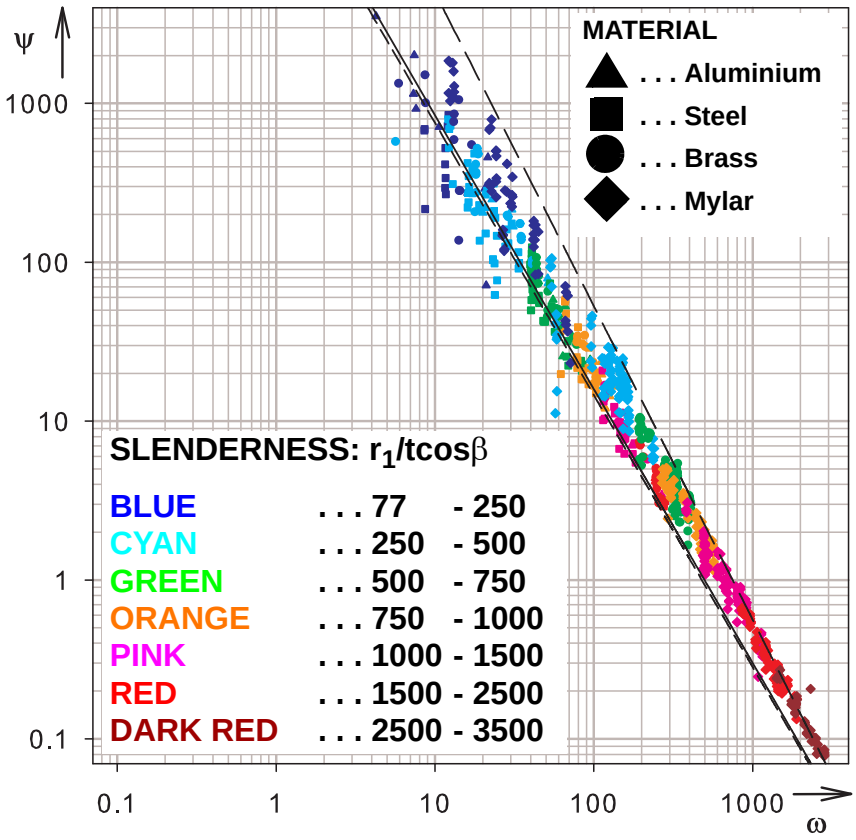

Figure 5.39 Gent log-log plot: different material types and different slenderness values

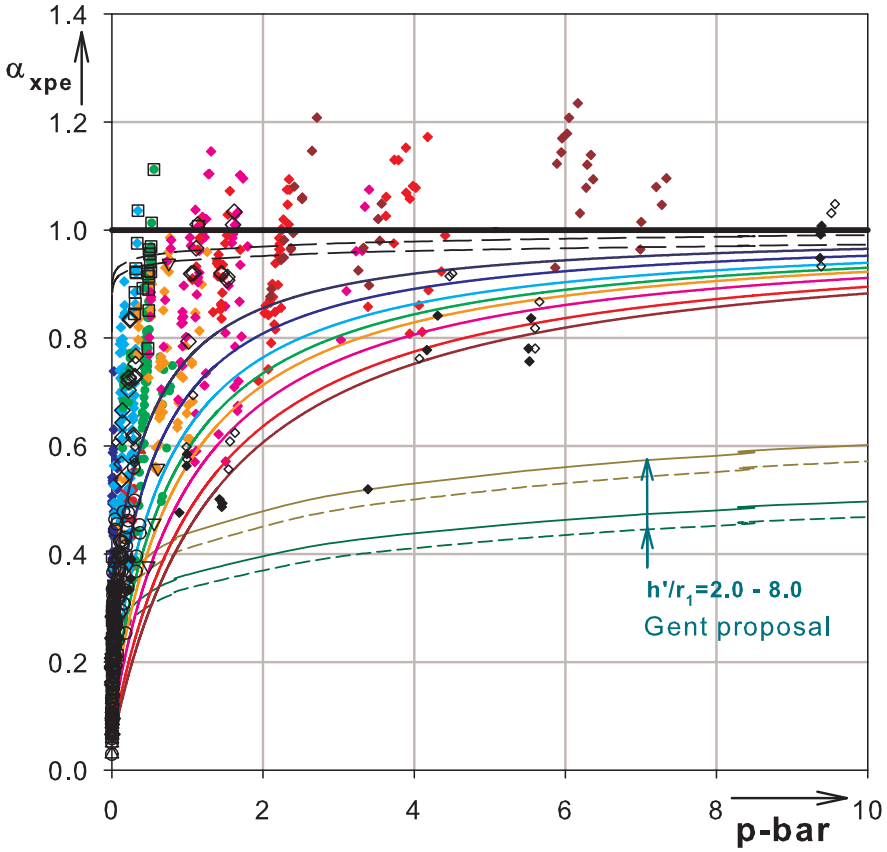

Figure 5.40 LFC linear-linear plot: cleaning out of the test data

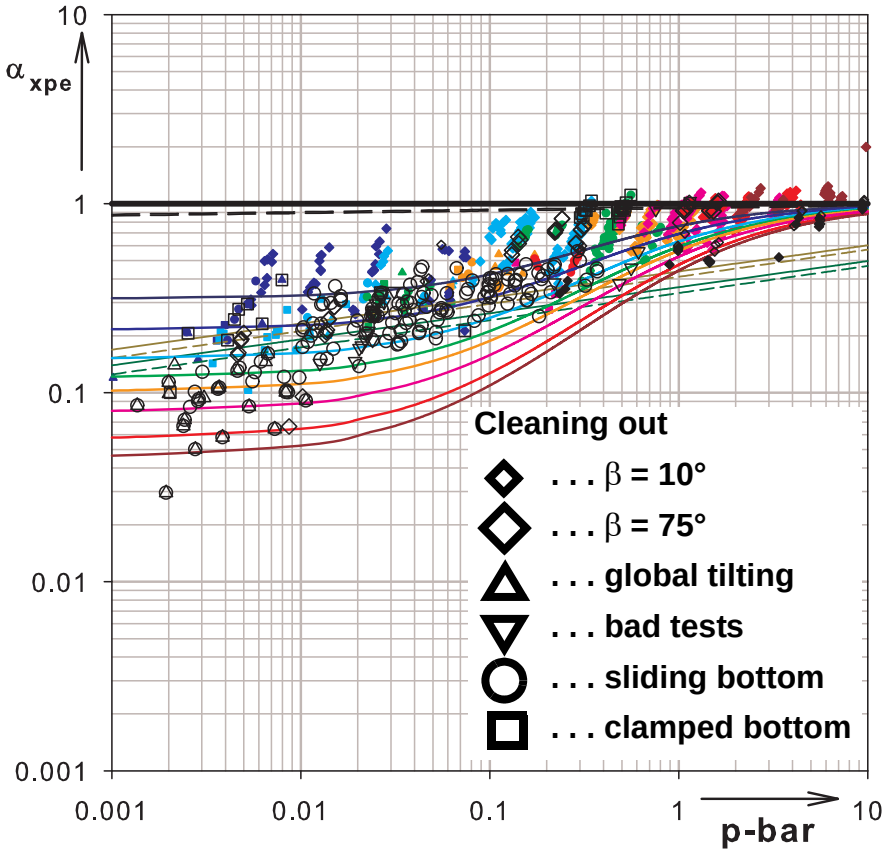

Figure 5.41 LFC log-log plot: cleaning out of the test data

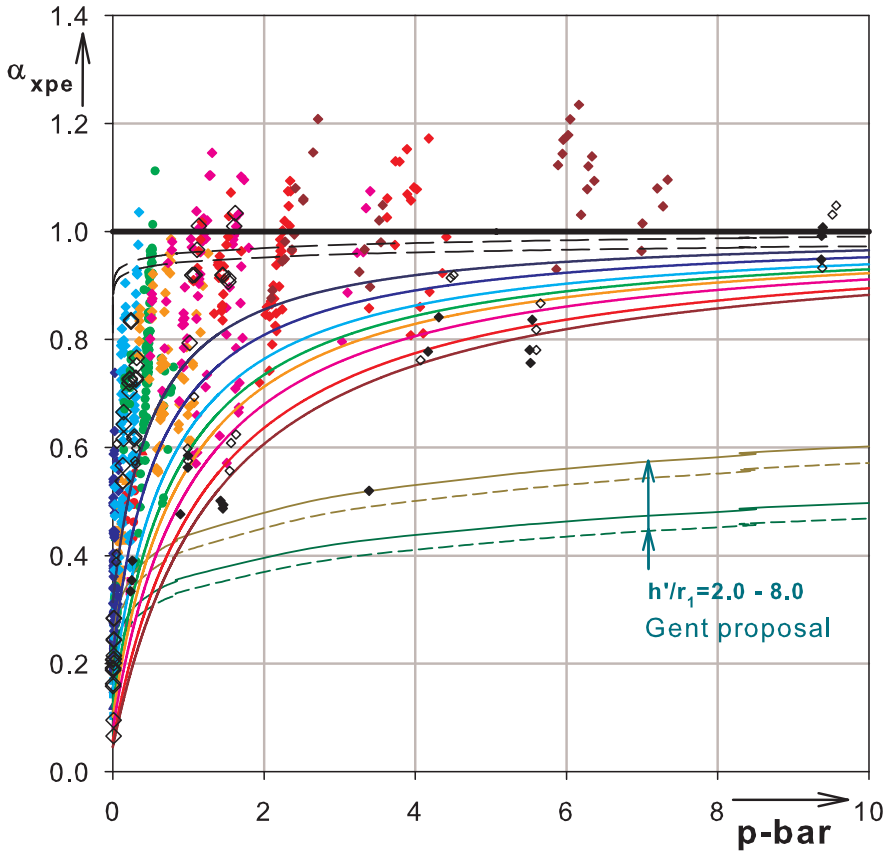

Figure 5.42 LFC linear-linear plot: cleaning out tests with extreme apex half-angles

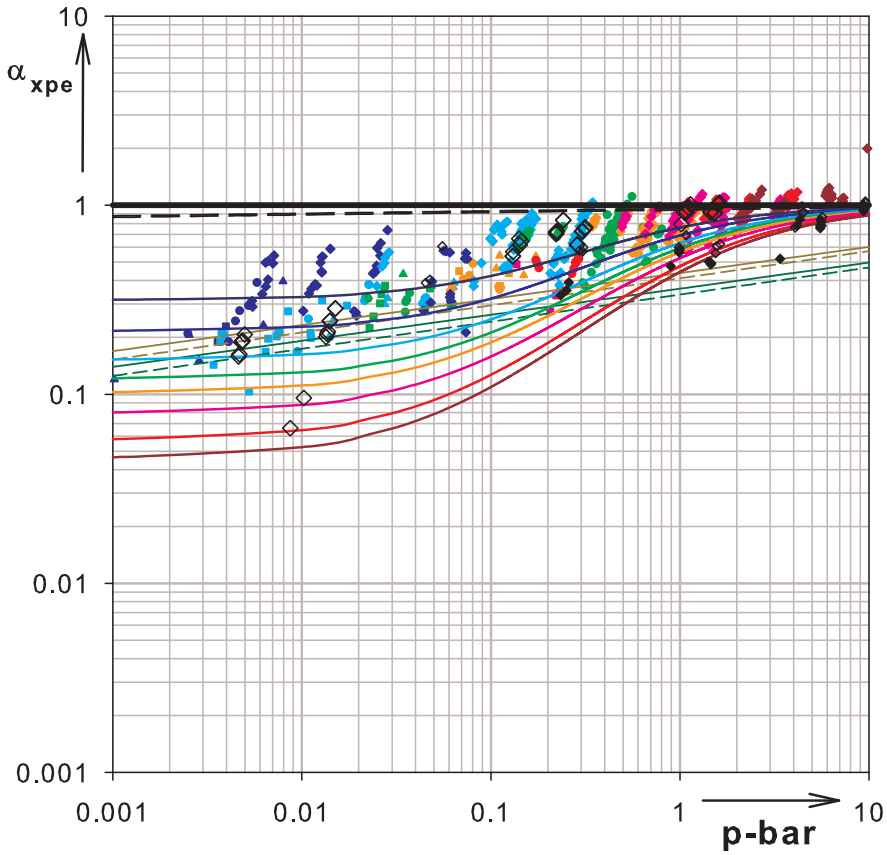

Figure 5.43 LFC log-log plot: cleaning out tests with extreme apex-half angles

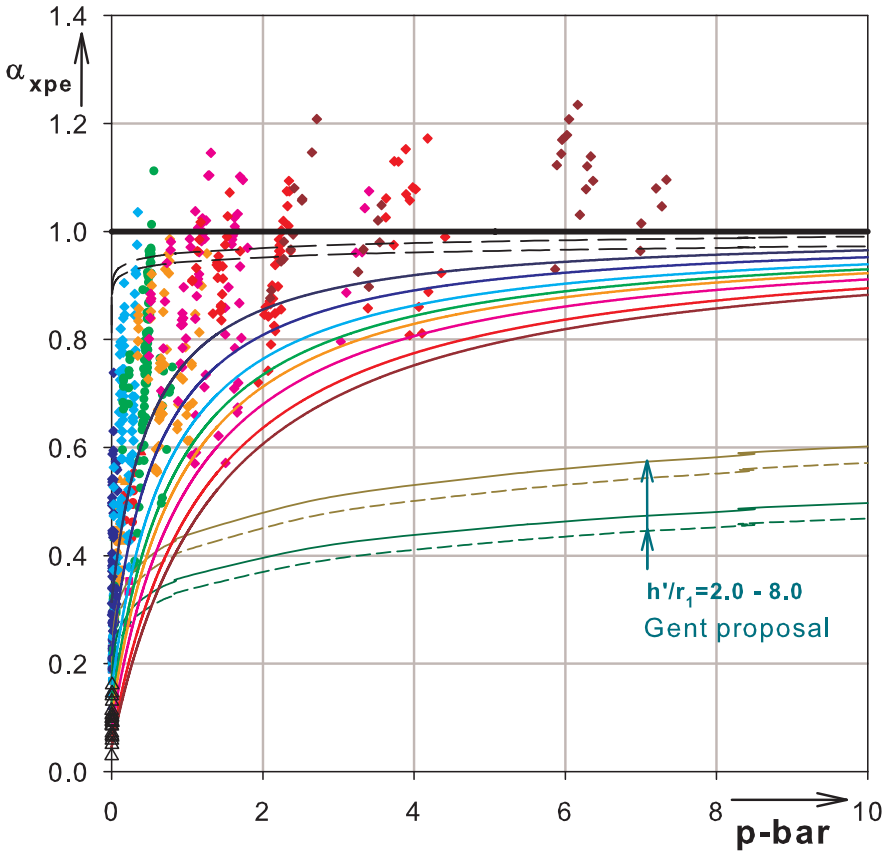

Figure 5.44 LFC linear-linear plot: cleaning out tests which failed sideways (global tilting)

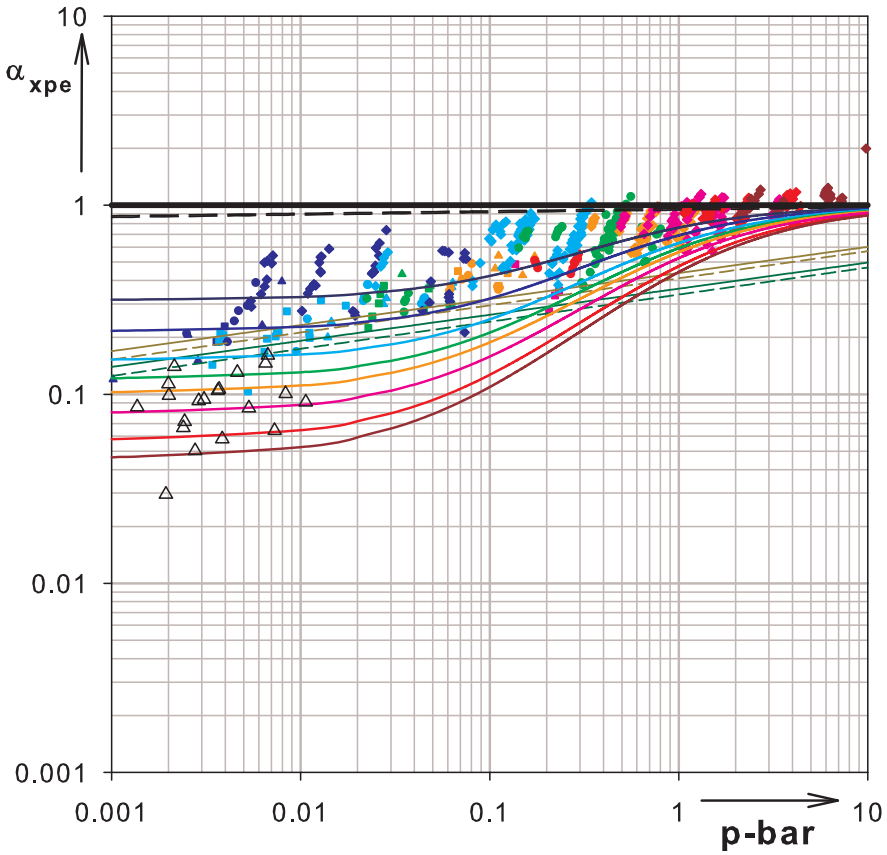

Figure 5.45 LFC log-log plot: cleaning out tests which failed sideways (global tilting)

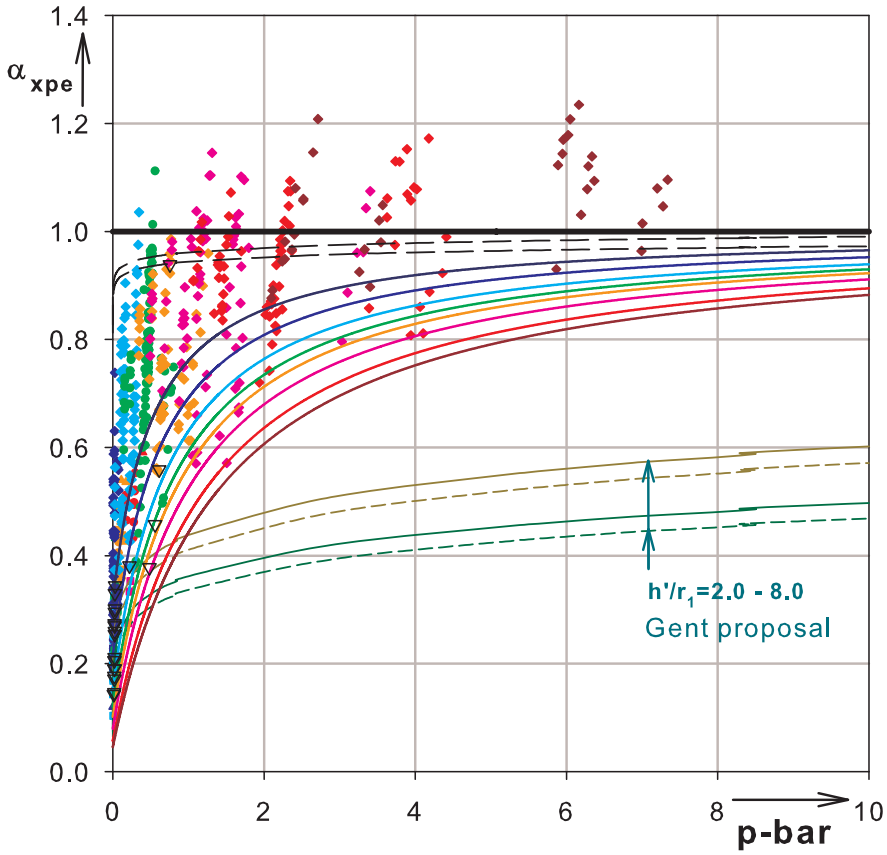

Figure 5.46 LFC linear-linear plot: cleaning out bad (faulty) test configurations

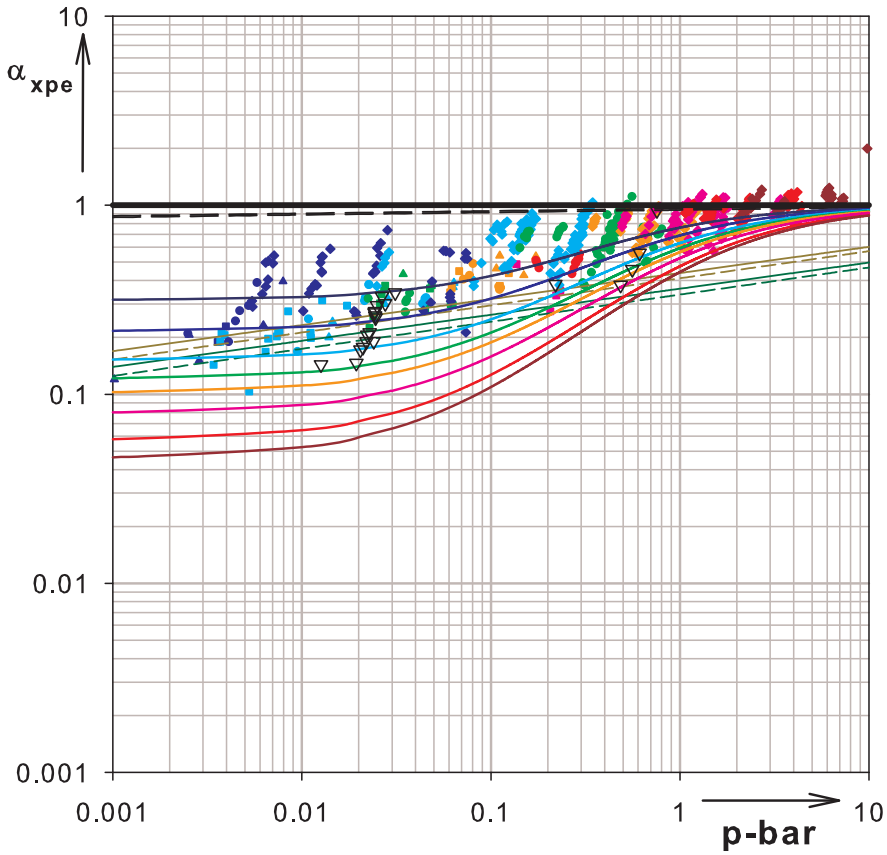

Figure 5.47 LFC log-log plot: cleaning out bad (faulty) test configurations

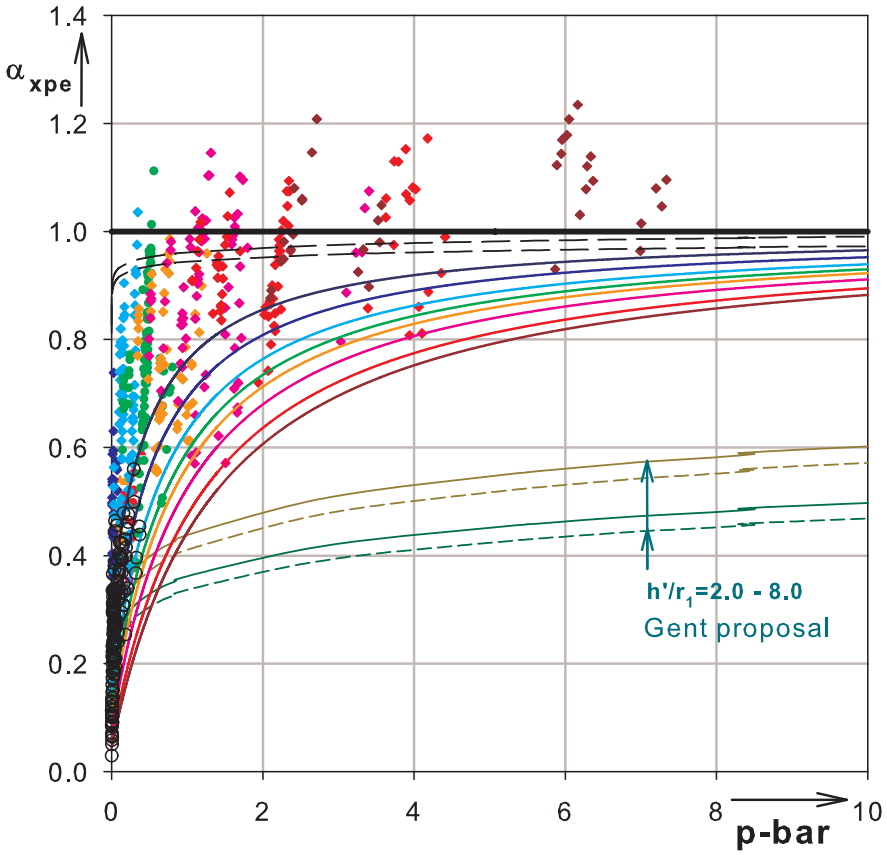

Figure 5.48 Linear-linear plot: cleaning out tests with sliding bottom boundary condition

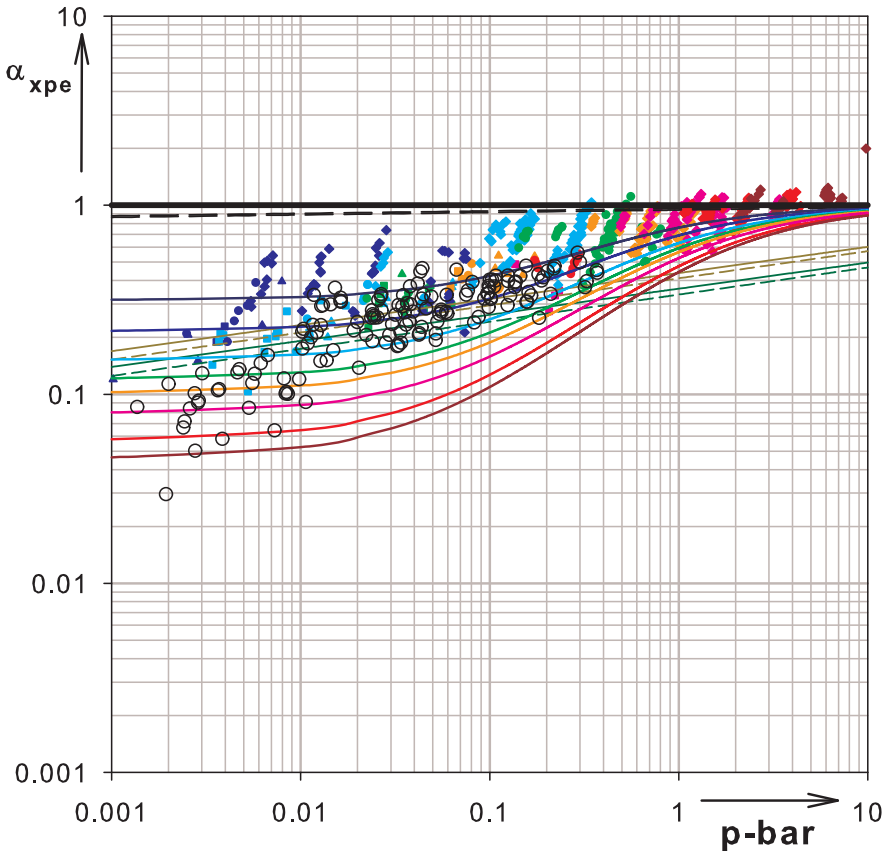

Figure 5.49 LFC log-log plot: cleaning out tests with sliding bottom boundary condition

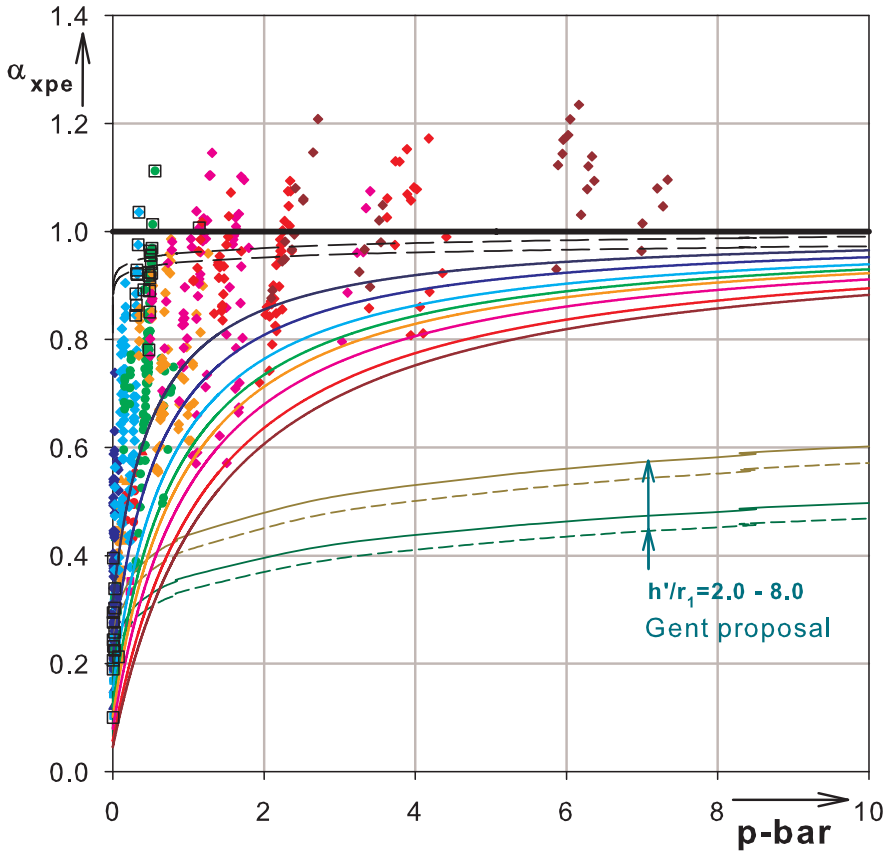

Figure 5.50 Linear-linear plot: cleaning out tests with clamped boundary condition

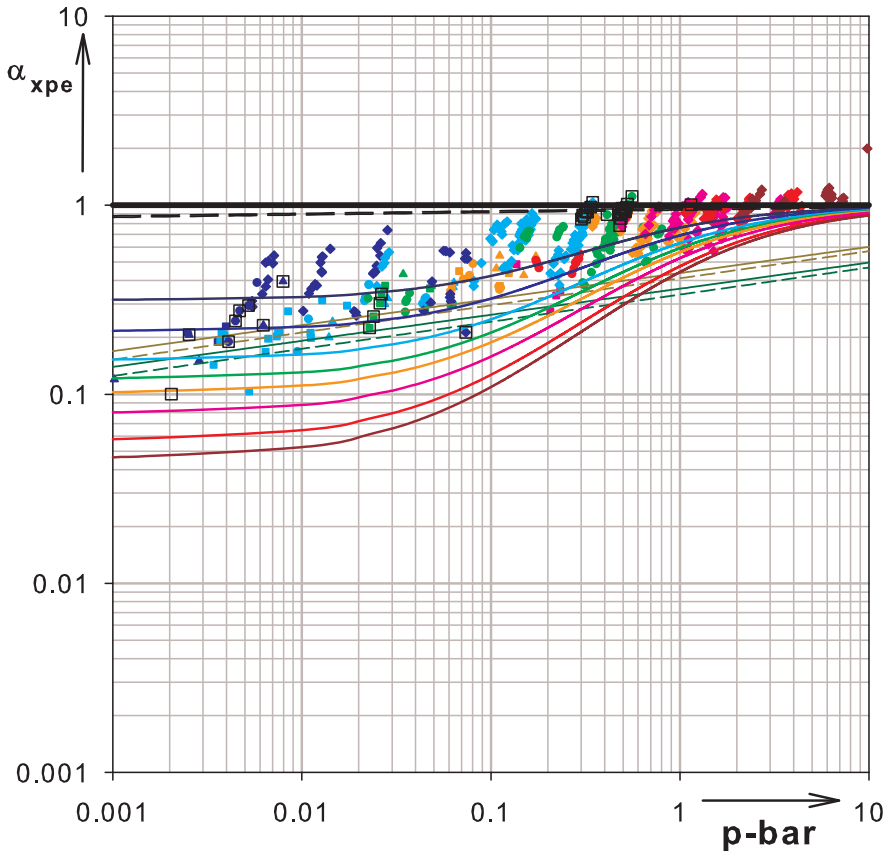

Figure 5.51 LFC log-log plot: cleaning tests with clamped bottom boundary condition

5.7.2 Detailed study of test results based on the slenderness ratio parameter ($r_1/t\cos\beta$)

The cones tested in the Gent experiment cover a very wide slenderness ratio range $r_1/t\cos\beta$ = 77 - 3760. In this detailed study, the test data are separated according to their slenderness ratio and grouped them in seven groups having smaller slenderness ratio ranges of 100-250 (includes also those less than 100), 250-500, 500-750, 750-1000, 1000-1500, 1500-2500, and 2500-3500 (includes also those larger than 3500). Besides, for each bounding slenderness ratio value of the test results, LFC curves with fabrication tolerance quality classes A and C are used for comparison purposes. Investigations of the different slenderness ratio ranges of the test data have been done one after the other. For a better view, specially for small $\bar{p}$ values, and parallel comparison of the results, the α_{xpe} - $\bar{p}$ log-log representation is plotted in addition to the α_{xpe} - $\bar{p}$ linear-linear representation.

The previously cleaned out results and the Gent lower-bounding curves are also included in each plot for the sake of clarity and better comparison. An overall explanation of the plots is shown in Table 5.3.

Figure No.	$r_1/t\cos\beta$ range of test data points	$r_1/t\cos\beta$ of group-bounding LFC curves	quality classes considered	Remark
Figure 5.52	77 - 250	100 and 250	A and C	(1) the LFC lower-bounding curves on each plot, when seen from top down, are class-A of the smaller slenderness, class-A of the larger slenderness, class-C of the smaller slenderness, and class-C of the larger slenderness, respectively. (2) the gray shading is between quality classes A and C of the slender LFC curve in each group (3) the Gent bounding curves are computed for h'/r_1 values of 2.0 and 8.0
Figure 5.53				
Figure 5.54	250 - 500	250 and 500		
Figure 5.55				
Figure 5.56	500 - 750	500 and 750		
Figure 5.57				
Figure 5.58	750 - 1000	750 and 1000		
Figure 5.59				
Figure 5.60	1000 - 1500	1000 and 1500		
Figure 5.61				
Figure 5.62	1500 - 2500	1500 and 2500		
Figure 5.63				
Figure 5.64	2500 - 3760	2500 and 3500		
Figure 5.65				

Table 5.3 Summary of figures (Figure 5.52 - Figure 5.65)

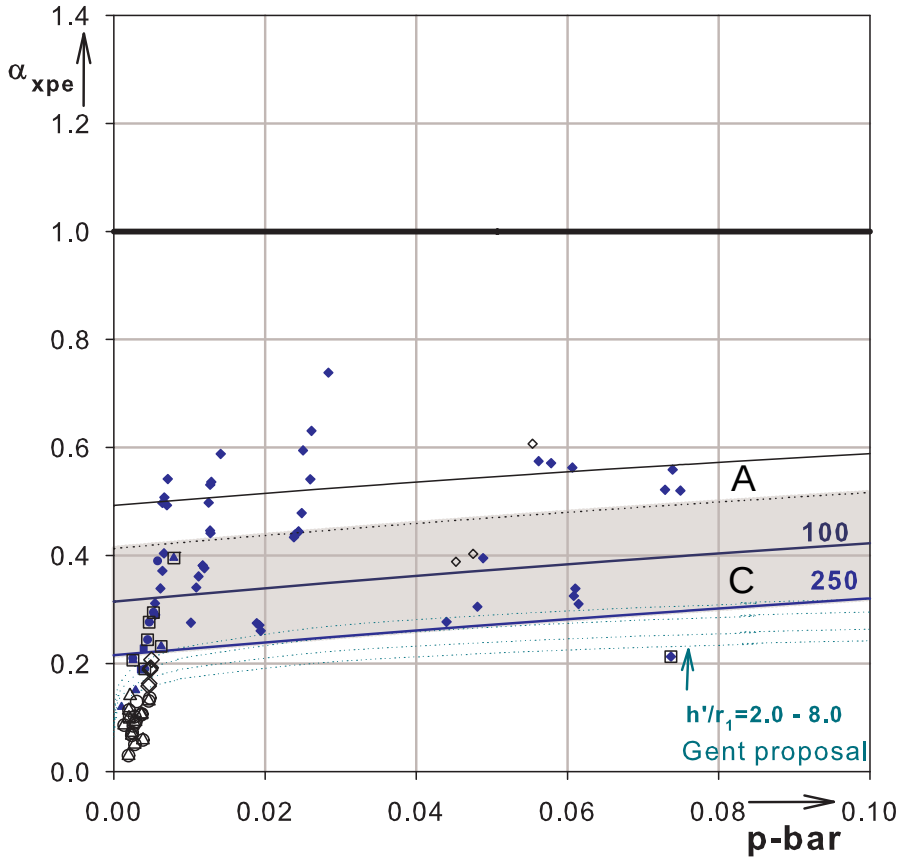

Figure 5.52 LFC linear-linear plot: $r_1/t\cos\beta$ = 77 - 250

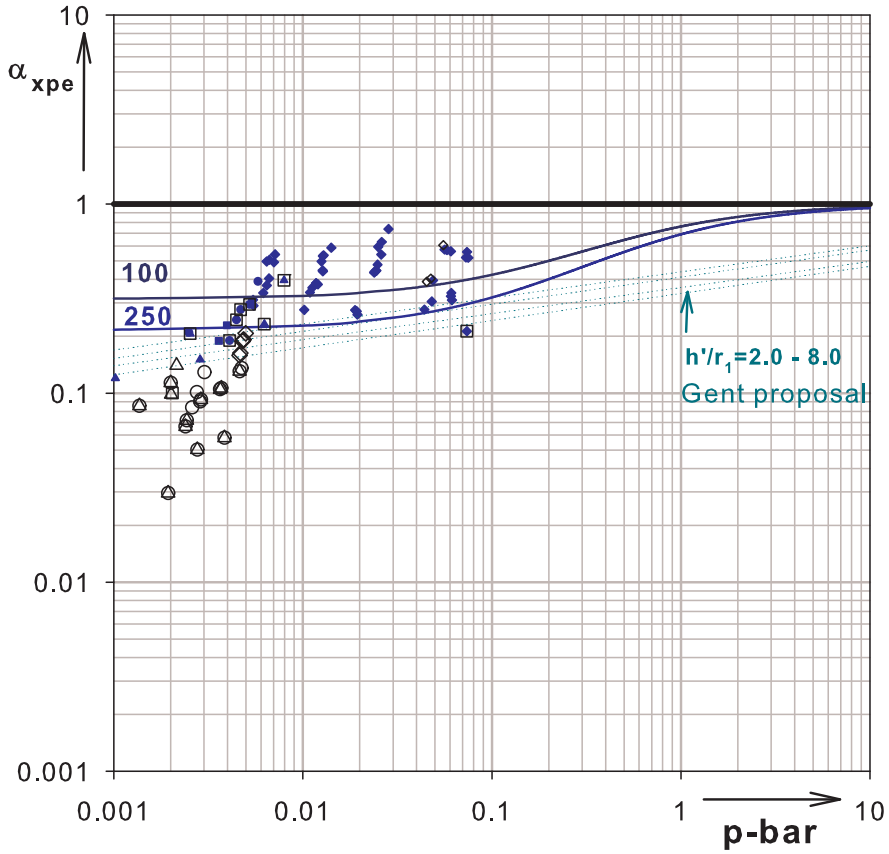

Figure 5.53 LFC log-log plot: $r_1/t\cos\beta$ = 77 - 250

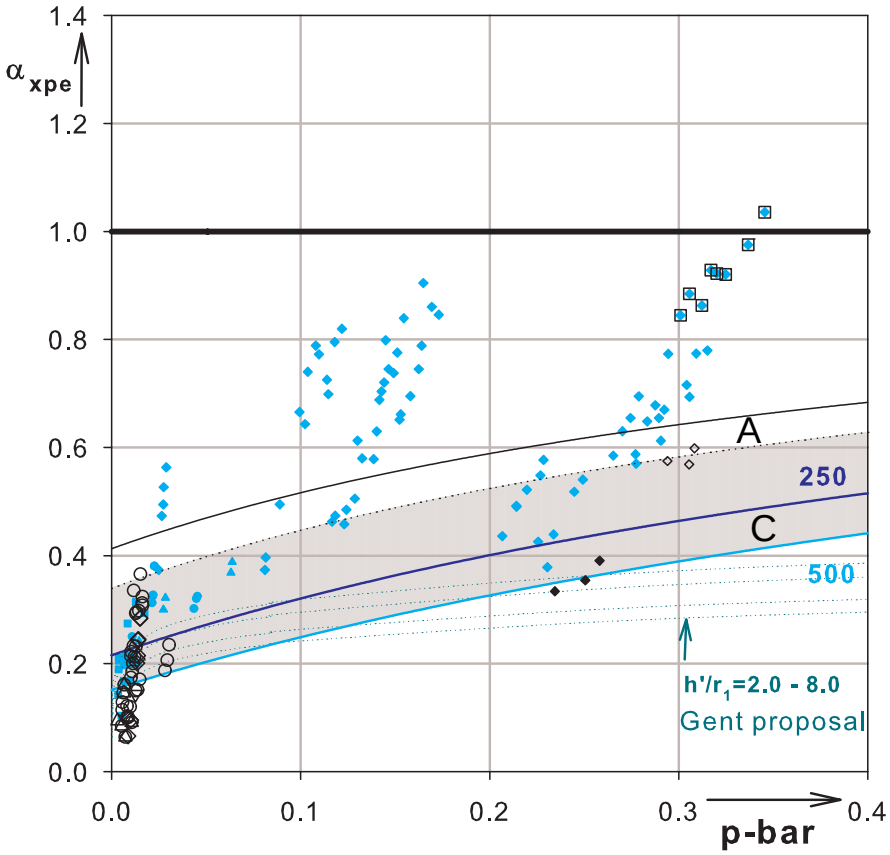

Figure 5.54 LFC linear-linear plot: $r_1/t\cos\beta$ = 250 - 500

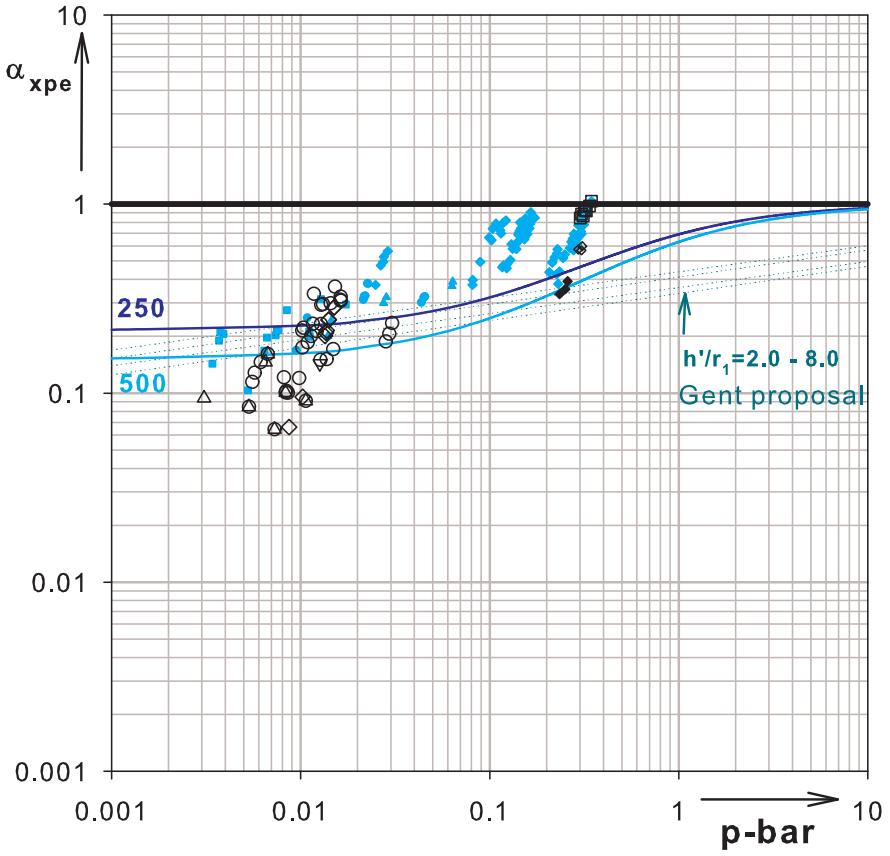

Figure 5.55 LFC log-log plot: $r_1/t\cos\beta$ = 250 - 500

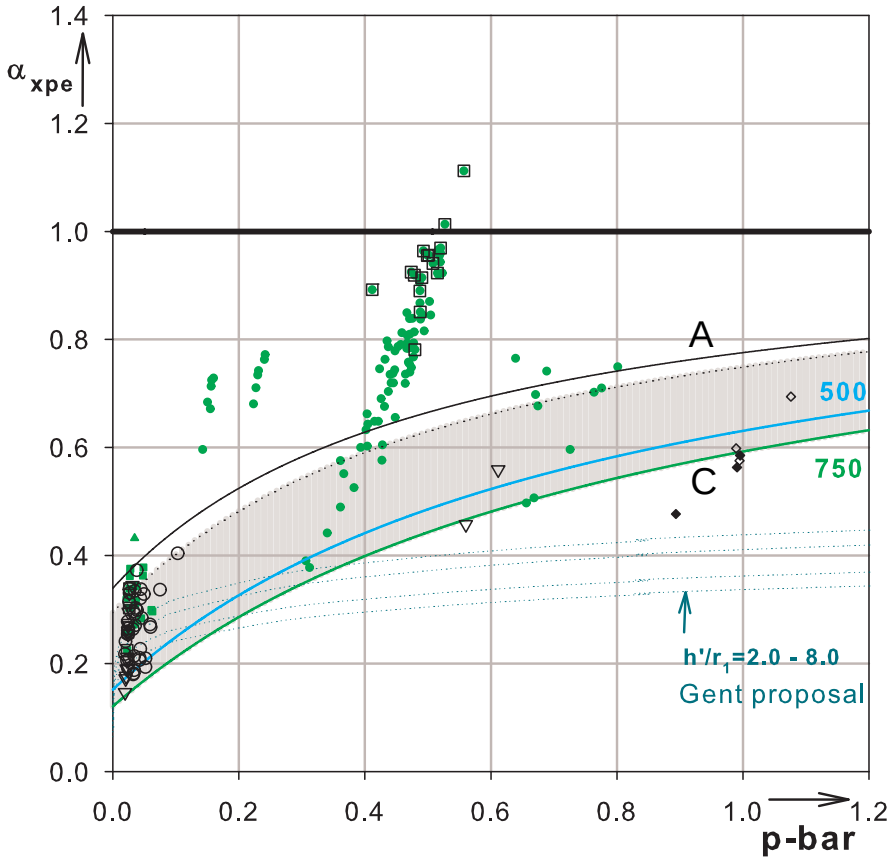

Figure 5.56 LFC linear-linear plot: $r_1/t\cos\beta$ = 500 - 750

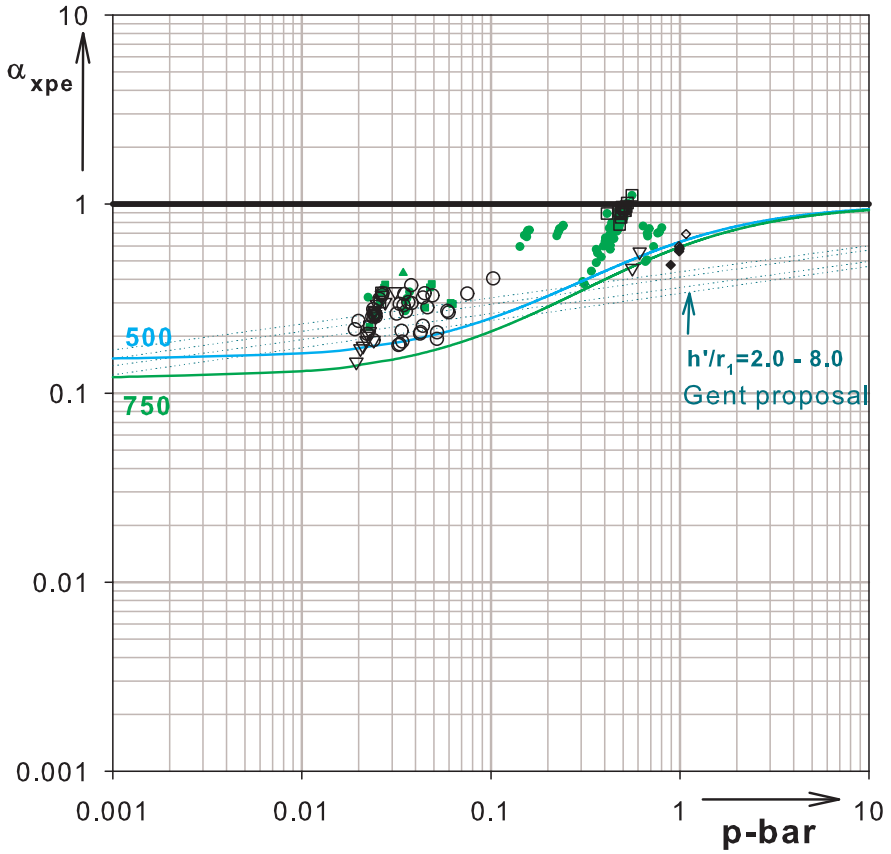

Figure 5.57 LFC log-log plot: $r_1/t\cos\beta$ = 500 - 750

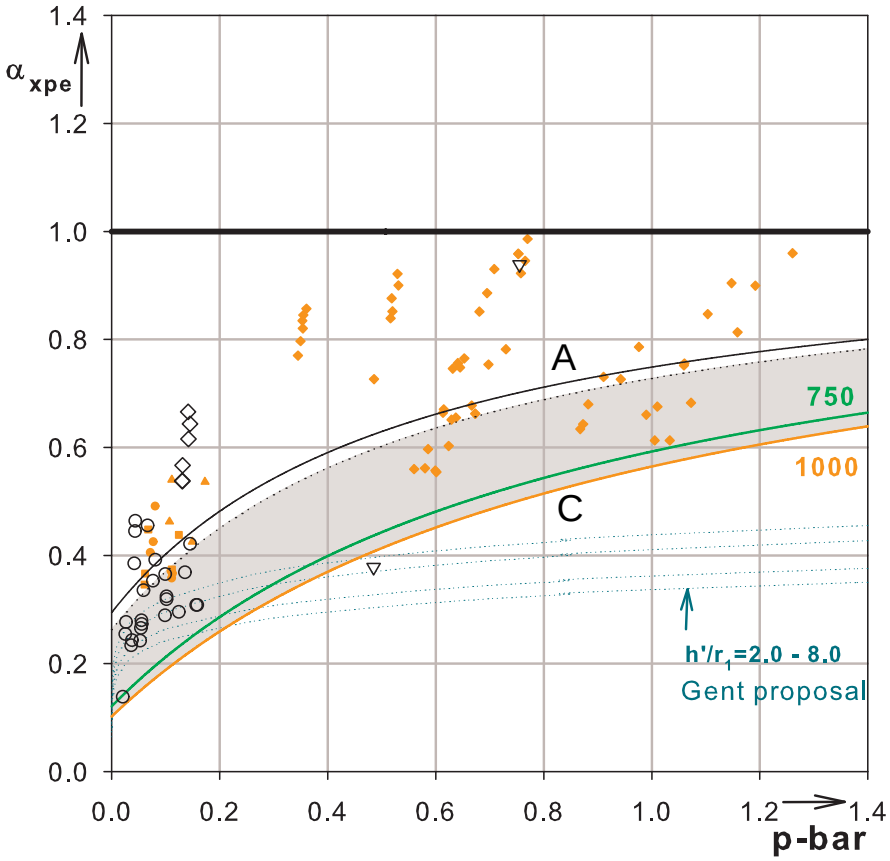

Figure 5.58 LFC linear-linear plot: $r_1/t\cos\beta$ = 750 - 1000

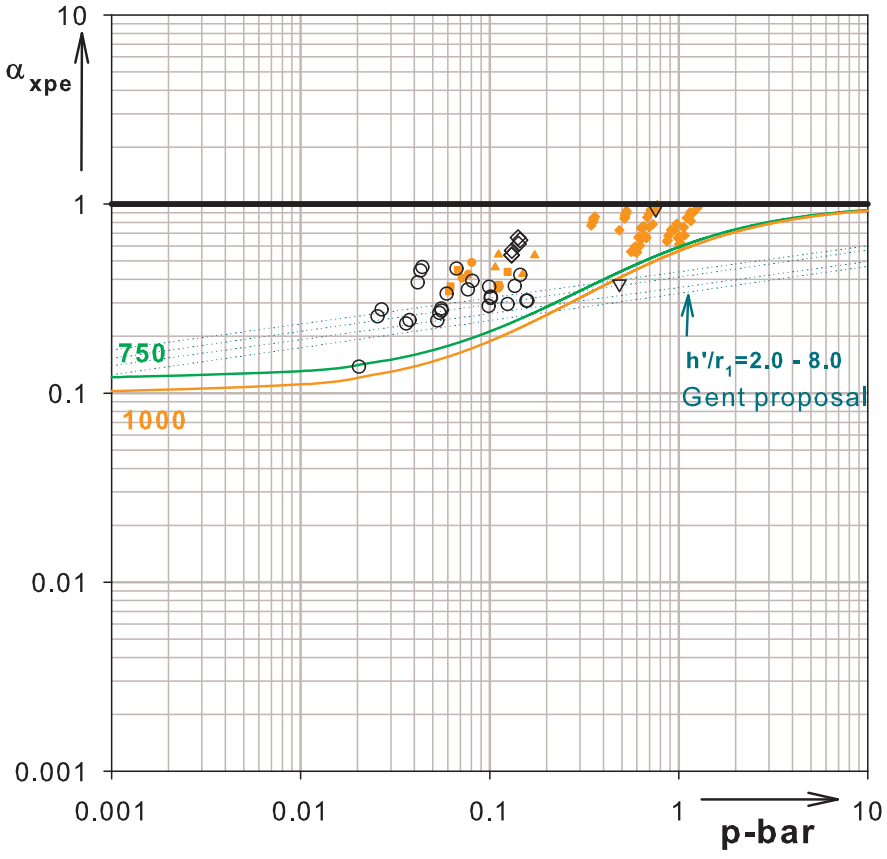

Figure 5.59 LFC log-log plot: $r_1/t\cos\beta$ = 750 - 1000

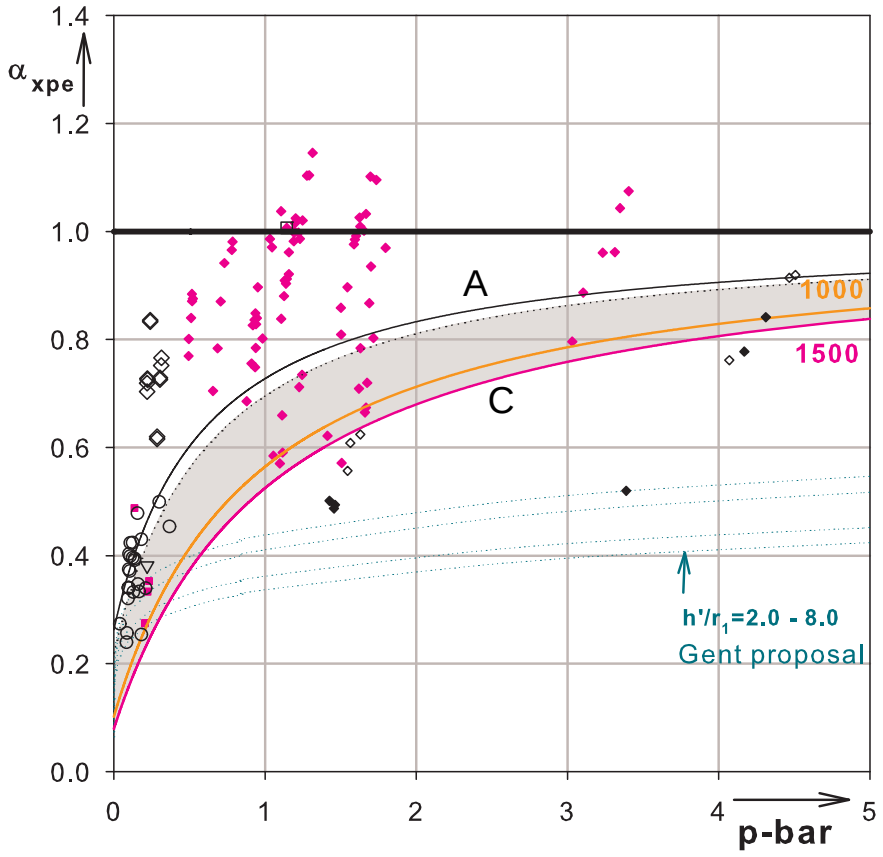

Figure 5.60 LFC linear-linear plot: $r_1/t\cos\beta$ = 1000 - 1500

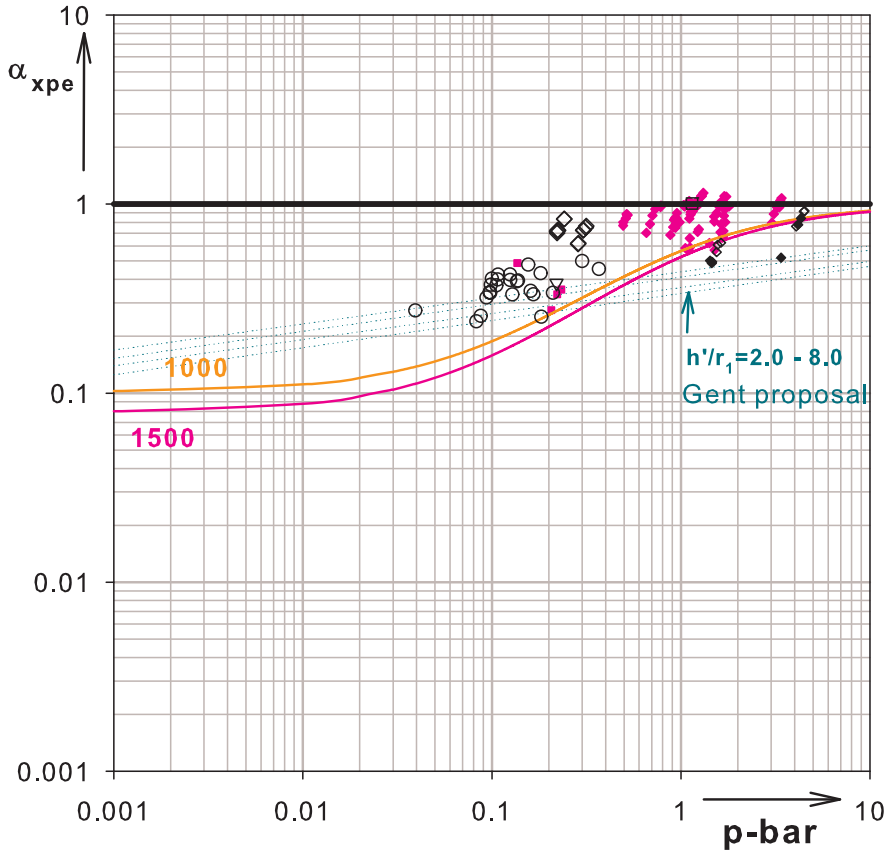

Figure 5.61 LFC log-log plot: $r_1/t\cos\beta$ = 1000 - 1500

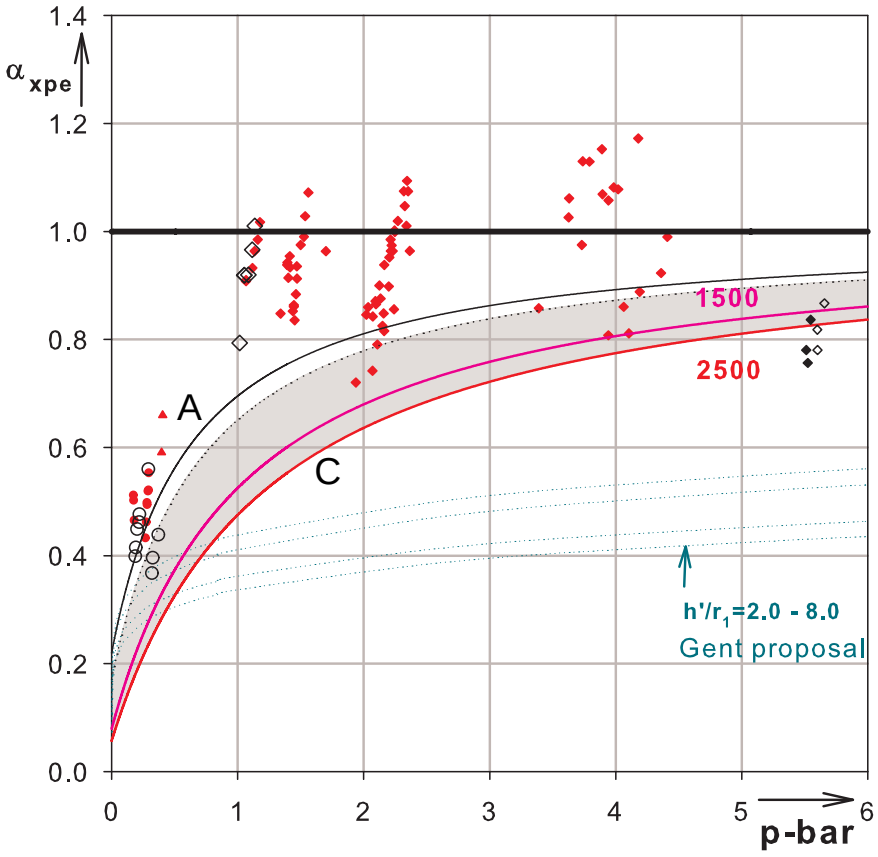

Figure 5.62 LFC linear-linear plot: $r_1/t\cos\beta$ = 1500 - 2500

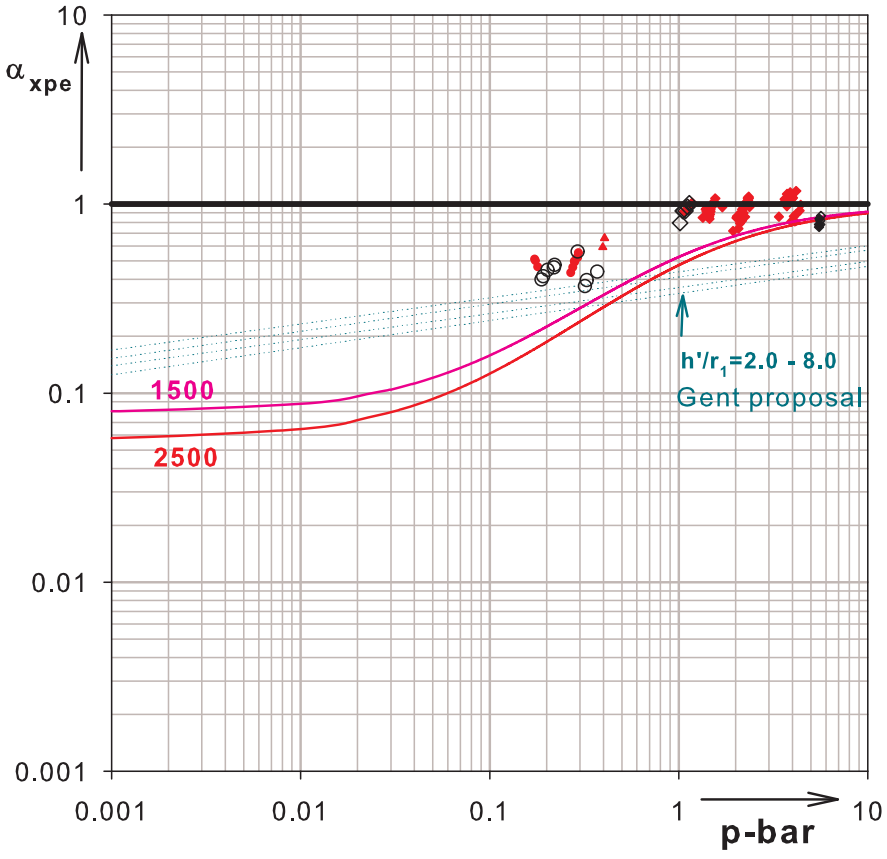

Figure 5.63 LFC log-log plot: $r_1/t\cos\beta$ = 1500 - 2500

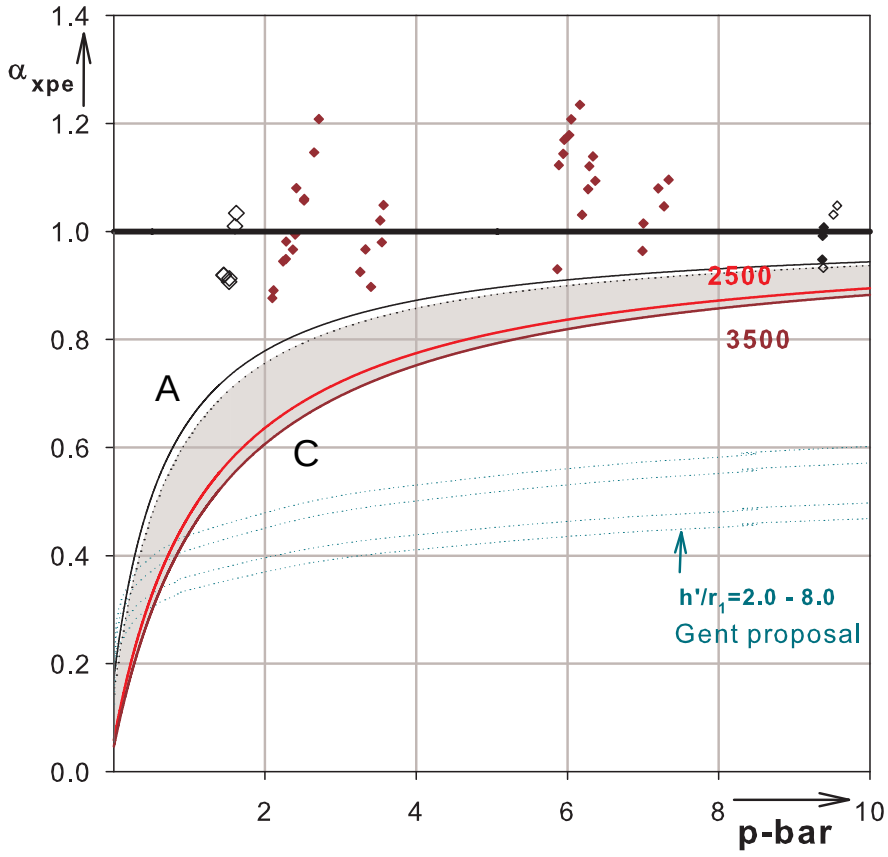

Figure 5.64 LFC linear-linear plot: $r_1/t\cos\beta$ = 2500 - 3760

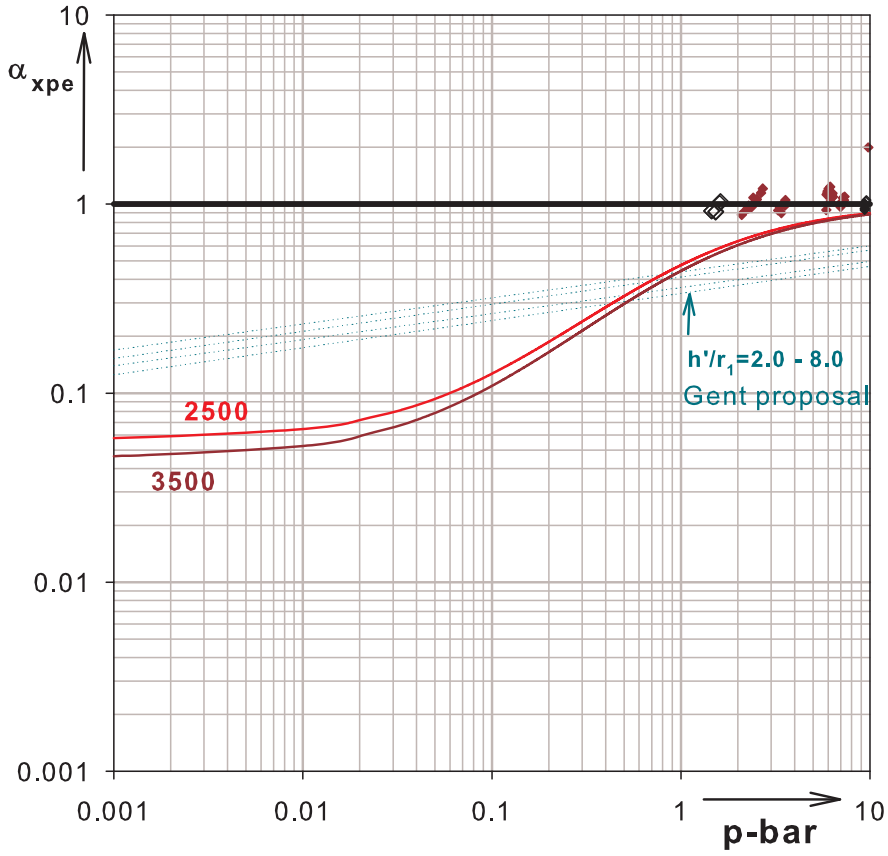

Figure 5.65 LFC log-log plot: $r_1/t\cos\beta$ = 2500 - 3760

5.8 Detailed comparison based on the LFC-elastic buckling limits

All the discussions so far were for an imperfection reduction factor which is applied to the case where the perfect elastic linear buckling (LBA) strength is given by the horizontal line $\alpha_{xpe} = 1.0$, i.e. when the perfect elastic buckling stress, $\sigma_{x,LBA}$, is scaled down to the classical reference buckling stress, $\sigma_{x,Rcr}$. However, unlike that of an axially compressed and internally pressurized cylindrical shell where the internal pressurization does not have a significant effect on the perfect elastic linear buckling strength ($\alpha_{xpe} = 1.0$), liquid-filled conical shells' LBA strength vary with the value of the internal pressure parameter $\bar{p}$. Therefore, as has been previously discussed, LFC imperfection reduction factors should be applied to the varying LBA buckling strength (with varying $\bar{p}$) of the liquid-filled conical shells instead of the $\alpha_{xpe} = 1.0$ line.

As a result, all the LFC curves that have been used for the different slenderness ratios of each group and representing the elastic buckling strength of the imperfect liquid-filled conical shells should all be scaled up in line with the LBA results of the LFC. Figure 5.66 shows the LFC LBA curves for the thicker and thinner shells (for both fixed and pinned bottom) in the grouping, the test data points and Gent curves.

This up scaling is applied to each $r_1/t\cos\beta$ group values discussed so far and is shown in Figure 5.67 to Figure 5.73. To avoid congestion, only the LFC curves representing the slender shell in each group with quality class-C is considered. Both the "fixed" and "pinned" bottom boundary condition cases are shown. The gray shaded area shows the region between the upper (perfect elastic) and lower (imperfect elastic) bounding curves of the slender shell in each group with "pinned" bottom boundary condition.

It can be seen from the plots that about 25 test data points lie outside this range, below the corresponding lower (imperfect elastic) curves for quality class-C. A comparison of the imperfection amplitudes in these test specimens and that of quality class-C has been made as shown in Table 5.4 and it turns out that 22 of the test data points have imperfection amplitudes larger than that permitted for quality class-C and hence can not be compared with the strength curves of that specific group. These test data points are shown in all the plots with an overlying bigger circular rings.

All the clamped bottom test data (shown with square shaped hollow symbols) have also been included in the respective group plots. These data points should be compared with their corresponding strength curves, i.e. they should be compared with the "FIX" curves.

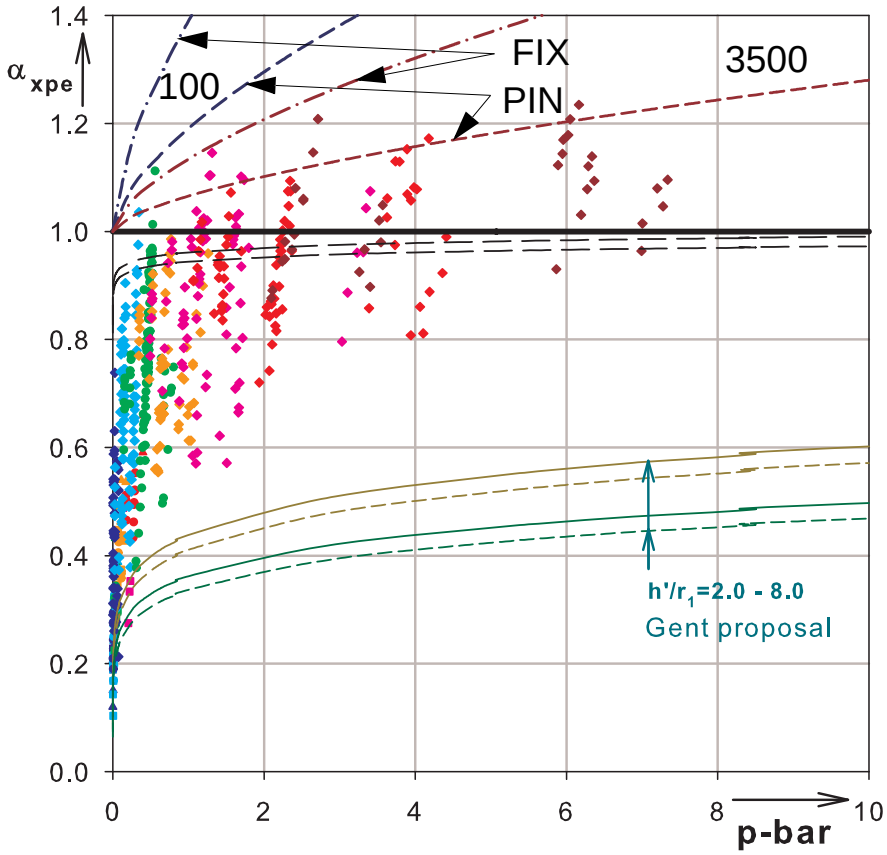

Figure 5.66 LFC linear-linear plot: LBA curves, Gent bounding curves & test data points

$r_1/t\cos\beta$ range of test data points	$r_1/t\cos\beta$ value	$\bar{p}$	α_{xpe}	test normalized imperfection amplitude, wo/t	quality class-C normalized imperfection amplitude, $\Delta w_k/t$
77 - 250	97.90	0.00102	0.11976	**0.802**	**0.618**
	192.73	0.00249	0.20957	**1.649**	**0.868**
	243.62	0.00302	0.12902	**1.719**	**0.976**
250 - 500	288.66	0.00555	0.11462	**1.609**	**1.062**
	303.58	0.00652	0.14587	**2.095**	**1.089**
500 - 750	726.63	0.66857	0.50642	**4.454**	**1.685**
	735.64	0.65632	0.49678	**4.589**	**1.695**
750 - 1000	889.38	1.00545	0.61289	**2.942**	**1.864**
	917.68	1.03357	0.61306	**4.100**	**1.893**
1000 - 1500	1079.37	1.05528	0.58472	**4.908**	**2.053**
	1108.42	1.09798	0.57061	**4.351**	**2.081**
	1195.30	1.41317	0.62181	**3.622**	**2.161**
	1330.15	1.62068	0.70918	**4.609**	**2.279**
	1344.37	1.66048	0.66509	**6.283**	**2.292**
	1367.01	1.50640	0.57150	**6.056**	**2.311**
	1471.93	3.10387	0.88680	**6.726**	**2.398**
	1491.08	3.03136	0.79619	**5.852**	**2.413**
1500 - 2500	1967.31	4.10510	0.81113	**7.457**	**2.772**
	1981.56	3.94071	0.80790	**9.263**	**2.782**
	2020.80	4.18952	0.88842	**7.768**	**2.810**
2500 - 3760	3037.87	7.00335	1.01484	**7.917**	**3.445**
	3293.50	5.86658	0.93006	**4.856**	**3.587**

Table 5.4 Comparison of test imperfection amplitudes vs. LFC quality class-C imperfection amplitudes

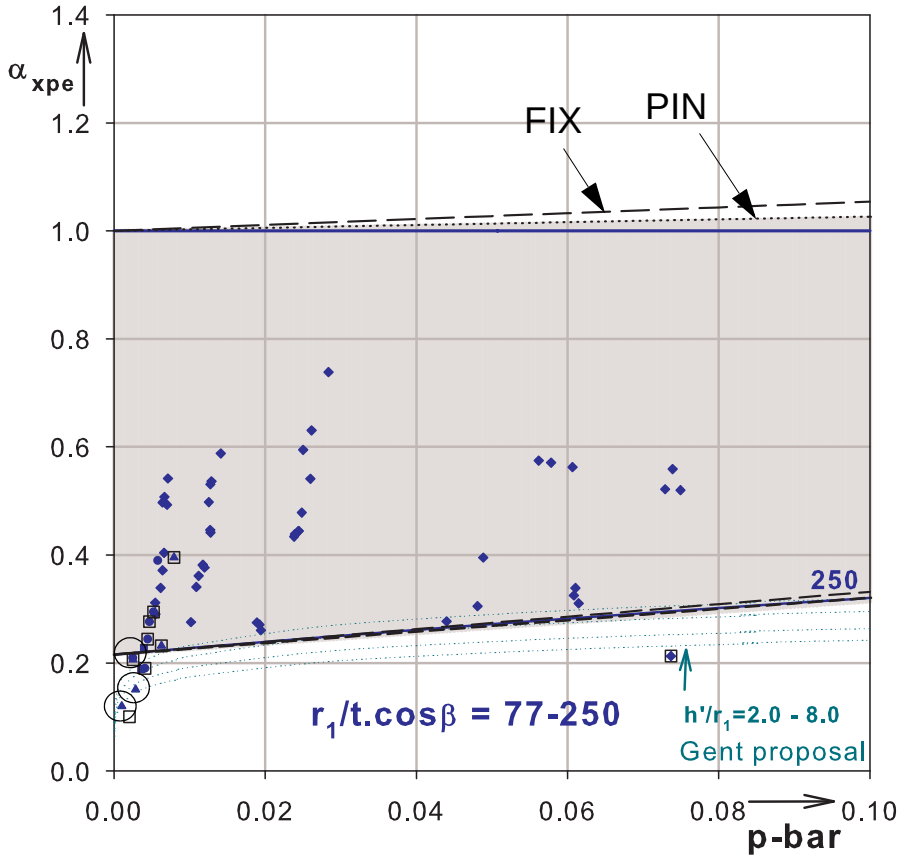

Figure 5.67 LFC curve: $r_1/t\cos\beta = 250$; pinned and fixed bottom

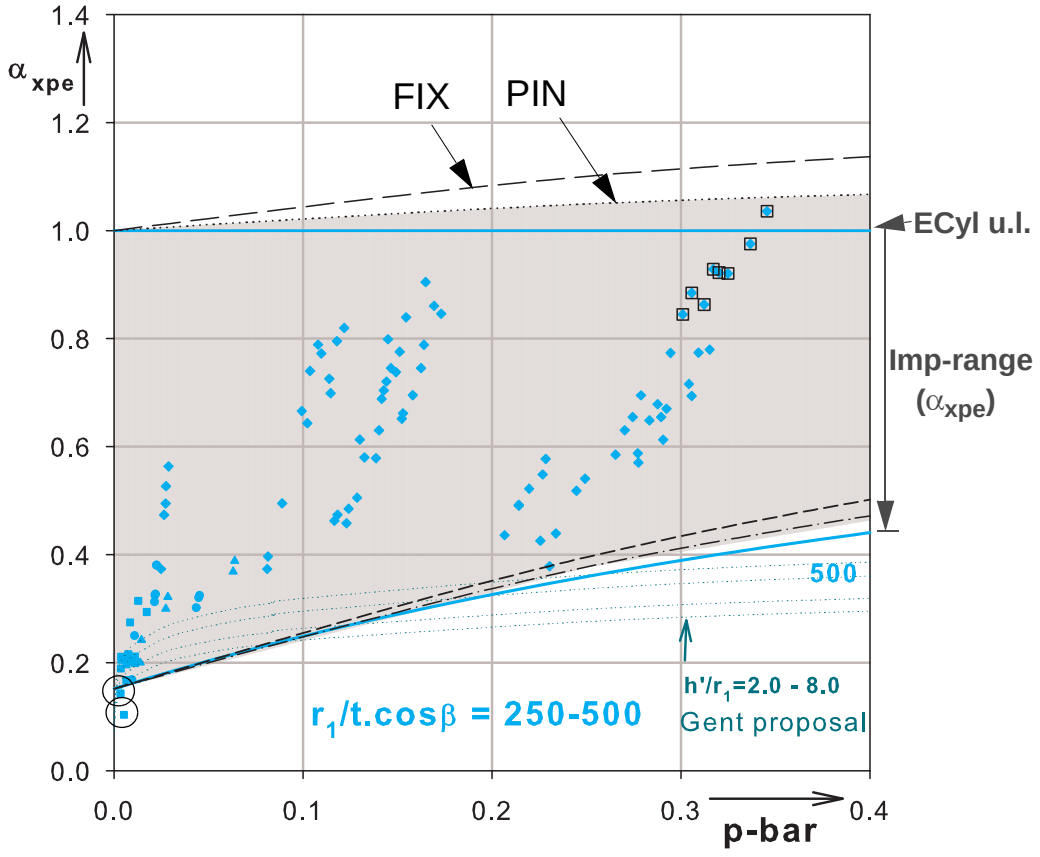

Figure 5.68 LFC curve: $r_1/t\cos\beta = 500$; pinned and fixed bottom

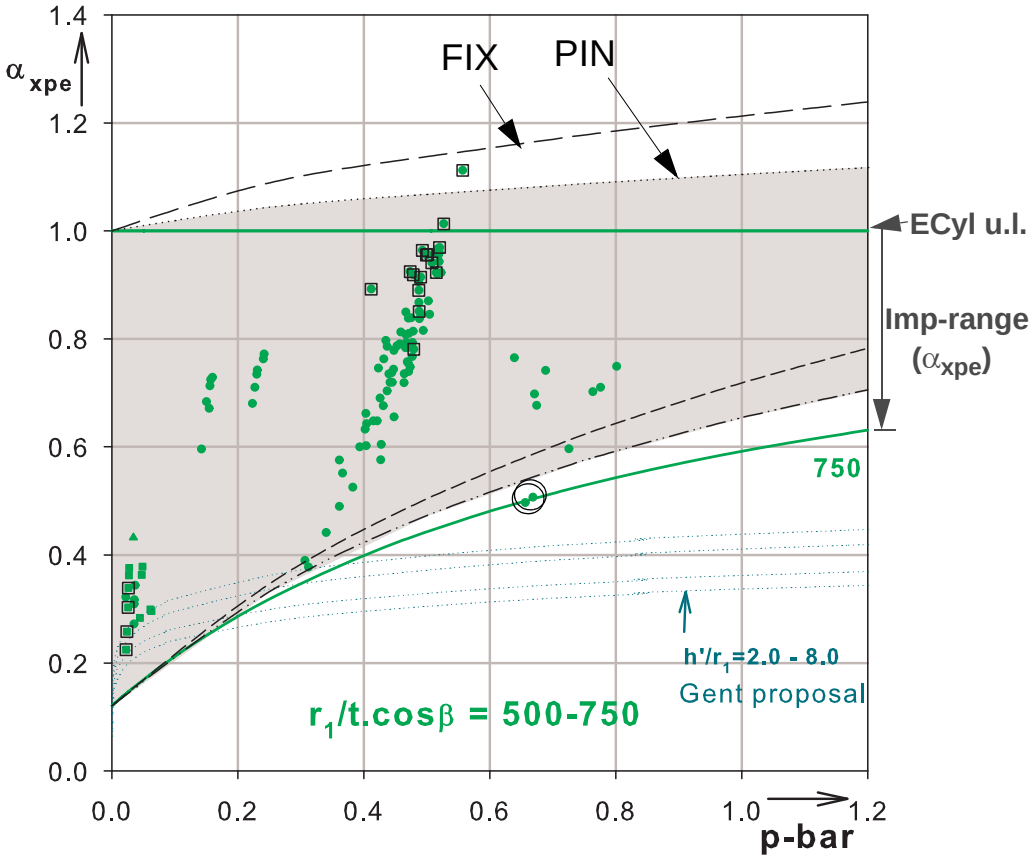

Figure 5.69 LFC curve: $r_1/t\cos\beta = 750$; pinned and fixed bottom

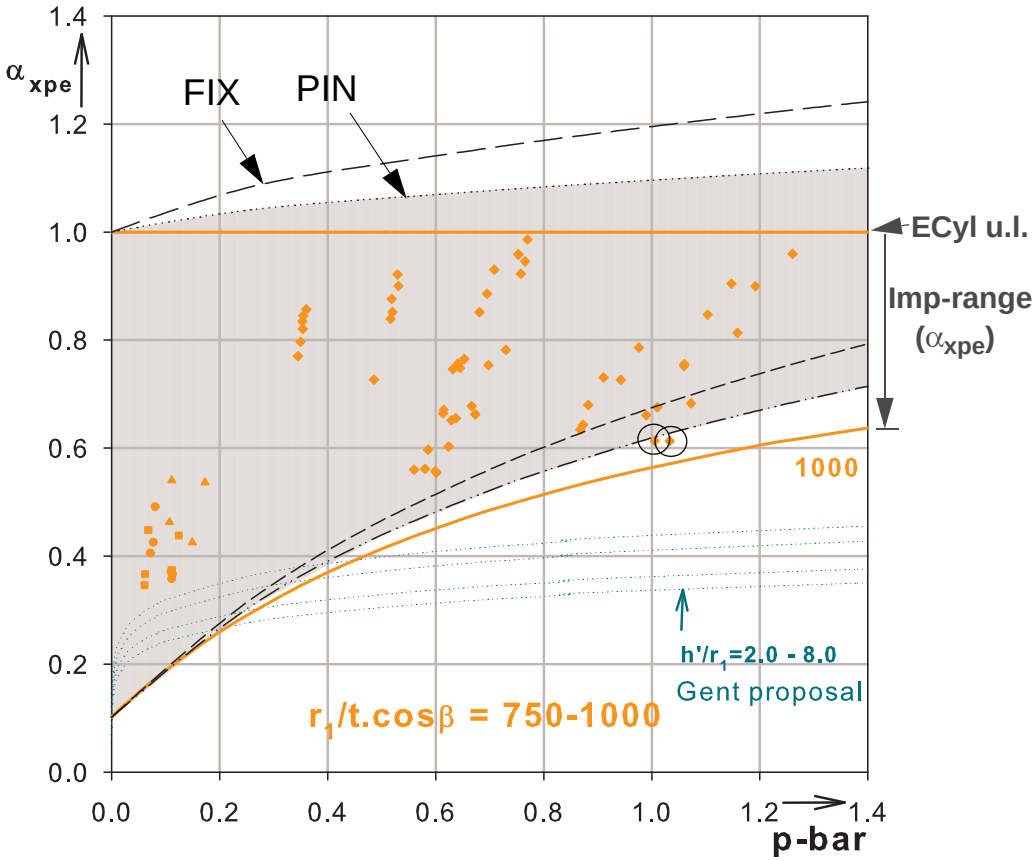

Figure 5.70 LFC curve: $r_1/t\cos\beta = 1000$; pinned and fixed bottom

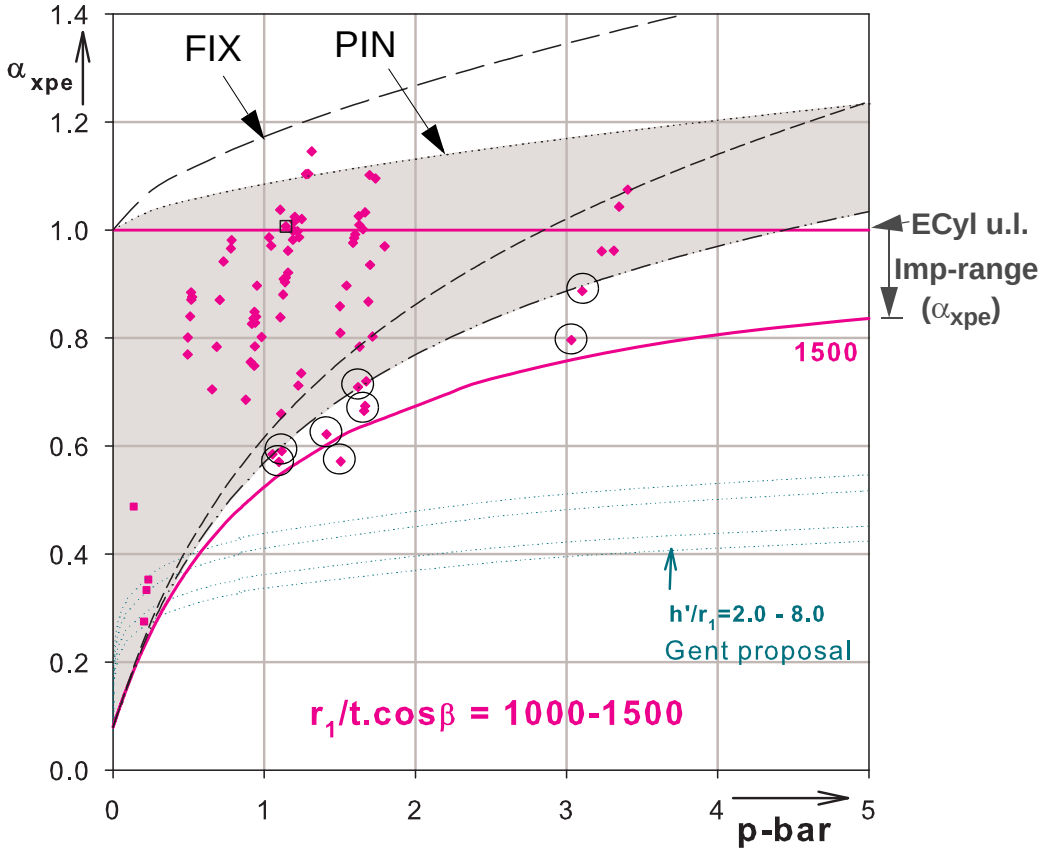

Figure 5.71 LFC curve: $r_1/t\cos\beta = 1500$; pinned and fixed bottom

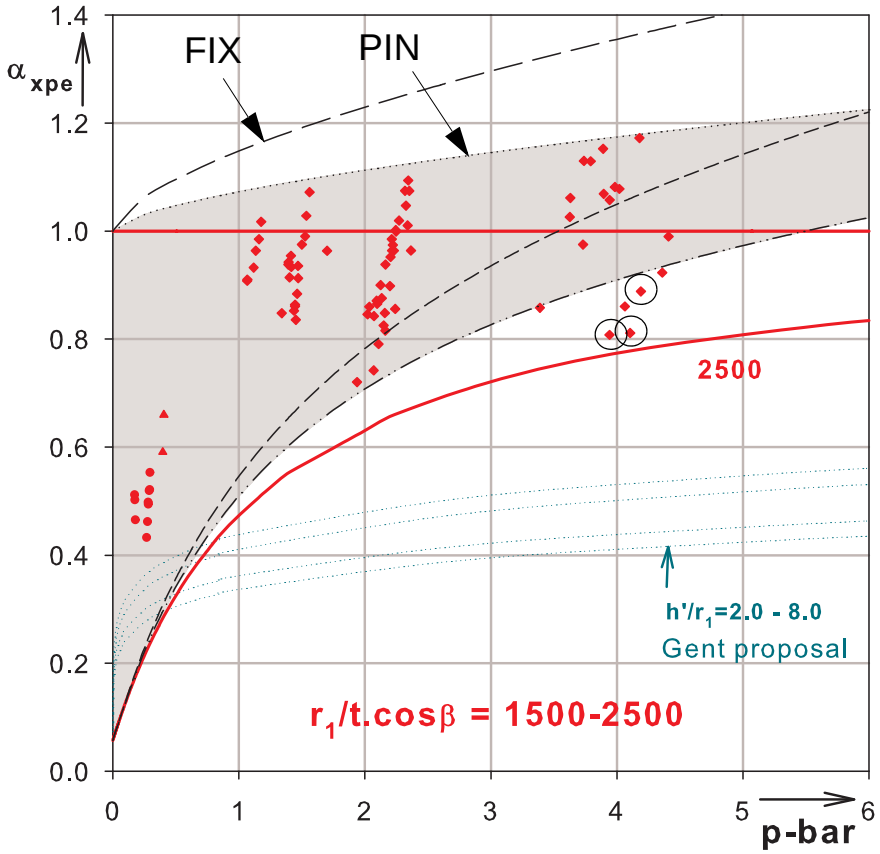

Figure 5.72 LFC curve: $r_1/t\cos\beta = 2500$; pinned and fixed bottom

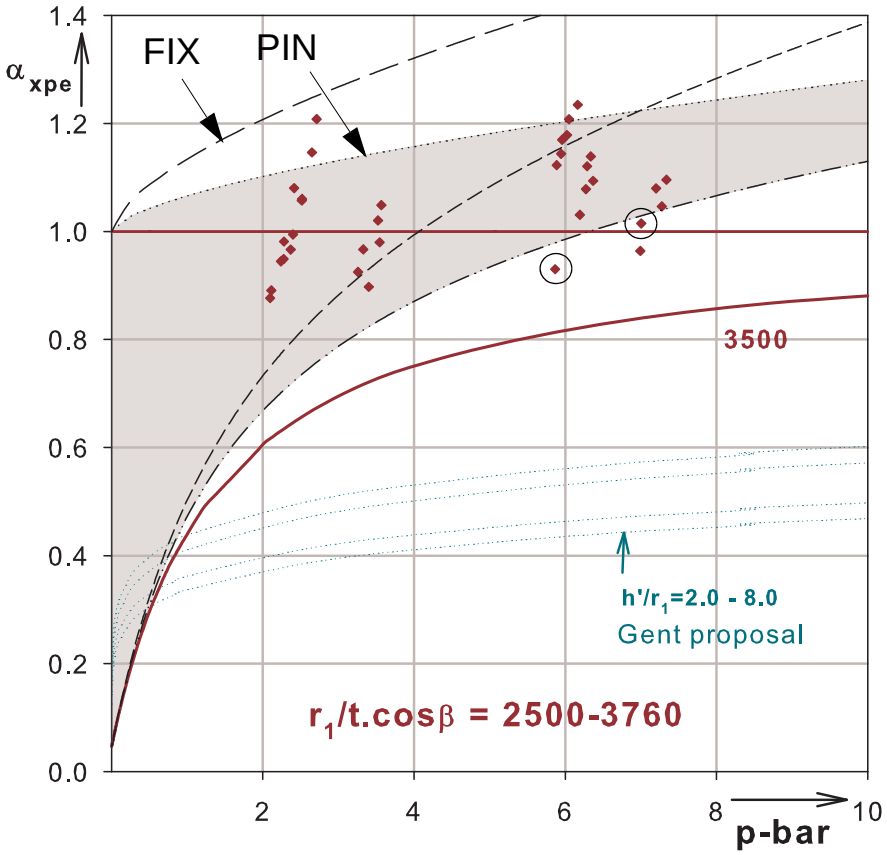

Figure 5.73 LFC curve: $r_1/t\cos\beta = 3500$; pinned and fixed bottom

5.9 LFC-imperfection reduction factor

From the detailed investigation of the Gent test results and an interpretation which is in line with the stress design and LBA-MNA buckling design principles, liquid-filled conical shells have the same strength reduction due to imperfections as those of cylindrical shells under axial compression and internal pressure.

$$\alpha_{xpe,\,LFC} \approx \alpha_{xpe,\,CYLINDER} \qquad \text{(Eq. 5.66)}$$

For verification purposes, the Belgium and Canada collapsed steel water towers have been analyzed and checked as follows.

5.9.1 Belgium collapsed steel water tower

The shell had two cone segments, lower and upper, with different thicknesses and apex-half angles. A complete buckling check has been made at the most critical locations of the tower: the lower cone base and upper cone base (junction between the two cones). The analyses made are summarized in Table 5.5. Additional comments and conclusions are also given at the end of this section.

Basic geometry, loading, and material variables (dimensions used: kN, mm)

lower cone base*:*	**upper cone base*:***
$h'_U = 6960$	$h'_U = 6210$
$r_1 = 2920$	$r_1 = 3794$
$\beta = 49.4$	$\beta = 51.0$
$t = 15.0$	$t = 8.0$

$\gamma' = 9.81*10^{-9}$ ... the only loading considered, i.e. shell own weight and roof loading excluded

Material properties (for both cones)

$E = 196.2$

$f_y = 0.236$ (will not be used in the present elastic buckling check!)

$\nu = 0.3$

5.9.2 Canada collapsed steel water tower

The shell had three cone segments: lowest, lower, and upper with different thicknesses but same apex half angle and a cylinder topping. The liquid surface level during buckling was within the cylindrical topping. The lowest, short (215.0 mm long) and thick (19.05 mm thickness), cone acts as a transition ring connecting the base plate and the lower cone. A complete buckling check has been made at two different critical locations: the lower cone base (junction between the lowest and lower cones) and upper cone base (junction between the lower and upper cones). The analyses made are summarized in Table 5.5. Additional comments and conclusions are also given at the end of this section.

Basic geometry, loading, and material variables (dimensions used: kN, mm)

lower cone base:	***upper cone base:***
h'_U = 8781.0 ... for $\sigma_{\theta,1}$ computation, existing liquid depth	h'_U = 6825.2 ... for $\sigma_{\theta,1}$ computation
h'_U = 8313.17...for $\sigma_{x,1}$ computation, replaced by full cone	h'_U = 6357.37...for $\sigma_{x,1}$ computation
r_1 = 5105.0	r_1 = 7060.8
β = 45.0	β = 45.0
t = 11.11	t = 9.525

$\gamma' = 9.81*10^{-9}$ ... the only loading considered, i.e. shell own weight and roof loading excluded

Material properties

lower cone base:	***upper cone base:***
E = 255	E = 214
f_y = 0.297 (will not be used in the elastic buckling check!)	f_y = 0.462
ν = 0.3	ν = 0.3

		Belgium tower		Canada tower	
		lower cone	upper cone	lower cone	upper cone
Shell slenderness	$r_1/(t\cos\beta)$	**299.13**	**753.59**	**649.83**	**1048.3**
Applied load computation	$\zeta' = h'\tan\beta/r_1$	2.781	2.021	1.56 (back calculated)	0.85 (back calculated)
	$\bar{\psi} = \frac{\zeta'}{6}(\zeta' + 3)$	2.679	1.692	1.19 (back calculated)	0.55 (back calculated)
	$\sigma_{\theta,u,1} = \frac{(\gamma' h'_U) r_1}{t\cos\beta}$	0.0204	0.0459	0.0560	0.0702
	$\sigma_{x,u,1} = \bar{\psi} \cdot \sigma_{\theta,u,1}$	0.0587	0.0777	0.0666	0.0383
	$\sigma_{x,Rcr} = 0.605\frac{Et\cos\beta}{r_1}$	0.3968	0.1575	0.2374	0.1235
	$\bar{p} = \frac{\sigma_{\theta,u,1}}{\sigma_{x,Rcr}}$	**0.0515**	**0.2915**	**0.2358**	**0.5684**
	$\alpha_{xpe,Load} = \frac{\sigma_{x,u,1}}{\sigma_{x,Rcr}}$	**0.1479**	**0.4930**	**0.2804**	**0.3099**
LFC_LBA buckling load factor, assuming “pinned” bottom	$\alpha_{LBA} = 1 + a\ (\varepsilon_b \cdot \bar{p})^{0.6}$	1.0254	1.0564	1.0458	1.0672
Imperfection Reduction Factor (IRF), assuming quality class-C	$IRF = \alpha_x + (1-\alpha_x)\frac{\bar{p}}{\bar{p} + 0.3/\alpha_x^{0.5}}$	0.2546	0.3420	0.3234	0.4353
Characteristic LFC buckling load factor, class-C	$\alpha_{xpe,LFC} = \alpha_{LBA} \cdot IRF$	**0.2610**	**0.3613**	**0.3382**	**0.4646**
Ratio of characteristic meridional stress to acting meridional stress, at cone base	$SafetyFactor = \frac{\alpha_{xpe,LFC}}{\alpha_{xpe,Load}}$	**1.7647**	**0.7329**	**1.2061**	**1.4992**
Immediate fulfilment of buckling criteria		**No**	**Yes**	**No**	**No**
Additional comments		see below for comments and conclusions			

Table 5.5 Results of the collapsed steel water towers, Belgium & Canada

Additional comments on the steel water tower collapse cases

From the above computations, the buckling phenomenon of the Belgium collapsed steel water tower should have been started on the base of the thin upper cone. The immediate fulfilment of the buckling criteria, even without considering any additional roof loading, own weight and load factor, indicates the fact that there was no any know-how about the possible occurrence of buckling at the time.

In the case of the Canada collapsed steel water tower, the safety factor (1.2061) obtained for the lower cone (without considering the loads coming from the tank wall and roofing) is too small to account for all (loading, boundary conditions, workmanship, material etc.) types of uncertainties. When the additional loading coming from the wall and roof (= 650 kN) is considered, the resulting additional meridional stress at the base of the cone is 0.0026, raising the value for $\alpha_{xpe,load}$ to 0.2914 and reducing the safety factor to 1.16. Therefore, if the collapse was really initiated by buckling, the buckling phenomenon of the Canada collapsed steel water tower should have been started on the base of the lower cone.

The loading situations during failure of both the Belgium upper cone and Canada lower cone segments already discussed are plotted in the classical critical buckling stress related pressure representation (α_{xpe} - $\overline{p}$ representation) along with the laboratory test results which lie on the same group of slenderness ratio values as shown in Figure 5.74.

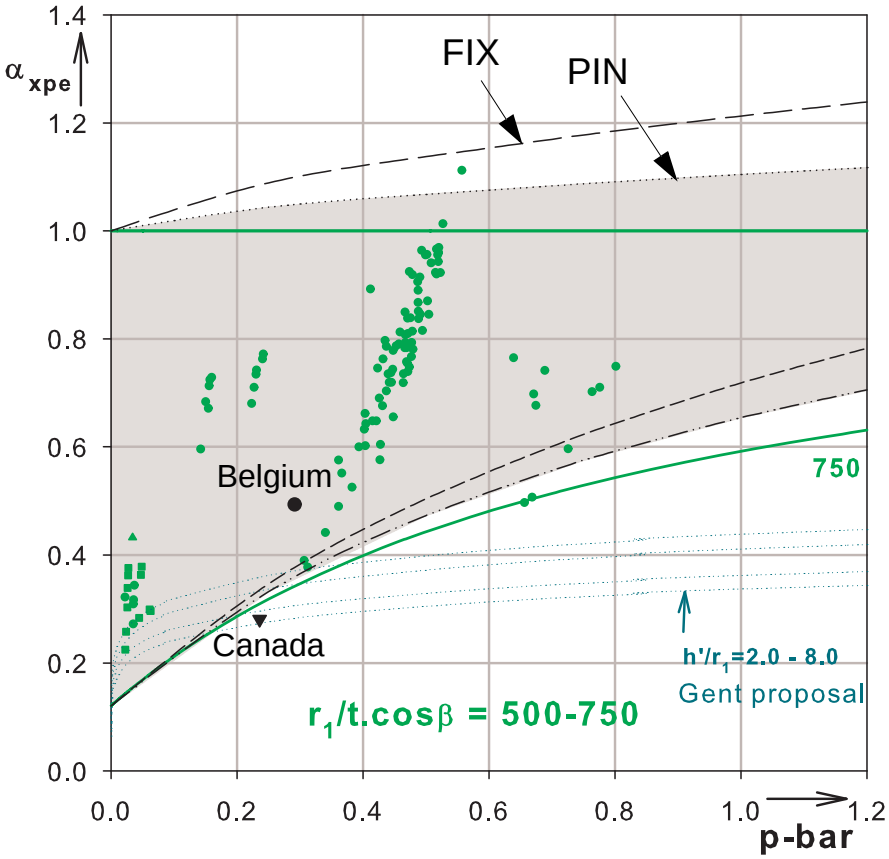

Figure 5.74 Water tower collapse situations & laboratory test results: $r_1/t\cos\beta$ = 500-750

5.10 Summary and Conclusion

- **Shell Slenderness** parameter, $r_1/t\cos\beta$, plays the most important role in every shell buckling phenomenon. The buckling strength of a shell depends on its slenderness ratio. The slenderness ratio parameter of conical shells is a function of the base radius, wall thickness, and apex half-angle of the cone and is given by $r_1/t\cos\beta$

- First, a rough comparison of the buckling behavior of "tip" compressed cones with the buckling behavior of an axially compressed internally unpressurized cylindrical shells; and liquid-filled conical shells with axially compressed internally pressurized cylindrical shells was made.

- Second, advanced judgment based on **LFC-specific LBA behavior** and **consistent** with cylinder imperfection reduction (α_{xpe}). The liquid-filled conical shells, because of the fast decaying meridional membrane section force distribution, have a higher LBA strength than cylindrical shells.

- The elastic buckling nature and the buckling strength reduction due to geometric imperfections of conical and cylindrical shells is similar.

- The Gent experimental results, according to the new interpretation and representation, show the quality of tests done. However, the Gent interpretation was not as clear as it is done in this study, to say the least. For example, the data points which are above the Gent perfect bounding lines were interpreted as might be caused by "unintended rotational restraint at the cone base instead of strictly simple support". The points, however, are high up because of the favorable buckling nature of liquid-filled conical shells. This fact has already been shown.

- At very **low** internal pressures, as $\overline{\mathbf{p}}$ approaches zero ($\overline{\psi}$ very large), a straight forward limit for the buckling strength of liquid-filled conical shells (same as for cylindrical shells) can be observed.

- At **medium** internal pressures, liquid-filled conical shells offer **higher stabilizing effect** due to internal pressurization than suggested by Gent proposal, i.e. the Gent proposal is too conservative for medium pressure values.

- Based on the new way of interpreting the test results, recommendations are made for the design of liquid-filled conical shells

- At **high** internal pressures, where plastic interaction is expected, **elephant's-foot** type buckling failure may happen close to the boundary and has already been investigated.

- Few additional specific numerical confirmation would be of interest and helpful.

6

Re-investigation of Gent test results:

Mercury-filled steel cones

6.1 Investigation of Gent mercury-test results

6.1.1 Gent mercury-test data

Following the extensive number of tests (more than 800) on elastic buckling strength assessment using water filling, relatively few (about 40, out of which only 38 are accepted) tests were made using mercury filling to measure the elastic-plastic buckling loads of liquid-filled thin-walled steel conical shells. The idea of using mercury filling as loading (instead of water) was to make use of its heavier specific weight in producing higher internal pressurization.

All the tests performed were made using steel cones with smaller radius of r_1 = 10 cm, apex-half angle of $\beta = 40°$ and varying the thickness between 0.05 cm and 0.1 cm. In terms of the shell slenderness ratio, the cones tested varies from $r_1/t\cos\beta = 130$ to 250. The material properties measured were modulus of elasticity E = 20000 kN/cm^2, Poisson's ratio $\nu = 0.29$, and uni-axial yield strength f_y varying between 15.3 kN/cm^2 and 33.3 kN/cm^2. Imperfection amplitudes were measured using a $3.6\sqrt{r_1/(t\cos\beta)}$ length stick in a $15\sqrt{r_1/(t\cos\beta)}$ wide region (sometimes even wider) along the meridian. The liquid-depth level at buckling was measured and recorded.

6.1.2 Current investigation

In the current investigation, the ultimate measured liquid-depth in terms of which the magnitude of the meridional membrane compressive stress and circumferential tensile stress at the base of the cone are computed step-by-step as follows:

$$\zeta' = \frac{h' \cdot \tan\beta}{r_1} \qquad \text{(Eq. 6.1)}$$

$$\bar{\psi} = \frac{\zeta'}{6}(3 + \zeta') \qquad \text{(Eq. 6.2)}$$

$$\sigma_{x,1} = \frac{\gamma' h' r_1}{t\cos\beta} \cdot \bar{\psi} \qquad \text{(Eq. 6.3)}$$

$$\sigma_{\theta,1} = \frac{\gamma' h' r_1}{t\cos\beta} = \frac{\sigma_{x,1}}{\bar{\psi}} \qquad \text{(Eq. 6.4)}$$

The intensity of internal pressurization is therefore inversely proportional to the liquid-depth measured when buckling occurs. All the above quantities have been calculated for all the mercury tests made and the results are compared with the elastic-plastic characteristic buckling strength computed using the interaction expression discussed above. As far as plasticity effect is concerned, yield strength related representations are used for graphical comparison of the results. The 38 mercury

tests are re-grouped into three categories depending on the shell slenderness ratio value. The first group comprises of cones with shell slenderness ratio values varying between $r_1/t\cos\beta = 130$ and 150, the results of which are plotted in the pressure representation shown in Figure 6.1. The second and third group comprise of cones with shell slenderness ratio values varying from $r_1/t\cos\beta = 165$ to 190 and $r_1/t\cos\beta = 220$ to 250, the results of which are shown in Figure 6.2 and Figure 6.3, respectively. The imperfection amplitudes measured during testing are compared with the maximum allowed for different fabrication quality class as recommended by EN 1993-1-6 and classification has been done accordingly. Different symbols are used for the different quality classes as shown in the respective figures. Quality class-D in this discussion refers to those measured imperfection amplitudes which are higher than that of class-C. In each of the plots the elastic and elastic-plastic characteristic buckling strengths of conical shells with the two bounding shell slenderness values of each group are included for fabrication tolerance quality classes A&C. Besides, the elastic-plastic interaction with membrane Mises plasticity using the basic plastic buckling parameters (as has been done for the cylindrical shell) is shown for comparison purposes.

Despite the above discussion and comparison of results, it should be noted here that the only imperfection information measured and recorded during testing was the amplitude (maximum depression from a measuring gauge) and nothing has been reported about the imperfection shape, imperfection wavelength, and exact imperfection location along the meridian. Even the imperfection amplitude reported for each test setup might have been as far located as $15\sqrt{r_1/(t\cos\beta)}$ (the region assessed during testing) while the buckling (elastic or elastic-plastic) phenomenon is more likely to happen in the bottom one-quarter of this length. This fact can clearly be seen from the inconsistency in the imperfection amplitudes measured and the buckling strength obtained during testing, i.e. a conical shell with an imperfection amplitude less than that allowed for quality class-A (close to perfect cone) failed at a load much lower than a similar cone having class-C imperfection amplitude; and a conical shell with an imperfection amplitude much larger than that allowed for quality class-C failed at a load as high as that of class-A. Generally speaking, the tests performed were not that consistent, to say the least, and much can not be drawn from the test results. Moreover, even though mercury filling has been used to make use of its heavier specific weight in producing higher internal pressurization, it was not as high as it might have been intended as the above discussion and re-examining of the test results reveal, see Figure 6.1 to Figure 6.3. In conclusion, a maximum of three tests would have been enough to get the same information obtained from performing all the 40 expensive tests which all result in similar and very low internal pressurization, i.e. all tests were done for a (nearly) constant big $\overline{\psi}$ value showing that the effect of internal pressurization on bi-axial plasticity can not be seen.

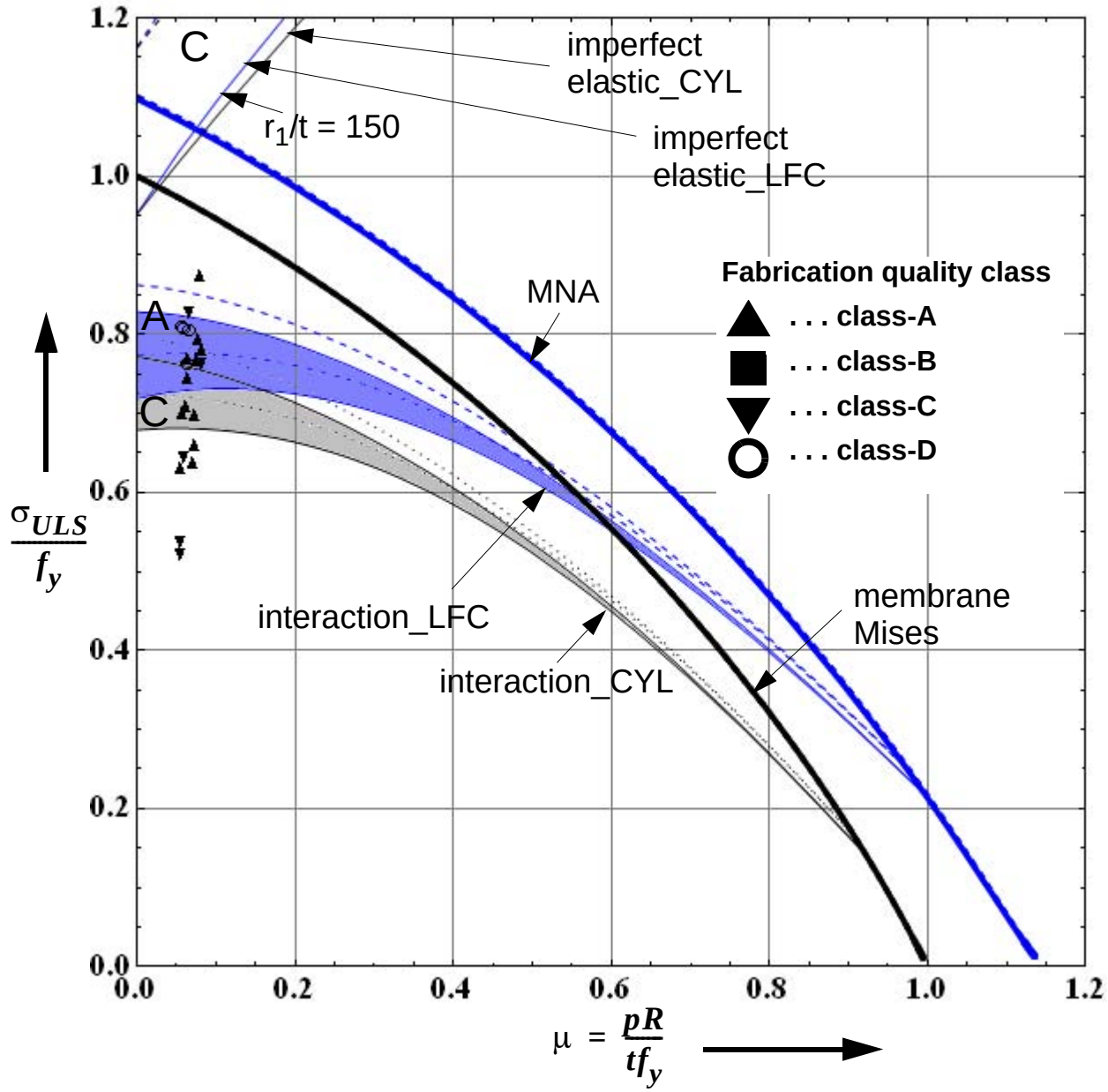

Figure 6.1 Gent mercury test data points $r_1/t\cos\beta$ = 130 - 150

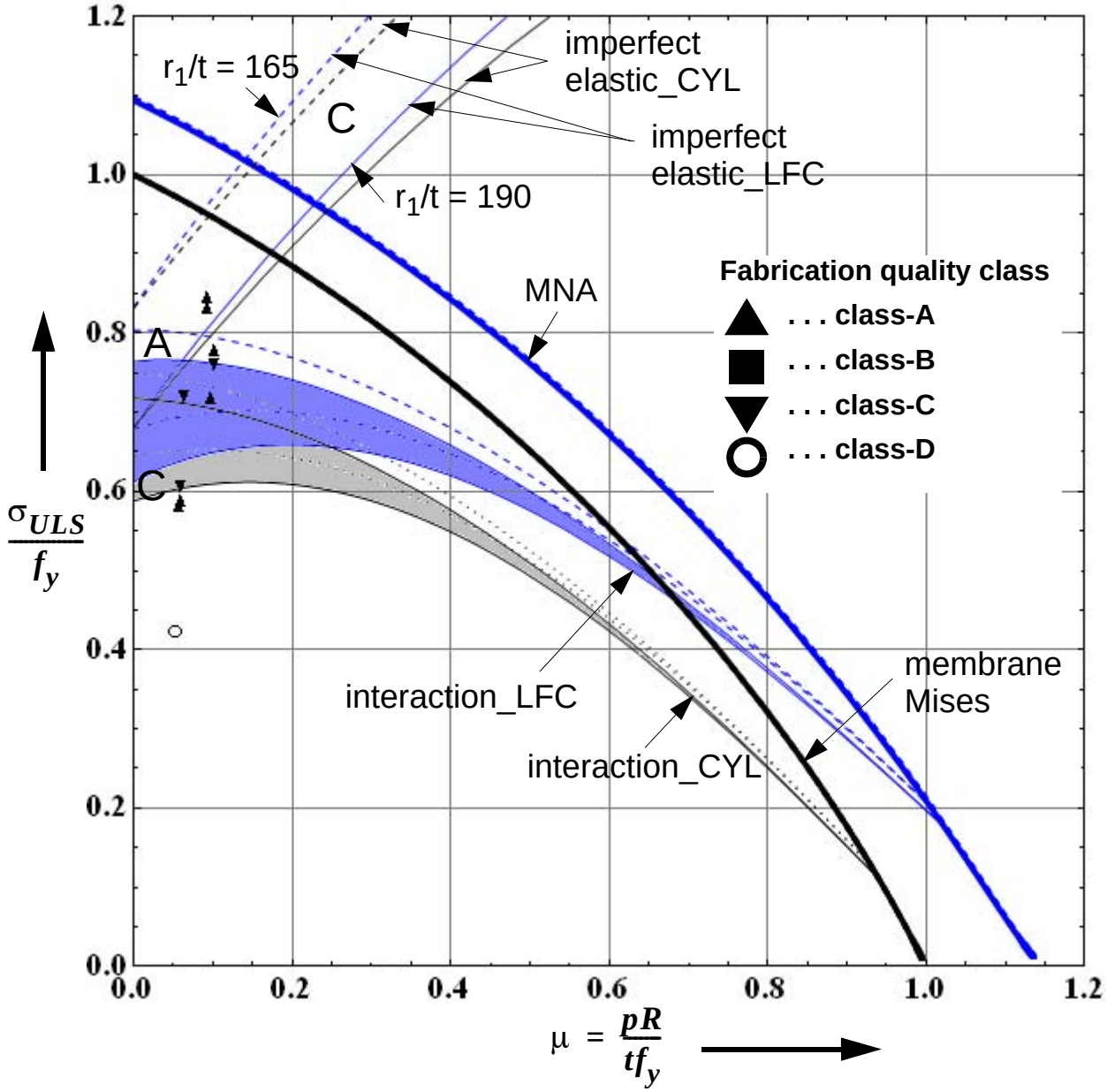

Figure 6.2 Gent mercury test data points $r_1/t\cos\beta$ = 165 - 190

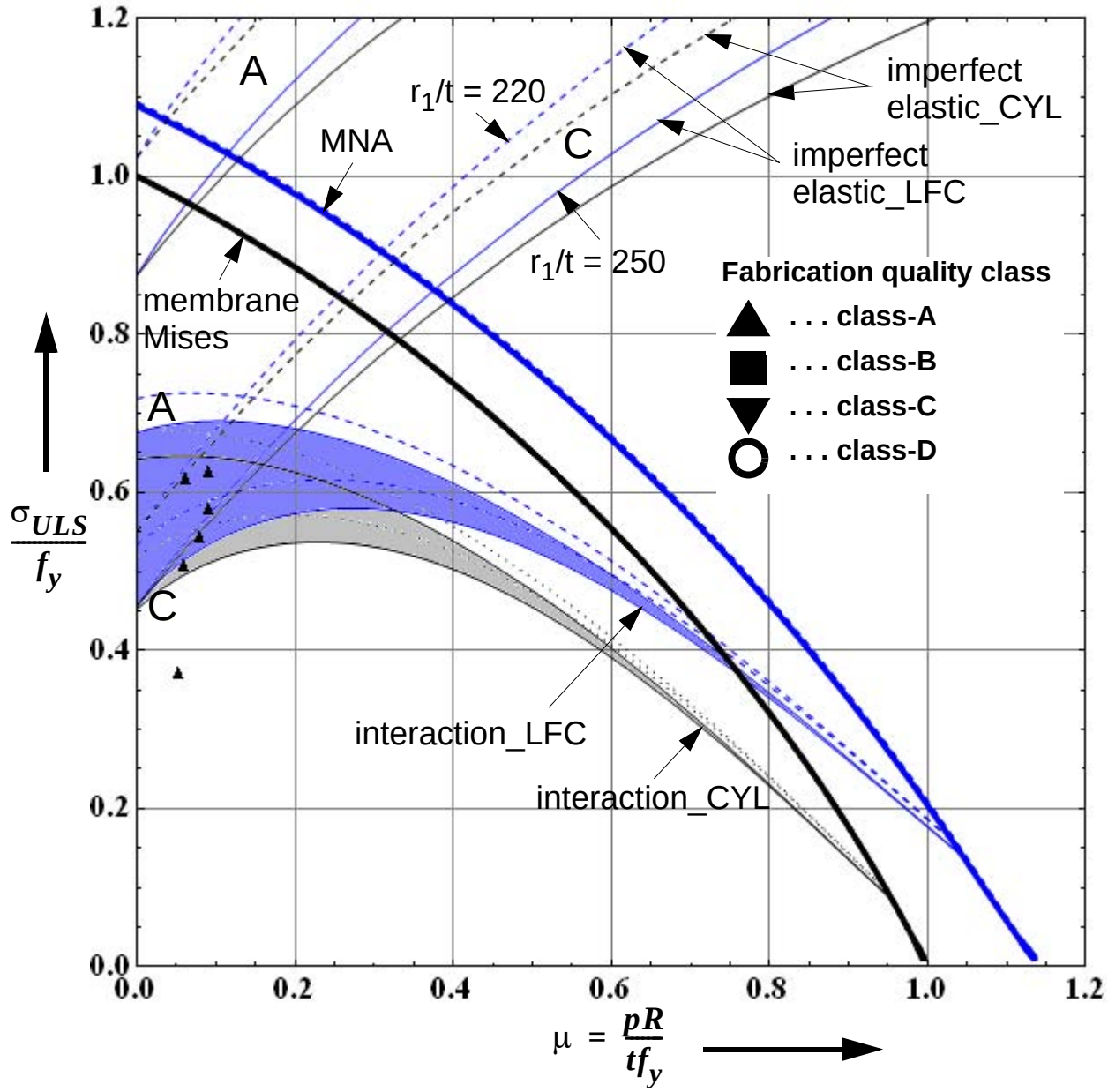

Figure 6.3 Gent mercury test data points $r_1/t\cos\beta$ = 220 - 250

6.2 Geometrically and materially nonlinear analysis of imperfect cones

Following the laboratory tests using mercury filling, Ramm (1991) made few nonlinear numerical analyses using axisymmetric shell model for pre-specified liquid-depths, three of which were taken from the Gent mercury tests. These three specific cases were modelled as used in the laboratory setup, i.e. informations concerning cone geometry, material, loading, bottom boundary condition, and imperfection amplitude were adopted from the report of the laboratory tests. Since there are no informations about the shape, wavelength, and along-meridian location of the measured imperfections, Ramm considered a linear buckling eigenmode-affine imperfection and made geometrically and materially nonlinear numerical analyses of the imperfect cones to compare his results with the results obtained from laboratory testing. He obtained 1% difference for two of the cones and 5% difference for the third cone concluding that there is a good correlation between the test results and his numerical analyses. It should, however, be recalled that the use of an LBA eigenmode-affine imperfection to simulate the laboratory test imperfection conditions may not be fair (to say the least) and the 1% and 5% correlation obtained should be a chance occurence.

A nonlinear numerical analyes have been made in the current work for one of the cones tested in the laboratory and also that analysed by Ramm (F275SAD), on one hand, to confirm Ramm's results and, on the other broader hand, to make an imperfection sensitivity study of the mercury-filled cone to an LBA eigenmode-affine imperfection by varying the imperfection amplitude. Besides, materially nonlinear analysis and geometrically & materially nonlinear analysis of the perfect cone will be compared to that of Ramm's corresponding results. It should, however, again be noted that an LBA eigenmode-affine imperfection shape is very far from the possible imperfection shape in laboratory experiments and, generally speaking, the results obtained from the numerical analyses will have no direct relation with the result obtained from testing. The details of the cone under consideration are as follows:

Geometry: $r_1 = 10$ cm; $t = 0.05166$ cm; $\beta = 40°$; $h' = 60$ cm

Boundary conditions: pinned bottom

Loading: mercury filling $\gamma' = 132.916 .10^{-6}$ kN/cm^3

Material properties: $E = 17459$ kN/cm^2; $\nu = 0.29$; $f_y = 21.73$ kN/cm^2

It can be seen from Figure 6.6 that for an LBA eigenmode-affine imperfection and an amplitude adopted from the test, Ramm's results differ by about 5% from the results obtained in this work. This difference in the GMNIA results, taking the overlapping MNA and GMNA results obtained into consideration, may result from a possible procedural difference in measuring an imperfection amplitude. In this work the imperfection amplitude is measured according to the guage length

procedure of EN 1993-1-6, i.e. method-1 in Figure 6.4. The results of the imperfection sensitivity study is also shown in Figure 6.5 where the normalized strength, GMNIA/GMNA versus the imperfection amplitude (ratio with respect to the wall thickness) of an LBA eigenmode-affine imperfection is plotted. To investigate the effect of imperfection-orientation on the shell buckling strength, the eigenmode has been considered twice once with first half wave oriented outward and once with first half wave oriented inward. Both results are included in Figure 6.5.

On the other hand, Vanlaere (2008) did nonlinear numerical simulations using full cone models of seven liquid-filled cones (one of which was purely elastic) and compared his results with those obtained using the procedure recommended by EN 1993-1-6. In his numerical simulations, Vanlaere used the iterative load increase procedure discussed above to compute the ultimate liquid-depth which will result in a buckling load factor of 1.0 when water is used as loading. He performed GNIA, GMNA, and GMNIA for all the seven cones with separate iterations for each analysis type. An LBA eigenmode-affine imperfection with an amplitude equal to that of fabrication quality class-C was used when simulating the buckling strengths of the imperfect cones.

Despite the use of full cone models in the numerical analyses, the buckling modes for the LBA, GMNA and GMNIA cases were all axisymmetric where he later used an axisymmetric cone model with pre-specified liquid-depth to re-compute the nonlinear buckling strengths of one of his cones (cone-2) and obtained the same results. The buckling strength results he obtained for cone-2 using the different loading procedures, shown as “Gent, 2008”, along with the results of this study are shown in Figure 6.7. The details of Vanlaere’s cone-2 are as follows:

Geometry: $r_1 = 300$ cm; $t = 1$ cm; $\beta = 45°$

Boundary conditions: pinned bottom

Loading: water filling

Material properties: $E = 21000$ kN/cm^2; $\nu = 0.3$; $f_y = 24$ kN/cm^2

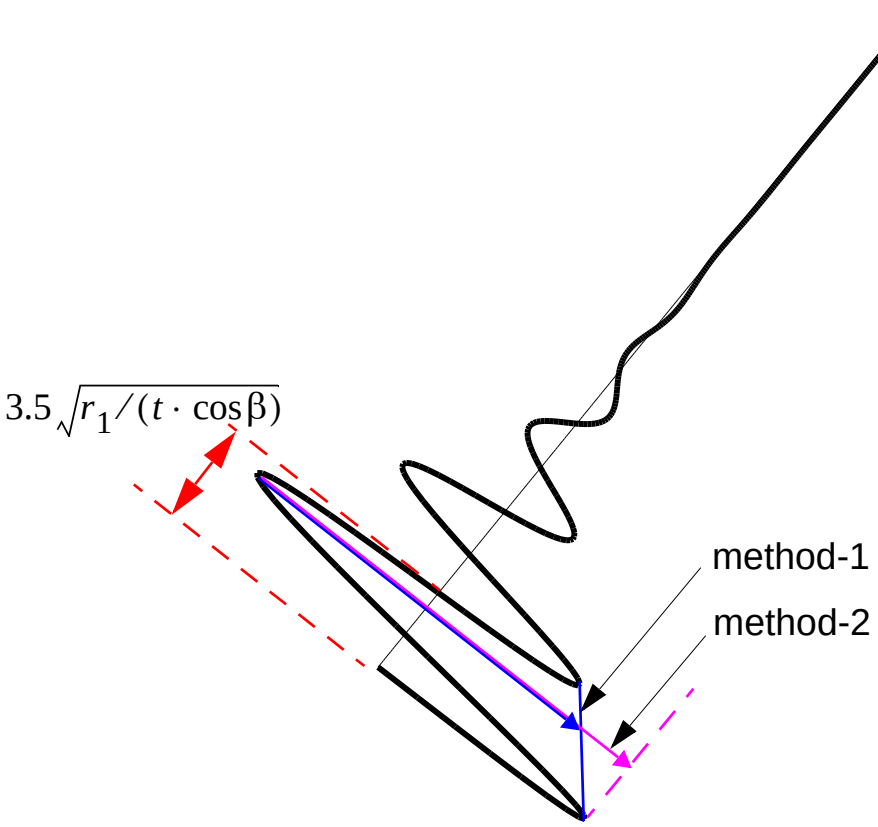

Figure 6.4 Linear buckling basic eigenmode: Pinned bottom

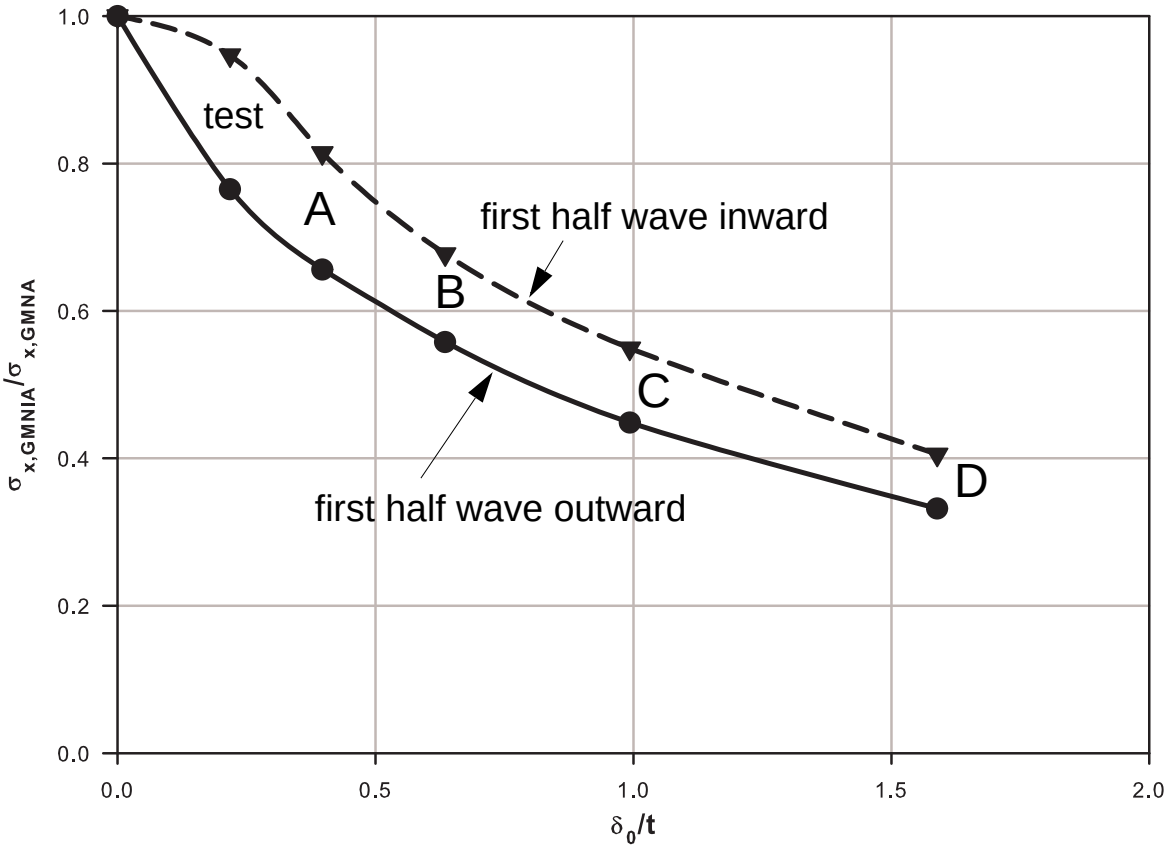

Figure 6.5 Geometrically and materially nonlinear analyses using an LBA eigenmode-affine imperfection: Pinned bottom

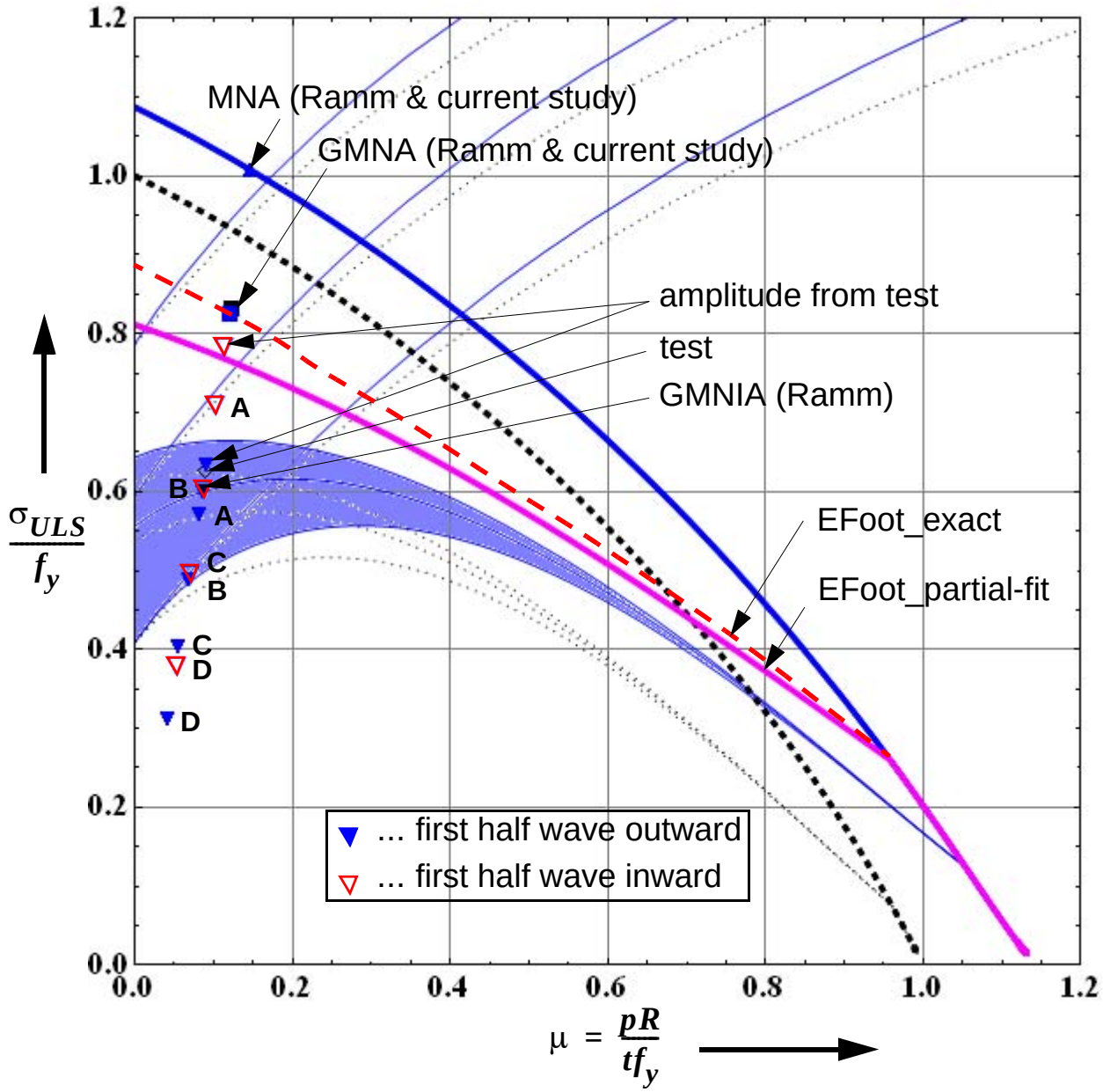

Figure 6.6 F275SAD test and numerical analysis results: $r_1/t\cos\beta = 255$

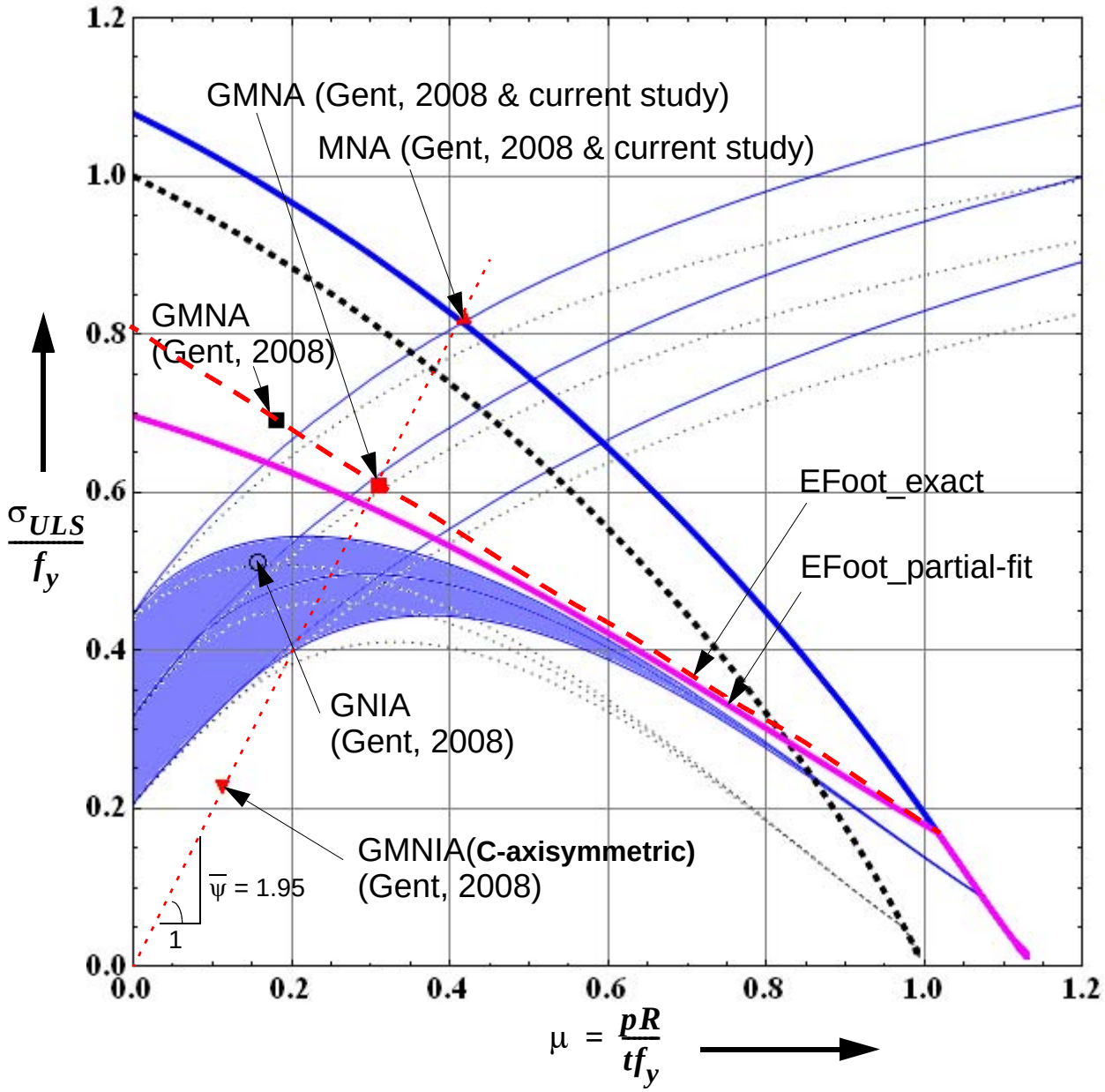

Figure 6.7 Vanlaere cone-2 numerical analysis results: $r_1/t\cos\beta = 425$

6.3 Summary and conclusions

Detailed investigation of Gent mercury test results along with detailed discussions, explanations, and conclusions have been done. Previous LFC-related research works on nonlinear simulation of liquid-filled conical shells with/out geometric imperfections have as well been discussed and few cases have been re-examined for confirmation and further studying purposes. Relevant explanations and conclusions have been given to the outcomes of those works.

7

Re-examination of two tank failure cases

7.1 Steel water tower failure cases

The failure cases of the steel water towers in Senefe, Belgium in 1972 and in Fredricton, Canada in 1990 are re-examined in this section to check if plasticity effects played a role during the collapse. It can be recalled that the Belgium tower had two cones, lower and upper, with different thicknesses and apex-half angles and hence the buckling check will be done at the base of each cone segment. Similarly, the Canada tower had three cone segments: lowest, lower, and upper with different wall thicknesses but same apex-half angle. With the lowest thick cone acting as a transition ring connecting the base plate and the lower cone, the buckling check has been made at the lower and upper cone bases of the tower.

The check has been done based on the procedure for liquid-filled conical shells discussed so far the results of which are plotted in the pressure representation as shown in Figure 7.1 to Figure 7.4 where the charactertsic buckling strength of the different conical shell segments are shown for fabrication quality classes of A, B, and C according to EN 1993-1-6 with which the loadings at the cone segments during collapse are compared. Figure 7.1 and Figure 7.2 show the results for the lower and upper cone segments, respectively, of the Belgium tower. Similarly, Figure 7.3 and Figure 7.4 show the results for the lower and upper cone segments, respectively, of the Canada tower.

It can be seen from these plots that there was no role played by plasticity effects in the failure phenomenon and hence the elastic buckling check and corresponding explanations which have already been done in the discussion of pure elastic buckling is sufficient.

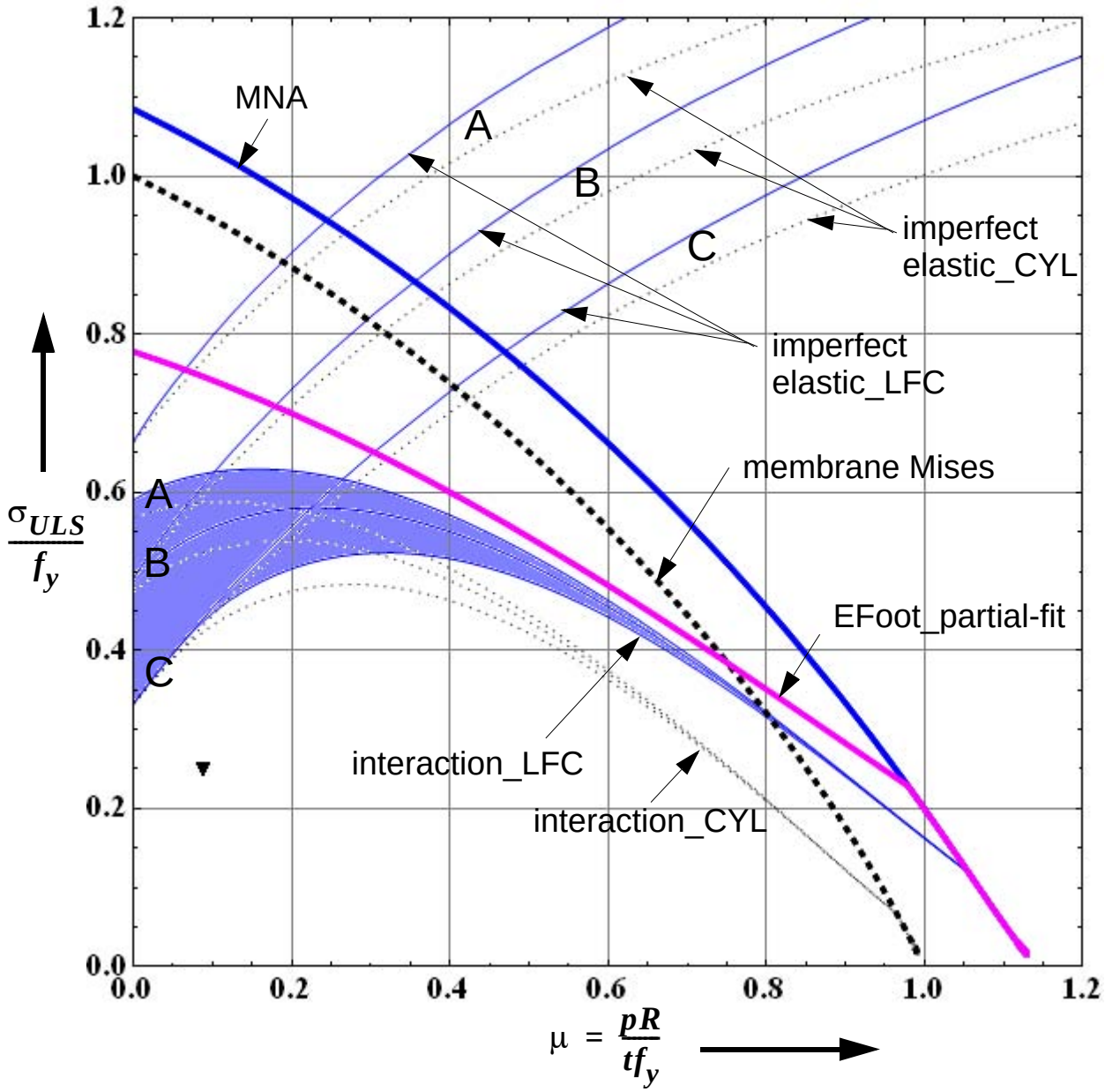

Figure 7.1 Belgium tower failure: lower cone with $r_1/t\cos\beta = 300$

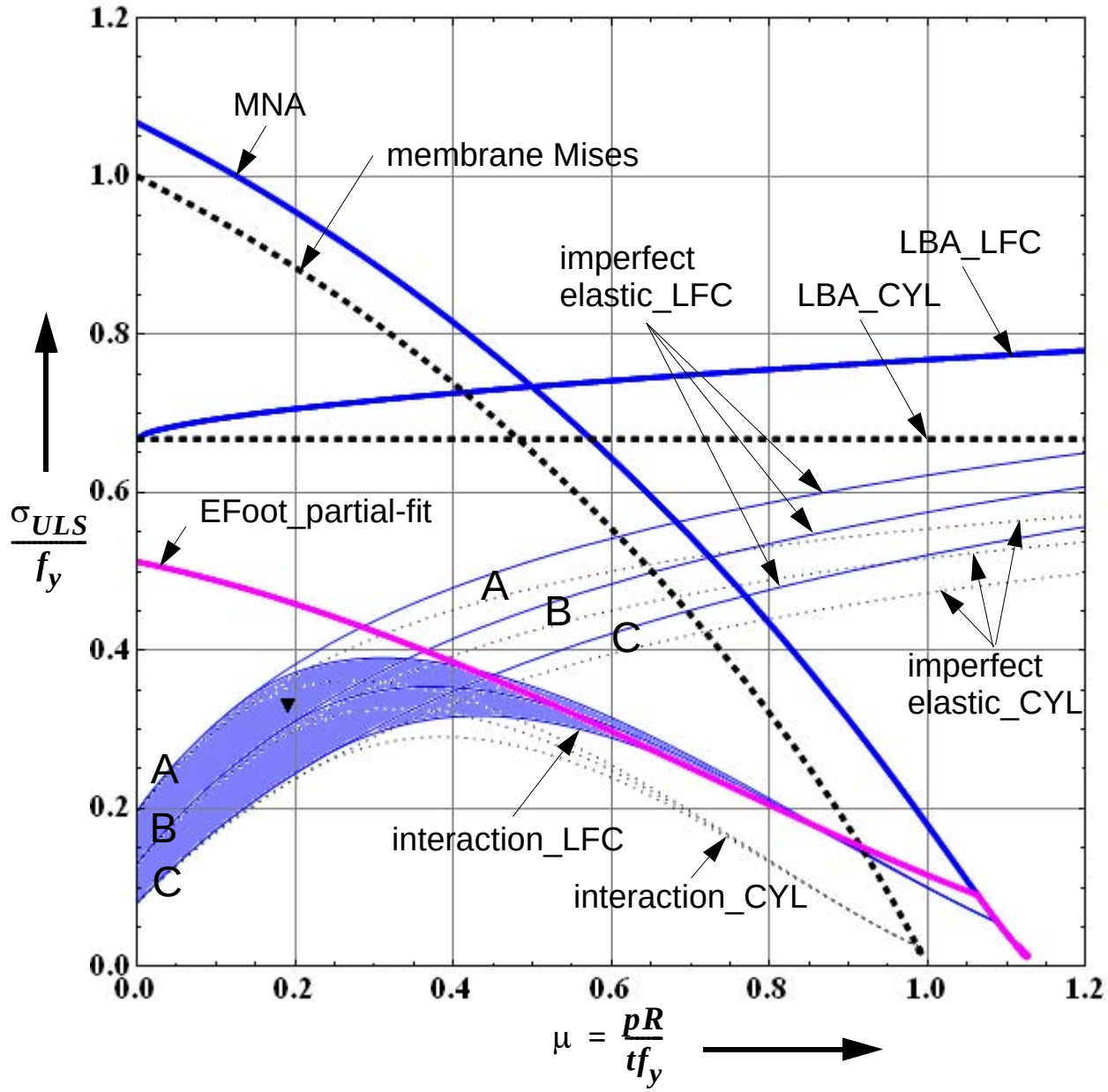

Figure 7.2 Belgium tower failure: upper cone with $r_1/t\cos\beta = 755$

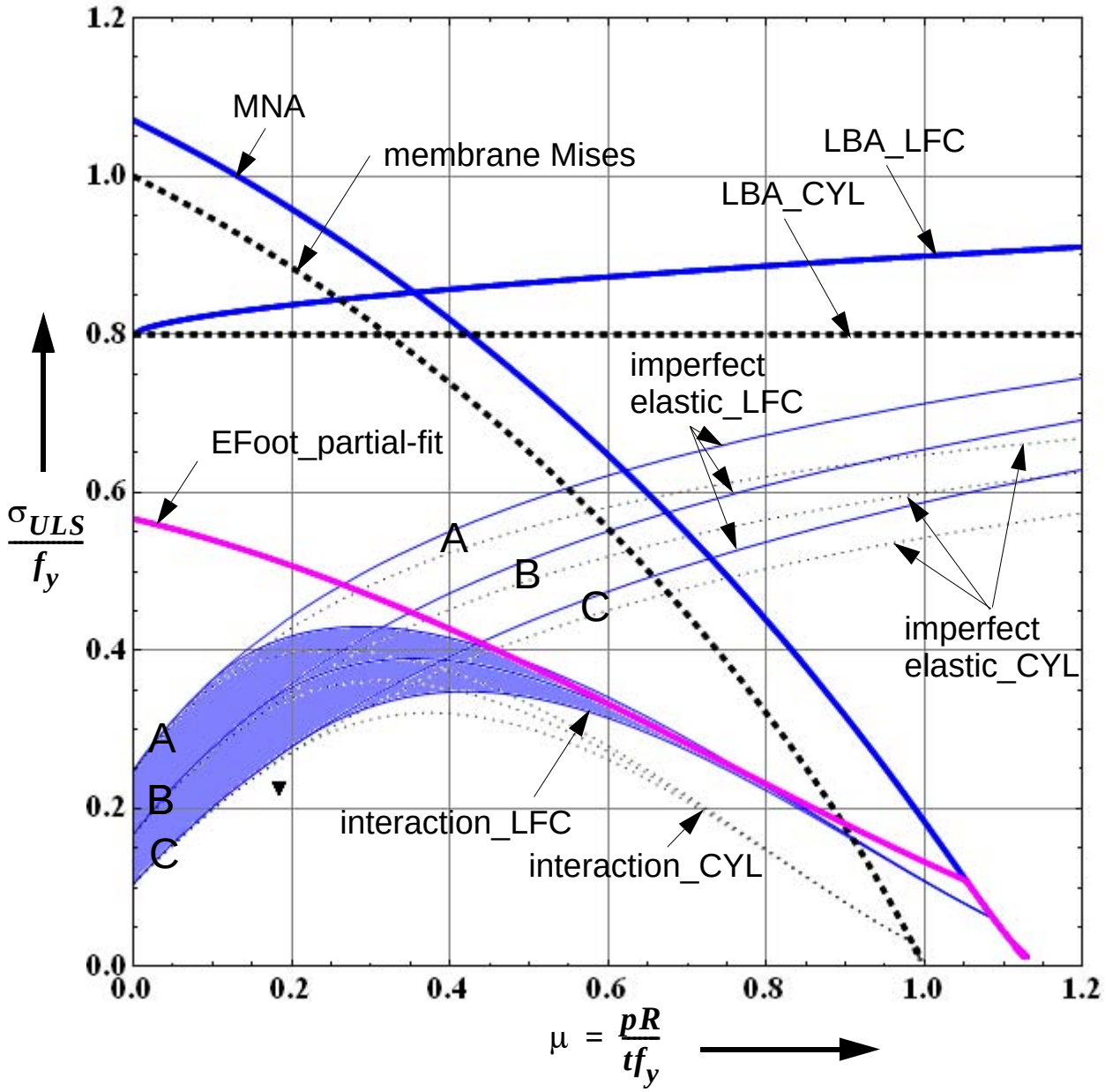

Figure 7.3 Canada tower failure: lower cone with $r_1/t\cos\beta = 650$

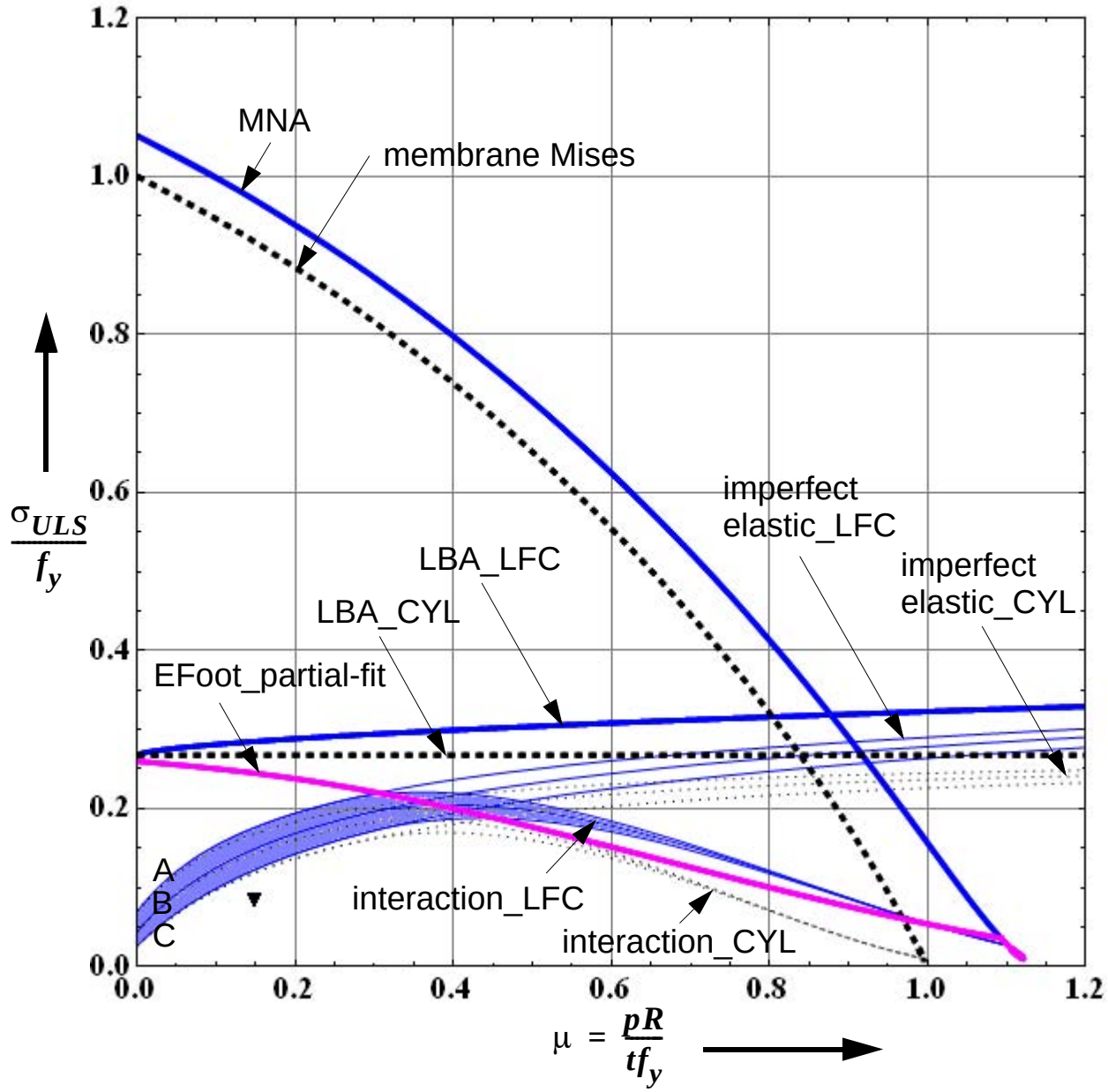

Figure 7.4 Canada tower failure: upper cone with $r_1/t\cos\beta = 1050$

7.2 Confronting previous research work results related to the collapse of steel water towers

Following the design proposal for elastic buckling of liquid-filled conical shells given by Vandepitte *et al.* which was based on the results of the extensive laboratory tests performed in Gent, many research works and collapse strength comparisons have been done with respect to this (Gent) design proposal. One of those cases where the Gent proposal was used to examine the situation of failure was the collapse of the Canada water tower. Vandepitte (1999), in his paper titled "The confrontation of shell buckling research results with the collapse of a steel water tower" examined the buckling failure of the conical steel tank of the Canada water tower and concluded that the collapse confirms the validity of his design proposal.

As the detailed re-examination done in the current work shows, however, the Gent proposal which was based on bounding straight lines in a log-log plot of the test results had interpretation problems leading to several questions. All the questions had been addressed during the detailed investigation of the current work which generally was based on different way of interpreting the test results.

As far as the failure of the Canada water tower is considered, however, the same conclusions as that of Vandepitte's would be reached. Even though the conclusion he made is similar to the conclusion arrived from the current work, the design proposals are completely different as already explained in the previous discussions. The two conclusions given are similar by chance only because the strength curves of the Canada steel cone as predicted by the two proposals coincide for the specific failure situation of the water tower.

A graphical comparison of the failure cases of both the Belgium and Canada water towers with the Gent proposal and that of the current work are shown in Figure 7.5 & Figure 7.6 for the steel cone segments of the Belgium tower and Figure 7.7 & Figure 7.8 for that of the Canada tower.

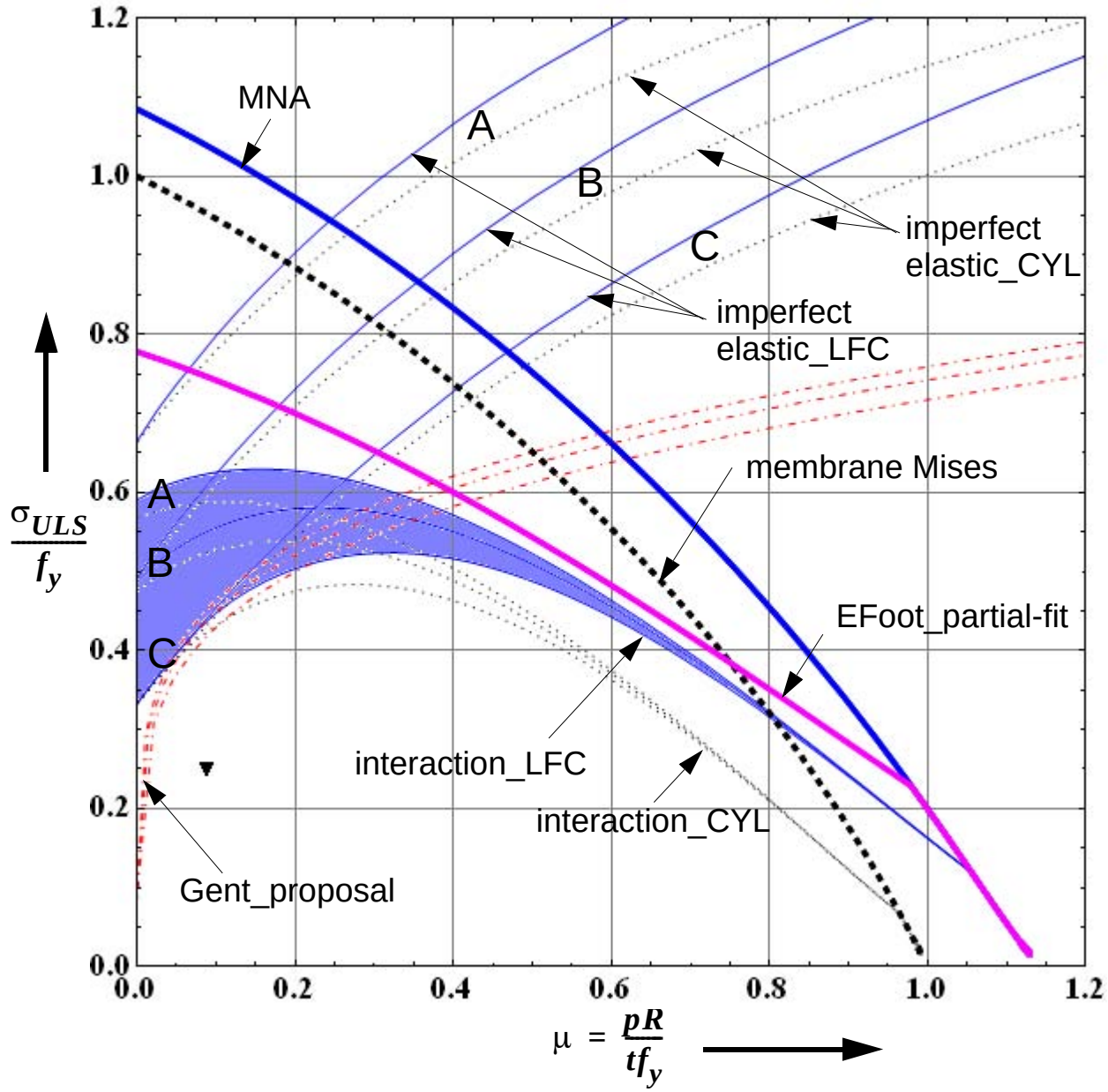

Figure 7.5 Belgium tower failure: lower cone with $r_1/t\cos\beta = 300$

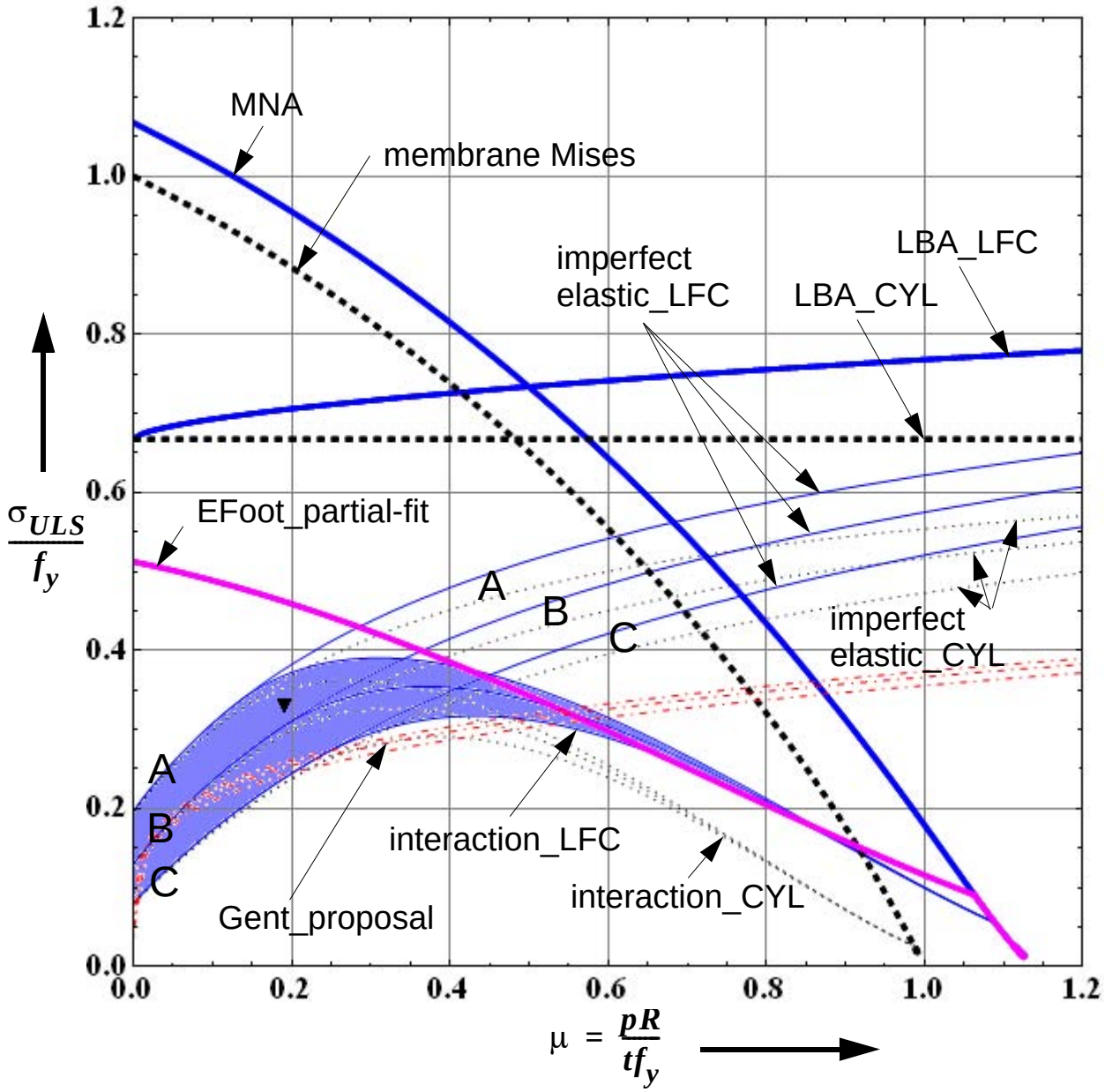

Figure 7.6 Belgium tower failure: upper cone with $r_1/t\cos\beta = 755$

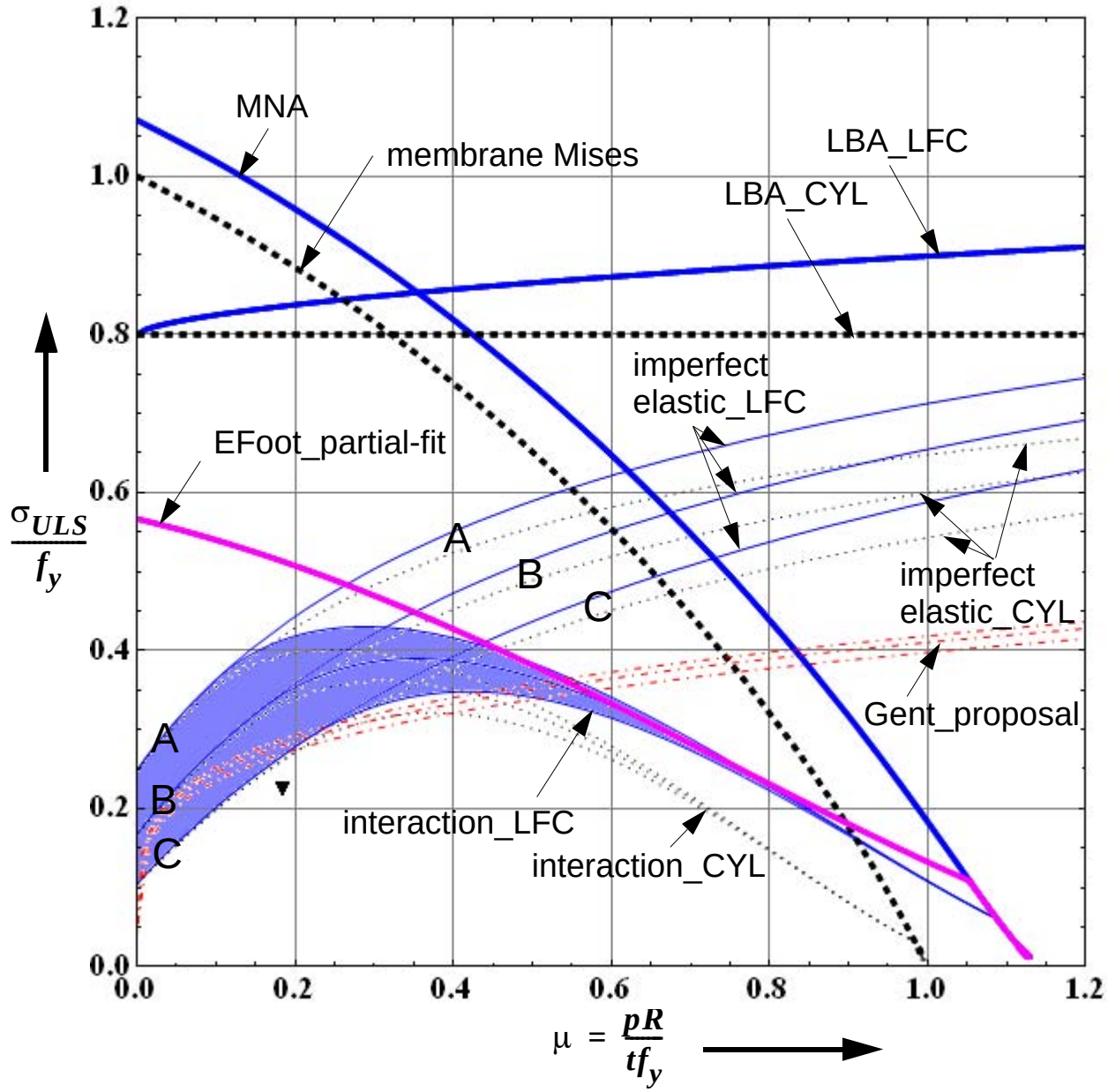

Figure 7.7 Canada tower failure: lower cone with $r_1/t\cos\beta = 650$

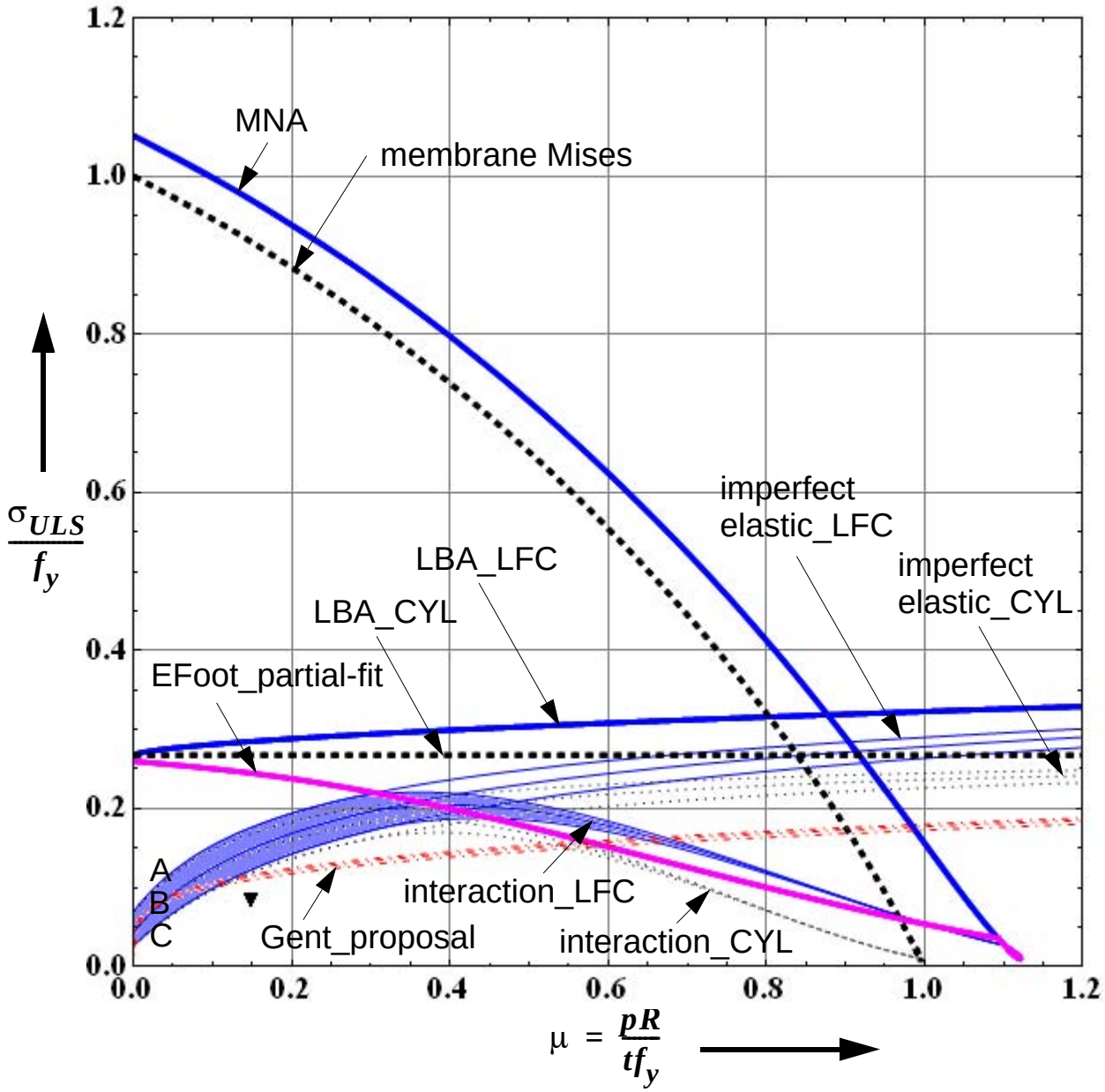

Figure 7.8 Canada tower failure: upper cone with $r_1/t\cos\beta = 1050$

7.3 Summary and conclusions

The Belgium and Canada steel water tower failure cases have been re-examined to check for any possible roles played by plasticity effects during the collapse. Previous research works related to the collapse of the water towers have also been discussed.

8

The notion of the “corresponding cylinder”

8.1 Introduction

For a better basic understanding of the behavioral similarities and differences of cylindrical and conical shells, a thorough investigation and comparison of the two shell types and their corresponding limit strengths (i.e. linear buckling strength, materially nonlinear strength, and geometrically & materially nonlinear strength of the perfect shell) have been done. Following is the complete discussion.

8.2 “Equivalent cylinder” of a conical shell

From the pure elastic buckling point of view, an “equivalent” cylindrical shell of a tip-meridionally-compressed conical shell is a cylinder with a slenderness ratio of $R/t = r_1/(t\cos\beta)$ where r_1, t, and β are geometric parameters at the cone base.

To assess the similarities and differences between uniformly compressed - internally pressurized cylindrical shells and liquid-filled conical shells, bridging loading cases (uniform axial compression with hydrostatic internal pressure; and linearly varying axial compression with hydrostatic internal pressure) of the cylindrical shell are considered and studied first. The cylindrical shell is preferred to the cone in studying their relationships and differences because the loading can easily be manipulated to independently vary the meridional and circumferential membrane stresses. In doing so, the small displacement materially nonlinear ultimate strength results (which for the uniformly loaded cylinder is governed by the bi-axial membrane Mises yield criterion and hence will be used as reference) will be referred to in the discussion.

As a first step in the comparison of a cylinder and a cone, a uniformly compressed and hydrostatically pressurized cylindrical shell with a pre-specified meridional to circumferential membrane stresses ratio ($\overline{\psi}$) at the base of the cylinder is studied by varying the liquid-depth (and therefore the liquid-density), Figure 8.1. The $\overline{\psi}$ and liquid-depth for a cylindrical shell can be made independent of each other which is not the case for a liquid-filled conical shell. Since plasticty of the shell and hence plastic limit strength is related with the development of a plastic zone, a uniformly compressed cylinder with a linearly decreasing (up the meridian) internal pressure produces a smaller bi-axial effective stress on the possible yield loacation when compared to a corresponding (same $\overline{\psi}$) uniformly pressurized case, hence it requires a load factor larger than 1.0 to produce yielding of the cylinder. This effect will be more pronounced as the liquid depth decreases. For a very big liquid-depth, on the other hand, the bi-axial state of stress at the possible yield zone location will be very close to a uniformly pressurized cylinder with the same $\overline{\psi}$ where

the bi-axial yield strength is governed by the membrane Mises yield criterion. Plots of small displacement materially nonlinear numerical analysis results for a uniformy compressed and hydrostatically pressurized cylindrical shell with R/t = 707 (equivalent cylinder of a cone with r_1/t = 500 and apex-half angle $\beta = 45°$), $\overline{\psi} = 2/3$, and fixed bottom boundary condition are shown in Figure 8.2 and Figure 8.3 where the effect of liquid-depth on the yield strength can be seen. Similar studies are done for different pre-specified values of $\overline{\psi}$ and varying the liquid-depth as shown in Figure 8.4.

The second step (which is one step closer to the LFC case) in the comparison of cylindrical shells and liquid-filled conical shells is to tip-compress the cylinder as in the first case but directly relate the parameter $\overline{\psi}$ with the liquid-depth in the same way as in the LFC, i.e. $\overline{\psi} = \zeta'(3 + \zeta')/6$ where $\zeta' = h' \cdot \tan\beta / r_1$ is taken from the LFC, Figure 8.5. Very big liquid-depth means very big $\overline{\psi}$ and hence very big meridional compression compared to the circumferential tension. This situation, for infinitely big $\overline{\psi}$, is similar to the pure axial compression of the cylinder where uni-axial meridional yielding governs the strength. In other words, as the liquid-depth increases, the materially nonlinear strength of the shell gets closer to the yield strength as predicted by the membrane Mises criterion. On the other hand, when the liquid-depth is very small, the relative magnitude of circumferential stretching at the possible yield zone of the shell is relatively small, compared to the uniform internally pressurized case, which results in a smaller effective bi-axial state of stress which inturn requires a bigger load factor to bring it to the plastic limit level, i.e. the smaller the liquid-depth gets the bigger the platsic load factor becomes and the more deviation from the yield strength predicted using the membrane Mises criterion. The results obtained from such treatment of the cylindrical shell are plotted on the pressure representation as shown in Figure 8.6. A comparison of these results with the materially nonlinear strengths of the liquid-filled conical shell (with the same $\overline{\psi}$ variations) is also shown in Figure 8.7.

The third step in the comparison of a cylinder and an LFC is the consideration of an unpressurized (or pure axial compression condition) cylinder and the corresponding yield strengths. In this case, however, it should be noted that pure axial compression doesn’t only mean tip-compression. A uniformly tip-compressed cylinder is compared to a cylinder loaded with linearly varying axial compression (i.e. uniform laoding along the meridian). The length upon which the linearly varying axial compression is acting will be varied (h/R = 0.2, 1, 10, 100 where “h” is the loaded meridional length of the cylinder) in such a way that an infinitely long compressed length apparently means a tip-compressed cylinder. In the numerical analysis of this comparison, a meridional tip-loading and a uniform along the meridian axial compressve loading are applied to both cylinders in such a way that the resulting meridional compressive stress at the base of both cylinders is equal to the uni-axial yield strength of the material under consideration. The effects of the loaded length on the materially nonlinear strength of the cylinder can be seen from the plot in Figure 8.8.

On the other hand, for a liquid-filled conical shell, an unpressurized situation means an infinitely big liquid-depth which technically is equivalent to the tip-meridionally-compressed cone. Once again, in the numerical analysis of this comparison, a meridional tip-loading is applied to both shell types in such a way that the resulting meridional compressive stress at the base is equal to the uni-axial yield strength of the material under consideration. It should then be clear that the tip-

compressed cylinder which is uniformly stressed at every point along the meridian yields at the applied tip-loading, i.e. a load factor equal to 1.0. However, because of its geometry, the resulting meridional stress distribution in the cone decays rapidly for points along the meridian other than the bottom. At the potential yield zone location, therefore, acts a smaller meridional stress than the uni-axial yield strength thereby requiring a load factor larger than 1.0 to bring it to the yield level. The exact magnitude of the load factor depends on the location of the yield zone and hence on the type of lower boundary condition. This comparison for the fixed-bottom cases of a cone and an equivalnet cylinder is shown in Figure 8.9.

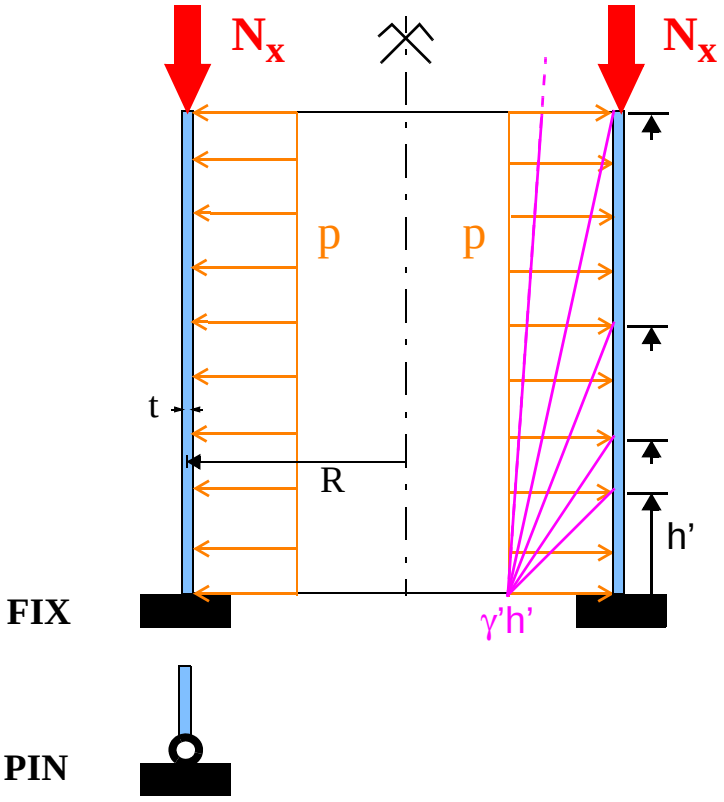

Figure 8.1 Liquid-depth variation for constant $\overline{\psi}$ and comparison with uniform pressure

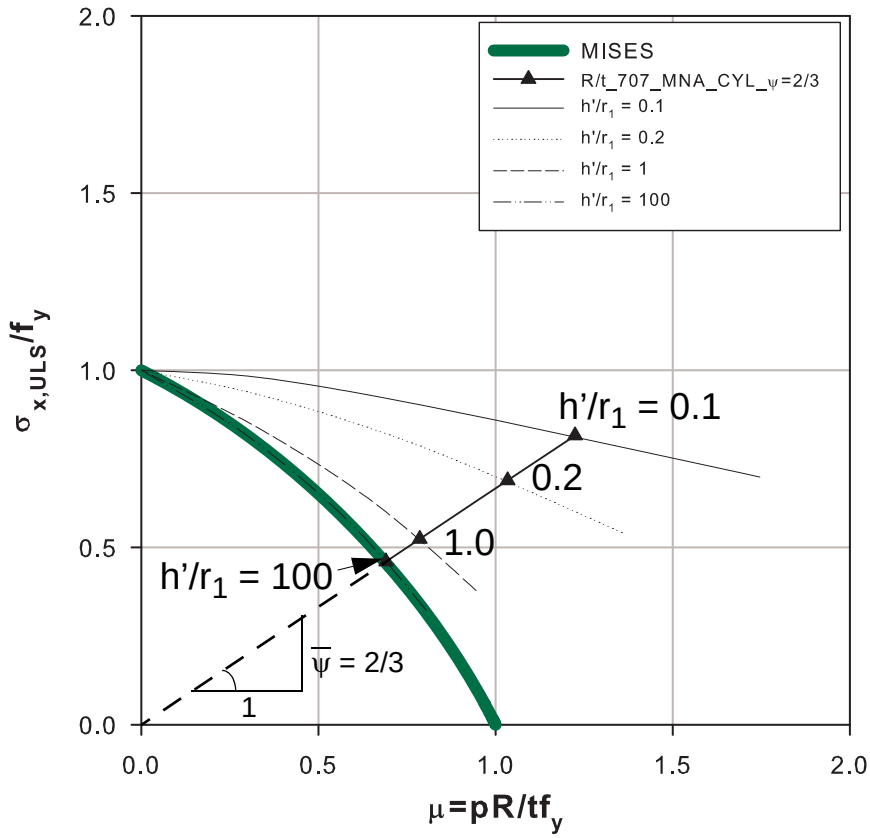

Figure 8.2 Small displacement materially nonlinear analysis: effects of liquid-depth

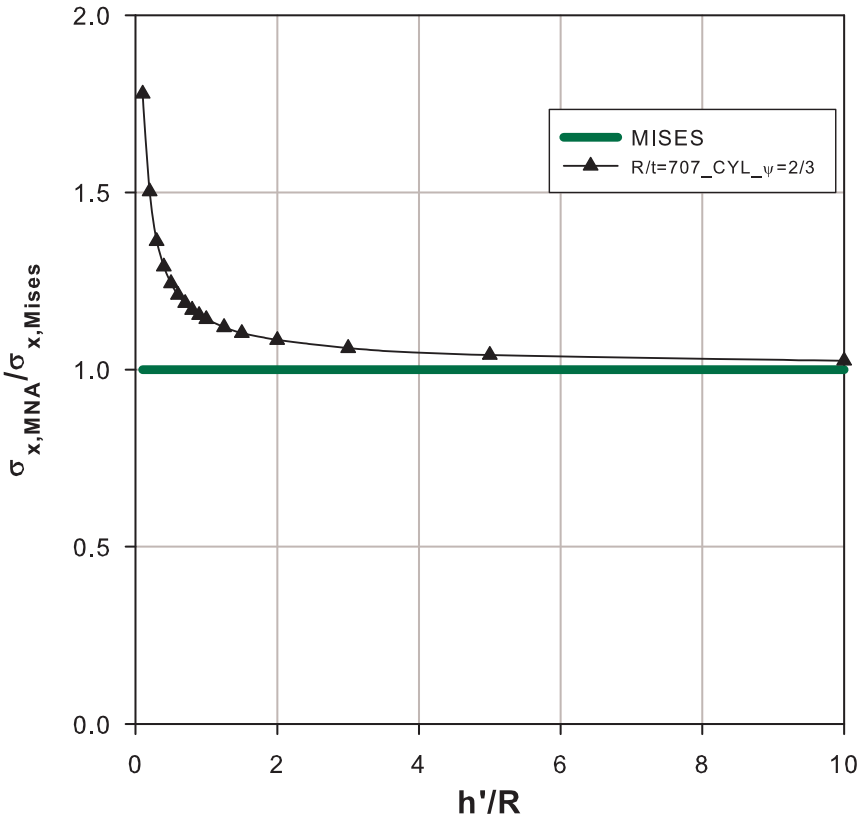

Figure 8.3 Small displacement materially nonlinear analysis: effects of liquid-depth

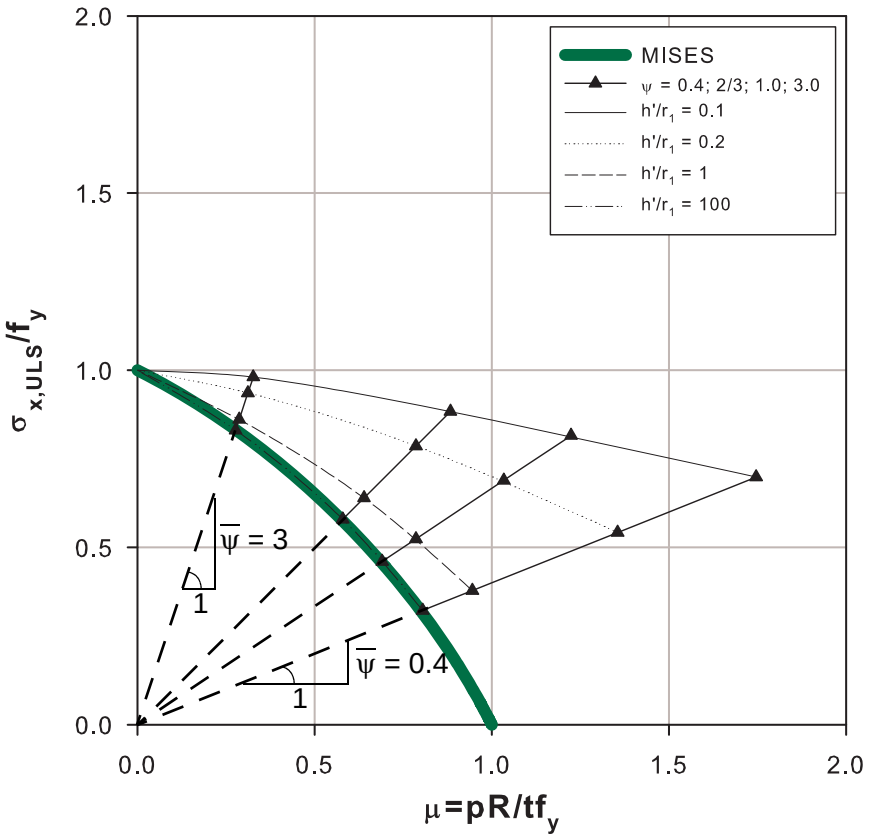

Figure 8.4 Small displacement materially nonlinear analysis: fixed bottom

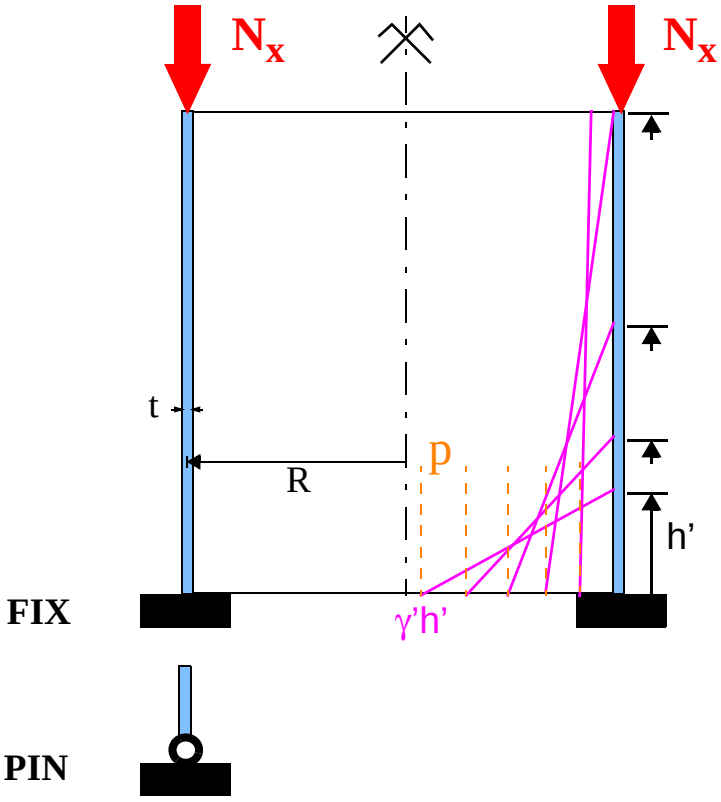

Figure 8.5 Liquid-depth variation for constant $\overline{\psi}$ and comparison with uniform pressure

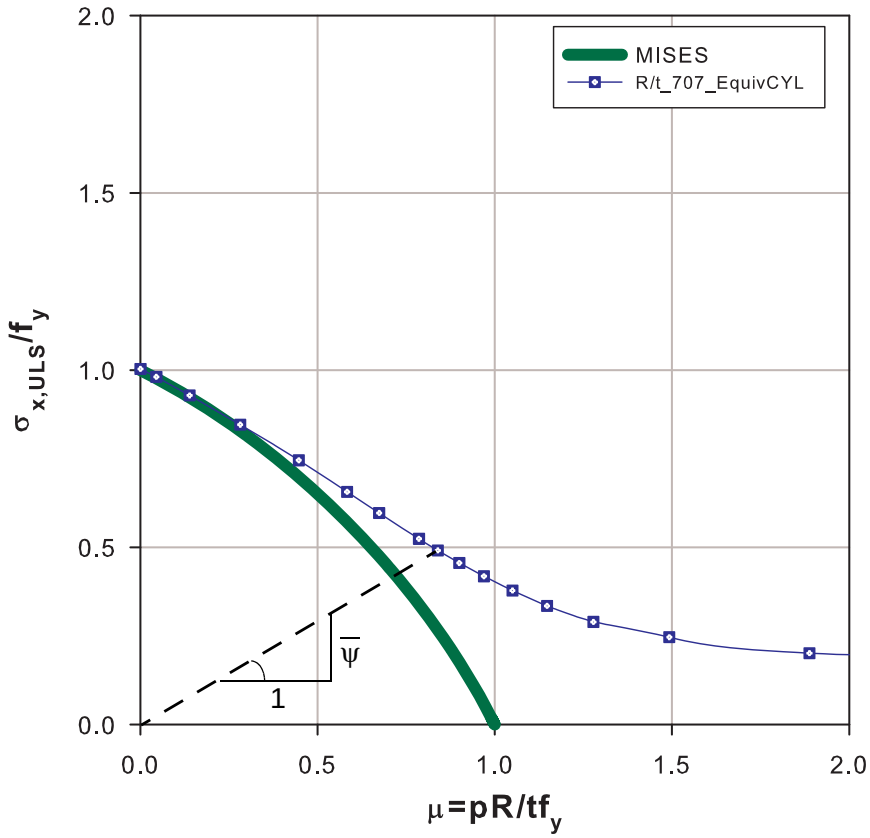

Figure 8.6 Small displacement materially nonlinear analysis: fixed bottom

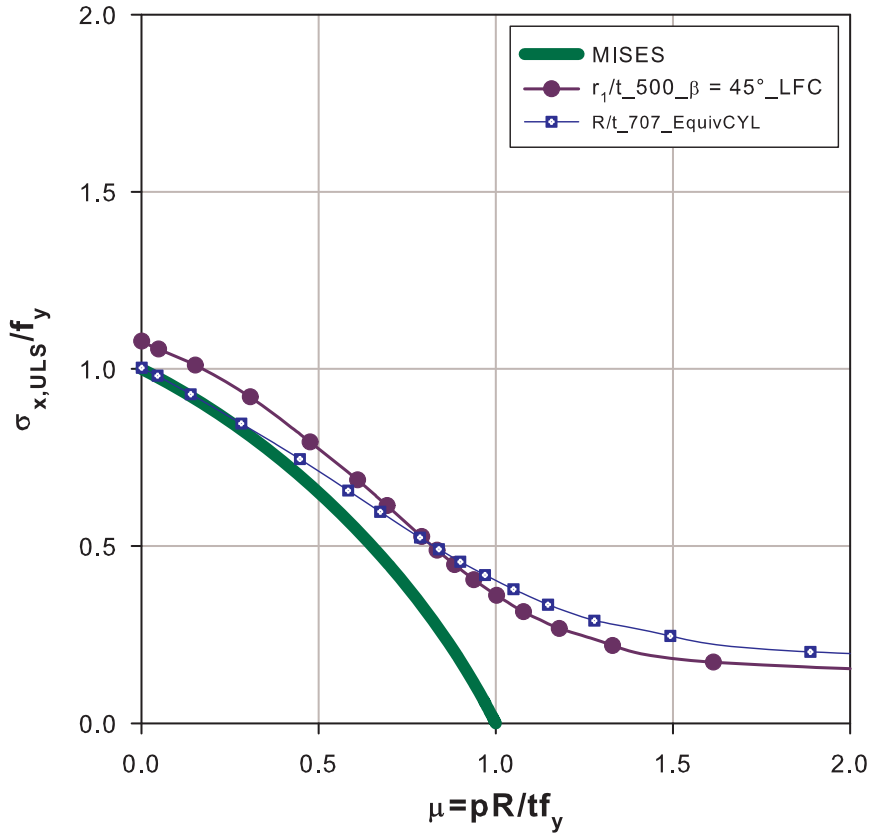

Figure 8.7 Small displacement materially nonlinear analysis: fixed bottom

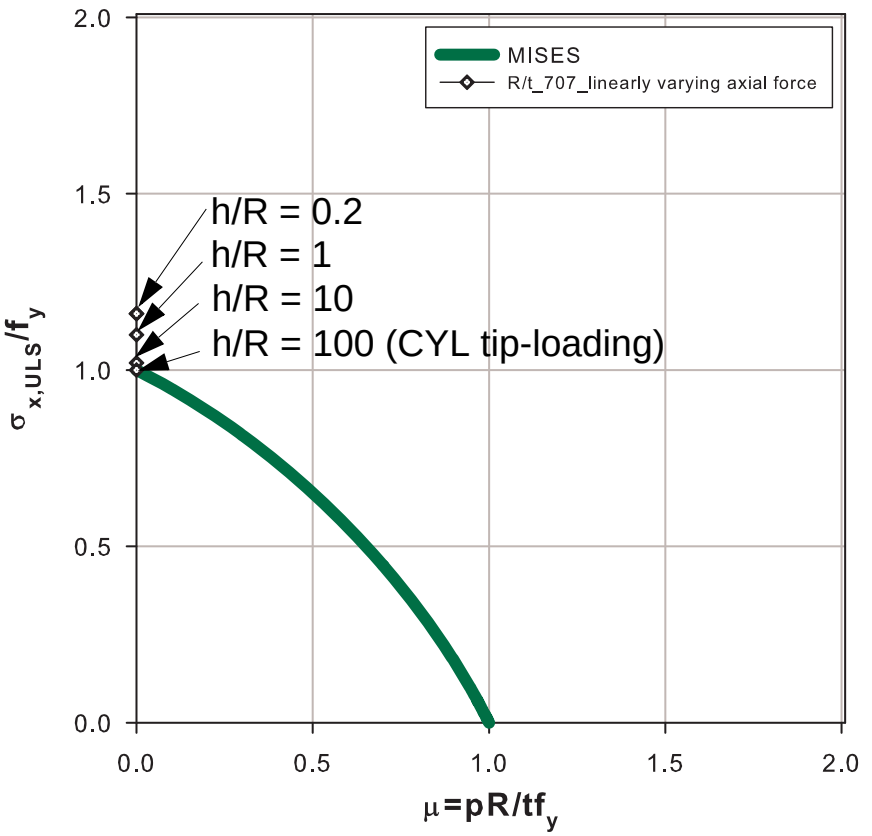

Figure 8.8 Small displacement materially nonlinear analysis: fixed bottom

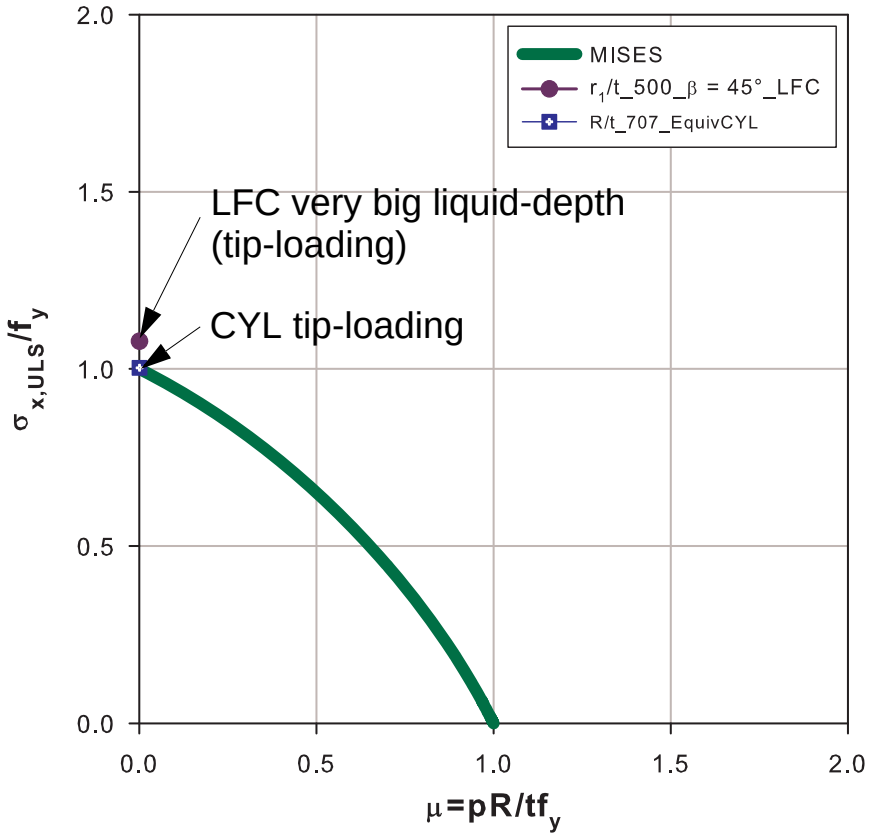

Figure 8.9 Small displacement materially nonlinear analysis: fixed bottom

8.3 “Corresponding cylinder” of a conical shell

A “corresponding” cylindrical shell of a conical shell is an “equivalent cylinder” having not only geometric equivalency but also loading equivalency. For a liquid-filled conical shell, where the meridional membrane compression rapidly decays up the meridian, buckling and plasticity occur on a region very close to the bottom boundary condition. For this reason an equivalent loading of an LFC to be used for the “corresponding” cylinder is computed as discussed below.

An equivalent meridional loading of the “corresponding cylinder” will be taken as a linearly varying meridional compressive loading which produces the same membrane stress at the cylinder base as in the LFC. The length (along the meridian) of the loaded part of the “corresponding cylinder” will be computed from the tangent of the meridional section force distribution of the LFC. Similarly, the equivalent internal pressure loading will be taken as a linearly varying pressure with a circumferential membrane section force distribution having the same tangent and producing the same membrane stress at the bottom of the cylinder as in the LFC. The length along the meridian of the corresponding cylinder over which the equivalent internal pressure should act will be the same as that of the meridional loading of the “corresponding cylinder”. The equivalent section force distributions of the “corresponding” cylinder are shown in Figure 8.10.

The tangent lines to the meridional and circumferential membrane section force distributions of the LFC can be computed as follows. The meridional and circumferential membrane stresses along the meridian of a liquid-filled conical shell are given as functions of the liquid-depth parameters ζ and ζ’ by

$$\sigma_x = \frac{\gamma' h' r_1}{t\cos\beta} \cdot \frac{1}{6} \cdot \frac{(\zeta' - \zeta)^2}{\zeta'} \cdot \left(3 + \frac{\zeta' - \zeta}{1 + \zeta}\right) \qquad \text{(Eq. 8.1)}$$

$$\sigma_\theta = \frac{\gamma' h' r_1}{t\cos\beta} \cdot (1 + \zeta) \cdot \left(\frac{\zeta' - \zeta}{\zeta'}\right) \qquad \text{(Eq. 8.2)}$$

where

$\zeta = \dfrac{z \cdot \tan\beta}{r_1}$ is a running depth parameter with z measured from bottom up of the cone, and

$\zeta' = \dfrac{h' \cdot \tan\beta}{r_1}$ is the maximum liquid level parameter with z = h’.

At the cone base $r = r_1$; $\zeta = 0$ and hence the membrane section forces at the cone base become

$$\sigma_{x,1} = \frac{\gamma' h' r_1}{t\cos\beta} \cdot \frac{1}{6} \cdot \zeta' \cdot (3 + \zeta') \qquad \text{(Eq. 8.3)}$$

$$\sigma_{\theta,\,1} = \frac{\gamma' h' r_1}{t\cos\beta} \qquad \text{(Eq. 8.4)}$$

The slope of the tangent line to the meridional membrane section force distribution will then be given interms of the normalized membrane section force $N_x/N_{x,1} = \sigma_x/\sigma_{x,1}$ shown in Figure 8.11 by

$$\frac{N_x}{N_{x,\,1}} = \left(1 - \frac{\zeta}{\zeta'}\right)^2 \cdot \frac{3 + \zeta' + 2\zeta}{(3 + \zeta') \cdot (1 + \zeta)} \qquad \text{(Eq. 8.5)}$$

$$\frac{\mathrm{d}}{\mathrm{d}s}(N_x) = N_{x,\,1} \cdot \frac{\mathrm{d}}{\mathrm{d}s}\left(\frac{N_x}{N_{x,\,1}}\right) \qquad \text{(Eq. 8.6)}$$

where “s” is a running meridional length parameter measured from bottom up the meridian of the cone and it is related to “z” using $s = z/\cos\beta$. Hence

$$\zeta = \frac{z \cdot \tan\beta}{r_1} = \frac{s \cdot \sin\beta}{r_1} \qquad \text{(Eq. 8.7)}$$

$$\frac{\mathrm{d}}{\mathrm{d}s}(\ ) = \frac{\sin\beta}{r_1} \cdot \frac{\mathrm{d}}{\mathrm{d}\zeta}(\ ) \qquad \text{(Eq. 8.8)}$$

Therefore,

$$\frac{\mathrm{d}}{\mathrm{d}s}\left(\frac{N_x}{N_{x,\,1}}\right) = \frac{\sin\beta}{r_1} \cdot \frac{\mathrm{d}}{\mathrm{d}\zeta}\left(\frac{N_x}{N_{x,\,1}}\right) \qquad \text{(Eq. 8.9)}$$

which gives

$$\frac{\mathrm{d}}{\mathrm{d}s}\left(\frac{N_x}{N_{x,\,1}}\right) = -\frac{\sin\beta}{r_1} \cdot \frac{1 - \zeta/\zeta'}{(3 + \zeta') \cdot (1 + \zeta)} \cdot \left(\left(1 - \frac{\zeta}{\zeta'}\right) \cdot \frac{1 + \zeta'}{1 + \zeta} + \frac{2}{\zeta'} \cdot (3 + \zeta' + 2\zeta)\right) \qquad \text{(Eq. 8.10)}$$

Substituting $\zeta = 0$ gives the slope of the tangent to the normalized section force at the cone base which is

$$\left.\frac{\mathrm{d}}{\mathrm{d}s}\left(\frac{N_x}{N_{x,\,1}}\right)\right|_{\zeta\,=\,0} = -\frac{\sin\beta}{r_1} \cdot \left(1 + \frac{2}{\zeta'} - \frac{2}{3 + \zeta'}\right) \qquad \text{(Eq. 8.11)}$$

The term in brackets on the right hand side of (Eq. 8.11) is plotted as a function of the maximum liquid-depth parameter ζ' as shown in Figure 8.12. The slope of the tangent to the un-normalized section force at the cone base will then be

$$\frac{\mathrm{d}}{\mathrm{d}s}(N_x)\Big|_{\zeta = 0} = -\frac{\sin\beta}{r_1} \cdot \left(1 + \frac{2}{\zeta'} - \frac{2}{3 + \zeta'}\right) \cdot N_{x,\,1} \qquad \text{(Eq. 8.12)}$$

Similarly. the slope of the tangent line to the circumferential membrane section force distribution of the LFC will be given interms of the normalized membrane section force $N_\theta/N_{\theta,1} = \sigma_\theta/\sigma_{\theta,1}$ shown in Figure 8.13 by

$$\frac{N_\theta}{N_{\theta,\,1}} = (1 + \zeta) \cdot \left(1 - \frac{\zeta}{\zeta'}\right) \qquad \text{(Eq. 8.13)}$$

$$\frac{\mathrm{d}}{\mathrm{d}s}(N_\theta) = N_{\theta,\,1} \cdot \frac{\mathrm{d}}{\mathrm{d}s}\left(\frac{N_\theta}{N_{\theta,\,1}}\right) \qquad \text{(Eq. 8.14)}$$

with

$$\frac{\mathrm{d}}{\mathrm{d}s}\left(\frac{N_\theta}{N_{\theta,\,1}}\right) = \frac{\sin\beta}{r_1} \cdot \frac{\mathrm{d}}{\mathrm{d}\zeta}\left(\frac{N_\theta}{N_{\theta,\,1}}\right) \qquad \text{(Eq. 8.15)}$$

gives

$$\frac{\mathrm{d}}{\mathrm{d}s}\left(\frac{N_\theta}{N_{\theta,\,1}}\right) = \frac{\sin\beta}{r_1} \cdot \left(1 - \frac{1 + 2\zeta}{\zeta'}\right) \qquad \text{(Eq. 8.16)}$$

Substituting $\zeta = 0$ gives the slope of the tangent to the normalized section force at the cone base which is

$$\frac{\mathrm{d}}{\mathrm{d}s}\left(\frac{N_\theta}{N_{\theta,\,1}}\right)\Big|_{\zeta = 0} = \frac{\sin\beta}{r_1} \cdot \left(1 - \frac{1}{\zeta'}\right) \qquad \text{(Eq. 8.17)}$$

The term in brackets on the right hand side of (Eq. 8.11) is plotted as a function of the maximum liquid-depth parameter ζ' as shown in Figure 8.12. The slope of the tangent to the un-normalized section force at the cone base will then be

$$\frac{\mathrm{d}}{\mathrm{d}s}(N_\theta)\Big|_{\zeta = 0} = \frac{\sin\beta}{r_1} \cdot \left(1 - \frac{1}{\zeta'}\right) \cdot N_{\theta,\,1} \qquad \text{(Eq. 8.18)}$$

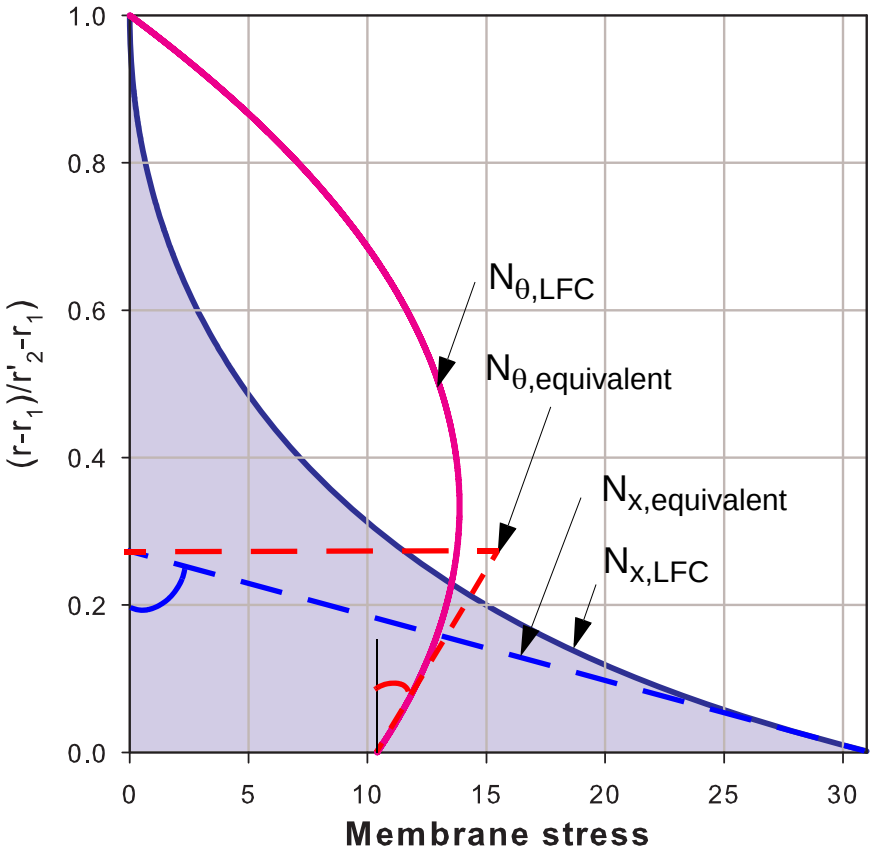

Figure 8.10 Equivalent load of the corresponding cylinder: $\overline{\psi}$ = 3.0

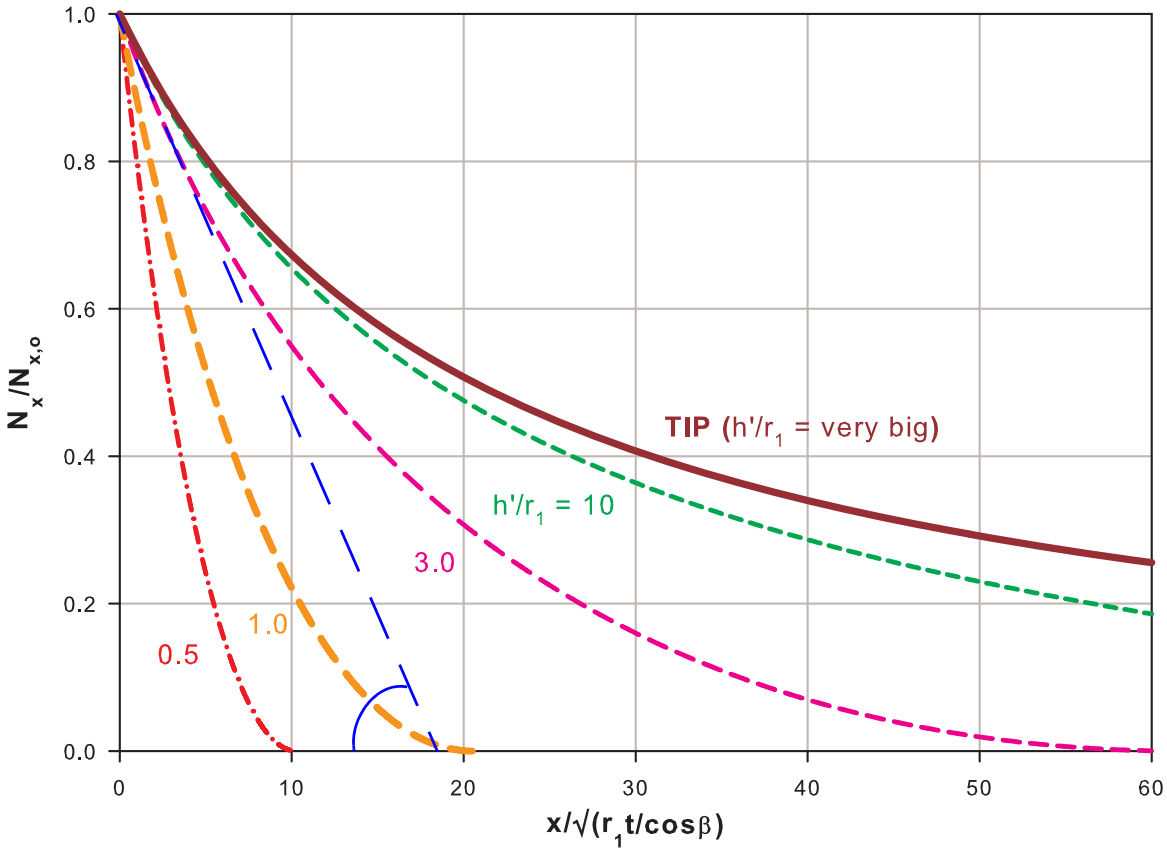

Figure 8.11 Meridional membrane section force distribution

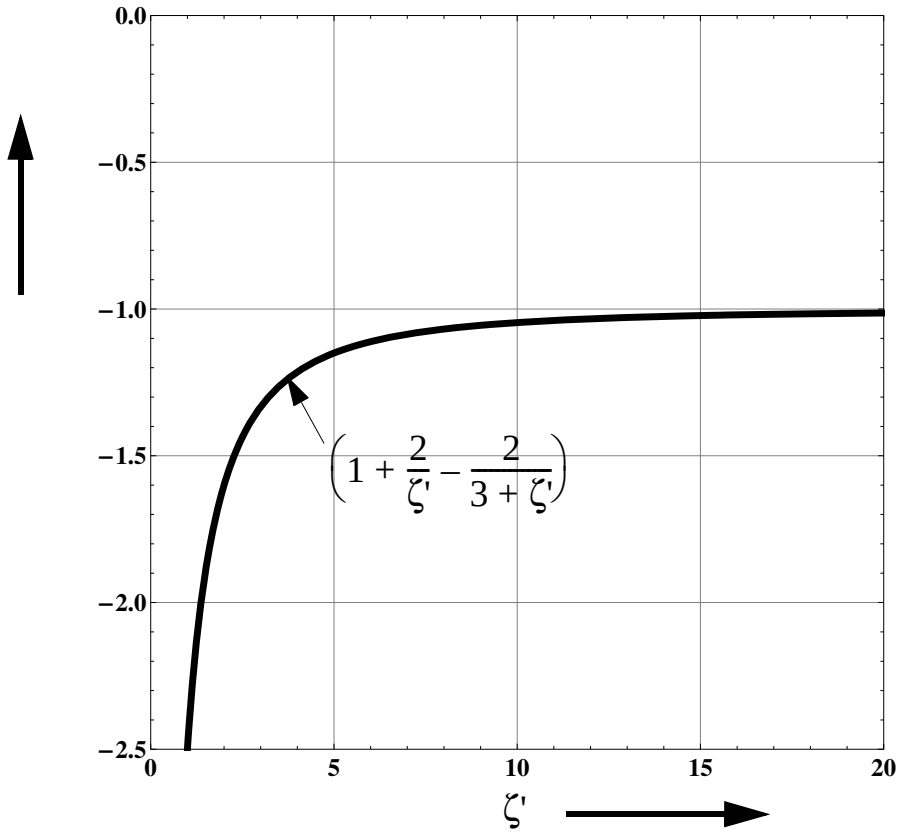

Figure 8.12 Slope of meridional membrane section force distribution at cone base

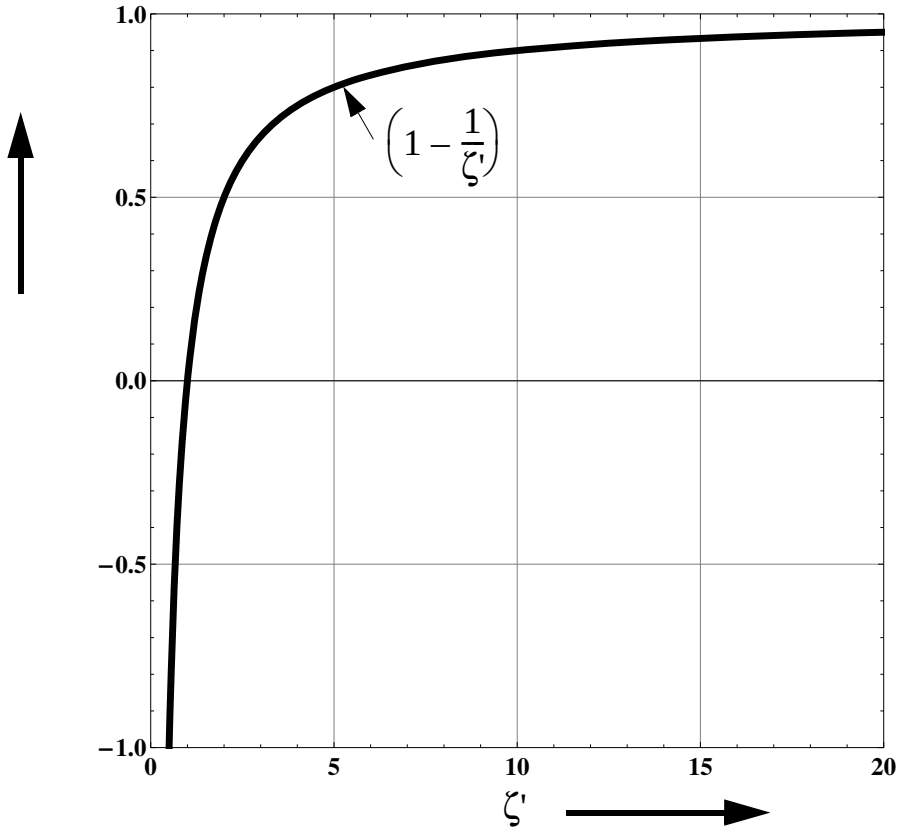

Figure 8.13 Slope of circumferential membrane section force distribution at cone base

Using the slope of the tangent to the normalized section force at the cone base (Eq. 8.12), the length of the region on the “corresponding cylinder” to be internally pressurized linearly to produce equivalent circumferential membrane section force and uniformly axially loaded to produce a linearly varying section force distribution with a maximum at the base (equal to that of the LFC), see Figure 8.10, will be given as follows:

$$\frac{\mathrm{d}}{\mathrm{d}s}(N_x)\bigg|_{\zeta = 0} = -\frac{\sin\beta}{r_1} \cdot \left(1 + \frac{2}{\zeta'} - \frac{2}{3 + \zeta'}\right) \cdot N_{x,\,1} \qquad \text{(Eq. 8.19)}$$

$$L_{axial,\,equivalent} = \frac{r_1}{\sin\beta} \cdot \frac{1}{\left(1 + \frac{2}{\zeta'} - \frac{2}{3 + \zeta'}\right)} \qquad \text{(Eq. 8.20)}$$

For an infinitely big liquid-depth (or ζ’) of the LFC, the second term on the right hand side of (Eq. 8.20) will be equal to 1.0 and the axially loaded region of the corresponding cylinder will have a length of

$$L_{axial,\,equivalent,\,TIP} = \frac{r_1}{\sin\beta} \qquad \text{(Eq. 8.21)}$$

The magnitude of the uniformly ditributed axial compressive loading of the corresponding cylinder will be given by

$$p_x = \frac{N_{x,\,1}}{L_{axial,\,equivalent}} \qquad \text{(Eq. 8.22)}$$

and the linearly varying internal pressure of the cylinder can be splitted into a uniform and hydrostaic pressure parts. With $N_{\theta,2}$ representing the circumferential membrane section force at top-end of the loaded region, the uniform, p_z, and hydrostatic, p_h, part (amplitude at the base of cylinder) of the linearly varying internal pressure are given by

$$\begin{aligned} N_{\theta,\,2} &= N_{\theta,\,1} + \frac{\mathrm{d}}{\mathrm{d}s}(N_\theta)\bigg|_{\zeta = 0} \cdot L_{axial,\,equivalent} \\ &= N_{\theta,\,1} \cdot \left(1 + \frac{1 - 1/\zeta'}{\left(1 + \frac{2}{\zeta'} - \frac{2}{3 + \zeta'}\right)}\right) \end{aligned} \qquad \text{(Eq. 8.23)}$$

$$p_z = \frac{N_{\theta,\,2}}{R} \qquad \text{(Eq. 8.24)}$$

$$p_h = \frac{N_{\theta,\,1} - N_{\theta,\,2}}{R} \qquad \text{(Eq. 8.25)}$$

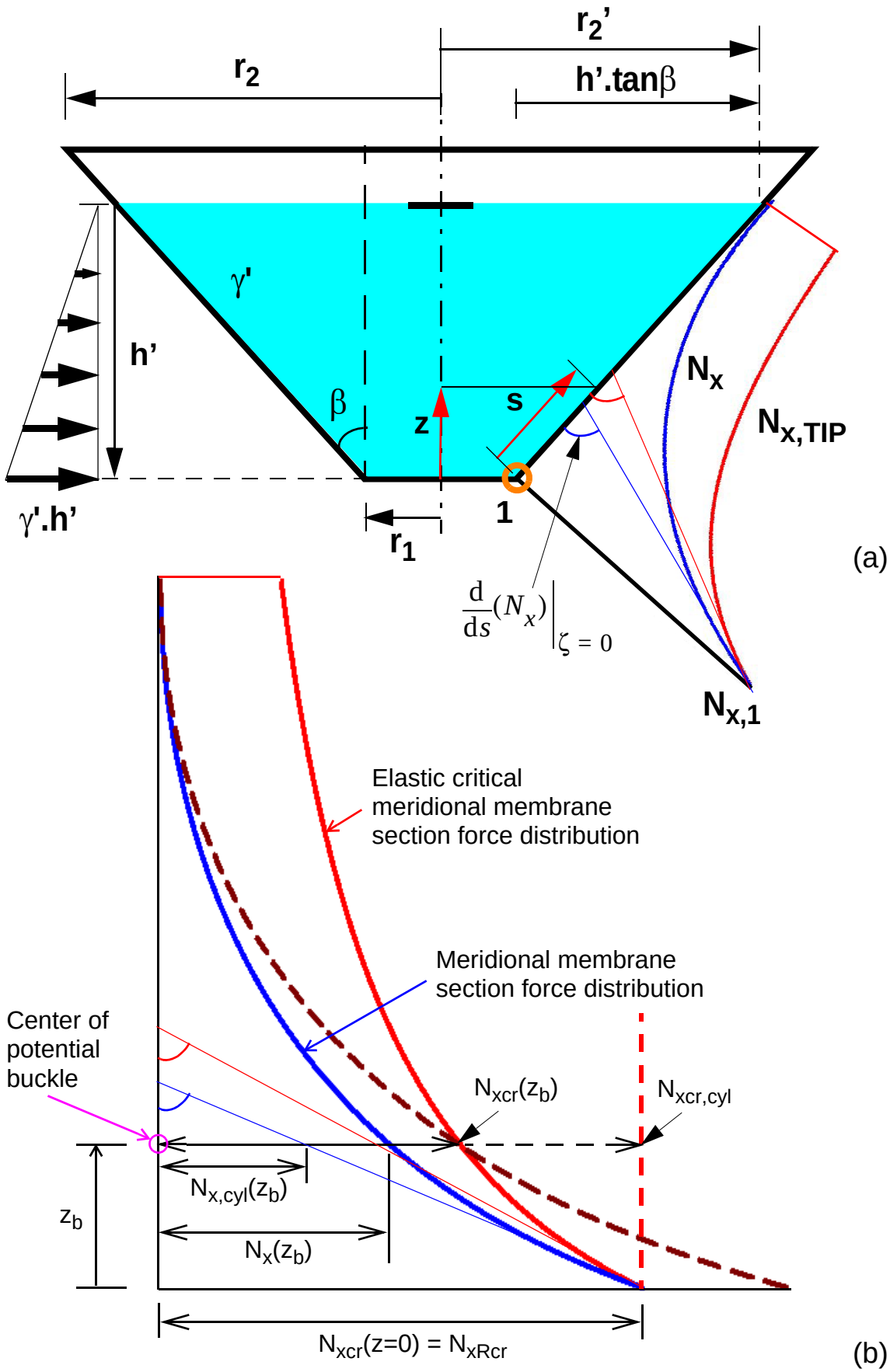

Figure 8.14 Meridional membrane section force distribution & approximate buckling load

8.3.1 Linear elastic buckling strength of the “corresponding cylinder”

Since the linear elastic buckling strength of a perfect cylindrical shell is independent of the internal pressurization, the equivalent meridional loading of the “corresponding cylinder” alone will be considered in the computation of the elastic buckling strength which will then be compared with the elastic buckling strength of the liquid-filled conical shell. In the course of doing this, the buckling strength of an LFC with an infinitely big liquid-depth (or a tip-loaded cone) will be qualitatively and quantitatively compared with that of the “corresponding” cylindrical shell under an equivalent axial loading as discussed above and the same reference meridional membrane stress at the bottom. It is, however, worth mentioning here that a meridionally-loaded cylindrical shell with exactly the same meridional membrane section force ditribution along the meridian as the tip-loaded cone buckles at a higher load factor (depending on the bottom boundary condition type) than the LFC. This is because of the the difference in buckling strength of the two shell types at the potential center of buckle, see Figure 8.14(b). The buckling load factor may even get higher when the ”corresponding cylinder” is considered with the equivalent axial loading instead of the actual distribution on the LFC, see Figure 8.14(b). This discussion applies similarly to smaller liquid-depth cases of the LFC.

The results of a linear elastic buckling analysis of an LFC and a “corresponding” cylinder for a fixed-bottom cone ($r_1/t = 500$; $\beta = 45°$; $E = 21000$ kN/cm^2; $f_y = 24$ kN/cm^2; $\nu = 0.3$ and varying the liquid-depth) are shown in Figure 8.17. The relative increase of the buckling load factor of the “corresponding cylinder” when compared to that of the LFC, however, decreases and hence comes closer to that of the LFC as the liquid-depth gets smaller since the equivalent section force distribution of the “corresponding cylinder” becomes more closer to the actual section force ditribution of the LFC. To qualitatively show this, a random 10% constant reduction has been applied to the buckling strengths of the corresponding cylinder and re-compared to the buckling strength of the LFC, see Figure 8.18. Had the geometric and section force equivalency of the LFC and “corresponding cylinder” been considered at the potential center of elastic buckling, the resulting buckling load would have been the same for both.

Basic linear buckling eigenmodes of the liquid-filled conical shell and its “corresponding cylinder” are shown in Figure 8.16 and Figure 8.17 for $\overline{\psi}$ values of 3.0 and tip-compressed (or $\overline{\psi}$ infinitely big), respectively.

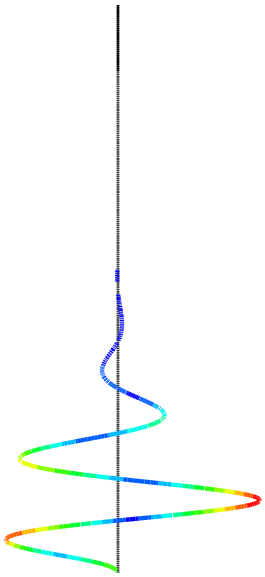

Step: Step–2, LINEAR BUCKLING ANALYSIS (LBA)
Mode 1: EigenValue = 1.3028
Primary Var: S, Mises
Deformed Var: U Deformation Scale Factor: +1.500e+02

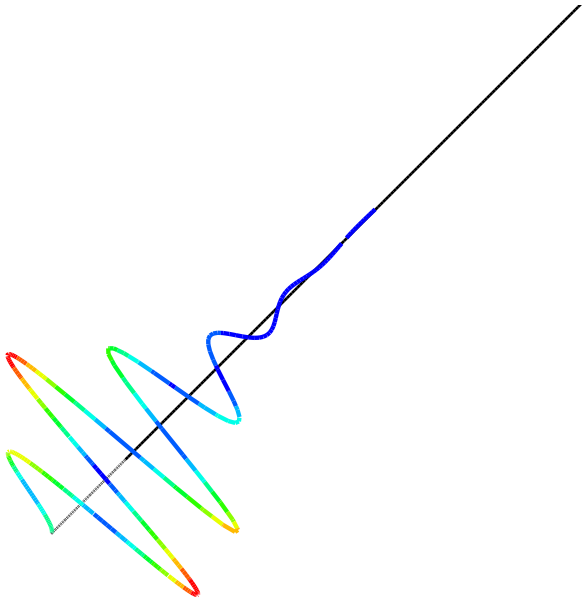

Step: Step–2, LINEARE BUCKLING(LBA) ANALYSIS
Mode 1: EigenValue = 1.1200
Primary Var: S, Mises
Deformed Var: U Deformation Scale Factor: +1.500e+02

Figure 8.15 Basic buckling eigenmodes: $\overline{\psi} = 3$

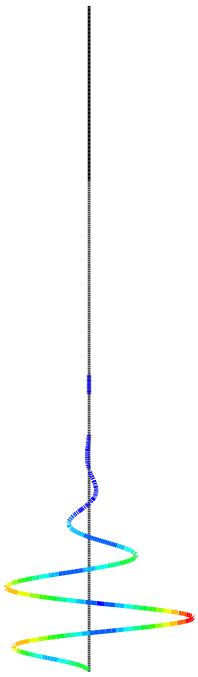

Step: Step–2, LINEAR BUCKLING ANALYSIS (LBA)
Mode 1: EigenValue = 1.2437
Primary Var: S, Mises
Deformed Var: U Deformation Scale Factor: +1.500e+02

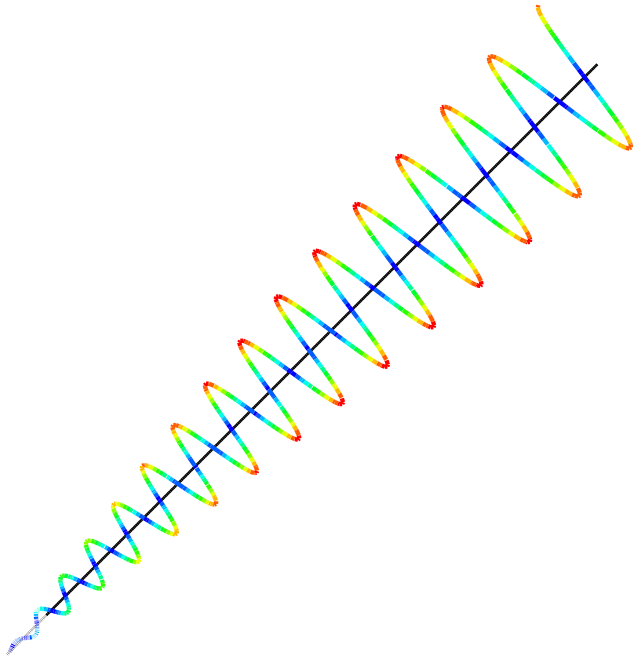

Step: Step–2, LINEARE BUCKLING(LBA) ANALYSIS
Mode 1: EigenValue = 1.0004
Primary Var: S, Mises
Deformed Var: U Deformation Scale Factor: +1.500e+02

Figure 8.16 Basic buckling eigenmodes: very high liquid-depth ($\overline{\psi}$ = infinity)

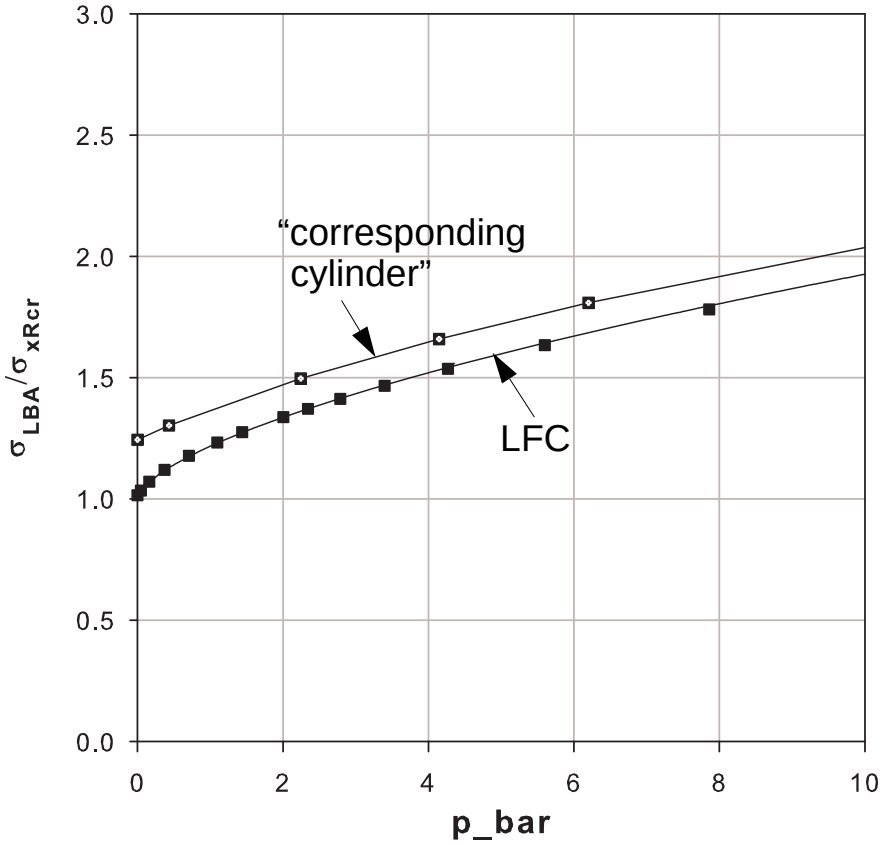

Figure 8.17 Linear buckling strengths of the perfect cone and “corresponding” cylinder

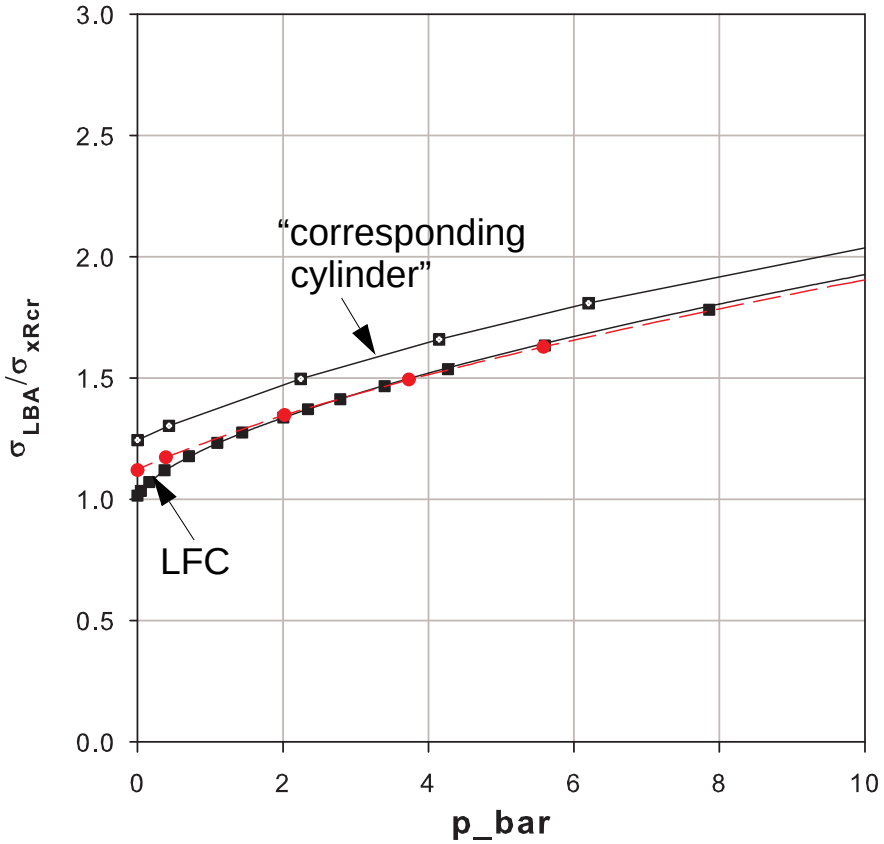

Figure 8.18 Linear buckling strengths of the perfect cone and “corresponding” cylinder

8.3.2 Materially nonlinear yield- and geometrically & materially nonlinear buckling- strengths of the “corresponding cylinder”

Since plasticity and elastic-plastic buckling phenomena of liquid-filled conical shells occur under the action of bi-axial state of stress in a region close to the bottom boundary, the combined effect of both the meridional and circumferential equivalent loadings of the “corresponding cylinder” should be considered. For relatively bigger liquid-depths where the axial equivalent section force on the “corresponding cylinder” is relatively not close (and hence relatively smaller when compared) to the actual meridional section force ditribution of the LFC, the tangent to the circumferential meridional section force distribution of the LFC leads to a somewhat higher circumferential section force dirtribution than the LFC thereby resulting in an overall balanced (lose & gain) bi-axial state of stress somehow comparable to that of the LFC. On the other hand, for relatively smaller liquid-depths, both the meridional and circumferential equivalent membrane section forces on the “corresponding cylinder” are relatively closer to the actual membrane section force ditributions and hence a direct equivalency in bi-axial state of stress will exist.

As far as geometrically and materially nonlinear buckling strengths are concerned, the widening radius (along the meridian) of the cone which results in a relatively bigger radius at the potential buckle center compared to the constant-radius “corresponding cylinder” will have a relatively bigger reduction in buckling strength due to geometric nonlinearity. This difference will, however, be very small as the buckling phenomenon happens close to the boundary, i.e. at a cone radius close to the base radius considered for the “corresponding cylinder”.

The comparison of the numerical MNA and GMNA results of the “corresponding” cylinder together with that of the LFC for a fixed-bottom cone ($r_1/t = 500$; $\beta = 45°$; $E = 21000$ kN/cm^2; $f_y = 24$ kN/cm^2; $\nu = 0.3$ and varying the liquid-depth) are shown in Figure 8.19. Thus, the “corresponding cylinder” of a liquid-filled conical shell behaves in exactly the same way as that of the LFC. **Hence, a liquid-filled conical shell is nothing but a *“wet cylinder”***.

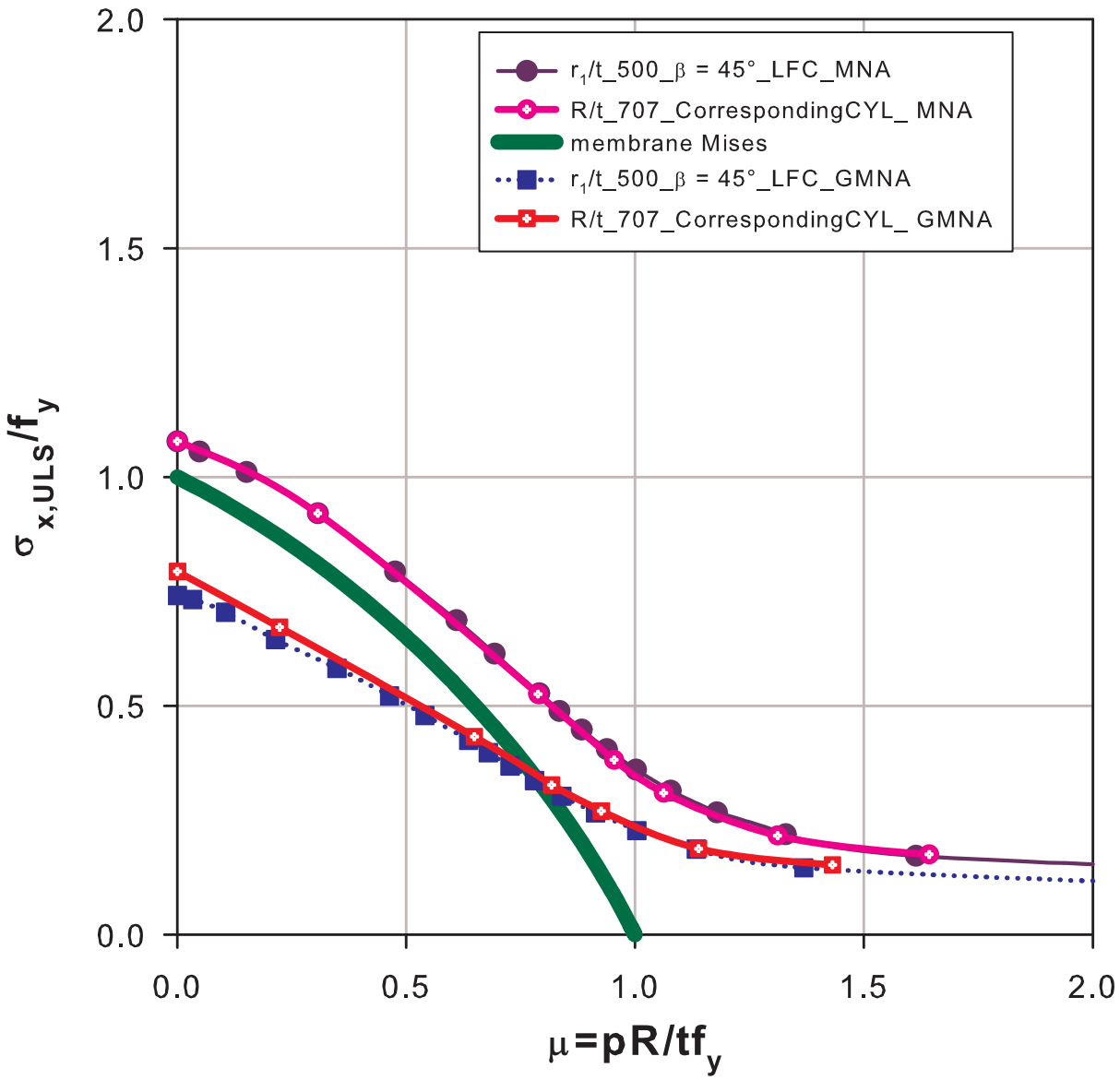

Figure 8.19 Small displacement materially nonlinear analysis: fixed bottom

8.4 Summary and conclusions

The “corresponding cylinder” of a liquid-filled conical shell has been introduced which behaves in exactly the same way as the LFC. Detailed investigation of the “corresponding cylinder” was then made which turned out to be that the liquid-filled cone is nothing but a “wet-cylinder”.

9

General summary & conclusion

9.1 General summary & conclusions

The general behaviour of thin-walled cylindrical & conical shells under meridional compression and circumferential tension has been analyzed using analytical and numerical linear analysis techniques from which the pure membrane and edge-bending effects on the section force distribution have been discussed. The general effects of edge restraining on the elastic-plastic buckling phenomena of such shells had been explained. The small displacement linear buckling (LB) strengths of cylindrical & conical shells have then been computed approximately and investigated numerically. The linear buckling strength has been used as a reference, throughout the whole study, to express other buckling strengths according to the frame work of EN 1993-1-6.

The possible loading procedures in dealing with liquid-filled conical shells have been discussed and clearly explained. Besides, which loading procedure should be used in what circumstances and for what purposes has been pointed out.

The effects of axisymmetric and non-axisymmetric imperfections on the elastic buckling strength of thin-walled cylindrical and conical shells have been discussed in detail for different fabrication quality classes as recommended in EN 1993-1-6 and comparisons between the cylinder and cone have been made. LFC-specific buckling phenomenon and corresponding elastic buckling strengths have been throughly discussed and clearly explained. Simplified expressions for the prediction of linear buckling strengths of liquid-filled general cones with pinned and fixed bottom boundary conditions have been obtained. The numerous Gent laboratory tests made on liquid-filled conical shells have been examined and re-investigated in detail. Comparisons of the perfect and imperfect linear buckling strengths of cylindrical and conical shells have been made.

Nonlinear buckling and plastic strengths of cylindrical and conical shells have been computed approximately using analytical models with second order effects included and numerically using a finite element package (ABAQUS). The pure plastic limit strengths of the two shell types have been computed approximately using von Mises membrane yield criterion taking the membrane stresses at the shell-base as references; and using generalized stress resultant oriented approximate yield criteria. The effects of material nonlinearity, geometric nonlinearity and imperfections on the buckling strength of thin-walled cylindrical and conical shells have been numerically investigated. Comparisons of the results obtained using the analytical model and numerical simulations have been made on which detailed comments and explanations were given.

The numerical simulation results have been used to derive a set of basic data that can be used in a straight forward buckling design by hand calculations in-line with the underlying structure of the European standard EN1993-1.6. Design recommendations were proposed which have been compared with previous research results and code recommendations. Additional comments and de-

tailed explanations concerning the results have been given. The comparison in buckling strength prediction between the design recommendation of the current work and the existing design regulation according EN 1993-1-6 for the cylindrical shell is summarized as follows:

EN1993-1-6 buckling design recommendation:

- the overall procedure in predicting the characteristic buckling strength of cylindrical shell involves many steps
- the reduction factor α_{xpp}, which really is a plastic buckling reduction factor, is being treated as if it is an elastic reduction factor. Besides, it is referred to as an imperfection reduction factor while it has nothing to do with imperfections.
- applies plasticity conditions twice, first in α_{xpp} itself as it basically includes material and geometric nonlinear effects and a second elastic-plastic buckling interaction of α_{xpp} with the uni-axial yield condition
- predicts elastic-plastic buckling strengths higher than the pure bi-axial plastic resistance of the cylinder
- needs additional separate plasticity check against bi-axial yielding
- even if separate plasticity condition is applied to it, the strength results are inconsistent with those computed numerically
- inconsistency in buckling strength predictions at very low pressure level and zero-pressure level resulting in a jump of strength
- applies only for pinned bottom cases (with more safety for fixed cases?)

Buckling design recommendation of the current work:

- considers bi-axial plasticity from the very beginning
- strictly differentiates typical buckling failure modes: buckling in the free shell interior and buckling adjacent to the boundary (elephant's-foot buckling mode)
- it is easy to follow and apply; straight forward approach
- differentiates pinned and fixed bottom boundary condition cases

On the other hand, from the axisymmetric elastic-plastic buckling analysis results of the liquid-filled conical shells, it can be concluded that that elephant's-foot type buckling in such shells, where the only loading is liquid-filling, may not be probable unless there exist a worst imperfection or a global bending moment resulting from, say, earthquake causing one-sided buldge or global tilting of the shell. A very little global bending effect, in the general case of cones supported from bottom (i.e. on the smaller radius), will have a very big meridional compression on one side of the

cone due to the shorter lever-arm at the smaller radius. It is this big meridional compression along with the existing circumferential stretching which results in bi-axial state of stress causing local yielding and hence elephant's-foot buckling. On the other hand, if there exists an additional, say, roof loading on top of the existing liquid-loading, an additional meridional compression will result. This higher meridional commpression along with the existing circumferential tension (plus small addition due to poisonn's effect) may therefore lead to the possibility of elephant's-foot type buckling.

Detailed investigation of Gent mercury-filled laboratory test results along with detailed discussions, explanations, and conclusions have been done. Previous LFC-related research works on nonlinear simulation of liquid-filled conical shells with or without geometric imperfections have been discussed and few cases have been re-examined for confirmation and further studying purposes. Relevant explanations and conclusions were given to the outcomes of those works. Moreover, the Belgium and Canada steel water tower failure cases have been re-examined to check if they really were under designed for elastic buckling and check for any possible roles played by plasticity effects during the collapse. Previous research works related to the collapse of the water towers have also been discussed.

A "corresponding" cylinder of a liquid-filled conical shell has been introduced which behaves in exactly the same way as the liquid-filled conical shell. Detailed invetigation of the "corresponding" cylinder has then been made.

9.2 Outlook & proposed future work

Axisymmetric shell models have been used in all the numerical simulations performed to study the axisymmetric elastic-plastic buckling phenomena, buckling modes and strengths of meridionally compressed and internally pressurized perfect and imperfect cylindrical and conical shells. Axisymmetric imperfection shapes have been used to study the effects of sinusoidal & local imperfections on the elastic-plastic buckling strengths of the aforementioned shells for different imperfection wavelengths, locations along the meridian, orientations, and imperfection amplitudes. On the other hand, in the study on the elastic-plastic buckling of liquid-filled conical shells, the cones considered were solely loaded with liquid. For these reasons, following is a list of possible areas where, in the eye of the current work, further researching is needed.

- **Investigation of real (i.e. that can be found in practical civil engineering shells) imperfection shapes, imperfection amplitudes, possible locations along the meridian, orientations and their effects on the elastic-plastic buckling strength of thin-walled cylindrical and conical shells.**

- **Investigation of the effects of local non-axisymmetric imperfection shapes and the corresponding buckling modes and buckling strengths for different internal pressurization.**

- **Investigation on the effects of an imperfection in the form of global tilting on the elastic and elastic-plastic buckling phenomena and buckling strength of liquid-filled conical shells.**

- **Investigation on the effects of using elephant's-foot buckling mitigation mechanisms and resulting elastic-plastic buckling phenomena and buckling strength of thin-walled cylindrical shells.**

9.3 Proposed European design recommendation (EDR) & European Standard EN 1993-1-6 modifications

The following list is a brief summary of what has been obtained from the whole work which can directly be integrated as modifications and/or incorporations into the existing European design recommendation and European Standard EN 1993-1-6.

i Proposal for modification of buckling strength prediction of cylindrical shells under axial compression with co-existent internal pressure

Buckling strength prediction using simple expressions which resulted through systematic interpretation of nonlinear buckling analysis results which considered bi-axial plasticity from the very beginning have been presented in Chapter-3 of this work. These modifications strictily differentiates between pinned and fixed bottom boundary condition cases.

ii Establishing a new proposal for the buckling strength prediction of conical shells under meridional compression with co-existent internal pressure

A similar-to-the-cylinder buckling strength prediction of meridionally compressed and internally pressurized conical shells can be established.

iii Proposal for modification and integration to the existing buckling strength prediction of liquid-filled conical shells (LFC)

Liquid-filled-specific buckling behavior and consistent with cylinder imperfection reduction (α_{xpe}) have been presented in Chapter-4 and Chapter-5.8. Simplified expressions for the prediction of buckling strengths of liquid-filled conical shells with pinned and fixed bottom boundary conditions have been obtained and hence proposed for future design purposes.

iv Proposal for modification of the linear-analysis-based plastic limit strength estimation using Ilyushin yield criterion

Ilyushin's yield criterion is incorrectly refered to in EN 1993-1-6 and hence, it needs to be modified according to the discussion in Annex-A of this work. Ivanov-I yield criterion is recommended to be used as it is accurate enough for 1D and axisymmetric conditions and simple to apply.

v Generalization of EN elastic-plastic buckling representation

The elastic-plastic buckling interaction expression given using an exponent parameter η should be modified using possible general shape functions as presented in Chapter-4.8.2.1.

10

References

ABAQUS (2002). ABAQUS/Standard: Theory Manual & User's Manual, Abaqus Version 6.3. Hibbit, Karlson & Sorensen, Inc.

Bornscheuer, F. W., Bornscheuer, F. (1987). Contribution to Simplified Handling of the Shell Buckling Concept without α-coefficient. ECCS Colloquium on Stability of Plate and Shell Structures, Ghent, Belgium, 261-272.

Burgoyne, C. J., Brennan, M. G. (1993). Exact Ilyushin Yield Surface. Int. J. Solids Structures, Vol. 30, No. 8, 1113 - 1131.

Bushnell, D. (1985). Computerized Buckling Analysis of Shells. Mechanics of Elastic Stability 9, Martinus Nijhoff Publishers, Dordrecht, The Netherlands.

Calladine, C. R. (1983). Theory of Shell Structures. Cambridge University Press, Cambridge, England.

Chryssanthopoulos, M. K., Poggi, C. (2001). Collapse Strength of Unstiffened Conical Shells under Axial Compression. Journal of Constructional Steel Research 57, 165-184.

Dawe, J. L., Seah, C. K., Abdel-Zahr, A. K. (1993). Investigation of the Regent Street Water Tower Collapse. Management & Operations, AWWA Journal , 34-47.

ECCS (1976). European Recommendations for Steel Construction: Buckling of Shells. European Convention for Constructional Steelwork, Brussels, Second Edition.

ECCS (1984). European Recommendations for Steel Construction: Buckling of Shells. European Convention for Constructional Steelwork, Brussels, Third Edition.

ECCS (1988). European Recommendations for Steel Construction: Buckling of Shells. European Convention for Constructional Steelwork, Brussels, Fourth Edition.

El Damatty, A. A., El-Attar, M., Korol, R. M. (1999). Simple Design Procedure for Liquid-Filled Steel Conical Tanks. Journal of Structural Engineering, Vol. 125, No. 8, 879-890.

EN 1993-1-6 (2006). Eurocode-3. Design of Steel Structures, part 1-6: Strength and Stability of Shells, CEN, Brussels.

Esslinger, M., Geier, B. (1975). Postbuckling Behavior of Structures. CISM, Springer-Verlag, Wien-New York.

Flügge, W. (1973). Stresses in Shells. Springer-Verlag, Berlin, Second Edition.

Guggenberger, W. (1994). Collapse Design of Large Steel Digester Tanks. Thin-Walled Structures 20, 109-128.

Guggenberger, W., Linder, C. (2004a). Analogy Model for the Axisymmetric Elastic Edge Bending problem in Shells of Revolution based on Geckeler's Approximation. In: Zingoni, A. (editor). Progress in Structural Engineering, Mechanics and Computation, Taylor & Francis, London, 269–274.

Guggenberger, W. (2004b). Proposed Modified Hierarchy of Shell Buckling Design Procedures in

Eurocode EN 1993-1-6. submission to ECCS TWG 8.4 “Buckling of Steel Shells“, April 2004.

Guggenberger, W. (2005a). Imperfection Assumptions and their Effects on Elastic Shell Buckling. Proceedings of the 5th IASS/IACM International Conference on Computation of Shell and Spatial Structures, Salzburg, Austria.

Guggenberger, W. (2005b). Discretely Supported Thin-Walled Steel Silo Shells: Advanced Buckling Design and Modelling Aspects. Paper 51, Proceedings of the Tenth International Conference on Civil, Structural and Environmental Engineering Computing, Rome, 30 August-2 September 2005.

Guggenberger, W. (2007). Lecture notes: Plates and Shell Structures, Institute for Steel and Shell Structures, Graz University of Technology.

Guggenberger, W. (2008). Lecture notes: Stability of Structures, Institute for Steel and Shell Structures, Graz University of Technology.

Guggenberger, W. (2009). Lecture notes: Nonlinear Structural Analysis, Institute for Steel and Shell Structures, Graz University of Technology.

Hamadan, F. H. (2000). Seismic Behavior of Cylindrical Steel Liquid Storage Tanks. Journal of Constructional Steel Research 53, 307-333.

Hamilton, R., Boyle, J. T. (2002). Simplified Lower Bound Limit Analysis of Transversely Loaded Thin Plates using Generalized Yield Criteria. Thin-Walled Structures 40, 503 - 522.

Haroun, M. A. (2005). Mitigation of Elephant-foot Bulge Formation in Seismically-excited Steel Storage Tanks. 18th International Conference on Structural Mechanics in Reactor Technology (SMiRT 18), Beijing, China, 3664-3675.

Hutchinson, J. (1965). Axial Buckling of Pressurized Imperfect Cylindrical Shells. AIAA Journal, Vol. 3, No. 8, 1461-1466.

Ilyushin, A.A, (1948). Plasticity. Gostekhizdat, Moscow (in Russian).

Jullien, J. F. (1991). Buckling of Shell Structures, on Land, in the Sea and in the Air. Elsevier Applied Science, London.

Khamlichi, A., Bezzazi, M., Limam, A. (2004). Buckling of Elastic Cylindrical Shells considering the Effect of Localized Axisymmetric Imperfections. Thin-Walled Structures 42, 1035-1047.

Lagae, G. and Vanlaere, W. (2008, 2009). Private communications, University of Gent, Belgium.

Linder, C. (2001). Theorie der allgemeinen Rotationsschale und Entwicklung eines Kreisringträger-Analogiemodells zur Berechnung Axialsymmetrischer Biegerandstörungen. Diploma Thesis, Institut für Stahlbau und Flächentragwerke, Technische Universität Graz.

Mathon, C., Limam, A. (2006). Experimental Collapse of Thin Cylindrical Shells submitted to Internal Pressure and Pure Bending. Thin-Walled Structures 44, 39-50.

NASA (1968). Buckling of Thin-Walled Truncated Cones. NASA Space Vehicle Design Criteria, National Aeronautics and Space Administration, NASA SP-8019.

Paridaens, R., Vandepitte, D., Lagae, G., Rathe, J., Van Den Steen, A. (1987). Design Equations accounting for Elastic Buckling of Liquid-Filled Conical Shells. ECCS Colloquium on Stability of Plate and Shell Structures, Ghent, Belgium, 425-430.

Pircher, M., Bridge, R. (2001). The Influence of Circumferential Weld-Induced Imperfections on the Buckling of Silos and Tanks. Journal of Constructional Steel Research 57, 569-580.

Pircher, M. (2004). The Influence of Weld-Induced Axisymmetric Imperfections on the Buckling of a medium-length Silo under Wind Loading. International Journal of Solids and Structures 41, 5595-5610.

Ramm, E., Büchter, N. (1991). Buckling of Cylindrical and Conical Shells under Concentrated Loading. In: Jullien J.F. (editor). Buckling of Shell Structures, on Land, in the Sea and in the Air, 313-322

Robinson, M. (1971). A Comparison of Yield Surfaces for Thin Shells. Int. J. Mech. Sci., Vol. 13, 345 - 354.

Robinson, M. (1988). The Yield Surface for Axisymmetric Thin Cylinders. Int. J. Mech. Sci., Vol. 30, No. 12, 959 - 962.

Rotter, J. M., Seide, P. (1987). On the Design of Unstiffened Cylindrical Shells subject to Axial Load and Internal Pressure. Proceedings of an International Colloquium on Stability of Plate and Shell Structures, Ghent, Belgium, 539-548.

Rotter, J. M., Teng, J. G. (1989). Elastic Stability of Cylindrical Shells with Weld Depressions. Journal of Structural Engineering, Vol. 115, No. 5, 1244-1263.

Rotter, J. M. (1990). Local Collapse of Axially Compressed Pressurized Thin Steel Cylinders. Journal of Structural Engineering, Vol. 116, No. 7, 1955-1970.

Rotter, J. M. (1998). Shell structures: The New European Standard and Current Research Needs. Thin-Walled Structures 31, 3-23.

Rotter, J. M. (2001). Guide for the Economic Design of Circular Metal Silos. Spon Press, London.

Rotter, J. M. (2006a). Elephant’s Foot Buckling in Pressurized Cylindrical Shells. Stahlbau 75, Heft 9, Ernst & Sohn Verlag.

Rotter, J. M. (2006b). The Practical Design of Shell Structures Exploiting Different Methods of Analysis. In: Shell Structures: Theory and Applications, Edited by Pietraszkiewicz & Szymczak, Taylor & Francis Group, London.

Seitzberger, M. (2000). Contributions to an Efficient Numerical Analysis of the Plastic Collapse Behavior of Thin-Walled Structures. Fortschritt-Berichte VDI, Reihe 18, Nr. 247, Düsseldorf

Singer, J., Arbocz, J., Weller, T. (eds). (2002). Buckling Experiments: Experimental Methods in Buckling of Thin-Walled Structures. Volume-2, John & Wiley, Inc., New York.

Teng, J. G., Rotter, J. M. (1992). Buckling of Pressurized Axisymmetrically Imperfect Cylinders under Axial Loads. Journal of Engineering Mechanics, Vol. 118, No. 2, 229-247.

Teng, J. G., Rotter, J. M. (eds). (2004). Buckling of Thin Metal Shells. Spon Press.

Vandepitte, D., Rathe, J., Verhegghe, B., Paridaens, R., Verschaeve, C. (1982). Experimental Investigation of Buckling of Hydrostatically Loaded Conical Shells and Practical Evaluation of the Buckling Load. Proceedings State-of-the-Art Colloquium, Springer-Verlag, Stuttgart, Germany, 375-399.

Vandepitte, D., Van Den Steen, A., Paridaens, R., Van Impe, R., Lagae, G., Rathe, J. (1988). Elastic and Elastic-Plastic Buckling of Liquid-Filled Conical Shells. Buckling of Structures, Elishakoff et. al. (eds), Elsevier, Amsterdam, The Netherlands, 433-449.

Vandepitte, D. (1999). Confrontation of Shell Buckling Research Results with the Collapse of a Steel Water Tower. Journal of Constructional Steel Research 49, 303-314.

Vanlaere W., Lagae G., Guggenberger, W., Van Impe, R. (2008). Numerical study of Imperfect Liquid-Filled Conical Shells: Verifying the Present Design Rule. EUROSTEEL 2008, Graz, Austria.

Weingarten, V. I., Morgan, E. J., Seide, P. (1965). Elastic Stability of Thin-Walled Cylindrical and Conical Shells under Axial Compression. AIAA Journal, Vol. 3, No. 3, 500-505.

Winterstetter, Th. A., Schmidt, H. (2002). Stability of Circular Cylindrical Steel Shells under Combined Loading. Thin-Walled Structures 40, 893-909.

Wolfram, S. (2008). Mathematica, Version 6, Wolfram Research, Inc.

Yamaki, N. (1984). Elastic Stability of Circular Cylindrical Shells. North-Holland, Amsterdam, Netherlands.

Zotter, J. (2007). Automatisierte Modellbildung und Berechnung komplexer Metallsilo-konstruktionen. Doctoral Dissertation, Institut für Stahlbau und Flächentragwerke, Technische Universität Graz.

ANNEX

A

Ilyushin yield criterion and related approximations

A.1 Introduction

In the estimation of plastic limit loads of plate and shell structures, the small displacement materially nonlinear numerical analysis is known to give accurate results. In cases of no sophisticated numerical analysis packages other simpler ways are sought to estimate the plastic limit load. For pure membrane stress states, the Von Mises membrane yield criterion gives exact estimates. When there exist bending stresses (or secondary stresses) in addition to the membrane stresses (or primary stresses), other simple methods are used. EN 1993-1-6 (2006) proposes alternative ways of estimating the plastic limit load based on linear analysis results. Two of such methods which use linear analyis results are the first outer-surface-yield at a point of the shell's bounding surfaces (parallel to the mid-surface), corresponding to the first outer-fiber-yield in beams; and "Ilyushin's" through-the-thickness yield criterion. This section discusses the Ilyushin yield criterion and different related approximate yield criteria (in addition to those proposed by EN 1993-1-6) and their corresponding limit load estimates which, for an illustrative shell structure, will later be compared with the plastic limit loads obtained from small displacement materially nonlinear analysis (MNA).

A.2 Ilyushin's yield criterion for plates & shells

A.2.1 Ilyushin's exact yield criterion

Ilyushin (1948), developed a parametrically expressed stress resultant (section forces N_1, N_2 & N_{12} and section moments M_1, M_2 & M_{12}) based generalized plasticity criterion which deals with through-the-thickness yielding in plates and shells with elastic-perfectly-plastic isotropic plasticity based on the Von Mises yield criterion. In other words, when Ilyushin's yield criterion is satisfied at a point of the shell mid-surface, yielding occurs over the full thickness of the structure at this particular location. Ilyushin used three basic non-dimensional yield parameters (q_N, q_M, and q_{NM}) which are quadratic functions of the normalized section forces and section moments (n_1, n_2, n_{12}, m_1, m_2, and m_{12}). The normalization is achieved by relating the actual section force and section moment components to the respective plastic limit components N_{pl} and M_{pl}, (Eq. A.7), in the uni-axial case.

Ilyushin's original representation of the exact through-the-thickness yield criterion was given in parametric form, expressing his three basic non-dimensional yield parameters (q_N, q_M, and q_{NM}) as functions of two abstract parameters. Because of its complexity in practical applications, Ilyushin later proposed a linear approximation (the best known linear approximation) to his yield surface given in implicit form, Figure A.1, which is easier to apply and lies between 6% on the safe side and 3.5% on the unsafe side (Robinson, 1971).

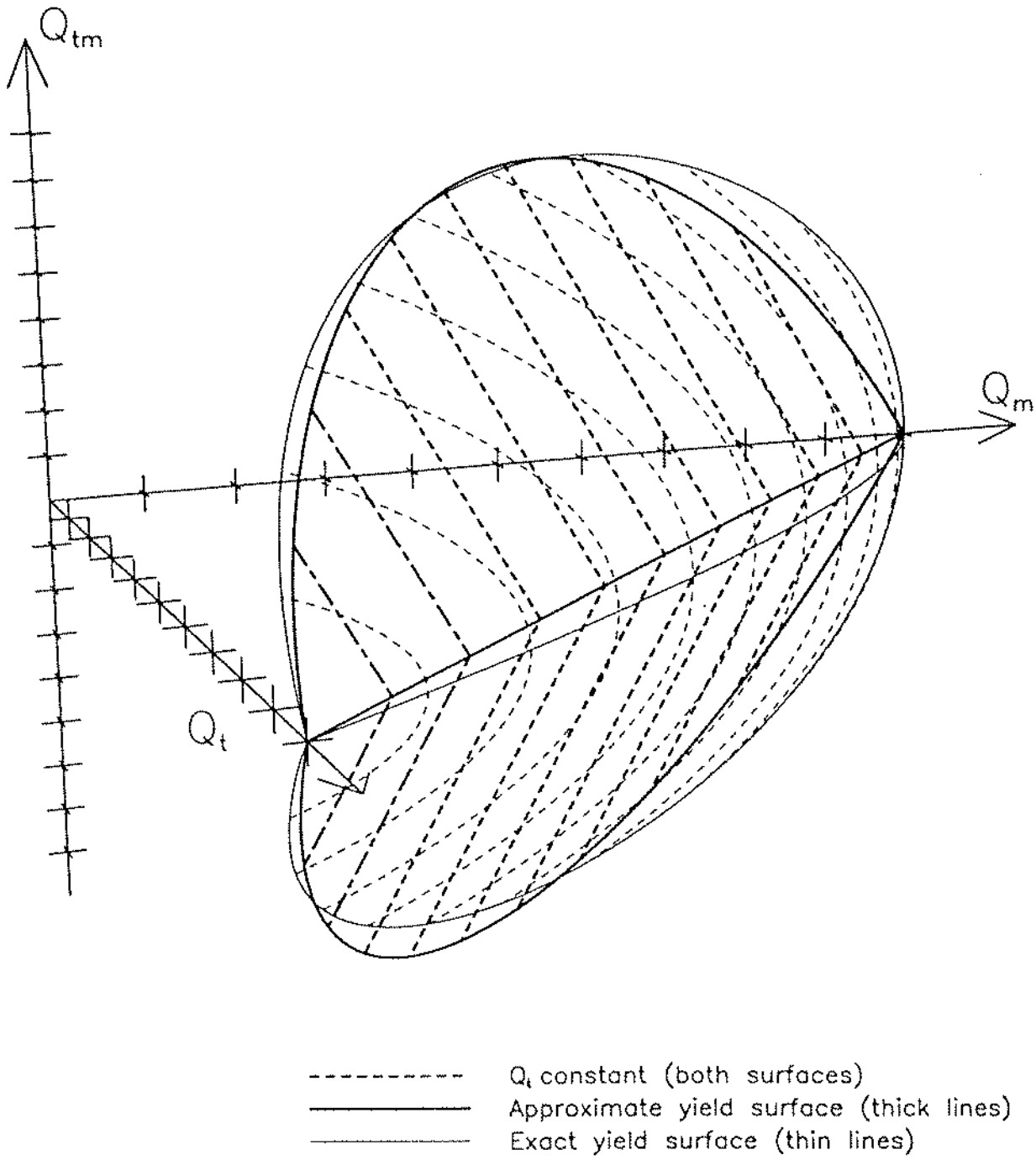

Figure A.1 Exact and approximate Ilyushin yield surfaces (Burgoyne, 1993)

A.2.2 Ilyushin's linear approximation

Ilyushin's linear approximate yield criterion is given as follows:

$$F(q_N, q_M, q_{NM}) = q_N + q_M \pm \frac{1}{\sqrt{3}} q_{NM} - 1 = 0 \qquad \text{(Eq. A.1)}$$

with the three basic parameters q_N, q_M, and q_{NM} given as

$$q_N = n_1^2 + n_2^2 - n_1 n_2 + 3n_{12}^2 \qquad \text{(Eq. A.2)}$$

$$q_M = m_1^2 + m_2^2 - m_1 m_2 + 3m_{12}^2 \qquad \text{(Eq. A.3)}$$

$$q_{NM} = n_1 m_1 + n_2 m_2 - \frac{1}{2}(n_1 m_2 + n_2 m_1) + 3n_{12} m_{12} \qquad \text{(Eq. A.4)}$$

where the normalized section force and moment components are given by

$$n_1 = \frac{N_1}{N_{pl}}; \quad n_2 = \frac{N_2}{N_{pl}}; \quad n_{12} = \frac{N_{12}}{N_{pl}} \qquad \text{(Eq. A.5)}$$

$$m_1 = \frac{M_1}{M_{pl}}; \quad m_2 = \frac{M_2}{M_{pl}}; \quad m_{12} = \frac{M_{12}}{M_{pl}} \qquad \text{(Eq. A.6)}$$

in which

$$N_{pl} = f_y \cdot t \text{ and } M_{pl} = f_y \cdot \frac{t^2}{4} \qquad \text{(Eq. A.7)}$$

Note:

i If applied to the 1D-stress situation of beams under bending and normal force, the terms q_N, q_M, and q_{NM} become:

$$q_N = n_1^2;\ q_M = m_1^2 \text{ and } q_{NM} = n_1 m_1 \qquad \text{(Eq. A.8)}$$

$$F(q_N, q_M, q_{NM}) = n_1^2 + m_1^2 \pm n_1 m_1 = 0 \qquad \text{(Eq. A.9)}$$

The 1D-plastic interaction n_1-m_1 in the linear-ilyushin-representation turns out to be symmetric with respect to the $n_1 = \pm m_1$ axis.

ii The linear-Ilyushin-representation does not exactly match the correct plastic interaction for the 1D-situation but is very close to it with a maximum deviation of about 5%. The correct interaction for beams with rectangular cross-sections is not symmetric with respect to the $n_1 = \pm m_1$ axis.

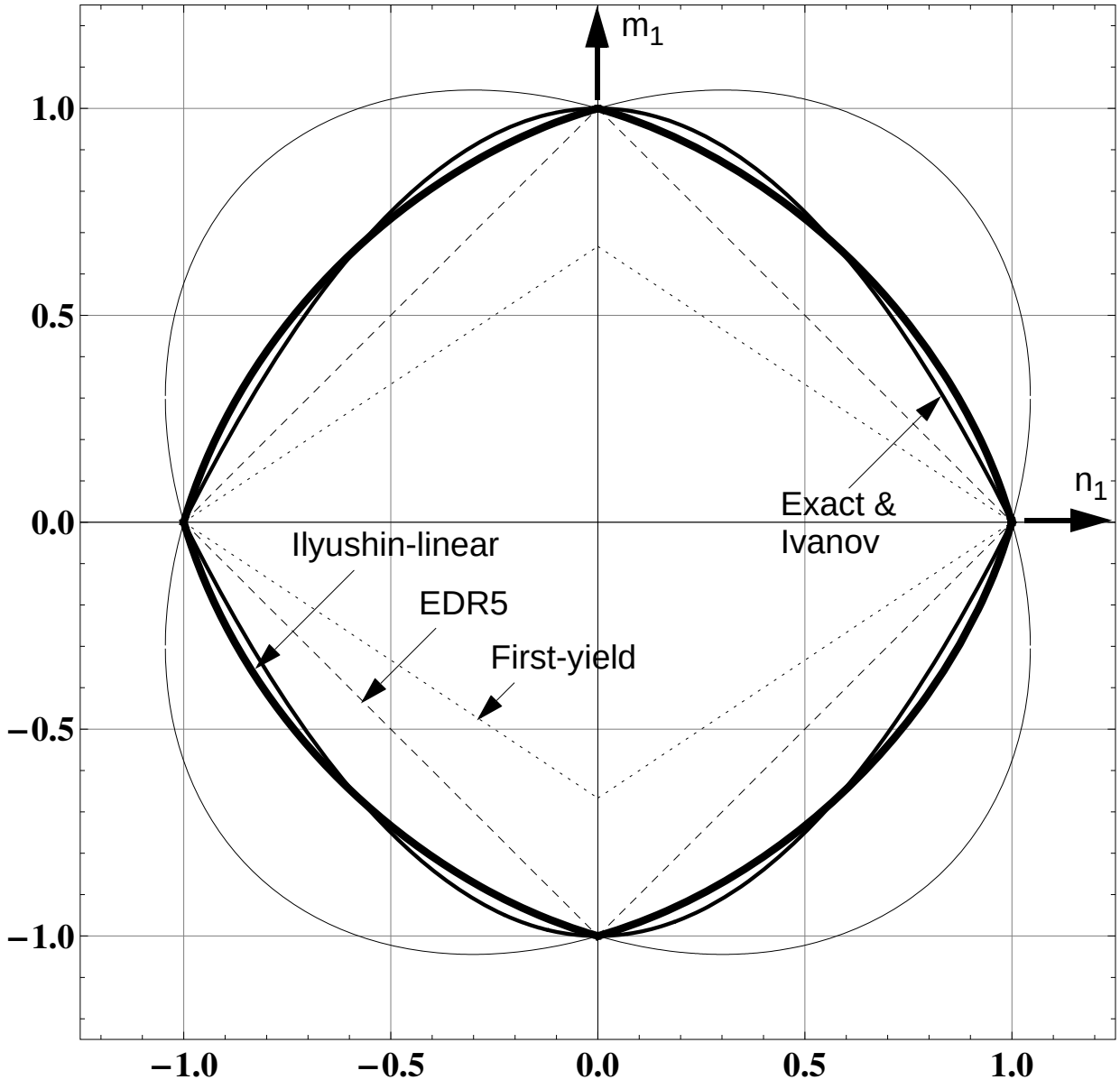

Figure A.2 Yielding under 1D bending and normal section forces situation

Example:

For illustration purposes, consider an axisymmetric axially compressed and internally uniformly pressurized cylindrical shell loaded in such a way that the pure membrane yield condition $q_N = 1.0$ is fulfilled in the free shell interior (i.e. in the bending free region). The cylindrical shell will have the following set of conditions:

Geometry: R/t = 500 cm; t = 1.0 cm; L/R = 1.0

Boundary conditions: pinned or fixed bottom

Loading: axial compressive loading & uniform internal pressure $p = 0.5\ t\ f_y/R$

Material properties: $E = 21000\ kN/cm^2$; $\nu = 0.3$; $f_y = 24.0\ kN/cm^2$

The internal pressure value ($p = 0.5\ t\ f_y/R$) is chosen only for demonstration purposes. Applying such an internal pressure intensity means 50% membrane plastic utilization in the circumferential direction. With this internal pressure,

$$n_{\phi,\,membrane} = \mu = \frac{p \cdot R}{t \cdot f_y} = 0.5 \qquad \text{(Eq. A.10)}$$

Assuming tensile forces as positive and compressive forces as negative, the circumferential tensile membrane section force will be positive and an axial compressive section force $n_{x,\,membrane} = N_x / N_{pl}$ as negative. Hence, an axial compressive section force n_x which, along with n_ϕ, produces a pure membrane yield condition $q_N = 1.0$ in the free shell interior is computed as follows:

$$q_N = n_x^2 + n_\phi^2 - n_x n_\phi \qquad \text{(Eq. A.11)}$$

$$q_N = n_x^2 + n_\phi^2 + |n_x| \cdot n_\phi \qquad \text{(Eq. A.12)}$$

Solving for n_x will then give $n_x = 0.651$.

Under the aforementioned loading conditions, the elastic normalized section forces (n_x, n_ϕ, m_x, and m_ϕ), Ilyushin's basic parameters (q_N, q_M, and q_{NM}), and Ilyushin's linear approximation ($q_N + q_M \pm q_{NM}/\sqrt{3}$) of the illustrative cylindrical shell have been computed. The results obtained are shown in Figure A.3 and Figure A.4.

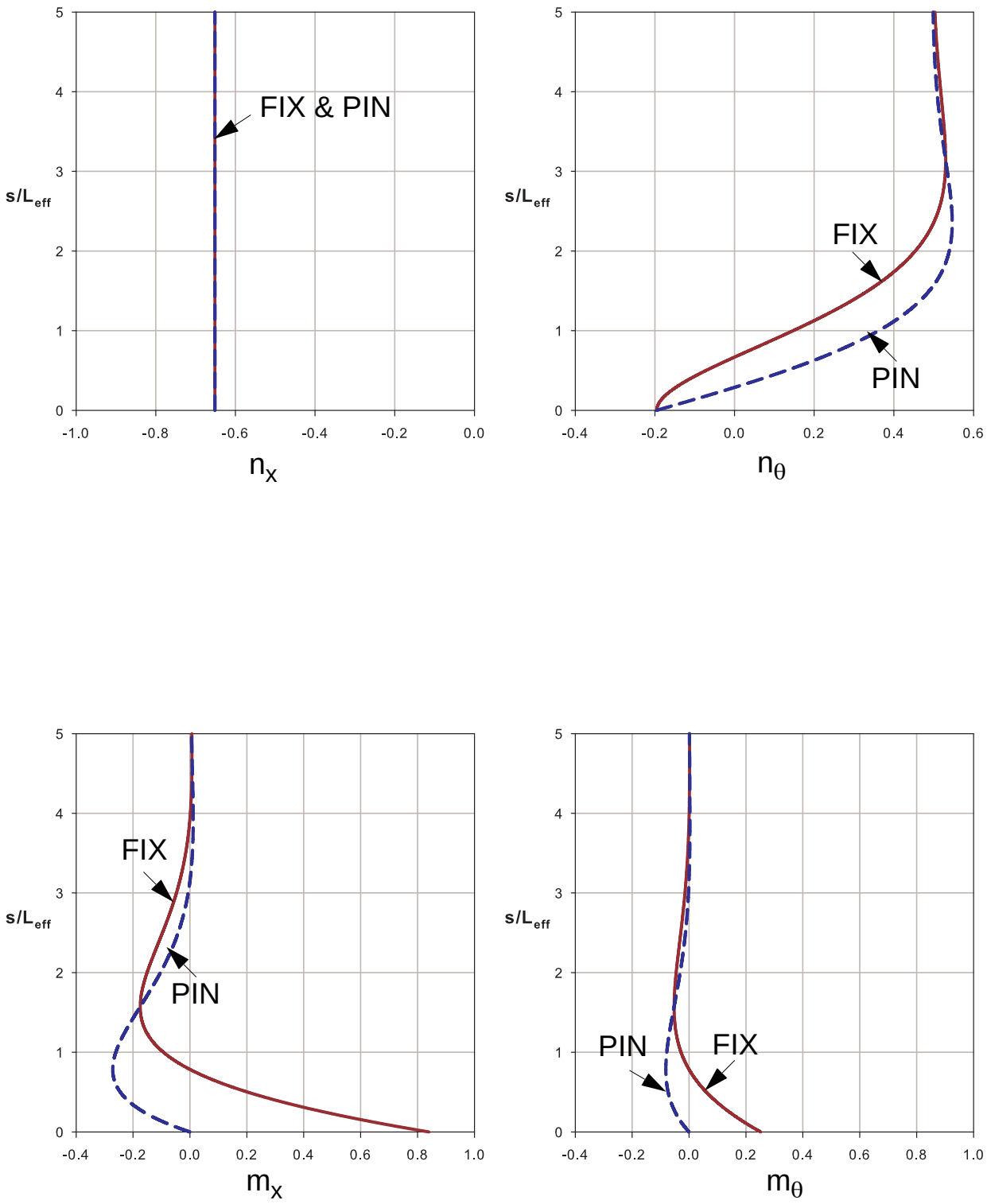

Figure A.3 Normalized elastic section forces

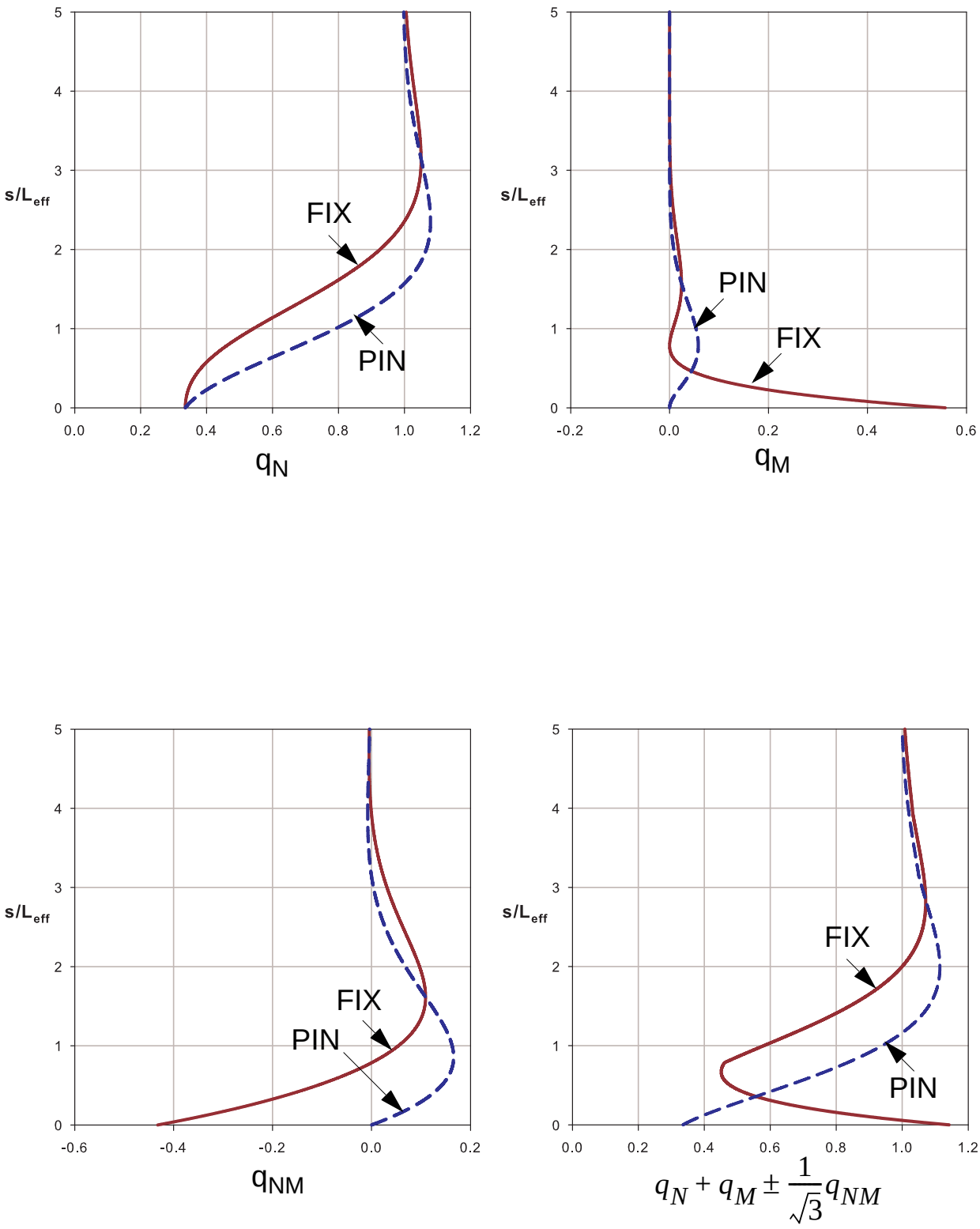

Figure A.4 Ilyushin's yield parameters

A.2.3 Ivanov's approximations

Following Ilyushin's stress resultant oriented yield criterionand his linear approximation, further improved approximations to the exact Ilyushin yield surface have been made. Ivanov used a quadratic approximation to Ilyushin's exact yield surface which has been proved to be more accurate than the Ilyushin's linear approximation and found to lie within 0.5% of the exact Ilyushin yield surface, Robinson (1971). In addition, Ivanov's approximate yield criterion, when compared to Ilyushin's linear approximation, avoids corner discontinuity problems of the yield surface when plotted on a 3D q_N-q_M-q_{NM}-space (Burgoyne & Brennan, 1993). For this reason, Ivanov's approximate yield criterion will be considered and discussed first.

Besides, other somehow crude yield criteria are commonly used in structural engineering including the first yield criterion and one that is proposed in EN 1993-1-6 and named as "Ilyushin yield criterion" eventhough it behaves like a 3-layer Von Mises sandwich shell yield criterion as will be explained later. Moreover, the two forms of Ivanov's approximate yield expressions (I and II), valid for beam-like 1D and "proportional" axisymmetric situations, are re-written in an alternative format which will help easily recognize the correct 1D plastic interactions.

A.2.3.1 Ivanov's approximate yield condition

Ivanov proposed two approximate yield surfaces which differ in a single correction term (Eq. A.14). Ivanov's yield criterion-II (will shortly be written as Ivanov-II in the upcoming discussions) is given by (Eq. A.15) whereas Ivanov-I yield criterion neglects the effects of the term in (Eq. A.14) and hence it is relatively easy to use. Ivanov-II yield criterion and its applications to special simple cases will be first discussed. Ivanov-I yield criterion, along with the other approximate yield criteria, will be discussed afterwards where a comparison will also be made using an illustrative shell example.

Ivanov-I approximate yield criterion:

$$f_I = q_N + \frac{q_M}{2} + \sqrt{\frac{q_M^2}{4} + q_{NM}^2} = 1 \qquad \text{(Eq. A.13)}$$

Ivanov-II approximate yield criterion:

With

$$\varepsilon = \frac{1}{4}\left(\frac{q_N q_M - q_{NM}^2}{q_N + 0.48 q_M}\right) \quad \ldots \text{ nonlinear correction term} \qquad \text{(Eq. A.14)}$$

Ivanov-II yield criterion is given by:

$$f_{II} = f_I - \varepsilon = q_N + \frac{q_M}{2} + \sqrt{\frac{q_M^2}{4} + q_{NM}^2} - \varepsilon = 1 \qquad \text{(Eq. A.15)}$$

(Eq. A.15) can be rewritten as

$$\frac{q_M^2}{4} + q_{NM}^2 = \left(1 - q_N - \frac{q_M}{2} + \varepsilon\right)^2 \quad \text{(Eq. A.16)}$$

$$q_{NM}^2 = (1 - q_N)^2 + q_N q_M - q_M + 2\varepsilon\left(1 - q_N - \frac{q_M}{2} + \frac{\varepsilon}{2}\right) \quad \text{(Eq. A.17)}$$

It can easily be shown directly that with

$$\tilde{q}_{NM} = q_N q_M - q_{NM}^2 \quad \text{(Eq. A.18)}$$

(Eq. A.17) now becomes,

$$(1 - q_N)^2 - q_M + \tilde{q}_{NM} + 2\varepsilon\left(1 - q_N - \frac{q_M}{2} + \frac{\varepsilon}{2}\right) = 0 \quad \text{(Eq. A.19)}$$

The terms $\tilde{q}_{NM}$ and ε are explicitly computed as follows

$$\tilde{q}_{NM} = 3\left(\frac{n_1 m_2 - n_2 m_1}{2}\right)^2 + 3(m_{12}^2 q_N - 2 n_{12} m_{12} q_{NM} + n_{12}^2 q_M) \quad \text{(Eq. A.20)}$$

$$\varepsilon = \frac{1}{4} \cdot \left(\frac{\tilde{q}_{NM}}{q_N + 0.48 q_M}\right) \quad \text{(Eq. A.21)}$$

A.2.3.2 Simple cases of Ivanov approximate yield criterion

Case-1: uni-axial normal force and bending moment

$$n_1 = n; \qquad m_1 = m; \qquad n_2 = m_2 = n_{12} = m_{12} = 0 \tag{Eq. A.22}$$

$$\Rightarrow q_N = n^2; \qquad q_M = m^2; \qquad q_{NM} = n \cdot m; \tag{Eq. A.23}$$

$$\Rightarrow q_N \cdot q_M = q_{NM}^2 \rightarrow \varepsilon = 0 \tag{Eq. A.24}$$

$$\Rightarrow q_M = (1 - q_N)^2 \tag{Eq. A.25}$$

$$\Rightarrow m = 1 - n^2 \tag{Eq. A.26}$$

Refer to Figure A.2 for the m-n plot of (Eq. A.26).

Case-2: fixed ratio of bending-to-membrane section forces

$$\frac{m_1}{n_1} = \frac{m_2}{n_2} = \frac{m_{12}}{n_{12}} = f \tag{Eq. A.27}$$

$$\Rightarrow q_M = f^2 \cdot q_N; \qquad q_{NM} = f \cdot q_N; \qquad q_N \cdot q_M = q_{NM}^2 \rightarrow \varepsilon = 0 \tag{Eq. A.28}$$

$$\Rightarrow q_M = (1 - q_N)^2 \tag{Eq. A.29}$$

$$\Rightarrow f^2 \cdot q_N = (1 - q_N)^2 \tag{Eq. A.30}$$

Compute q_N as function of *f*.

Case-3: Principal section forces

No shear and twisting components or axisymmetric condition ($n_{12} = m_{12} = 0$)

- ***general axisymmetric case:***

$$q_N = n_1^2 + n_2^2 - n_1 n_2 \tag{Eq. A.31}$$

$$q_M = m_1^2 + m_2^2 - m_1 m_2 \tag{Eq. A.32}$$

$$q_{NM} = n_1 m_1 + n_2 m_2 - \frac{1}{2}(n_1 m_2 + n_2 m_1) \quad \text{(Eq. A.33)}$$

and

$$\tilde{q}_{NM} = 3\left(\frac{n_1 m_2 - n_2 m_1}{2}\right)^2 \quad \text{(Eq. A.34)}$$

(Eq. A.19) will be written, for this particular case as,

$$(1 - q_N)^2 - q_M + \frac{3}{4}(n_1 m_2 - n_2 m_1)^2 + 2\varepsilon\left(1 - q_N - \frac{q_M}{2} + \frac{\varepsilon}{2}\right) \quad \text{(Eq. A.35)}$$

and

$$\varepsilon = \frac{3}{16} \cdot \left(\frac{(n_1 m_2 - n_2 m_1)^2}{q_N + 0.48 q_M}\right) \quad \text{(Eq. A.36)}$$

The term ε is usually omitted, on one hand, to make it easier to use and on the other hand it results in very little difference as will be seen later in the cylindrical analysis examples. If this is applied to (Eq. A.35), it simplifies to

$$(1 - q_N)^2 - q_M + \frac{3}{4}(n_1 m_2 - n_2 m_1)^2 \quad \text{(Eq. A.37)}$$

- ***special axisymmetric case with fixed ratio of bending-to-membrane section forces***

$$\frac{m_1}{n_1} = \frac{m_2}{n_2} = f \quad \text{(Eq. A.38)}$$

$$q_M = (1 - q_N)^2 \quad \text{(Eq. A.39)}$$

$$f^2 \cdot q_N = (1 - q_N)^2 \quad \text{(Eq. A.40)}$$

$$q_N = \left(1 + \frac{f^2}{2}\right) \pm \sqrt{\left(1 + \frac{f^2}{2}\right)^2 - 1} \quad \text{(Eq. A.41)}$$

$$q_N = \left(1 + \frac{f^2}{2}\right) \pm \left(f\sqrt{1 + \frac{f^2}{4}}\right) \quad \text{(Eq. A.42)}$$

A.2.4 Rewriting different yield criteria

In this section, different yield criteria will be discussed and compared one another. In doing so, the different yield criteria are grouped into two main groups depending on the capability of representing exact 1D-beam plasticity and other specific situations.

Group-1:

The first group (named as the "nonlinear-group" because the non-dimensional yield parameters q_N, q_M and q_{NM} are combined nonlinearly) comprising of three yield criteria (Ivanov-I, Ivanov-II and "Simple") which exactly represent 1D-beam plasticity will be discussed first. For the sake of clarity and easy comparison, these yield criteria will be re-written in the same format as will be discussed below.

Group-2:

The second group (named as the "linear-group" because the non-dimensional yield parameters q_N, q_M and q_{NM} are combined linearly) comprises of three yield criteria (Linear-Ilyushin, EDR5 and First-yield) which are not capable of representing exact 1D-beam plasticity. The "linear-group" yield criteria will be discussed later.

GROUP-1: THE "NONLINEAR GROUP"

A.2.4.1 Ivanov's yield criterion-I

$$q_N + \frac{q_M}{2} + \sqrt{\frac{q_M^2}{4} + q_{NM}^2} = 1 \qquad \text{(Eq. A.43)}$$

Then Ivanov's yield surface-I can be rewritten in a step by step simplification as

$$\sqrt{\frac{q_M^2}{4} + q_{NM}^2} = 1 - \left(q_N + \frac{q_M}{2}\right) \qquad \text{(Eq. A.44)}$$

Squaring both sides will give

$$\frac{q_M^2}{4} + q_{NM}^2 = \left(1 - \left(q_N + \frac{q_M}{2}\right)\right)^2 \qquad \text{(Eq. A.45)}$$

$$\Rightarrow q_{NM}^2 = 1 + q_N^2 + q_N q_M - 2q_N - q_M \qquad \text{(Eq. A.46)}$$

$$\Rightarrow (1 - q_N)^2 - q_M + \underbrace{q_N q_M - q_{NM}^2}_{\tilde{q}_{NM}} = 0 \qquad \text{(Eq. A.47)}$$

$$\Rightarrow (1 - q_N)^2 - q_M + \tilde{q}_{NM} = 0 \qquad \text{(Eq. A.48)}$$

A.2.4.2 Ivanov's yield criterion-II

$$q_N + \frac{q_M}{2} + \sqrt{\frac{q_M^2}{4} + q_{NM}^2} - \varepsilon = 1 \qquad \text{(Eq. A.49)}$$

Using 0.5 instead of 0.48 in the denominator of the "usually" omitted term ε (applying a small change on the very small term is almost negligible) will give:

$$\varepsilon = \frac{1}{4}\left(\frac{\tilde{q}_{NM}}{q_N + 0.5q_M}\right) \qquad \text{(Eq. A.50)}$$

Following a step by step simplification as above,

$$\sqrt{\frac{q_M^2}{4} + q_{NM}^2} = 1 - \left(q_N + \frac{q_M}{2}\right) + \varepsilon \qquad \text{(Eq. A.51)}$$

Squaring both sides will give

$$\frac{q_M^2}{4} + q_{NM}^2 = \left(1 - \left(q_N + \frac{q_M}{2}\right) + \varepsilon\right)^2 \qquad \text{(Eq. A.52)}$$

expanding and rearranging will then give

$$\Rightarrow (1 - q_N)^2 - q_M + \tilde{q}_{NM} + \varepsilon^2 + 2\varepsilon\left(1 - q_N - \frac{q_M}{2}\right) = 0 \qquad \text{(Eq. A.53)}$$

$$\Rightarrow (1 - q_N)^2 - q_M + \tilde{q}_{NM}\left[1 + \underbrace{\frac{1}{2}\left(\frac{1}{(q_N + 0.5q_M)} - 1\right) + \frac{1}{4}\frac{\varepsilon}{(q_N + 0.5q_M)}}_{\varepsilon^*}\right] = 0 \qquad \text{(Eq. A.54)}$$

$$\Rightarrow (1 - q_N)^2 - q_M + \tilde{q}_{NM} \cdot (1 + \varepsilon^*) = 0 \qquad \text{(Eq. A.55)}$$

A.2.4.3 "Simple" yield criterion

This "Simple" yield criterion which exactly is the same as that of Ivanov-II yield criterion when the fixed ratio of bending-to-membrane section forces, see (Eq. A.27) to (Eq. A.29) or (Eq. A.38) to (Eq. A.39) for axisymmetric cases, is considered here as a separate yield criterion. This yield criterion gives the exact yield capacity for beams under uni-axial situation, i.e. uni-axial normal force and bending moment.

$$(1 - q_N)^2 - q_M = 0 \qquad \text{(Eq. A.56)}$$

GROUP-2: THE "LINEAR GROUP"

A.2.4.4 Ilyushin's linear approximate yield criterion

$$q_N + q_M \pm \frac{1}{\sqrt{3}} q_{NM} = 1 \qquad \text{(Eq. A.57)}$$

Ilyushin's linear yield criterion has been fully discussed on the beginning of the current chapter.

A.2.4.5 EN 1993-1-6 proposed yield criterion

This yield criterion named in EN 1993-1-6 (EDR5) as "Ilyushin's yield criterion" is not really Ilyushin's yield criterion but instead a Von Mises sandwich shell (a shell with three through-thickness layers) yield criterion where the middle layer is modelled to carry transverse shear stresses (assumed negligble in the present discussion) and the outer two layers carrying combined (normal and bending) stress effects equal to n_1+m_1, n_2+m_2, $n_{12}+m_{12}$ on one of the two outer layers and n_1-m_1, n_2-m_2, $n_{12}-m_{12}$ on the other outer layer. It is true that for few special conditions the Von Mises sandwich shell yield criterion will be equal to the Ilyushin yield criterion (Robinson, 1971) but generally this is not true as will be seen later with the help of an illustrative shell example.

The EDR5 yield criterion is given as follws:

$$(n_1 \pm m_1)^2 + (n_2 \pm m_2)^2 - (n_1 \pm m_1)\cdot(n_2 \pm m_2) + 3(n_{12} \pm m_{12})^2 = 1 \qquad \text{(Eq. A.58)}$$

Expanding, simplifying & re-arranging (Eq. A.58) will give:

$$\underbrace{(n_1^2 + n_2^2 - n_1 n_2 + 3n_{12}^2)}_{q_N} + \underbrace{(m_1^2 + m_2^2 - m_1 m_2 + 3m_{12}^2)}_{q_M} \pm 2 \underbrace{\left(n_1 m_1 + n_2 m_2 - \frac{n_1 m_2 + n_2 m_1}{2} + 3n_{12} m_{12}\right)}_{q_{NM}} = 1 \qquad \text{(Eq. A.59)}$$

Re-writing the complete equation for EDR5 yield criterion will then give:

$$q_N + q_M \pm 2q_{NM} = 1 \qquad \text{(Eq. A.60)}$$

Thus, the EDR5 yield criterion will be equivalent to the Ilyushin-linear-approximate yield criterion when the mixed term q_{NM} is zero. This condition is fulfilled only in situations where the following expression holds true:

$$\frac{m_2}{m_1} = -\frac{2 - (n_2/n_1)}{2(n_2/n_1) - 1} \qquad \text{(Eq. A.61)}$$

For a 1D bending (m) and normal force (n) situation the non-dimensional yield parameters q_N, q_M and q_{NM} will be $q_N = n^2$; $q_M = m^2$; $q_{NM} = n \cdot m$. The EDR5 yield criterion will be given by:

$$n^2 + m^2 \pm 2nm = (n \pm m)^2 = 1 \qquad \Rightarrow n \pm m = \pm 1 \qquad \text{(Eq. A.62)}$$

Refer to Figure A.2 for the m-n plot of (Eq. A.62).

A.2.4.6 “First-yield” yield criterion

The “first-yield” yield criterion is the same as the EDR5 yield criterion except the fact that this yield criterion is fulfilled when the combined elastic stress on either of the two outer surfaces reaches the 1D-yield strength of the material. Hence, the section moments should be related to the section moment at first-yield, i.e. the reference plastic moment $M_{pl} = f_y \cdot t^2/6$ should be used instead of $f_y \cdot t^2/4$. The reference plastic normal force remains $N_{pl} = f_y \cdot t$ since first-yield under membrane stress results in through-the-thickness yielding. Thus, the “first-yield” yield criterion is fulflled when:

$$\left(n_1 \pm \frac{3}{2}m_1\right)^2 + \left(n_2 \pm \frac{3}{2}m_2\right)^2 - \left(n_1 \pm \frac{3}{2}m_1\right) \cdot \left(n_2 \pm \frac{3}{2}m_2\right) + 3\left(n_{12} \pm \frac{3}{2}m_{12}\right)^2 = 1 \qquad \text{(Eq. A.63)}$$

Expanding, simplifying & re-arranging (Eq. A.63) will give:

$$\underbrace{(n_1^2 + n_2^2 - n_1 n_2 + 3n_{12}^2)}_{q_N} + \frac{9}{4}\underbrace{(m_1^2 + m_2^2 - m_1 m_2 + 3m_{12}^2)}_{q_M} \pm 3 \underbrace{\left(n_1 m_1 + n_2 m_2 - \frac{n_1 m_2 + n_2 m_1}{2} + 3n_{12}m_{12}\right)}_{q_{NM}} = 1 \qquad \text{(Eq. A.64)}$$

Re-writing the complete equation for the “first-yield” yield criterion will then give:

$$q_N + 2.25 q_M \pm 3 q_{NM} = 1 \qquad \text{(Eq. A.65)}$$

For a 1D bending (m) and normal force (n) situation the non-dimensional yield parameters q_N, q_M and q_{NM} will be $q_N = n^2$; $q_M = m^2$; $q_{NM} = n \cdot m$. The “first-yield” yield criterion will be given by:

$$n^2 + 2.25m^2 \pm 3nm = \left(n \pm \frac{3}{2}m\right)^2 = 1 \qquad \Rightarrow n \pm \frac{3}{2}m = \pm 1 \qquad \text{(Eq. A.66)}$$

Refer to Figure A.2 for the m-n plot of (Eq. A.66).

A.2.5 Example: comparison of different yield conditions

To compare the degree of "safety" of using each yield criterion, a numerical comparison of the corresponding limit load factors is given in Table A.1. In this comparison, the plastic limit load factor according to Ivanov-II yield criterion is used as a reference. The information in Table A.1 should be interpreted relative to the plastic limit load factor according to Ivanov-II yield criterion, for example, for the plastic limit load factor according to Ilyushin's linear approximate yield criterion, it will be as follows:

$$0.9377 \cdot \Lambda_{Ivanov-II} \leq \Lambda_{Ilyushin-linear} \leq 1.0343 \cdot \Lambda_{Ivanov-II} \qquad \text{(Eq. A.67)}$$

where Λ is the plastic limit load factor based on elastic section forces.

	Ivanov-I	Ivanov-II	Ilyushin_linear	EDR5	Simple
Minimum	0.9554	1	0.9377	0.8000	0.8338
Maximum	1	1	1.0343	1	1

Table A.1 Ivanov-II as a reference

Moreover, along meridian comparison of the different yield criteria can be made as shown in Figure A.5 and Figure A.6 for the illustrative axially compressed and internally uniformly pressurized cylindrical shell discussed above with fixed and pinned bottom boundary conditions, respectively. The circumferential membrane utilization due to internal pressure is considered to be $\mu = \sigma_\theta / f_y = 0.5$. The membrane Mises yield criterion is included for reference purposes. Besides, the influences of the edge bending effect on the different yield criteria can be seen.

The approximate plastic strengths for cylindrical and conical shells have been computed using the section forces and moments obtained using linear elastic shell analysis for different intensities of internal pressurization. The results have been included in the respective discussions on the plastic strengths of cylindrical and conical shells in this work.

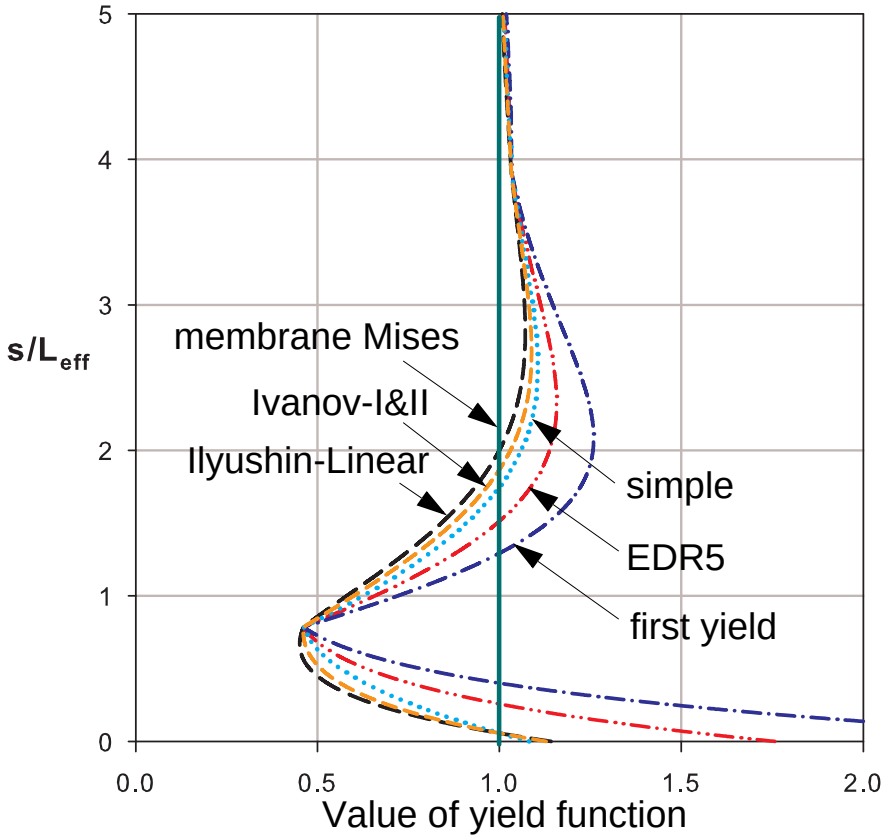

Figure A.5 Comparison of yield function for R/t = 500, μ = 0.5: **fixed bottom**

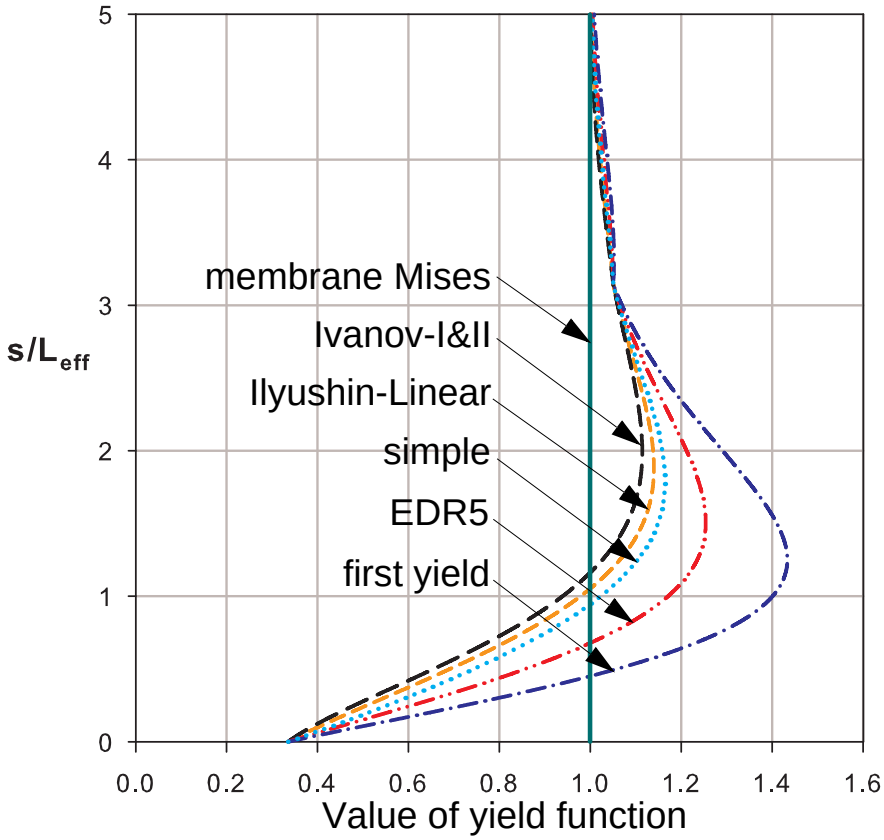

Figure A.6 Comparison of yield function for R/t = 500, μ = 0.5: **pinned bottom**

B

Axisymmetric rigid plastic plate & shell analysis

B.1 Introduction

This chapter is concerned with the anayltical computation of rigid-perfect-plastic limit strengths and corresponding section force distributions of axisymmetric plate and shell structures. In doing so, Ilyushin's yield criterion and the related approximations will be used along with the basic equations, i.e. equilibrium and kinematic relationships. To show this, a circular plate and a cylindrical shell under different loading and boundary conditions will be considered.

First, circular and annular plates under uniform or ring lateral loads and fixed or pinned outer edges will be analyzed. Later, cylindrical shells under radial ring loading with and without axial loading & internal pressurization will be considered. All the results will be compared with the recommendations according to EN 1993-1-6 and with small displacement materially nonlinear numerical analysis (ABAQUS) results.

The general concept of rigid-perfectly-plastic analysis will comprise of the following basic components:

- **Equilibrium condition should be fulfilled**
- **Kinematic relationships should hold true**
- **Elastic deformations and strains are neglected and hence the total strain is equal to the plastic strain**
- **No strain hardening is considered and hence perfect plastic**
- **A yield criterion which will be expressed by using a yield function should be fulfilled**
- **A plastic flow/normality rule that relates plastic strains with the yield function should be fulfilled**

B.2 Rigid plastic analysis of axisymmetric circular & annular plates

In this section, the rigid plastic limit strengths of uniformly or ring laterally loaded (i.e. normal to the plate surface) and outer-edge supported solid circular and annular plates will be computed. The radial distributions of of the deformations and section forces corresponding to the rigid plastic limit load will as well be computed and plotted. Axisymmetric loading and boundary conditions are considered. The following assumptions are taken into account:

- **isotropic & homogeneous** material behavior
- **Kirchhoff's hypothesis**, i.e., a straight fiber perpendicular to the middle plane before bending remains straight after bending and hence transverse shear strains are neglected ($\gamma_{rz} = 0$)
- **small deflection theory**, i.e. the vertical deflection of the plate middle plane is assumed to be very small compared to the plate thickness; and hence, there will be no role to be played by membrane actions that may result from large deflections

A solid circular plate and an annular plates are shown in Figure B.1(a) and Figure B.1(b), respectively. The different geometrical, loading and boundary condition terminologies used are as follows:

t plate thickness

R plate outer radius

a inner radius (for both geometry and loading)

b loading outer radius ($a \le b \le R$, i.e. $a = b = 0$ would mean a solid circular plate under concentrated central load)

r running radius

q lateral load

The "FIX" and "PIN" outer boundary conditions are shown in Figure B.1(a) & (b). A cut-out element along with the possible internal section forces is shown in Figure B.1(c) & (d).

The basic equations which will be needed in computing the rigid plastic limit strength and its corresponding deformation and section force distributions will be obtained as will be discussed in the following sections.

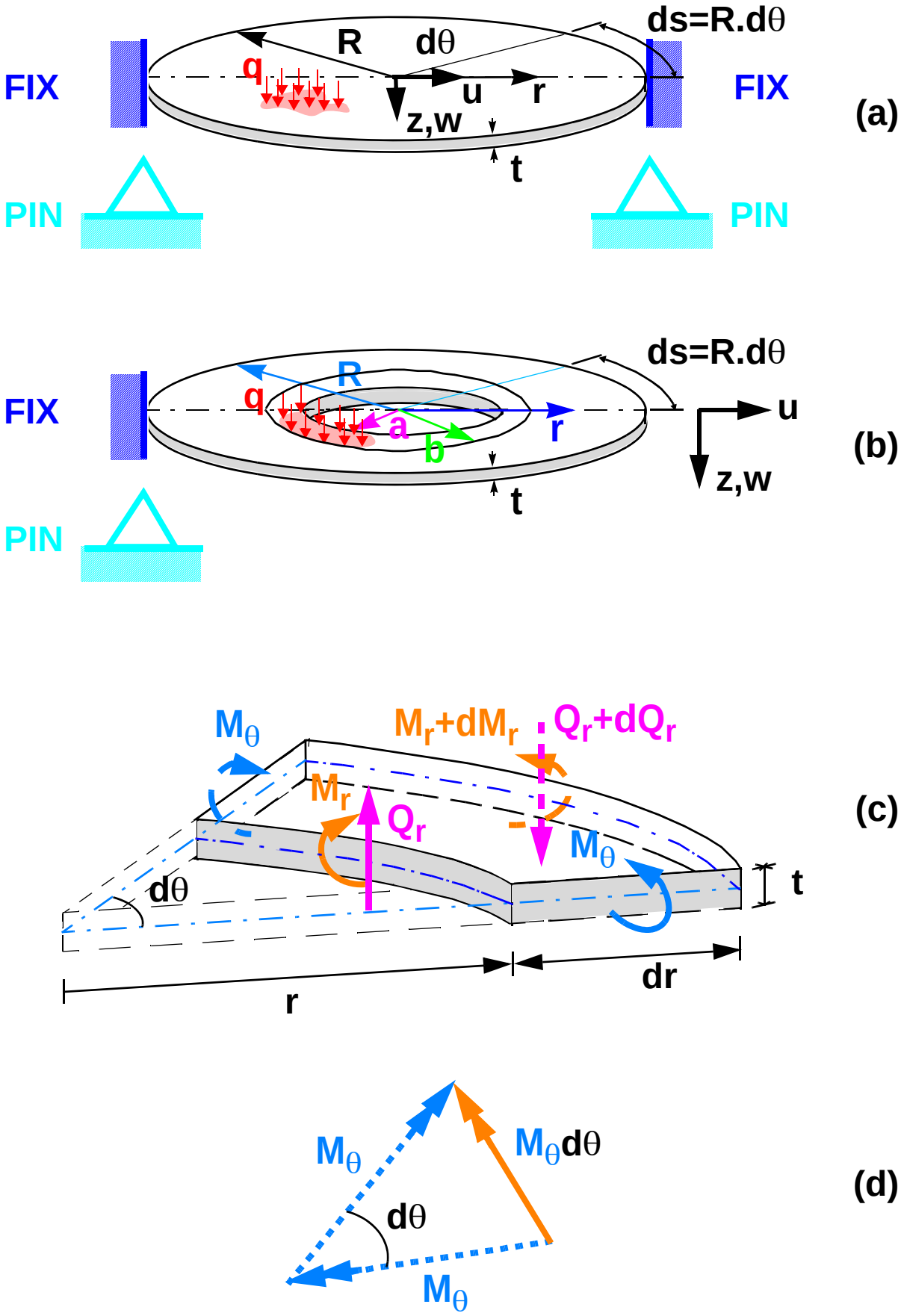

Figure B.1 Geometry, loading boundary conditions and section forces

B.2.1 Equilibrium relationships

Equilibrium of forces along the transverse direction:

$$Q_r r d\theta - \left(Q_r + \frac{\partial Q_r}{\partial r} dr\right)(r + dr)d\theta - q(r + dr)dr d\theta = 0 \qquad \text{(Eq. B.1)}$$

$$\Rightarrow \frac{\mathrm{d}}{\mathrm{d}r}(rQ_r) = -qr \qquad \text{(Eq. B.2)}$$

Equilibrium of moments:

$$M_r r d\theta - \left(\mathrm{M}_r + \frac{\partial \mathrm{M}_r}{\partial r} dr\right)(r + dr)d\theta + M_\theta dr d\theta + rQ_r dr d\theta = 0 \qquad \text{(Eq. B.3)}$$

$$\Rightarrow \frac{\mathrm{d}}{\mathrm{d}r}(rM_r) = rQ_r + M_\theta \qquad \text{(Eq. B.4)}$$

When written in matrix form, a summary of the equilbrium equations will be given as

$$\left[\begin{array}{c|c|c} \frac{\mathrm{d}}{\mathrm{d}r}(\ ) & 0 & 0 \\ \hline -1 & \frac{\mathrm{d}}{\mathrm{d}r}(\ ) & -1 \end{array}\right] \cdot \begin{bmatrix} rQ_r \\ rM_r \\ M_\theta \end{bmatrix} + \begin{bmatrix} rq \\ 0 \end{bmatrix} = \begin{bmatrix} 0 \\ 0 \end{bmatrix} \qquad \text{(Eq. B.5)}$$

The transverse shear section force can be eliminated using the two equilibrium equations (i.e. substituting (Eq. B.4) in (Eq. B.2)) to give the following relationship:

$$\begin{bmatrix} \frac{\mathrm{d}^2}{\mathrm{d}r^2}(\ ) & -\frac{\mathrm{d}}{\mathrm{d}r}(\ ) \end{bmatrix} \cdot \begin{bmatrix} rM_r \\ M_\theta \end{bmatrix} + rq = 0 \qquad \text{(Eq. B.6)}$$

B.2.2 Kinematic (geometry) relationships

***3D axisymmetric Strains*:**

$$\begin{bmatrix} \varepsilon_r \\ \varepsilon_\theta \\ \gamma_{rz} \end{bmatrix}_{3D} = \left[\begin{array}{c|c} \frac{\partial}{\partial r}(\ ) & 0 \\ \hline \frac{1}{r} & 0 \\ \hline \frac{\partial}{\partial z}(\ ) & \frac{\partial}{\partial r}(\ ) \end{array}\right] \cdot \begin{bmatrix} u \\ w \end{bmatrix}_{3D} \qquad \text{(Eq. B.7)}$$

***3D displacement assumption*:**

$$\begin{aligned} u &= z \cdot \beta_r \\ w &= W = \text{ constant with z} \end{aligned} \qquad \text{(Eq. B.8)}$$

or in matrix form:

$$\left[\begin{array}{c} u \\ \hline w \end{array}\right]_{3D} = \left[\begin{array}{c|c} z & 0 \\ \hline 0 & 1 \end{array}\right] \cdot \begin{bmatrix} \beta_r \\ W \end{bmatrix} \qquad \text{(Eq. B.9)}$$

The 3D axisymmetric strains will then be given by

$$\begin{bmatrix} \varepsilon_r \\ \varepsilon_\theta \\ \gamma_{rz} \end{bmatrix}_{3D} = \left[\begin{array}{c|c} \frac{\partial}{\partial r}(\ ) & 0 \\ \hline \frac{1}{r} & 0 \\ \hline \frac{\partial}{\partial z}(\ ) & \frac{\partial}{\partial r}(\ ) \end{array}\right] \cdot \begin{bmatrix} z & 0 \\ 0 & 1 \end{bmatrix} \cdot \begin{bmatrix} \beta_r \\ W \end{bmatrix} = \left[\begin{array}{c|c} z\frac{\partial}{\partial r}(\ ) & 0 \\ \hline \frac{z}{r} & 0 \\ \hline 1 & \frac{\partial}{\partial r}(\ ) \end{array}\right] \cdot \begin{bmatrix} \beta_r \\ W \end{bmatrix} \qquad \text{(Eq. B.10)}$$

from Kirchhoff's hypothesis, the transverse shear strain is zero

$$\gamma_{rz} = \beta_r + \frac{\partial W}{\partial r} = 0 \qquad \Rightarrow \beta_r = -\frac{\partial W}{\partial r} \qquad \text{(Eq. B.11)}$$

***Reduced 3D-strains and plate curvatures*:**

$$\begin{bmatrix}\varepsilon_r\\ \varepsilon_\theta\end{bmatrix} = z\begin{bmatrix}\frac{\partial}{\partial r}(\ )\\ \frac{1}{r}\end{bmatrix}\cdot\beta_r = -z\begin{bmatrix}\frac{\partial^2}{\partial r^2}(\ )\\ \frac{1}{r}\frac{\partial}{\partial r}(\ )\end{bmatrix}\cdot W = z\begin{bmatrix}\kappa_r\\ \kappa_\theta\end{bmatrix} \qquad \text{(Eq. B.12)}$$

Hence,

$$\begin{bmatrix}\kappa_r\\ \kappa_\theta\end{bmatrix} = -\begin{bmatrix}\frac{\partial^2}{\partial r^2}(\ )\\ \frac{1}{r}\frac{\partial}{\partial r}(\ )\end{bmatrix}\cdot W \qquad \text{(Eq. B.13)}$$

In rigid plastic analysis, there is no elastic deformation included. Hence, in this context the deformations and curvatures correspond to the rigid plastic limit mode incremental components:

$$\begin{aligned} W &= W_{plastic}\\ \beta_r &= \beta_{r,\,plastic}\\ \kappa_r &= \kappa_{r,\,plastic}\\ \kappa_\theta &= \kappa_{\theta,\,plastic}\end{aligned} \qquad \text{(Eq. B.14)}$$

B.2.3 Yield functions and yield criterion based on stress resultants

B.2.3.1 Yield function

$$F(q_N, q_M, q_{NM}) \qquad \text{(Eq. B.15)}$$

B.2.3.2 Yield condition

$$F(q_N, q_M, q_{NM}) = 0 \qquad \text{(Eq. B.16)}$$

Table B.1 lists the different yield function approximations to Ilyushin exact yield function. The correction term ε* in Ivanov-II yield function is given by (See Annex-A):

$$\varepsilon^* = \frac{1}{2}\left(\frac{1}{(q_N + 0.5q_M)} - 1\right) + \frac{1}{4}\frac{\varepsilon}{(q_N + 0.5q_M)} \qquad \text{(Eq. B.17)}$$

yield criterion	yield function, F
Ivanov-I	$(1-q_N)^2 - q_M + \tilde{q}_{NM}$
Ivanov-II	$(1-q_N)^2 - q_M + \tilde{q}_{NM} \cdot (1+\varepsilon^*)$
Simple	$(1-q_N)^2 - q_M$
Ilyushin Linear	$q_N + q_M \pm \frac{1}{\sqrt{3}} q_{NM} - 1$
EDR5	$q_N + q_M \pm 2q_{NM} - 1$
First-yield	$q_N + 2.25q_M \pm 3q_{NM} - 1$

Table B.1 Approximate yield functions

For the particular case of the considered circular (i.e. solid and annular) plates where the deflection is assumed to be very small and hence no membrane effects, the following condition will apply

$$q_N = 0; \qquad q_{NM} = 0 \qquad \text{(Eq. B.18)}$$

With these conditions, all approximate yield criteria, except the “first-yield” for which a 2.25 factor should be applied to q_M in the following equation, will be given by

$$F(q_M) = q_M - 1 = 0 \qquad \text{(Eq. B.19)}$$

When re-written in terms of the section moments, the yield function in (Eq. B.19) will be

$$F(M_r, M_\theta) = M_r^2 + M_\theta^2 - M_r M_\theta - M_{pl}^2 = 0 \qquad \text{(Eq. B.20)}$$

B.2.4 Associated flow/normality rule

The incremental plastic curvatures are proportional to the gradient of the yield surface. Using a plastic load increment parameter, $\lambda_{plastic}$, the associated flow rule is given by

$$\kappa_{plastic} = \begin{bmatrix} \kappa_r \\ \kappa_\theta \end{bmatrix}_{plastic} = \lambda_{plastic} \begin{bmatrix} \frac{\partial}{\partial M_r}(\ ) \\ \frac{\partial}{\partial M_\theta}(\ ) \end{bmatrix} \cdot F \qquad \text{(Eq. B.21)}$$

B.2.5 Summary of equations for rigid plastic analysis of circular plates

A detailled summary of the different relationships needed for rigid plastic analysis of circular plates is shown in Table B.2. In this table, the different relationships along with the total number and type of unknown terms to be computed & the number of equations available in each relationship are given. The mathematical solvability of the whole problem will depend on the total numbers of unknown terms and available equations. In the particular circular plate problem, there exist as many unknowns as available equations, hence it is solvable (determinate).

relationship	unknown terms	# unknowns	# equations
	(Q_r)	**(3)**	**(2)**
equilibrium [(Eq. B.5)], (Eq. B.6)	**M_r** **M_θ**	**2**	**1**
kinematics (Eq. B.13)	**$\kappa_{r,plastic}$** **$\kappa_{\theta,plastic}$** **$W_{plastic}$**	**3**	**2**
yield function (Eq. B.20)	**-**	**0**	**1**
flow rule (Eq. B.21)	**$\lambda_{plastic}$**	**1**	**2**
Total		**(7) 6**	**(7) 6**

Table B.2 Number of unknowns and unknown terms

B.2.5.1 Simplification of equations

The plastic multiplier, $\lambda_{plastic}$, can be eliminated using the two equations given by the flow rule, i.e. using the ratio of the two plastic curvature terms. The plastic curvatures can aslo be eliminated by substituting them using the kinematic relationships.

***Kinematics + yield function + flow rule*:**

$$(2M_\theta - M_r) \cdot \frac{\mathrm{d}^2 W_{plastic}}{\mathrm{d}r^2} - (2M_r - M_\theta) \cdot \frac{1}{r}\frac{\mathrm{d}W_{plastic}}{\mathrm{d}r} = 0 \qquad \text{(Eq. B.22)}$$

or can also be re-written in terms of two first order differential equations as

$$\frac{\mathrm{d}\beta_{r,\,plastic}}{\mathrm{d}r} - \frac{(2M_r - M_\theta)}{(2M_\theta - M_r)} \cdot \frac{1}{r}\beta_{r,\,plastic} = 0 \qquad \text{(Eq. B.23)}$$

$$\frac{\mathrm{d}W_{plastic}}{\mathrm{d}r} + \beta_{r,\,plastic} = 0 \qquad \text{(Eq. B.24)}$$

Yield function and derivatives:

$$F(M_r, M_\theta) = 0 \qquad \text{(Eq. B.25)}$$

$$M_\theta = M_r/2 \pm \sqrt{M_{pl}^2 - 3/4 M_r^2} \qquad \text{(Eq. B.26)}$$

$$\frac{\partial F}{\partial M_r} = 2M_r - M_\theta$$
$$\frac{\partial F}{\partial M_\theta} = 2M_\theta - M_r \qquad \text{(Eq. B.27)}$$

With the above simplifications and the equilibrium equations given in (Eq. B.5) and (Eq. B.6), the summary of equations for rigid plastic analysis of circular plates will reduce to:

relationship	unknown terms	# unknowns	# equations
equilibrium [(Eq. B.5)], (Eq. B.6)	**(Q_r)** **M_r** **M_θ**	**(3)** **2**	**(2)** **1**
yield function (Eq. B.26)	**-**	**0**	**1**
kinematics + yield function + flow rule (Eq. B.23) & (Eq. B.24)	**$W_{plastic}$** $\beta_{r,plastic}$	**2**	**2**
Total		**(5) 4**	**(5) 4**

Table B.3 Number of unknowns and unknown terms

B.2.5.2 Boundary conditions

The boundary conditions of the considered circular plate which will be required in solving the set of differential equations are given as follows:

***Interior free edge (r = a)*:**

$$Q_r = 0 \text{; and } M_r = 0 \text{;} \qquad \text{(Eq. B.28)}$$

***Exterior supported edge (r = R)*:**

Pin supported:

$$M_r = 0 \text{; and } W_{plastic} = 0 \text{;} \qquad \text{(Eq. B.29)}$$

Clamped edge:

$$W_{plastic} = 0 \text{; and } \beta_r = \frac{\partial W_{plastic}}{\partial r} = 0 \text{;} \qquad \text{(Eq. B.30)}$$

B.2.6 Introduction of non-dimensional parameters

Geometry-related non-dimensional parameters:

$$\rho = \frac{r}{R}; \qquad \rho_a = \frac{a}{R}; \qquad \rho_b = \frac{b}{R} \tag{Eq. B.31}$$

$$\xi = \frac{r-a}{R-a} = \frac{\rho-\rho_a}{1-\rho_a} \tag{Eq. B.32}$$

the relationship between the derivatives will then become

$$\Rightarrow \frac{d(\ )}{dr} = (\ )' = \frac{1}{R(1-\rho_a)} \cdot \frac{d(\ )}{d\xi} = \frac{1}{R(1-\rho_a)} \cdot (\dot{\ }) \tag{Eq. B.33}$$

$$\Rightarrow \frac{d^2(\ )}{dr^2} = (\ )'' = \frac{1}{R^2(1-\rho_a)^2} \cdot \frac{d^2(\ )}{d\xi^2} = \frac{1}{R^2(1-\rho_a)^2} \cdot (\ddot{\ }) \tag{Eq. B.34}$$

*Section forces and deformations-related non-dimensional parameters***:**

$$Q_r^* = \frac{Q_r \cdot R}{M_{pl}}$$
$$q^* = \frac{q \cdot R^2}{M_{pl}} \tag{Eq. B.35}$$

$$\begin{aligned} \beta_{r,\,plastic}^* &= R \cdot \beta_{r,\,plastic} \\ \lambda_{plastic}^* &= R^2 M_{pl} \cdot \lambda_{plastic} \\ \kappa_{r,\,plastic}^* &= R^2 \cdot \kappa_{r,\,plastic} \\ \kappa_{\theta,\,plastic}^* &= R^2 \cdot \kappa_{\theta,\,plastic} \end{aligned} \tag{Eq. B.36}$$

$$m_r = \frac{M_r}{M_{pl}}; \qquad m_\theta = \frac{M_\theta}{M_{pl}}; \qquad M_{pl} = f_y \cdot \frac{t^2}{4} \tag{Eq. B.37}$$

B.2.7 Condensed rigid plastic equations of annular/solid circular plates

The equations which completely describe circular plate rigid plasticity will reduce to the following set of erdinary differential equations. The yield condition, $F(M_r,M_\theta) = 0$, has been used to eliminate M_θ.

$$Q_r^* + \left(\frac{\rho_a}{1-\rho_a} + \xi\right) \cdot \dot{Q}_r^* + q^*(1-\rho_a)\left(\frac{\rho_a}{1-\rho_a} + \xi\right) = 0 \qquad \text{(Eq. B.38)}$$

$$m_r + 2\left(\frac{\rho_a}{1-\rho_a} + \xi\right)\dot{m}_r - \sqrt{4-3m_r^2} - 2(1-\rho_a)\left(\frac{\rho_a}{1-\rho_a} + \xi\right)Q_r^* = 0 \qquad \text{(Eq. B.39)}$$

$$\sqrt{4-3m_r^2} \cdot (\dot{\beta}_{r,\,plastic}^*) - \frac{1}{2} \cdot \frac{1}{\left(\frac{\rho_a}{1-\rho_a} + \xi\right)}(3m_r - \sqrt{4-3m_r^2}) \cdot (\beta_{r,\,plastic}^*) = 0 \qquad \text{(Eq. B.40)}$$

$$(\beta_{r,\,plastic}^*) + \frac{1}{(1-\rho_a)}\dot{W}_{plastic} = 0 \qquad \text{(Eq. B.41)}$$

Thus, the rigid plastic limit analysis of circular plates has been reduced to four first order ordinary differential equations with four unkown non-dimensional section force and deformation quantities (Q_r^*, m_r, $W_{plastic}$, and $\beta_{r,\,plastic}^*$).

Boundary conditions in terms of the non-dimensional parameters:

Interior free edge ($\rho = \rho_a$):

$$Q_r^* = 0 \text{; and } m_r = 0 \qquad \text{(Eq. B.42)}$$

Exterior supported edge ($\rho = 1$):

Pin supported:

$$m_r = 0 \text{; and } W_{plastic} = 0 \qquad \text{(Eq. B.43)}$$

Clamped edge:

$$W_{plastic} = 0 \text{; and } \beta_{r,\,plastic}^* = 0 \qquad \text{(Eq. B.44)}$$

Back calculated section force and deformation variables:

Once the four quantities (Q_r*, m_r, $W_{plastic}$, and $\beta_{r,\,plastic}$*) are computed using the set of ordinary differential equations, the following section force and deformation variables can then be back calculated.

$$m_\theta = 0.5m_r + \sqrt{1 - 0.75m_r^2} \qquad \text{(Eq. B.45)}$$

$$q_M = m_r^2 + m_\theta^2 - m_r m_\theta \qquad \text{(Eq. B.46)}$$

$$\lambda_{plastic}^* = -\frac{1}{(1-\rho_a)^2}\frac{1}{\left(\frac{\rho_a}{1-\rho_a} + \xi\right)}\frac{1}{(2m_\theta - m_r)}\dot{W}_{plastic} \qquad \text{(Eq. B.47)}$$

$$\kappa_{r,\,plastic}^* = -\frac{1}{(1-\rho_a)^2}\ddot{W}_{plastic} \qquad \text{(Eq. B.48)}$$

$$\kappa_{\theta,\,plastic}^* = -\frac{1}{(1-\rho_a)^2}\frac{1}{\left(\frac{\rho_a}{1-\rho_a} + \xi\right)}\dot{W}_{plastic} \qquad \text{(Eq. B.49)}$$

B.2.8 Solution procedure

The condensed set of first order differential equations (o.d.e.) has been solved with the help of the boundary conditions and using MATHEMATICA program package (Wolfram, 2008). This software has the ability to accurately solve set of differential equations both analytically and numerically. Thus it enables to solve the set of o.d.e. and compute the lateral plastic load q* and corresponding section force and deformation variables in such a way that the boundary conditions are fulfilled. This way of solving equations to fulfill constraint conditions (it is like adjusting conditions at one end to satisfy requirements the other end) is usually called SHOOTING!

Since the presentaion of the condensed set of differential equations is in non-dimensional geometric, section force and deormation variables, the solution of the problem can be applied to different geometry conditions.

B.2.9 Examples, result plots and comparison

Rigid-plastic analyses of circular plates with varying values of the interior radius a and loading outer radius b have been done. For illustration purposes, the results of a rigid plastic analysis of a solid circular plate (a = 0) under uniform lateral loading (b = R) have been perfeormed. The circular plate has the following set of conditions:

Geometry: general for all R and t values

Boundary conditions: pinned or fixed outer edges

Loading: uniform lateral load q

Material properties: general for all material properties

For the solid circular plate under the uniform loading, MATHEMATICA has been used to numerically compute the rigid plastic load and the corresponding section force and deformation distributions along the radius of the plate. The results obtained are plotted as shown in Figure B.3 to Figure B.10.

A materially nonlinear numerical analysis (MNA) has been done using ABAQUS for a solid circular plate with similar geometry and loading conditions. In this case geometric variables with R = 500 cm and t = 1 cm has been used. The results obtained, however, have been converted into non-dimensional form in order to be able to make comparisons with those of the MATHEMATICA results discussed above. The ABAQUS materially nonlinear numerical analyis results are also shown in the same plots shown in Figure B.3 to Figure B.10. The materially nonlinear plastic deflection and slope are computed as normalized differences between the deflections and slopes of two neighbouring increments on the plastic plateau of the load-deflection diagram, Figure B.2.

Figure B.11 shows the effects of local load distribution (varying b/R) on the plastic load capacity of the solid circular plate and corresponding plastic load as predicted by EN 1993-1-6 recommendations. In all the computations both fixed and pinned outer-edge boundary conditions have been considered and shown. It can be seen from all the comparisons that a good fit exists between the analytical and numerical results & the analytical and EN 1993-1-6 recommendations.

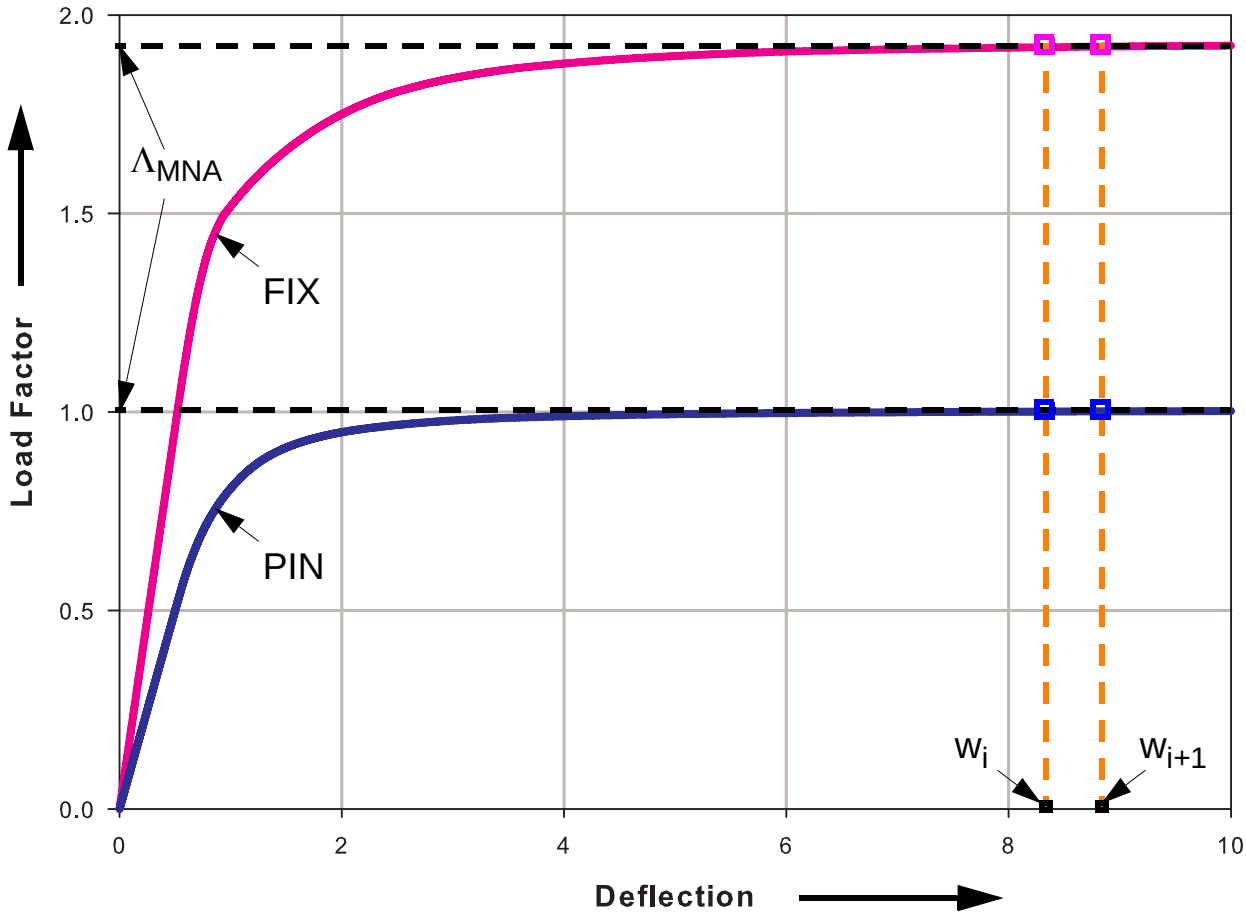

Figure B.2 Load-deflection diagram: FEM

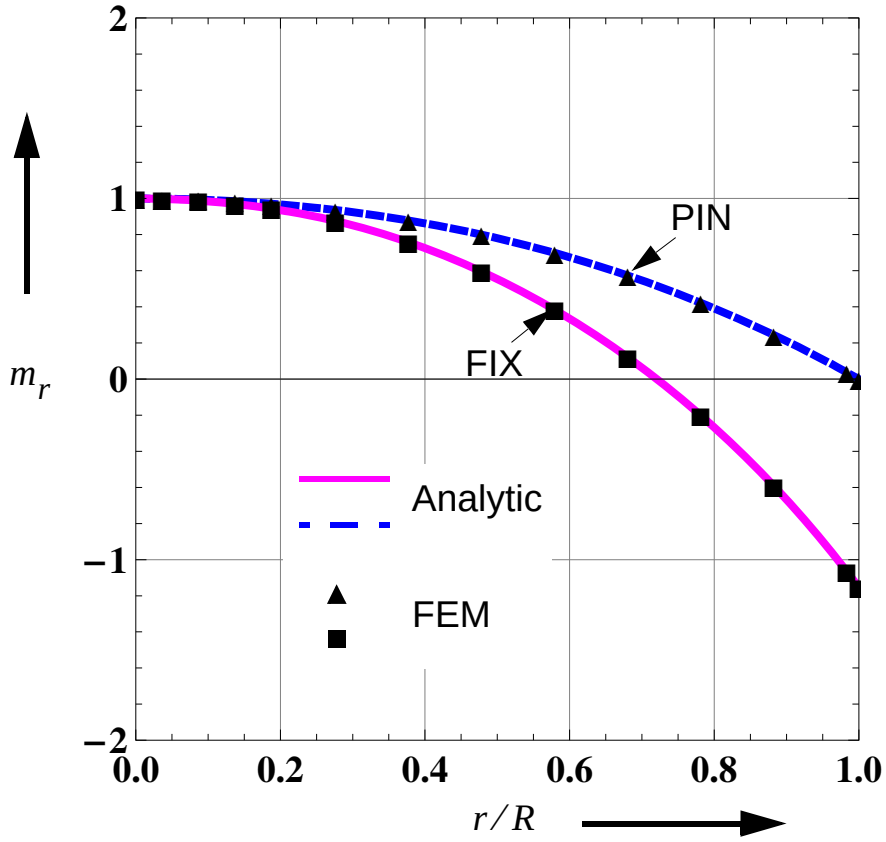

Figure B.3 Radial plastic moment, m_r

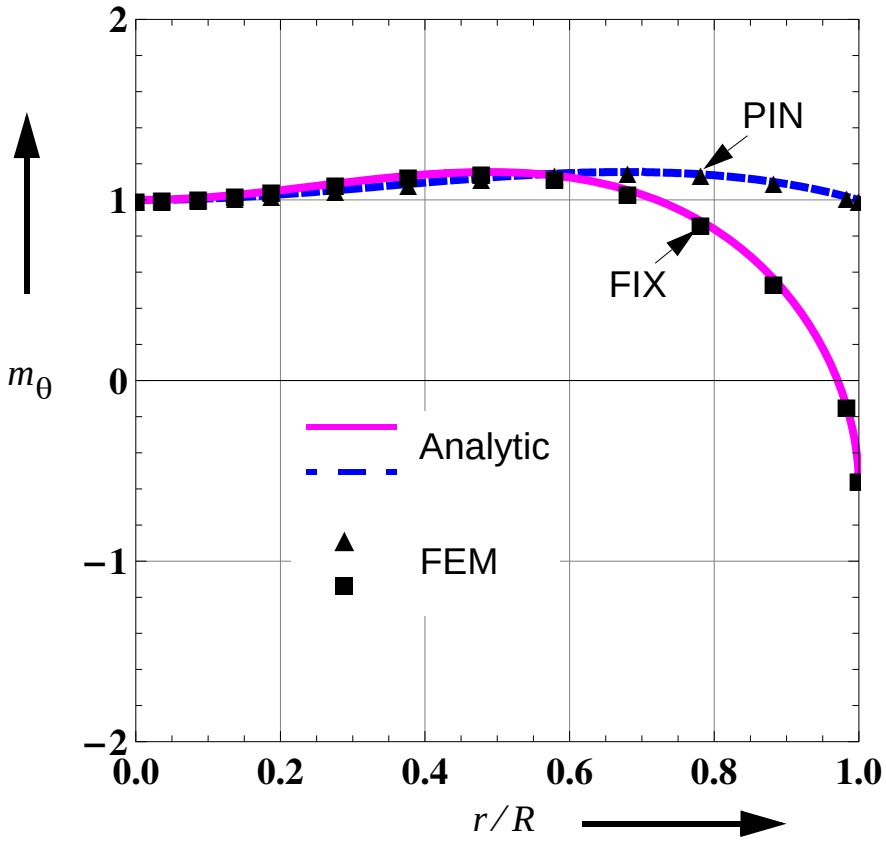

Figure B.4 Circumferential plastic moment, m_θ

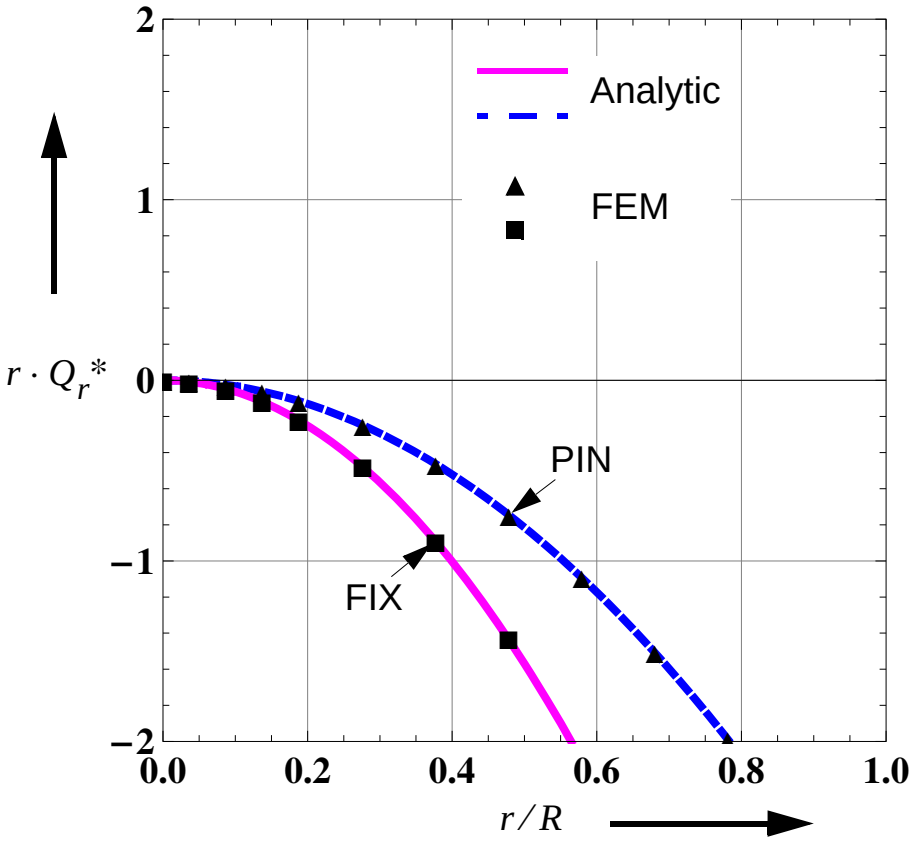

Figure B.5 Transverse shear, $r.Q_r^*$

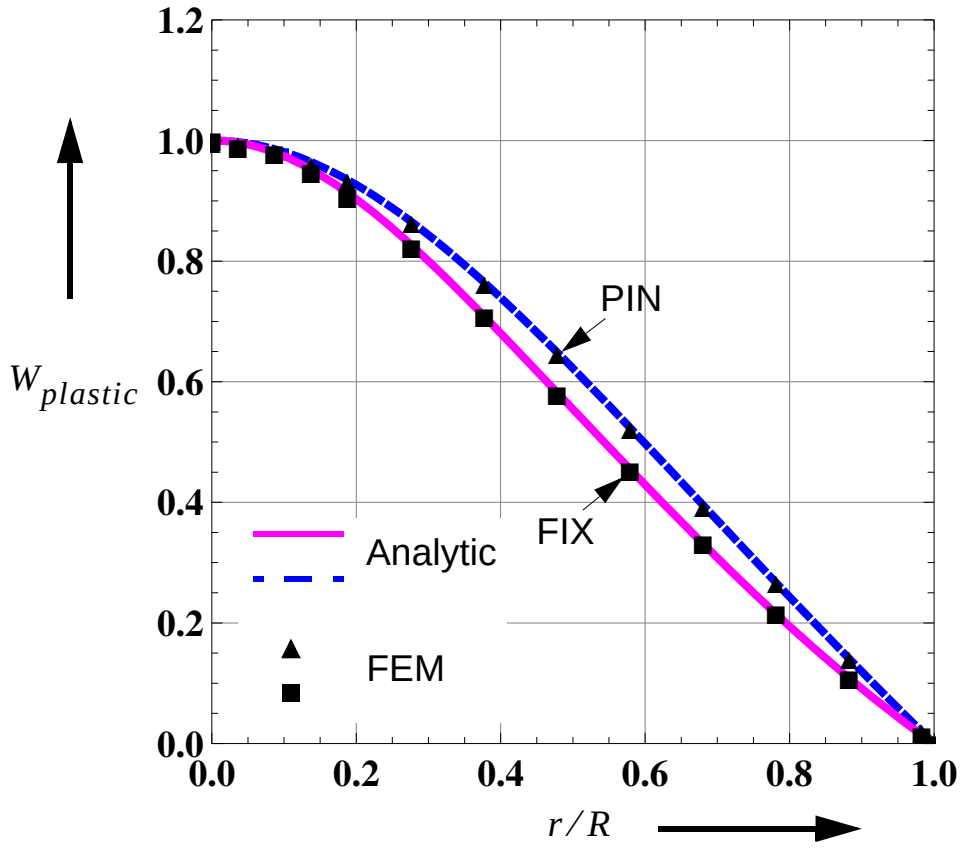

Figure B.6 Lateral plastic deflection, $W_{plastic}$

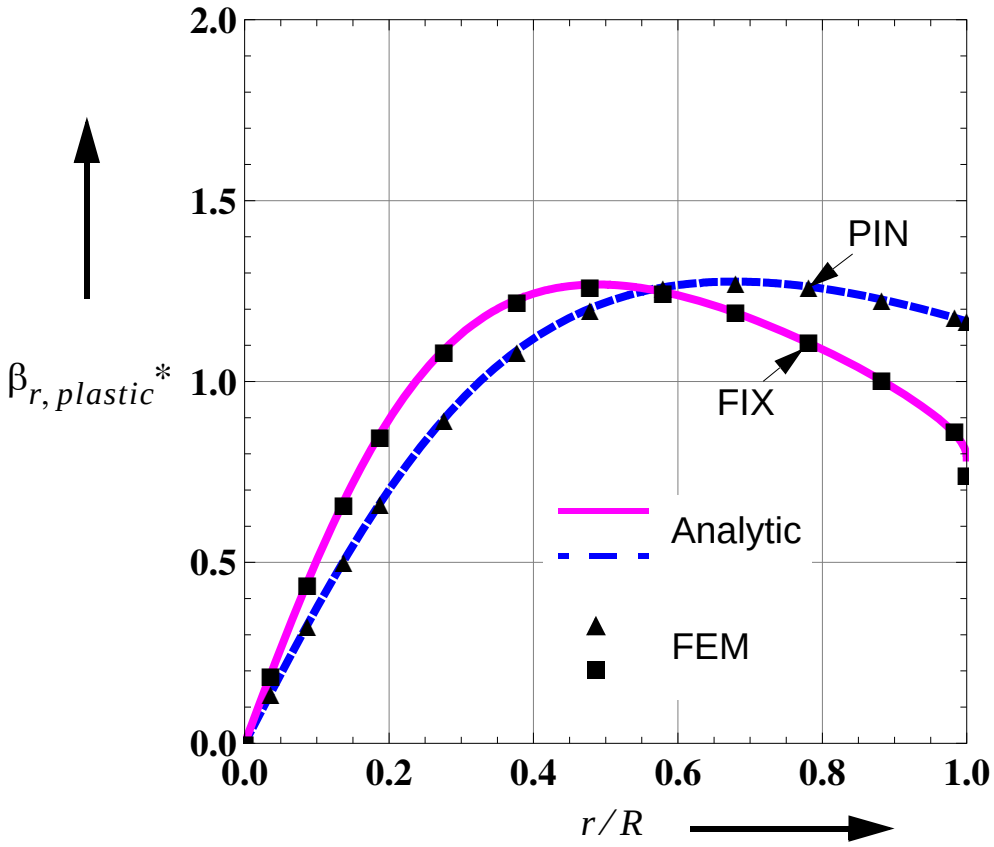

Figure B.7 Radial plastic rotation, R. $\beta_{r,plastic}$

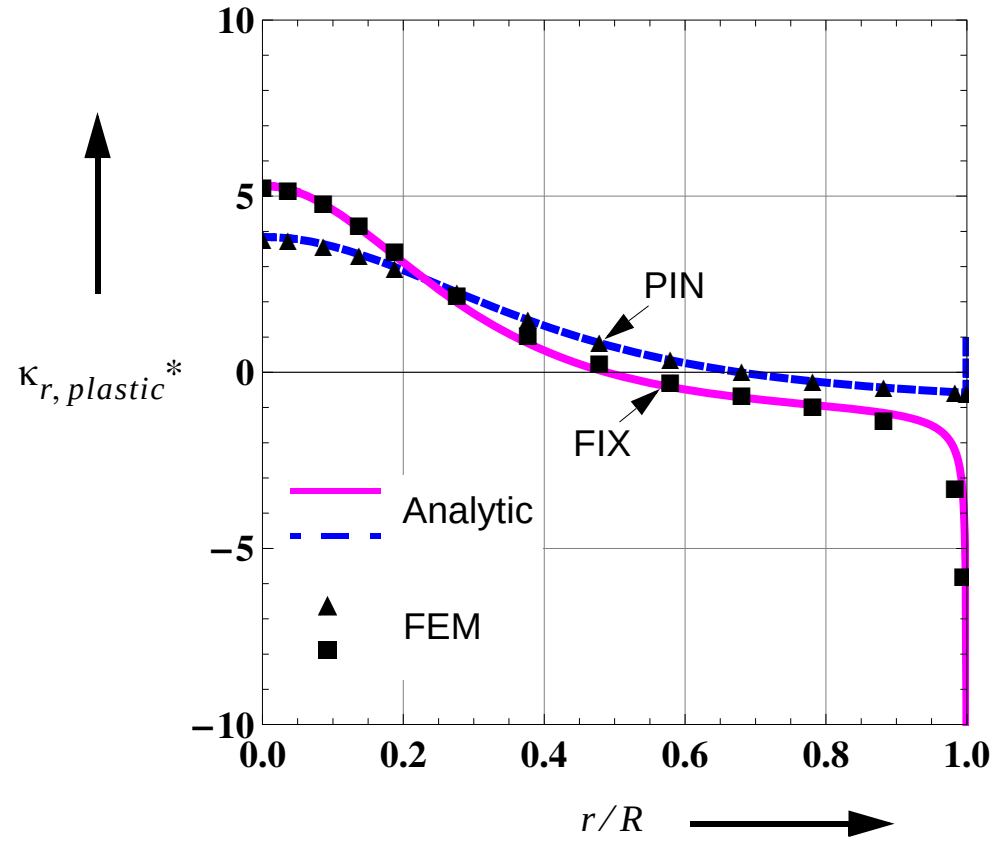

Figure B.8 Radial plastic curvature, $R^2.k_{r,plastic}$

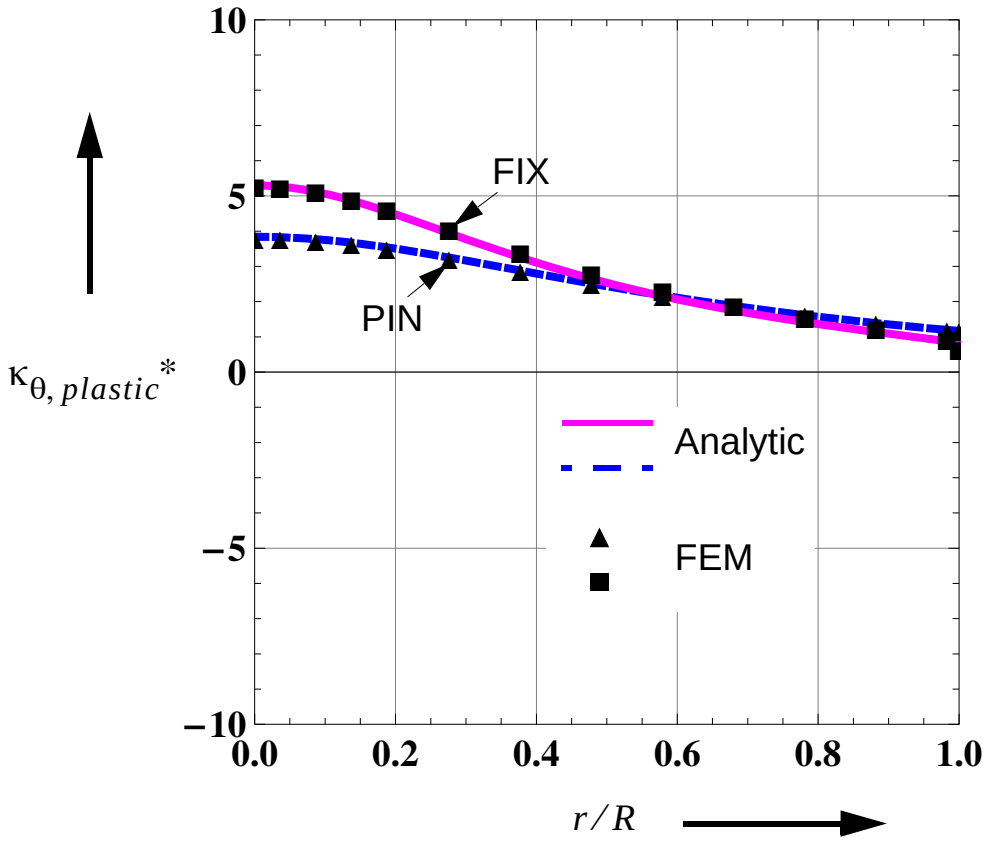

Figure B.9 Circumferential plastic curvature, $R^2.k_{\theta,plastic}$

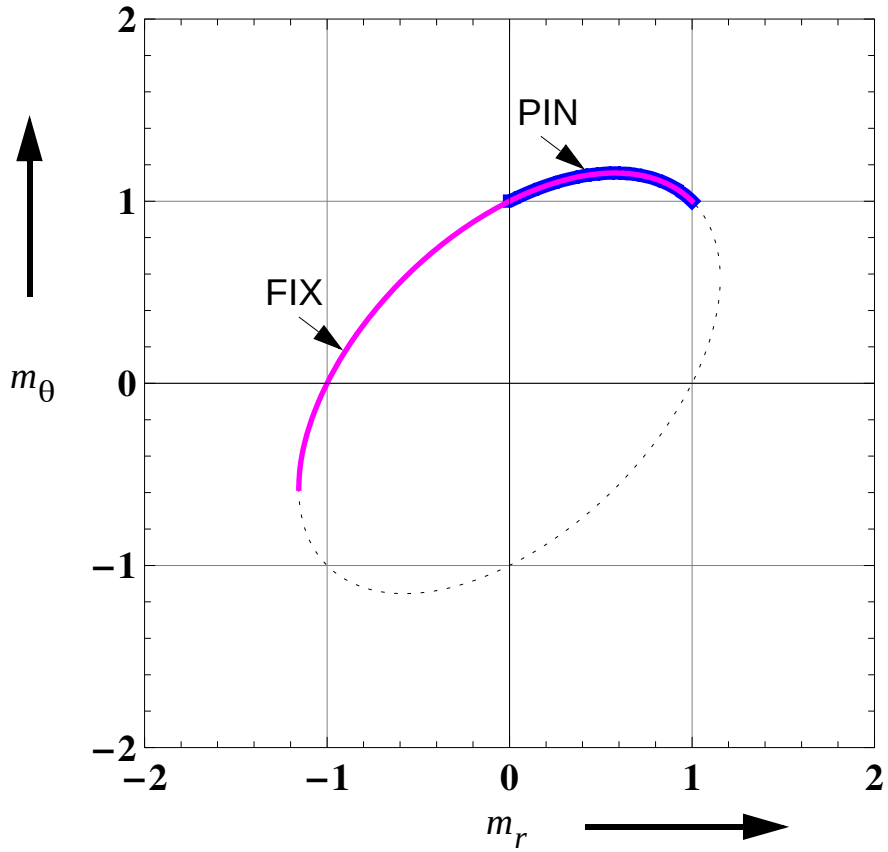

Figure B.10 Plastic section moments: Analytic & FEM

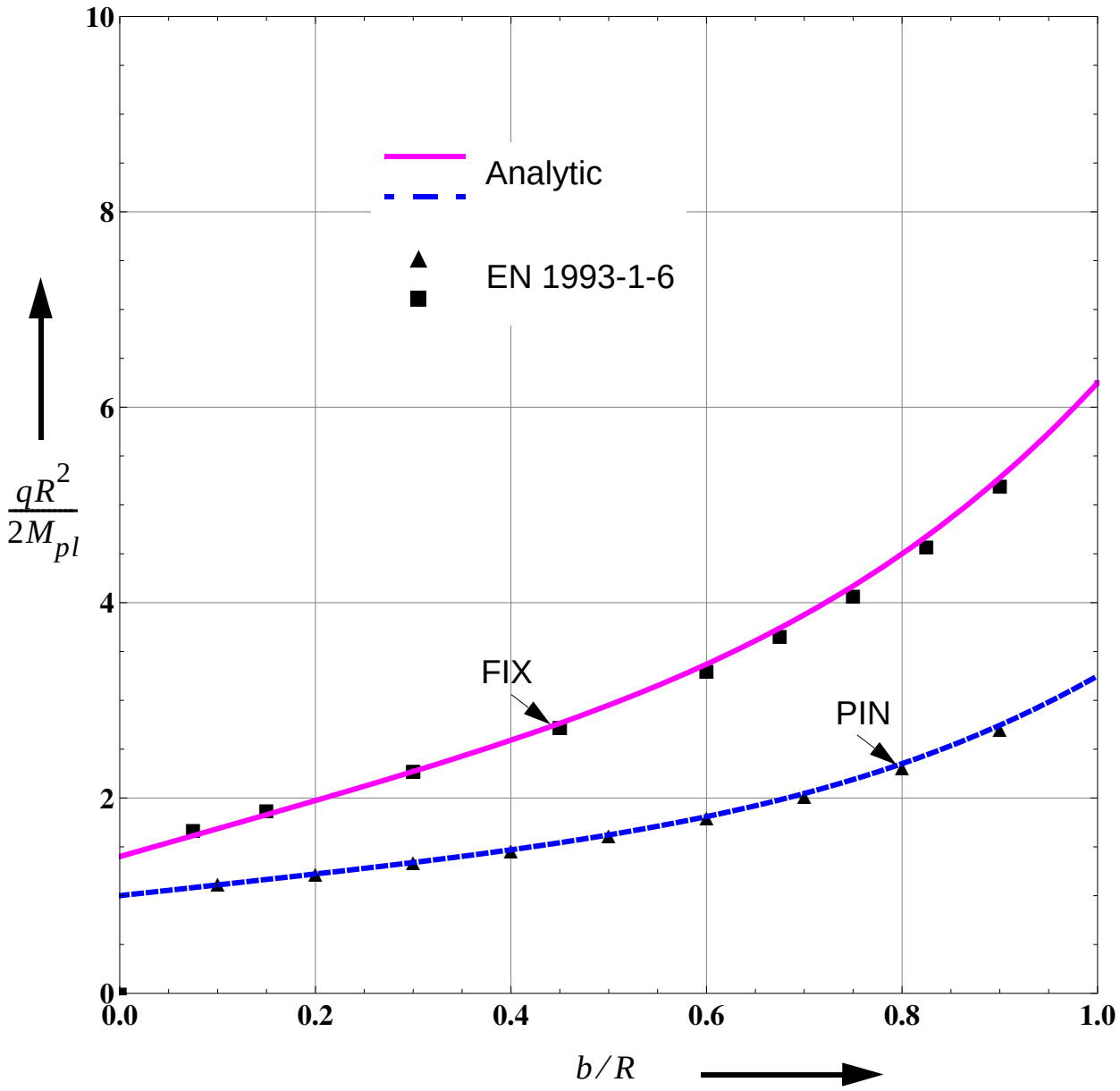

Figure B.11 Plastic limit load: effects of local load distribution; Analytic & EN 1993-1-6

B.3 Rigid plastic analysis of cylindrical shells under axisymmetric radial loading

In this section, the rigid plastic limit strengths of ring radially loaded long cylindrical shells with and without axial loading and internal pressure will be computed. In this case, the plasticity effect will be confined to an effective region symmetric about the loaded circumferential circle. The meridional distributions of of the deformations and section forces corresponding to the rigid plastic limit load will as well be computed and plotted. Axisymmetric loading conditions are considered. The following assumptions are taken into account:

- **isotropic & homogeneous** material behavior
- **long cylinder**, i.e. no **edge-restraint** effect
- **Normal hypothesis**, i.e., a straight fiber perpendicular to the thickness before deformation remains straight after deformation and hence transverse shear strains are neglected
- **small deformation theory**, i.e. the radial deformation of the cylinder middle surface is assumed to be very small compared to the shell thickness in the sense that the rigid-plastic load is the load at which a small radial deformation is possible.

A long cylindrical shell is shown in Figure B.12(a). The different geometrical, loading and section force terminologies used are shown in Figure B.12(a) & (b). The model used in a materially nonlinear numerical analysis is also shown on the right-hand-side in Figure B.12(a). A cut-out element along with the possible internal section forces is shown on the right-hand-side in Figure B.12(b).

The basic equations which will be needed in computing the rigid plastic limit strength and its corresponding deformation and section force distributions will be obtained as will be discussed in the following sections.

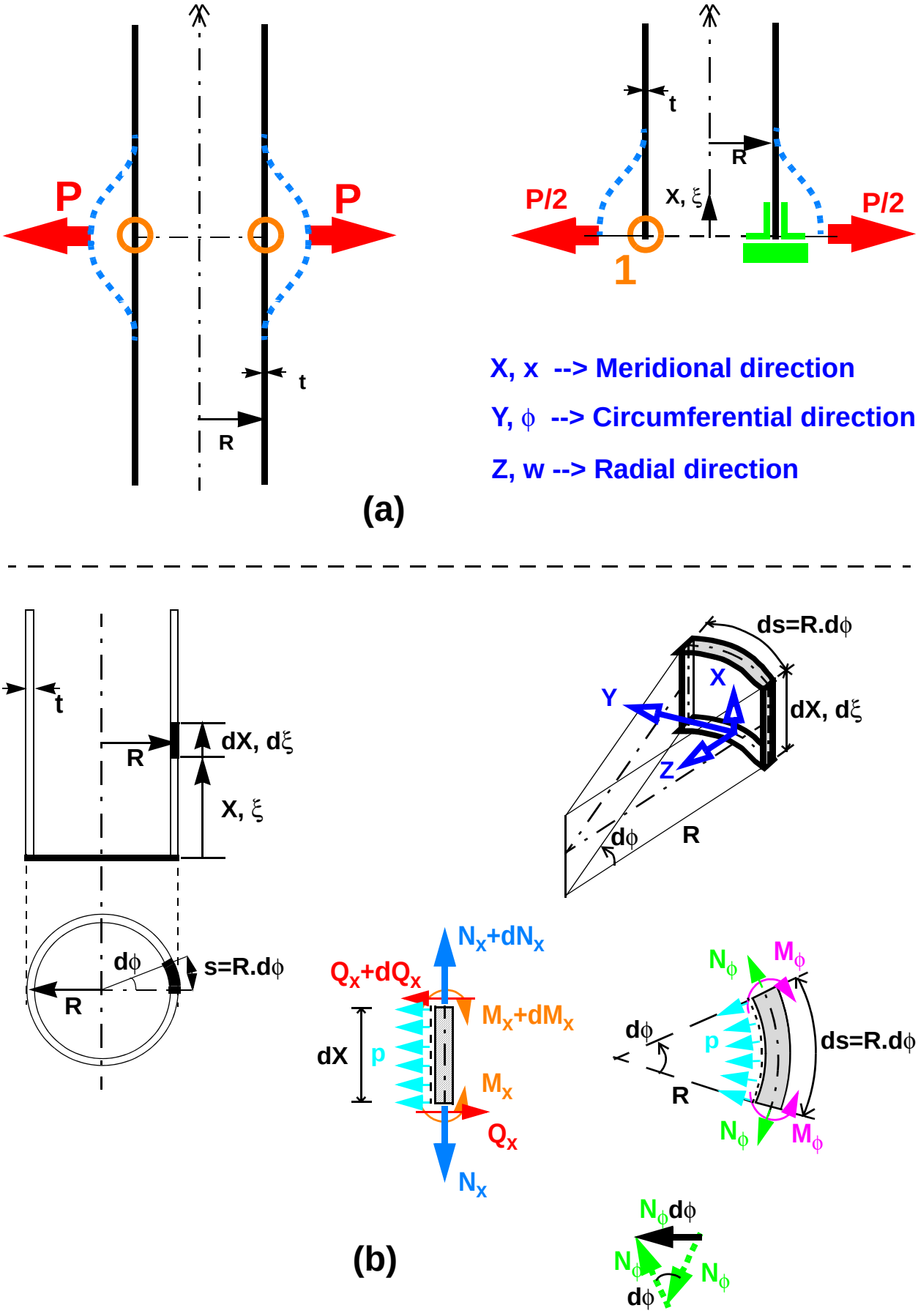

Figure B.12 Geometry, loading and section forces

B.3.1 Equilibrium relationships

B.3.1.1 Equilibrium of forces

in the axial direction:

$$(-N_x + (N_x + dN_x)) \cdot Rd\phi = 0 \qquad \text{(Eq. B.50)}$$

$$N_x' = 0 \qquad \text{(Eq. B.51)}$$

in the radial direction:

$$(-Q_x + (Q_x + dQ_x)) \cdot Rd\phi + N_\phi d\phi dx + p \cdot Rd\phi dx = 0 \qquad \text{(Eq. B.52)}$$

$$Q_x' + \frac{N_\phi}{R} + p = 0 \qquad \text{(Eq. B.53)}$$

B.3.1.2 Equilibrium of moments

$$(-M_x + (M_x + dM_x)) \cdot Rd\phi - Q_x \cdot Rd\phi dx = 0 \qquad \text{(Eq. B.54)}$$

$$Q_x = M_x' \qquad \text{(Eq. B.55)}$$

When written in matrix form, a summary of the equilbrium equations will be given as

$$\begin{bmatrix} \frac{\mathrm{d}}{\mathrm{d}x}(\ ) & 0 & 0 & 0 \\ 0 & \frac{1}{R} & \frac{\mathrm{d}}{\mathrm{d}x}(\ ) & 0 \\ 0 & 0 & -1 & \frac{\mathrm{d}}{\mathrm{d}x}(\ ) \end{bmatrix} \cdot \begin{bmatrix} N_x \\ N_\phi \\ Q_x \\ M_x \end{bmatrix} + \begin{bmatrix} 0 \\ p \\ 0 \end{bmatrix} = \begin{bmatrix} 0 \\ 0 \\ 0 \end{bmatrix} \qquad \text{(Eq. B.56)}$$

B.3.2 Kinematic (geometry) conditions

The general relationship between the strains and deformations of thin-walled cylindrical shells with normal hypothesis is given as follows, Linder (2001):

$$\begin{bmatrix} \varepsilon_x \\ \varepsilon_\phi \\ \kappa_x \\ \kappa_\phi \end{bmatrix} = \left[\begin{array}{c|c|c} \frac{\partial}{\partial x}(\ ) & 0 & 0 \\ \hline 0 & \frac{1}{R}\frac{\partial}{\partial \phi}(\ ) & -\frac{1}{R} \\ \hline 0 & 0 & -\frac{\partial^2}{\partial x^2}(\ ) \\ \hline 0 & \frac{1}{R^2}\frac{\partial}{\partial \phi}(\ ) & -\frac{1}{R^2}\frac{\partial^2}{\partial \phi^2}(\ ) \end{array}\right] \cdot \begin{bmatrix} U \\ V \\ W \end{bmatrix} \qquad \text{(Eq. B.57)}$$

For cylindrical shells under axisymmetric conditions, all the derivatives with respect to ϕ will be zero because of symmetry. The kinematic relationships will then reduce to:

$$\begin{bmatrix} \varepsilon_x \\ \varepsilon_\phi \\ \kappa_x \\ \kappa_\phi \end{bmatrix} = \begin{bmatrix} \frac{\partial U}{\partial x} \\ -\frac{W}{R} \\ -\frac{\partial^2 W}{\partial x^2} \\ 0 \end{bmatrix} \qquad \text{(Eq. B.58)}$$

Once again, it should be noted that the rigid-plastic deformation and strain quantities refer to the incremental rigid-plastic eigenmode.

B.3.3 Yield functions and yield criteria based on stress resultants

B.3.3.1 Yield function

$$F(q_N, q_M, q_{NM}) \qquad \text{(Eq. B.59)}$$

B.3.3.2 Yield condition

$$F(q_N, q_M, q_{NM}) = 0 \qquad \text{(Eq. B.60)}$$

Refer to Table B.1 for a list of the different approximate yield functions. As it will be seen later, Ivanov-II yield criterion has been used for illustrative purposes.

B.3.4 Associated flow/normality rule

The incremental plastic strains and curvatures are proportional to the gradient of the yield surface. Using a plastic load increment parameter, $\lambda_{plastic}$, the associated flow rule is given by

$$\begin{bmatrix} \varepsilon_x \\ \varepsilon_\phi \\ \kappa_x \\ \kappa_\phi \end{bmatrix}_{plastic} = \lambda_{plastic} \cdot \begin{bmatrix} \frac{\partial}{\partial N_x}(\ ) \\ \frac{\partial}{\partial N_\phi}(\ ) \\ \frac{\partial}{\partial M_x}(\ ) \\ \frac{\partial}{\partial M_\phi}(\ ) \end{bmatrix} F \qquad \text{(Eq. B.61)}$$

B.3.5 Summary of equations for rigid plastic analysis of cylindrical shells under radial ring load

A detailled summary of the different relationships needed for rigid-plastic analysis of long cylindrical shells is shown in Table B.4. In this table, the different relationships along with the total number and type of unknown terms to be computed & the number of equations available in each relationship are given. There exist as many unknowns as available equations, hence the problem is solvable.

relationship	unknown terms	# unknowns	# equations
equilibrium (Eq. B.56)	N_x N_ϕ Q_x M_x	**4**	**3**
kinematics (Eq. B.58)	$\varepsilon_{x,plastic}$ $\varepsilon_{\phi,plastic}$ $\kappa_{x,plastic}$ $\kappa_{\phi,plastic}$ $U_{plastic}$ $W_{plastic}$	**6**	**4**
yield function (Eq. B.60)	M_ϕ	**1**	**1**
flow rule (Eq. B.61)	$\lambda_{plastic}$	**1**	**4**
Total		**12**	**12**

Table B.4 Number of unknowns and unknown terms

Boundary conditions:

at a point in the shell interior ($x = x_0$):

$$Q_x = 0 \qquad \text{(Eq. B.62)}$$

$$M_x = maximum \qquad \text{(Eq. B.63)}$$

at the point of ring load application ($x = 0$):

$$W_{plastic} = maximum; \text{ and } \frac{dW_{plastic}}{dx} = 0 \qquad \text{(Eq. B.64)}$$

$$Q_x = \frac{P}{2} \qquad \text{(Eq. B.65)}$$

B.3.6 Introduction of non-dimensional parameters

Geometry-related non-dimensional parameters:

$$\xi = \frac{x}{\sqrt{R \cdot t}} \tag{Eq. B.66}$$

with the following derivative relationships

$$\Rightarrow \frac{d(\ )}{d\xi} = (\dot{\ }) = \sqrt{R \cdot t} \cdot \frac{d(\ )}{dx} = \sqrt{R \cdot t} \cdot (\ )' \tag{Eq. B.67}$$

$$\Rightarrow (\ddot{\ }) = (R \cdot t)(\ )'' \tag{Eq. B.68}$$

*Section forces and deformations-related non-dimensional parameters***:**

$$n_x = \frac{N_x}{N_{pl}}; \qquad n_\phi = \frac{N_\phi}{N_{pl}}; \qquad m_x = \frac{M_x}{M_{pl}}; \qquad m_\phi = \frac{M_\phi}{M_{pl}}; \qquad \mu = \frac{pR}{f_y t} \tag{Eq. B.69}$$

$$N_{pl} = f_y \cdot t; \qquad M_{pl} = f_y \cdot \frac{t^2}{4} \tag{Eq. B.70}$$

$$Q_x^* = \frac{Q_x}{f_y t} \cdot \sqrt{\frac{R}{t}} \tag{Eq. B.71}$$

$$\beta_{x,\,plastic}^* = \beta_{x,\,plastic} \cdot \sqrt{Rt} \tag{Eq. B.72}$$

$$\lambda_{plastic}^* = \lambda_{plastic} \cdot \frac{Rt}{M_{pl}} \tag{Eq. B.73}$$

$$\kappa_{x,\,plastic}^* = \kappa_{x,\,plastic} \cdot Rt \tag{Eq. B.74}$$

B.3.7 Simplification of equations

The equations which completely describe rigid plasticity of ring-loaded cylindrical shells reduce to:

Equilibrium equations:

$$\begin{bmatrix} \frac{d(\ )}{d\xi} & 0 & 0 & 0 \\ 0 & 1 & \frac{d(\ )}{d\xi} & 0 \\ 0 & 0 & -1 & \frac{1}{4}\frac{d(\ )}{d\xi} \end{bmatrix} \cdot \begin{bmatrix} n_x \\ n_\phi \\ Q_x^* \\ m_x \end{bmatrix} + \begin{bmatrix} 0 \\ \mu \\ 0 \end{bmatrix} = \begin{bmatrix} 0 \\ 0 \\ 0 \end{bmatrix} \qquad \text{(Eq. B.75)}$$

Elimination of transverse shear:

The second and third rows of (Eq. B.75) can be combined and reduced to a single differential equation of second order given by

$$0.25 \cdot \ddot{m}_x + n_\phi + \mu = 0 \qquad \text{(Eq. B.76)}$$

Plastic/yield condition:

$$F(n_x, n_\phi, m_x, m_\phi) = 0 \qquad \text{(Eq. B.77)}$$

Kinematic + flow rule:

Using the zero circumferential curvature of an axisymmetric cylindrical shell, the following relationship will be obtained:

$$\kappa_{\phi,\,plastic} = \lambda_{plastic} \cdot \frac{\partial F}{\partial M_\phi} = 0 \quad \Rightarrow \frac{\partial F}{\partial m_\phi} = 0 \qquad \text{(Eq. B.78)}$$

The plastic multiplier, $\lambda_{plastic}$, can be eliminated using the $\varepsilon_{\phi,plastic}$ and $\kappa_{x,plastic}$ equations given by the flow rule, i.e. using the ratio of the two plastic strain terms. The $\varepsilon_{\phi,plastic}$ and $\kappa_{x,plastic}$ can then be eliminated by substituting them using the respective kinematic relationships. Combining the kinematic and flow rule relationships with further simplification will then give:

$$-\frac{\partial F}{\partial n_{\phi}} \cdot \dot{\beta}_{x,\,plastic}{}^{*} - 4\frac{\partial F}{\partial m_{x}} \cdot \frac{W_{plastic}}{R} = 0 \qquad \text{(Eq. B.79)}$$

$$\beta_{x,\,plastic}{}^{*} = -\dot{W}_{plastic} \qquad \text{(Eq. B.80)}$$

(Eq. B.79) and (Eq. B.80) can also be combined and reduced to a single differential equation of second order given by

$$\frac{\partial F}{\partial n_{\phi}} \cdot \ddot{W}_{plastic} - 4\frac{\partial F}{\partial m_{x}} \cdot \frac{W_{plastic}}{R} = 0 \qquad \text{(Eq. B.81)}$$

B.3.8 Condensed rigid plastic equations of cylindrical shells under radial ring load

The equations which completely describe rigid plasticity of radially ring loaded cylindrical shells with or without axial load and internal pressure reduce to:

$$\dot{n}_x = 0 \qquad \text{(Eq. B.82)}$$

$$0.25 \cdot \ddot{m}_x + n_\phi + \mu = 0 \qquad \text{(Eq. B.83)}$$

$$F(n_\phi, m_x, m_\phi) = 0 \qquad \text{(Eq. B.84)}$$

$$\frac{\partial F}{\partial m_\phi} = 0 \qquad \text{(Eq. B.85)}$$

$$\frac{\partial F}{\partial n_\phi} \cdot \ddot{W}_{plastic} - 4\frac{\partial F}{\partial m_x} \cdot \frac{W_{plastic}}{R} = 0 \qquad \text{(Eq. B.86)}$$

relationship	unknown terms	# unknowns	# equations
equilibrium (Eq. B.82) & (Eq. B.83)	$\mathbf{n_x}$ $\mathbf{n_\phi}$ $\mathbf{m_x}$	**3**	**2**
yield function (Eq. B.84)	$\mathbf{m_\phi}$	**1**	**1**
kinematic + flow rule (Eq. B.85) & (Eq. B.86)	**w**	**1**	**2**
Total		**5**	**5**

Table B.5 Number of unknowns and unknown terms

Boundary conditions in terms of the non-dimensional section force & deformation variables

at a point in the shell interior ($x = x_0$):

$$\dot{m}_x = 0 \text{ and } m_x = maximum \qquad \text{(Eq. B.87)}$$

at the point of ring load application ($x = 0$):

$$W_{plastic} = maximum \text{ and } \dot{W}_{plastic} = 0 \qquad \text{(Eq. B.88)}$$

$$Q_x^* = \frac{P}{2} \cdot \frac{1}{f_y t}\sqrt{\frac{R}{t}} \qquad \text{(Eq. B.89)}$$

B.3.9 Derivatives of the yield function

The general expression for the derivative of the yield function $F(q_N, q_M, q_{NM})$ with respect to the normalized section force parameters n_ϕ, m_x, m_ϕ is given as follows:

$$\frac{\partial F}{\partial n_\phi} = \frac{\partial F}{\partial q_N}\cdot\frac{\partial q_N}{\partial n_\phi} + \frac{\partial F}{\partial q_M}\cdot\frac{\partial q_M}{\partial n_\phi} + \frac{\partial F}{\partial q_{NM}}\cdot\frac{\partial q_{NM}}{\partial n_\phi} \quad \text{(Eq. B.90)}$$

$$\frac{\partial F}{\partial m_x} = \frac{\partial F}{\partial q_N}\cdot\frac{\partial q_N}{\partial m_x} + \frac{\partial F}{\partial q_M}\cdot\frac{\partial q_M}{\partial m_x} + \frac{\partial F}{\partial q_{NM}}\cdot\frac{\partial q_{NM}}{\partial m_x} \quad \text{(Eq. B.91)}$$

$$\frac{\partial F}{\partial m_\phi} = \frac{\partial F}{\partial q_N}\cdot\frac{\partial q_N}{\partial m_\phi} + \frac{\partial F}{\partial q_M}\cdot\frac{\partial q_M}{\partial m_\phi} + \frac{\partial F}{\partial q_{NM}}\cdot\frac{\partial q_{NM}}{\partial m_\phi} \quad \text{(Eq. B.92)}$$

in which

$$\frac{\partial}{\partial n_\phi}\begin{bmatrix} q_N \\ q_M \\ q_{NM} \end{bmatrix} = \begin{bmatrix} 2n_\phi - n_x \\ 0 \\ (2m_\phi - m_x)/2 \end{bmatrix} \quad \text{(Eq. B.93)}$$

$$\frac{\partial}{\partial m_x}\begin{bmatrix} q_N \\ q_M \\ q_{NM} \end{bmatrix} = \begin{bmatrix} 0 \\ 2m_x - m_\phi \\ (2n_x - n_\phi)/2 \end{bmatrix} \quad \text{(Eq. B.94)}$$

$$\frac{\partial}{\partial m_\phi}\begin{bmatrix} q_N \\ q_M \\ q_{NM} \end{bmatrix} = \begin{bmatrix} 0 \\ 2m_\phi - m_x \\ (2n_\phi - n_x)/2 \end{bmatrix} \quad \text{(Eq. B.95)}$$

and the derivatives of the yield function with respect to q_N, q_M, q_{NM}, for example, for Ivanov-II yield function will be given by

$$\begin{bmatrix} \frac{\partial}{\partial q_N} \\ \frac{\partial}{\partial q_M} \\ \frac{\partial}{\partial q_{NM}} \end{bmatrix} F = \begin{bmatrix} 1 - \dfrac{q_M/4}{q_N + 0.48q_M} + \dfrac{(q_N q_M - {q_{NM}}^2)}{4(q_N + 0.48q_M)^2} \\ \dfrac{1}{2} + \dfrac{q_M/2}{\sqrt{{q_M}^2 + 4{q_{NM}}^2}} - \dfrac{({q_N}^2 + 0.48{q_{NM}}^2)}{4(q_N + 0.48q_M)^2} \\ q_{NM}\left(\dfrac{2}{\sqrt{{q_M}^2 + 4{q_{NM}}^2}} + \dfrac{0.5}{q_N + 0.48q_M}\right) \end{bmatrix} \quad \text{(Eq. B.96)}$$

B.3.10 Determination of plastic section forces, plastic deformation, slope, curvature and plastic loading parameter $\lambda_{plastic}$

The axial section force term n_x is constant and can be directly computed using the applied axial loading, i.e. pure axial membrane section force. For the computation of other section force terms, the following solution procedure is followed:

Using (Eq. B.83) to (Eq. B.85) and starting conditions at a point in the shell interior (i.e. at a meridional distance ξ_0 from the ring-load location) of zero transverse shear (or $\dot{m}_x = 0$) and maximum m_x without violating the equilibrium, yield and flow rule conditions. The later starting condition is equivalent to producing a maximum transverse shear section force at the ring-load location which can be reached without violating the equilibrium, yield and flow rule conditions (SHOOTING!).

While shooting for the maximum possible transverse shear at the ring-load location, the corresponding plastic section force terms ($n_\phi, \dot{m}_x, m_x, m_\phi$) at the ring-load location can simultaneously be computed. With these plastic section force terms and fulfillment of deformation conditions at $\xi = 0$ (i.e. $W_{plastic}$ = maximum, which is chosen to be 1.0 in the current computation and $\dot{W}_{plastic} = 0$) as initial conditions, the set of differential equations (Eq. B.83) to (Eq. B.86) can then be mathematically solved to give the complete rigid-plastic solution.

Directly computed section force and deformation variables:

$$n_\phi, m_x, m_\phi, W_{plastic} \qquad \text{(Eq. B.97)}$$

Back calculated section force and deformation variables:

$$Q_x^* = \frac{1}{4} \cdot \dot{m}_x \qquad \text{(Eq. B.98)}$$

$$\begin{aligned} \beta_{x,\,plastic}^* &= -\dot{W}_{plastic} \\ \kappa_{x,\,plastic}^* &= -\ddot{W}_{plastic} \end{aligned} \qquad \text{(Eq. B.99)}$$

$$\lambda_{plastic}^* = \lambda_{plastic} \cdot \frac{R \cdot t}{M_{pl}} \qquad \text{(Eq. B.100)}$$

B.3.11 Complete section force distributions along the meridian

Rigid-plastic analyses of long cylindrical shells with different loading situtaions have been done. It should be noted here that the plastic section forces will be distributed along a limited length along the meridian (plastic zone) symmetric about the the ring-loaded circumferential circle. All meridional points out of this plastic zone of the long cylinder will behave elastically and hence, the section force distributions along these points will be governed by pure elastic relationships. Hence, there should be a transition point along the meridian which should fulfill both rigid-plastic and pure elastic properties. For this reason, the elastic behavior is discussed below which will later be used to compute the complete section force distributions along the meridian of the shell.

Elastic section force and deformation relationship

The elastic section forces and deformations at the boundary point of the elastic region of a long cylindrical shell are related, Linder (2001), using:

$$\begin{bmatrix} Q_x \\ M_x \end{bmatrix} = -\frac{EA_{eff}}{2R^2} \cdot \begin{bmatrix} 2 & -h \\ -h & h^2 \end{bmatrix} \cdot \begin{bmatrix} W_{edge\text{-}effect} \\ \beta_x \end{bmatrix} \quad \text{(Eq. B.101)}$$

where

$$W_{edge\text{-}effect} = W - W_{part} \quad \text{(Eq. B.102)}$$

$$h = L_{eff} = \frac{1}{\sqrt[4]{3(1-\nu^2)}} \sqrt{R \cdot t} \quad \text{(Eq. B.103)}$$

W is the total radial deformation and W_{part} represents the particular (or membrane) solution. For an axially loaded and internally uniformly pressurized cylinder, the membrane solution using the sign convention shown in Figure B.12 is given by:

$$W_{part} = \nu \cdot \frac{N_x \cdot R}{E \cdot t} + \frac{p \cdot R^2}{E \cdot t} \quad \text{(Eq. B.104)}$$

(Eq. B.101) can be reduced to a single equation by substituting β_x from one row to the other to give the following relationship:

$$Q_x + \frac{M_x}{h} = -\frac{EA_{eff}}{2R^2} \cdot (W - W_{part}) \quad \text{(Eq. B.105)}$$

On the other hand, considerations of kinematic and elastic constitutive relationships in the circumferential direction, the following equation can be obtained:

$$N_\phi = -\frac{Et}{R} \cdot W + \nu \cdot N_x \quad \text{(Eq. B.106)}$$

Substituting W from (Eq. B.106) into (Eq. B.105) will give:

$$Q_x + \frac{M_x}{h} - \frac{h}{2} \cdot \left(\frac{N_\phi}{R} + p \right) = 0 \qquad \text{(Eq. B.107)}$$

When (Eq. B.107) is combined with the equilibrium equations (Eq. B.53) and (Eq. B.55), it will give the following reduced relationship for elastic section moment, m_x:

$$\ddot{m}_x + 2\frac{\sqrt{R \cdot t}}{h} \cdot \dot{m}_x + 2\frac{R \cdot t}{h^2} \cdot m_x = 0 \qquad \text{(Eq. B.108)}$$

For example, for $\nu = 0.3$ (Eq. B.108) will be:

$$\ddot{m}_x + 2.5705\dot{m}_x + 3.3042 m_x = 0 \qquad \text{(Eq. B.109)}$$

(Eq. B.108) represents the complete relationship for an elastic cylindrical shell from which the other section forces will be computed as will be discussed later.

Meridional plastic-elastic transition point

The rigid plastic section forces computed previously should be checked at every meridional point (starting from the radial-ring-load location) for the fulfillment of the elastic section force relationship given in (Eq. B.107). at the transtion point to the elastic region of the shell. This in other words means, the rigid plastic meridional section moment m_x and its derivatives should be checked for the fulfillment of the relationship given in (Eq. B.108) at every meridional point. There will be a single meridional point (the transition point from plastic to elastic zone of the cylinder) where the plastic section forces will exactly fulfill the elastic relationships. That is, when the plastic section forces are used in the elastic relationships (Eq. B.107) and (Eq. B.108) will respectively lead to:

$$Q_{x,\,plastic} + \frac{M_{x,\,plastic}}{h} - \frac{h}{2} \cdot \left(\frac{N_{\phi,\,plastic}}{R} + p \right) = 0 \qquad \text{(Eq. B.110)}$$

and

$$\ddot{m}_{x,\,plastic} + 2\frac{\sqrt{R \cdot t}}{h} \cdot \dot{m}_{x,\,plastic} + 2\frac{R \cdot t}{h^2} \cdot m_{x,\,plastic} = 0 \qquad \text{(Eq. B.111)}$$

Upon fulfillment of (Eq. B.110) or (Eq. B.111), the meridional coordinate of the transition point and all the corresponding section forces and moments can be computed. These section forces and moments represent the coincident of the plastic and elastic section forces and section moments at the trasnsition point. From the transition point onwards, the shell behaves elasticically.

Elastic section force and section moment distributions

With those computed values for the location of the transition point, section forces and section moments at the transition point, two different approaches can be utilized for the computation of the distribution of elastic section forces and section moments as will be discussed below.

Alternative-1:

The computed values of the section forces and section moments at the transition point can be used as boundary values to numerically solve (using MATHEMATICA) the ordinary differential equation of the elastic cylinder given in (Eq. B.108) to directly compute along-the-meridion distribution of the meridional section moment m_x and its derivatives from which the other section forces can be back calculated using the following expressions:

$$\begin{aligned} n_{\phi,el} &= -(0.25\ddot{m}_{x,el} + \mu) \\ Q_{x,el}^{*} &= 0.25\dot{m}_{x,el} \\ m_{\phi,el} &= \nu \cdot m_{x,el} \end{aligned} \qquad \text{(Eq. B.112)}$$

Alternative-2:

The same ordinary differential equation (Eq. B.108) can also be solved analytically as will be shown in the following discussion. For simplicity, a modified non-dimensional length parameter is defined as follows:

$$\xi^{*} = \frac{x}{L_{eff}} \qquad \text{(Eq. B.113)}$$

with the following derivative relationships

$$\Rightarrow \frac{d(\ )}{d\xi^{*}} = (\dot{\ }) = L_{eff} \cdot \frac{d(\ )}{dx} = L_{eff} \cdot (\ )' \qquad \text{(Eq. B.114)}$$

$$\Rightarrow (\ddot{\ }) = L_{eff}^{2}(\ )'' \qquad \text{(Eq. B.115)}$$

With this modified non-dimensional length parameter, the elastic relationship (Eq. B.108) will be given as:

$$\ddot{M}_x + 2\dot{M}_x + 2M_x = 0 \qquad \text{(Eq. B.116)}$$

The general solution of such second order ordinary differential equations is given by

$$M_x = c_M \cdot e^{\lambda \cdot \xi^{*}} \qquad \text{(Eq. B.117)}$$

The characteristic equation of the differential equation will be:

$$(\lambda^2 + 2\lambda + 2 = 0) \qquad \Rightarrow \lambda = -1 \pm i \qquad \text{(Eq. B.118)}$$

Thus, with the substituion of λ into (Eq. B.117), the meridional elastic section moment will be given by:

$$M_x = c_{1M} \cdot f_1 + c_{2M} \cdot f_2 \qquad \text{(Eq. B.119)}$$

where the solution functions f_1 and f_2 are given by

$$\begin{bmatrix} f_1 \\ f_2 \end{bmatrix} = e^{-\xi^*} \cdot \begin{bmatrix} \sin\xi^* \\ \cos\xi^* \end{bmatrix} \qquad \text{(Eq. B.120)}$$

The derivatives of the solution functions will then be

$$\begin{bmatrix} \dot{f}_1 \\ \dot{f}_2 \end{bmatrix} = \begin{bmatrix} -1 & 1 \\ -1 & -1 \end{bmatrix} \cdot \begin{bmatrix} f_1 \\ f_2 \end{bmatrix} \qquad \text{(Eq. B.121)}$$

With the plastic-to-elastic transition point considered as $\xi^* = 0$ (the starting point of the elastic zone), the values of the solution functions and their derivatives at this location is given by

$$\begin{bmatrix} f_1 \\ f_2 \\ \dot{f}_1 \\ \dot{f}_2 \end{bmatrix}_{\xi^* = 0} = \begin{bmatrix} 0 \\ 1 \\ 1 \\ -1 \end{bmatrix} \qquad \text{(Eq. B.122)}$$

The constants c_{1M} and c_{2M} will be computed from the shear force and meridional moment conditions at the transition point. These section force and section moment values at the transition point are equal to those obtained from the rigid-plastic analysis and hence they are known, i.e.

$$\begin{bmatrix} M_{x,\,elastic} \\ Q_{x,\,elastic} \end{bmatrix}_{\xi^* = 0} = \begin{bmatrix} M_{x,\,elastic} \\ M'_{x,\,elastic} \end{bmatrix}_{\xi^* = 0} \qquad \text{(Eq. B.123)}$$

$$\begin{bmatrix} M_{x,\,elastic} \\ Q_{x,\,elastic} \end{bmatrix}_{\xi^* = 0} = \left[\begin{array}{c:c} c_{1M} & c_{2M} \\ \hdashline -\frac{1}{L_{eff}} \cdot (c_{1M} + c_{2M}) & \frac{1}{L_{eff}} \cdot (c_{1M} - c_{2M}) \end{array}\right] \cdot \begin{bmatrix} f_1 \\ f_2 \end{bmatrix}_{\xi^* = 0} = \begin{bmatrix} M_{x,\,plastic} \\ Q_{x,\,plastic} \end{bmatrix}_{\xi^* = 0}$$

(Eq. B.124)

Using the values of the solution functions f_1 and f_2 at the boundary point $\xi^* = 0$ given by (Eq. B.122), the constants c_{1M} and c_{2M} will give:

$$\begin{bmatrix} c_{1M} \\ c_{2M} \end{bmatrix} = \left[\begin{array}{c:c} 1 & L_{eff} \\ \hdashline 1 & 0 \end{array}\right] \cdot \begin{bmatrix} M_{x,\,plastic} \\ Q_{x,\,plastic} \end{bmatrix}_{\xi^* = 0} \qquad \text{(Eq. B.125)}$$

The meridional distribution of the elastic section forces M_x and Q_x can then be computed using (Eq. B.119) and its derivative, i.e.

$$\begin{bmatrix} M_{x,\,elastic} \\ L_{eff} \cdot Q_{x,\,elastic} \end{bmatrix} = \left[\begin{array}{c:c} c_{1M} & c_{2M} \\ \hdashline -(c_{1M} + c_{2M}) & (c_{1M} - c_{2M}) \end{array}\right] \cdot \begin{bmatrix} f_1 \\ f_2 \end{bmatrix} \qquad \text{(Eq. B.126)}$$

The other section forces can then be back-calculated.

B.3.12 Illustrative examples, results and comparison

For illustration purposes, the results of a rigid plastic analysis of a cylindrical shell under pure radial ring loading, Figure B.13, will be discussed first. The separately computed rigid-plastic and elastic section force distributions including the transition point along the meridian are shown in Figure B.14 to Figure B.16 for the circumferential section force, transverse shear force and meridional section moment, respectively. Comparative plots of the analytically solved complete section force ($n_\phi, m_x, m_\phi, Q_x^*$) distributions and those computed using materially nonlinear numerical analyis (MNA) are shown in Figure B.17 to Figure B.24.

A second illustrative example has been done for a cylindrical shell under radial ring loading with axial compressive and internal pressure loads as shown in Figure B.25. For this loading situation, the comparative plots of the analytically solved complete section force ($n_\phi, m_x, m_\phi, Q_x^*$) distributions and those computed using materially nonlinear numerical analyis (MNA) are shown in Figure B.26 to Figure B.33.

In both of the above illustrative examples, Ivanov-II yield criterion has been used.

B.3.12.1 Long cylindrical shell under radial ring loading

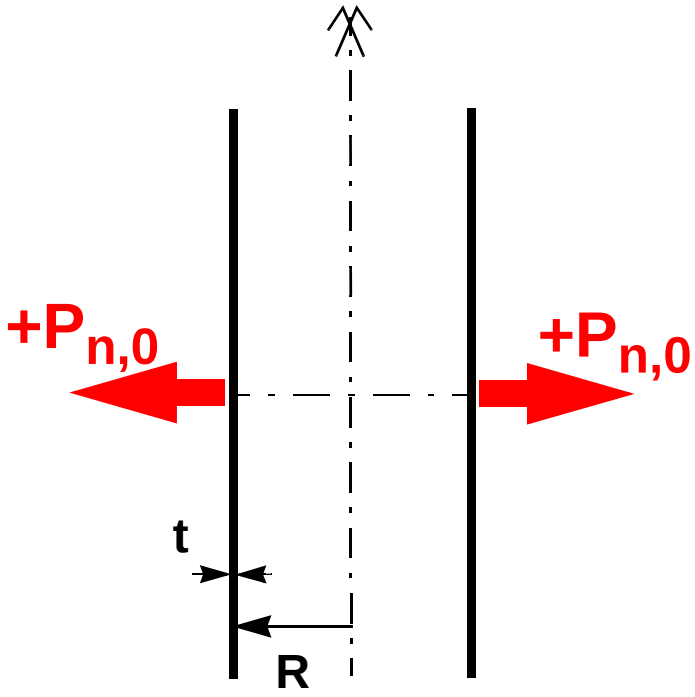

Figure B.13 Ring-loaded long cylindrical shell

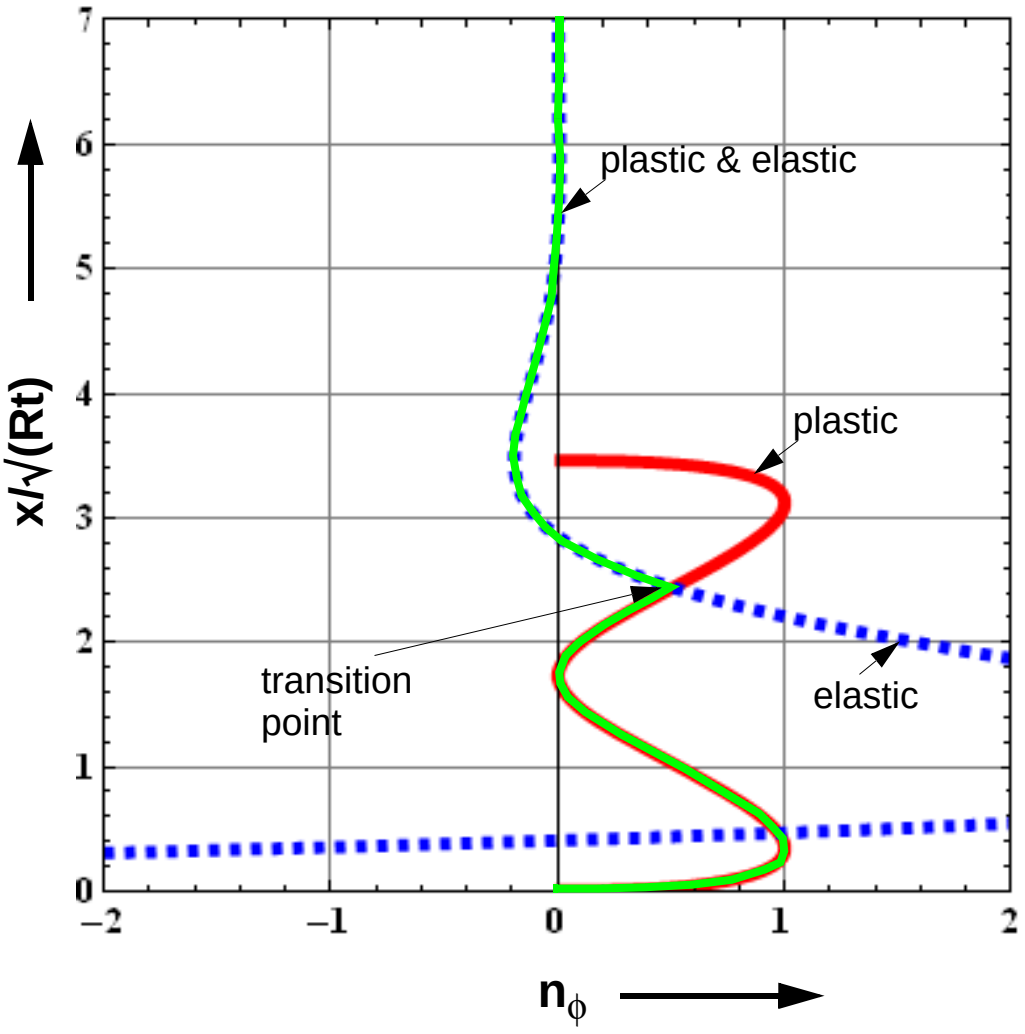

Figure B.14 Circumferential section force, n_ϕ

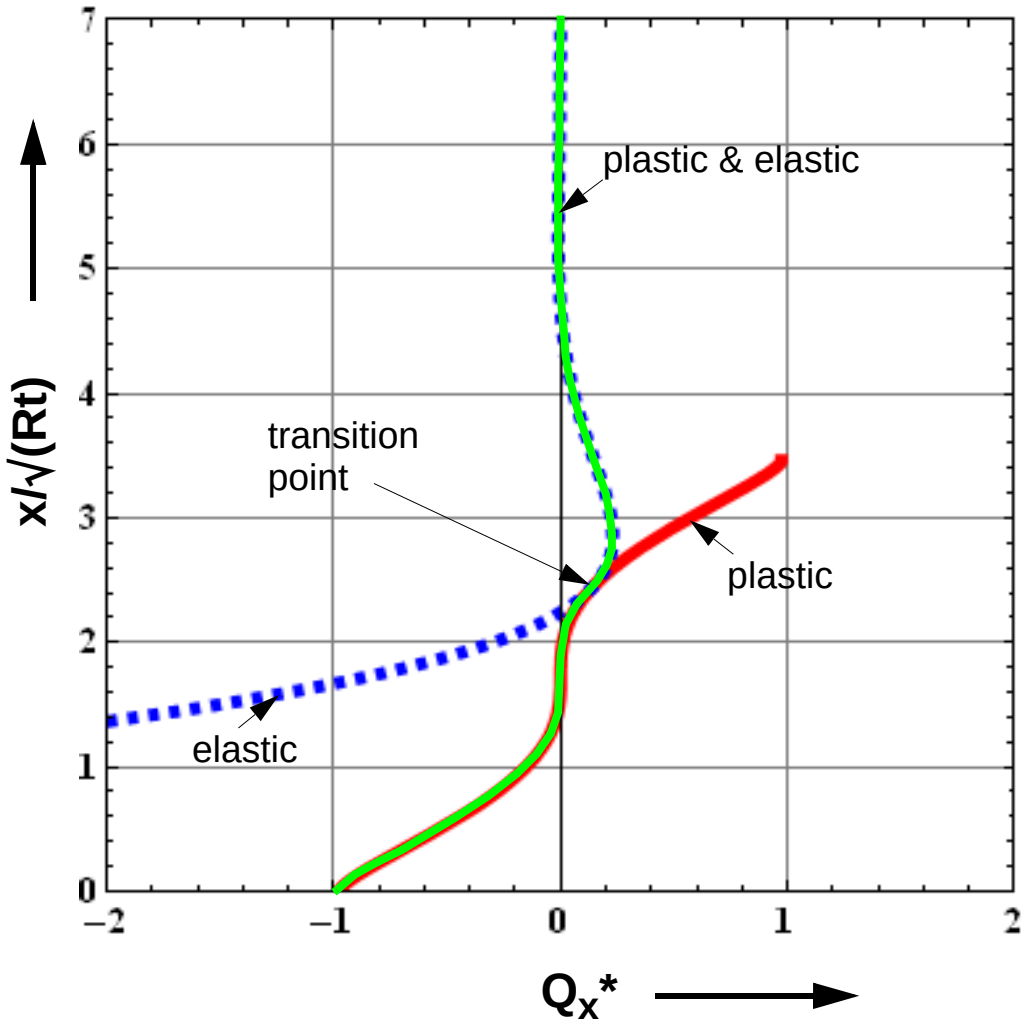

Figure B.15 Transverse shear force, Q_x^*

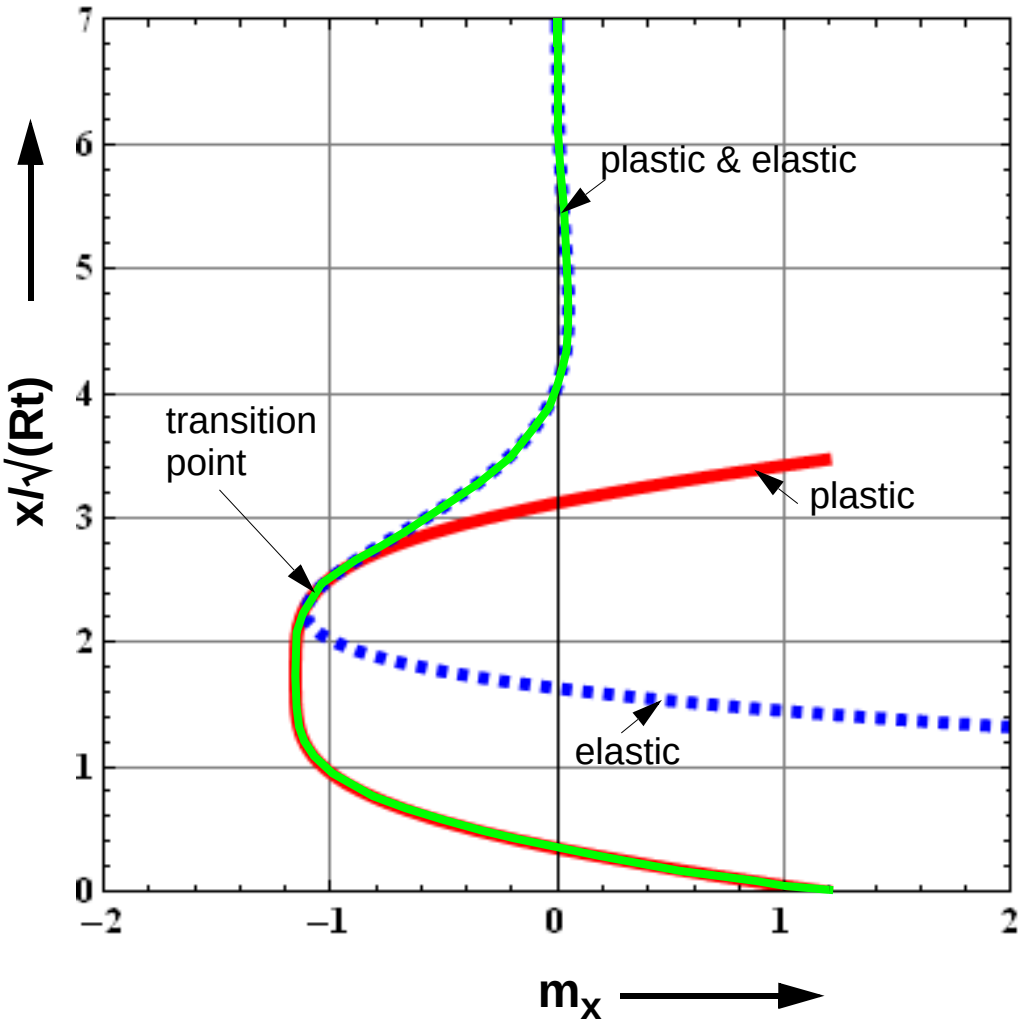

Figure B.16 Meridional section moment, m_x

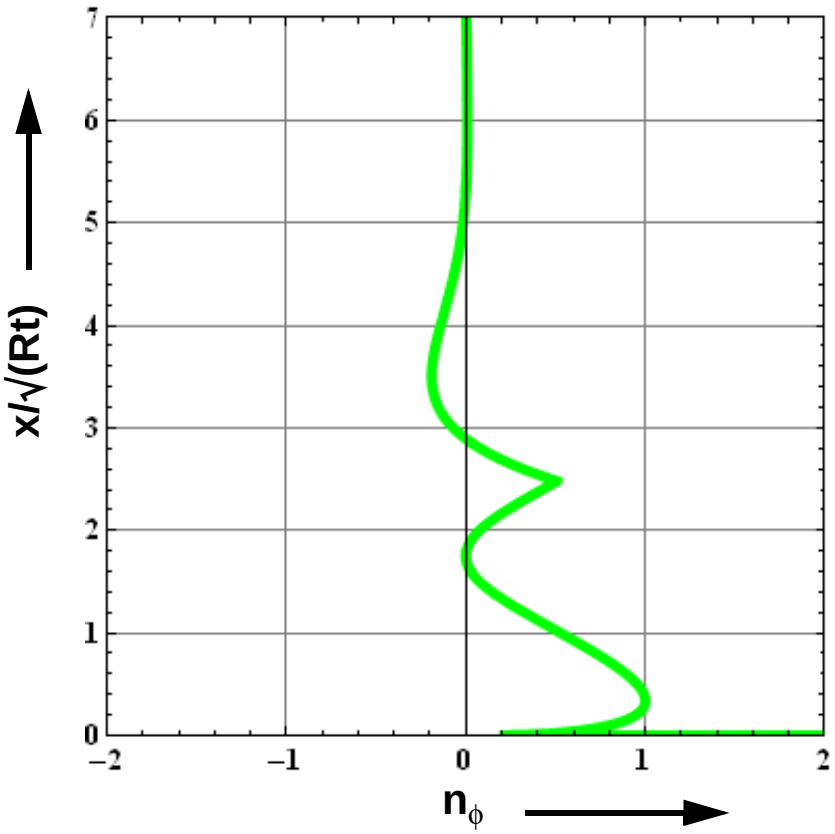

Figure B.17 Circumferential section force, n_ϕ: Analytic

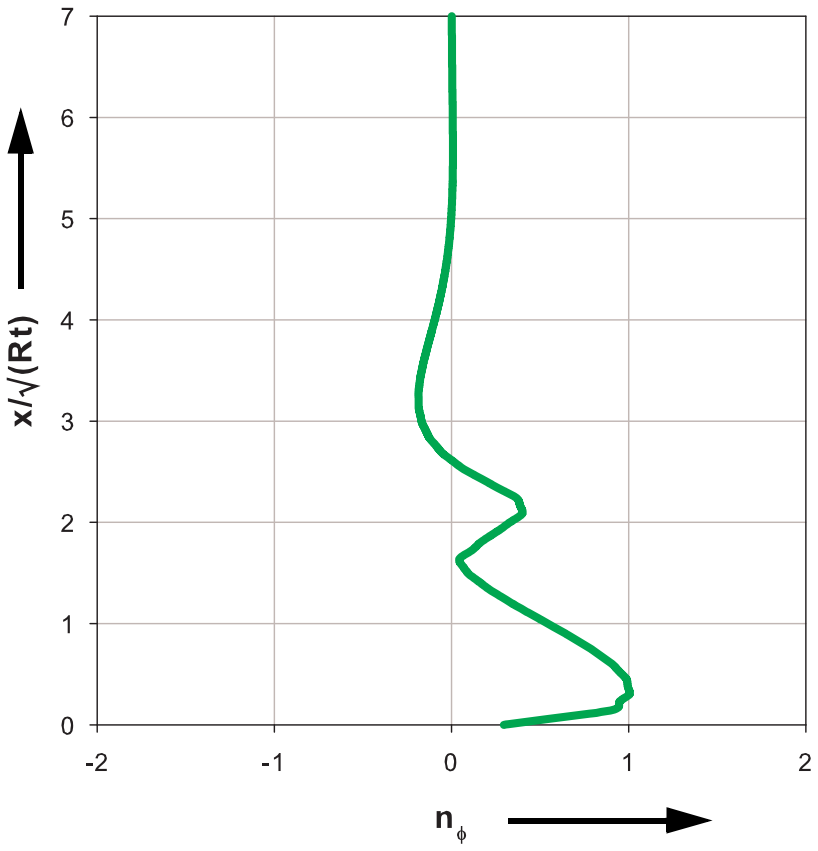

Figure B.18 Circumferential section force, n_ϕ: FEM

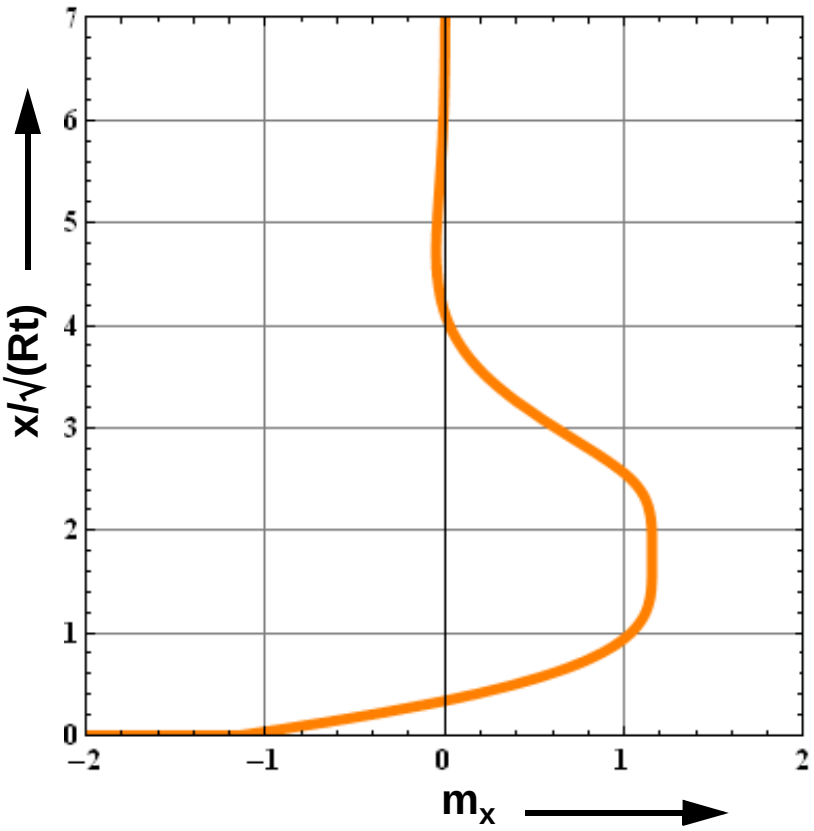

Figure B.19 Meridional section moment, m_x: Analytic

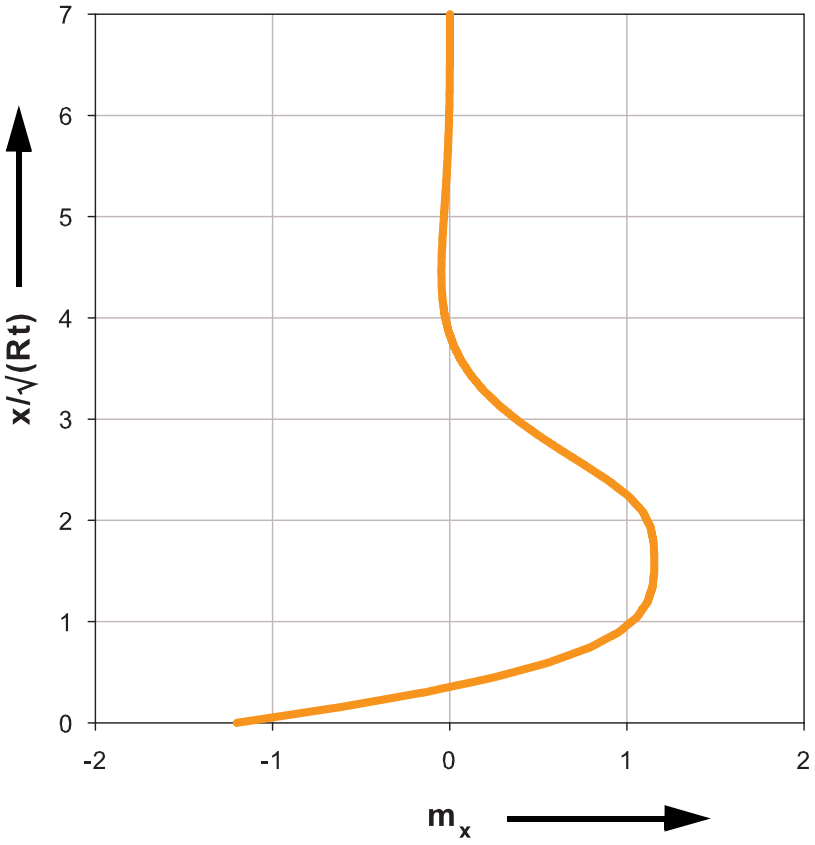

Figure B.20 Meridional section moment, m_x: FEM

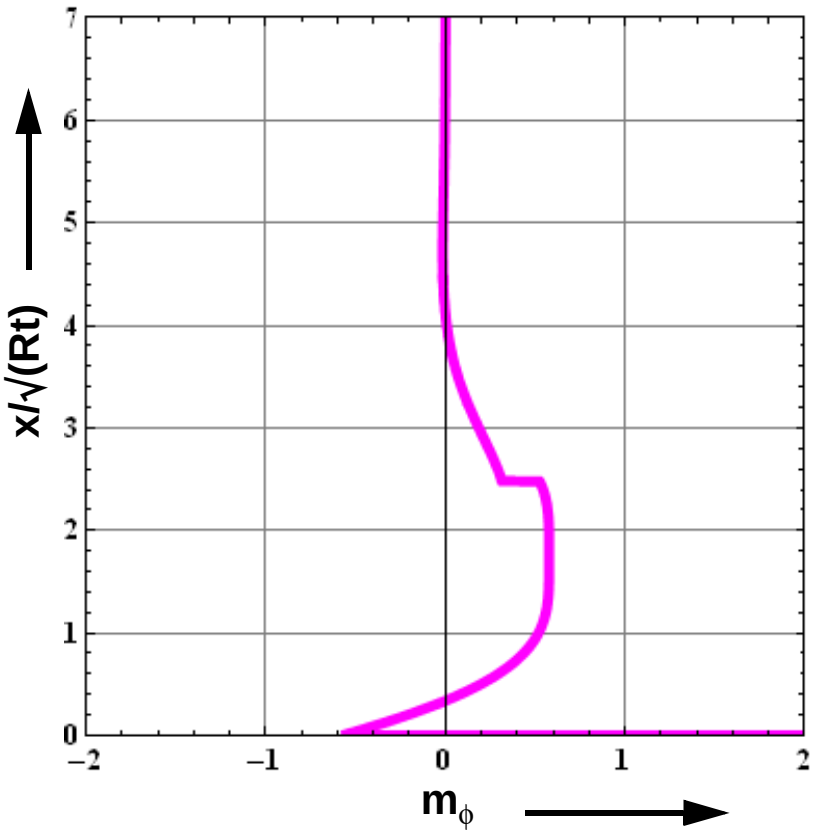

Figure B.21 Circumferential section moment, m_ϕ: Analytic

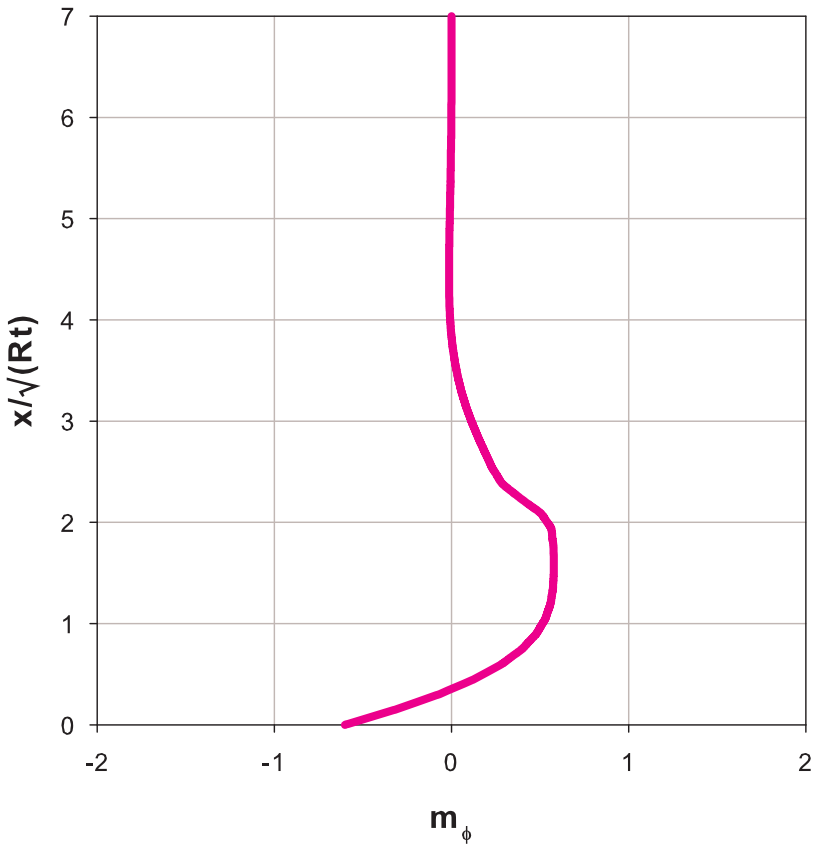

Figure B.22 Circumferential section moment, n_ϕ: FEM

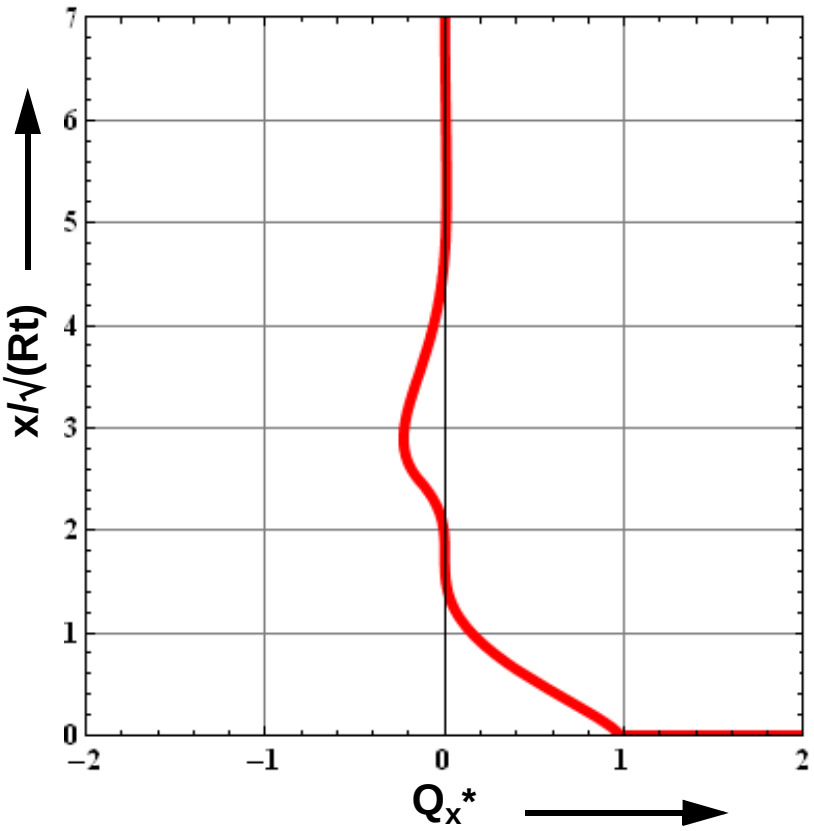

Figure B.23 Transverse shear force, Q_x*: Analytic

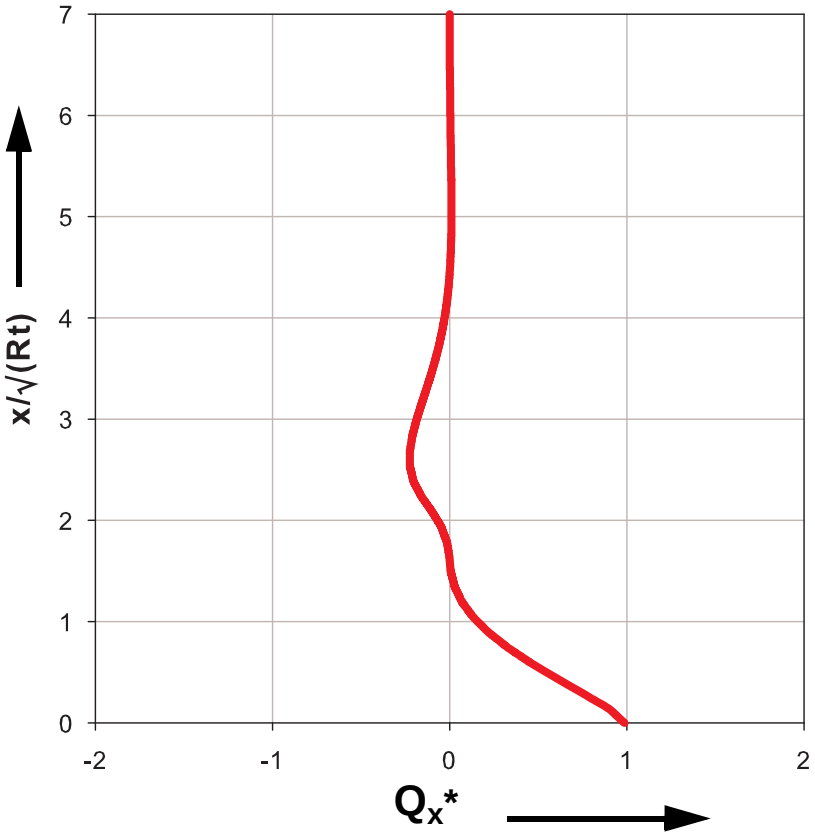

Figure B.24 Transverse shear force, Q_x*: FEM

B.3.12.2 Long cylindrical shell under radial ring loading with axial compressive and internal pressure loads

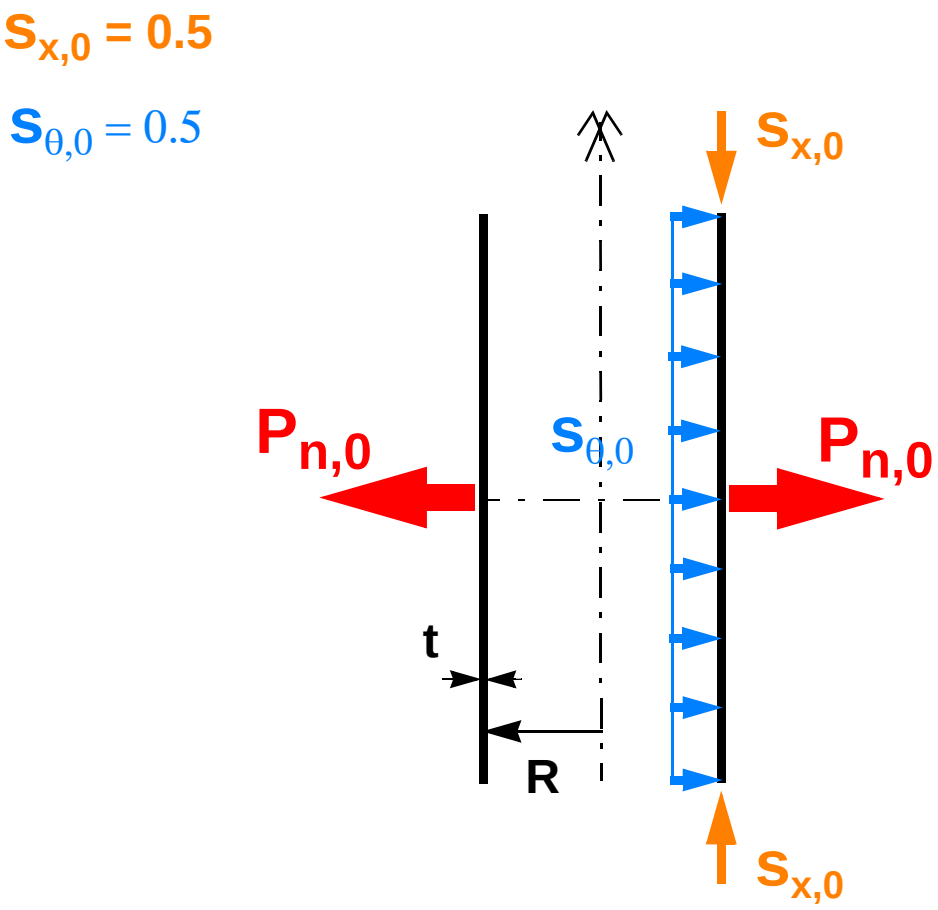

Figure B.25 Ring-loaded long cylindrical shell with axial load & internal pressure

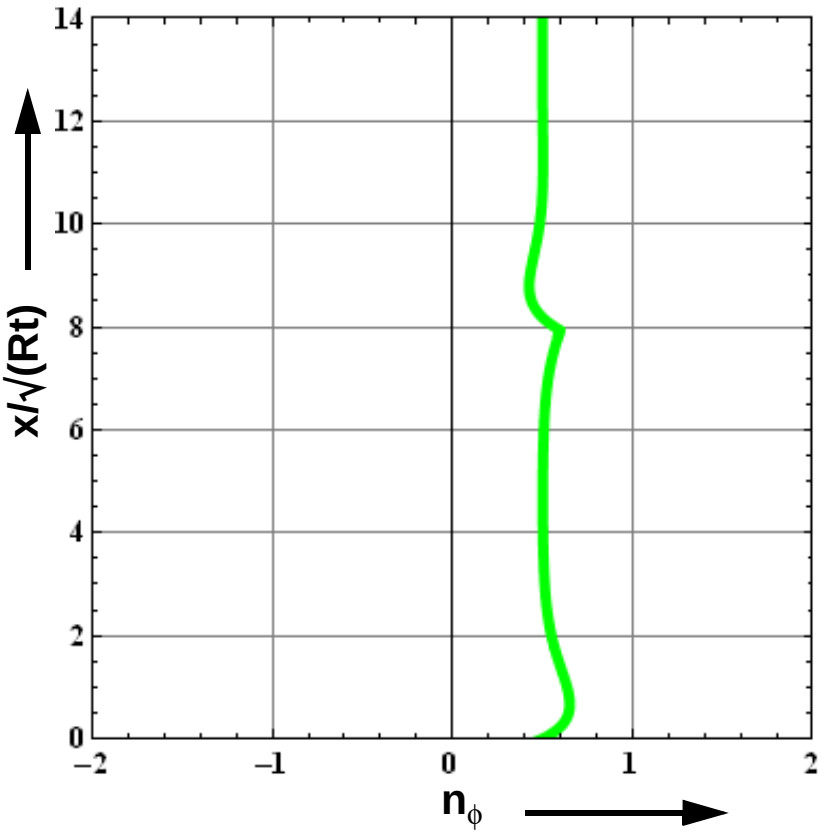

Figure B.26 Circumferential section force, n_ϕ: Analytic

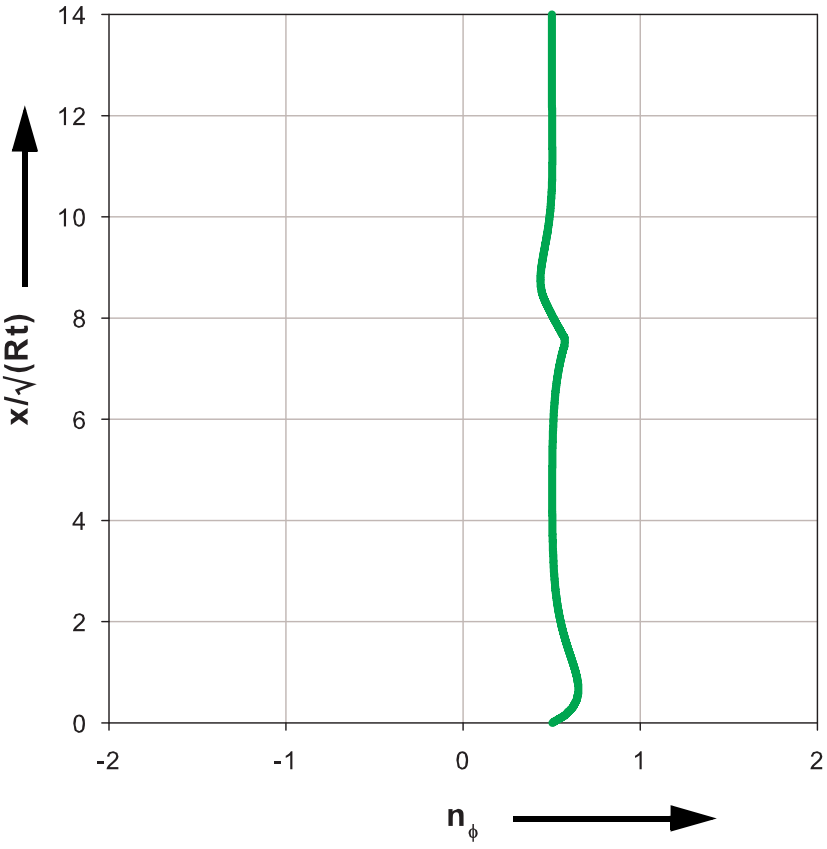

Figure B.27 Circumferential section force, n_ϕ: FEM

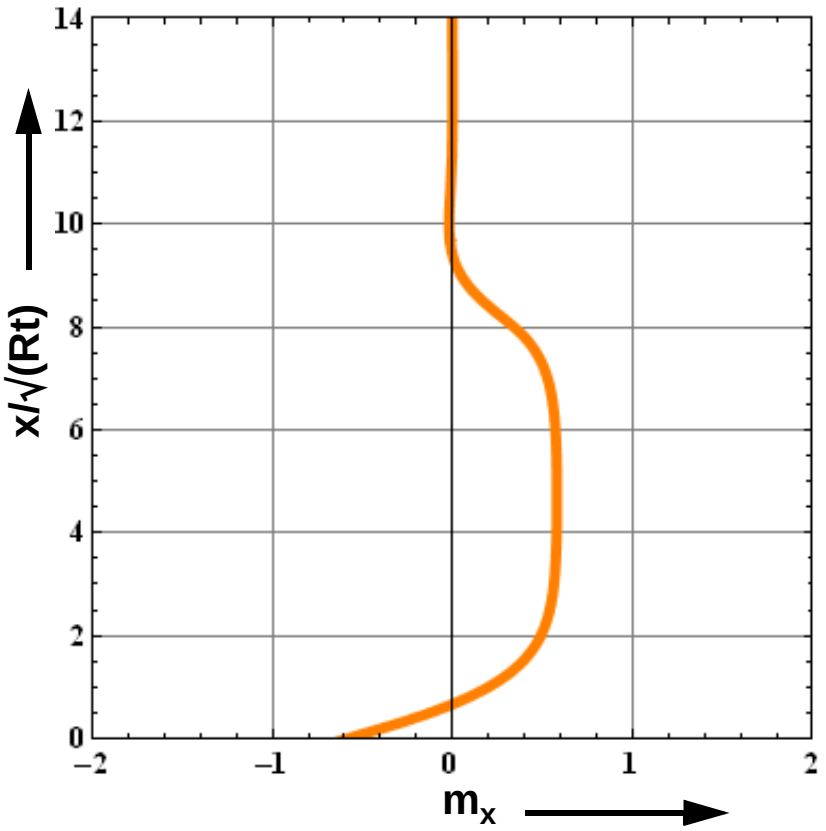

Figure B.28 Meridional section moment, m_x: Analytic

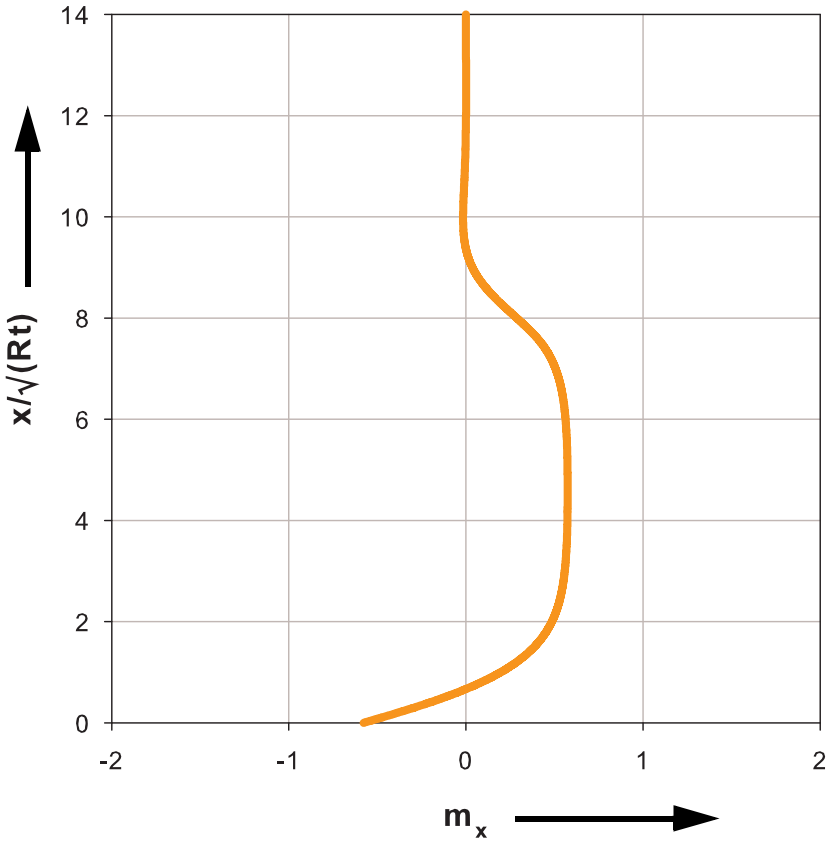

Figure B.29 Meridional section moment, m_x: FEM

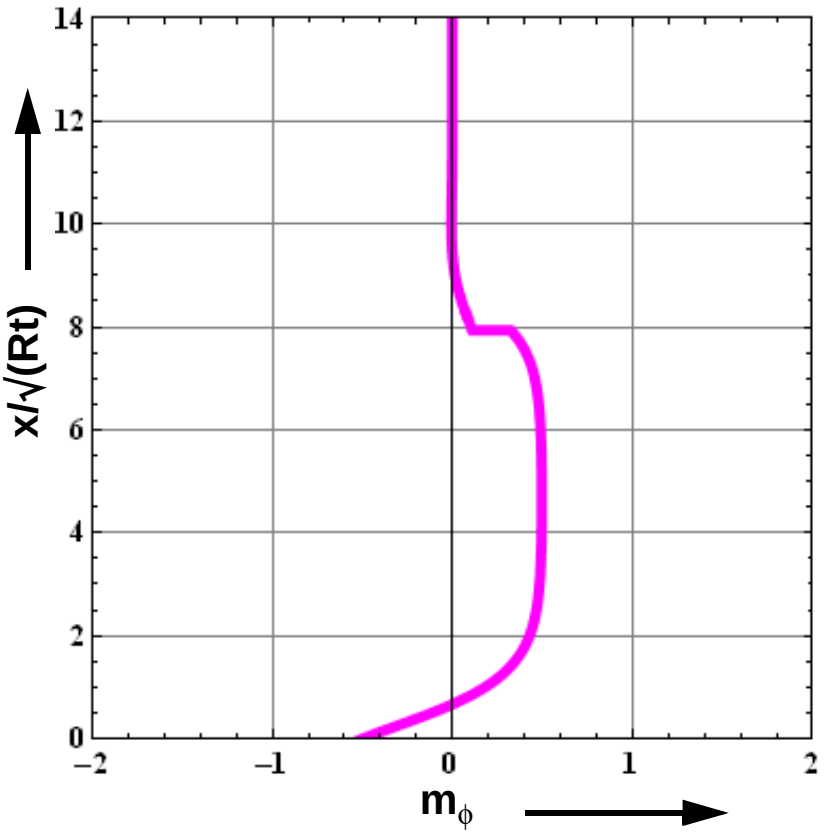

Figure B.30 Circumferential section moment, m_ϕ: Analytic

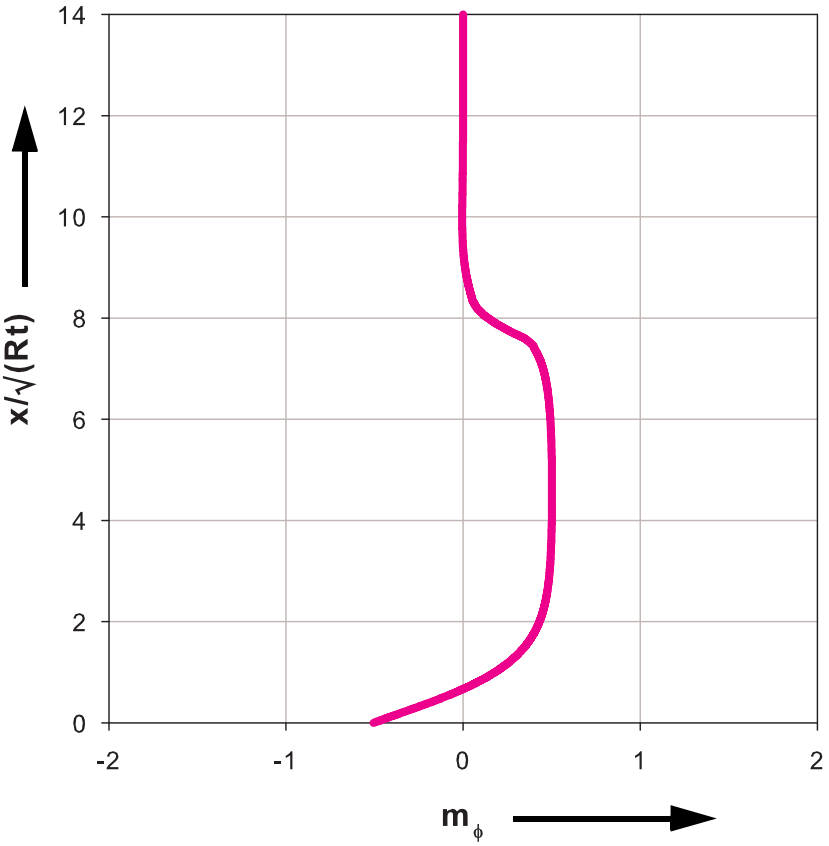

Figure B.31 Circumferential section moment, n_ϕ: FEM

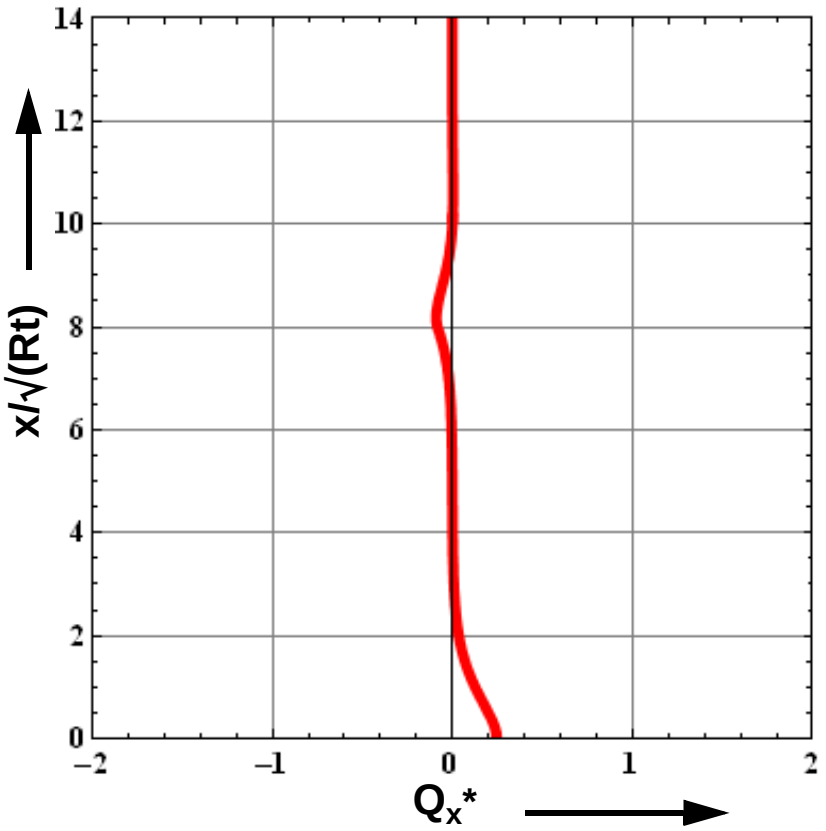

Figure B.32 Transverse shear force, Q_x*: Analytic

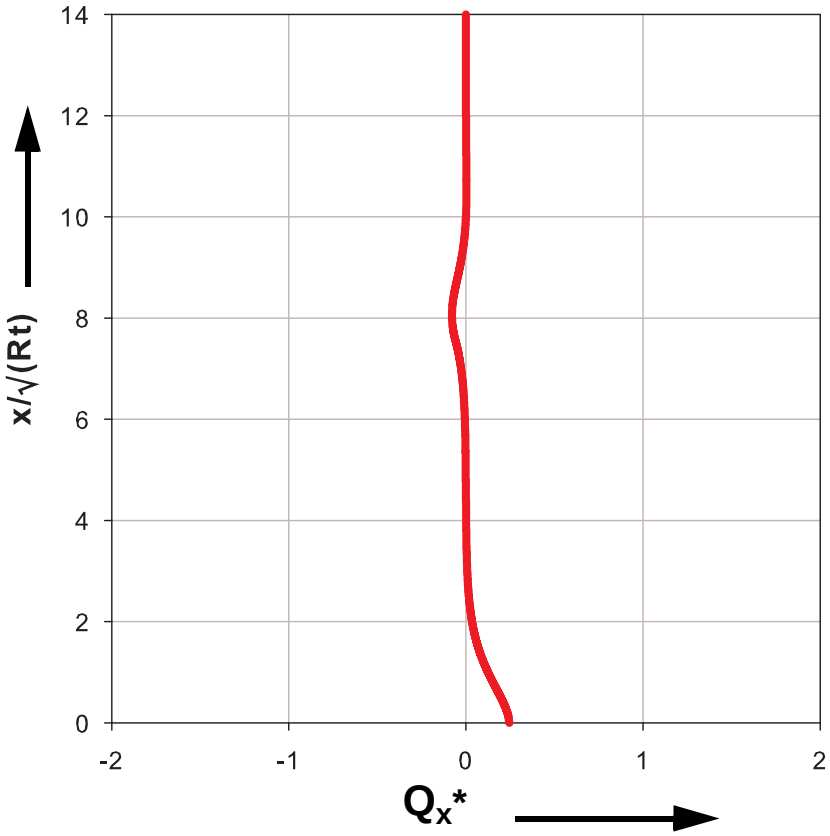

Figure B.33 Transverse shear force, Q_x*: FEM

A.4 Summary and conclusion

The chapter was concerned with the anayltical computation of rigid-perfect-plastic limit strengths and corresponding section force distributions of axisymmetric plate and shell structures. In doing so, Ilyushin's yield criterion related approximations have been used along with the equilibrium and kinematic relationships.

Circular and annular plates under uniform or ring lateral loads and fixed or pinned outer edges have been analyzed. Besides, long cylindrical shells under radial ring loading with and without axial loading & internal pressurization have been considered. The results have been compared with recommendations according to EN 1993-1-6 and with small displacement materially nonlinear numerical analysis (ABAQUS) results which turns out that the analytical rigid-plastic analysis with the help of the approximate stress resultant oriented yield criteria produces accurate results.

C

Analytical elastic buckling analysis of cylindrical shells

C.1 Introduction

The axisymmetric linear and nonlinear buckling behavior and buckling strength of axially compressed and internally pressurized cylindrical shells have been computed in Chapter-3 of this thesis. In all the numerical simulations, the cylinder was modeled using an axisymmetric shell element. i.e. a one-dimensional segment in meridional direction with two-dimensional loading, deformation and section force distributions has been used to model and simulate the complete axisymmetric behavior of the three-dimensional cylindrical shell problem. All the computations have been made numerically using the finite element package ABAQUS, Version 6.7-1 (2007).

This chapter, like Chapter-3, deals with the axisymmetric elastic buckling behavior and strength of axially compressed cylindrical shells modeled as a one-dimensional shell segment in meridonal direction with two-dimensional loading, deformation and section forces but will be solved analytically. In doing so, a beam on elastic foundation with the same axial and flexural rigidities as that of a unit circumferential length of the cylinder will be used. The circumferential membrane stiffness of the cylindrical shell will be modeled as an elastic foundation spring with a spring stiffness equal to the circumferential membrane stretching stiffness of the cylinder, usually known as foundation modulus, C.

The basic relationships (equilibrium, kinematics and constitutive equations) including second order effects will be presented first and the necessary set of ordinary differential equations which will be used in the buckling analysis will be derived. Figure C.1 shows the equivalent geometry, loading and section force components of a cylindrical shell and a beam on an elastic foundation.

Once the basic relationships including second order effects and the complete set of analytical solutions are at hand, they will be used to assess the approximate elastic-plastic buckling loads of cylindrical shells with the help of the stress resultant oriented Ilyushin-related yield criteria (See Annex-A and B). The elastic-plastic buckling strengths obtained in this way will approximately represent the geometrically and materially nonlinear strength of the perfect cylindrical shell, the results of which have already been fully discussed in Chapter 3.7.

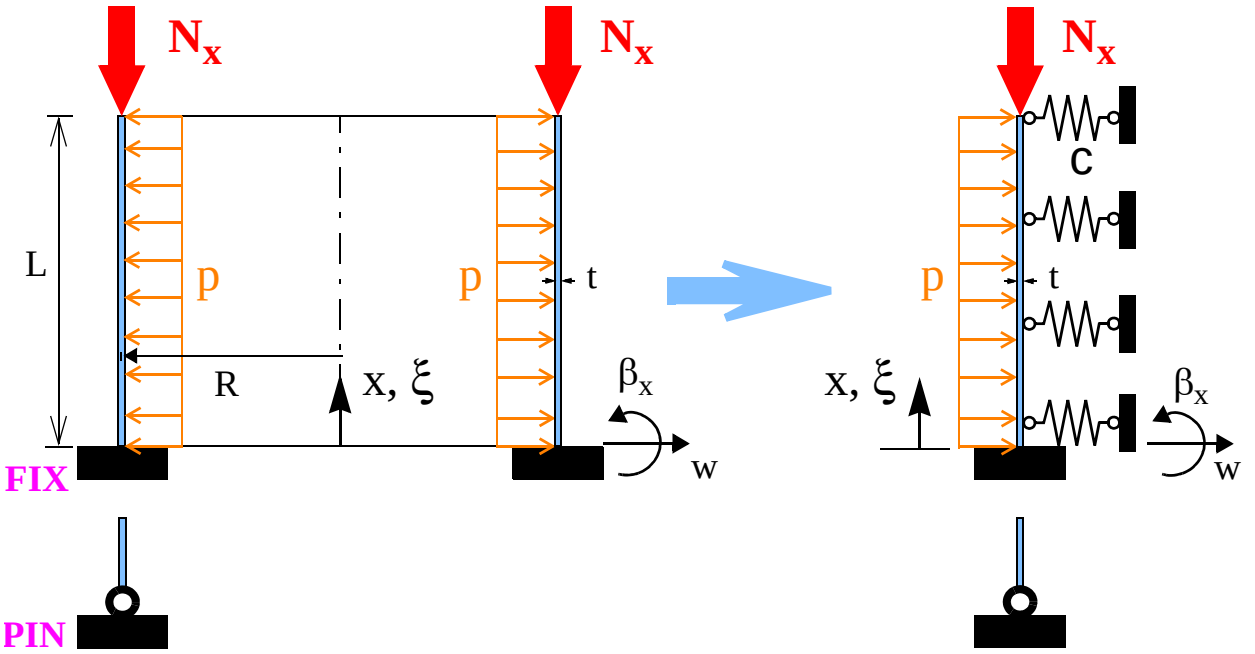

(a)

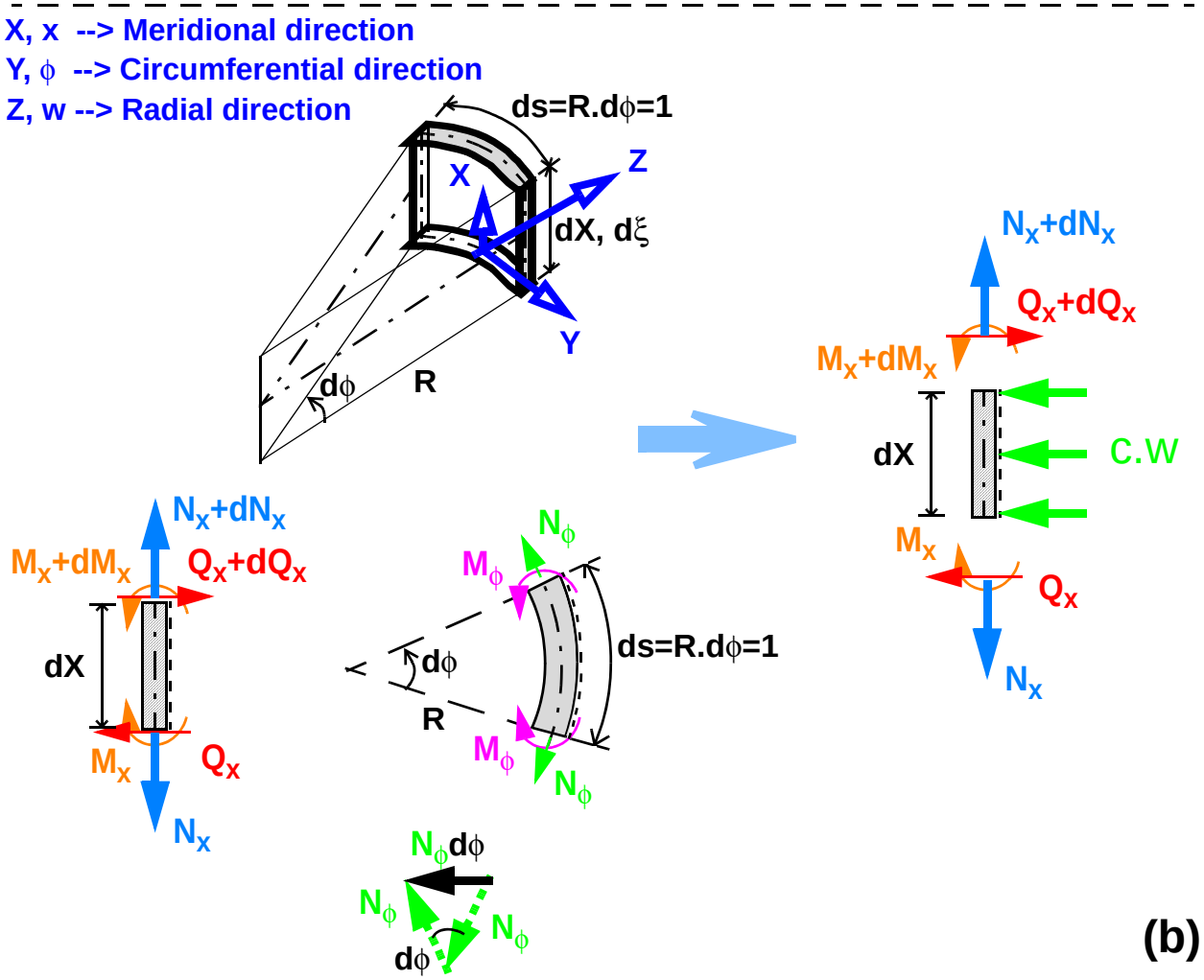

(b)

Figure C.1 Geometry, loading and section forces

C.2 Theory of second order

Generally speaking, stability criterion is related to the nonlinear characterization of a specific problem. In this chapter, the geometic nonlinear (deformation) effects will be considered by taking the second order effects into account. These second order effects will inturn be considered by taking the deformed geometry of the structure as a reference for the fulfillment of equilibrium equations, i.e. the section force variables are defined with respect to the cross-section of the deformed structure thereby the equilibrium equations will be based on the deformed configuration of the structure. In doing so, the global longitudinal and transverse section forces which correspond to the undeformed geometry will be computed from the deformed geometry. Figure C.2(a) shows geometry, loading and boundary conditions of a beam on an elastic foundation. Figure C.2(b) shows the section forces on the undeformed and deformed configurations of the beam structure. The relationships between the global-oriented and local-oriented section forces is graphically shown on the right-hand-side of Figure C.2(b). The meanings of the variables used in this figure are listed below:

L global longitudinal section force

T_x global transverse section force

N_{xo} local axial section force tangent to the neutral axis

Q_x local shear force parallel to the cross-section

w’ rotation of the neutral axis

β_x rotation of the cross-section

γ_{xz} shear strain (angular deformation)

It can easily be seen, with the help of Figure C.2(b), that the second order effect can be included in the shear equilibrium equation, i.e. an additional shear section force equal to $N_{xo}.w’$ will result due to second order effects. This effect can also be considered as an additional distributed lateral load equal to $(N_{xo}.w’)’$ which in turn is equal to $N_{xo}.w’’$ for a constant axial loading. The directions of the additional shear force or distributed lateral load will depend on the direction (tensile or compressive) of the axial loading.

In the upcoming discussions, the equilibrium equations will first be written in terms of the local section forces along with the consideration of the second order effects. Later, when discussing about edge forces in the global orientation, the global oriented section forces will be used.

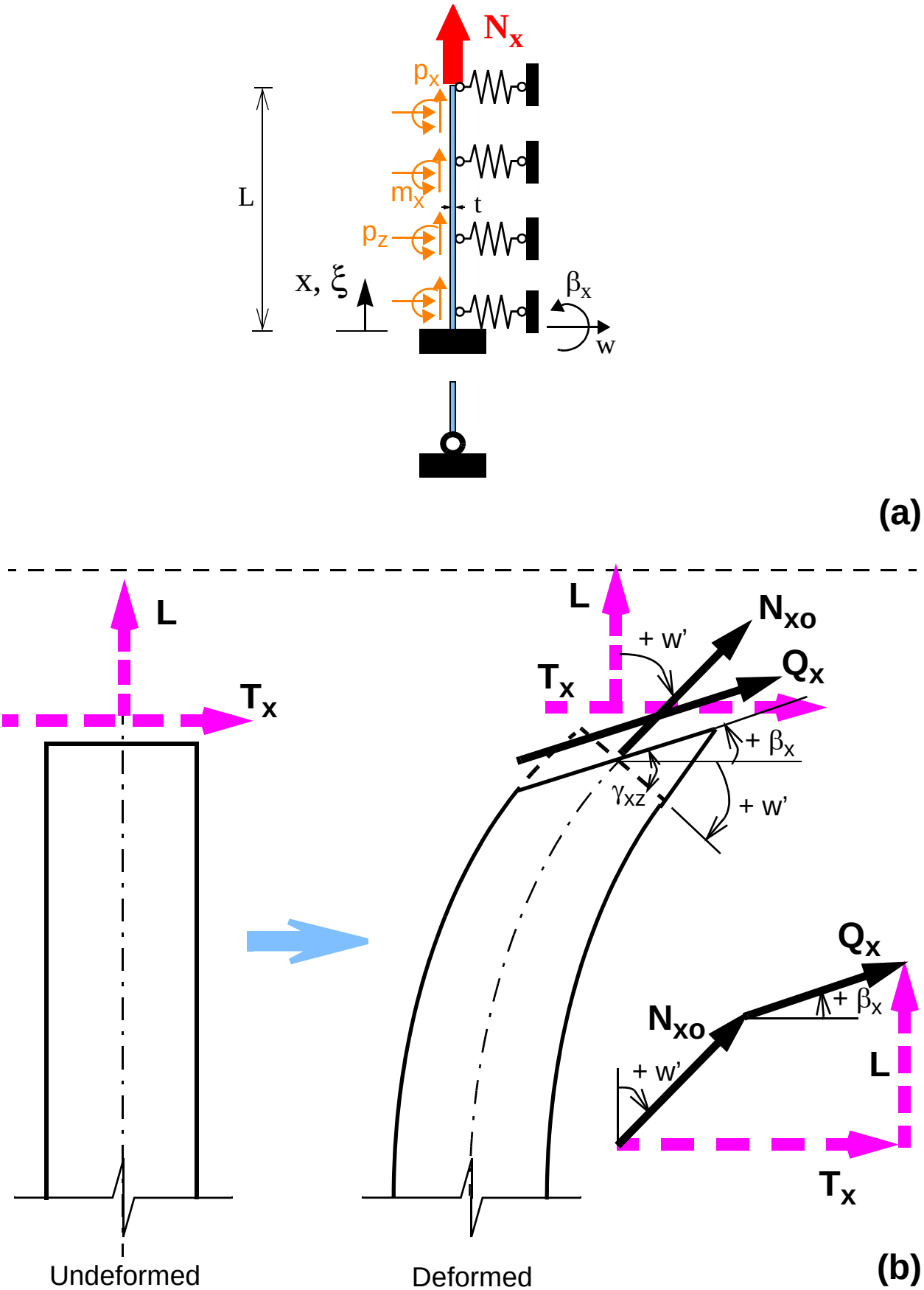

Figure C.2 Geometry, loading and section forces

C.3 Basic differential equations for an axisymmetric cylindrical shell

The basic differential equations for an axisymmetric cylindrical shell with out considering the second order effects have been discussed in ANNEX-B. The second order effect (See Figure C.2b) will appear in the force equilibrium equation along the radial direction. It can equivalently be treated as a radial distributed pressure loading with magnitude (axial loading assumed tensile) equal to:

$$p_{z,\,Th-2-O} = N_{xo} \cdot w''\,;\; N_{xo} > 0 \;\ldots \text{tension} \qquad \text{(Eq. C.1)}$$

With this additional radial distributed loading coming from theory of second order, the basic differential equations (equilibrium, kinematics and constitution) for an axisymmetric cylindrical shell with normal hypothesis (i.e. transverse shear deformation neglected) can be summarized as given below. Thereby it is assumed that the axial normal force is a known quantitiy (N_{xo}) and the shell is able to deform freely in axial direction.

$$\frac{\partial(\;)}{\partial x}\begin{bmatrix} w \\ \beta_x \\ Q_x \\ M_x \end{bmatrix} + \left[\begin{array}{cc|cc} & & 1 & \\ & & & -\frac{1}{K} \\ \hline -C & & & -\frac{N_{xo}}{K} \\ & & -1 & \end{array}\right] \cdot \begin{bmatrix} w \\ \beta_x \\ Q_x \\ M_x \end{bmatrix} + \begin{bmatrix} 0 \\ 0 \\ p_z \\ m_x \end{bmatrix} = \begin{bmatrix} 0 \\ 0 \\ 0 \\ 0 \end{bmatrix} \qquad \text{(Eq. C.2)}$$

with the following parameters being used:

$$K = \frac{E \cdot t^3}{12(1-\nu^2)} \;\ldots \text{plate flexural rigidity} \qquad \text{(Eq. C.3)}$$

$$C = \frac{E \cdot t}{R^2} \;\ldots \text{circumferential membrane stiffness} \qquad \text{(Eq. C.4)}$$

E elastic modulus

t wall thickness

R cylinder radius

p_z applied radial pressure loading

Note: The membrane solution for the axial loading N_{xo} accounting for the Poisson's effect in circumferential direction has to be separately superimposed.

C.4 Basic differential equations for a beam on elastic foundation analogy model

The basic system ordinary differential equations (equilibrium, kinematics and constitution) including second order effects of a beam are discussed below. In all the discussions, the shear rigidity of the beam is assumed to be infinitely large and hence the transverse shear deformation is negligible. Once again, it is assumed that the axial force is a known quantitiy (N_{xo}) and the beam is able to deform freely in axial direction.

C.4.1 Deformation geometry relationships (Kinematics)

This is the relationship between the strains and displacements, and is given by:

$$\begin{bmatrix} \gamma_{xz} \\ \kappa_x \end{bmatrix} = \left[\begin{array}{c:c} \frac{\partial}{\partial x}(\ ) & 1 \\ \hdashline 0 & \frac{\partial}{\partial x}(\ ) \end{array}\right] \cdot \begin{bmatrix} w \\ \beta_x \end{bmatrix} \qquad \text{(Eq. C.5)}$$

with the normal hypothesis, $\gamma_{xz} = \frac{\partial w}{\partial x} + \beta_x = 0 \qquad \Rightarrow \beta_x = -\frac{\partial w}{\partial x}$

C.4.2 Material relationships (Constitution)

The constitutive or strain - section force (stress) relationship will be as follows

$$\begin{bmatrix} \gamma_{xz} \\ \kappa_x \end{bmatrix} = \left[\begin{array}{c:c} \frac{1}{S_{xz}} & 0 \\ \hdashline 0 & \frac{1}{K} \end{array}\right] \cdot \begin{bmatrix} Q_x \\ M_x \end{bmatrix} \quad \text{with } S_{xz} = G \cdot t \to \infty \text{ or } \frac{1}{S_{xz}} \to 0 \qquad \text{(Eq. C.6)}$$

C.4.3 Equilibrium relationships (Kinetics)

The equilbrium (or section forces - applied loads) relationship will be given by:

$$\left[\begin{array}{c:c} \frac{\partial}{\partial x}(\ ) & 0 \\ \hdashline -1 & \frac{\partial}{\partial x}(\ ) \end{array}\right] \cdot \begin{bmatrix} Q_x \\ M_x \end{bmatrix} + \begin{bmatrix} p_z + p_{z,\,total} \\ m_x \end{bmatrix} = \begin{bmatrix} 0 \\ 0 \end{bmatrix} \qquad \text{(Eq. C.7)}$$

where

$$p_{z,\,total} = p_z + p_{z,\,Th-2-O} + p_{z,\,foundation} = p_z + N_{xo} \cdot w'' - C \cdot w \qquad \text{(Eq. C.8)}$$

$p_{z,\,Th-2-O} = + N_{xo} \cdot w''$ results from consideration of second order effects (N_{xo} assumed tension) and $p_{z,\,foundation} = -C \cdot w$ results from the stiffness of the elastic foundation.

C.4.4 Kinematics + Constitution + Kinetics (all - in - one beam equation matrix)

the three relationships written above can be squeezed to:

$$\frac{\partial(\ )}{\partial x}\begin{bmatrix} w \\ \beta_x \\ Q_x \\ M_x \end{bmatrix} + \left[\begin{array}{c|c} \begin{matrix} \ \end{matrix} & 1 \\ \hline -C & -\frac{N_{xo}}{K} \end{array}\right] \cdot \begin{bmatrix} w \\ \beta_x \\ Q_x \\ M_x \end{bmatrix} + \begin{bmatrix} 0 \\ 0 \\ p_z \\ m_x \end{bmatrix} = \begin{bmatrix} 0 \\ 0 \\ 0 \\ 0 \end{bmatrix} \qquad \text{(Eq. C.9)}$$

with the following parameters being used:

$K = E \cdot J$	beam flexural rigidity
E	elastic modulus
J	moment of inertia of the cross-section
C	foundation stiffness
p_z	applied transverse loading

C.4.5 Correspondence of axisymmetric cylinder and beam on elastic foundation

With the following analogy taken into account, an axisymmetric cylindrical shell and a beam on elastic foundation will behave in exactly the same manner. Therefore, the upcoming discussions will by default address both structures.

parameter	cylinder	beam	comment
K	$\frac{E \cdot t^3}{12(1-\nu^2)}$	$E \cdot J$	J is the moment of inertia of the beam cross-section
C	$\frac{E \cdot t}{R^2}$	C	C is the elastic foundation modulus and hence not specific

Table C.1 Analogy between the axisymmetric cylinder & the beam on elastic foundation

Note: p_z for the shell is the radial pressure loading; p_z for the beam is the transverse line load.

N_{xo} for the shell is the axial membrane section force; N_{xo} for the beam is the normal section force.

C.4.6 Reduction of the set of 1st order differential equations into a single 4th order differential equation

The set of ordinary differential equations (Eq. C.9) can be reduced to the following fourth order differential equation:

$$K \cdot w'''' - N_{xo} \cdot w'' + C \cdot w - \underbrace{(m_x' + p_z)}_{p_z^*} = 0 \qquad \text{(Eq. C.10)}$$

Introducing a non-dimensional running parameter ξ, with the following relationships:

$$\xi = \frac{X}{L} \qquad \Rightarrow \qquad (\,)' = \frac{\dot{(\,)}}{L}; \qquad (\,)'' = \frac{\ddot{(\,)}}{L^2} \qquad \text{(Eq. C.11)}$$

The differential equation will then be given by:

$$\frac{K}{L^4} \cdot \dddot{w} - \frac{N_{xo}}{L^2} \cdot \ddot{w} + C \cdot w - \underbrace{\left(\frac{\dot{m}_x}{L} + p_z\right)}_{p_z^*} = 0 \qquad \text{(Eq. C.12)}$$

$$\dddot{w} - \frac{N_{xo} L^2}{K} \ddot{w} + \frac{C L^4}{K} w = \frac{L^4}{K} p_z^* \qquad \text{(Eq. C.13)}$$

C.4.6.1 Solution for the 4th order differential equation - homogeneous fundamental solution

The analytic solution to the elastic buckling problem will be obtained by solving the homogeneous differential equation (i.e. no external loading) which can be written in a general form as:

$$\dddot{w} + 2\beta^2 \ddot{w} + \alpha^4 w = 0 \qquad \text{(Eq. C.14)}$$

$$\beta^2 = \frac{N_{xo} L^2}{2K}; \qquad \alpha^4 = \frac{CL^4}{K}; \qquad \kappa = \frac{\beta^2}{\alpha^2} = \frac{N_{xo}}{2\sqrt{C \cdot K}} = \frac{N_{xo}}{N_{xo,\,cr,\,\infty}} \qquad \text{(Eq. C.15)}$$

Note: $N_{xo,\,cr,\,\infty}$ represents the critical buckling load for the infinitely long beam and appears here as a unified reference value (See Chapter C.8.1 where it appears as $N_{xo,\,cr}$).

Assuming a solution of the form:

$$w(\xi) = e^{\lambda\xi} \qquad \Rightarrow \qquad (\lambda^4 + 2\beta^2\lambda^2 + \alpha^4)e^{\lambda\xi} = 0 \qquad \text{(Eq. C.16)}$$

the characteristic equation becomes:

$$\lambda^4 + 2\beta^2\lambda^2 + \alpha^4 = 0 \qquad \text{(Eq. C.17)}$$

C.4.6.2 General solution of the homogeneous differential equation

The solution to the characteristic polynomial will be given by:

$$\lambda_{1,\,2} = \pm\sqrt{-\beta^2 + \sqrt{\beta^4 - \alpha^4}} = \pm\alpha\sqrt{-\kappa + \sqrt{\kappa^2 - 1}} = \pm i\left(\alpha\sqrt{\kappa - \sqrt{\kappa^2 - 1}}\right) = \pm i\mu_1$$

$$\lambda_{3,\,4} = \pm\sqrt{-\beta^2 - \sqrt{\beta^4 - \alpha^4}} = \pm\alpha\sqrt{-\kappa - \sqrt{\kappa^2 - 1}} = \pm i\left(\alpha\sqrt{\kappa + \sqrt{\kappa^2 - 1}}\right) = \pm i\mu_2 \qquad \text{(Eq. C.18)}$$

where

$$\mu_1 = \alpha\sqrt{\kappa - \sqrt{\kappa^2 - 1}}; \qquad \mu_2 = \alpha\sqrt{\kappa + \sqrt{\kappa^2 - 1}} \qquad \text{(Eq. C.19)}$$

the general homogeneous solution will then be

$$W(\xi) = c_1 \cdot e^{i\mu_1\xi} + c_2 \cdot e^{-i\mu_1\xi} + c_3 \cdot e^{i\mu_2\xi} + c_4 \cdot e^{-i\mu_2\xi} \qquad \text{(Eq. C.20)}$$

or it can also be written as

$$W(\xi) = \boldsymbol{f}^T(\xi) \cdot \boldsymbol{c}; \qquad \boldsymbol{c} = \begin{bmatrix} c_1 & c_2 & c_3 & c_4 \end{bmatrix}^T \qquad \text{(Eq. C.21)}$$

C.5 Different solution cases of the 4th order homogeneous o.d.e.: fundamental function and accompanying derivative matrix

Depending on the value of the parameter κ, three distinct fundamental solution cases may exist. These distinct solution cases are discussed below:

C.5.1 Case - 1

$$\kappa = \frac{\beta^2}{\alpha^2} < 1 \qquad \mu_1 = \alpha\sqrt{\frac{1-\kappa}{2}} \qquad \mu_2 = \alpha\sqrt{\frac{1+\kappa}{2}} \tag{Eq. C.22}$$

Fundamental solution function:

$$\boldsymbol{f} = \begin{bmatrix} e^{-\mu_1\xi}\cdot\sin(\mu_2\xi) \\ e^{-\mu_1\xi}\cdot\cos(\mu_2\xi) \\ e^{-\mu_1(1-\xi)}\cdot\sin(\mu_2(1-\xi)) \\ e^{-\mu_1(1-\xi)}\cdot\cos(\mu_2(1-\xi)) \end{bmatrix} \tag{Eq. C.23}$$

Derivative and derivative matrix of the function:

$$\dot{\boldsymbol{f}} = \boldsymbol{D}\cdot\boldsymbol{f} \qquad \Rightarrow \qquad \boldsymbol{D} = \begin{bmatrix} -\mu_1 & \mu_2 & 0 & 0 \\ -\mu_2 & -\mu_1 & 0 & 0 \\ 0 & 0 & \mu_1 & -\mu_2 \\ 0 & 0 & \mu_2 & \mu_1 \end{bmatrix} \tag{Eq. C.24}$$

C.5.2 Case - 2

$$\kappa = \frac{\beta^2}{\alpha^2} = 1 \qquad \mu = \mu_1 = \mu_2 = \alpha = \beta \tag{Eq. C.25}$$

Fundamental solution function:

$$\boldsymbol{f} = \begin{bmatrix} \sin(\mu\xi) \\ \cos(\mu\xi) \\ (1-\xi)\cdot\sin(\mu(1-\xi)) \\ (1-\xi)\cdot\cos(\mu(1-\xi)) \end{bmatrix} \tag{Eq. C.26}$$

Derivative and derivative matrix of the function:

$$\dot{\boldsymbol{f}} = \boldsymbol{D}\cdot\boldsymbol{f} \qquad \Rightarrow \qquad \boldsymbol{D} = \begin{bmatrix} 0 & \mu & 0 & 0 \\ -\mu & 0 & 0 & 0 \\ 0 & 0 & -\frac{1}{1-\xi} & -\mu \\ 0 & 0 & \mu & -\frac{1}{1-\xi} \end{bmatrix} \tag{Eq. C.27}$$

C.5.3 Case - 3

$$\kappa = \frac{\beta^2}{\alpha^2} > 1 \qquad \mu_1 = \alpha\sqrt{\kappa - \sqrt{\kappa^2 - 1}} \qquad \mu_2 = \alpha\sqrt{\kappa + \sqrt{\kappa^2 - 1}} \tag{Eq. C.28}$$

Fundamental solution function:

$$\boldsymbol{f} = \begin{bmatrix} \sin(\mu_1\xi) \\ \cos(\mu_1\xi) \\ \sin(\mu_2\xi) \\ \cos(\mu_2\xi) \end{bmatrix} \tag{Eq. C.29}$$

Derivative and derivative matrix of the function:

$$\dot{\boldsymbol{f}} = \boldsymbol{D}\cdot\boldsymbol{f} \qquad \Rightarrow \qquad \boldsymbol{D} = \begin{bmatrix} 0 & \mu_1 & 0 & 0 \\ -\mu_1 & 0 & 0 & 0 \\ 0 & 0 & 0 & \mu_2 \\ 0 & 0 & -\mu_2 & 0 \end{bmatrix} \tag{Eq. C.30}$$

C.6 Derivation of beam stiffness matrix

C.6.1 General - for all solution cases

C.6.1.1 Displacement vector

The general expression for the displacement vector will be given as follows:

$$w_{hom}(\xi) = \boldsymbol{f}^T(\xi) \cdot \boldsymbol{c}; \qquad \boldsymbol{c} = \begin{bmatrix} c_1 & c_2 & c_3 & c_4 \end{bmatrix}^T \tag{Eq. C.31}$$

$$\beta_{hom}(\xi) = -\frac{\dot{w}_{hom}(\xi)}{L} = -\frac{1}{L}\dot{\boldsymbol{f}}^T(\xi) \cdot \boldsymbol{c} \qquad \Rightarrow \qquad L \cdot \beta_{hom}(\xi) = -\boldsymbol{f}^T \cdot \boldsymbol{D}^T \cdot \boldsymbol{c} \tag{Eq. C.32}$$

$$\boldsymbol{W}^* = \begin{bmatrix} W \\ L \cdot \beta \end{bmatrix} = \begin{bmatrix} \boldsymbol{f}^T \\ -\dot{\boldsymbol{f}}^T \end{bmatrix} \cdot \boldsymbol{c} = \begin{bmatrix} \boldsymbol{f}^T \cdot \boldsymbol{I}_{(4,4)} \\ \boldsymbol{f}^T \cdot (-\boldsymbol{D}^T) \end{bmatrix} \cdot \boldsymbol{c} = \underbrace{\begin{bmatrix} \boldsymbol{f}^T & \boldsymbol{0} \\ \boldsymbol{0} & \boldsymbol{f}^T \end{bmatrix}}_{\boldsymbol{F}^T_{(2,8)}} \cdot \begin{bmatrix} \boldsymbol{I} \\ -\boldsymbol{D}^T \end{bmatrix} \cdot \boldsymbol{c} \tag{Eq. C.33}$$

C.6.1.2 Beam-end displacements and homogeneous edge-displacement matrix

With “A” and “E” representing the starting edge and ending edge of the beam, the edge displacements will be given by:

$$\hat{\boldsymbol{W}}^* = \begin{bmatrix} \boldsymbol{W}^*_A \\ \boldsymbol{W}^*_E \end{bmatrix} = \begin{bmatrix} W_A \\ L \cdot \beta_A \\ W_E \\ L \cdot \beta_E \end{bmatrix} = \underbrace{\begin{bmatrix} \boldsymbol{F}^T_A \\ \boldsymbol{F}^T_E \end{bmatrix} \cdot \begin{bmatrix} \boldsymbol{I} \\ -\boldsymbol{D}^T \end{bmatrix}}_{U_{hom}} \cdot \boldsymbol{c} \tag{Eq. C.34}$$

C.6.1.3 Computation of the integration constants vector c

Once the beam-end displacements and the homogeneous edge-displacement matrix $\mathbf{U_{hom}}$ are known, the integration constants vector **c** can be computed from:

$$\hat{\boldsymbol{W}}^* = \boldsymbol{U}_{hom} \cdot \boldsymbol{c} \tag{Eq. C.35}$$

$$\boldsymbol{c} = \boldsymbol{U}^{-1}_{hom} \cdot \hat{\boldsymbol{W}}^* \tag{Eq. C.36}$$

C.6.1.4 Section and edge forces

Local section forces:

$$M_x = K \cdot \beta_x' = -K \cdot W'' = -\frac{K}{L^2} \cdot \ddot{W}$$

$$Q_x = M_x' = -K \cdot W''' = -K \cdot \frac{1}{L^3} \cdot \dddot{W} \qquad \text{(Eq. C.37)}$$

$$\boldsymbol{Q}^* = \begin{bmatrix} Q_x \\ \frac{M_x}{L} \end{bmatrix} = -K \cdot \frac{1}{L^3} \begin{bmatrix} \ddot{\boldsymbol{f}}^T \\ \ddot{\boldsymbol{f}}^T \end{bmatrix} \boldsymbol{c} = -\frac{K}{L^3} \begin{bmatrix} \boldsymbol{f}^T & \cdot \boldsymbol{D}^{3T} \\ \boldsymbol{f}^T & \cdot \boldsymbol{D}^{2T} \end{bmatrix} \boldsymbol{c} \text{ ... section-forces vector} \qquad \text{(Eq. C.38)}$$

$$\boldsymbol{Q}^* = -\frac{K}{L^3} \underbrace{\begin{bmatrix} \boldsymbol{f}^T & \boldsymbol{0}^T \\ \boldsymbol{0}^T & \boldsymbol{f}^T \end{bmatrix}}_{\boldsymbol{F}^T} \begin{bmatrix} \boldsymbol{D}^{3T} \\ \boldsymbol{D}^{2T} \end{bmatrix} \boldsymbol{c} \qquad \text{(Eq. C.39)}$$

Global section forces:

The global transversal and longitudinal section forces of the beam including second order effects are given, Figure C.2, by:

$$T_x = Q_x - N_{xo} \cdot W' \text{ ... Transversal section force} \qquad \text{(Eq. C.40)}$$

$$L = N_{0x} + Q_x \cdot W' \approx N_{xo} \text{ ... Longitudinal section force} \qquad \text{(Eq. C.41)}$$

C.6.1.5 computation of the transversal section force

$$T_x = Q_x - N_{xo} \cdot W' = -K \cdot W''' - N_{xo} \cdot W' = -\frac{K}{L^3} \cdot \dddot{W} - \frac{N_{xo}}{L} \cdot \frac{\partial W}{\partial \xi}$$

$$T_x = -\frac{K}{L^3} \cdot \left(\dddot{W} + \frac{N_{xo} \cdot L^2}{K} \cdot \dot{W} \right) = -\frac{K}{L^3} \cdot (\dddot{W} + 2\beta^2 \dot{W}) \qquad \text{(Eq. C.42)}$$

- **Section-forces vector in terms of the transversal force T:**

$$\boldsymbol{T}^* = \begin{bmatrix} T_x \\ M_x / L \end{bmatrix} = -\frac{K}{L^3} \cdot \begin{bmatrix} \dddot{W} + 2\beta^2 \cdot \dot{W} \\ \ddot{W} \end{bmatrix} = -\frac{K}{L^3} \cdot \underbrace{\begin{bmatrix} \boldsymbol{f}^T & \boldsymbol{0}^T \\ \boldsymbol{0}^T & \boldsymbol{f}^T \end{bmatrix}}_{\boldsymbol{F}^T} \cdot \begin{bmatrix} \boldsymbol{D}^{3T} + 2\beta^2 \boldsymbol{D}^T \\ \boldsymbol{D}^{2T} \end{bmatrix} \cdot \boldsymbol{c} \qquad \text{(Eq. C.43)}$$

C.6.1.6 Global edge-forces vector

$$\hat{\boldsymbol{T}}^* = \begin{bmatrix} \boldsymbol{T}^*_A \\ \boldsymbol{T}^*_E \end{bmatrix} = \begin{bmatrix} T_A \\ M_A/L \\ T_E \\ M_E/L \end{bmatrix} = \underbrace{-\frac{K}{L^3} \cdot \begin{bmatrix} \boldsymbol{F}_A^T \\ \boldsymbol{F}_E^T \end{bmatrix} \cdot \begin{bmatrix} \boldsymbol{D}^{3T} + 2\beta^2 \boldsymbol{D}^T \\ \boldsymbol{D}^{2T} \end{bmatrix}}_{\boldsymbol{S}_{hom}} \cdot \boldsymbol{c} \qquad \text{(Eq. C.44)}$$

C.6.1.7 Stiffness matrix using theory of second order

$$\hat{\boldsymbol{T}}^* = \boldsymbol{S}_{Hom} \cdot \boldsymbol{c} = (\boldsymbol{S}_{Hom} \cdot \boldsymbol{U}_{Hom}^{-1}) \cdot \hat{\boldsymbol{W}}^* = \begin{bmatrix} T_A \\ M_A/L \\ T_E \\ M_E/L \end{bmatrix} \text{ ... edge-forces vector} \qquad \text{(Eq. C.45)}$$

$$\hat{\boldsymbol{W}}^* = \begin{bmatrix} W_A \\ \beta_A \cdot L \\ W_E \\ \beta_E \cdot L \end{bmatrix} \text{ ... edge displacements vector} \qquad \text{(Eq. C.46)}$$

$$\hat{\boldsymbol{R}}^* = \hat{\boldsymbol{K}}^* \cdot \hat{\boldsymbol{W}}^* \qquad \text{(Eq. C.47)}$$

$$\hat{\boldsymbol{K}}^* = (\boldsymbol{T} \cdot \boldsymbol{S}_{Hom} \cdot \boldsymbol{U}_{Hom}^{-1}) \text{ ... beam stiffness matrix} \qquad \text{(Eq. C.48)}$$

$$\boldsymbol{T} = \begin{bmatrix} -1 & 0 & 0 & 0 \\ 0 & -1 & 0 & 0 \\ 0 & 0 & 1 & 0 \\ 0 & 0 & 0 & 1 \end{bmatrix}$$

... matrix to convert from section force orientation to global edge force sign-convention (Eq. C.49)

C.6.2 Specific - for each solution case

C.6.2.1 Case - 1

$$\kappa = \frac{\beta^2}{\alpha^2} < 1 \qquad \mu_1 = \alpha\sqrt{\frac{1-\kappa}{2}} \qquad \mu_2 = \alpha\sqrt{\frac{1+\kappa}{2}} \tag{Eq. C.50}$$

- **Displacement vector**

$$\boldsymbol{W}^* = \begin{bmatrix} e^{-\mu_1\xi}\sin(\mu_2\xi) & e^{-\mu_1\xi}[\mu_1\sin(\mu_2\xi)-\mu_2\cos(\mu_2\xi)] \\ e^{-\mu_1\xi}\cos(\mu_2\xi) & e^{-\mu_1\xi}[\mu_2\sin(\mu_2\xi)+\mu_1\cos(\mu_2\xi)] \\ e^{-\mu_1(1-\xi)}\sin(\mu_2(1-\xi)) & e^{-\mu_1(1-\xi)}[-\mu_1\sin(\mu_2(1-\xi))+\mu_2\cos(\mu_2(1-\xi))] \\ e^{-\mu_1(1-\xi)}\cos(\mu_2(1-\xi)) & -e^{-\mu_1(1-\xi)}[\mu_2\sin(\mu_2(1-\xi))+\mu_1\cos(\mu_2(1-\xi))] \end{bmatrix}^T \cdot \boldsymbol{c} \tag{Eq. C.51}$$

- **Beam-end displacements and homogeneous edge-displacement matrix**

$$\hat{\boldsymbol{W}}^* = \boldsymbol{U}_{hom} \cdot \boldsymbol{c} \tag{Eq. C.52}$$

$$\boldsymbol{U}_{hom} = \begin{bmatrix} \bar{\bar{a}}_1 & \bar{\bar{\bar{f}}} & \bar{\bar{c}} & -\bar{\bar{\bar{g}}} \\ \bar{\bar{\bar{b}}} & \bar{\bar{a}}_2 & -\bar{\bar{e}} & -\bar{\bar{\bar{d}}} \\ \bar{\bar{c}} & \bar{\bar{\bar{g}}} & \bar{\bar{a}}_1 & \bar{\bar{\bar{f}}} \\ \bar{\bar{e}} & \bar{\bar{\bar{d}}} & -\bar{\bar{\bar{b}}} & -\bar{\bar{a}}_2 \end{bmatrix} \tag{Eq. C.53}$$

where

$$\begin{bmatrix} \bar{\bar{a}}_1 = 0 \\ \bar{\bar{a}}_2 = \mu_1 \\ \bar{\bar{b}} = -\mu_2 \\ \bar{\bar{c}} = e^{-\mu_1} \cdot \sin(\mu_2) \\ \bar{\bar{d}} = e^{-\mu_1} \cdot [\mu_1 \cos(\mu_2) + \mu_2 \sin(\mu_2)] \\ \bar{\bar{e}} = e^{-\mu_1} \cdot [\mu_1 \sin(\mu_2) - \mu_2 \cos(\mu_2)] \\ \bar{\bar{f}} = 1 \\ \bar{\bar{g}} = e^{-\mu_1} \cdot \cos(\mu_2) \end{bmatrix} \quad \text{(Eq. C.54)}$$

- **Computation of the integration constants vector c**

$$\boldsymbol{c} = \boldsymbol{U}_{hom}^{-1} \cdot \hat{\boldsymbol{W}}^* \quad \text{(Eq. C.55)}$$

$$\boldsymbol{U}_{hom}^{-1} = \frac{1}{\bar{N}} \begin{bmatrix} \bar{\bar{a}}_1 & \bar{\bar{f}} & \bar{\bar{c}} & -\bar{\bar{g}} \\ \bar{\bar{b}} & \bar{\bar{a}}_2 & \bar{\bar{e}} & -\bar{\bar{d}} \\ \bar{\bar{c}} & \bar{\bar{g}} & \bar{\bar{a}}_1 & -\bar{\bar{f}} \\ \bar{\bar{e}} & \bar{\bar{d}} & \bar{\bar{b}} & -\bar{\bar{a}}_2 \end{bmatrix} \quad \text{(Eq. C.56)}$$

where

$$N = det(\boldsymbol{U}_{hom}) = e^{-2\mu_1}[4\mu_1^2 \sin(\mu_2)^2 + \mu_2^2(-1 + e^{-2\mu_1})] \quad \text{(Eq. C.57)}$$

$$\begin{bmatrix} \bar{\bar{a}}_1 = -[\mu_1^2 e^{-2\mu_1} \sin(2\mu_2) + \mu_1\mu_2(1 - e^{-2\mu_1} \cos(2\mu_2))] \\ \bar{\bar{a}}_2 = 2e^{-2\mu_1} \cdot \mu_1 \sin(\mu_2)^2 \\ \bar{\bar{b}} = -\mu_2^2 + e^{-2\mu_1} \cdot [2\mu_1^2 \sin(\mu_2)^2 - \mu_1\mu_2 \sin(2\mu_2) + \mu_2^2] \\ \hline \bar{\bar{c}} = e^{-\mu_1} \cdot [2\mu_1^2 \sin(\mu_2) - \mu_1\mu_2(-1 + e^{-2\mu_1}) \cos(\mu_2) - \mu_2^2(-1 + e^{-2\mu_1}) \sin(\mu_2)] \\ \bar{\bar{d}} = e^{-\mu_1} \cdot \mu_2(-1 + e^{-2\mu_1}) \sin(\mu_2) \\ \bar{\bar{e}} = \mu_2 e^{-\mu_1} \cdot [\mu_1(1 + e^{-2\mu_1}) \sin(\mu_2) - \mu_2(-1 + e^{-2\mu_1}) \cos(\mu_2)] \\ \bar{\bar{f}} = \mu_2 - e^{-2\mu_1} \cdot [\mu_1 \sin(2\mu_2) + \mu_2] \\ \bar{\bar{g}} = -e^{-\mu_1} \cdot [2\mu_1 \sin(\mu_2) + \mu_2(-1 + e^{-2\mu_1}) \cos(\mu_2)] \end{bmatrix} \quad \text{(Eq. C.58)}$$

- **homogeneous edge-forces matrix**

$$\boldsymbol{S}_{hom} = \frac{EJ}{L^3}\begin{bmatrix} \bar{a}_1 & \bar{f} & -\bar{c} & -\bar{g} \\ \bar{b} & \bar{a}_2 & \bar{e} & \bar{d} \\ \bar{c} & \bar{g} & -\bar{a}_1 & -\bar{f} \\ \bar{e} & \bar{d} & \bar{b} & \bar{a}_2 \end{bmatrix} \qquad \text{(Eq. C.59)}$$

where

$$\begin{bmatrix} \bar{a}_1 = -\mu_2\alpha^2 \\ \bar{a}_2 = 2\beta^2 \\ \bar{b} = 2\mu_1\mu_2 \\ \bar{c} = -e^{-\mu_1}\alpha^2 \cdot [\mu_1\sin(\mu_2) + \mu_2\cos(\mu_2)] \\ \bar{d} = -e^{-\mu_1} \cdot [2\mu_1\mu_2\sin(\mu_2) - 2\beta^2\cos(\mu_2)] \\ \bar{e} = e^{-\mu_1} \cdot [2\mu_1\mu_2\cos(\mu_2) + 2\beta^2\sin(\mu_2)] \\ \bar{f} = -\mu_1\alpha^2 \\ \bar{g} = -e^{-\mu_1}\alpha^2 \cdot [\mu_1\cos(\mu_2) - \mu_2\sin(\mu_2)] \end{bmatrix} \qquad \text{(Eq. C.60)}$$

- **Stiffness matrix and Stiffness coefficients**

$$\hat{\boldsymbol{K}}^* = \frac{1}{N} \cdot \frac{EJ}{L^3} \cdot \begin{bmatrix} a_1 & b & c & e \\ b & a_2 & -e & d \\ c & -e & a_1 & -b \\ e & d & -b & a_2 \end{bmatrix} \qquad \text{(Eq. C.61)}$$

where

$$N = det(\boldsymbol{U}_{hom}) = 4\mu_1^2 e^{-2\mu_1}\sin(\mu_2)^2 - \mu_2^2(-1 + e^{-2\mu_1})^2 \qquad \text{(Eq. C.62)}$$

$$\begin{bmatrix} a_1 = & 2\mu_1\mu_2(\mu_1^2+\mu_2^2)[\mu_2(-1+e^{-4\mu_1})-2\mu_1 e^{-2\mu_1}\sin(2\mu_2)] \\ a_2 = & 2\mu_1\mu_2[\mu_2(-1+e^{-4\mu_1})+2\mu_1 e^{-2\mu_1}\sin(2\mu_2)] \\ b = & (\mu_1^2+\mu_2^2)[4\mu_1^2 e^{-2\mu_1}\sin(\mu_2)^2-\mu_2^2(-1+e^{-2\mu_1})^2] \\ c = & 4\mu_1\mu_2(\mu_1^2+\mu_2^2)e^{-\mu_1}[\mu_1(1+e^{-2\mu_1})\sin(\mu_2)-\mu_2(-1+e^{-2\mu_1})\cos(\mu_2)] \\ d = & -4\mu_1\mu_2 e^{-\mu_1}[\mu_1(1+e^{-2\mu_1})\sin(\mu_2)+\mu_2(-1+e^{-2\mu_1})\cos(\mu_2)] \\ e = & -4\mu_1\mu_2(\mu_1^2+\mu_2^2)e^{-\mu_1}(-1+e^{-2\mu_1})\sin(\mu_2) \end{bmatrix} \quad \text{(Eq. C.63)}$$

These non-dimensional stiffness coefficients can be brought into a compact unified shape by introducing the parameters μ and κ and thus replacing μ_1 and μ_2 as follows:

$$\mu_1 = \frac{\alpha}{\sqrt{2}}\sqrt{1-\kappa} = \mu\sqrt{1-\kappa} \quad \text{(Eq. C.64)}$$

$$\mu_2 = \frac{\alpha}{\sqrt{2}}\sqrt{1+\kappa} = \mu\sqrt{1+\kappa} \quad \text{(Eq. C.65)}$$

with $\mu = \alpha/\sqrt{2}$

and therefore,

$$\mu_1 \cdot \mu_2 = \mu^2\sqrt{1-\kappa} \quad \text{(Eq. C.66)}$$

$$\mu_1^2+\mu_2^2 = \mu^2\cdot((1-\kappa)+(1+\kappa)) = 2\mu^2 \quad \text{(Eq. C.67)}$$

For vanishing axial force $N_{x0} \to 0$, we have also $\kappa \to 0$ and therefore $\mu_1 = \mu_2 = \mu$ holds. These substitutions enable therefore a compact and unified representation for all values of the axial normal force which is hidden in the parameter κ.

C.6.2.2 Case - 2

$$\kappa = \frac{\beta^2}{\alpha^2} = 1 \qquad \mu = \mu_1 = \mu_2 = \alpha = \beta \tag{Eq. C.68}$$

- **Displacement vector**

$$\boldsymbol{W}^* = \begin{bmatrix} \sin(\mu\xi) & -\mu\cos(\mu\xi) \\ \cos(\mu\xi) & \mu\sin(\mu\xi) \\ (1-\xi)\sin(\mu(1-\xi)) & \sin(\mu(1-\xi)) + \mu(1-\xi)\cos(\mu(1-\xi)) \\ (1-\xi)\cos(\mu(1-\xi)) & -\mu\sin(\mu(1-\xi)) + \cos(\mu(1-\xi)) \end{bmatrix}^T \cdot \boldsymbol{c} \tag{Eq. C.69}$$

- **Beam-end displacements and homogeneous edge-displacement matrix**

$$\hat{\boldsymbol{W}}^* = \boldsymbol{U}_{hom} \cdot \boldsymbol{c} \tag{Eq. C.70}$$

$$\boldsymbol{U}_{hom} = \begin{bmatrix} 0 & 1 & \sin(\mu) & \cos(\mu) \\ -\mu & 0 & \sin(\mu) + \mu\cos(\mu) & -\mu\sin(\mu) + \cos(\mu) \\ \sin(\mu) & \cos(\mu) & 0 & 0 \\ -\mu\cos(\mu) & \mu\sin(\mu) & 0 & 1 \end{bmatrix} \tag{Eq. C.71}$$

- **Computation of the integration constants vector c**

$$\boldsymbol{c} = \boldsymbol{U}_{hom}^{-1} \cdot \hat{\boldsymbol{W}}^* \tag{Eq. C.72}$$

$$\boldsymbol{U}_{hom}^{-1} = \frac{1}{N}\begin{bmatrix} -\cos(\mu)[\sin(\mu)+\mu\cos(\mu)] & \sin(\mu)\cos(\mu) & \sin(\mu)+\mu[\cos(\mu)-\mu\sin(\mu)] & \mu\cos(\mu) \\ \sin(\mu)[\sin(\mu)+\mu\cos(\mu)] & -\sin(\mu)^2 & -\mu[\sin(\mu)+\mu\cos(\mu)] & -\mu\sin(\mu) \\ -\mu^2\sin(\mu) & \sin(\mu)-\mu\cos(\mu) & \mu\sin(\mu)^2 & \mu-\sin(\mu)\cos(\mu) \\ -\mu[\sin(\mu)+\mu\cos(\mu)] & \mu\sin(\mu) & \mu[\mu+\sin(\mu)\cos(\mu)] & \sin(\mu)^2 \end{bmatrix} \tag{Eq. C.73}$$

$$N = det(\boldsymbol{U}_{hom}) = \frac{1}{2}[1-2\mu^2-\cos(2\mu)] \tag{Eq. C.74}$$

- **homogeneous edge-forces matrix**

$$\boldsymbol{S}_{hom} = \frac{EJ}{L^3}\begin{bmatrix} -\mu^3 & 0 & -\mu^2\sin(\mu)+\mu^3\cos(\mu) & -\mu^3\sin(\mu)-\mu^2\cos(\mu) \\ 0 & \mu^2 & \mu^2\sin(\mu)-2\mu\cos(\mu) & 2\mu\sin(\mu)+\mu^2\cos(\mu) \\ -\mu^3\cos(\mu) & \mu^3\sin(\mu) & 0 & -\mu^2 \\ \mu^2\sin(\mu) & \mu^2\cos(\mu) & -2\mu & 0 \end{bmatrix} \quad \text{(Eq. C.75)}$$

- **Stiffness matrix and Stiffness coefficients**

$$\hat{\boldsymbol{K}}^* = \frac{1}{N}\cdot\frac{EJ}{L^3}\cdot\begin{bmatrix} a_1 & b & c & e \\ b & a_2 & -e & d \\ c & -e & a_1 & -b \\ e & d & -b & a_2 \end{bmatrix} \quad \text{(Eq. C.76)}$$

$$N = det(\boldsymbol{U}_{hom}) = \frac{1}{2}[1-2\mu^2-\cos(2\mu)] \quad \text{(Eq. C.77)}$$

$$\begin{bmatrix} a_1 = -2\mu^3[\mu+\sin(\mu)\cos(\mu)] \\ a_2 = \mu[-2\mu+\sin(2\mu)] \\ b = \frac{1}{2}\mu^2[1+2\mu^2-\cos(2\mu)] \\ c = 2\mu^3[\sin(\mu)+\mu\cos(\mu)] \\ d = -2\mu[\sin(\mu)-\mu\cos(\mu)] \\ e = 2\mu^3\sin(\mu) \end{bmatrix} \quad \text{(Eq. C.78)}$$

C.6.2.3 Case - 3

$$\kappa = \frac{\beta^2}{\alpha^2} > 1 \qquad \mu_1 = \alpha\sqrt{\kappa - \sqrt{\kappa^2 - 1}} = \sqrt{\beta^2 - \sqrt{\beta^4 - \alpha^4}}$$

$$\mu_2 = \alpha\sqrt{\kappa + \sqrt{\kappa^2 - 1}} = \sqrt{\beta^2 + \sqrt{\beta^4 - \alpha^4}} \qquad \text{(Eq. C.79)}$$

- **Displacement vector**

$$\boldsymbol{W}^* = \begin{bmatrix} \sin(\mu_1\xi) & \cos(\mu_1\xi) & \sin(\mu_2\xi) & \cos(\mu_2\xi) \\ -\mu_1\cos(\mu_1\xi) & \mu_1\sin(\mu_1\xi) & -\mu_2\cos(\mu_2\xi) & \mu_2\sin(\mu_2\xi) \end{bmatrix} \cdot \boldsymbol{c} \qquad \text{(Eq. C.80)}$$

- **Beam-end displacements and homogeneous edge-displacement matrix**

$$\hat{\boldsymbol{W}}^* = \boldsymbol{U}_{hom} \cdot \boldsymbol{c} \qquad \text{(Eq. C.81)}$$

$$\boldsymbol{U}_{hom} = \begin{bmatrix} 0 & 1 & 0 & 1 \\ -\mu_1 & 0 & -\mu_2 & 0 \\ \sin(\mu_1) & \cos(\mu_1) & \sin(\mu_2) & \cos(\mu_2) \\ -\mu_1\cos(\mu_1) & \mu_1\sin(\mu_1) & -\mu_2\cos(\mu_2) & \mu_2\sin(\mu_2) \end{bmatrix} \qquad \text{(Eq. C.82)}$$

- **Computation of the integration constants vector c**

$$\boldsymbol{c} = \boldsymbol{U}_{hom}^{-1} \cdot \hat{\boldsymbol{W}}^* \qquad \text{(Eq. C.83)}$$

$$\boldsymbol{U}_{hom}^{-1} = \frac{1}{N}\begin{bmatrix} \mu_2^2 c_1 s_2 - \mu_1\mu_2 s_1 c_2 & \mu_1 s_1 s_2 - \mu_2(1 - c_1 c_2) & \mu_1\mu_2 s_1 - \mu_2^2 s_2 & \mu_2(c_2 - c_1) \\ \mu_1\mu_2(1 - c_1 c_2) - \mu_2^2 s_1 s_2 & \mu_1 c_1 s_2 - \mu_2 s_1 c_2 & \mu_1\mu_2(c_1 - c_2) & \mu_2 s_1 - \mu_1 s_2 \\ \mu_1^2 s_1 c_2 - \mu_1\mu_2 c_1 s_2 & \mu_2 s_1 s_2 - \mu_1(1 - c_1 c_2) & \mu_1\mu_2 s_2 - \mu_1^2 s_1 & \mu_1(c_1 - c_2) \\ \mu_1\mu_2(1 - c_1 c_2) - \mu_1^2 s_1 s_2 & \mu_2 s_1 c_2 - \mu_1 s_2 c_1 & \mu_1\mu_2(c_2 - c_1) & \mu_1 s_2 - \mu_2 s_1 \end{bmatrix} \qquad \text{(Eq. C.84)}$$

$$N = det(\boldsymbol{U}_{hom}) = 2\alpha^2[1 - \cos(\mu_1)\cos(\mu_2)] - 2\beta^2\sin(\mu_1)\sin(\mu_2) \qquad \text{(Eq. C.85)}$$

$$s_1 = \sin(\mu_1) \qquad c_1 = \cos(\mu_1)$$

$$s_2 = \sin(\mu_2) \qquad c_2 = \cos(\mu_2) \qquad \text{(Eq. C.86)}$$

- **homogeneous edge-forces matrix**

$$\boldsymbol{S}_{hom} = \frac{EJ}{L^3}\begin{bmatrix} \mu_1(\mu_1^2-2\beta^2) & 0 & \mu_2(\mu_2^2-2\beta^2) & 0 \\ 0 & \mu_1^2 & 0 & \mu_2^2 \\ \mu_1 c_1(\mu_1^2-2\beta^2) & -\mu_1 s_1(\mu_1^2-2\beta^2) & \mu_2 c_2(\mu_2^2-2\beta^2) & -\mu_2 s_2(\mu_2^2-2\beta^2) \\ \mu_1^2 s_1 & \mu_1^2 c_1 & \mu_2^2 s_2 & \mu_2^2 c_2 \end{bmatrix} \quad \text{(Eq. C.87)}$$

- **Stiffness matrix and Stiffness coefficients**

$$\hat{\boldsymbol{K}}^* = \frac{EJ}{L^3}\cdot\begin{bmatrix} a_1 & b & c & e \\ b & a_2 & -e & d \\ c & -e & a_1 & -b \\ e & d & -b & a_2 \end{bmatrix} \quad \text{(Eq. C.88)}$$

$$N = det(\boldsymbol{U}_{hom}) = 2\alpha^2[1-\cos(\mu_1)\cos(\mu_2)] - 2\beta^2\sin(\mu_1)\sin(\mu_2) \quad \text{(Eq. C.89)}$$

$$\begin{bmatrix} a_1 = \alpha^2(\mu_1^2-\mu_2^2)[\mu_1\sin(\mu_1)\cos(\mu_2) - \mu_2\cos(\mu_1)\sin(\mu_2)] \\ a_2 = (\mu_1^2-\mu_2^2)[\mu_2\sin(\mu_1)\cos(\mu_2) - \mu_1\cos(\mu_1)\sin(\mu_2)] \\ b = 2\alpha^4\sin(\mu_1)\sin(\mu_2) - 2\alpha^2\beta^2[1-\cos(\mu_1)\cos(\mu_2)] \\ c = \alpha^2(\mu_1^2-\mu_2^2)[\mu_2\sin(\mu_2) - \mu_1\sin(\mu_1)] \\ d = (\mu_1^2-\mu_2^2)[\mu_1\sin(\mu_2) - \mu_2\sin(\mu_1)] \\ e = \alpha^2(\mu_1^2-\mu_2^2)[\cos(\mu_1) - \cos(\mu_2)] \end{bmatrix} \quad \text{(Eq. C.90)}$$

C.7 Procedure for analytical computation of elastic buckling strengths and buckling eigenmodes

In order to make the above discussion clearer, following is a step-by-step procedure for the analytic computation of elastic buckling strengths and buckling eigenmodes of perfect cylindrical shells under axiall compressive loading.

- Assume a solution case:

$$\kappa = \frac{\beta^2}{\alpha^2} \begin{matrix} \leq \\ = \\ > \end{matrix} 1 \qquad \text{(Eq. C.91)}$$

- Select a fundamental solution function, f, corresponding to the solution case

- Compute $\boldsymbol{U}_{hom}$, S_{hom} and

$$\hat{\boldsymbol{K}}^* = (\boldsymbol{T} \cdot \boldsymbol{S}_{Hom} \cdot \boldsymbol{U}_{Hom}^{-1}) \text{ ... beam stiffness matrix} \qquad \text{(Eq. C.92)}$$

with

$$\boldsymbol{T} = \begin{bmatrix} -1 & 0 & 0 & 0 \\ 0 & -1 & 0 & 0 \\ 0 & 0 & 1 & 0 \\ 0 & 0 & 0 & 1 \end{bmatrix}$$

... matrix to convert from section force orientation to global edge force Sign-convention (Eq. C.93)

- Compute the reduced stiffness matrix, $\hat{\boldsymbol{K}}^*_{red}$, by applying the boundary conditions on $\hat{\boldsymbol{K}}^*$

- Set the determinant of $\hat{\boldsymbol{K}}^*_{red}$ to zero and symbolically compute μ, μ_1, μ_2 depending on the specific solution case

- Compute the corresponding parameters β, α and κ

- Check if κ agrees with the assumption made in the first step. If not, assume another solution case and repeat the above steps. ***If yes, follow the next steps***:

- Compute the critical buckling load: plot κ vs. α, i.e. when the $N_{cr,min}$ is used as a reference axial loading on the beam, it will be equivalent to saying Λ_{LBA} vs. $\sqrt{2} \cdot L / L_{eff}$ where $L_{eff} = 0.778\sqrt{Rt}$ for ν = 0.3

- For a given α value, compute the different κ values corresponding to different buckling modes. Compute the corresponding μ, μ_1, μ_2 values for each α and κ combination and substitute them in $\hat{\boldsymbol{K}}^*_{red}$

- Compute $\hat{\boldsymbol{W}}^* = \left[W_A, \quad L \cdot \beta_A, \quad W_E, \quad L \cdot \beta_E\right]^T$ from the given boundary conditions and eigenvector of $\hat{\boldsymbol{K}}^*_{red}$ corresponding to the zero eigenvalue

- Compute $\boldsymbol{c} = \left[c_1, \quad c_2, \quad c_3, \quad c_4\right]^T$ from $\hat{\boldsymbol{W}}^* = \boldsymbol{U}_{hom} \cdot \boldsymbol{c}$ for a given (α, κ) pair

- Compute the buckling eigenmode using the fundamental solution function for the respective solution case $w(\xi) = f^T(\xi) \cdot \boldsymbol{c}$. Vary the value of the already computed κ values to produce other buckling modes

C.8 Illustrative examples, results and comparison

For illustration purposes, the elastic buckling strength and buckling eigenmodes of a cylindrical shell, Figure C.3, with the following same set of geometric, material and loading conditions but with different boundary conditions will be analytically computed.

***Geometry*:** R/t = 500; t = 1.0 cm; L/R = 1.0

***Loading*:** meridional ring compressive loading

***Material properties*:** E = 21000 kN/cm^2; ν = 0.3; f_y = 24.0 kN/cm^2

In the analytical computation of the elastic buckling strength and buckling eigenmodes, the step-by-step procedure discussed in Chapter C.7 will be followed.

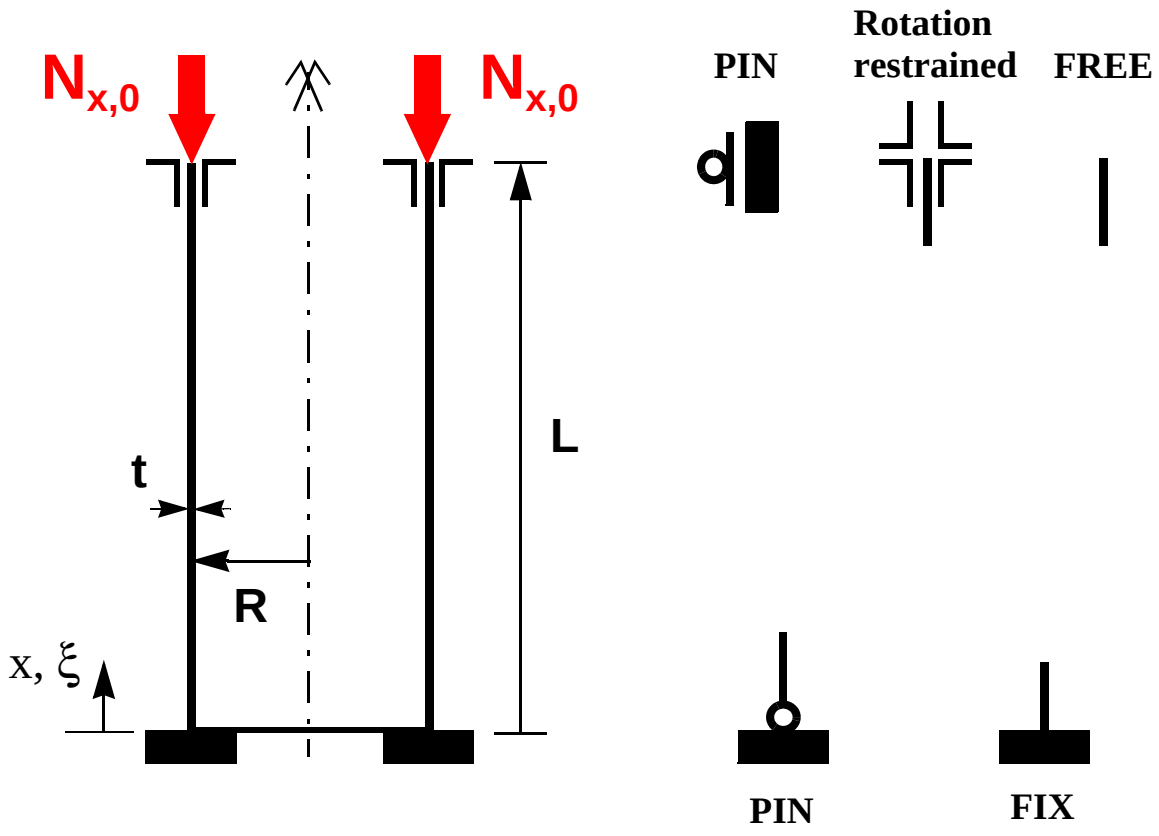

Figure C.3 Axially compressed cylindrical shell

C.8.1 Elastic buckling strength computation

C.8.1.1 Example-1: Pinned bottom and top edges

From the given boundary conditions,

$$w(\xi = 0) = w(\xi = 1) = 0 \qquad \text{(Eq. C.94)}$$

Using the already developed beam stiffness matrix and the boundary conditions of the current problem, it can be seen that the reduced beam stiffness matrix will be a 2 x 2 matrix. To obtain the buckling eigenvalues, the determinant of the reduced beam stiffness matrix should be zero. In doing so, a solution case is assumed and the parameters μ, μ_1, μ_2 will be computed depending on the specific solution case which will be used in computing the corresponding parameters β, α and κ. A check will be made if the value of the computed κ agrees with the assumed value. If there is no such agreement or if there exist no solution to the case considered, a different case is assumed and the computations are repeated until a solution which agrees with the assumption exists. This procedure is discussed below for the current problem.

Case - 1:

$$\kappa = \frac{\beta^2}{\alpha^2} < 1 \qquad \mu_1 = \alpha\sqrt{\frac{(1-\kappa)}{2}} \qquad \mu_2 = \alpha\sqrt{\frac{(1+\kappa)}{2}} \qquad \text{(Eq. C.95)}$$

Setting the determinant of the reduced beam stiffness matrix to zero will give

$$(1 + e^{4\mu_1}) - 2e^{2\mu_1}\cos(2\mu_2) = 0 \qquad \text{(Eq. C.96)}$$

which leads to

$$\cos(2\mu_2) = \frac{(1 + e^{4\mu_1})}{2e^{2\mu_1}} \qquad \text{(Eq. C.97)}$$

(Eq. C.97) will lead to a single possible solution with $\mu_1 = \mu_2 = 0$ at which the left and right-hand-side expressions intersect. For a given α, this solution leads to no specific value for κ. Hence, no buckling is possible under this solution case and therefore another solution case needs to be considered, as discussed below.

Case - 2:

$$\kappa = \frac{\beta^2}{\alpha^2} = 1 \qquad \mu = \mu_1 = \mu_2 = \alpha = \beta \tag{Eq. C.98}$$

Setting the determinant of the reduced beam stiffness matrix to zero will give

$$\sin(\mu) = 0 \tag{Eq. C.99}$$

which leads to

$$\mu = n \cdot \pi = \alpha = \beta \tag{Eq. C.100}$$

with n representing the number of buckle half-waves. It can also be written as

$$\alpha^2 = \beta^2 = n^2 \cdot \pi^2 \tag{Eq. C.101}$$

Substituting the expresssion for α, (Eq. C.101) gives the number of buckle half-waves for buckling under the current solution case as:

$$n^2 = \frac{L^2}{\pi^2} \cdot \sqrt{\frac{c}{EJ}} \tag{Eq. C.102}$$

The buckle half-wave length can then be computed from the axial length of the beam (or meridional length of the cylinder) and using the number of buckle half-waves as follows:

$$l_{half-wave} = \frac{L}{n} = \pi \cdot \sqrt[4]{\frac{EJ}{c}} = \frac{\pi}{\sqrt{2}} \cdot \frac{\sqrt{R \cdot t}}{\sqrt[4]{3(1-\nu^2)}} \tag{Eq. C.103}$$

$$l_{half-wave} = \frac{\pi}{\sqrt{2}} \cdot L_{eff} = 2.444 \frac{\sqrt{R \cdot t}}{\sqrt{2}} \tag{Eq. C.104}$$

Substituting the expresssion for β and using (Eq. C.102), (Eq. C.101) gives the expression for the buckling load as

$$N_{xo,\,cr} = 2 \cdot \frac{n^2 \pi^2}{L^2} \cdot EJ = 2\sqrt{c \cdot EJ} \tag{Eq. C.105}$$

This axial load will be the minimum possible buckling load if there will exist a solution under case-3 (i.e. $\kappa > 0$) or will be the only buckling load if there will exist no possible buckling solution under case-3. The first argument comes from the fact that the buckling load is proportional to the κ value and the κ value in solution case-3 is greater than that of solution case-2.

Case - 3:

$$\kappa = \frac{\beta^2}{\alpha^2} > 1 \qquad \mu_1 = \alpha\sqrt{\kappa - \sqrt{\kappa^2 - 1}} = \sqrt{\beta^2 - \sqrt{\beta^4 - \alpha^4}}$$

$$\mu_2 = \alpha\sqrt{\kappa + \sqrt{\kappa^2 - 1}} = \sqrt{\beta^2 + \sqrt{\beta^4 - \alpha^4}} \qquad \text{(Eq. C.106)}$$

Setting the determinant of the reduced beam stiffness matrix to zero will give

$$(\mu_1^2 - \mu_2^2)^2 \sin(\mu_1)\sin(\mu_2) = 0 \qquad \text{(Eq. C.107)}$$

There are different possibilities which make (Eq. C.107) true. One of these possibilities is when $\mu_1 = \mu_2$ which will lead to $\kappa = 1$, contradicting the solution case and therefore can not be a solution. The other possibilities are when $\sin(\mu_1) = 0$ or $\sin(\mu_2) = 0$ or both are zero at the same time. The general solution for this particular situation is when

$$\mu_1 = n \cdot \pi \qquad \text{(Eq. C.108)}$$

$$\mu_2 = m \cdot \pi \qquad \text{(Eq. C.109)}$$

with the following two necessary conditions:

- $n \neq m$ **otherwise it contradicts the current solution case; and**
- $n \in Integer$ **and m having any value or vice versa (i.e. only the letter changes: n or m, otherwise the same).**

The following discussion uses the variable n as the integer. It can be checked that using m as the integer will result in the same expressions as will be obtained using n as an integer.

$$\mu_1^2 = (n \cdot \pi)^2 = \beta^2 - \sqrt{\beta^4 - \alpha^4} \qquad \text{(Eq. C.110)}$$

which can be re-written as

$$(n^2\pi^2 - \beta^2)^2 = \beta^4 - \alpha^4 \qquad \text{(Eq. C.111)}$$

$$2\beta^2 = n^2\pi^2 + \frac{\alpha^4}{n^2\pi^2} \qquad \text{(Eq. C.112)}$$

Substituting the values for β and α & letting $\gamma = \alpha^4/\pi^4$, the buckling load can be expressed as

$$N_{xo,\,cr,\,n} = \frac{n^2\pi^2 \cdot EJ}{L^2} \cdot \left(1 + \left(\frac{\alpha}{n\pi}\right)^4\right) \qquad \text{(Eq. C.113)}$$

$$N_{xo,\,cr,\,n} = \frac{\pi^2 \cdot EJ}{L^2} \cdot \left(n^2 + \frac{\gamma}{n^2}\right) \qquad \text{(Eq. C.114)}$$

When n = 1 and there is no elastic foundation (c = 0), (Eq. C.114) represents the Euler's buckling load for a pin-ended column, i.e.

$$N_{cr,\,Euler} = \frac{\pi^2 \cdot EJ}{L^2} \qquad \text{(Eq. C.115)}$$

Thus the buckling load in (Eq. C.114) can be expressed in terms of the Euler's buckling load for a pin-ended column as follows

$$\frac{N_{xo,\,cr,\,n}}{N_{cr,\,Euler}} = n^2 + \frac{\gamma}{n^2} = n^2 + \left(\frac{\sqrt{\gamma}}{n}\right)^2 \qquad \text{(Eq. C.116)}$$

The buckling load according to the current solution case (i.e. case-3) can also be expressed in terms of the minimum buckling load obtained using solution case-2 as follows:

$$\frac{N_{xo,\,cr,\,n}}{N_{xo,\,cr,\,min}} = \frac{1}{2\sqrt{\gamma}} \cdot \left(n^2 + \left(\frac{\sqrt{\gamma}}{n}\right)^2\right) \qquad \text{(Eq. C.117)}$$

where

$$\frac{N_{xo,\,cr,\,min}}{N_{cr,\,Euler}} = 2\sqrt{\gamma} \qquad \text{(Eq. C.118)}$$

On the other hand, it can easily be checked that when a reference axial loading equal to the classical buckling load of a cylindrical shell is used, the variable κ represents the buckling load factor Λ_{LBA}, i.e.

$$\kappa = \beta^2/\alpha^2 = \Lambda_{LBA} = \frac{N_{xo,\,cr,\,n}}{N_{xo,\,cr,\,min}} \qquad \text{(Eq. C.119)}$$

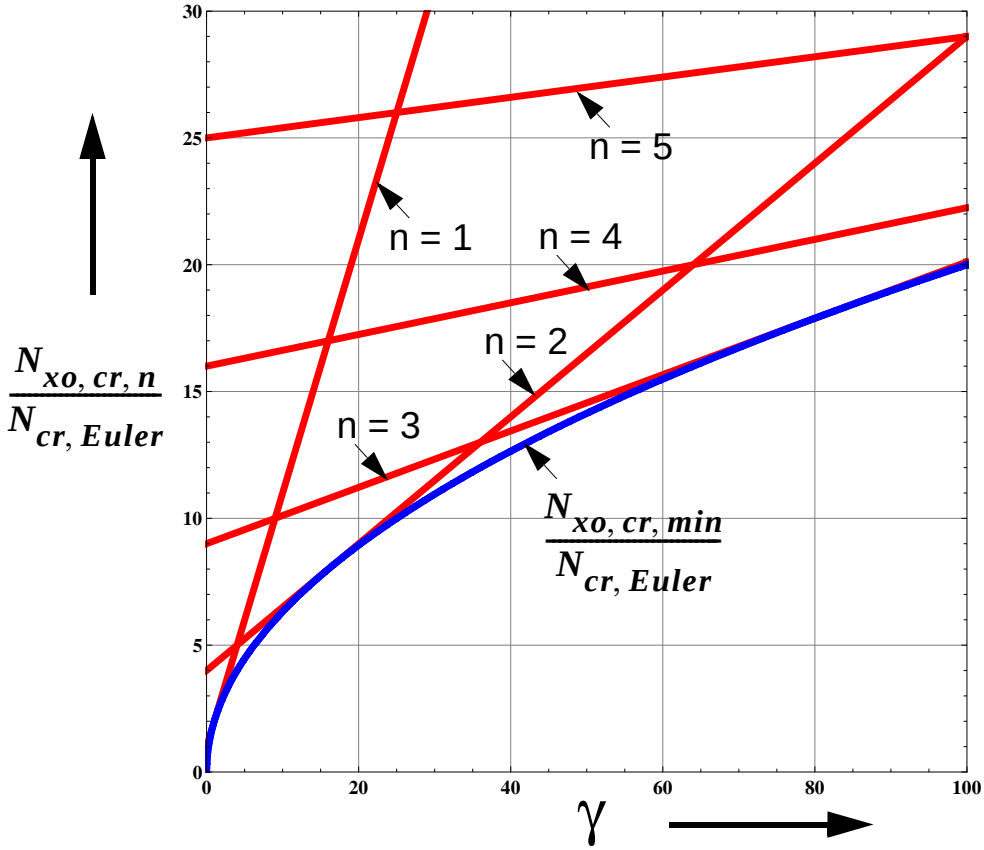

Figure C.4 Linear elastic buckling strength: Pin-pin, case-3

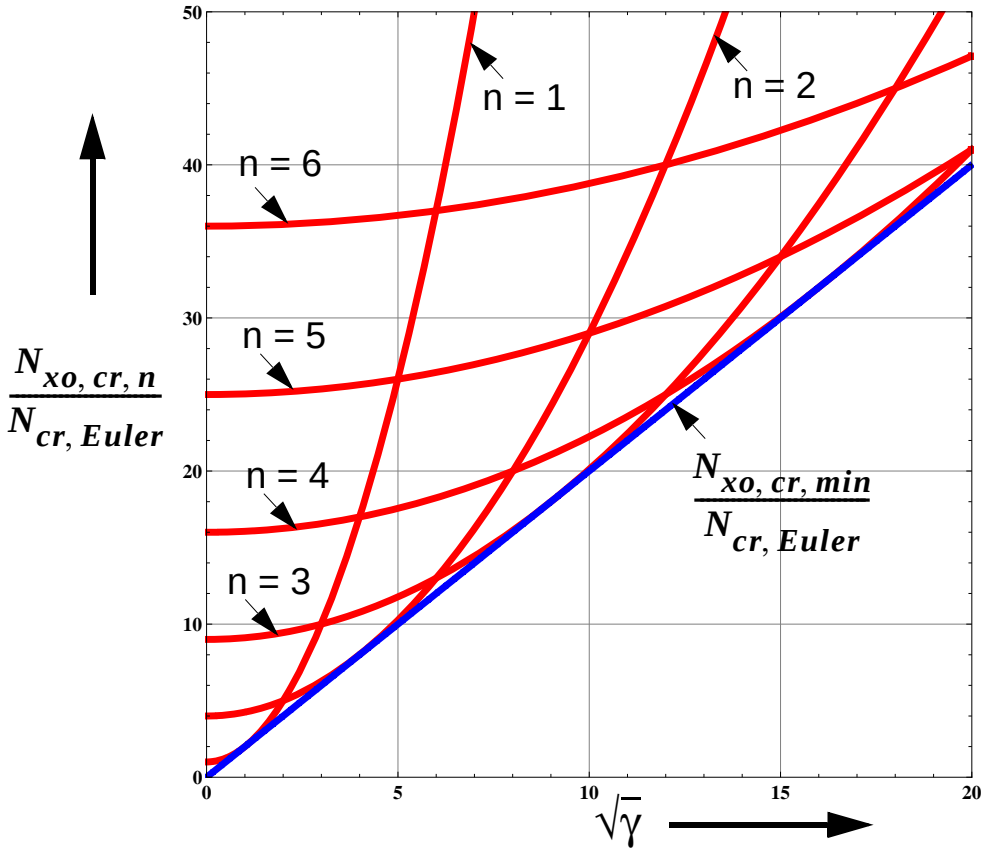

Figure C.5 Linear elastic buckling strength: Pin-pin, case-3

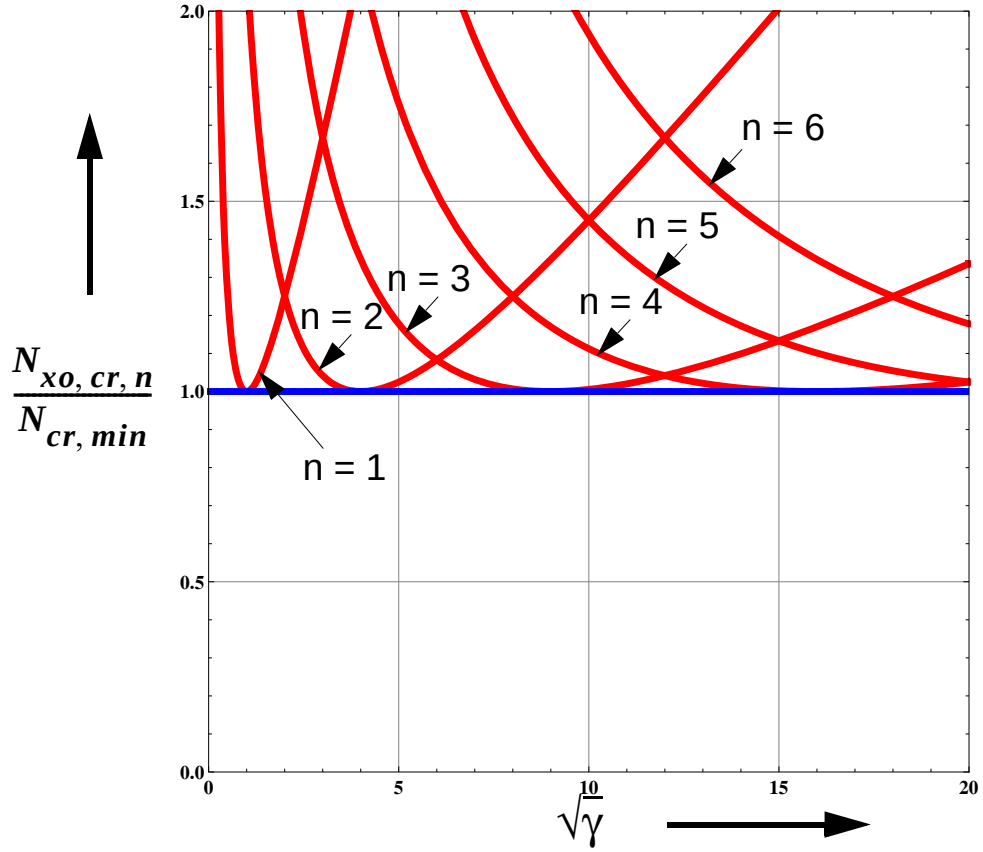

Figure C.6 Linear elastic buckling strength: Pin-pin, case-3

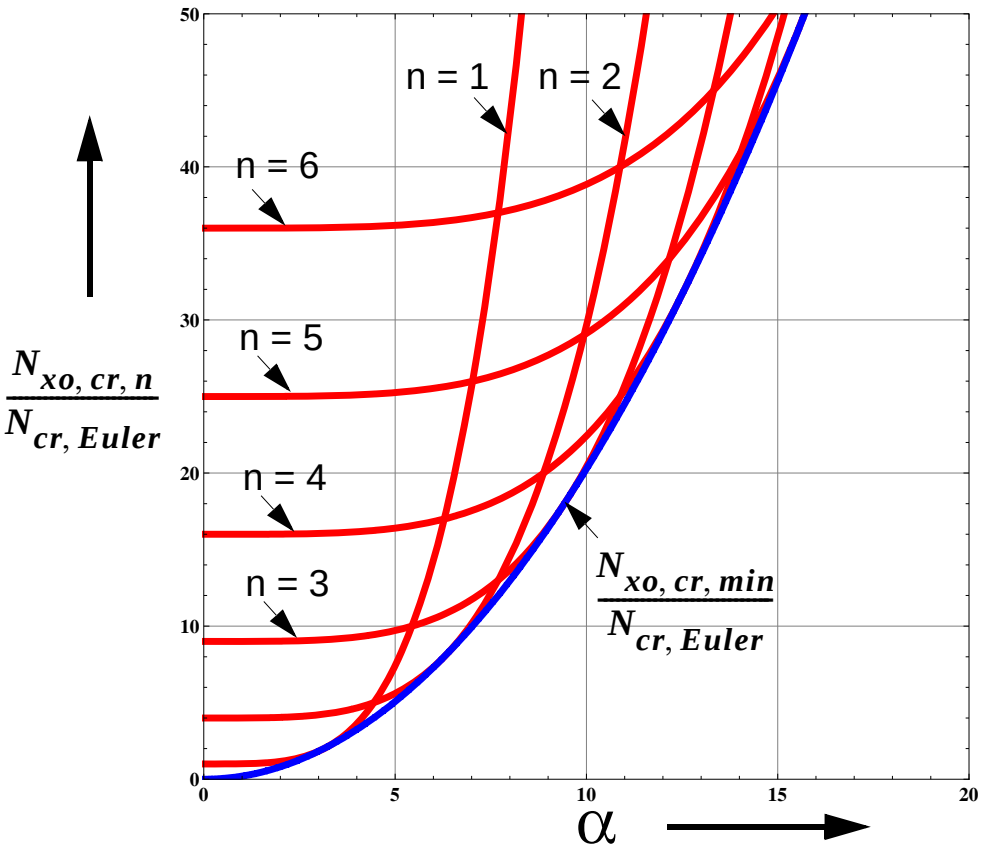

Figure C.7 Linear elastic buckling strength: Pin-pin, case-3

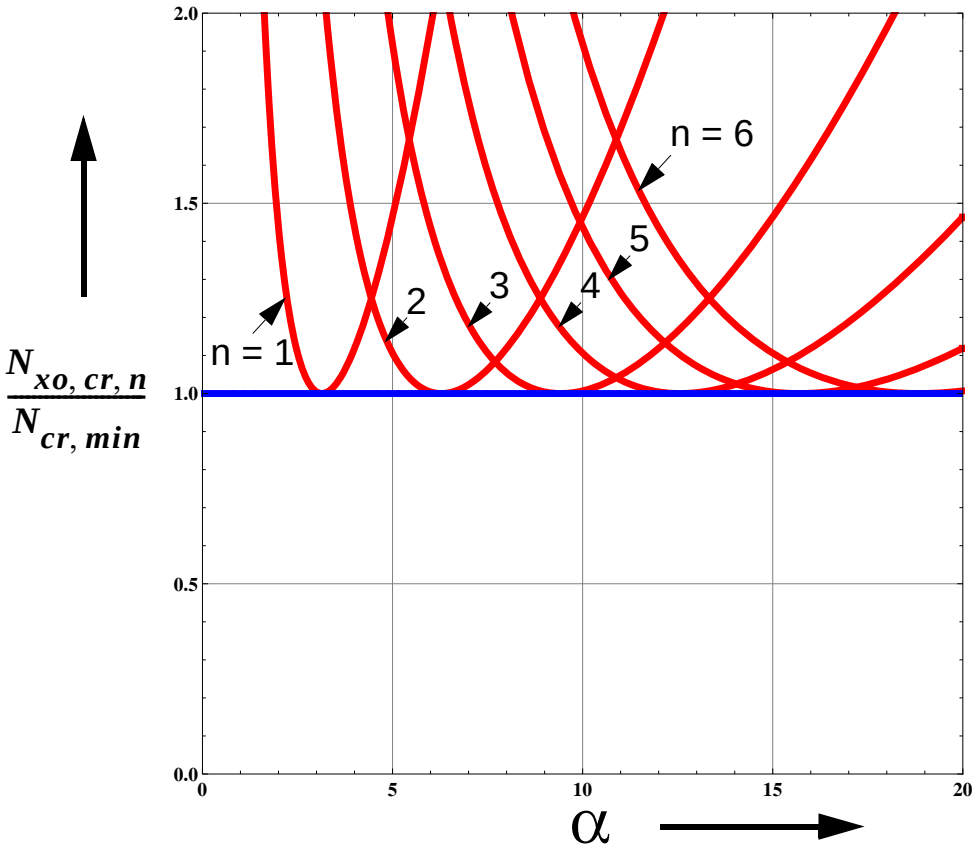

Figure C.8 Linear elastic buckling strength: Pin-pin, case-3

C.8.1.2 Example-2: Pinned bottom and rotationally restrained top edges

From the given boundary conditions,

$$w(\xi = 0) = \beta_x(\xi = 1) = 0 \qquad \text{(Eq. C.120)}$$

Using the already developed beam stiffness matrix and the boundary conditions of the current example, it can be seen that the reduced beam stiffness matrix will be a 2 x 2 matrix. To obtain the buckling eigenvalues, the determinant of the reduced beam stiffness matrix should be zero. In doing so, a solution case is assumed and the parameters μ, μ_1, μ_2 will be computed depending on the specific solution case which will be used in computing the corresponding parameters β, α and κ. A check will be made if the value of the computed κ agrees with the assumed value. If there is no such agreement or if there exist no solution to the case considered, a different case is assumed and the computations are repeated until a solution which agrees with the assumption exists. This procedure is discussed below for the current example.

Case - 1:

$$\kappa = \frac{\beta^2}{\alpha^2} < 1 \qquad \mu_1 = \alpha\sqrt{\frac{(1-\kappa)}{2}} \qquad \mu_2 = \alpha\sqrt{\frac{(1+\kappa)}{2}} \qquad \text{(Eq. C.121)}$$

Setting the determinant of the reduced beam stiffness matrix to zero will give

$$(1 + e^{4\mu_1}) + 2e^{2\mu_1}\cos(2\mu_2) = 0 \qquad \text{(Eq. C.122)}$$

which leads to

$$\cos(2\mu_2) = -\frac{(1 + e^{4\mu_1})}{2e^{2\mu_1}} \qquad \text{(Eq. C.123)}$$

(Eq. C.123) will lead to no possible solution since the left and right-hand-side expressions do not intersect. Hence, no buckling is possible under this solution case and therefore another solution case needs to be considered, as discussed below.

Case - 2:

$$\kappa = \frac{\beta^2}{\alpha^2} = 1 \qquad \mu = \mu_1 = \mu_2 = \alpha = \beta \tag{Eq. C.124}$$

Setting the determinant of the reduced beam stiffness matrix to zero will give

$$\cos(\mu) = 0 \tag{Eq. C.125}$$

which leads to

$$\mu = \frac{n \cdot \pi}{2} = \alpha = \beta \tag{Eq. C.126}$$

with n representing the number of buckle half-waves. It can also be written as

$$\alpha^2 = \beta^2 = \frac{n^2 \cdot \pi^2}{4} \tag{Eq. C.127}$$

Substituting the expresssion for α, (Eq. C.127) gives the number of buckle half-waves for buckling under the current solution case as:

$$n^2 = 4\frac{L^2}{\pi^2} \cdot \sqrt{\frac{c}{EJ}} \tag{Eq. C.128}$$

The buckle half-wave length can then be computed from the axial length of the beam (or meridional length of the cylinder) and using the number of buckle half-waves as follows:

$$l_{half-wave} = \frac{L}{n} = \frac{\pi}{2} \cdot \sqrt[4]{\frac{EJ}{c}} = \frac{\pi}{2\sqrt{2}} \cdot \frac{\sqrt{R \cdot t}}{\sqrt[4]{3(1-\nu^2)}} \tag{Eq. C.129}$$

$$l_{half-wave} = \frac{\pi}{2\sqrt{2}} \cdot L_{eff} = 1.222\frac{\sqrt{R \cdot t}}{\sqrt{2}} \tag{Eq. C.130}$$

Substituting the expresssion for β and using (Eq. C.128), (Eq. C.127) gives the expression for the buckling load as

$$N_{xo,\,cr} = \frac{1}{2} \cdot \frac{n^2\pi^2}{L^2} \cdot EJ = 2\sqrt{c \cdot EJ} \tag{Eq. C.131}$$

This axial load will be the minimum possible buckling load if there will exist a solution under case-

3 (i.e. $\kappa > 0$) or will be the only buckling load if there will exist no possible buckling solution under case-3. The first argument comes from the fact that the buckling load is proportional to the κ value and the κ value in solution case-3 is greater than that of solution case-2.

Case - 3:

$$\kappa = \frac{\beta^2}{\alpha^2} > 1 \qquad \mu_1 = \alpha\sqrt{\kappa - \sqrt{\kappa^2 - 1}} = \sqrt{\beta^2 - \sqrt{\beta^4 - \alpha^4}}$$

$$\mu_2 = \alpha\sqrt{\kappa + \sqrt{\kappa^2 - 1}} = \sqrt{\beta^2 + \sqrt{\beta^4 - \alpha^4}} \qquad \text{(Eq. C.132)}$$

Setting the determinant of the reduced beam stiffness matrix to zero will give

$$(\mu_1^2 - \mu_2^2)^2 \cos(\mu_1)\cos(\mu_2) = 0 \qquad \text{(Eq. C.133)}$$

There are different possibilities which make (Eq. C.133) true. One of these possibilities is when $\mu_1 = \mu_2$ which will lead to $\kappa = 1$, contradicting the solution case and therefore can not be a solution. The other possibilities are when $\cos(\mu_1) = 0$ or $\cos(\mu_2) = 0$ or both are zero at the same time. The general solution for this particular situation is when

$$\mu_1 = \frac{n \cdot \pi}{2} \qquad \text{(Eq. C.134)}$$

$$\mu_2 = \frac{m \cdot \pi}{2} \qquad \text{(Eq. C.135)}$$

with the following two necessary conditions:

- $n \neq m$ **otherwise it contradicts the current solution case; and**
- $n \in Odd\ \ Integer$ **and m having any value or vice versa (i.e. only the letter changes: n or m, otherwise the same).**

The following discussion uses the variable n as the odd integer. It can be checked that using m as the odd integer will result in the same expressions as will be obtained using n as an odd integer.

$$\mu_1^2 = \left(\frac{n \cdot \pi}{2}\right)^2 = \beta^2 - \sqrt{\beta^4 - \alpha^4} \qquad \text{(Eq. C.136)}$$

which can be re-written as

$$\left(\frac{n^2\pi^2}{4} - \beta^2\right)^2 = \beta^4 - \alpha^4 \qquad \text{(Eq. C.137)}$$

$$2\beta^2 = \frac{n^2\pi^2}{4} + \frac{4\alpha^4}{n^2\pi^2} \quad \text{(Eq. C.138)}$$

Substituting the values for β and α & letting $\gamma = \alpha^4/\pi^4$, the buckling load can be expressed as

$$N_{xo,\,cr,\,n} = \frac{n^2\pi^2 \cdot EJ}{4L^2} \cdot \left(1 + \left(\frac{2\alpha}{n\pi}\right)^4\right) \quad \text{(Eq. C.139)}$$

$$N_{xo,\,cr,\,n} = \frac{\pi^2 \cdot EJ}{L^2} \cdot \left(\frac{n^2}{4} + \frac{4\gamma}{n^2}\right) \quad \text{(Eq. C.140)}$$

When n = 1 and there is no elastic foundation (c = 0), (Eq. C.140) represents the Euler's buckling load for a column pinned at one edge and rotationally restrained at the other edge, i.e.

$$N_{cr,\,Euler} = \frac{\pi^2 \cdot EJ}{4L^2} \quad \text{(Eq. C.141)}$$

Thus the buckling load in (Eq. C.114) can be expressed in terms of the Euler's buckling load for a such a column as follows

$$\frac{N_{xo,\,cr,\,n}}{N_{cr,\,Euler}} = n^2 + \frac{16\gamma}{n^2} = n^2 + \left(\frac{4\sqrt{\gamma}}{n}\right)^2 \quad \text{(Eq. C.142)}$$

The buckling load according to the current solution case (i.e. case-3) can also be expressed in terms of the minimum buckling load obtained using solution case-2 as follows:

$$\frac{N_{xo,\,cr,\,n}}{N_{xo,\,cr,\,min}} = \frac{1}{8\sqrt{\gamma}} \cdot \left(n^2 + \left(\frac{4\sqrt{\gamma}}{n}\right)^2\right) \quad \text{(Eq. C.143)}$$

where

$$\frac{N_{xo,\,cr,\,min}}{N_{cr,\,Euler}} = 8\sqrt{\gamma} \quad \text{(Eq. C.144)}$$

It can again be checked that when a reference axial loading equal to the classical buckling load of a cylindrical shell is used, the variable κ represents the buckling load factor Λ_{LBA}, i.e.

$$\kappa = \beta^2/\alpha^2 = \Lambda_{LBA} = \frac{N_{xo,\,cr,\,n}}{N_{xo,\,cr,\,min}} \quad \text{(Eq. C.145)}$$

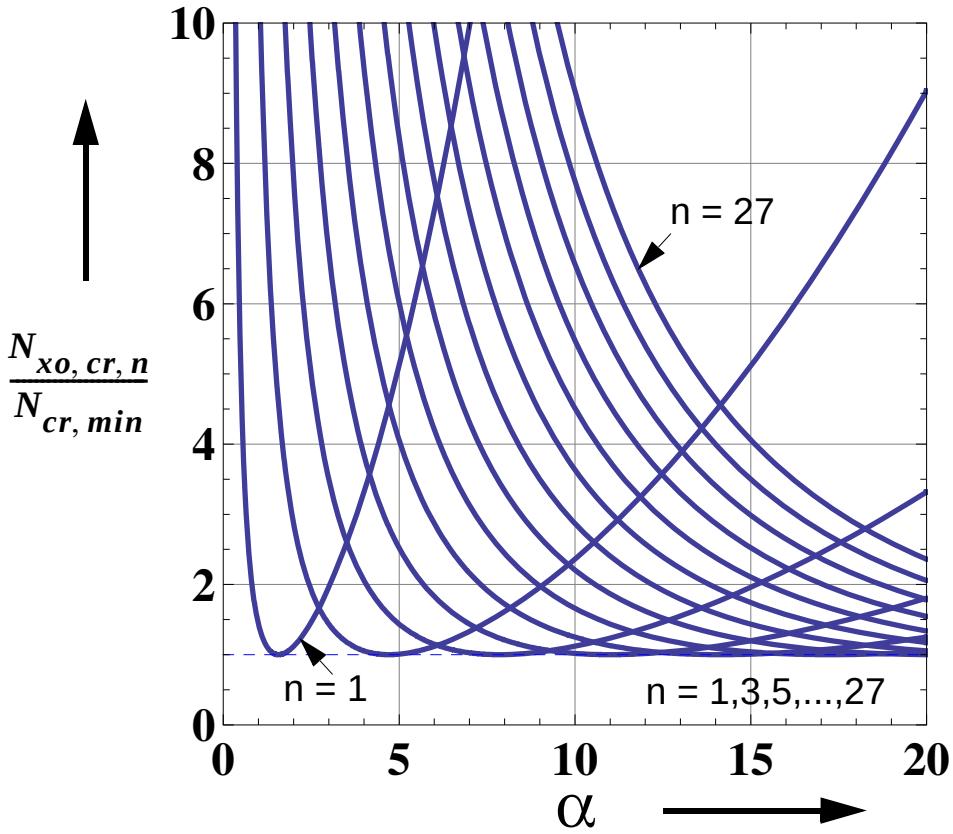

Figure C.9 Linear elastic buckling strength: Pin-RotFix, case-3

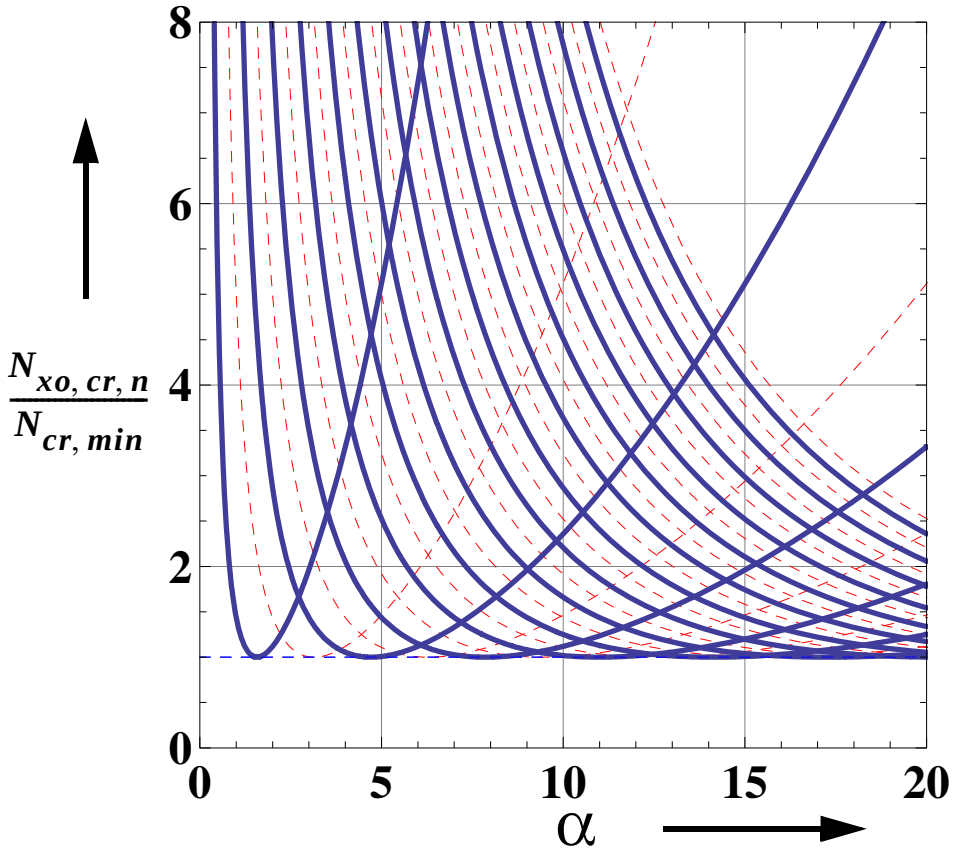

Figure C.10 Linear elastic buckling strength: Pin-RotFix & Pin-Pin, case-3

C.8.1.3 Example-2: Fixed bottom and free top edges

From the given boundary conditions,

$$w(\xi = 0) = \beta_x(\xi = 0) = 0 \qquad \text{(Eq. C.146)}$$

Using the already developed beam stiffness matrix and the boundary conditions of the current example, it can be seen that the reduced beam stiffness matrix will be a 2 x 2 matrix.. To obtain the buckling eigenvalues, the determinant of the reduced beam stiffness matrix should be zero. In doing so, a solution case is assumed and the parameters μ, μ_1, μ_2 will be computed depending on the specific solution case which will be used in computing the corresponding parameters β, α and κ. A check will be made if the value of the computed κ agrees with the assumed value. If there is no such agreement or if there exist no solution to the case considered, a different case is assumed and the computations are repeated until a solution which agrees with the assumption exists. This procedure is discussed below for the current problem.

Case - 1:

$$\kappa = \frac{\beta^2}{\alpha^2} < 1 \qquad \mu_1 = \alpha\sqrt{\frac{(1-\kappa)}{2}} \qquad \mu_2 = \alpha\sqrt{\frac{(1+\kappa)}{2}} \qquad \text{(Eq. C.147)}$$

Setting the determinant of the reduced beam stiffness matrix to zero will give

$$4\mu_1^4 e^{2\mu_1}\sin(\mu_2)^2 + \mu_1^2\mu_2^2 \cdot (3 + 4e^{2\mu_1} + 3e^{4\mu_1} + 6e^{2\mu_1}\cos(2\mu_2)) - \mu_2^4(-1 + e^{2\mu_1})^2 = 0 \qquad \text{(Eq. C.148)}$$

(Eq. C.148) can be directly expressed interms of α and κ, (Eq. C.147), where the relationship can be plotted (κ vs. α) from which the buckling load factor can be read, Figure C.11.

Case - 2:

$$\kappa = \frac{\beta^2}{\alpha^2} = 1 \qquad \mu = \mu_1 = \mu_2 = \alpha = \beta \tag{Eq. C.149}$$

Setting the determinant of the reduced beam stiffness matrix to zero will give

$$5 - 2\mu^2 + 3\cos(2\mu) = 0 \tag{Eq. C.150}$$

This relationship will only be true for $\mu = \pm 1.1896$ which means $\alpha = \beta = 1.1896$ and hence, a single possible solution occurs only when $(\alpha, \kappa) = (1.1896, 1)$. This solution will not be applicable to the illustrative example since for the considered cylindrical shell $\alpha = 40.65$.

Case - 3:

$$\kappa = \frac{\beta^2}{\alpha^2} > 1$$

$$\mu_1 = \alpha\sqrt{\kappa - \sqrt{\kappa^2 - 1}} = \sqrt{\beta^2 - \sqrt{\beta^4 - \alpha^4}}$$

$$\mu_2 = \alpha\sqrt{\kappa + \sqrt{\kappa^2 - 1}} = \sqrt{\beta^2 + \sqrt{\beta^4 - \alpha^4}} \tag{Eq. C.151}$$

Setting the determinant of the reduced beam stiffness matrix to zero will give

$$2\mu_1^2\mu_2^2 - \mu_1\mu_2(\mu_1^2 + \mu_2^2)\sin(\mu_1)\sin(\mu_2) - (\mu_1^4 + \mu_2^4)\cos(\mu_1)\cos(\mu_2) = 0 \tag{Eq. C.152}$$

(Eq. C.152) can be directly expressed interms of α and κ, (Eq. C.151), where the relationship can be plotted (κ vs. α) from which the buckling load factor can be read, Figure C.12. A comparison plot is also shown in Figure C.13 where the current solution case is compared with that of the pinned bottom and rotationally restrained top edges beam. The number of half-wave buckles for a given cylindrical shell of the current example type and solution case can be estimated with the help of the comparison with the solution for the pinned bottom and rotationally restrained top edges beam.

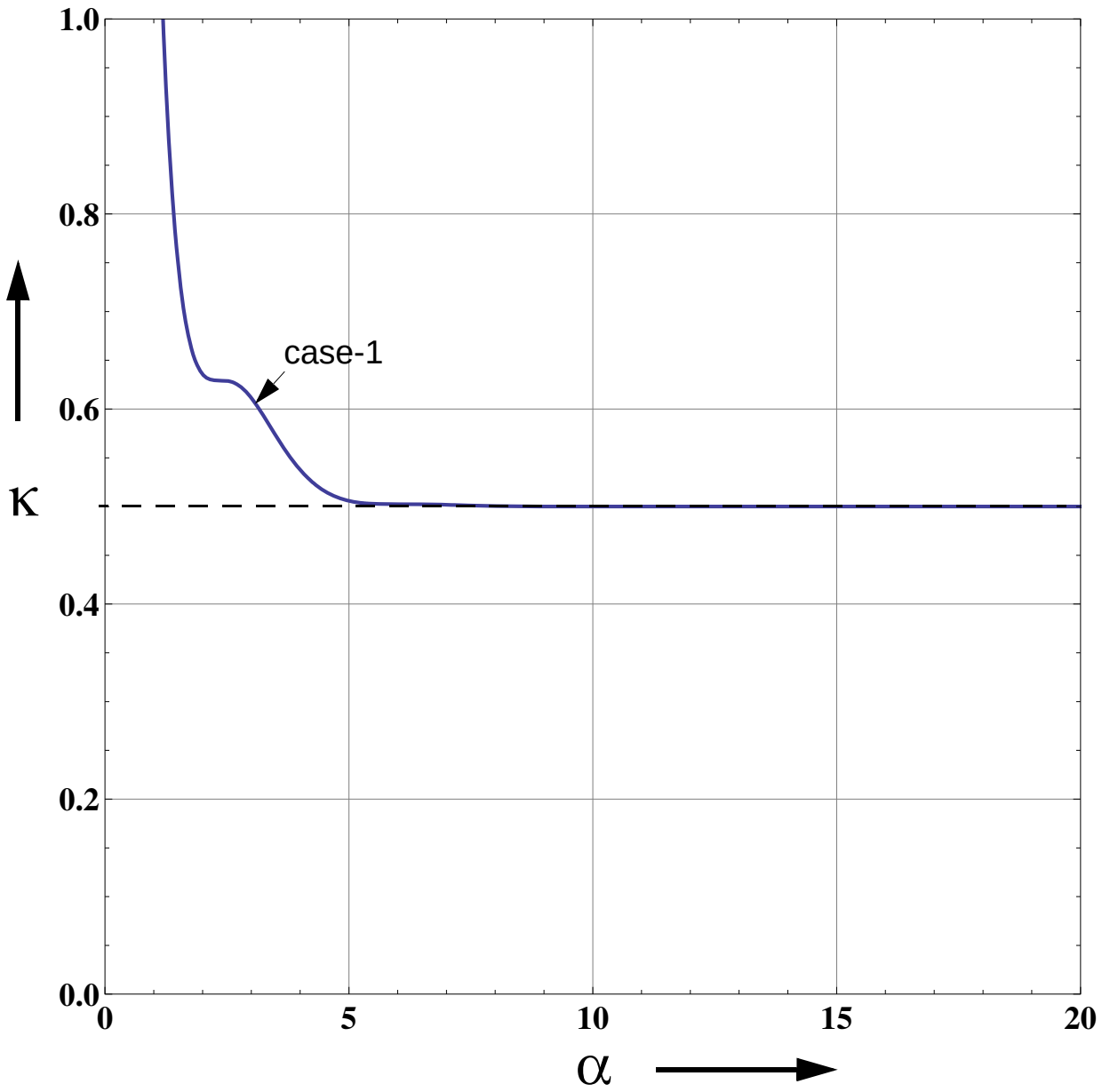

Figure C.11 Linear elastic buckling strength: Fix-Free, case-1

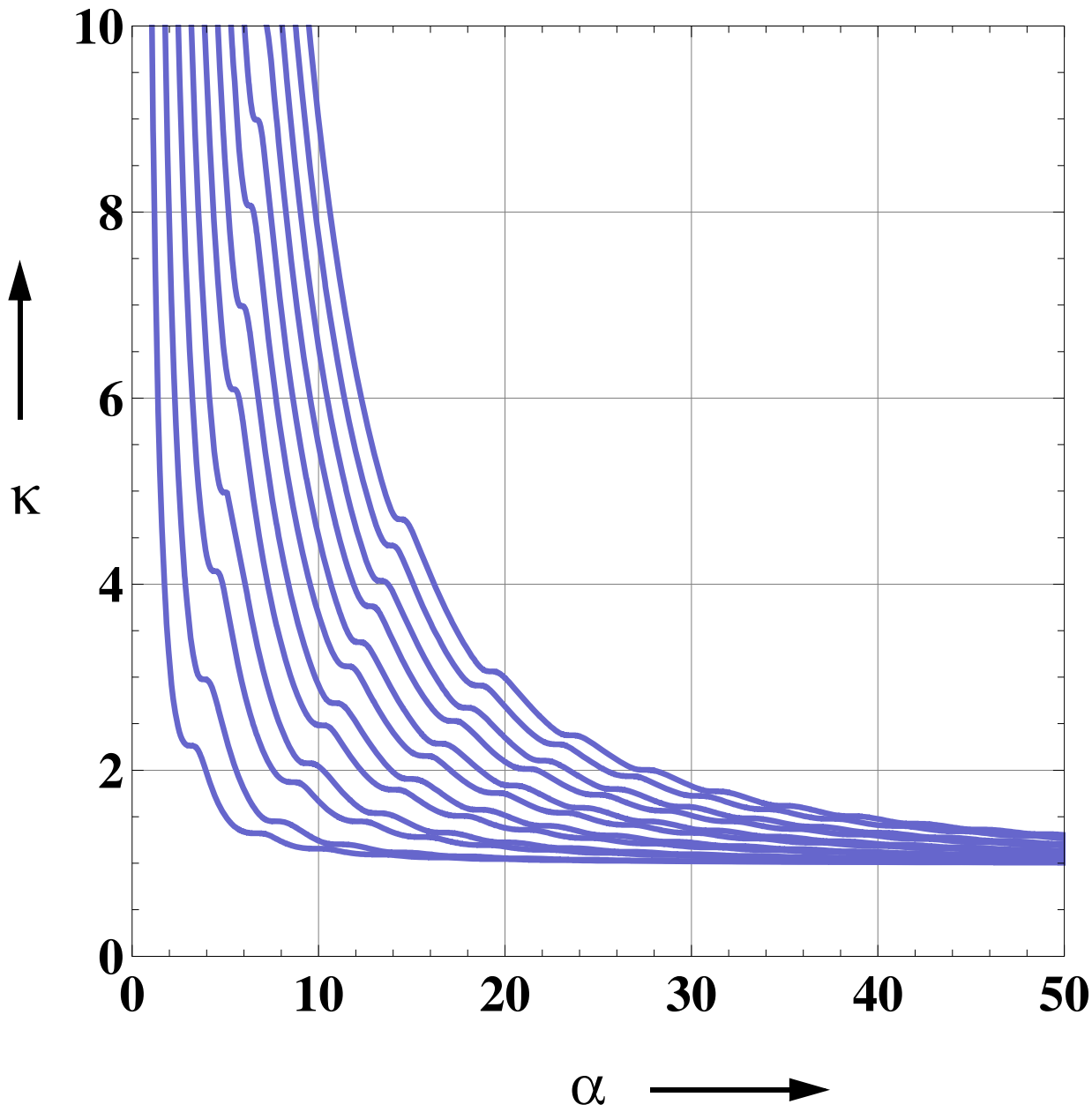

Figure C.12 Linear elastic buckling strength: Fix-Free, case-3

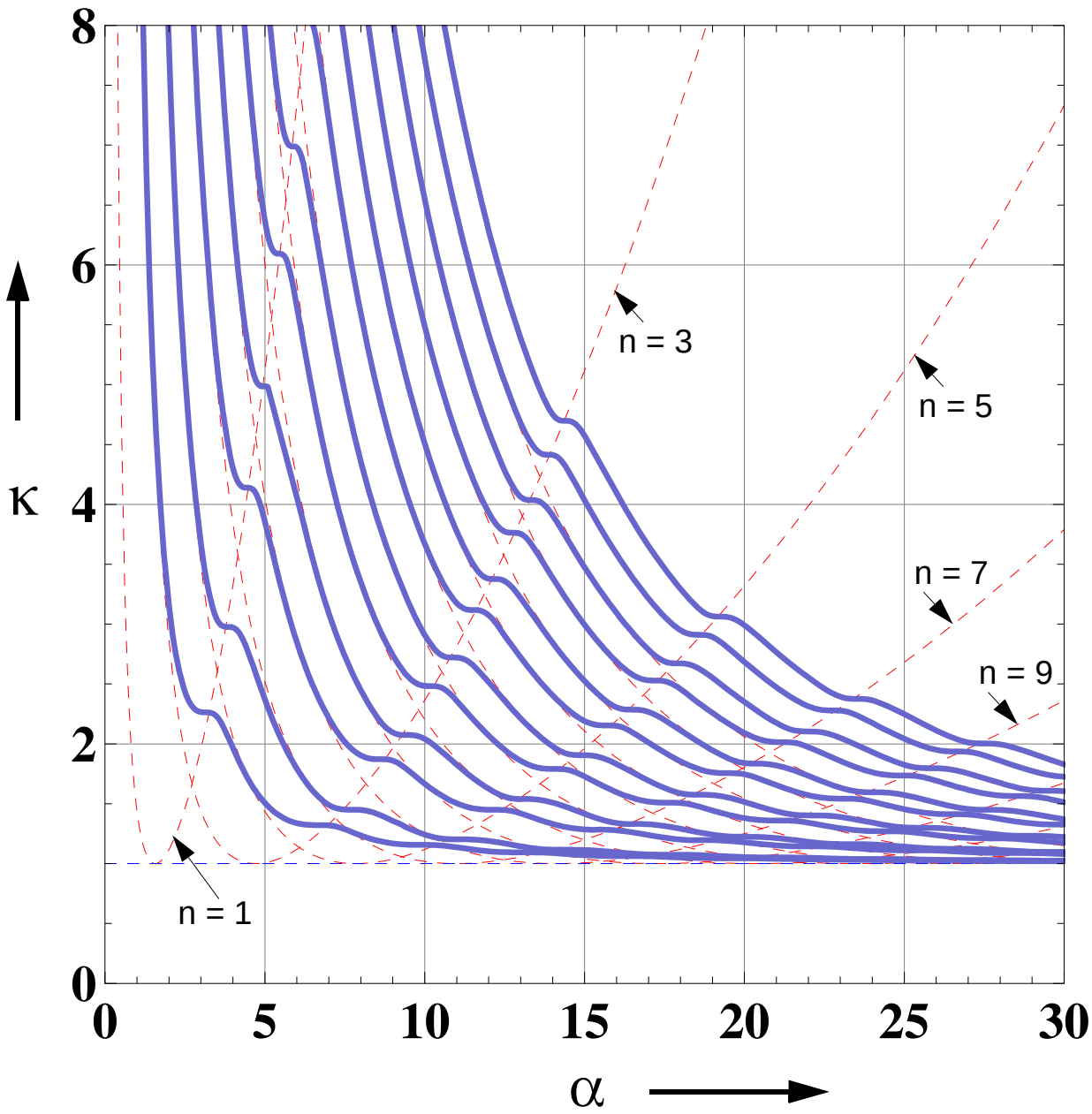

Figure C.13 Linear elastic buckling strength: Fix-Free & Pin-RotFix, case-3

C.8.1.4 Example-4: Fixed bottom and rotationally restrained top edges

From the given boundary conditions,

$$w(\xi = 0) = \beta_x(\xi = 0) = \beta_x(\xi = 1) = 0 \quad \text{(Eq. C.153)}$$

Using the already developed beam stiffness matrix and the boundary conditions of the current problem, it can be seen that the reduced beam stiffness matrix will have a single element. To obtain the buckling eigenvalues, the determinant of the reduced beam stiffness matrix should be zero. This, in the current context, means the single element of the reduced stiffness matrix should set to zero. In doing so, a solution case is assumed and the parameters μ, μ_1, μ_2 will be computed depending on the specific solution case which will be used in computing the corresponding parameters β, α and κ. A check will be made if the value of the computed κ agrees with the assumed value. If there is no such agreement or if there exist no solution to the case considered, a different case is assumed and the computations are repeated until a solution which agrees with the assumption exists. This procedure is discussed below for the current problem.

Case - 1:

$$\kappa = \frac{\beta^2}{\alpha^2} < 1 \qquad \mu_1 = \alpha\sqrt{\frac{(1-\kappa)}{2}} \qquad \mu_2 = \alpha\sqrt{\frac{(1+\kappa)}{2}} \quad \text{(Eq. C.154)}$$

Setting the determinant of the reduced beam stiffness matrix to zero will give

$$\mu_2(1 - e^{-4\mu_1}) - 2\mu_1 e^{2\mu_1}\sin(2\mu_2) = 0 \quad \text{(Eq. C.155)}$$

$$\frac{\sin(2\mu_2)}{\mu_2} = \frac{(1 - e^{-4\mu_1})}{2\mu_1 e^{2\mu_1}} \quad \text{(Eq. C.156)}$$

(Eq. C.97) will lead to no possible solution as the left and right-hand-terms will not intersect each other. Hence, no buckling is possible under this solution case and therefore another solution case needs to be considered, as discussed below.

Case - 2:

$$\kappa = \frac{\beta^2}{\alpha^2} = 1 \qquad \mu = \mu_1 = \mu_2 = \alpha = \beta \tag{Eq. C.157}$$

Setting the determinant of the reduced beam stiffness matrix to zero will give

$$\mu + \sin(\mu)\cos(\mu) = 0 \tag{Eq. C.158}$$

$$2\mu + \sin(2\mu) = 0 \tag{Eq. C.159}$$

This relationship will only be true for $\mu = 0$ which means $\alpha = \beta = 0$ and hence, no buckling will occur under this solution case and therefore another solution case needs to be considered.

Case - 3:

$$\kappa = \frac{\beta^2}{\alpha^2} > 1 \qquad \begin{aligned} \mu_1 &= \alpha\sqrt{\kappa - \sqrt{\kappa^2 - 1}} = \sqrt{\beta^2 - \sqrt{\beta^4 - \alpha^4}} \\ \mu_2 &= \alpha\sqrt{\kappa + \sqrt{\kappa^2 - 1}} = \sqrt{\beta^2 + \sqrt{\beta^4 - \alpha^4}} \end{aligned} \tag{Eq. C.160}$$

Setting the determinant of the reduced beam stiffness matrix to zero will give

$$\mu_1 \sin(\mu_1)\cos(\mu_2) - \mu_2 \cos(\mu_1)\sin(\mu_2) = 0 \tag{Eq. C.161}$$

$$\mu_1 \tan(\mu_1) - \mu_2 \tan(\mu_2) = 0 \tag{Eq. C.162}$$

$\mu_1 = \mu_2$ would lead to $\kappa = 1$ which contradicts the assumption $\kappa > 1$. Instead, (Eq. C.162) can be directly expressed interms of α and κ, (Eq. C.160), where the relationship can be plotted (κ vs. α) from which the buckling load factor can be read, Figure C.14 (or when zoomed Figure C.15). A comparison plot is also shown in Figure C.16 where the current solution case is compared with that of the pinned bottom and top edges beam. The number of half-wave buckles for a given cylindrical shell of the current example type and solution case can be estimated with the help of the comparison with the solution for the pinned bottom and top edges beam.

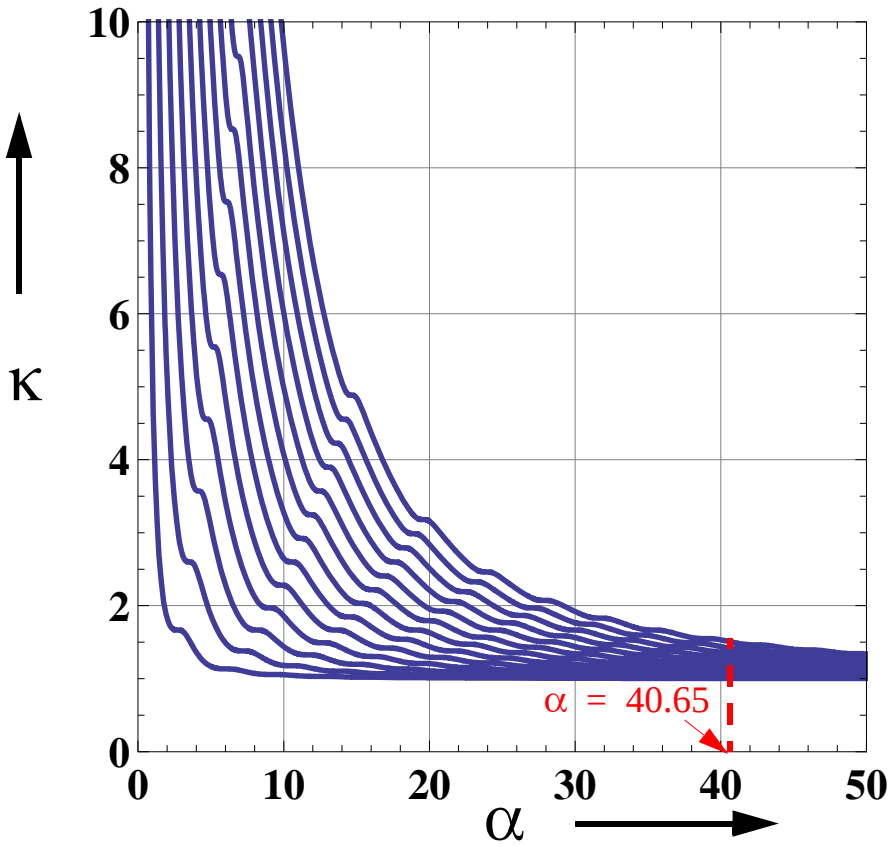

Figure C.14 Linear elastic buckling strength: Fix-RotFix, case-3

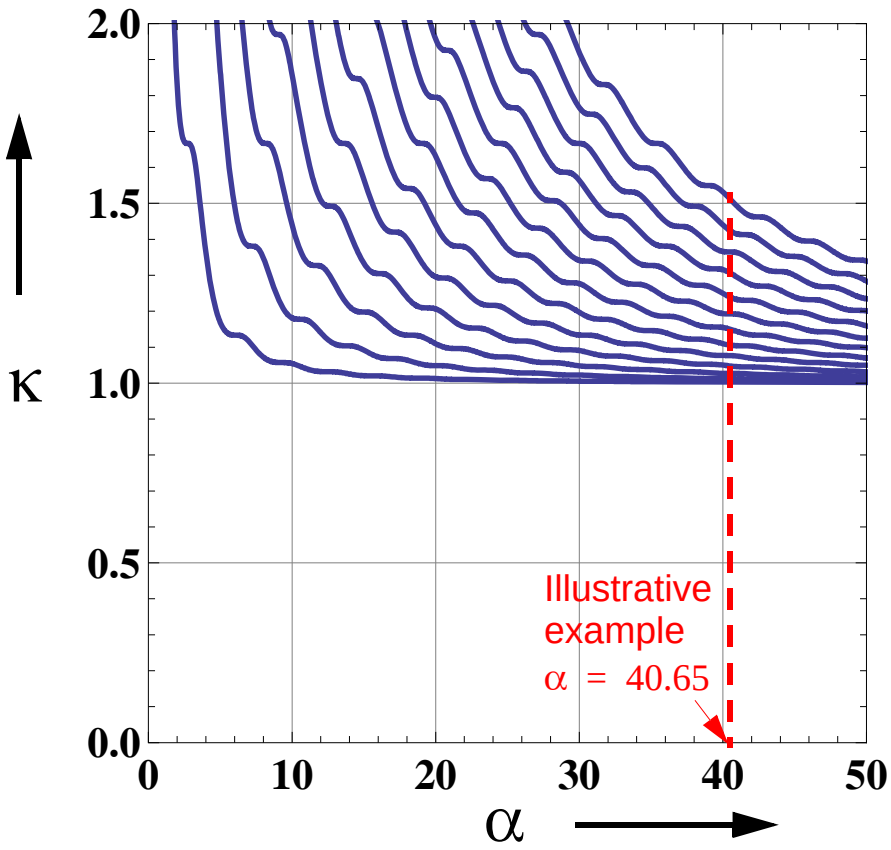

Figure C.15 Linear elastic buckling strength: Fix-RotFix, case-3 (Figure C.14 zoomed)

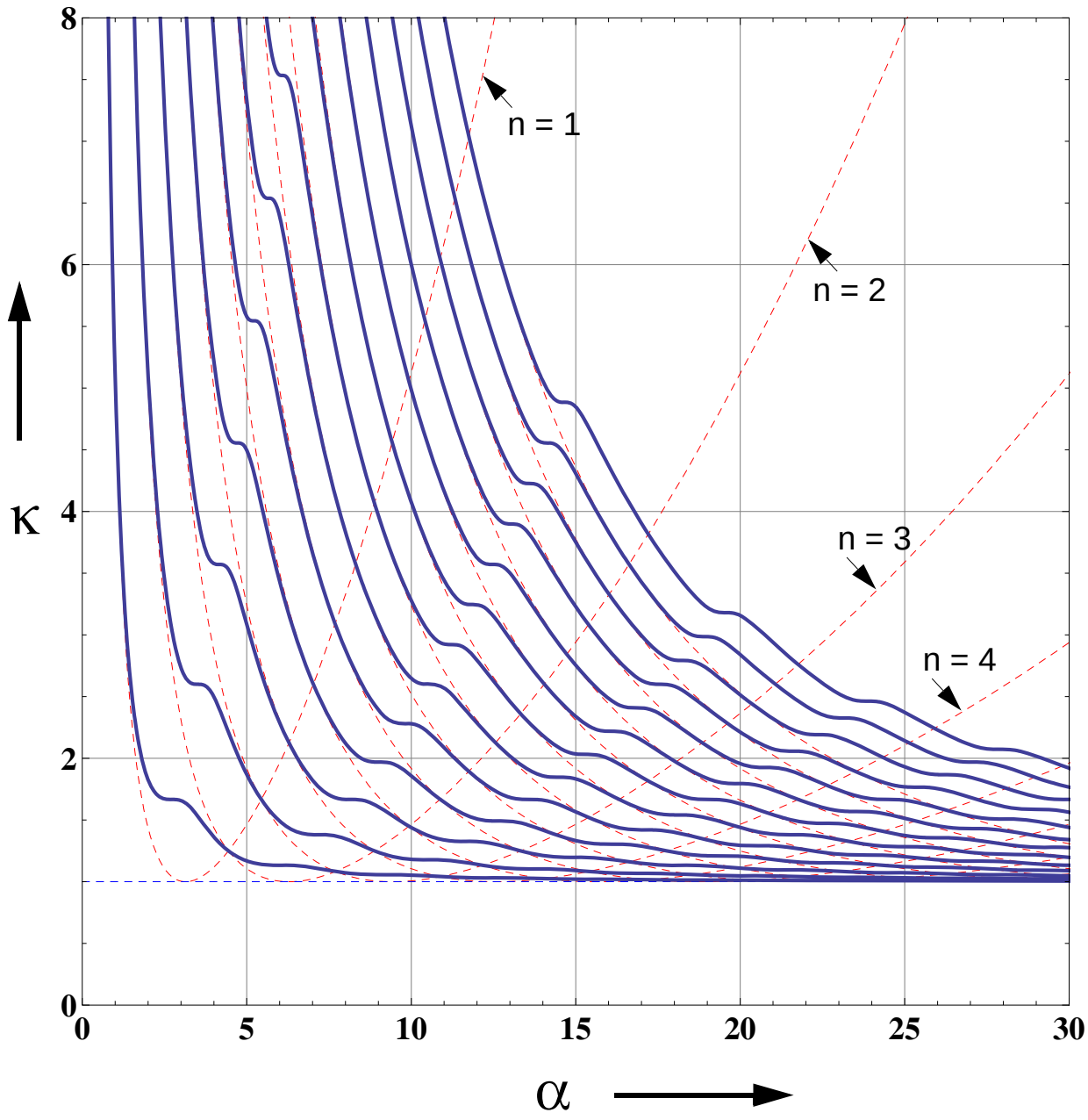

Figure C.16 Linear elastic buckling strength: Fix-RotFix & Pin-Pin, case-3

C.8.2 Elastic buckling eigenmode computation

Once the k versus a relationships are known for a given cylindrical shell and a specific solution case, the following step-by-step procedure (part of the procedure discussed in Chapter C.7) will be used to compute the elastic buckling eigenmodes.

- For a given α value, compute the different κ values corresponding to different buckling modes. Compute the corresponding μ, μ_1, μ_2 values for each α and κ combination and substitute them in $\hat{\boldsymbol{K}}^*_{red}$

- Compute $\hat{\boldsymbol{W}}^* = \left[W_A, \quad \mathrm{L} \cdot \beta_A, \quad W_E, \quad \mathrm{L} \cdot \beta_E\right]^T$ from the given boundary conditions and eigenvector of $\hat{\boldsymbol{K}}^*_{red}$ corresponding to the zero eigenvalue

- Compute $\boldsymbol{c} = \left[c_1, \quad c_2, \quad c_3, \quad c_4\right]^T$ from $\hat{\boldsymbol{W}}^* = \boldsymbol{U}_{hom} \cdot \boldsymbol{c}$ for a given (α, κ) pair

- Compute the buckling eigenmode using the fundamental solution function for the respective solution case $w(\xi) = f^T(\xi) \cdot \boldsymbol{c}$. Vary the value of the already computed κ values to produce other buckling modes

For the illustrative cylindrical shell example considered,

$$\alpha = L \cdot \sqrt[4]{c/EJ} = \sqrt{2} \cdot L/L_{eff} = 40.65 \qquad \text{(Eq. C.163)}$$

where

$$L_{eff} = \frac{1}{\sqrt[4]{3(1-\nu^2)}} \sqrt{R \cdot t} \qquad \text{(Eq. C.164)}$$

C.8.2.1 Fixed bottom and free top edges

The analytical solution for the first elastic buckling eigenmode (for solution case-1) and corresponding buckling strength for the illustrative cylindrical shell with fixed bottom and free top edges are shown in Figure C.17. The respective finite element small displacement linear buckling analysis results are also shown in Figure C.18 for comparison purposes.

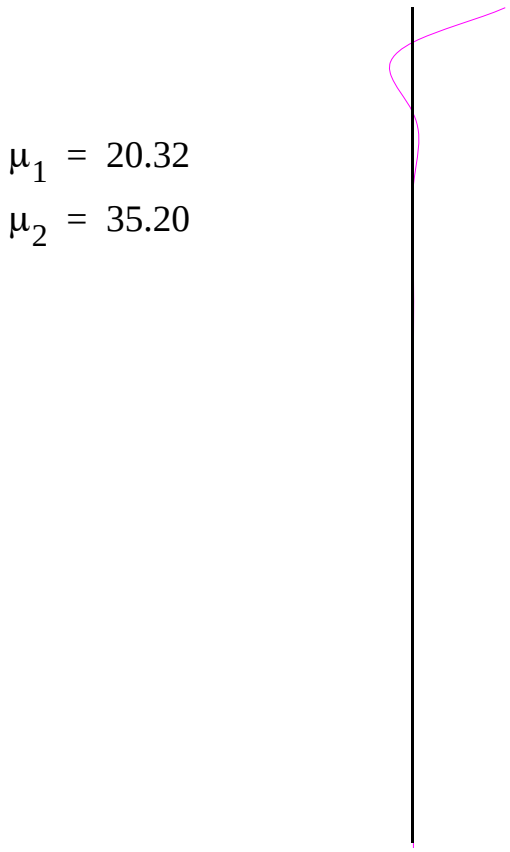

Figure C.17 Analytic linear elastic buckling eigenmode-1: $\Lambda_{LBA} = 0.5$, Fix-RotFix

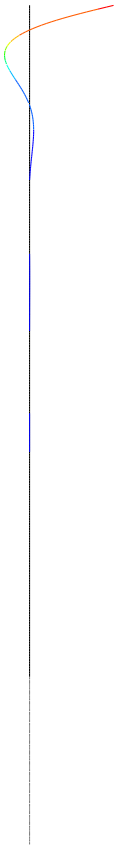

Figure C.18 FEM linear elastic buckling eigenmode-1: $\Lambda_{LBA} = 0.5$, Fix-RotFix

C.8.2.2 Fixed bottom and rotationally restrained top edges

The analytical solution for the first six elastic buckling eigenmodes (for solution case-3) and corresponding buckling strengths for the illustrative cylindrical shell with fixed bottom and rotationally restrained top edges are shown in Figure C.19 to Figure C.30. The respective finite element small displacement linear buckling analysis results are also shown for comparison purposes.

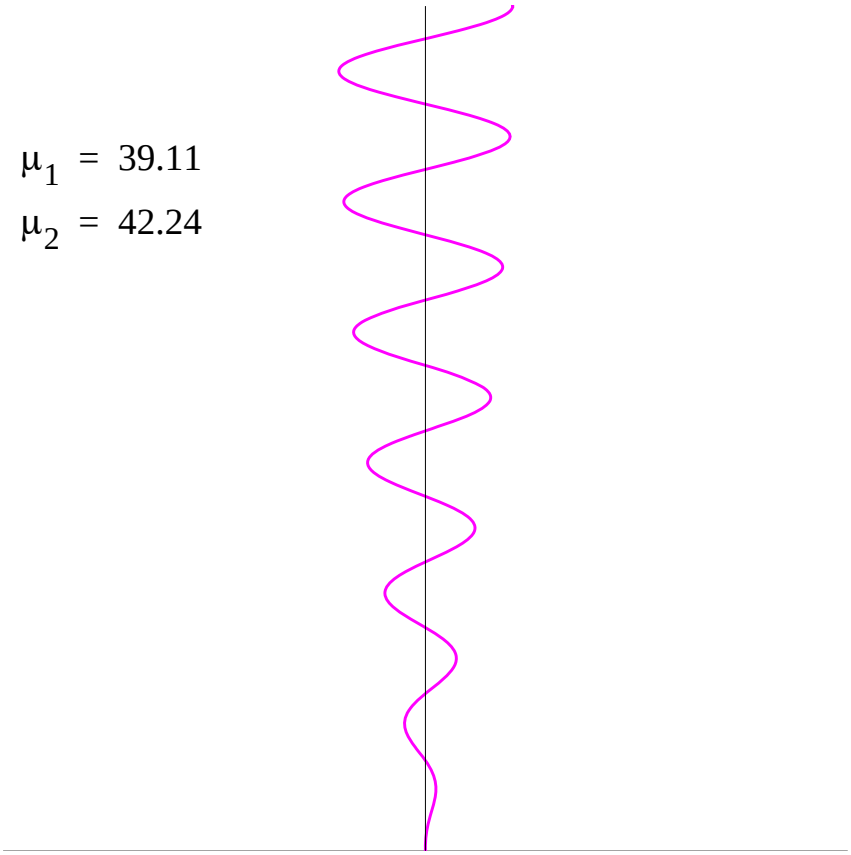

Figure C.19 Analytic linear elastic buckling eigenmode-1: $\Lambda_{LBA} = 1.0030$, Fix-RotFix

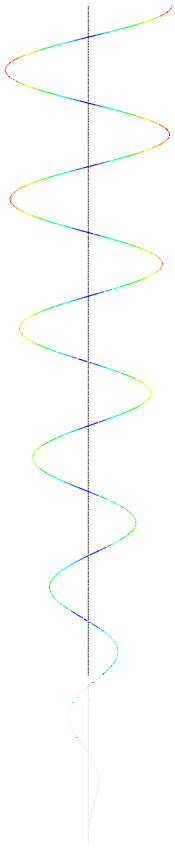

Figure C.20 FEM linear elastic buckling eigenmode-1: $\Lambda_{LBA} = 1.0024$, Fix-RotFix

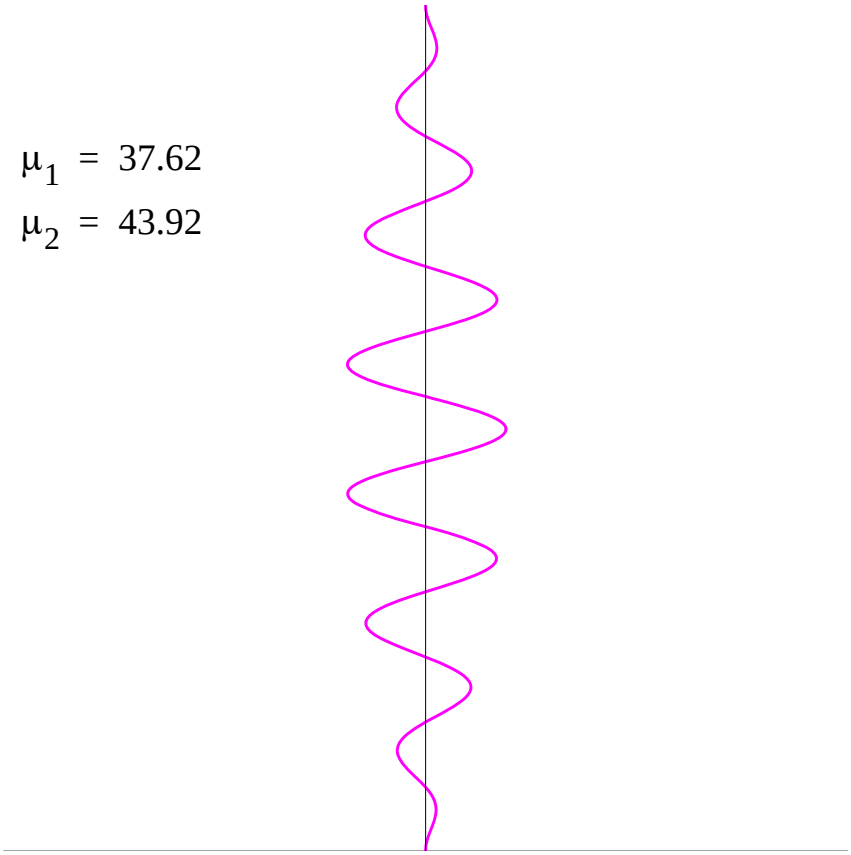

Figure C.21 Analytic linear elastic buckling eigenmode-2: $\Lambda_{LBA} = 1.0120$, Fix-RotFix

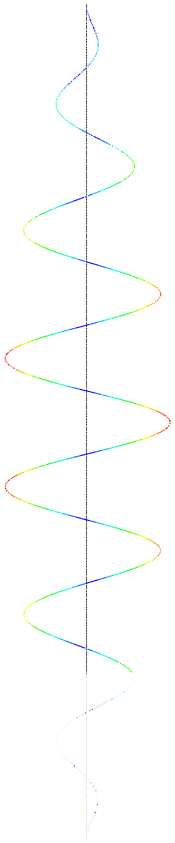

Figure C.22 FEM linear elastic buckling eigenmode-2: $\Lambda_{LBA} = 1.0113$, Fix-RotFix

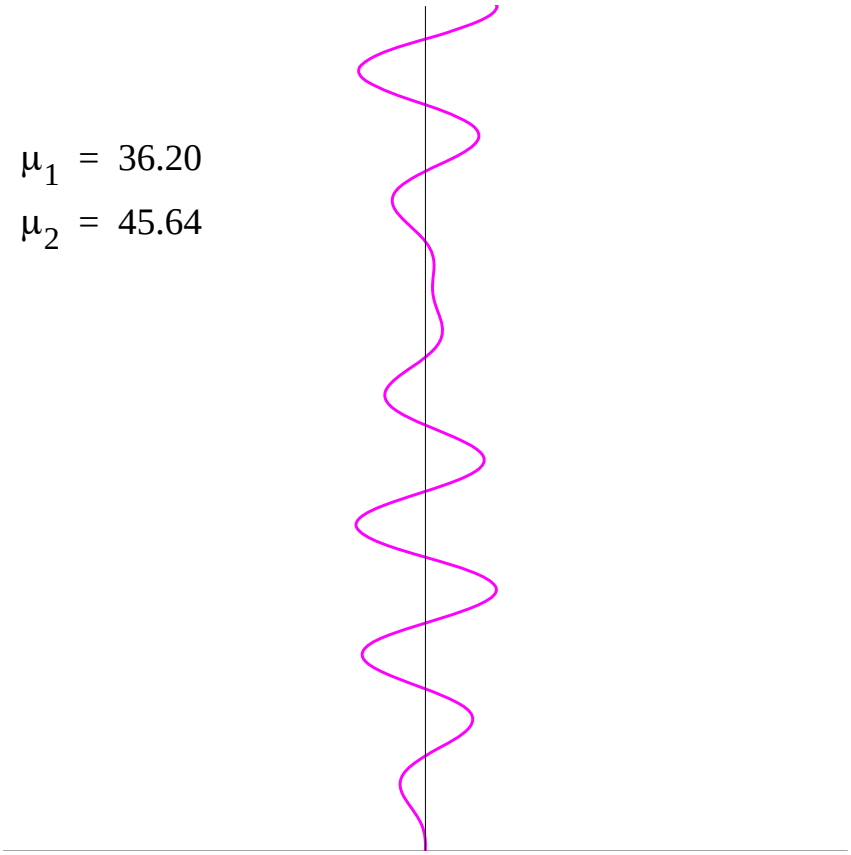

Figure C.23 Analytic linear elastic buckling eigenmode-3: $\Lambda_{LBA} = 1.0270$, Fix-RotFix

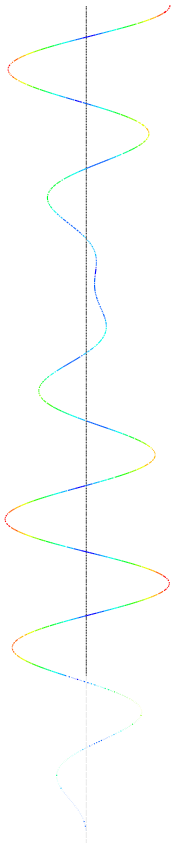

Figure C.24 FEM linear elastic buckling eigenmode-3: $\Lambda_{LBA} = 1.0263$, Fix-RotFix

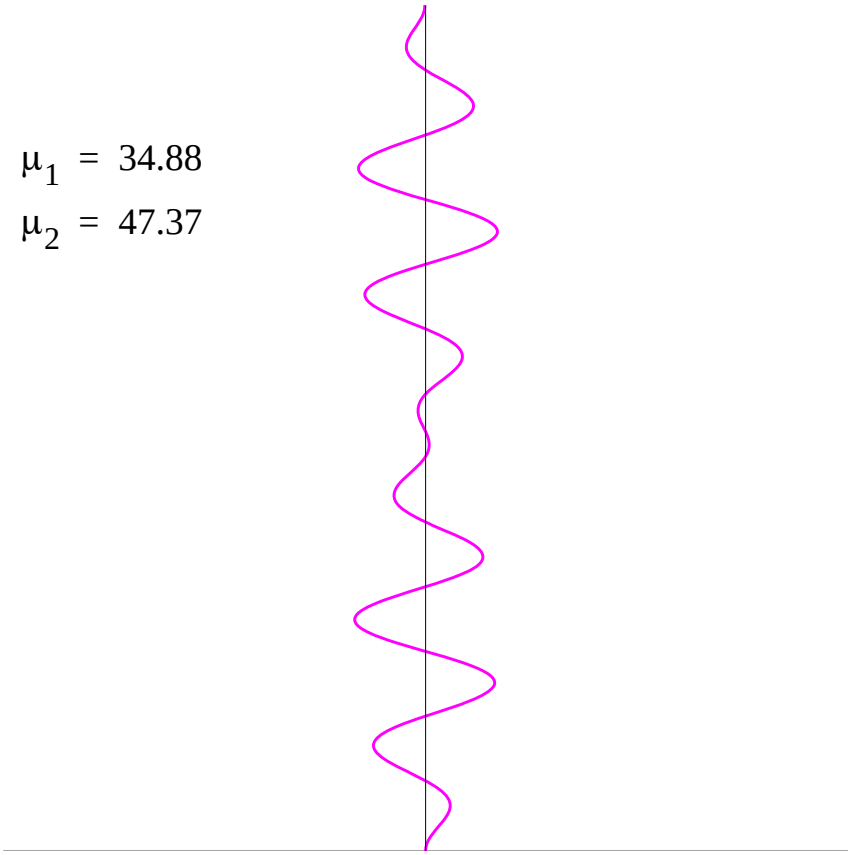

Figure C.25 Analytic linear elastic buckling eigenmode-4: $\Lambda_{LBA} = 1.0472$, Fix-RotFix

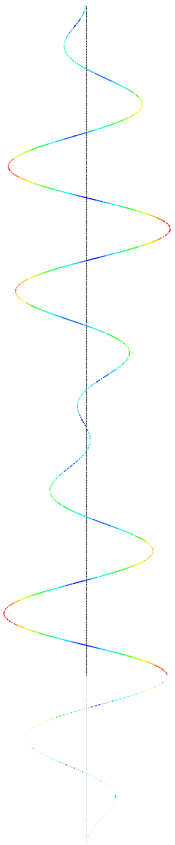

Figure C.26 FEM linear elastic buckling eigenmode-4: $\Lambda_{LBA} = 1.0462$, Fix-RotFix

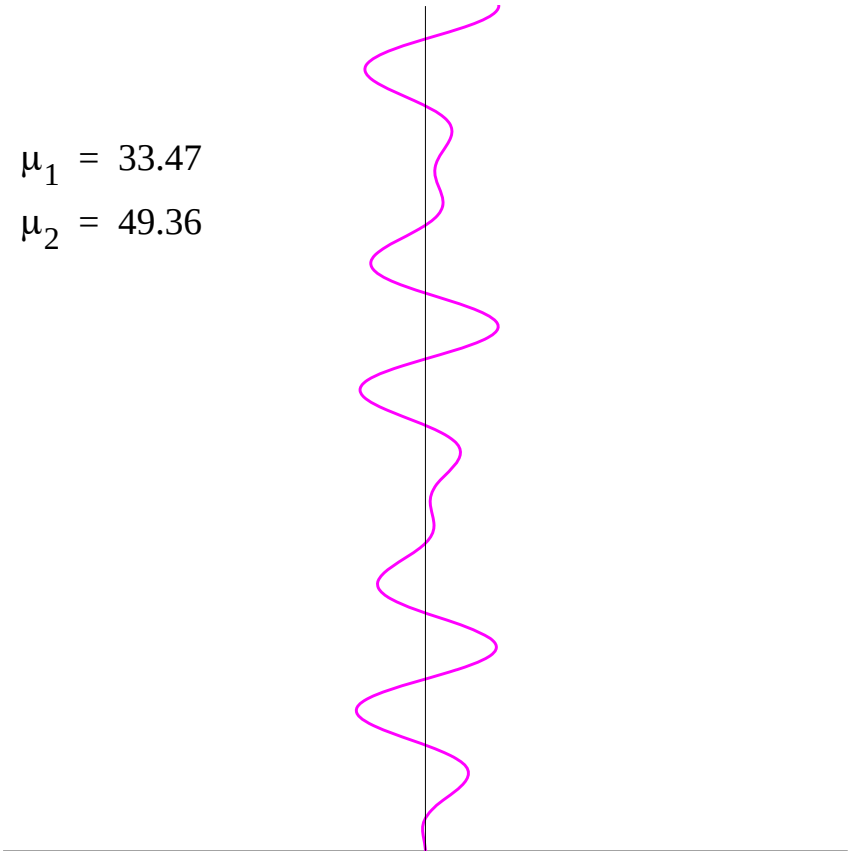

Figure C.27 Analytic linear elastic buckling eigenmode-5: $\Lambda_{LBA} = 1.0764$, Fix-RotFix

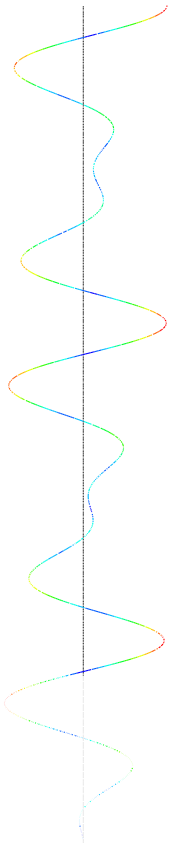

Figure C.28 FEM linear elastic buckling eigenmode-5: $\Lambda_{LBA} = 1.0754$, Fix-RotFix

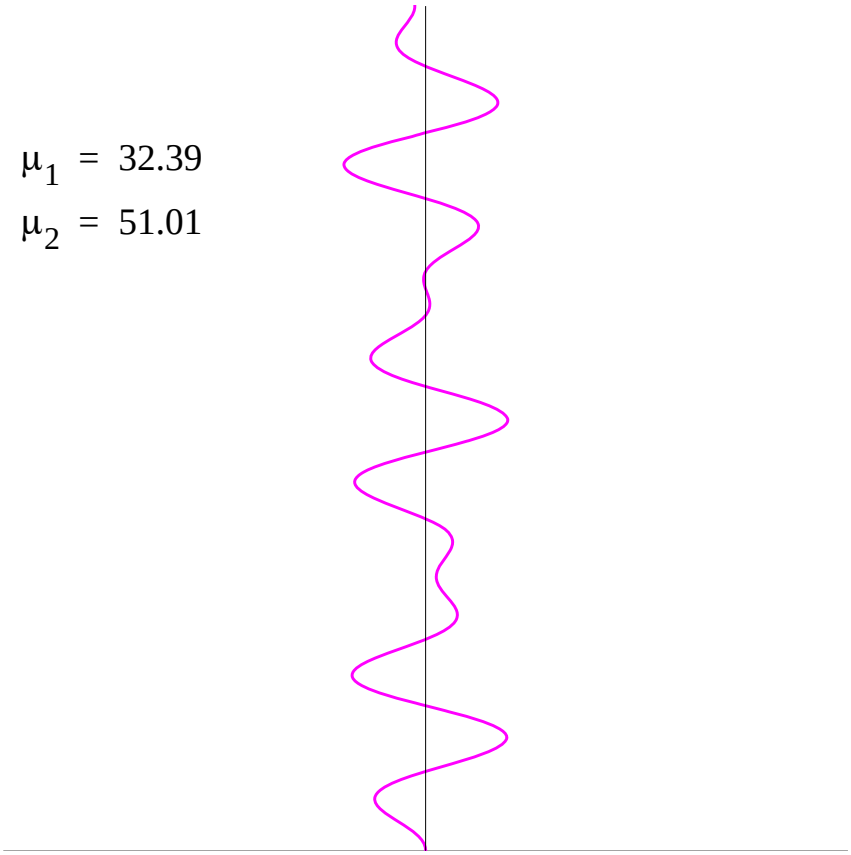

Figure C.29 Analytic linear elastic buckling eigenmode-6: Λ_{LBA} = 1.1050, Fix-RotFix

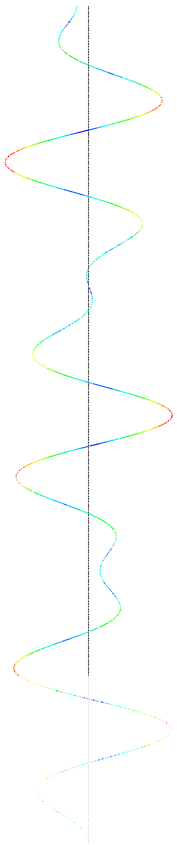

Figure C.30 FEM linear elastic buckling eigenmode-6: Λ_{LBA} = 1.1038, Fix-RotFix

C.9 Summary and conclusion

The axisymmetric elastic buckling behavior and strength of axially compressed cylindrical shells exihibts a direct analogy to a one-dimensional beam on elastic foundation. For this structural system the general solution for deformations and section forces has been obtained analytically. These analytical results have been compared with the corresponding results obtained from small displacement linear buckling numerical analysis. A perfect match between the buckling eigenmodes and the buckling strengths has been obtained (the differences in buckling strengths being insignificant).

Approximate plastic buckling analysis based on elastic-second-order analysis

On the other hand, the beam-on-elastic-foundation model of a cylindrical shell has been used to analytically compute the geometric and material nonlinear effects of a cylindrical shell using a combination of the theory-of-second-order and the stress-resultant-oriented approximate Ilyushin yield criteria. The elastic-plastic buckling loads, Figure 3.47 to Figure 3.52, were computed in an inherently iterative manner. Once the second order effect due to axial compression is considered in the force equilibrium equation (in the transverse direction), a trial load factor has been applied with which the section force distributions along the meridian were computed. Using these section forces (stress resultants), a check has been made for possible yield at each point along the meridian using one of the approximate yield criteria discussed. When the yield criterion is not fulfilled with the trial load factor, another trial load factor has been applied depending on the result obtained, i.e. if the yield surface defined by the approximate yield function is exceeded, a smaller load factor has been applied; if the result lies within the yield surface, a larger load factor has been applied. This procedure has been repeatedly used until the yield criterion was exactly fulfilled. Thus the fulfilment of the plastic yield criterion, when combined with the theory of second order, represents an approximate elastic-plastic buckling condition. This procedure in shells corresponds directly to the well-known second-order plastic-hinge approach in beams. Comparison of these analytic approximate results with those results obtained using the geometrically and materially nonlinear numerical analysis have been discussed in Chapter 3.7.